Secondary loss reduction in rotor blades by non-axisymmetric end-wall profiling.

Hartland, Jonathan

Secondary Loss Reduction in Rotor Blades by Non-Axisymmetric End-Wall Profiling

Jonathan Hartland

A Thesis submitted in partial fulfilment of the requirements for the degree of Doctor of Philosophy

School of Engineering

University of Durham

2001

The right of Jonathan Hartland to be identified as the author of this work has been asserted by him in accordance with the Copyright Designs and Patents Act 1988.

Declaration.

The work contained in this thesis has not been submitted elsewhere for any other degree or qualification, and unless otherwise referenced is the authors own work.

Acknowledgements.

The author is grateful to Dr David Gregory-Smith in his role as supervisor. His encouragement, guidance and patience have been invaluable during the course of this work.

The assistance of Gary Parker with the assembly of the cascade must also be recognised. The help of Jim Swift, Milos Kolar and Alan Swan with the setting up of the CNC machine and subsequent manufacture of end-wall segments is also acknowledged, and the assistance of all of the workshop staff must also be recognised. Also the assistance of all of the staff in the School of Engineering must be acknowledged.

Special thanks must be made to Dr Martin Rose, Dr Neil Harvey and Andrew Smith at Rolls Royce plc for their assistance with this work and the running of the CFD code.

Finally, the financial support of Rolls Royce plc, DERA and EPSRC is acknowledged.

In memory of Tom Spicer-Wilson.

Secondary Loss Reduction in Rotor Blades by Non-Axisymmetric End-Wall Profiling

Jonathan Hartland.

Abstract

The work presented in this thesis comprises an investigation into the design of end-wall profiles for secondary loss reduction. The investigation was carried out in the Durham Linear Cascade, a large scale, low speed linear cascade of high turning blades typical of a high pressure turbine rotor blade passage.

A system for manufacturing end-walls has been developed using high density polyurethane foam, and the existing planar wall flow measurements in the cascade were repeated to ensure that effects of surface roughness of the machined end-walls were accounted for.

CFD design studies have been carried out to investigate a number of profiles using CFDS, and selected profiles have been manufactured and tested within the Cascade. Measurements of end-wall static pressures are made using an end wall segment fitted with pressure tappings, and the cascade flow-field has been investigated at a number of axial traverse planes using a 5-hole probe. Simple flow visualisation has been carried out by injecting an oil/dye mixture through selected end-wall pressure tappings.

The first of these studies was to redesign the profile proposed by Rose [1994] for use within the Durham cascade. The resulting profile was manufactured and tested. The aim of this profile is to reduce rim-seal leakage by reducing end-wall pressure non-uniformities at the rim-seal location. The profile achieved a 60% reduction in RMS pressure at the assumed rim seal location used in the design procedure. The CFD predictions of pressure agree very well with the experimental data, as do the flow predictions. The loss predictions are not as accurate and only trends are predicted.

The second study was to design an end-wall profile to reduce secondary flow using the FAITH design code. This profile was also manufactured and tested. Again, the flow was predicted well with the CFD predicting a 49% reduction in secondary kinetic energy, with the experimental investigation showing a 48% reduction. The CFD under-predicts the changes in end-wall pressure, and the loss predictions are again poor with only trends being correctly predicted.

The third study involved a CFD only investigation of three profiles for secondary flow reduction. The best of these achieved a predicted 61% reduction in secondary kinetic energy, which could be assumed to be accurate, and a 6% reduction in secondary loss, which cannot be relied upon as accurate.

A system of boundary layer intermittency measurement using surface mounted hot film gauges was also developed, and measurements were made within the cascade. The suction surface and end-wall intermittencies agree well with previous work of Moore [1995] in this cascade. Flow features such as the interaction between passage vortex and suction surface, and the growth of a new laminar end-wall boundary layer, both seen in Moore's data were also captured by the hot film measurements. However the results of the hot film measurements along the pressure surface were poor, and the reason for this was attributed to the method of gauge attachment.

Contents.

1 Introduction 1

2 Literature Review 4

2.1 Secondary Flow 5

2.1.1 Secondary Flow Structure 5

2.1.2 Secondary Loss Generation 7

2.1.3 Secondary Loss Prediction 8

2.2 Secondary Flow Reduction 10

2.2.1 General Methods 10

2.2.2 End-wall Profiling 11

2.3 Hot Film Gauges and Intermittency Measurement 13

3 Intermittency Measurements 18

3.1 Introduction 18

3.2 Measurement Technique and Data Processing 19

3.2.1 Probe Calibration 19

3.2.2 Measurement Technique 20

3.3 Discussion of Experimental Results 22

3.4 Conclusions 24

4 Measurement Techniques, Data Processing and End-Wall Manufacture 30

4.1 Introduction 30

4.2 The Durham Cascade 30

4.3 Measurement Technique 32

4.3.1 End-wall Pressure Measurement 32

4.3.2 Area Traverses 33

4.4 End-Wall Profile Manufacture 37

5 Repeat of Datum Case 46

5.1 Introduction 46

5.2 The CFD Code 47

5.3 CFD Results 48

5.3.1 Blade and End-Wall C_P Values 48

5.3.2 Area and Pitch Averaged Results 48

5.3.3 Contour Maps and Secondary Velocity Vectors 49

5.4 Experimental Results 50

5.4.1 End-Wall Cp Values 50

5.4.2 Area and Pitch Averaged Results 50

5.4.3 Contour Maps and Secondary Velocity Vectors 53

5.5 Conclusions 54
6 Reduction of Circumferential Pressure Non-uniformities at Exit from the Cascade 75
6.1 Introduction 75
6.2 CFD Design 76
6.3 CFD Results 80
6.3.1 End-Wall Height and Cp Values 80
6.3.2 Area and Pitch Averaged Results 80
6.3.3 Contour Maps and Secondary Velocity Vectors 81
6.4 Experimental Results 83
6.4.1 End-Wall Cp Values 83
6.4.2 Area and Pitch Averaged Results 83
6.4.3 Contour Maps and Secondary Velocity Vectors 84
6.4.4 Flow Visualisation 85
6.5 Discussion 86
6.5.1 C_{SKE} Compensation for End-Wall Slope 86
6.6 Conclusions 88
7 End-wall Profiling to Reduce Secondary Loss 119
7.1 Introduction 119
7.2 Design Philosophy and FAITH Design Code 120
7.3 CFD Results 122
7.3.1 End-Wall Height and Cp Values 122
7.3.2 Area and Pitch Averaged Results 123
7.3.3 Contour Maps and Secondary Velocity Vectors 125
7.3.4 Compensated C_{SKE} 126
7.4 Experimental Results 127
7.4.1 End-Wall Cp Values 127
7.4.2 Area and Pitch Averaged Results 127
7.4.3 Contour Maps and Secondary Velocity Vectors 130
7.4.4 Compensated C_{SKE} 131
7.4.5 Flow Visualisation 131
7.5 Conclusions 132
8 Alternative End-wall Design Method 160
8.1 Axial Mean Profile Design Philosophy 160
8.2 Axial Mean Profile Design Philosophy 161
8.3 Discussion of Results 163
8.3.1 End-wall Cp Contours 163
8.3.2 Area and Pitch Averaged Results 163
8.3.3 Contour Maps and Secondary Velocity Vectors 165
8.4 Conclusions 167

9 Overall Conclusions and Future Work 176
9.1 Conclusions 176
9.1.1 Intermittency Measurements 176
9.1.2 End-wall Profile Manufacture 177
9.1.3 Repeat of Datum Case 177
9.1.4 Reduction of Circumferential Pressure Non-uniformities at Exit from the Cascade 178
9.1.5 End-wall Profiling to Reduce Secondary Loss 178
9.1.6 Alternative End-wall Design Method 178
9.2 Future Work 180
9.2.1 Intermittency Measurements 180
9.2.2 Reduction of Circumferential Pressure Non-uniformities at Exit from the Cascade 180
9.2.3 End-wall Profiling to Reduce Secondary Loss 181
9.2.4 Alternative End-wall Design Method 181

Appendix A 182
Appendix B 185
References/Bibliography 191

Figures.

2.1 General Secondary Flow Structure 15
2.2 Contraction Shape (after Diech[1960]) 16
2.3 Optimum Contraction Ratio (after Diech[1960]) 17
3.1 Calibration Curve Assuming Different Exponents 25
3.2 Fluctuating Suction Surface Shear Stress Traces 100mm From the End-Wall 26
3.3 Probability Density Functions 100mm From the End-wall 27
3.4 End-wall Measurement Locations 28
3.5 Suction Surface Intermittency Contours 29
3.6 End-wall Intermittency Contours 29
4.1 Layout of the Durham Linear Cascade 40
4.2 Planar End-Wall Pressure Tappings 41
4.4 FAITH End-Wall Pressure Tappings 41
4.3 Profile3 End-Wall Pressure Tappings 41
4.5 Cobra Type Probe 41
4.6 Flow Diagram of the Processing Algorithm 42
4.7 Typical Calibration Map 43
4.8 Iterative Algorithm used to Calculate Flow Angles 44
4.9 Inlet Total Pressure Non-uniformity at the Reference Probe Location 45
4.10 Variable Convention for Equations 4.13 to 4.20 45
5.1 Coarse CFD Grid 55
5.2 End-wall Cp Contours for both CFD Grids 56
5.3 CFD Blade Cp Plots for the Fine Grid 57
5.4 Pitch Averaged CFD Data at Slot 1 (Both Grids Shown) 58
5.5 Pitch Averaged CFD Data at Slot 6 (Both Grids Shown) 59
5.6 Pitch Averaged CFD Data at Slot 8 (Both Grids Shown) 60
5.7 Pitch Averaged CFD Data at Slot 10 (Both Grids Shown) 61
5.8 Fine Grid CFD Data at Slot 1 62
5.9 Fine Grid CFD Data at Slot 6 62
5.10 Fine Grid CFD Data at Slot 8 63
5.11 Fine Grid CFD Data at Slot 10 63
5.12 Coarse Grid CFD Data at Slot 10 64
5.13 Experimental and Fine Grid CFD End-wall C_p Contours 65
5.14 Measured Total Pressure Coefficient 100% C_{ax} Upstream 66
5.15 Pitch Averaged Experimental and CFD Data at Slot 1 (Both Grids Shown) 67
5.16 Pitch Averaged Experimental and CFD Data at Slot 6 (Both Grids Shown) 68

5.17 Pitch Averaged Experimental and CFD Data at Slot 8 (Both Grids Shown) 69
5.18 Pitch Averaged Experimental and CFD Data at Slot 10 (Both Grids Shown) 70
5.19 Comparison of Data with Previous Research 71
5.20 Growth of Secondary Kinetic Energy Through the Cascade 72
5.21 Experimental Data at Slot 1 73
5.22 Experimental Data at Slot 6 73
5.23 Experimental Data at Slot 8 74
5.24 Experimental Data at Slot 10 74
6.1 Schematic Pressure Field Downstream of a Blade Row 89
6.2 Schematic View of the Axial Shape of the Profile 89
6.3 Non-Dimensional Pressure at Platform Trailing Edge (Coarse Grid CFD) 90
6.4 Change in Non-Dimensional Pressure at Platform Trailing Edge (Profile1 - Planar) 91
6.6 Change in Non-Dimensional Pressure at Platform Trailing Edge (Profile3 - Planar) 91
6.5 Change in Non-Dimensional Pressure at Platform Trailing Edge (Profile2 - Planar) 91
6.7 Designed Non-Dimensional Pressure at Platform Trailing Edge (Coarse Grid CFD) 91
6.8 End-wall Pressure Coefficients (Coarse Grid CFD) 92
6.9 Change in End-wall Pressure Coefficient (Profile 3 - Planar) and End-wall Height (Profile 3) 93
6.10 CFD Non-Dimensional Pressures at Platform Trailing Edge 94
6.11 End-wall Pressure Coefficients (Fine Grid CFD) 95
6.12 CFD Blade Cp Plots for Profile 3 and the Planar End-wall 96
6.13 Pitch Averaged CFD Data at Slot 1 97
6.14 Pitch Averaged CFD Data at Slot 6 98
6.15 Pitch Averaged CFD Data at Slot 8 99
6.16 Pitch Averaged CFD Data at Slot 10 100
6.17 CFD Data at Slot 1 101
6.18 CFD Data at Slot 6 102
6.19 CFD Data at Slot 8 103
6.20 CFD Data at Slot 10 104
6.21 Experimental End-wall Pressure Coefficients 105
6.22 Experimental Non-Dimensional Pressures at Platform Trailing Edge 106
6.23 Measured Total Pressure Coefficient 100% C_{ax} Upstream 106
6.24 Pitch Averaged Experimental Data at Slot 1 107
6.25 Pitch Averaged Experimental Data at Slot 6 108
6.26 Pitch Averaged Experimental Data at Slot 8 109

6.27 Pitch Averaged Experimental Data at Slot 10 110
6.28 Growth of C_{SKE} Through the Cascade 111
6.29 Experimental Data at Slot 1 112
6.30 Experimental Data at Slot 6 113
6.31 Experimental Data at Slot 8 114
6.32 Experimental Data at Slot 10 115
6.33 End-wall Flow Visualisation 116
6.34 Compensated CFD C_{SKE} Throughout the Cascade (Uncompensated and Planar Data Included for Comparison) 117
6.35 Compensated Experimental C_{SKE} Throughout the Cascade (Uncompensated and Planar Data Included for Comparison) 118
7.1 Wind Tunnel Modifications to Allow Large End-wall Segments to be Mounted 133
7.2 CFD End-wall Pressure Distributions with Compound Blade Lean 134
7.3 Pitch Averaged CFD Data for Compound Leant Blades at Slot 10 135
7.4 Contours of End-wall Height and CFD C_p Values 136
7.5 CFD Blade Cp Plots for the FAITH profile 137
7.6 Pitch Averaged CFD Data at Slot 1 (Planar Wall Included for Comparison) 138
7.7 Pitch Averaged CFD Data at Slot 6 (Planar Wall Included for Comparison) 139
7.8 Pitch Averaged CFD Data at Slot 8 (Planar Wall Included for Comparison) 140
7.9 Pitch Averaged CFD Data at Slot 10 (Planar Wall Included for Comparison) 141
7.10 CFD Data at Slot 1 142
7.11 CFD Data at Slot 6 143
7.12 CFD Data at Slot 8 144
7.13 CFD Data at Slot 10 145
7.14 Pitch Averaged Compensated CFD C_{SKE} Through the Cascade 146
7.15 Experimental End-wall C_p Contours 147
7.16 Measured Total Pressure Coefficient 100% C_{ax} Upstream 148
7.17 Pitch Averaged Experimental Data at Slot 1 (Planar Wall and CFD Data Included for Comparison) 149
7.18 Pitch Averaged Experimental Data at Slot 6 (Planar Wall and CFD Data Included for Comparison) 150
7.19 Pitch Averaged Experimental Data at Slot 8 (Planar Wall and CFD Data Included for Comparison) 151
7.20 Pitch Averaged Experimental Data at Slot 10 (Planar Wall and CFD Data Included for Comparison) 152
7.21 Growth of C_{SKE} Through the Cascade 153
7.22 Experimental Data at Slot 1 154
7.23 Experimental Data at Slot 6 155
7.24 Experimental Data at Slot 8 156

7.25 Experimental Data at Slot 10 157
7.26 Pitch Averaged Compensated Experimental C_{SKE} Through the Cascade 158
7.27 End-wall Flow Visualisation 159
8.1 Modification of the Blade Mean Line 168
8.2 Axial Component of Profile AXM2 168
8.3 Contours of Profile Height (mm) 169
8.4 CFD End-wall Pressure Coefficients for the AXM, AXM2, AXMe Profiles and the Planar Wall 170/71
8.5 Pitch Averaged CFD Data at Slot 10 for AXM, AXM2, AXMe and Planar End-walls 172
8.6 Pitch Averaged CFD Data at Slot 10 for FAITH, AXMe and Planar End-walls 173
8.7 CFD Data at Slot 10 174/5

Tables.

3.1 Co-ordinates on the Blade Suction Surface 21
4.1 Cascade Design Details 31
4.2 Inlet Conditions to the Cascade 31
4.3 Measurement Slot Locations 31
4.4 Data File Control Codes 37
5.1 Area Averaged CFD Data Through the Cascade 49
5.2 Net CFD Losses Through the Cascade 49
5.3 Area Averaged Experimental Data Through the Cascade 51
5.4 Net Experimental Losses Through the Cascade 51
6.1 Changes in Profile and Flow Parameters 78
6.2 Area Averaged Values for the Profile 3 CFD 81
6.3 Area Averaged Values for the Planar Wall CFD 81
6.4 Net Area Averaged C_{Po} at Slot 10 for Planar and Profile 3 CFD 81
6.5 Area Averaged Experimental Values for the Profile 3 Wall 84
6.6 Area Averaged Experimental Values for the Planar Wall 84
6.7 Net Area Averaged Experimental C_{Po} for the Planar and Profile 3 Walls at Slot 10 84
7.1 Area Averaged Values for the FAITH Profiled Wall CFD 124
7.2 Area Averaged Values for the Planar Wall CFD 124
7.3 Net Area Averaged C_{Po} at Slot 10 for Planar and FAITH Profiled Wall CFD 124
7.4 Area Averaged Experimental Values for the FAITH Profiled Wall 128
7.5 Area Averaged Experimental Values for the Planar Wall 128
7.6 Net Area Averaged Experimental C_{Po} for the Planar and FAITH Profiled Walls at Slot 10 129
8.1 Area Averaged CFD Data At Slot 10. 164

Nomenclature.

A	Constant
B	Constant
C_{ax}	Axial Chord
C_L	Lift Coefficient
C_P	Static Pressure Coefficient
C_{Po}	Total Pressure Coefficient
C_{Pt}	Rim Seal Location Local Static Pressure Coefficient
C_{SKE}	Secondary Kinetic Energy Coefficient
C_{total}, C_{static}	5-Hole Probe Pressure Coefficients (also C_t, C_s)
C_{yaw}, C_{pitch}	5-Hole Probe Flow Angle Coefficients (also C_y, C_p)
c	Blade Chord
E	Voltage supplied to Wheatstone Bridge
E_0	Voltage supplied to Wheatstone Bridge with no Flow
h	Blade Span
k	Constant
P	Static Pressure
Po	Total Pressure
Q_w	Heat Flux from Hot Film Gauge
Re_x	Reynolds Number Based on Distance Along a Plate
δr	Profile Height w.r.t Rose Profile
s	Blade Pitch
ΔT_0	Temperature Difference between Flow and Hot Film Gauge
t	Time
U	Mean Flow Velocity
u	Fluctuating flow velocity
Y	Total Pressure Loss Coefficient (Ainley & Mathieson)

y_{mean}	Blade Mean Line
Z	Loading Parameter (Ainley & Mathieson)
z	Axial Co-ordinate in Polar Co-ordinate Systems
z	Profile Height in Cartesian Co-ordinate Systems
α	Pitch Angle
α_1	Inlet Yaw Angle (Ainley & Mathieson)
α_2	Exit Yaw Angle (Ainley & Mathieson)
α_m	Mean Yaw Angle (Ainley & Mathieson)
β	Yaw Angle
β_1	Inlet Pitch Angle (Ainley & Mathieson)
δ^*	Boundary Layer Displacement Thickness
λ	Area Parameter (Ainley & Mathieson)
μ_T	Turbulent Viscosity
ρ	Air Density
τ_w	Wall Shear Stress

Subscripts

1	Axial
2	Spanwise
3	Pitchwise
inlet	One Axial Chord Upstream
inv	Inviscid
le	Leading Edge Axial Plane
m	Maximum
mid	Mid-Span
pte	Assumed Rim Seal Axial Location
∞	Free-Stream

1 Introduction.

The fuel costs for a Boeing 747 amount to approximately $22,000,000 per year and so, in a competitive market, the efficiency of gas turbines is of great importance. With the costs of fuel set to rise, methods of designing yet more efficient turbines continue to be essential.

The pressures within a turbine blade row propagate downstream of the trailing edges of the blades and interact with the rim seal between the stator and rotor. To prevent ingestion of hot gas into the hub and casing, the coolant flow must be pressurised to the maximum pressure over the rim seal. As the pressure over the rim seal is non-uniform due to the propagation of the blade pressures, coolant flow leaks into the turbine. Between 15% and 23% of the core mass flow is used as coolant and, as each rim seal looses about 0.5%, rim seal leakage may represent 0.1% of efficiency, or $22,000 per year for the 747.

When the end-wall boundary layer entering a blade row is turned, it is subject to a pressure gradient generated across the blade passage. The mid-span pressure gradient is imposed on the low momentum flow in the boundary layer, resulting in overturning of the flow. This flow rolls up into a passage vortex. Losses arise due to the spanwise migration of low momentum fluid from the boundary layer towards mid-span, the growth of a new boundary layer on the end-wall behind the passage vortex and interactions between the passage vortex and the end-wall and blade suction surface. The loss arising from this secondary flow can contribute to half of the total loss in a modern high-pressure turbine. This flow structure also has a detrimental effect on the following blade row as the passage vortex results in a non-uniform spanwise exit angle and relative motion of the rotating and stationary blades results in periodically unsteady inlet flow. It is therefore important to investigate methods of reducing secondary flows and loss. End-wall profiling is one such method, and previous researchers (Diech et al [1960], Kopper & Milano[1975]) achieved a reduction in loss. Some researchers (Ewen [1973], Haas [1982]) carried out tests in rotating model turbines and attributed the efficiency rise to improved flow at inlet to the rotor.

As mentioned above, losses also arise due to the growth of the new boundary layer behind the passage vortex. The understanding of this boundary layer is still limited, and CFD modelling usually ignores its laminar nature, restricting the capacity to model loss generation accurately (Moore [1996])

This research addresses these three aspects of loss generation within a turbine. Experimental investigations have been carried out into boundary layer state measurements and CFD and experimental investigations into the design of non-axisymmetric end-wall profiles to reduce secondary flows and end-wall pressure non-uniformities at the rim seal location have been carried out. The Work has been supported by Rolls Royce plc and DERA.

This thesis covers work carried out from 1995 to 1998, and a brief overview of the contents follows.

A literature review has been carried out covering secondary flows and reduction methods, concentrating on end-wall profiling. methods of boundary layer state detection were also briefly investigated. The results of the literature are presented in Chapter 2.

A method of boundary layer state detection using surface mounted hot film gauges has been developed, and measurements on the cascade end-wall and blade suction surface are presented and briefly compared with the hot wire measurements of Moore [1995] in Chapter 3.

The experimental techniques used to investigate the effects of end-wall profiling on the flow within the cascade and a brief overview of the CFD code are presented in Chapter 4. A description of the end-wall profile manufacturing system developed to allow easy manufacture of arbitrary three dimensional surfaces is also presented here.

The datum case (planar end-wall) measurements were repeated due to the repositioning of the reference probe and uncertainties over the effect of the surface roughness of the machined end-walls on the flow. The results of this repeat datum case are presented in Chapter 5 along

with CFD data for comparison with both the experimental planar case and CFD designs in later chapters.

The profile proposed by Rose [1994] has been redesigned for the Durham linear cascade, and the design method and CFD results are presented in Chapter 6. The redesigned profile was manufactured as described in Chapter 4 and tested in the cascade. End-wall pressures were measured to verify the CFD design and flow field measurements were taken to investigate the effect of the profile on the cascade flow.

An end-wall profile was then designed with the sole purpose of reducing the secondary flow within the cascade. The profile was designed using the Rolls Royce FAITH design code, and results of CFD calculations, flow-field measurements and end-wall pressure measurements are presented and discussed in Chapter 7. A brief overview of the FAITH design code is also given here.

A further three non-axisymmetric profiles were designed in Durham with the aim of reducing the secondary flows and losses within the cascade. The results of the CFD design calculations for these profiles are presented and discussed in Chapter 8.

The conclusions drawn in Chapter 3 and Chapters 5 to 8 are summarised in Chapter 9, along with some additional general conclusions. Suggestions for further work arising from these conclusions are also made here.

2 Literature Review.

The three dimensionality of turbomachinery flows has been accepted for some time. However, it has only recently been practical to engage in fully three dimensional design of turbomachines. The effects of sweep, dihedral and curved blades have been studied, as have boundary layer fences, and other devices. One method that can be employed is end-wall profiling. Suggestions have been made, and different geometries have been proposed, but most appear to have been limited to a single blade profile, or based on design rules produced from early work in the 1960's. Much work has been done based on the original design of Diech et al [1960, 1965], but few researchers have gone further than to verify this simple correlation. A literature review has been carried out on this subject and the findings are summarised below.

2.1 Secondary Flow.

Secondary flows are of great importance to the performance of turbomachines, especially those with low aspect ratios where the secondary losses can be the most significant loss mechanism. The secondary flow structure both convects low momentum fluid from the boundary layers into the free stream and causes radial non-uniformities in the blade row exit flow angle, both of which may have a detrimental effect on the performance of the following blade row. Not only do secondary flows introduce radial variations in the exit flow, but also result in pitchwise periodic variations which, in a rotating frame of reference create unsteady loading on the downstream blades.

Turbomachinery secondary flow has been studied in detail by a number of authors over the past 20 years [eg, Marchal & Sieverding, 1977. Tall, 1977. Langston & Boyle, 1982. Moustapha et al, 1985 Harrison, 1989. Joslyn & Dring, 1992. Denton, 1993.]. In 1985, Sieverding carried out a comprehensive review of the existing work at that time, when the main aspects of the secondary flow were fairly well understood. Denton also reviewed the current knowledge of losses in Turbomachinery in 1993. The main aspects of the secondary flow are briefly described below and can be seen in Figure 2.1 [Klein 1966. Langston 1976. reproduced from Sieverding, 1985].

2.1.1 Secondary Flow Structure.

As fluid is turned through the blade channel, a cross channel pressure gradient is set up. The pressure gradient resulting from the essentially 2 dimensional mid-span flow (Primary Flow) is imposed on the low momentum fluid in the end-wall boundary layer, causing over-turning of the flow near the end-wall, resulting in migration from the pressure surface to the suction surface. When this boundary layer fluid reaches the suction surface, it moves radially away from the end-wall along the blade surface. New fluid moves radially towards the end-wall to replace the old boundary layer, and a large vortex structure is formed against the suction surface, although it can occupy almost the whole blade passage. This is known as the passage vortex. The new boundary layer that forms on the end-wall is very thin, highly skewed, and is mainly laminar up

boundary layer which causes the secondary flow is a viscous phenomenon, the resulting passage vortex is an inviscid phenomenon, although viscous effects can play a part in the dissipation and movement of the passage vortex [Moore & Gregory-Smith, 1996].

When the end-wall boundary layer upstream of the blade row meets the blade leading edge, it rolls up to form a horseshoe vortex. This consists of two legs which flow around both sides of the leading edge of the blade. The pressure surface leg of the horseshoe vortex quickly moves away from blade pressure surface and migrates across the end-wall where it is believed to merge with the passage vortex [Langston, 1977]. This theory was verified using smoke and surface flow visualisation [Marchal & Sieverding, 1977]. The suction side leg of the horseshoe vortex is convected up the blade suction surface by the passage vortex and is still visible downstream of the blade row [Sieverding & Van Den Bosche, 1983. Moore & Smith 1983]

A small counter vortex can form in the end-wall / suction surface corner. The counter vortex is detectable by a small reduction in the overturning of the flow close to the end-wall [Gregory-Smith & Graves, 1983], and end-wall flow visualisation.

Trailing vorticity is also detectable behind the blade trailing edge, rotating in the opposite sense to the passage vortex [Armstrong, 1955], and stems from two sources [Sieverding 1985]. The first being trailing filament vortices, which arise due to the stretching of the inlet vortex filaments when passing through the cascade with different velocities between suction side and pressure side. The second being trailing shed vorticity, which is due to the spanwise change of the blade circulation. This vorticity would eventually mix out, but it is believed that by the time the next blade row is reached, this will not happen.

2.1.2 Secondary Loss Generation.

Sieverding [1985] summarised the main factors contributing to loss in a blade passage. These are as follows.

a) The natural increase of the inlet boundary layer up to the separation lines of the horseshoe vortex.

b) A stagnant separation bubble in the leading edge region between the two separation lines.

c) Growth of a new boundary layer behind the separation line defining the pressure side leg of the horseshoe vortex and passage vortex.

d) Corner loss in the suction surface/end-wall corner, and to a lesser extent in the pressure surface/end-wall corner.

e) Shear stress effects along all three-dimensional separation lines.

f) Losses due to the shear action of the passage vortex on the blade suction surface and the mixing process between the cross-flow and the blade flow along a three-dimensional separation line on the blade suction surface towards the mid-span side of the passage vortex.

g) Dissipation of all vortices and complete mixing of the non-uniform outlet flow-field downstream of the cascade.

Denton [1993] also summarised the loss generation mechanisms in an in-depth review of turbomachinery losses. The main sources of loss outlined are viscous effects in both boundary layers and mixing processes, shock waves and heat transfer across temperature differences. Among other sources of loss considered in this review are unsteady losses caused by pitchwise non-uniformities at exit to upstream blade rows and windage and disc coolant losses. The steady sources of loss can be divided into three categories. These are, profile loss, or losses due to the two dimensional flow, secondary (or end-wall) loss, and leakage loss. However, Denton also states that these flow phenomena are highly interdependent, and cannot be easily separated, suggesting that secondary loss often includes any losses that cannot be otherwise accounted for.

2.1.3 Secondary Loss Prediction.

A number of correlations have been proposed, based on empirical data, and a brief outline of some of these follows.

In 1970, Dunham reviewed the existing loss correlations at that time and found that the loading parameter used by Ainley and Mathieson [1951], and shown in Equation 2.2, produced the best correlations. Ainley & Mathieson's secondary loss correlation for average loss non-dimensionalised by exit dynamic head is shown in Equation 2.1.

$$Y = \lambda\left(\frac{C_L}{s/c}\right)^2 \frac{\cos^2\alpha_2}{\cos^3\alpha_m} \qquad \text{Equation 2.1}$$

Where $\tan\alpha_m = \frac{1}{2}(\tan\alpha_1 + \tan\alpha_2)$, λ is a function of inlet and exit area, s and c are the pitch and chord and α_1 and α_2 are the mean inlet and exit flow angles respectively.

$$Z = \left(\frac{C_L}{s/c}\right)^2 \frac{\cos^2\alpha_2}{\cos^3\alpha_m} \qquad \text{Equation 2.2}$$

Dunham took $\lambda \propto \frac{\cos(\alpha_2)}{\cos(\beta_{1)}}$, where β_1 is the blade inlet angle, and proposed the relationship of Equation 2.3, where $f(\delta^*/c) = 0.0055 + 0.078\sqrt{\delta^*/c}$ and δ^* is the boundary layer displacement thickness.

$$Y = \frac{c}{h} Z \frac{\cos\alpha_2}{\cos\beta_1} f(\delta^*/c) \qquad \text{Equation 2.3}$$

Dunham and Came [1970] suggested $f(\delta^*/c) = 0.0334$ to overcome the problem of not knowing the boundary layer thickness. and later, Came [1973] proposed $f(\delta^*/c) = 0.008 + 0.64\sqrt{\delta^*/c}$.

Gregory-Smith [1982] proposed that the secondary losses could be divided into three components:

a) the upstream boundary layer which is shed downstream as a loss core;

b) the new skewed boundary layer on the end-wall, and

c) an "extra" secondary loss due to the (passage) vortex and its interaction with the blade and end-wall boundary layers.

The gross secondary loss is the sum of these and the net secondary loss is the sum of b and c. Gregory-Smith modelled an approximation of the passage vortex with a triangular region on the blade suction surface having the same mass flow and loss as the upstream boundary layer. The new boundary layer on the end-wall was modelled along the mid-passage line using a two dimensional calculation method, neglecting skew. The "extra" loss was assumed to be equal to the secondary kinetic energy, which in turn was calculated using the classical secondary flow theory originally described by Hawthorne [1955] and calculated using the formula of Came and Marsh [1974].

Okan and Gregory-Smith [1992,1995] used a similar approach, but tracing streamlines and the rolling up of the inlet boundary layer, hence avoiding the triangular passage vortex of Gregory-Smith[1982]

2.2 Secondary Flow Reduction.

2.2.1 General Methods.

Whilst the aim of this literature review is to concentrate on secondary loss reduction by end-wall profiling, a brief summary of alternative secondary flow reduction techniques follows.

A number of different methods of reducing secondary flow have been suggested, including dihedral or compound lean (curving of the blades) [Lewis & Hill, 1971. Breugelmans et al, 1984. Han Wanjin et al, 1994. Harrison, 1990. Wright & Simmons, 1990]. This enables a radial component of the lift generated by the blades to counter the pressure gradients driving secondary flows with successful results.

In 1990, Devenport studied the effect of fillets around and at the leading edge of an aerofoil/flat plate boundary. It was observed that whilst a leading edge fillet reduced the strength of the horseshoe vortex, fillets around the whole blade had the effect of strengthening the horseshoe vortex and pushing it away from the aerofoil.

In 1975, Sieverding published an outline of the existing secondary flow reduction methods at that time, including radially varying blade profiles, meridional wall profiling, suction and blowing in the end-wall boundary layers and sheet metal fences, or grooves to modify the end-wall boundary layer.

At the same time Topunov and Nikolaev [1975] published a similar review of secondary loss reduction methods in Russia. Methods covered include circumferentially stepped axial end-wall profiles, the addition of a small blade or fence along the middle of the blade channel, and the drilling of special orifices in the blade suction surface to reduce the risk of flow separation in the suction surface end-wall corner.

Following the work of Walsh and Gregory-Smith [1987 & 1989], Biesinger [1993] attempted to reduce secondary flows by blowing air into the boundary layer to induce a skewed inlet boundary layer. This approach showed promising results, but the trade off between the

energy needed to inject extra flow and the reduction in secondary loss achieved made this impractical.

2.2.2 End-wall Profiling.

Of the work carried out on end-wall profiling, most attention has been given to axi-symmetric profiles, based on the findings of Diech and Zaryankin [1960] who carried out extensive tests on different end-wall geometries, optimising the position of the maximum curvature and the contraction ratio. Their results indicated that the blade passage should be reduced in height using a similar profile shape to that shown in Figure 2.2 on the tip end-wall, with the maximum curvature of the beginning of the 'kink' situated just behind the position of maximum channel curvature. The optimum contraction ratio can be found from Figure 2.3. Using the optimum profile, stage efficiency could be increased by up to 3.5% at very low aspect ratios (0.2). The curvature of the end-wall reduces the velocity along the blade surface, reducing the cross channel pressure gradient by almost half at the point of maximum channel curvature, and shifting the maximum acceleration at the endwalls toward the trailing edge of the blade passage. This significantly reduces the development of secondary flow and the associated losses.

The work of Diech et al was published again in more detail in 1965 in a text book for Russian students studying turbomachinery [Diech et al, 1965].

Most other work carried out using axisymmetric profiles has resulted in a reduction in secondary loss and an increase in overall performance. The majority of researchers have attributed this to a redistribution of pressure and hence loading of the blade near the end-wall, resulting in weaker secondary flows and less radial migration of low momentum fluid from the boundary layers into the free stream. However, some researchers carrying out tests in rotating stages [Ewen, 1973. Haas, 1982. Boletis, 1985], attributed the gain to improved flow at inlet to the rotor. In all cases where detailed internal measurements were presented, the main decrease in loss has been adjacent to the unprofiled wall, with some results [Kopper & Milano, 1975. Atkins, 1987] showing an increase in loss near the profiled wall. Most results show that the adverse effects behind the profile cancel out any positive effects against the profiled wall whilst

not significantly affecting the benefits along the unprofiled wall. It is clear from the work of some [Morris & Hoare, 1975. Atkins 1987] that the interaction between the end-wall and blade profiles must be taken into account if the optimum profile is to be found, and separation is to be avoided.

In the accounts of previous work, only three [Morris & Hoare, 1975. Atkins, 1987. Rose, 1994], attempted to use three dimensional profiles. The work done by Rose[1994] aimed to reduce circumferential pressure non-uniformities to reduce disc coolant flow leakage, and as such does not take account of the secondary loss reduction potential of the profile. In this case, the mean flow was hardly affected by the profiling although the objective was achieved. Atkins[1987] tried two non-axisymmetric profiles, both based on a bump adjacent to one blade surface reducing to no profile near the opposite surface, with the intention of reducing the maximum or minimum pressure on the relevant blade surface. Both profiles resulted in an overall increase in losses due to the adverse effects on the flow near the profiled end-wall causing separation or violent twisting of the blade wake. Morris and Hoare[1975] used the same profile as their axisymmetric case, but with the profile following, and perpendicular to, the mid passage streamline. The loss decrease by the unprofiled wall was found to be greater than in the axisymmetric case, but the advantages were cancelled by the adverse effects close to the profiled wall and violent twisting of the blade wake. The increase in loss close to the profiled wall was possibly due to separation along the blade suction surface caused by the profiling being more severe. As previously mentioned, this would indicate that care must be taken to allow for interaction between the blade surface and the end-wall profile.

Of the investigations mentioned, Atkins tried to use CFD to design the profiles, optimising them before actually constructing and testing them. Horton[1984] and Rose[1994] both carried out entirely CFD investigations, however, Horton used an inviscid time marching code, where Rose used the fully viscous code CFDS used by Rolls-Royce.

2.3 Hot Film Gauges and Intermittency Measurement.

Moore and Gregory-Smith [1996] measured the intermittency in the cascade boundary layers using a hot wire probe 1mm from the surface and showed that the boundary layer state on the end-wall plays a significant role in the generation of secondary loss. Different methods of boundary layer state detection have been briefly investigated, concentrating on surface mounted hot film shear stress gauges for intermittency measurement.

Surface mounted hot film gauges are a useful, unobtrusive method of measuring surface shear stresses, and boundary layer state. Power is supplied to a Wheatstone bridge, one arm being occupied by the film gauge. If the boundary layer shear stress over the gauge increases, then so does the heat transfer and the temperature of the gauge falls momentarily. This reduces the gauge resistance and unbalances the bridge. The resulting voltage output is then fed to a servo amplifier which increases the supply voltage to the bridge, heating the gauge and keeping the resistance of the gauge constant, thus maintaining a constant temperature. By operating the gauge in this way, the effects of the thermal inertia of the gauge and mounting surface are minimised and the frequency response of the gauge can be kept to a maximum.

It is possible to prove [Bellhouse & Schultz, 1966 & 1968] that the voltage required to keep the film at a constant temperature (related to the heat flux into the boundary layer) is also related to the wall shear by Equation 2.4.

$$\tau_w^{\frac{1}{3}} = A\left(\frac{Q_w}{\Delta T_0}\right) + B \qquad \text{Equation 2.4}$$

The values of A and B can be found by measuring a boundary layer profile and calculating the wall shear directly. However, Equation 2.4 can be reduced to Equation 2.5, which requires only a one point calibration to evaluate k. In Equation 2.5, E and E_o are the voltages applied to the bridge at the calibration flow and with no flow respectively.

$$\tau_w^{\frac{1}{3}} = k\left(E^2 - E_0^2\right) \qquad \text{Equation 2.5}$$

As well as directly measuring the wall shear stresses, valuable information can be obtained qualitatively from the form of the fluctuating voltage outputs [Hodson, 1985]. As a boundary layer undergoes the final stages of transition, the flow is neither turbulent nor laminar, but changes between laminar and turbulent as turbulent bubbles are convected downstream. It is possible to measure the proportion of time during which the boundary layer is turbulent, and this is known as intermittency. A very important result gained from hot film measurements is the determination of intermittency from the form of the fluctuating voltage outputs [Schneider, 1995. Walker & Solomon, 1992. Moore & Gregory-Smith 1996].

Moore & Gregory-Smith used a the Turbulent Energy Recognition Algorithm (TERA) of Falco and Gendrich[1990] to calculate the intermittency. This attempts to amplify the fluctuating shear stress by using Equation 2.6.

$$f(u) = \frac{u\frac{du}{dt}}{\overline{U}} \qquad \text{Equation 2.6}$$

Schneider [1995] developed a method using a probability density function (PDF). This is a common statistical function, so no description of the mathematics is given here. The PDF is calculated on the probability density that the shear stress will be between predefined levels, and is based on a burst of sampled data. The PDF is plotted, and should have the distinct characteristics of a sharp high peak at the laminar shear stress and a smooth normal distribution curve over the range of turbulent fluctuations. The normal distribution curve is then integrated, ignoring the laminar peak, to give an intermittency value.

Figure 2.1 General Secondary Flow Structure (after Klein [1966] and Langston [1976])

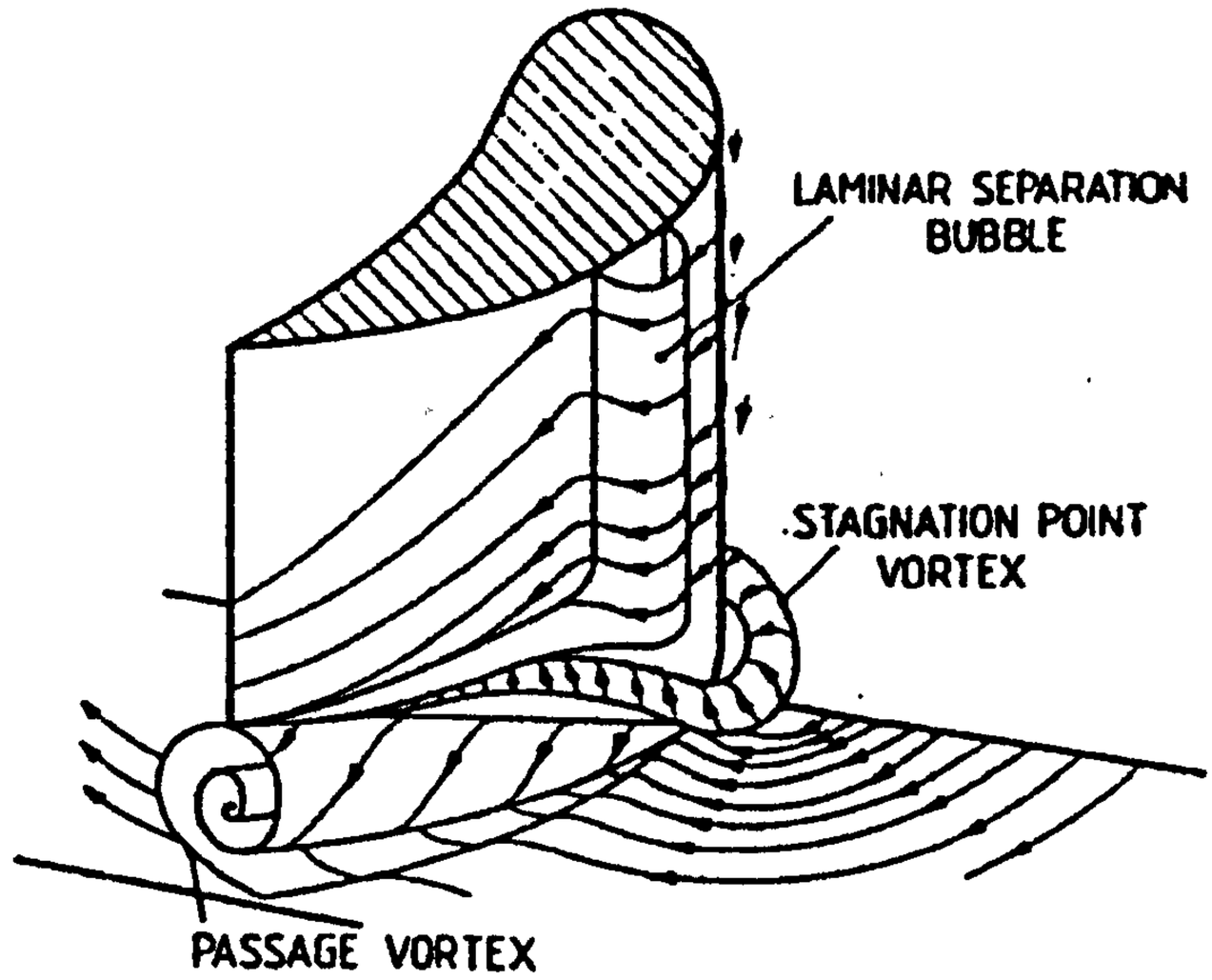

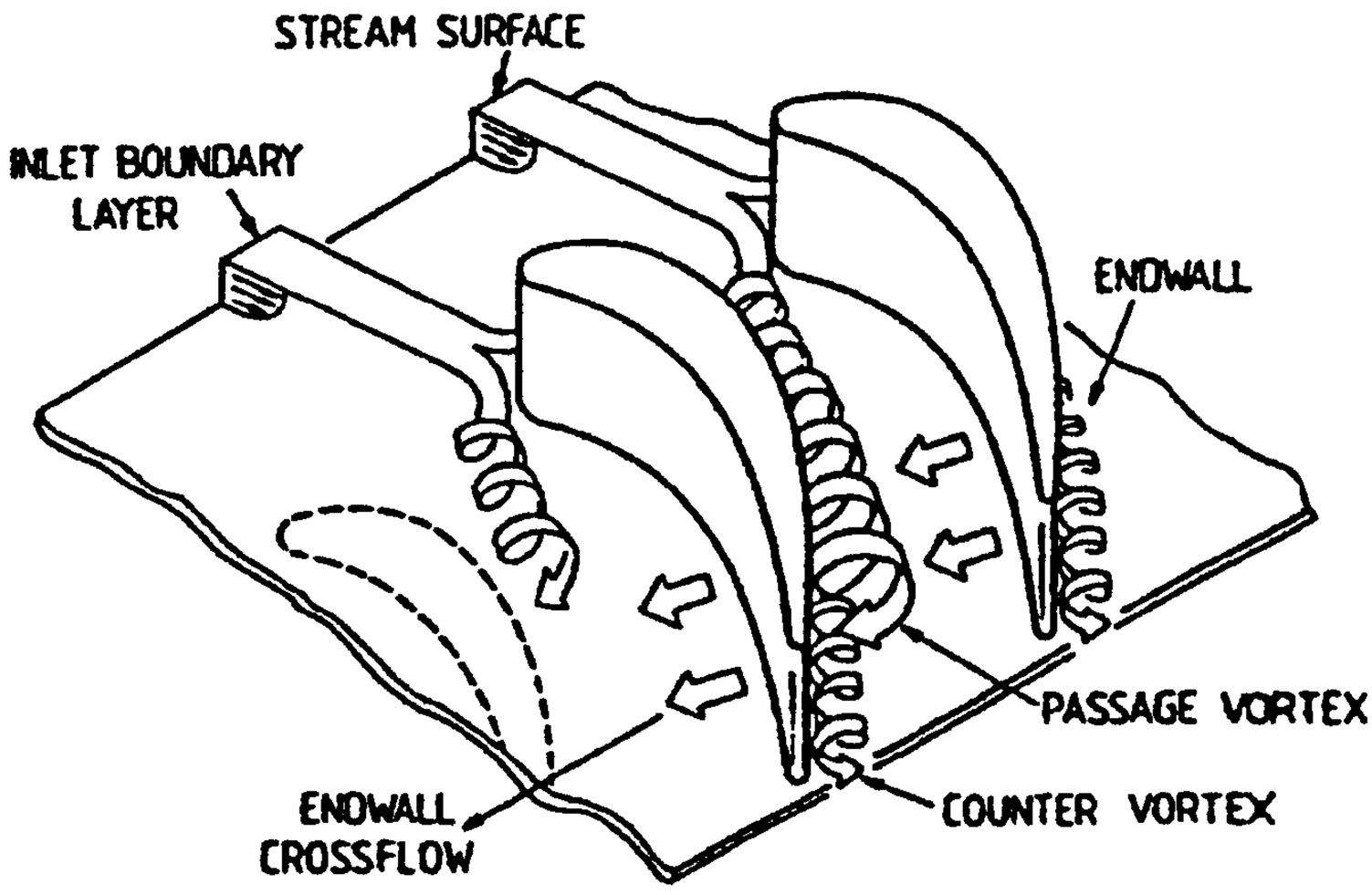

Figure 2.2 Contraction Shape (after Diech [1960])

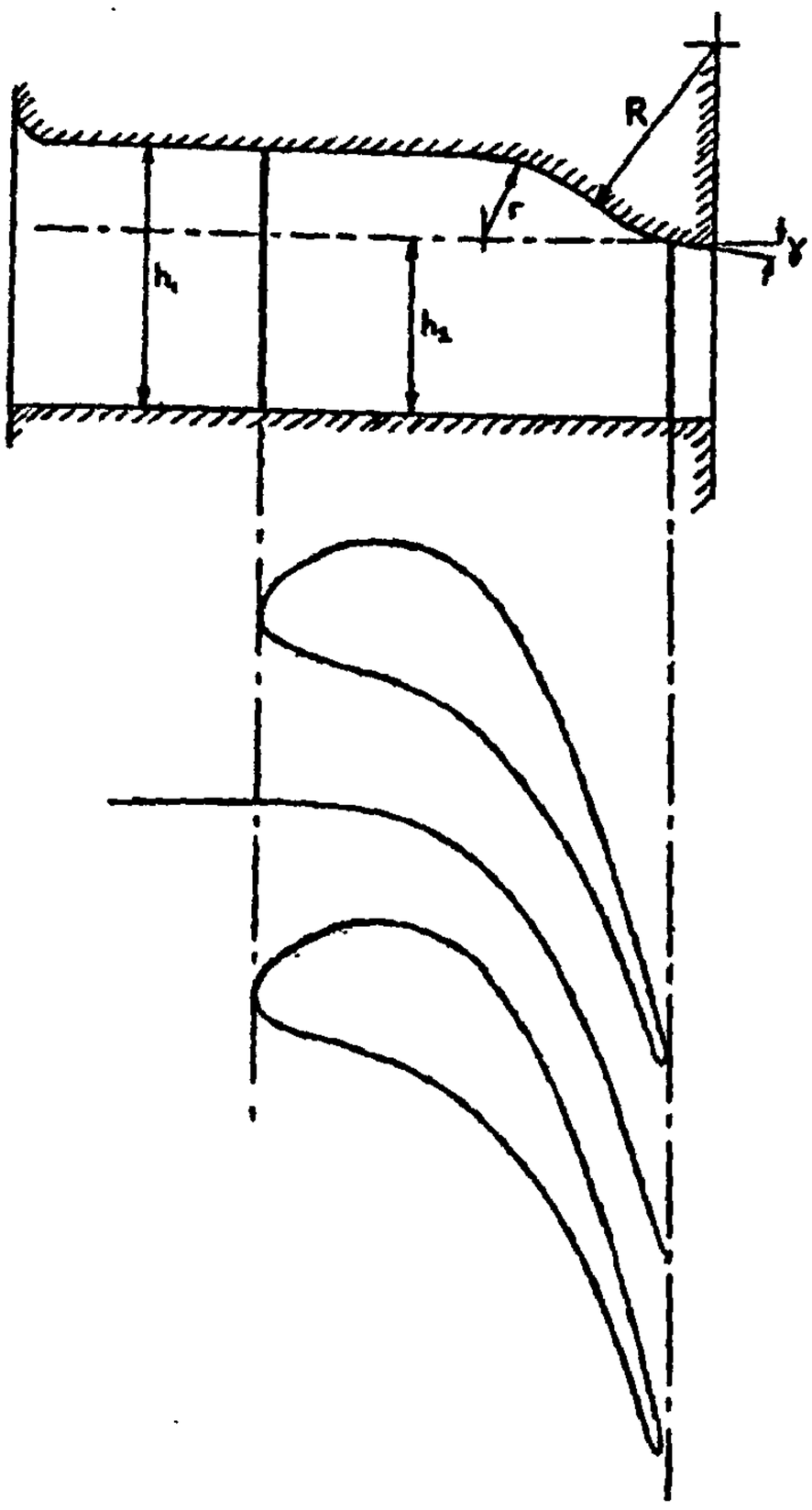

Figure 2.3 Optimum Contraction Ratio (after Diech [1960])

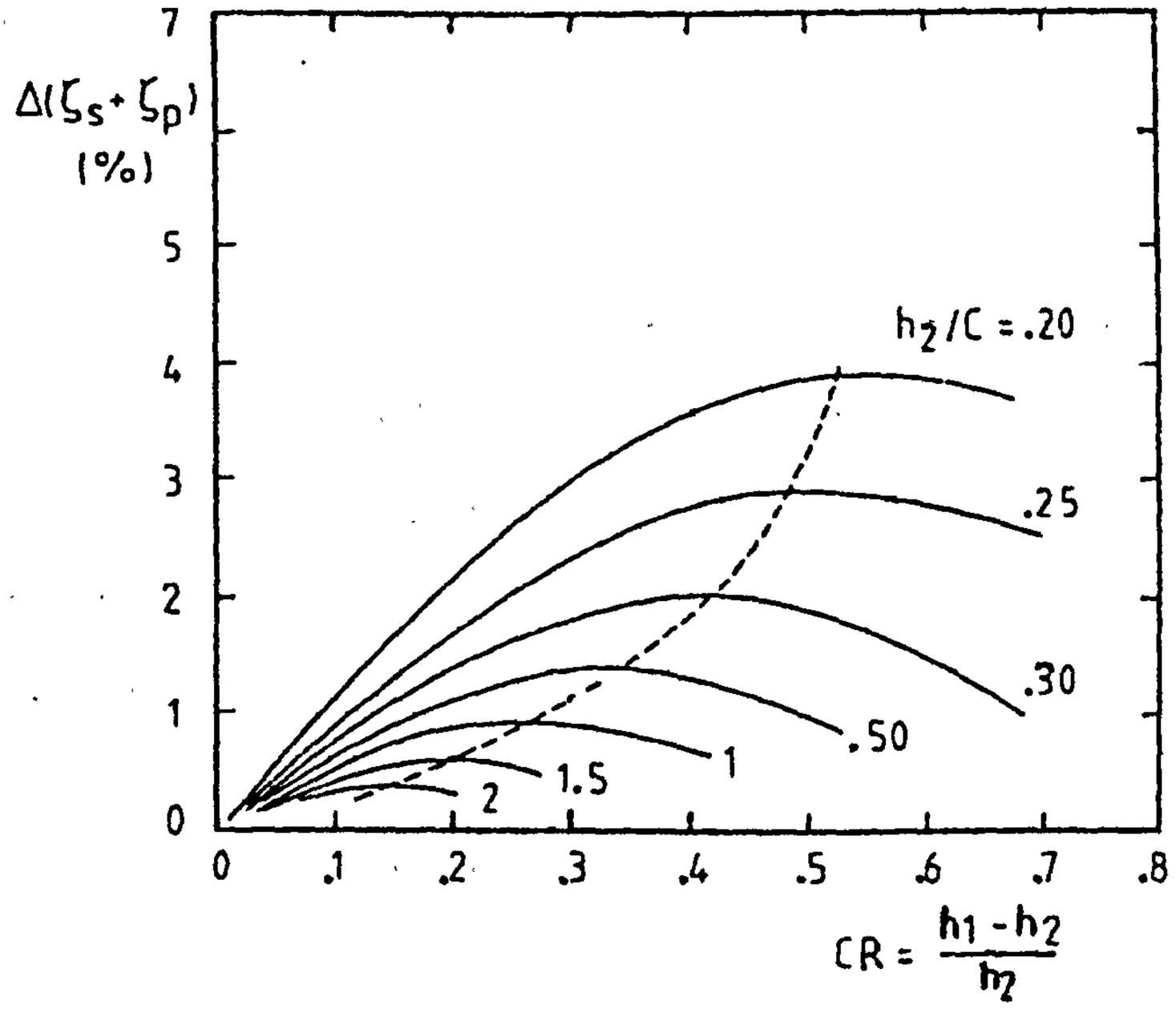

3 Intermittency Measurements.

3.1 Introduction.

As described by Sieverding [1985], the growth of a new boundary layer behind the separation line defining the pressure side leg of the horseshoe vortex and passage vortex is one of the primary contributors to loss generation within a blade row. Losses due to the shear action of the passage vortex on the blade suction surface and the mixing process between the cross-flow and the blade flow along a three-dimensional separation line on the blade suction surface towards the mid-span side of the passage vortex are also stated as a significant contributor to the loss generation. Denton [1993] also comments on the significance of viscous effects in boundary layers. It is therefore important to understand the flow in these regions.

A method of boundary layer state measurement has been developed, and measurements have been made on the blade suction surface, pressure surface and end-wall. These data add to the existing work of Moore [1995].

Different methods of boundary layer state detection were investigated, and a method using surface mounted hot film shear gauges was developed. Moore [1995] measured the intermittency in the cascade boundary layers using a hot wire probe 1mm from the surface. However the complex nature of the boundary layers warranted surface measurements to further investigate the boundary layer flow.

3.2 Measurement Technique and Data Processing.

3.2.1 Probe Calibration.

A Dantec 55R47 flush mounted hot film was used, with 100mm long enamelled copper leads changing to a thin single cored coaxial cable to minimise pickup of noise from the wind tunnel fan or other machinery. The enamelled wires were sandwiched between aluminium foil which is connected to the shielding of the coaxial cable to further reduce noise. The lead and probe resistance can be measured using the resistance measurement facilities of the Dantec 55M10 standard bridge. The gauge was attached to a double sided adherent plastic film which whilst adhering very well to both the gauge and blade surface, does not rely on adhesive, and so can be removed and reused many times over. Parcel tape was attached to the back of the plastic behind the gauge to prevent damage to the gauge by bending it and cracking the film when peeling it off the surface.

The gauge was calibrated by measuring shear stress along a flat Perspex plate with a sharp leading edge, and verified by measuring flow around a cylinder, The plate was mounted in a wind tunnel with very low free stream turbulence. To prevent separation at the leading edge, the plate had to be set at -5° incidence. It can be seen from Figure 3.1 a that the shear measured by the gauge is slightly high compared with the theoretical prediction for a laminar boundary layer assuming a correlation of the form of Equation 3.1 [Massey].

$$\tau_w = \frac{0.332\rho.U_\infty^2}{\sqrt{\mathrm{Re}_x}} \qquad \text{Equation 3.1}$$

This is thought to be due to thinning of the boundary layer due to a pressure gradient caused by the negative incidence. The value of k (Equation 2.5) was measured as 2.105. The exponent of τ was modified to give a least squares fit (Figure 3.1 b), hopefully cancelling out the effects of the pressure gradient, and giving an exponent of 0.235 and k as 1.818. It can also be seen from Figure 3.1 b that the values of shear can only be considered accurate to within about ±20%, the error being approximately constant in absolute magnitude at about ±0.25 Pa.

Despite these results, the original calibration curve with the exponent 1/3 was used in later tests in the linear cascade. This decision was taken because when measuring intermittency, the qualitative shape of the shear trace with time is more important than the absolute level, and in all previous experimental and theoretical accounts, the exponent 1/3 has been used.

3.2.2 Measurement Technique.

Using the calibration data from Figure 3.1 a, the data acquisition software used by Moore [1995] was modified to facilitate single measurements as opposed to traverses as carried out by Moore. The method used by Moore [1995] to process the data was not suitable for use with the hot films, due to the high level of noise on the signal, so a method was developed using a probability density function (PDF) after Schneider [1995]. This is a common statistical function, so no description of the mathematics is given here. The PDF is calculated on the probability density that the shear stress will be between pre-defined levels, and is based on a burst of sampled data. The trace from the hot film probe is sampled at 50kHz, and 8192 samples are recorded (~0.16 seconds). The film voltage is converted into a shear stress by the calibration discussed earlier before the PDF is calculated. The PDF is plotted and should have the distinct characteristics of a sharp high peak at the laminar shear stress and a smooth normal distribution curve over the range of turbulent fluctuations. A cut-off value is chosen in the trough between the laminar and turbulent values and the normal distribution curve of the PDF is interpolated between the minimum point at this cut-off value and the minimum shear stress measured (i.e. where the PDF returns to zero to the left of the laminar region). The normal distribution part of the PDF is then integrated using trapezium rule to give the intermittency. Figures 3.2 show typical shear stress traces on the blade suction surface 100mm from the end-wall. ,They show laminar, partially turbulent, almost completely turbulent and fully turbulent flow. The co-ordinate system for these plots has been translated to axial distance where the trailing edge is zero and the downstream direction is positive (Column 2 in Table 3.1). Figures 3.3 show corresponding PDFs for these shear stress traces.

The suction surface measurement co-ordinate system chosen was based on distance around the blade suction surface from the trailing edge and distance from the end-wall.

Measurements were taken on a 9 x 8 rectangular grid shown in Table 3.1 and the co-ordinates transformed into axial position are also tabulated along with the radial locations used.

Table 3.1 Co-ordinates on the Blade Suction Surface

Distance From Trailing Edge (mm)	Axial Co-ordinate (mm)	Radial Co-ordinates (mm)
25	-7.587	10
50	-15.441	20
100	-31.942	30
150	-52.346	40
200	-81.245	50
225	-101.188	60
250	-125.113	80
300	-166.063	100
325	-177.718	

The measurement locations on the end-wall correspond approximately to traverse slots 2 to 9 inclusive. Within the passage they were equally spaced at ten tangential locations, the first and last being 5% of the channel width from the blade surface. At slot 9, 11 equally spaced points were used, the first and last being one pitch apart to check for periodicity. The end-wall measurement positions are shown in Figure 3.4.

3.3 Discussion of Experimental Results.

Figures 3.5 a and b show contour maps of intermittency on the suction surface of the blade, those using hot wire measurements are taken from Moore [1995]. It can be seen that the two sets of results are very similar, both sets of results capturing the location of the passage vortex as it impinges on the suction surface and migrates radially along the blade surface. One interesting feature is that where Moore's results show a ridge in intermittency at about 50mm from the end-wall, the surface shear measurements show a slight trough. This could be due to fluid from the new laminar boundary layer on the end-wall being swept up onto the blade suction surface. The results from the hot film measurements have been linearly interpolated to allow contour plots to be drawn. It should also be noted that the lower span-wise limit of the hot film measurements is 10mm from the end-wall, compared with 1mm for the hot wire measurements.

Figures 3.6 a and b show contour maps of intermittency on the end-wall. The hot wire measurements are again taken from Moore [1995]. The low intermittency region between the pressure surface and passage vortex can be seen clearly in both plots. The migration of the pressure surface leg of the horseshoe vortex/passage vortex from leading edge to suction surface can also be seen from the hot film measurements, although not as clearly as from the hot wire measurements. The beginning of transition from a laminar to turbulent boundary layer can also be picked out downstream of the blade passage. The waviness in the hot film plot is probably caused by the interpolation routine used by the plotting software coupled with the relatively coarse nature of the measurement grid. It is interesting to note that the laminar region behind the passage vortex extends sufficiently far downstream for it to possibly enter the following blade row. Considering the work of Biesinger [1993], Gregory-Smith and Walsh [1987], it is possible that this laminar boundary layer may affect the flow within a following blade row.

Contour maps of pressure surface intermittency are not presented as no useful data can be extracted as the hot film measurements are poor. This is believed to be due to the concave nature of the pressure surface. The method used to prevent the gauge from bending and being damaged results in the gauge not being held tightly against the surface under these conditions. This is believed to cause instability in the traces obtained, and has a detrimental effect on the quality of

the measurements. The solution to this is to remove the tape that prevents the gauge itself from adhering to the end-wall but this would result in damage to the gauge when repositioning. Due to the cost involved this was not done as the pressure surface was considered to be of less value compared with the end-wall and suction surface measurements. Moore [1995] reported no significant flow features on the pressure surface that would justify this extra cost.

3.4 Conclusions

The hot film intermittency results over the suction surface and end-wall confirm the findings of Moore[1995] and prove that the measurements made 1mm from the surface are accurate, similar features of the flow being identified by both detection systems. the passage vortex and its migration across the end-wall and along the blade suction surface have been captured by the hot film measurements, along with the laminar region on the end-wall and the beginnings of its transition back to a turbulent state.

The measurements over the pressure surface are not sufficiently clear to allow valid conclusions to be drawn, however if the gauges were to be more firmly affixed to the blade surface (at the risk of destroying the film on removal) then better measurements should be possible.

As stated in section 3.1, an understanding of the boundary layer development through the cascade has important implications for the prediction and calculation of secondary flow. Before fully accurate modelling of the secondary flow structure can be achieved, the effects of the boundary layer development must be fully investigated. This also has implications for devising loss reduction methods.

Figure 3.1 Calibration Curve Assuming Different Exponents.

a) Exponent = 1/3.

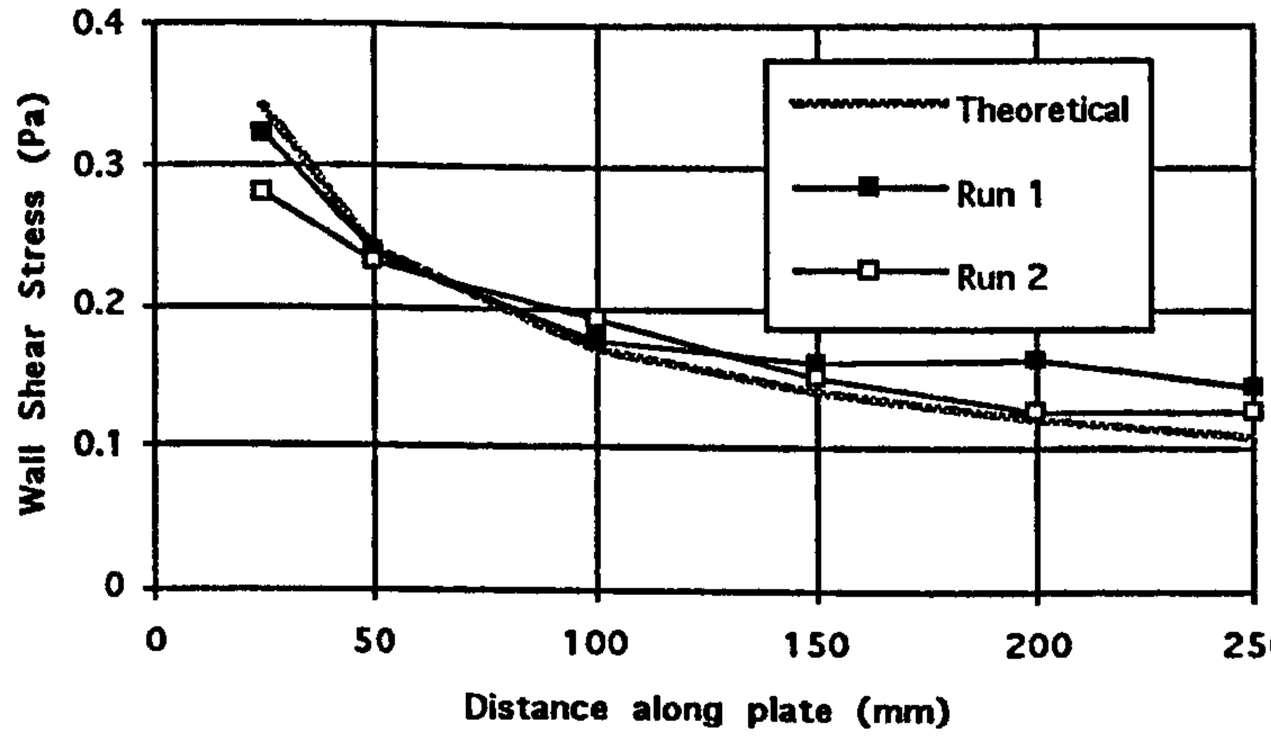

b) Exponent = 0.235.

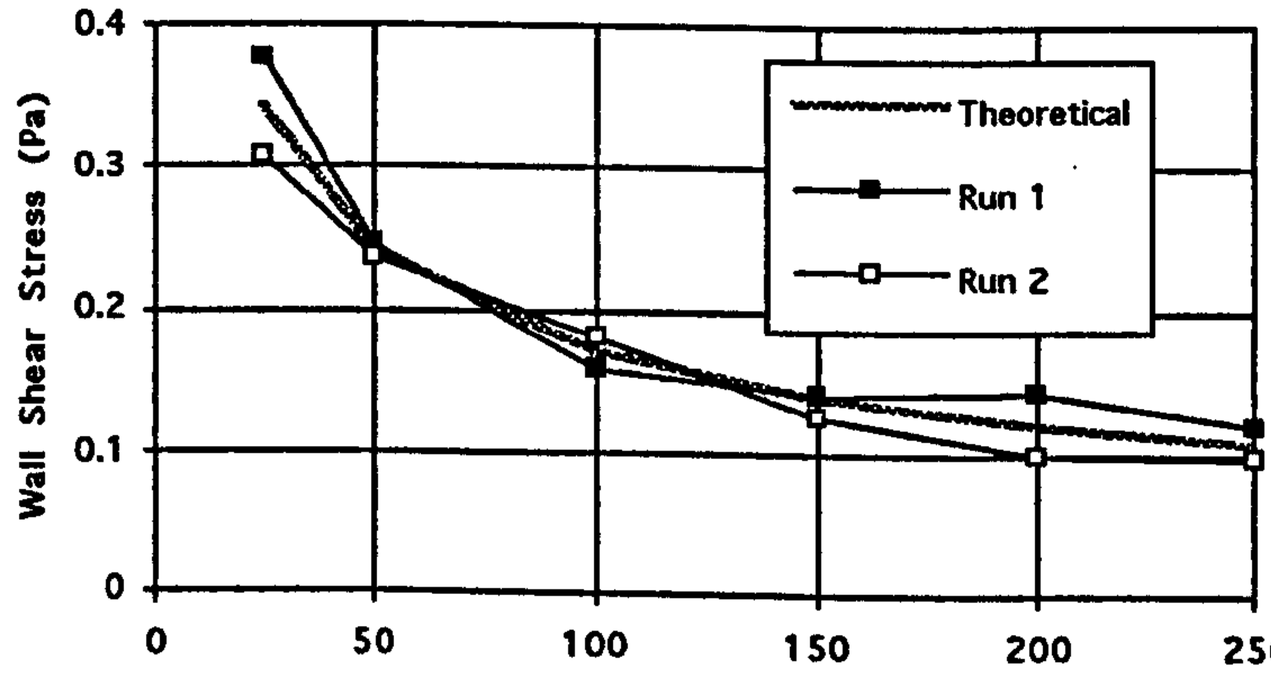

Figure 3.2 Fluctuating Suction Surface Shear Stress Traces 100mm From the End-Wall.

a) -81mm from Trailing Edge.

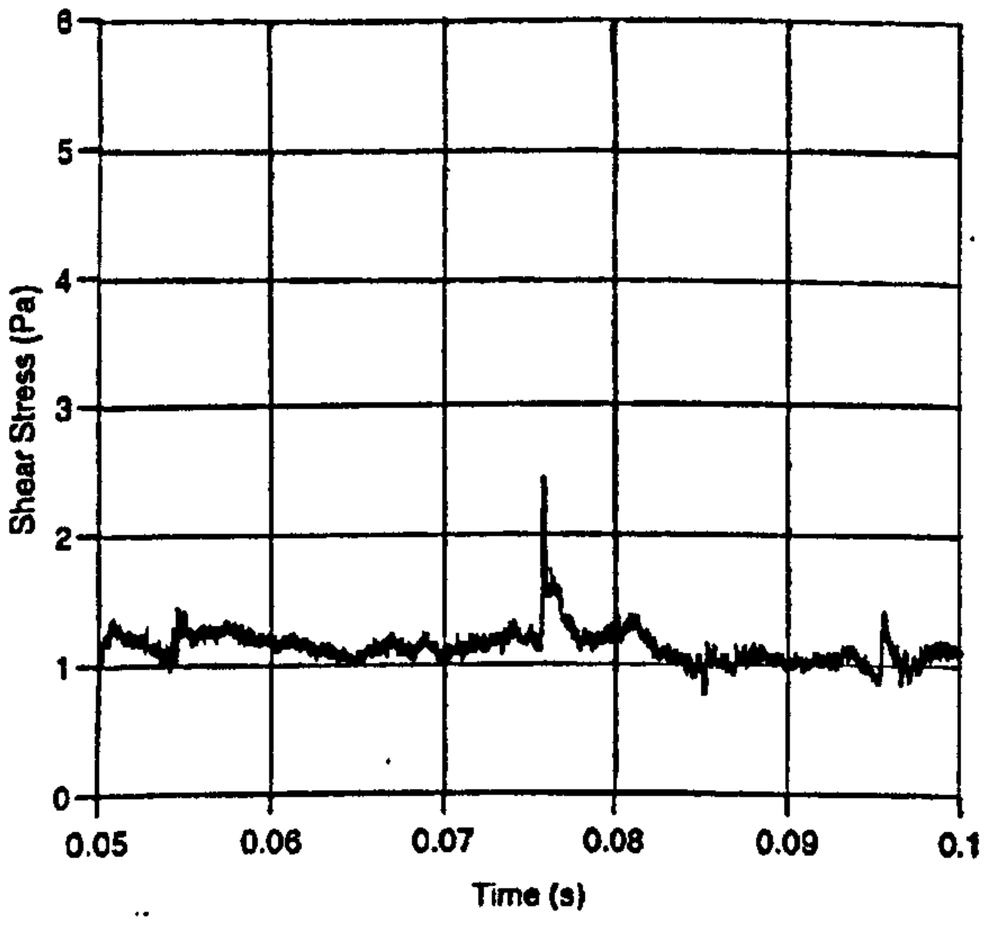

b) -52mm from Trailing Edge.

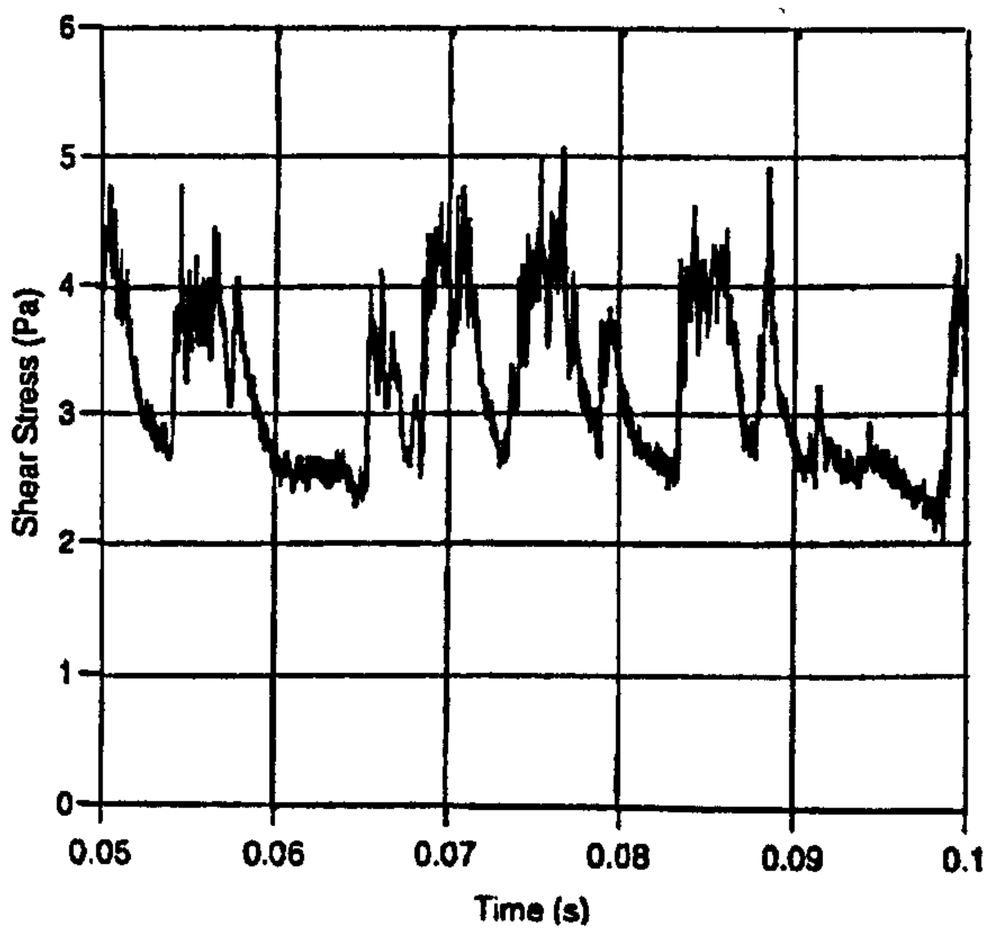

c) -32mm from Trailing Edge.

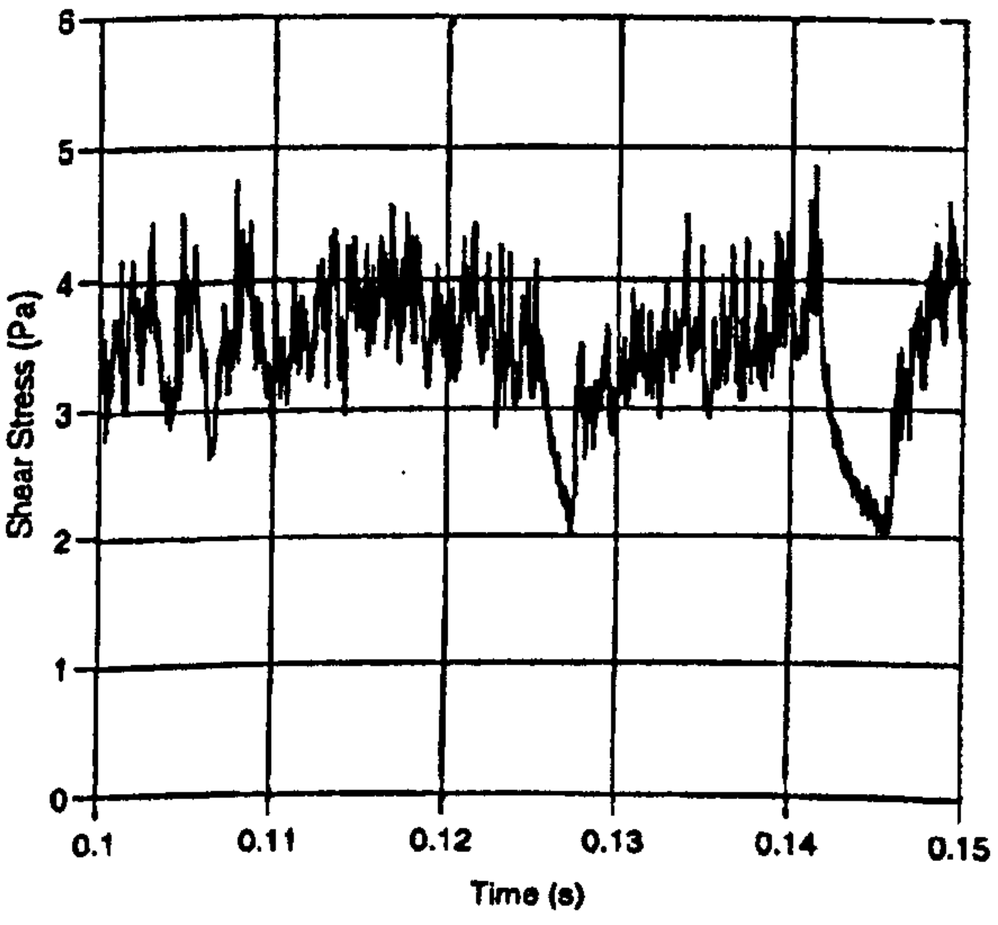

d) -15mm from Trailing Edge.

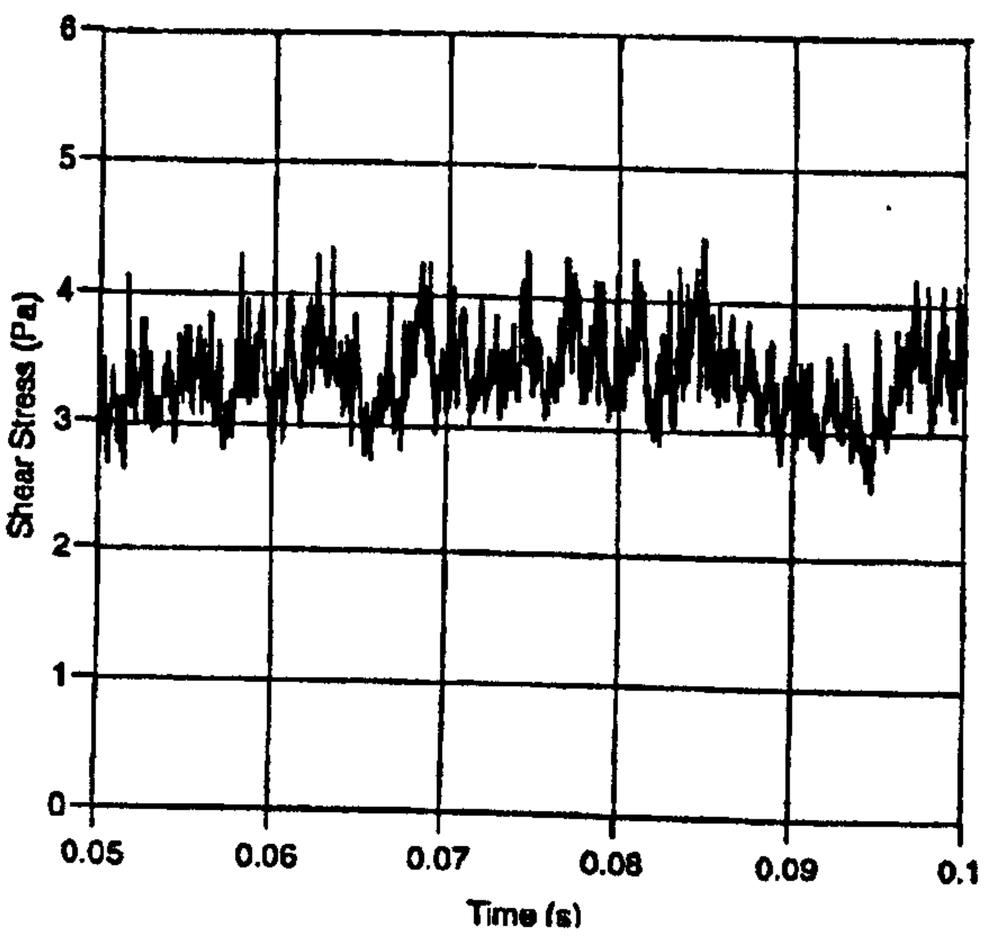

Figure 3.3 Probability Density Functions 100mm From the End-wall.

a) -81mm from Trailing Edge.

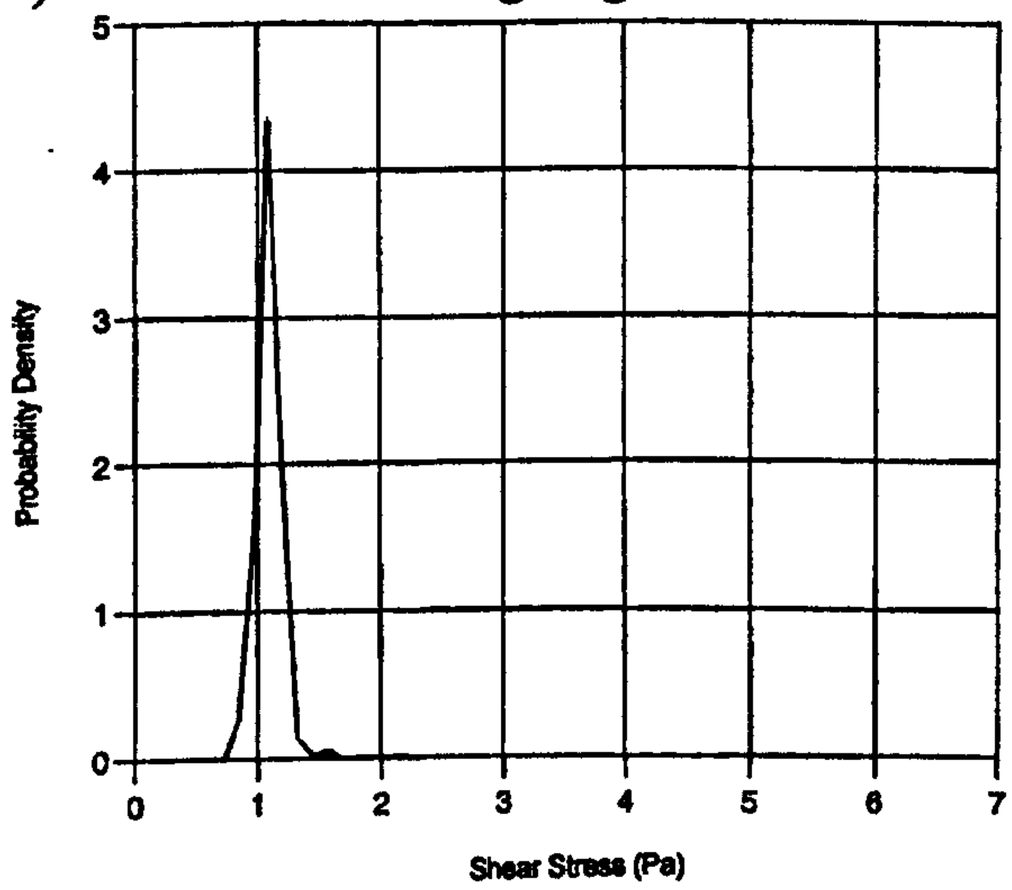

b) -52mm from Trailing Edge.

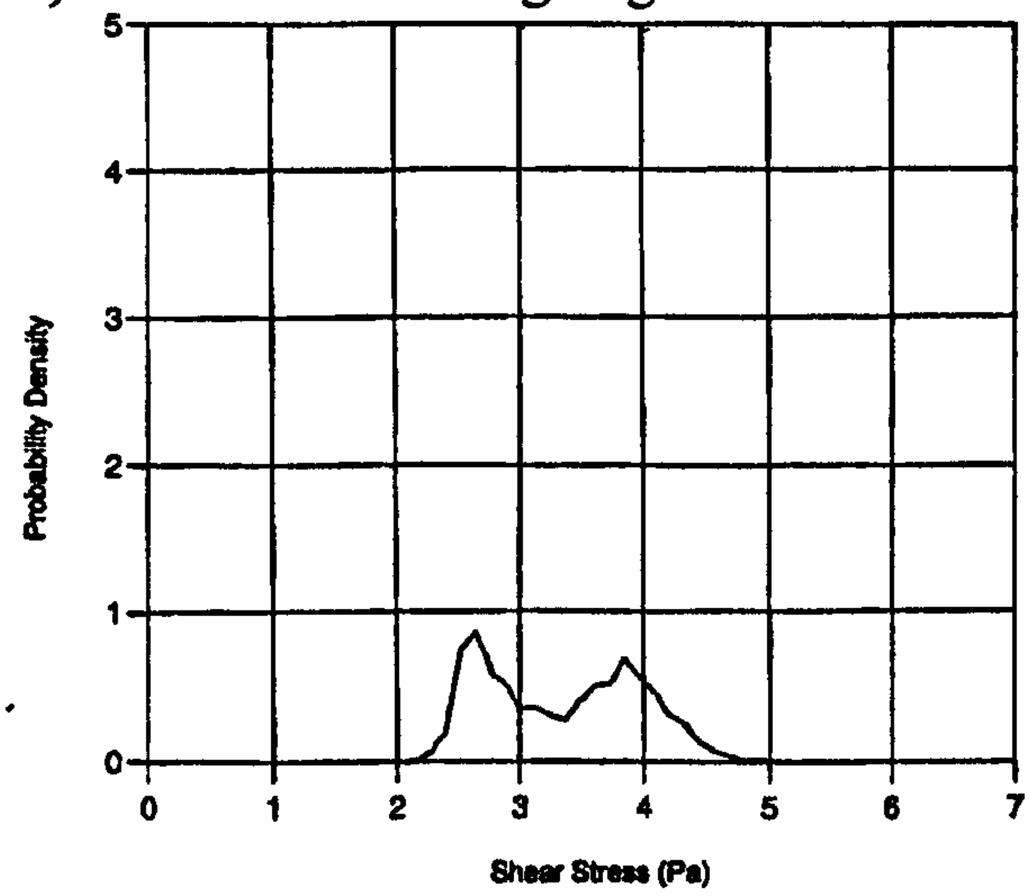

c) -32mm from Trailing Edge.

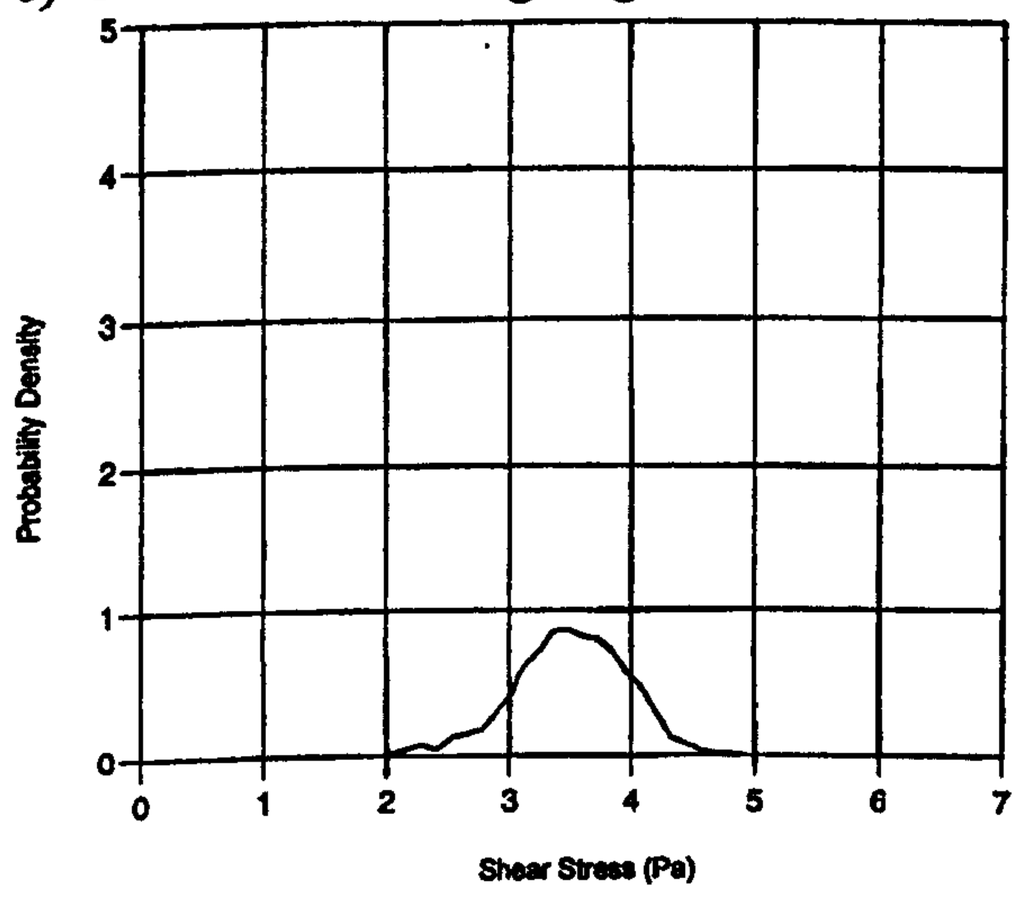

d) -15mm from Trailing Edge.

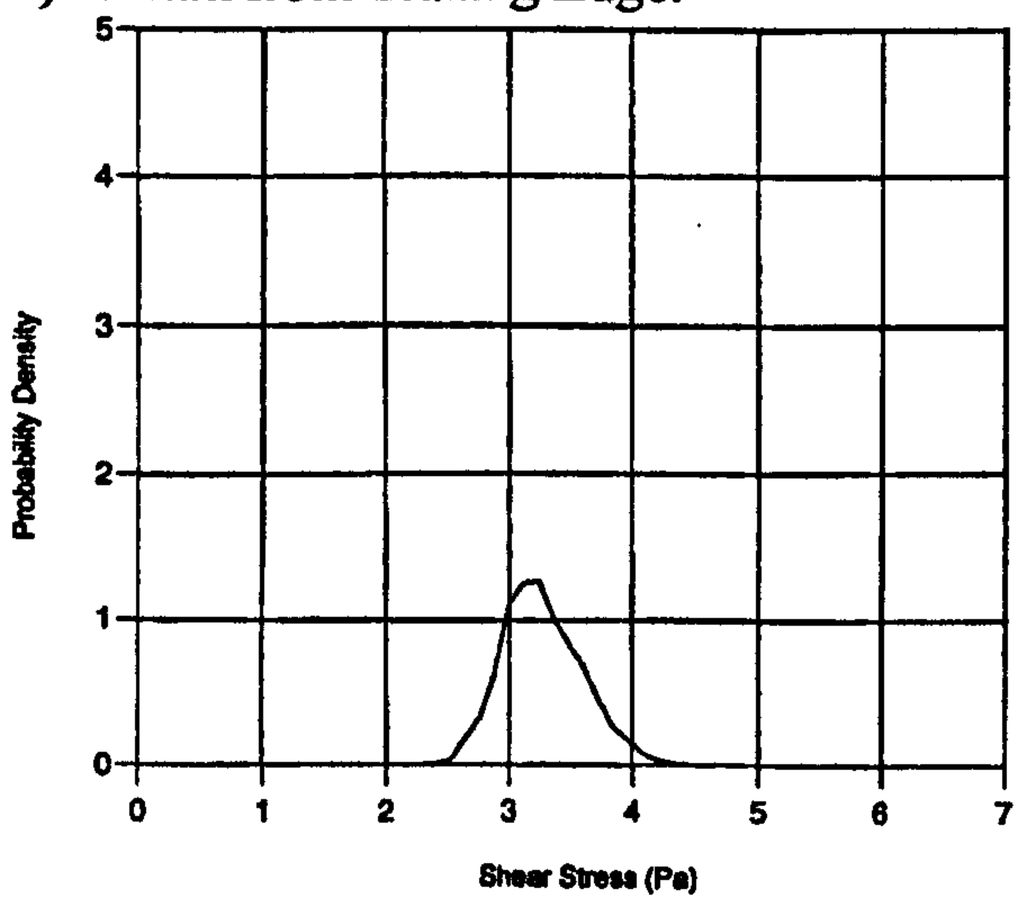

Figure 3.4 End-wall Measurement Locations.

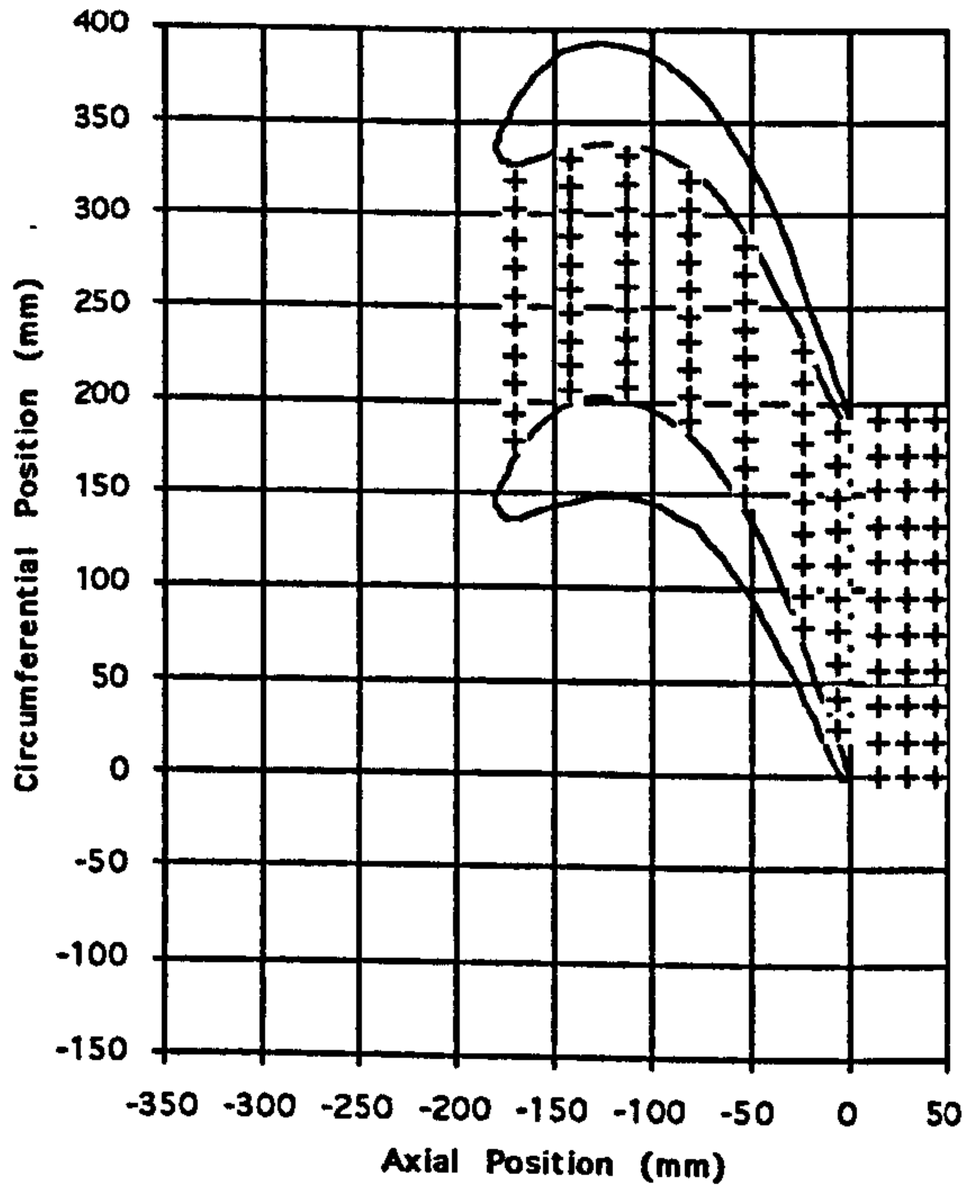

Figure 3.5 Suction Surface Intermittency Contours.

a) Hot Film Measurements.

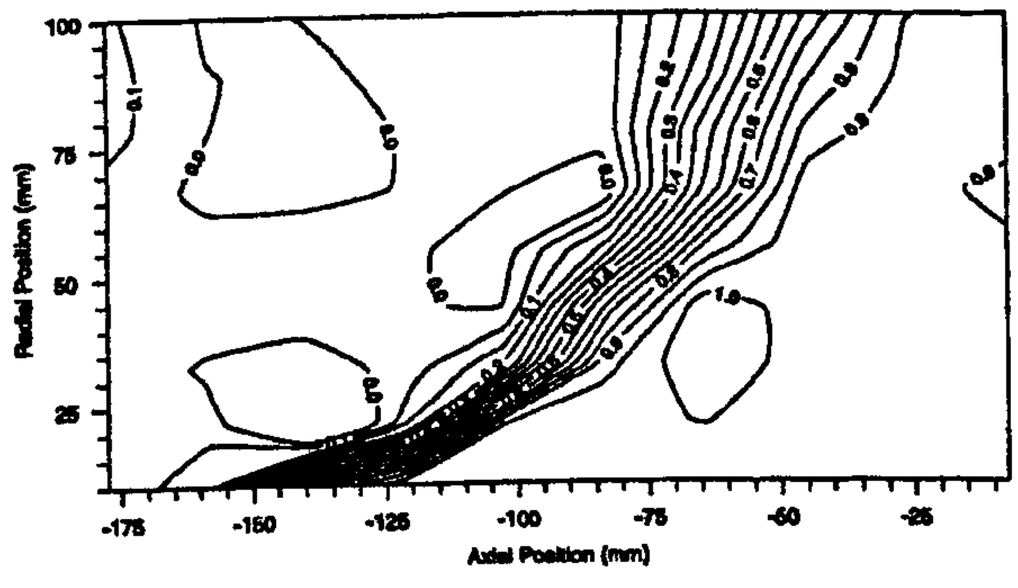

b) Hot Wire Measurements (Moore [1995]).

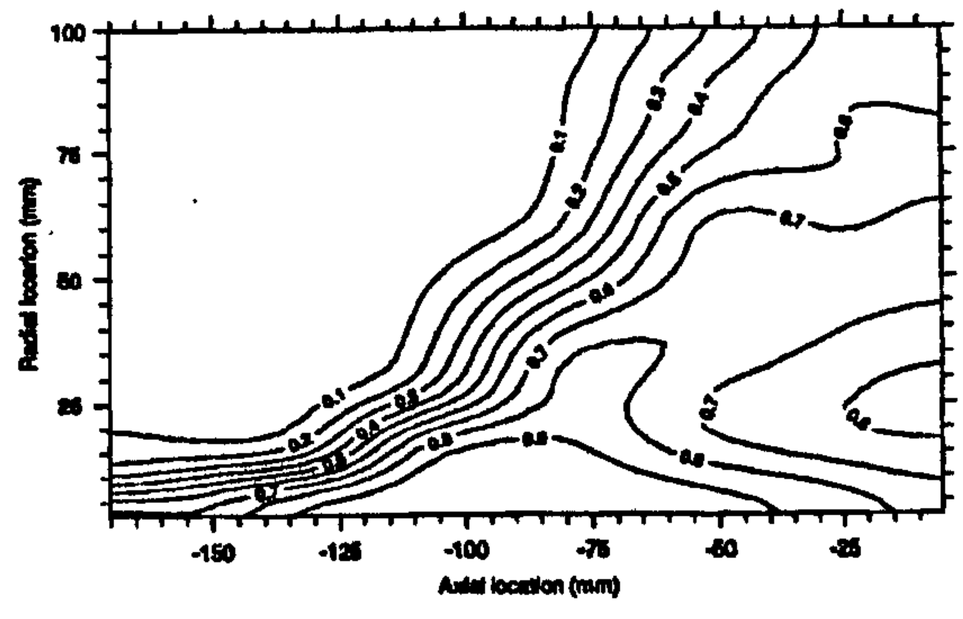

Figure 3.6 End-wall Intermittency Contours.

a) Hot Film Measurements.

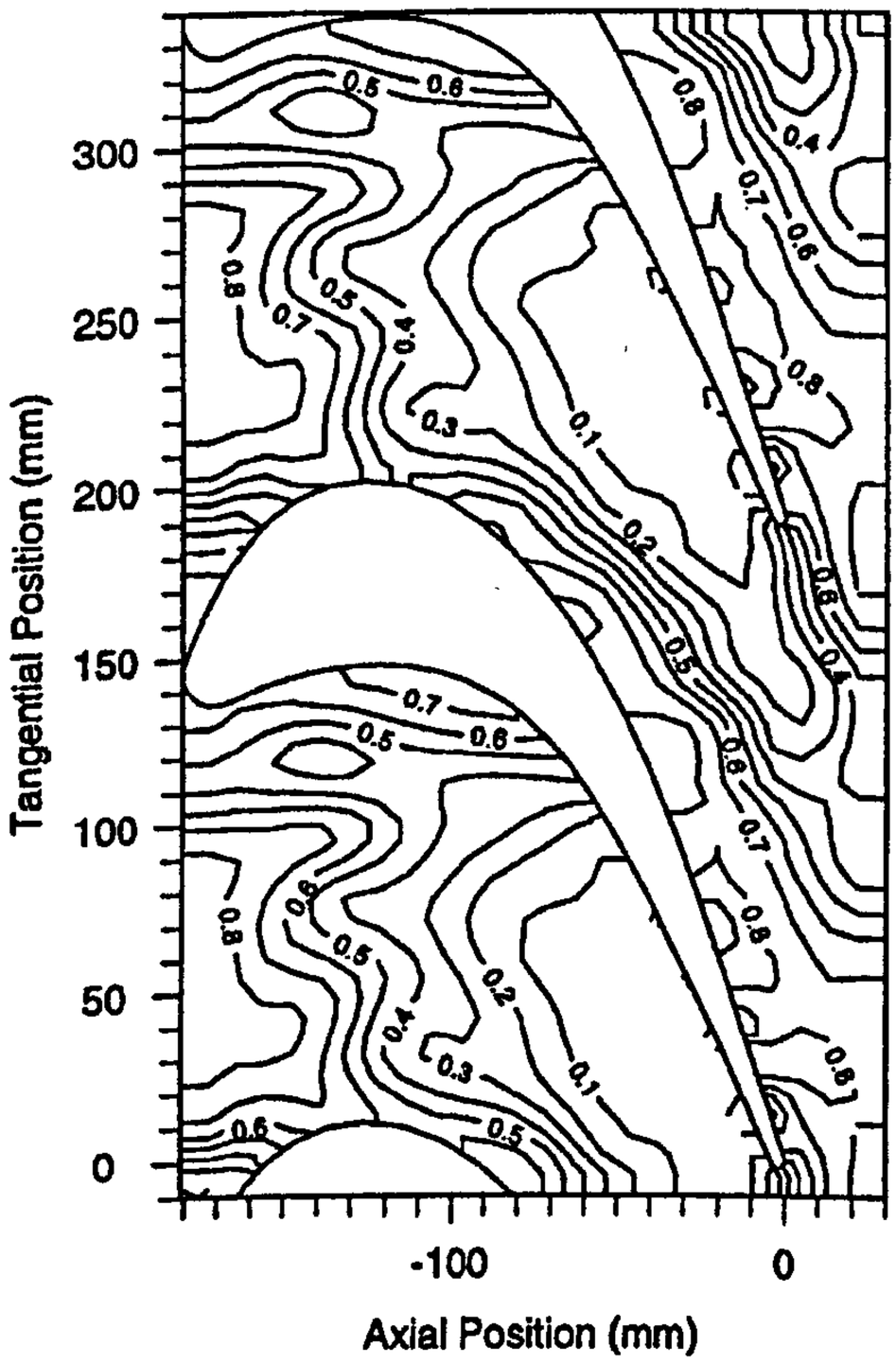

b) Hot Wire Measurements (Moore [1995]).

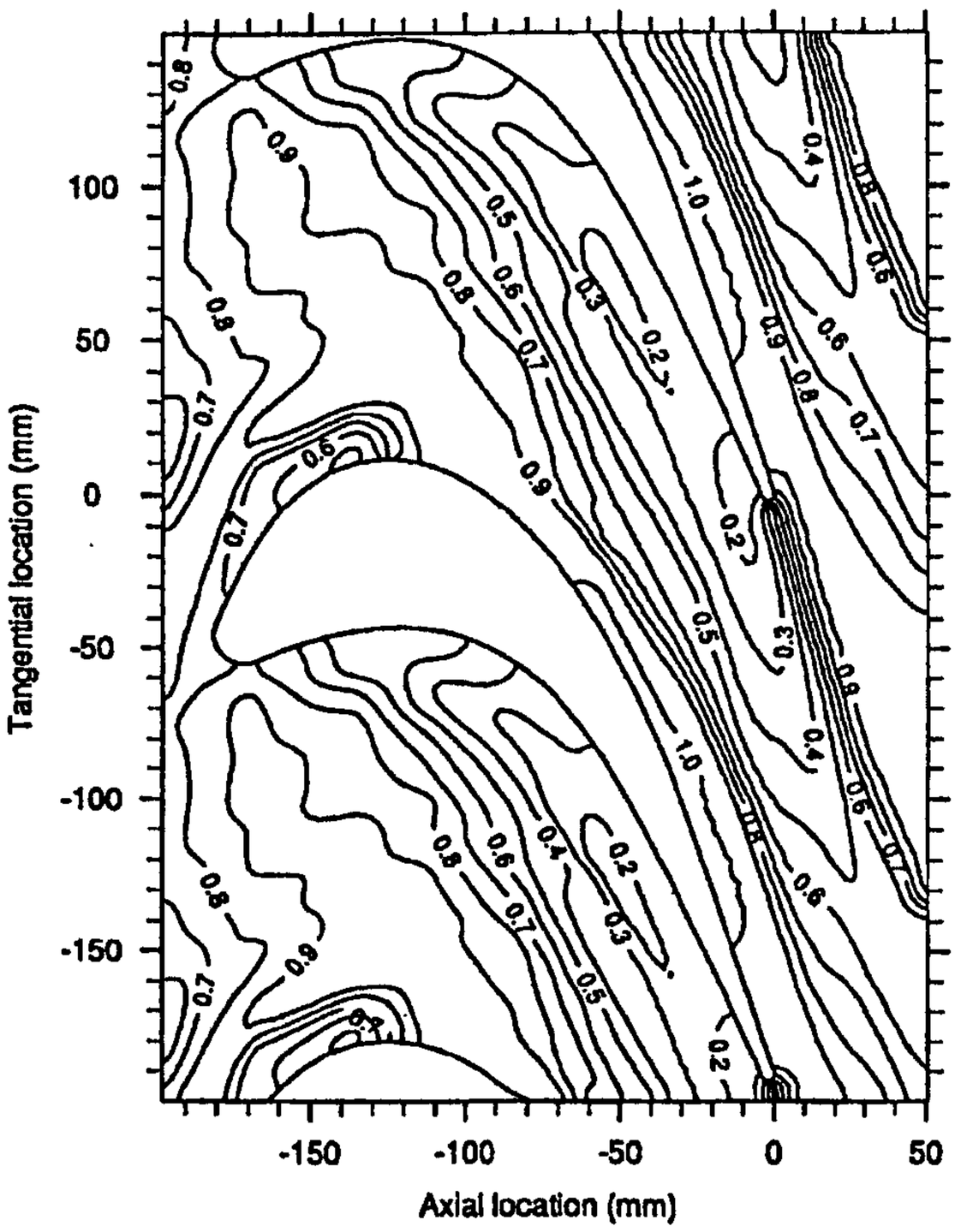

4 Measurement Techniques, Data Processing and End-Wall Manufacture.

4.1 Introduction.

Measurements have been made in the Durham Cascade using a five hole probe. In this chapter the cascade, five hole probe calibration, data processing algorithms and end-wall manufacturing system are covered.

4.2 The Durham Cascade.

The Durham cascade is a large scale, low speed, linear cascade, of high aspect ratio, designed to model the flow through a high pressure turbine rotor. The flow is characterised by strong secondary flows generated by the end-wall boundary layers, while at mid-span the flow is nearly two-dimensional. The cascade has a removable end-wall at one end, and slots cut out of the opposite end-wall to enable measuring probes to be inserted into the flow-field. The layout of the cascade, showing the positions of the measurement slots is shown in Figure 4.1. A grid of bars upstream of the blade row generates turbulence levels similar to those experienced in a true turbine, although no simulation is made of the periodic nature of the flow within a true turbine blade row as no means of modelling the passing of upstream blade exists. Tables 1 and 2 give the design details of the cascade. Further information is given by Gregory-Smith and Cleak [1992] and Moore and Gregory-Smith [1995]. Table 4.1 gives the cascade design details. Table 4.2 gives the inlet boundary layer parameters for the flow measured one axial chord upstream. Table 4.3 gives the measurement slot locations. Three parallel slots also exist for measuring the flow 1 chord upstream.

Table 4.1 Cascade Design Details

Inlet Flow Angle	42.75°
Blade Exit Angle	-68.7°
Blade Chord	224 mm
Blade Axial Chord	181 mm
Blade Pitch	191 mm
Blade Half-Span	200 mm
Reynolds Number (Axial Chord and Exit Velocity)	4.0×10^5

Table 4.2 Inlet Conditions to the Cascade

Dynamic Head	215 Pa
Free stream Velocity	19.1m/s
Density of Air	$1.179 kg/m^3$
Dynamic Viscosity	$1.814 * 10^{-5}$ Ns/m^2
Inlet Yaw Angle	43.5°
99% Thickness	40 mm
Displacement Thickness	2.8 mm
Momentum Thickness	2.3 mm
Shape Factor	1.22

Table 4.3 Measurement Slot Locations.

Slot	Position (%Cax)	Position (mm)
Slot 1	-9	-197
Slot 2	6	-170
Slot 3	22	-141
Slot 4	38	-112
Slot 5	55	-81
Slot 6	71	-52
Slot 7	87	-24
Slot 8	97	-5
Slot 9	116	29
Slot 10	128	51

4.3 Measurement Technique.

The cascade is run to a constant Reynolds Number. This ensures consistent flow for any atmospheric conditions. Pressures are non-dimensionalised by the upstream dynamic head and then multiplied by the standard day dynamic head before conversion to velocities, allowing accurate comparisons to be made between measured velocities.

4.3.1 End-wall Pressure Measurement.

The end-wall of the cascade is fitted with pressure tappings. These are in rows corresponding to slot positions, each row having 10 holes equally spaced. For the flat wall measurements the holes were 0.8mm internal diameter and for the profiled walls 0.76mm internal diameter. The pressure tappings for the profiled walls were made using polyethene tubing (1.22mm external diameter) set through the end-wall and glued in place with a small amount of tube protruding. The protruding tubing is then cut off and sanded to give a smooth finish. Figures 4.2 to 4.4 show the pressure tapping locations for the planar and profiled end-walls. The FAITH profile (designed using the Rolls Royce design code FAITH and described in Chapter 7) extended significantly upstream hence the extra rows of pressure tappings upstream of the blade leading edge. The pressure tappings were attached to an inclined multi-tube manometer set to 20° to horizontal, any unused tappings being blocked off. The specific gravity of the fluid used is 0.82.

4.3.2 Area Traverses.

The software originally written by Biesinger to enable automated traversing and measurement within the cascade has been re-written to suit current needs. The new software is significantly different in three main ways. The first is that the stepper motor driver was updated by Moore, and as such new traverse control routines were necessary. The second is that to enable measurements to be made over a profiled end-wall, the format of the measurement grid files needed re-organising. The third main difference is that due to slight fluctuations in the wind tunnel speed over a longer period than the 28Hz "Organ Pipe" effect reported by earlier researchers, the pressures were logged at a lower frequency and for a longer time period (~5 seconds at ~500Hz as opposed to 0.06 seconds at 2.7kHz).

Area traverses were carried out at slots 1, 6, 8 and 10 using a 5-hole pressure probe. Two cobra type probes were used, both of which were almost identical, and Figure 4.5 shows one of the cobra probes used. To enable a wider range of accurate flow angles the yaw and pitch angle coefficients are non-dimensionalised by the actual local dynamic head rather than an estimated dynamic head based on the difference between the front probe hole and the average of the 4 side holes. This increases the range as, at high angles, the estimated dynamic head used in the standard coefficients tends towards zero, stretching and skewing the calibration map and eventually inverting the outer most points as the dynamic head effectively becomes negative. Using the actual local dynamic head necessitates the use of an iterative method to determine the total and static pressures. Figure 4.6 shows a flow diagram for the solution of the flow variables at any point and Figures 4.7 show a typical set of calibration data. The definitions for the calibration coefficients used are given in Equations 4.1 to 4.4, along with the standard calibration coefficients in Equations 4.5 to 4.8.

Coefficient Definitions Used:

$$C_{pitch} = \frac{P_{bottom} - P_{top}}{P_{dynamic}} \qquad \text{Equation 4.1}$$

$$C_{yaw} = \frac{P_{right} - P_{left}}{P_{dynamic}} \qquad \text{Equation 4. 2}$$

$$C_{total} = \frac{P_{front} - P_{o}}{P_{dynamic}} \qquad \text{Equation 4. 3}$$

$$C_{static} = \frac{P_{avg} - P_{static}}{P_{dynamic}} \qquad \text{Equation 4. 4}$$

Standard Coefficient Definitions:

$$C_{pitch} = \frac{P_{bottom} - P_{top}}{P_{front} - P_{avg}} \qquad \text{Equation 4.5}$$

$$C_{yaw} = \frac{P_{right} - P_{left}}{P_{front} - P_{avg}} \qquad \text{Equation 4. 6}$$

$$C_{total} = \frac{P_{front} - P_{o}}{P_{front} - P_{avg}} \qquad \text{Equation 4. 7}$$

$$C_{static} = \frac{P_{avg} - P_{static}}{P_{front} - P_{avg}} \qquad \text{Equation 4. 8}$$

Where $P_{avg} = \frac{1}{4}\left(P_{left} + P_{right} + P_{top} + P_{bottom}\right)$

The measured pressures are processed using an iterative method which has been successfully tested on sample data. Initially a box test is performed to determine which pairs of pitch and yaw curves from Figure 4.7 a straddle the data point and are therefore required for the interpolation routine. The routine is then initialised using a yaw angle half way between the two curves of constant yaw selected by the box test. Pitch coefficients corresponding to this yaw angle are then calculated along the constant pitch curves. An estimate of pitch angle is then calculated using a and b from Figure 4.8 a. The above procedure is repeated to give an estimate of

yaw angle, using this pitch angle estimate, as shown in Figure 4.8 b. The procedure is repeated, alternately calculating pitch and yaw angles based on the previous iteration until a convergence criterion is met (Figures 4.8 c and d). Typically 2 or 3 iterations are needed to resolve the flow angles to within 0.1°.

The cobra type probes used are 90° pyramid probes with 0.5mm forward facing holes. The probe tip is approximately 3mm in diameter giving a probe Reynolds Number of approximately 8000. This is unfortunately in a region in which Reynolds Number effects can be significant [Dominy & Hodson 1993]. The probe was calibrated at the cascade exit velocity so that any Reynolds Number effects should be minimised. Re-calibration of the probe at a slightly lower speed to verify this did not indicate any significant changes in the probe characteristics, however Dominy and Hodson found typical errors of 1% of dynamic head and 0.5° in flow angle coefficients due to flow phenomena around the probe head.

The pressures are measured using 5 CMR "p-sensor" transducers (4 x 0-2000 Pa and 1 x 0-500 Pa) and one Furness FC040 (+/-200 Pa). These were calibrated by the manufacturers before use, and a brief check against a micro-manometer proved them to be accurate. Upstream dynamic head is measured on the 0-500 Pa CMR transducer, and local total pressure (centre hole) at the five holed probe is measured relative to upstream total pressure using the Furness transducer. The four side holes are measured relative to upstream total pressure using the remaining 0-2000 Pa CMR transducers.

The pressures are logged using a A/D card with a resolution of +/-2048 bits, which translates to approximately 0.05% of dynamic head for the +/-200Pa transducer and 0.5% Dynamic head for the 0-2000Pa transducers. Considering the calibration map (Figure 4.7 a) at zero pitch, zero yaw, a yaw coefficient of 0.3 relates to a yaw angle of 5° and a pitch coefficient of 0.2 relates to a pitch angle of 5°. Thus, an error of 0.5% dynamic head per side hole would relate to a total error of 1% dynamic head, or 0.17° yaw and 0.25° pitch. Combining the above with the flow induced errors , would give experimental errors up to 0.67° yaw, 0.75° pitch and 1% dynamic head for total pressure.

The positioning of the upstream reference probe is critical for loss measurements, as there is a large scale total pressure non-uniformity at the position where the reference probe is mounted (Figure 4.9). The probe is mounted 665mm downstream from the turbulence grid and 885mm upstream of the blade leading edge plane, and has previously been mounted 110mm from the wall of the wind tunnel. Static pressure is almost constant at -215Pa over the whole range of measurements. Previous researchers are thought to have checked this, but none reported such a large variation. The reference probe has been moved to 170mm from the wall to eliminate negative losses which occur when the reference total pressure is lower than at the 5 hole probe location.

This repositioning of the reference probe would result in an increase in measured total pressure loss of about 10 Pa (4 to 5% of dynamic head). As such, the measured losses would be expected to be about 4 to 5% higher than reported by Biesinger [1993].

Once the data has been processed, the flow angles are adjusted to give the same mass flow rate at mid-span as the inlet flow by adjusting the value of the setting angle to introduce a yaw angle offset. Within the cascade, the data is extrapolated to the blade surfaces to ensure that the area is correct and any variation in flow speed across the passage is accounted for. An adjustment is made to the mid-span mass flow rate to account for the boundary layers on the blade surfaces. This is based on an apparent error in the integrated CFD data, evident when the integrated mass flow rate from CFD data interpolated onto the experimental grid is compared with the integrated mass flow rate from the full CFD data-set. Typically the setting angle changes by between 0 and 3°. Whilst this seems large in comparison with the predicted experimental accuracy above, the existence of approximately 2° backlash in the dovetail slide of the traverse equipment would appear to be the explanation of this. Flow variables (Yaw, C_{SKE}, C_{Po} etc...) are then calculated and mass averaged as outlined in Appendix A. It should be noted that the pitchwise integration for profiled end-wall data is carried out over a curved quasi-constant spanwise path, based on the fractional distance between the end-wall and mid-span. The path also varies in thickness as it is stretched and squashed over the end-wall profile. This approach has been adopted as it was thought to be better to integrate over a path parallel to the end-wall and yet still accurately integrate the mid-span flow.

4.4 End-Wall Profile Manufacture.

To allow complex 3-D surfaces to be machined, the CNC milling machine in the CAM laboratory has been linked to an IBM PC, and software has been written for both the PC and CNC machine to facilitate downloading of ASCII files. The current file format for downloading requires 4 columns of numbers. The first column must contain a 2 digit integer command code, 11, 22 or 33 (see table 4.4) and the next 3 columns must contain 3 real numbers for the x, y, and z co-ordinates respectively. The number 123001 must appear on its own at the start of the file to initiate the machining cycle on the CNC machine (This is a security measure to avoid spurious co-ordinates from any data buffers being read). Comments can be added to the data file and these will be echoed on the PC screen but not transmitted to the CNC machine. Comments are enclosed by "#" symbols which must be separated from any other text or numbers by a space or tab mark. The software for both the CNC machine and PC can be seen in Appendix B along with the cable connections and a short example file which draws a circle.

The C program reads an ASCII file as described above, echoing the data and comments on the screen. The comments are then ignored and the data is sent to the serial port on the PC. At the end of the file, the program automatically stops itself. The last line in the ASCII file on the PC must be a 33 command to switch off the CNC machine on completion of the work. When the CNC program is started, the program continually reads in a number from the serial port until it receives 123001. The program then starts the machine tool spinning, then reads in an integer followed by three real numbers. The integer command is interpreted as above by way of a subroutine call and the co-ordinates are then used accordingly.

Table 4.4 Data File Control Codes

Code	Function
11	Move rapidly to x,y,z.
22	Machine to x,y,z at a pre-set feed-rate.
33	Move rapidly to x,y,z then stop the tool and terminate the CNC program.

If a ball ended cutter is used to machine a 3-D surface, the compensation for tool offset can be calculated using Equations 4.9 to 4.12. The offset calculation assumes that the uncompensated co-ordinates would be machined by the centre of the tip of the tool. Gradients are calculated numerically from an x,z,y dataset to allow arbitrary surfaces to be machined.

$$\delta z = \frac{R}{\sqrt{\left(\frac{\partial z}{\partial x}\right)^2 + \left(\frac{\partial z}{\partial y}\right)^2 + 1}} \qquad \text{Equation 4.9}$$

$$x_{new} = x_{old} - \frac{\partial z}{\partial x} \cdot \delta z \qquad \text{Equation 4. 10}$$

$$y_{new} = y_{old} - \frac{\partial z}{\partial y} \cdot \delta z \qquad \text{Equation 4. 11}$$

$$z_{new} = z_{old} - R + \delta z \qquad \text{Equation 4. 12}$$

For calculating tool offsets in 2 dimensions, Equations 4.13 to 4.20 are used. X and Y are the new co-ordinates based on original co-ordinates x,y and the conventions are as shown in Figure 4.10. These equations are only valid for increasing x. k_{LR} should be positive for left hand compensation (as in the Figure 4.10) and negative for right hand compensation.

$$S_- = \sqrt{(x - x_-)^2 + (y - y_-)^2} \qquad \text{Equation 4.13}$$

$$S+ = \sqrt{(x - x_+)^2 + (y - y_+)^2} \qquad \text{Equation 4.14}$$

$$x_a = x_- - k_{LR}\frac{R \cdot (y - y_-)}{S_-} \qquad \text{Equation 4.15}$$

$$x_b = x - k_{LR}\frac{R \cdot (y_+ - y)}{S_+} \qquad \text{Equation 4.16}$$

$$y_a = y_- - \frac{(x_a - x_-)}{\frac{dy}{dx}_-} \qquad \text{Equation 4.17}$$

$$y_b = y - \frac{(x_b - x)}{\frac{dy}{dx}_+} \qquad \text{Equation 4.18}$$

$$X = \frac{\left((y_b - y_a) + x_a \cdot \frac{dy}{dx}_- - x_b \cdot \frac{dy}{dx}_+\right)}{\frac{dy}{dx}_- - \frac{dy}{dx}_+} \qquad \text{Equation 4.19}$$

$$Y = (X - x_a) \cdot \frac{dy}{dx}_- + y_a \qquad \text{Equation 4.20}$$

Figure 4.1 Layout of the Durham Linear Cascade.

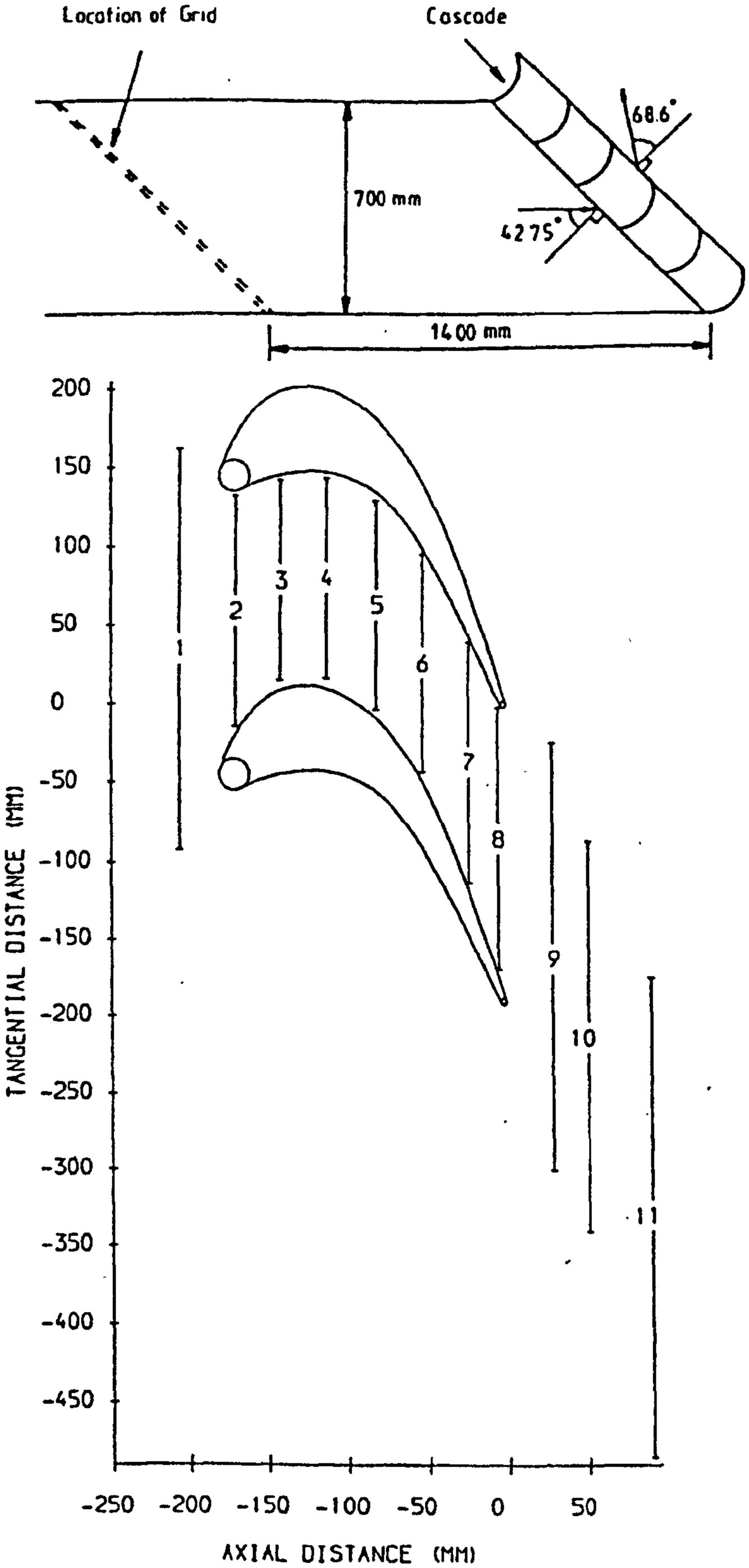

Figure 4.2 Planar End-Wall Pressure Tappings.

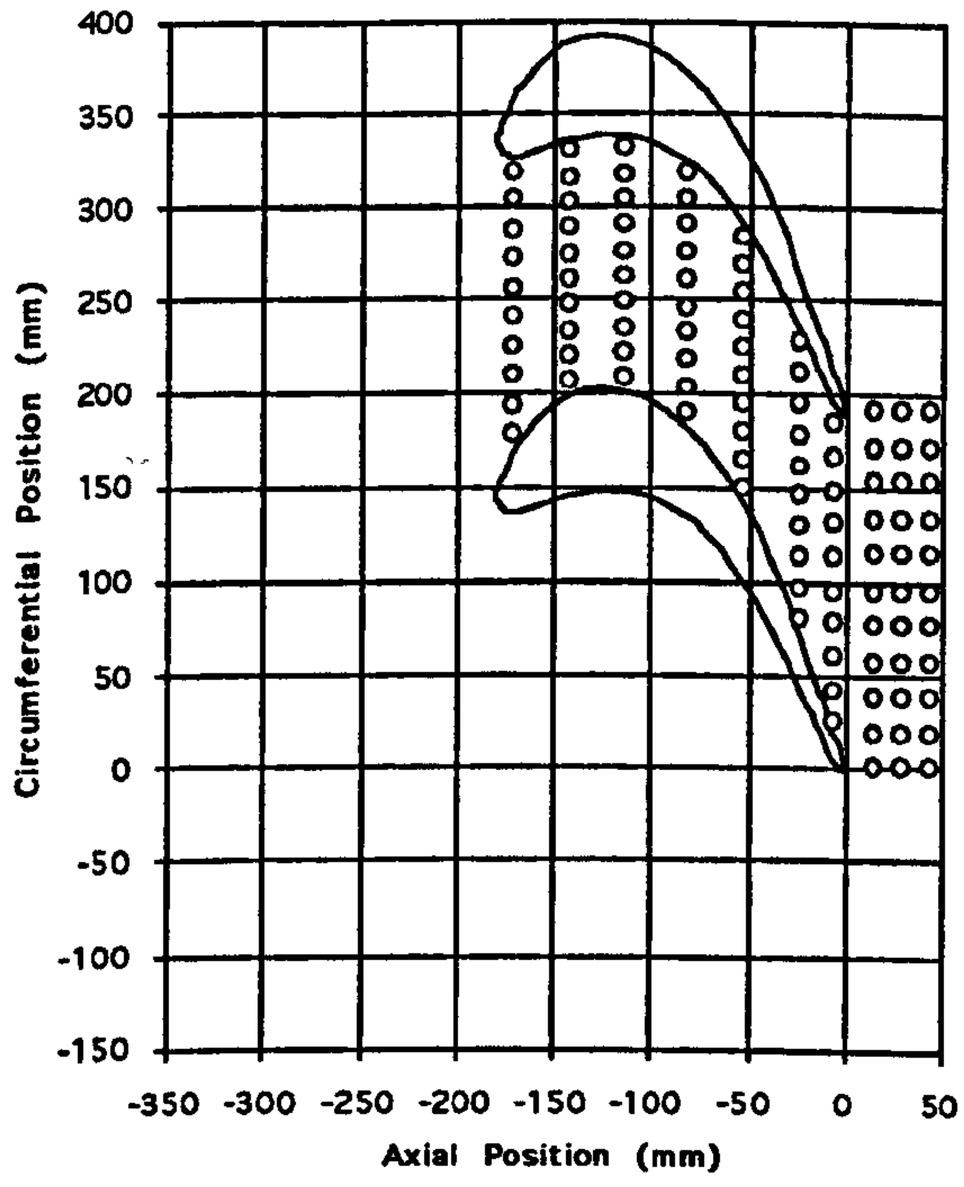

Figure 4.3 Profile3 End-Wall Pressure Tappings.

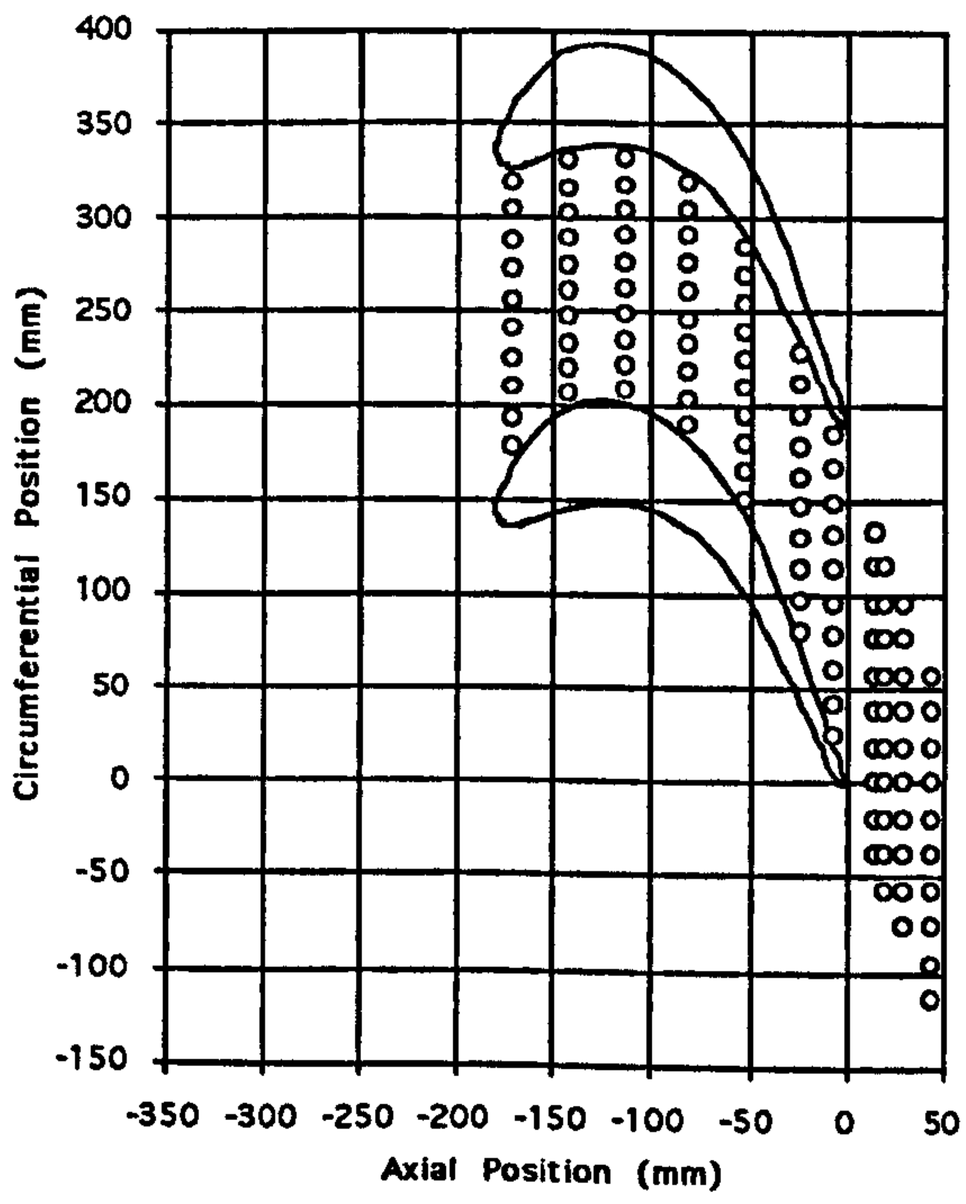

Figure 4.4 FAITH End-Wall Pressure Tappings.

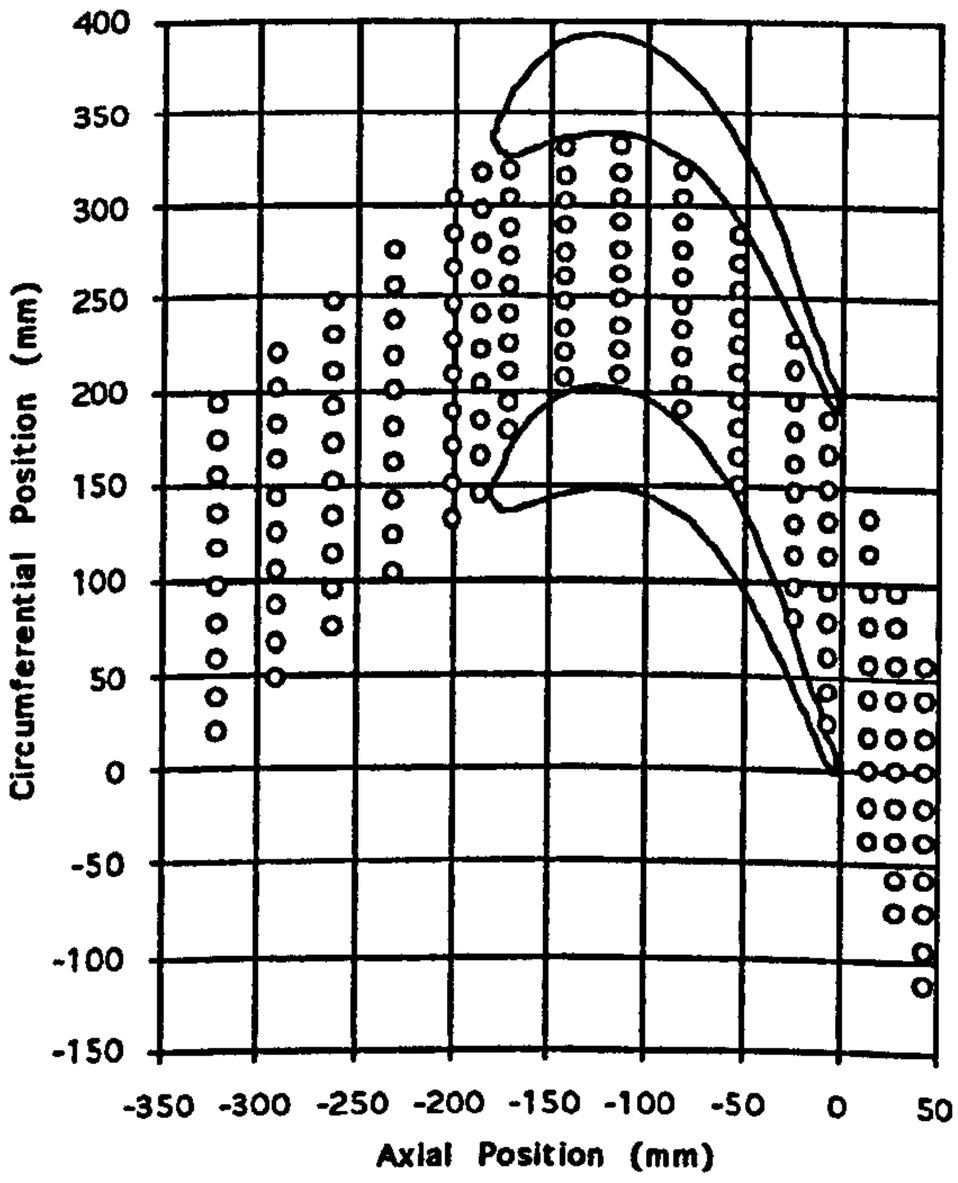

Figure 4.5 Cobra Type Probe.

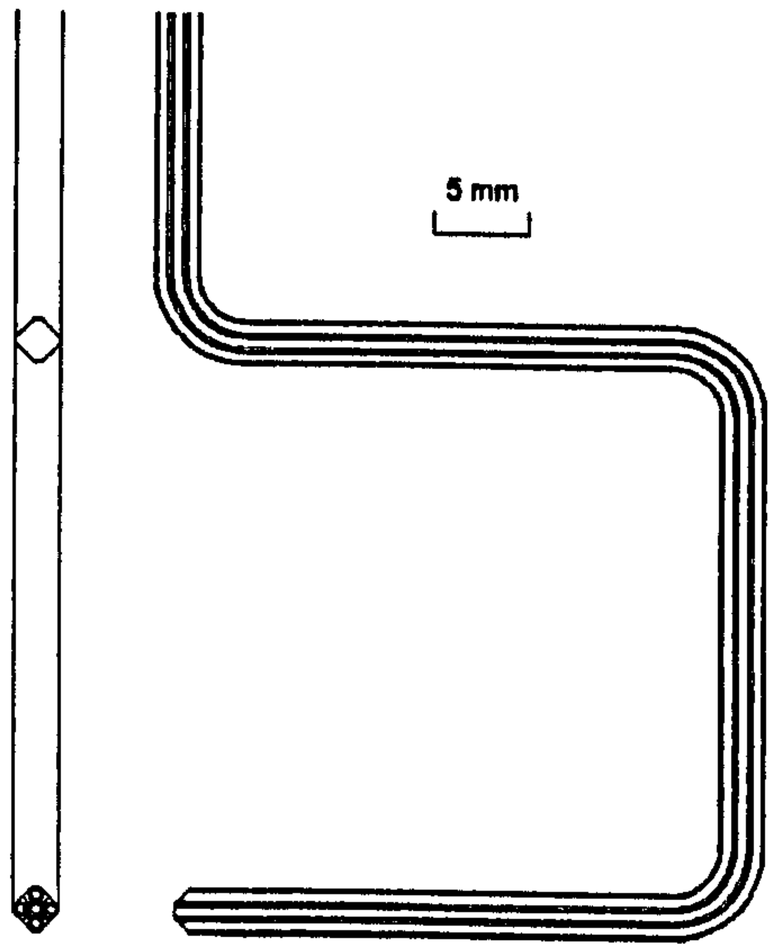

Figure 4.6 Flow Diagram of the Processing Algorithm.

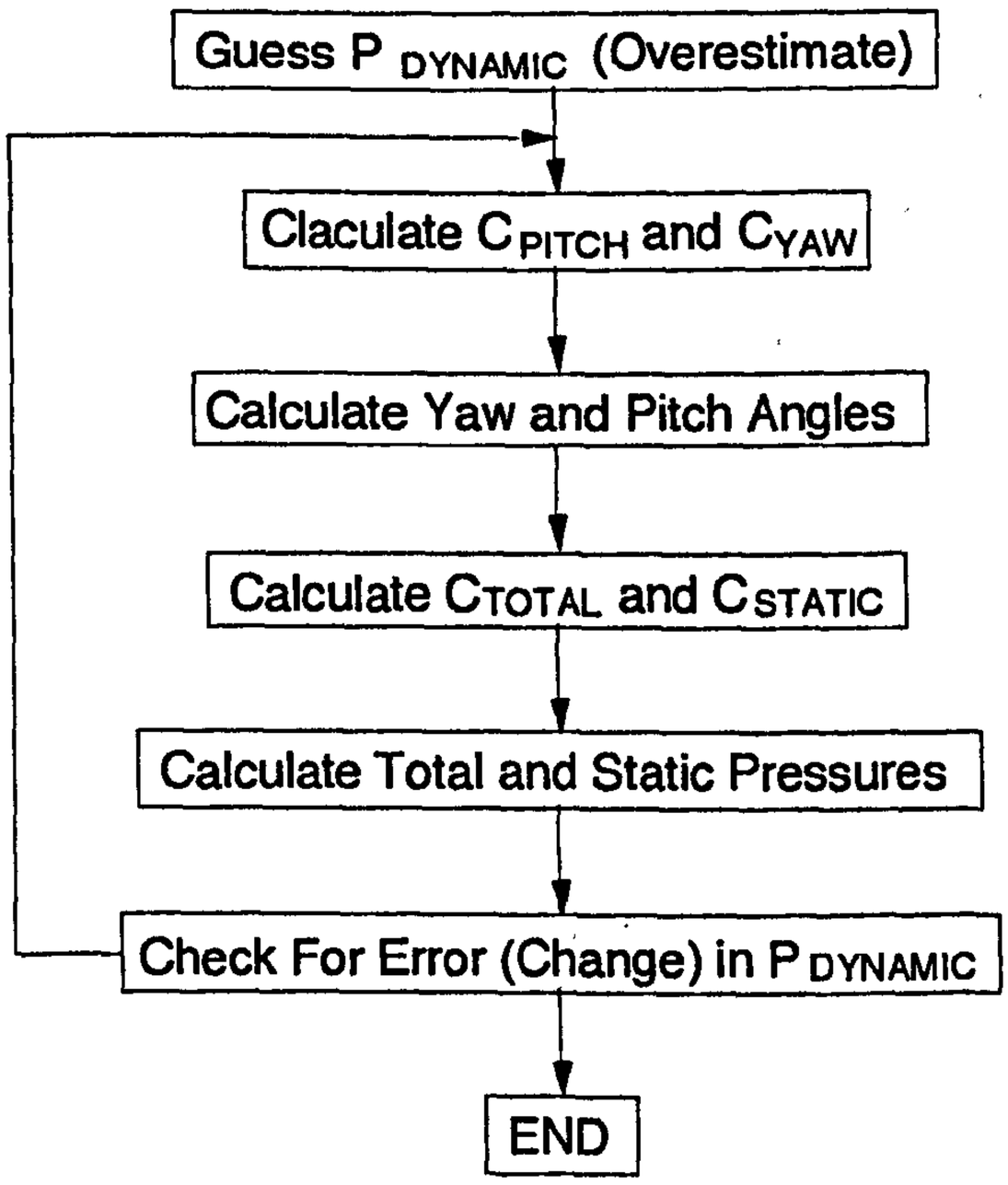

Figure 4.7 Typical Calibration Map.

a) Pitch and Yaw Coefficients.

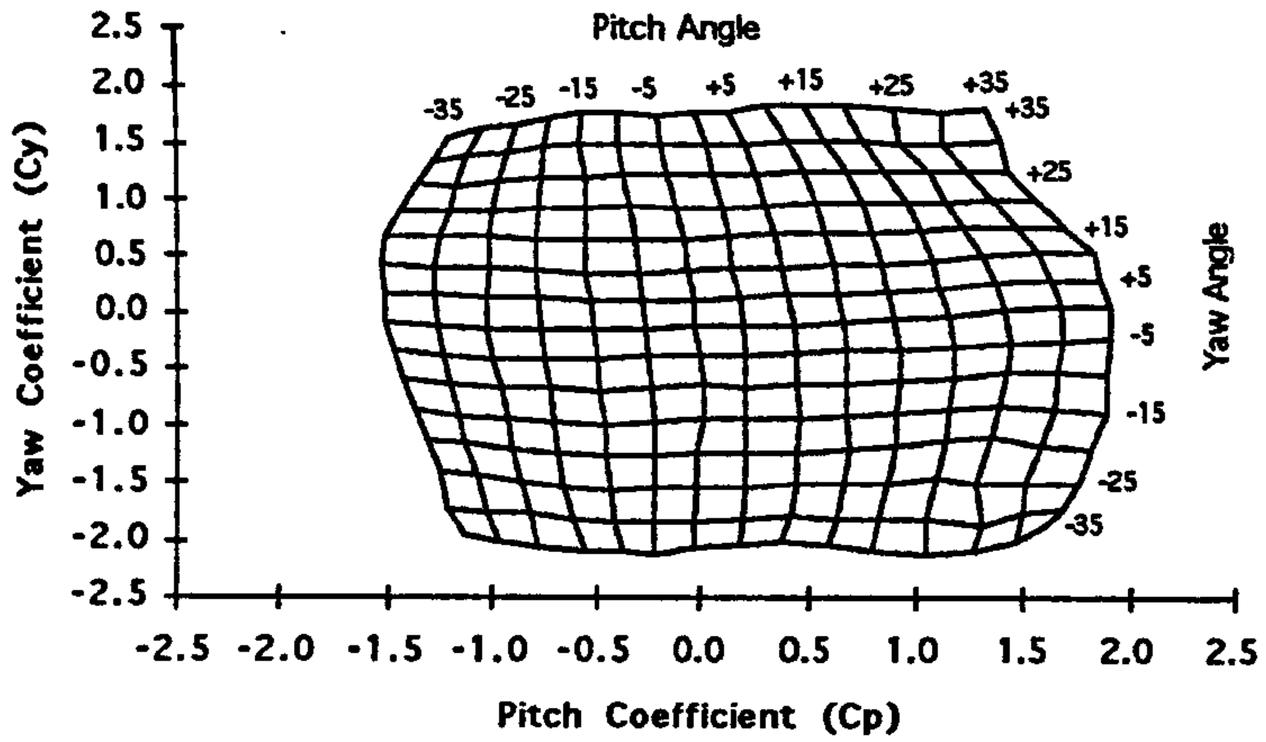

b) Total Pressure Coefficient.

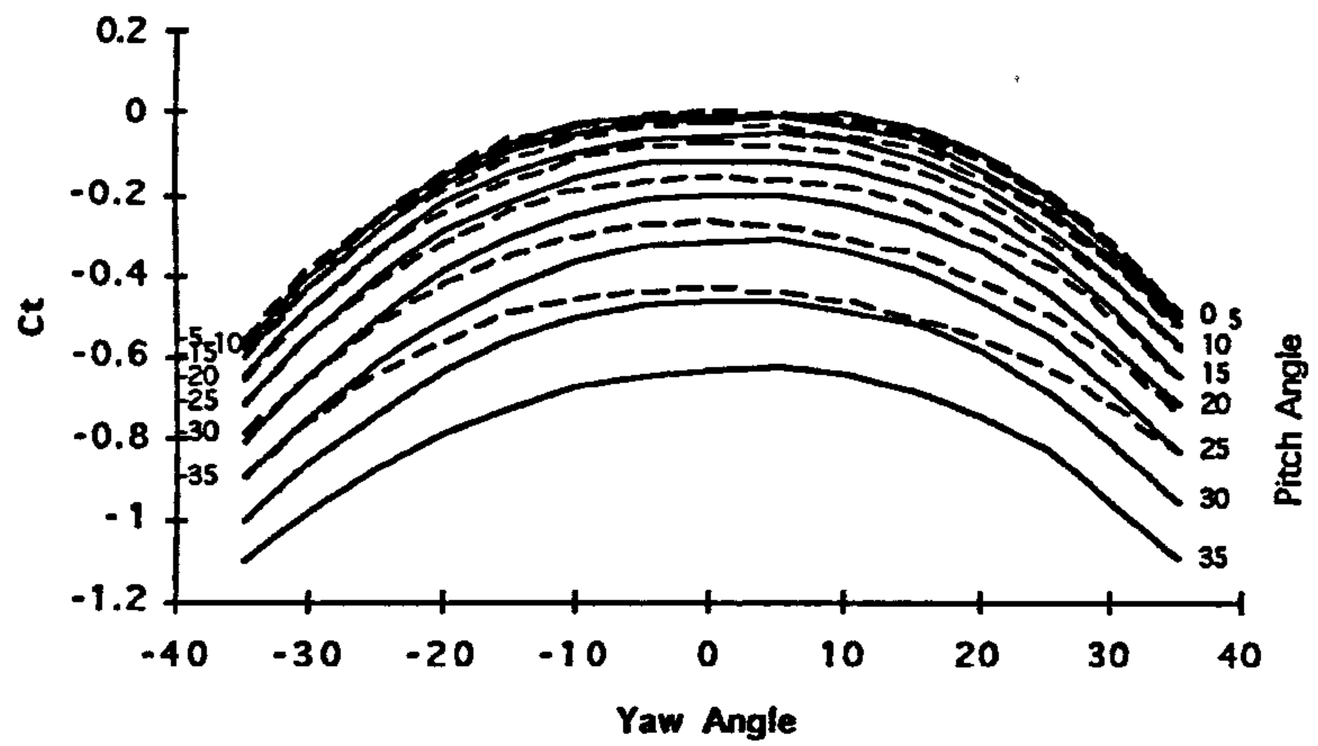

c) Static Pressure Coefficient.

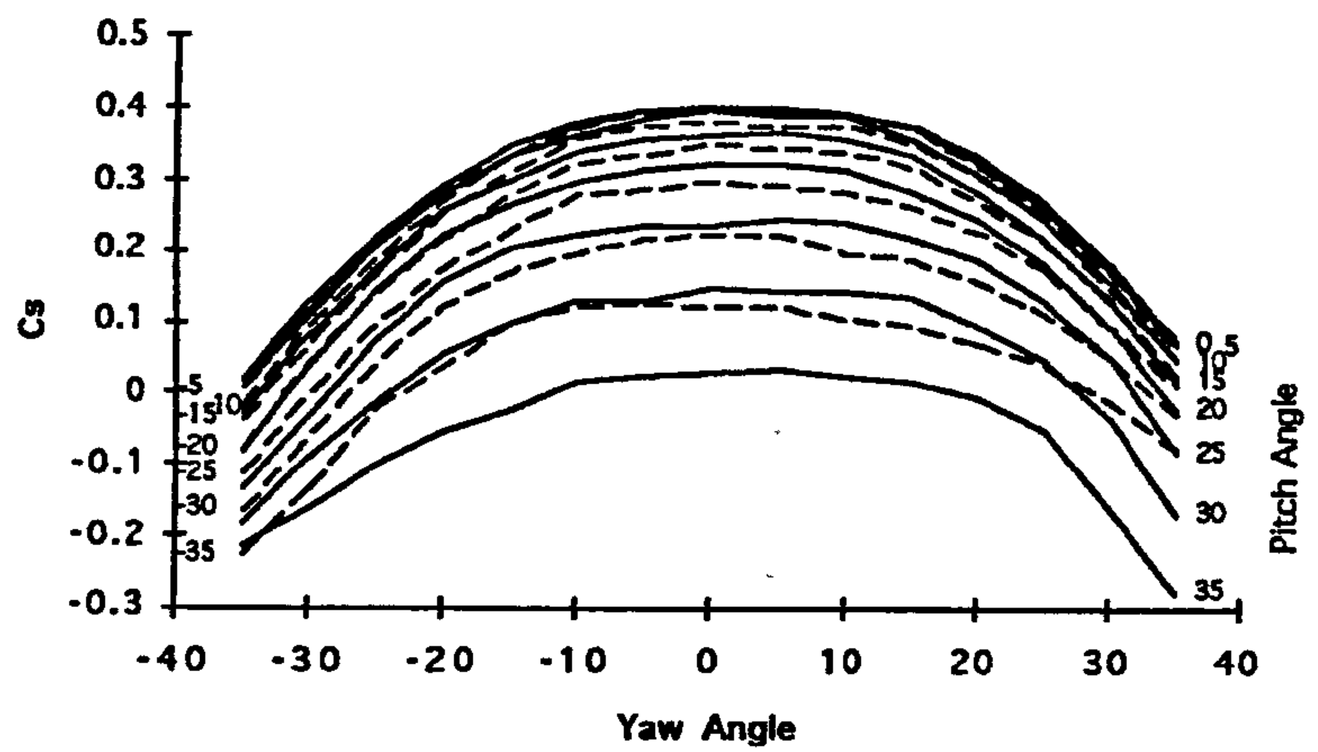

Figure 4.8 Iterative Algorithm used to Calculate Flow Angles.

a) Initial Guess

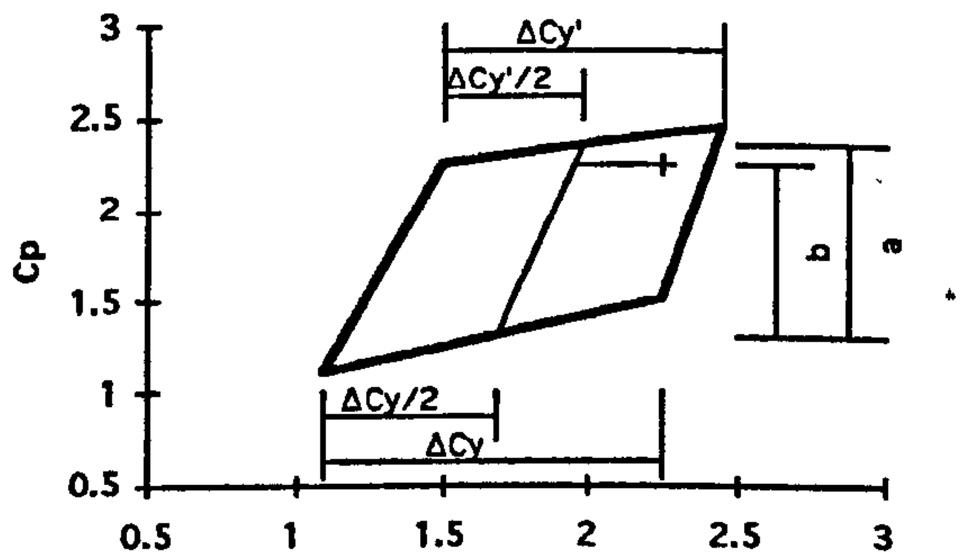

b) Second Half of Iteration 1

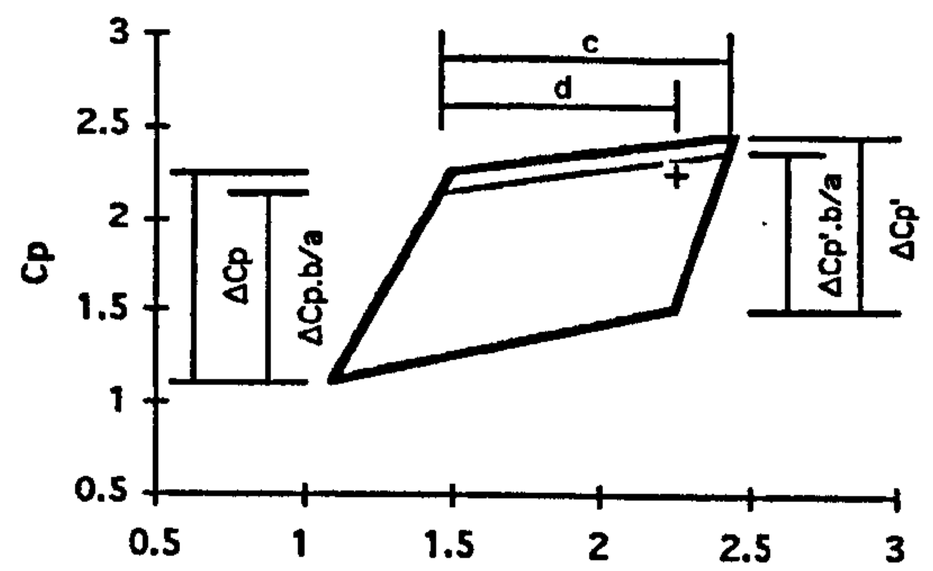

c) First Half of Iteration 2

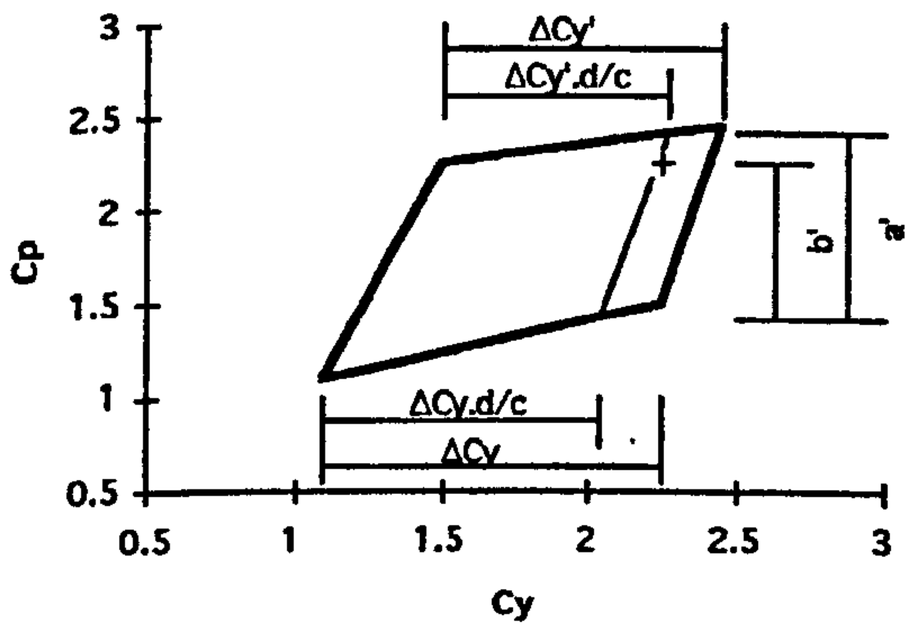

d) Second Half of Iteration 2

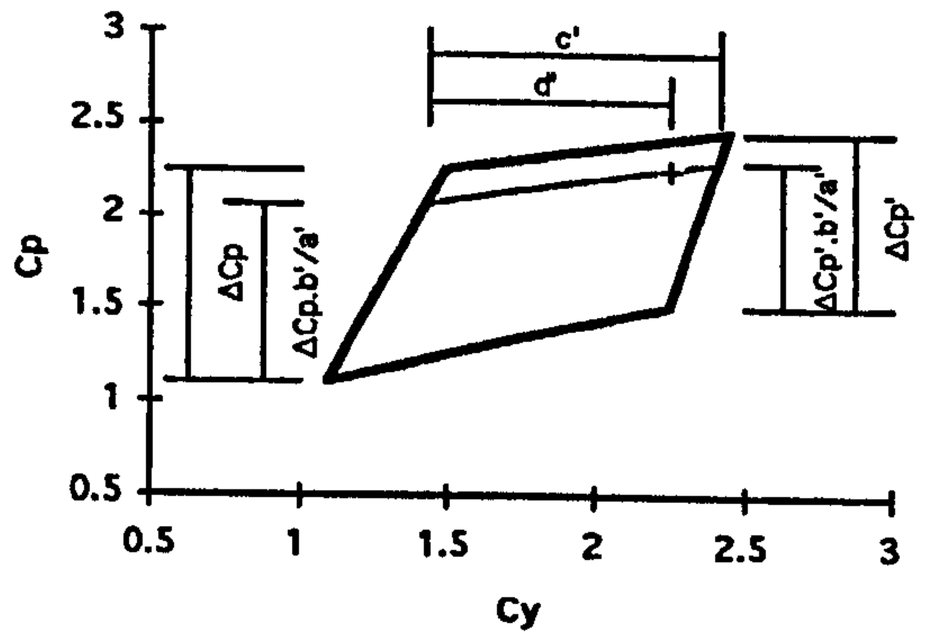

e) Both Iterations.

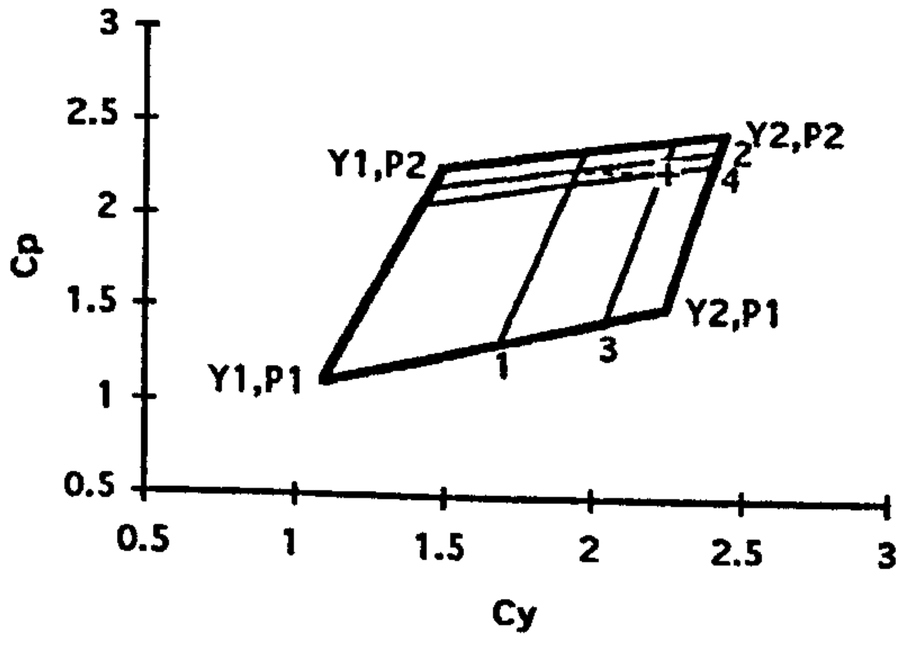

Figure 4.9 Inlet Total Pressure Non-uniformity at the Reference Probe Location.

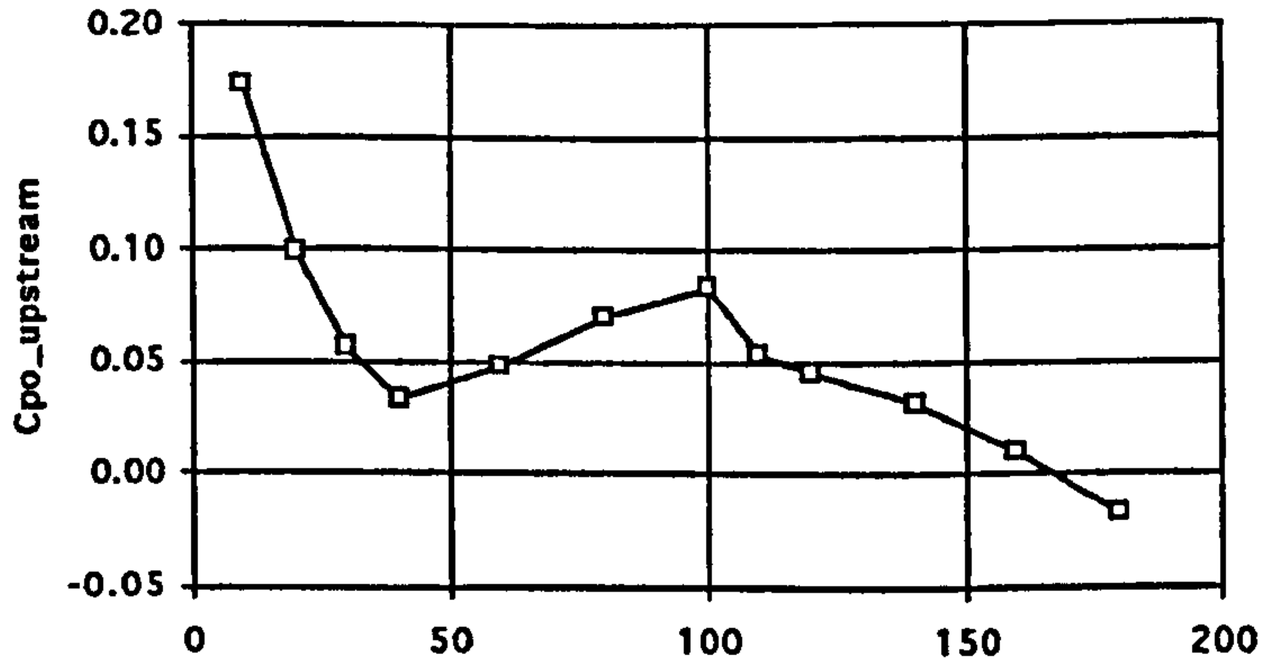

Figure 4.10 Variable Convention for Equations 4.13 to 4.20

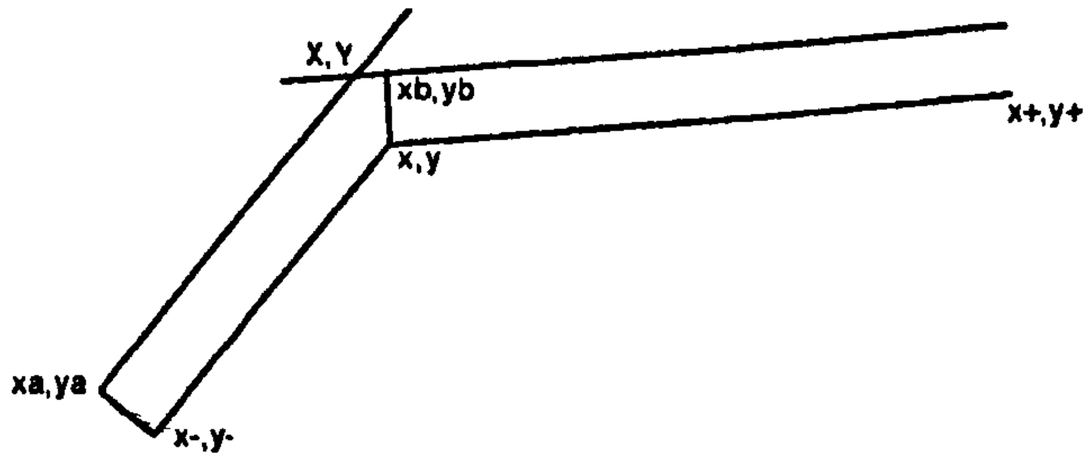

5 Repeat of Datum Case.

5.1 Introduction.

Investigation into the inlet total pressure profile revealed a total pressure deficit outside the boundary layer. As no previous work on this cascade has reported this, and to remove any uncertainties due to surface roughness (the profiled end-walls were to be made from machined polyurethane foam, varnished and sanded smooth, whereas all previous data have been taken with a perspex end-wall) it was thought necessary to repeat the datum case (flat wall) measurements. Also, the upstream reference probe was re-positioned to ensure a zero total pressure reading at Slot 10, mid-span mid-pitch. The inlet total pressure profile was measured with the new reference probe position, and traverses were carried out at Slots 1, 6, 8 and 10. The results of these traverses are presented in this chapter.

A full set of repeat CFDS calculations were carried out for comparison with the experimental data and these are discussed here. Due to the large size of the CFDS data files, these were not available from previous researchers.

5.2 The CFD Code.

The Rolls-Royce pressure correction CFD code, CFDS, was used for modelling the flow (and for design purposes later). Two grids were used for flow calculations. Both grids were identical in layout, having a letter box layout (i.e. an H type grid but with the blade in the centre and unbroken periodic boundaries at both top and bottom of the grid). The coarse grid has 75 axial, 27 tangential and 18 (half-span) spanwise grid points (36450 total) and the fine grid has 89 axial, 38 tangential and 29 (half-span) spanwise grid points (98078 total). Figure 5.1 Shows the coarse grid. The mixing length turbulence model used (due to Moore & Moore [1985]) is based on Prandtl's formulation for the length scale within a shear layer:

$$L = \min(\kappa y, \lambda \delta) \qquad \text{Equation 5.1}$$

where κ=0.41, λ=0.08 and δ is the thickness of the shear layer. Outside the shear layer the effect of free-stream turbulence is allowed for by varying L linearly to a specified free-stream length scale at a slope no greater than κ. The turbulent viscosity is then set by:

$$\mu_T = \rho L^2 S F_{vd}^2 \qquad \text{Equation 5.2}$$

where ρ is the density, S the strain rate and F_{vd} the Van Driest damping function. The inlet length scale has been reduced from 9.3mm to 0.93mm after Moore and Gregory-Smith (1996) to improve modelling of the passage vortex.

Inlet boundary conditions were based on the data from Table 4.2, and the boundary layer profile used was that found by Moore [1995]. This is essentially the same as that shown in Figure 5.14 if the data up to the maximum negative C_{Po} is considered (approximately 50mm from the end-wall).

5.3 CFD Results.

5.3.1 Blade and End-Wall C_P Values.

Figures 5.2 a and b show the end-wall static pressure coefficient contour plot for the planar wall for both CFD grids used. Comparing Figure 5.2 a and b, it can be seen that the pressure distribution is not changed significantly when the grid resolution is increased. This is to be expected as pressure field effects are first order and as such can be easily captured by a coarse grid. Blade C_P plots are given for the fine grid as this resolved the secondary flows with more accuracy, and hence the radial variations in pressure should be more accurately resolved. These are presented in Figures 5.3

5.3.2 Area and Pitch Averaged Results.

Figures 5.4 to 5.7 show mass weighted pitch averaged loss, yaw and pitch angles and secondary kinetic energy coefficient at Slots 1, 6, 8 and 10 for both CFD grids. It should be noted that the CFD Data has been interpolated onto the same grid as the experimental data for the purpose of integration to enable more accurate comparisons.

Area averaged total pressure loss coefficient and secondary kinetic energy coefficients at Slots 1, 6 and 8 are presented in Table 5.1 for the fine CFD grid, along with mixed out loss coefficients at Slot 10. Table 5.2 shows the net loss at Slot 10. The very slight negative mid-span loss at Slots 6 and 8 is probably due to the interpolation of the CFDS data onto the experimental grid for integration as this is not displayed by uninterpolated data.

Table 5.1 Area Averaged CFD Data Through the Cascade.

	Total Pressure Loss			Mixed Out Loss			
	Full	Mid-span	Secondary	Full	Mid-span	Secondary	C_{SKE}
Slot 1	0.015	0.000	0.016	0.016	0.000	0.016	0.0001
Slot 6	0.039	-0.002	0.041	-	-	-	0.0227
Slot 8	0.048	-0.010	0.059	-	-	-	0.0359
Slot 10	0.211	0.153	0.058	0.244	0.163	0.081	0.0218

Table 5.2 Net CFD Losses Through the Cascade.

	Full	Mid-span	Secondary
Total Pressure Loss	0.195	0.153	0.042
Mixed Out Loss	0.228	0.163	0.065

5.3.3 Contour Maps and Secondary Velocity Vectors.

Secondary velocity vectors and area plots for C_{Po}, yaw angle and C_{SKE} are presented for all 4 Slots in Figures 5.8 to 5.11 for the fine grid, and Slot 10 data for the coarse grid can be seen for comparison in Figure 5.12. From Figures 5.11 and 5.12, the improvement in the capture of the vortex can be seen from the shift of the vortex core from 50mm from the end-wall to 60mm from the end-wall.

5.4 Experimental Results

5.4.1 End-Wall Cp Values.

The end-wall pressure distribution was measured using tappings of 0.8mm internal diameter, and Figures 5.13 a and b show contours of the end-wall static pressure for the experimental data and fine CFD grid. Comparing Figure 5.13 with Figure 5.2 a shows that both CFD grids give an accurate representation of the end-wall static pressure, although the -1.0 contour intercepts the blade pressure surface further upstream in the experimental data, and exits the upstream boundary of the plot area before re-entering to intercept the suction surface near the leading edge. This would indicate a higher acceleration of the flow in the CFD calculation.

Due to the blade pressure tappings being severely blocked, and the problems associated with the radial arrangement of the pressure tappings for comparison later, measurement of blade pressures was unfortunately not possible. However, after comparison of the end-wall static pressures and the flow field it would seem safe to assume that the blade static pressures are achieved with reasonable accuracy at least by the fine grid CFD.

5.4.2 Area and Pitch Averaged Results.

Figure 5.14 shows the measured inlet boundary layer. As stated previously, the negative C_{Po} region between 25mm and 125mm has not been noted by previous researchers. However the presence or absence of this region is not clear from previous research. and is thought to be caused by the upstream turbulence grid. This region can be compensated for by calculating net loss (outlet loss -inlet loss) which shows the more important loss increase through the blade row rather than just the exit loss. Inlet loss is calculated at 100% Cax upstream of the leading edge.

Figures 5.15 to 5.18 show mass weighted pitch averaged loss, yaw and pitch angles and secondary kinetic energy coefficient at Slots 1, 6, 8 and 10 for the experimental data and both CFD grids. Throughout the cascade, it is clear that whereas the fine grid resolves the secondary flow quite well, the coarse grid is not sufficiently accurate to provide any useful information.

Area averaged total pressure loss coefficient and secondary kinetic energy coefficients (averaged over a full half-span) at Slots 1, 6 and 8 are presented in Table 5.3, along with mixed out loss coefficients at Slots 1 and 10. Table 5.4 shows the net loss at Slot 10.

Table 5.3 Area Averaged Experimental Data Through the Cascade.

	Total Pressure Loss			Mixed Out Loss			
	Full	Mid-span	Secondary	Full	Mid-span	Secondary	C_{SKE}
Slot 1	-0.002	0.016	-0.019	-0.002	0.016	-0.018	0.0005
Slot 6	0.013	0.008	0.005	-	-	-	0.0055
Slot 8	0.006	-0.001	0.007	-	-	-	0.0115
Slot 10	0.136	0.076	0.060	0.157	0.079	0.078	0.0192

Table 5.4 Net Area Averaged Experimental C_{Po} at Slot 10.

	Full	Mid-span	Secondary
Total Pressure Loss	0.148	0.068	0.080
Mixed Out Loss	0.169	0.071	0.098

The high value of mid-span loss and the near zero full loss at Slot 1 is caused by the inlet boundary layer profile described earlier and shown in Figure 5.13 a.

Comparing the data at Slots 6 and 8, the rolling up of the inlet boundary layer is clearly seen. At Slot 6 (Figures 5.16) a very small amount of under-turning is seen, although the predominant effect is the overturning of the boundary layer due to the action of the imposed blade pressures near the end-wall on the inlet boundary layer which has only just started to roll up into a weak vortex. By Slot 8 (Figures 5.17), a significant amount of under-turning is also present as the overturning seen at Slot 6 interacts with the blade suction surface and rolls up into a strong vortex. The fine grid CFD captures these effects accurately although at Slots 8 and 10 the CFD over predicts the flow deviations. Although at Slot 10 (Figures 5.18) the CFD still over predicts the mid-span loss, this can be put down to errors in the CFD modelling of the blade boundary layers and wake as discussed below, unlike within the blade row where the blade boundary layers are not included in the pitchwise integration of the experimental or CFD data. The differences in yaw angles shown at Slots 1, 6 and 8 are probably caused by a number of

errors. These could include the method used to compensate the experimental yaw angles, as this involves assumptions based on the CFD boundary layers which are not correctly modelled. The CFD yaw angles could also be incorrect due to the fully turbulent boundary layer model [Moore, 1995].

Comparing the current experimental data from the cascade with previous research from Biesinger [1993] and Moore [1995] (Figures 5.19 a and b), good agreement is seen for both yaw angle and C_{Po}. Overall, the losses are lower than measured by Biesinger, although this is possibly due to a reduction in cascade speed caused by the relocation of the reference probe.

Figure 5.20 shows the growth of secondary kinetic energy coefficient through the cascade for the Fine grid CFD and the experiments. Whilst is appears that the CFD over predicts the growth of secondary flow up to Slot 6, it under predicts the growth from Slot 6 to Slot 8. The CFD also under predicts the mixing out of the secondary flow between Slots 8 and 10.

Area averaged total pressure loss coefficient and secondary kinetic energy coefficients at Slots 1, 6, 8 and 10 are presented in Table 5.3 for the experimental data, along with mixed out loss coefficients at Slot 10. The CFD significantly over predicts the loss at Slot 10. This is due to the higher mid span loss, confirmed by the secondary loss being more accurately predicted than overall loss. The high mid-span loss is probably due to the assumption in the CFD code that the flow is fully turbulent, whereas regions of laminar flow which have been shown to exist on both the blade surfaces and end-wall in Chapter 3 and by Moore & Gregory-Smith [1996] will act to reduce the overall loss. Also, numerical errors within the CFD could cause errors in the loss predictions. It is also possible that the resolution of the wake by the experimental measurement grid, and interpolation of the CFD data onto the experimental grid, have an effect on the loss.

5.4.3 Contour Maps and Secondary Velocity Vectors.

Figures 5.21 to 5.24 show velocity vectors and area plots for C_{Po}, yaw angle and C_{SKE} for Slots 1, 6, 8 and 10. Comparing these with Figures 5.8 to 5.11, the fine grid CFD captures the secondary flow with reasonably accuracy, as also seen previously with the pitch averaged curves. The passage vortex, suction surface horseshoe vortex and the small counter-vortex at the end-wall are all predicted in their correct positions, although the passage vortex is predicted too close to the end-wall. The development of the passage vortex through Slots 6 and 8 is clearly visible from the secondary vectors and yaw angles, and the growth of the loss core can also be seen.

5.5 Conclusions

Whilst the change in position of the reference probe has changed the absolute values of loss, the flow-field is unchanged from previously reported research in this cascade. It is therefore highly likely that the non-uniformity in inlet total pressure existed for previous data from the cascade, even though it was not referenced directly. The effects of surface roughness do not seem to play a significant role in the flow development within the passage in comparison to the cross passage pressure gradients near the end-wall.

The coarse grid CFD resolved the static pressures within the cascade with reasonable accuracy, as did the fine grid. However, only the fine grid was able to resolve the flow within the passage accurately. From previous investigations into the grid dependency of solutions using different turbulence models and grid densities [Moore 1995], it is believed that the fine grid CFD solution is independent of the grid resolution. Two grids were used by Moore, a coarse grid which was identical to the fine grid used here and a fine grid having 99 axial, 55 tangential and 42 (half-span) spanwise grid points (228690 total). These two grids gave almost identical results for flow features at Slot 10, although the loss values for the fine grid were slightly higher mid-span. This was possibly caused by the near wall boundary layer treatment used due to the fine nature of the grid near the blade surfaces and end-wall. From Moore's results, and discussions with Rolls-Royce, it is believed that the solutions used in this study for flow features and surface static pressures are grid independent.

Figure 5.1 Coarse CFD Grid.

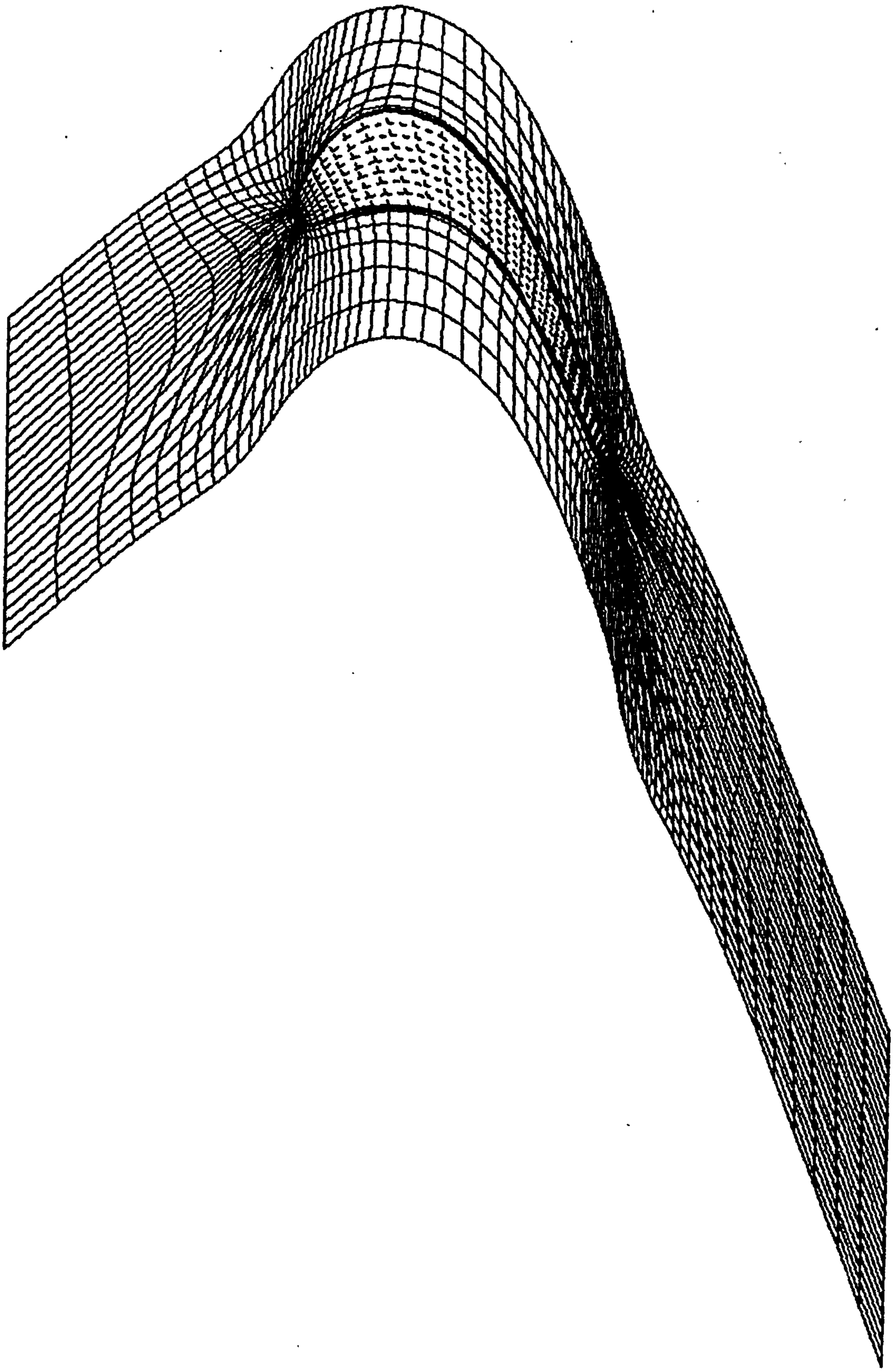

Figure 5.2 End-wall Cp Contours for both CFD Grids.

a) Coarse Grid.

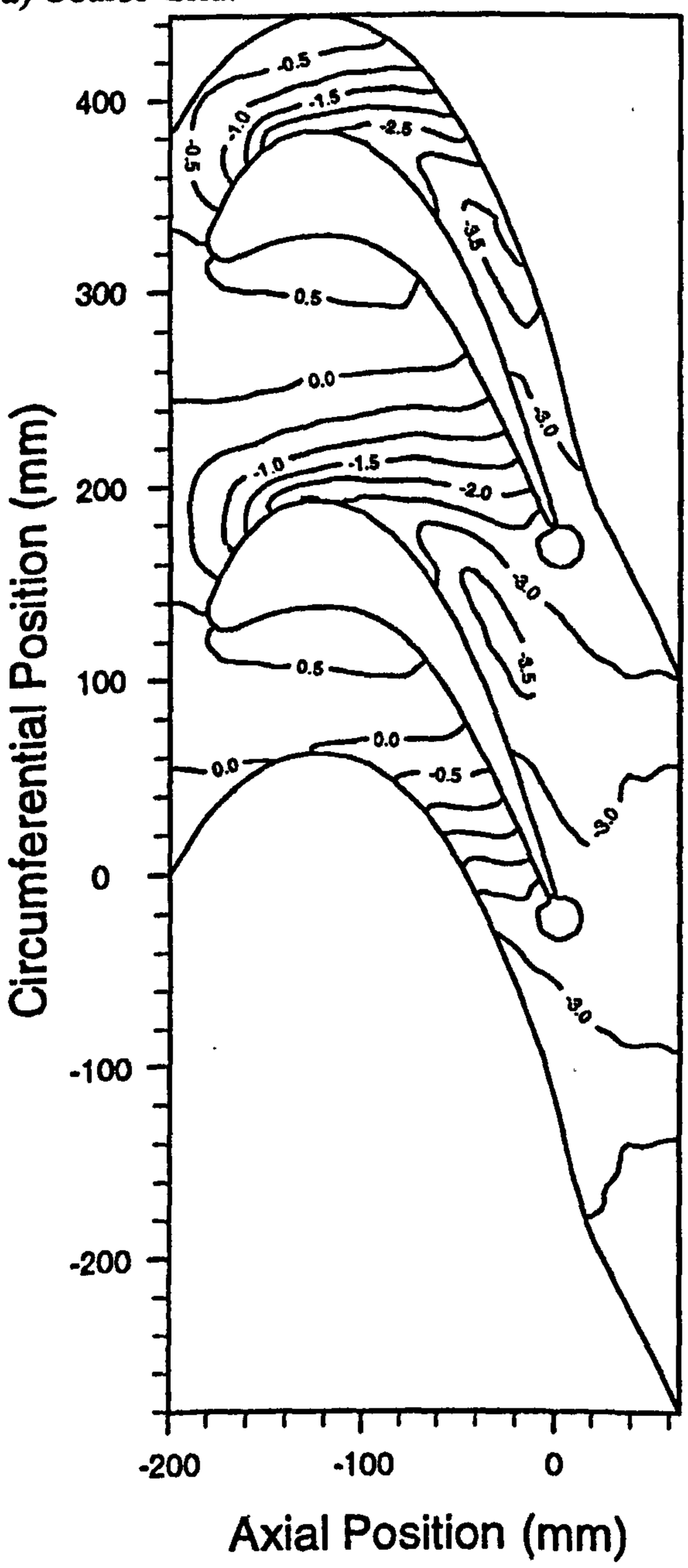

b) Fine Grid.

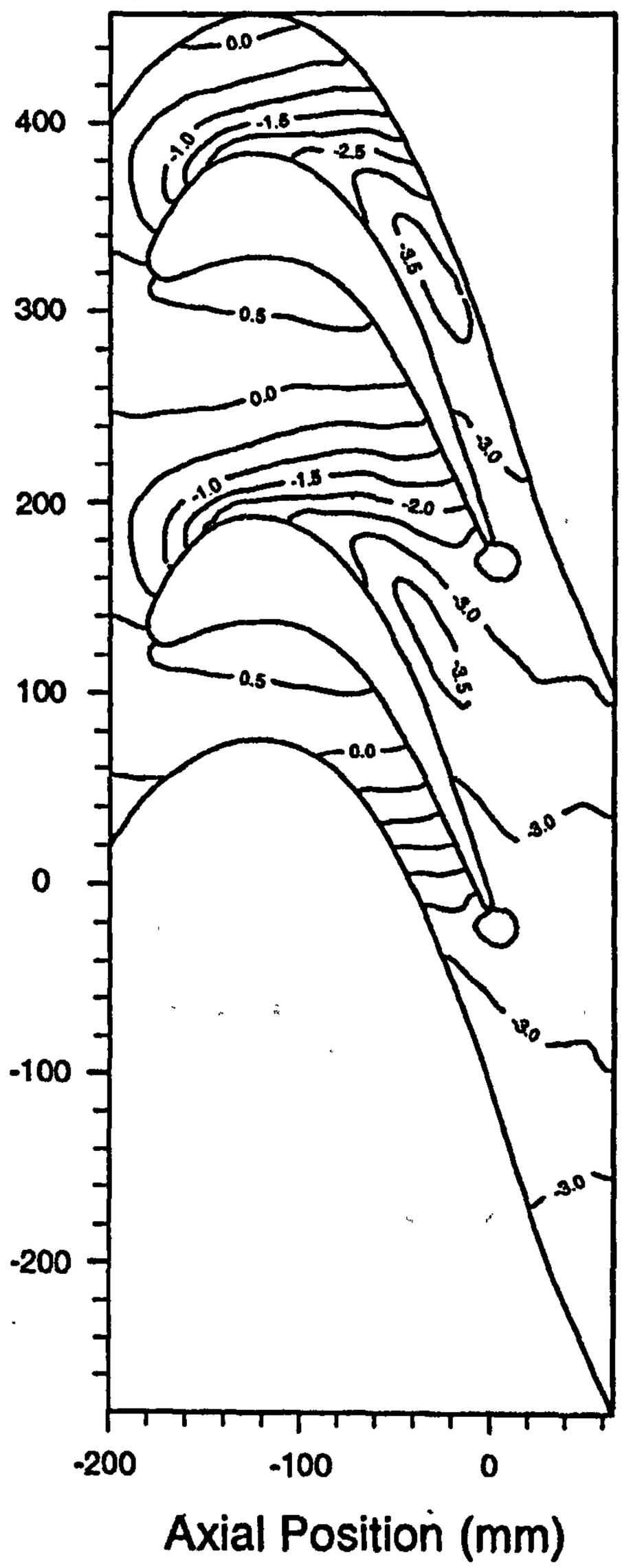

Figure 5.3 CFD Blade Cp Plots for the Fine Grid.

a) 0% Height.

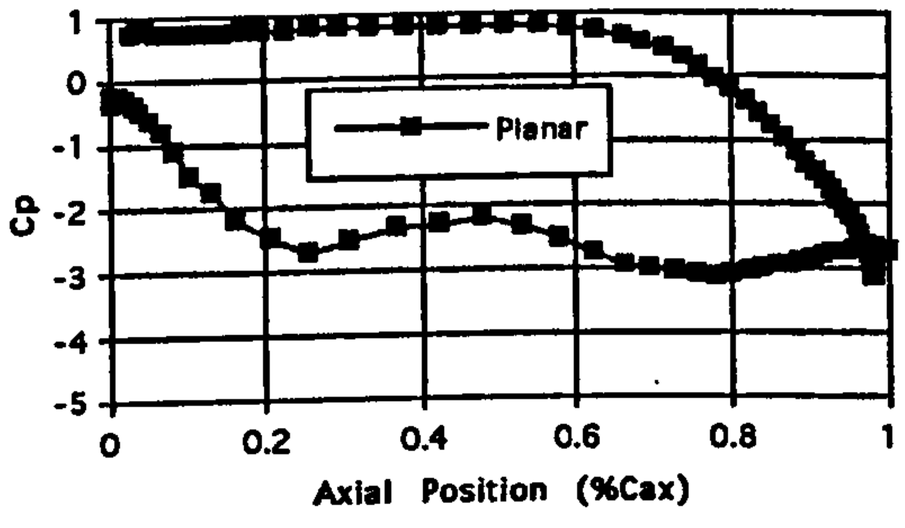

b) 4.65% Height.

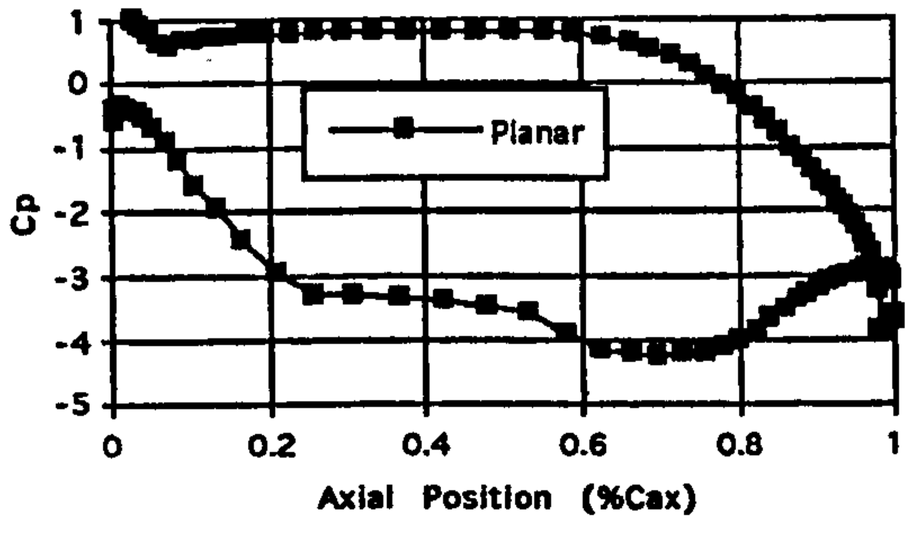

c) 10% Height.

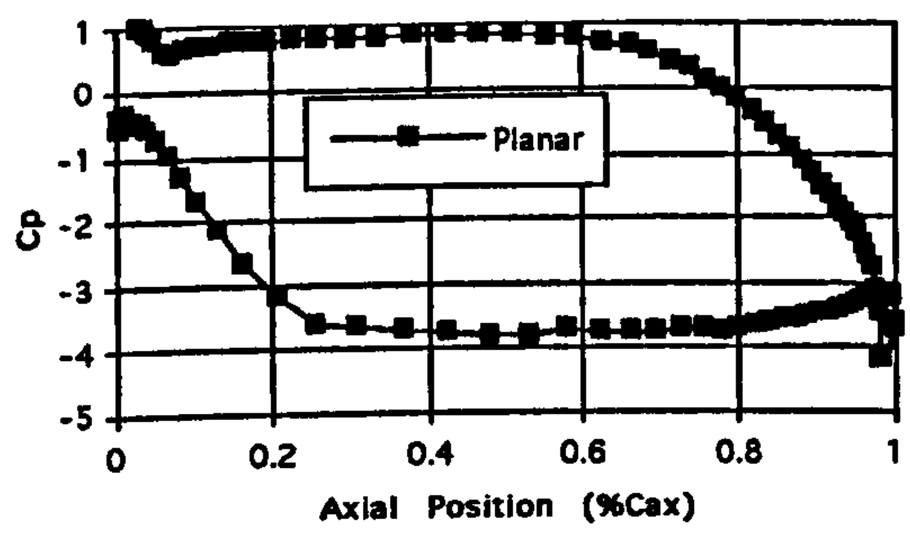

d) 15% Height.

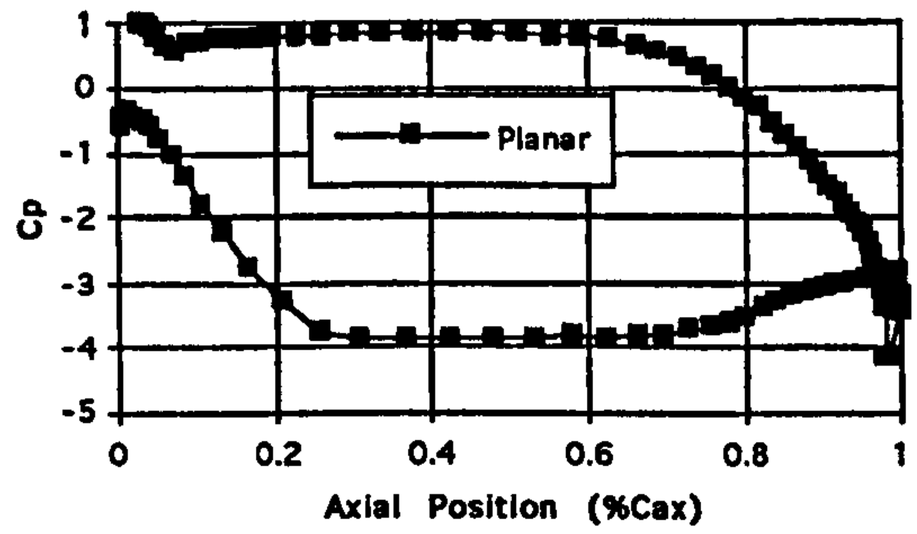

e) 20% Height.

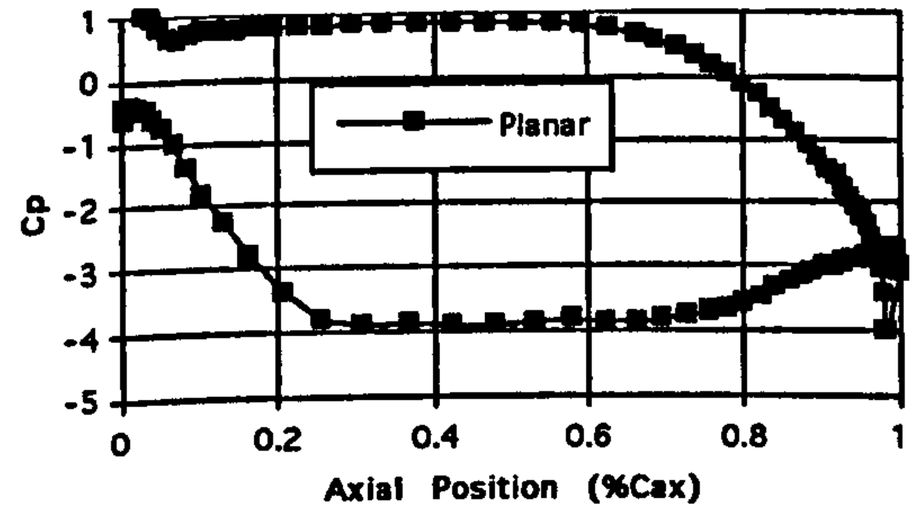

f) 50% Height.

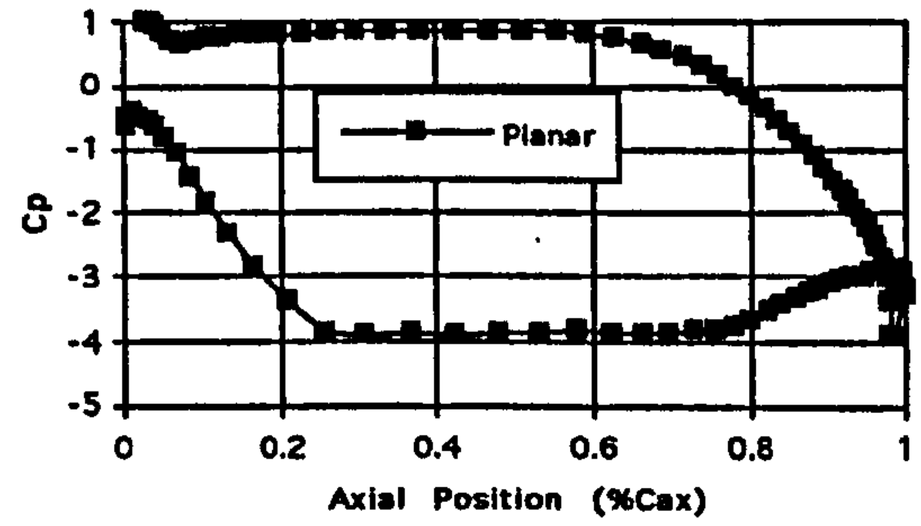

Figure 5.4 Pitch Averaged CFD Data at Slot 1 (Both Grids Shown).

a) Total Pressure Loss Coefficient.

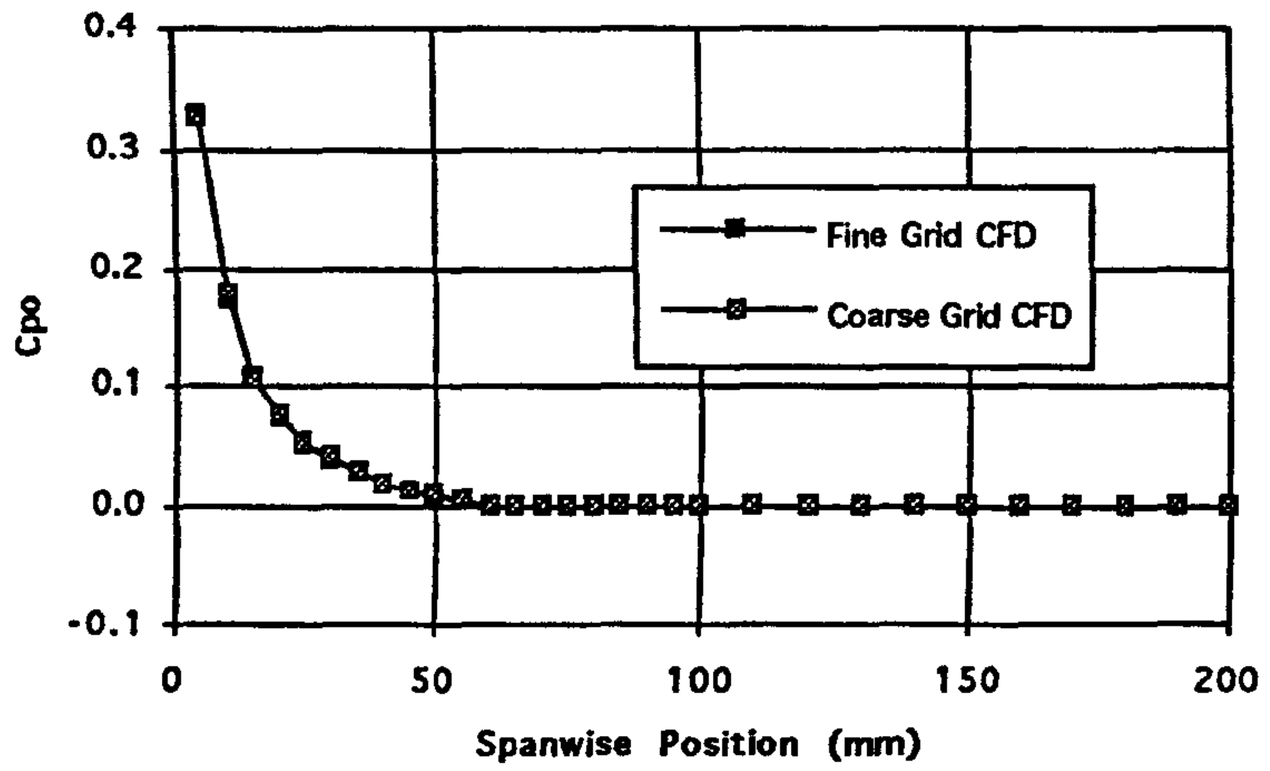

b) Yaw Angle.

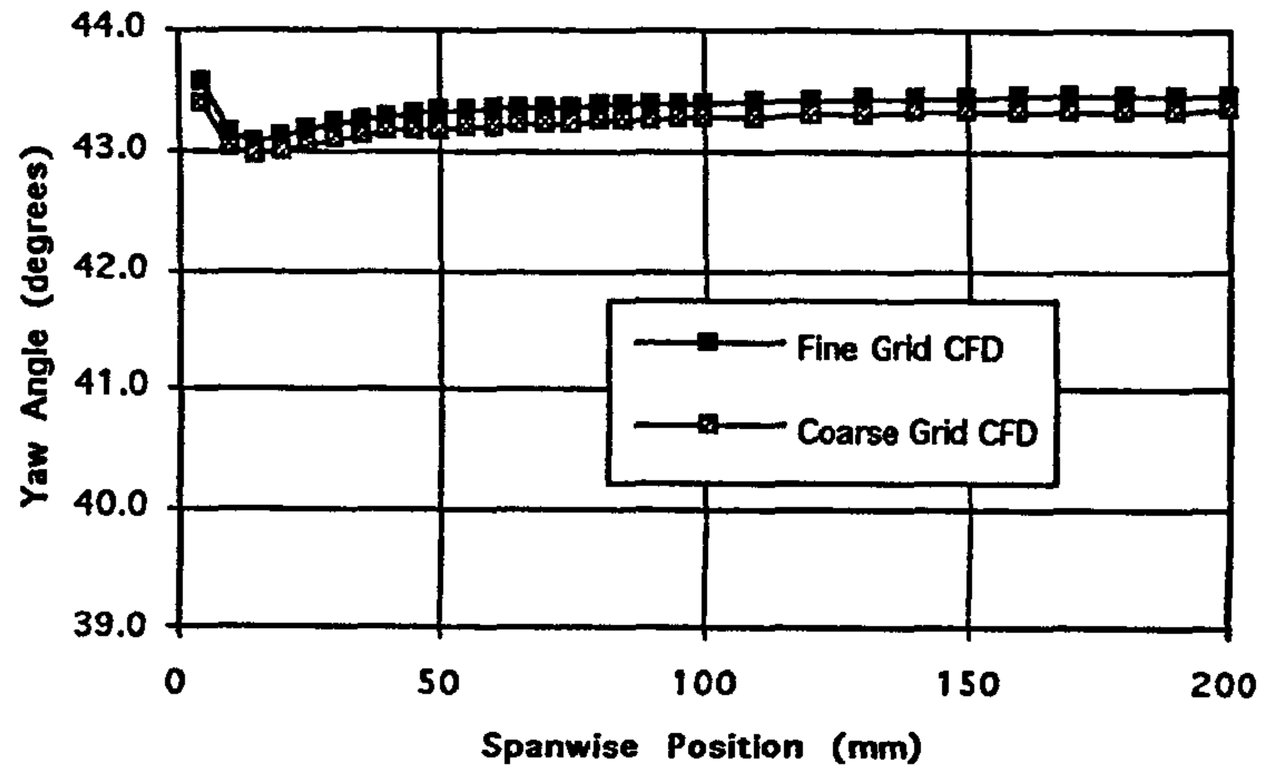

c) Pitch Angle.

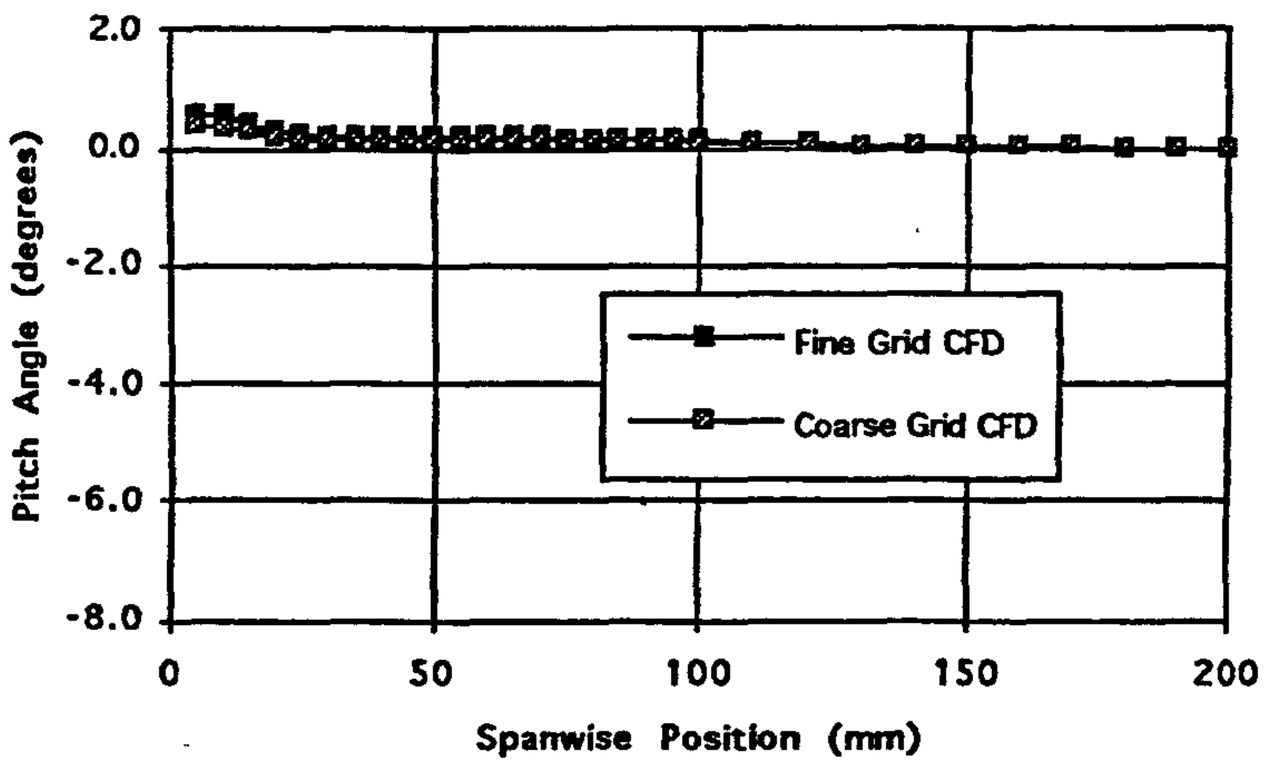

d) Secondary Kinetic Energy Coefficient.

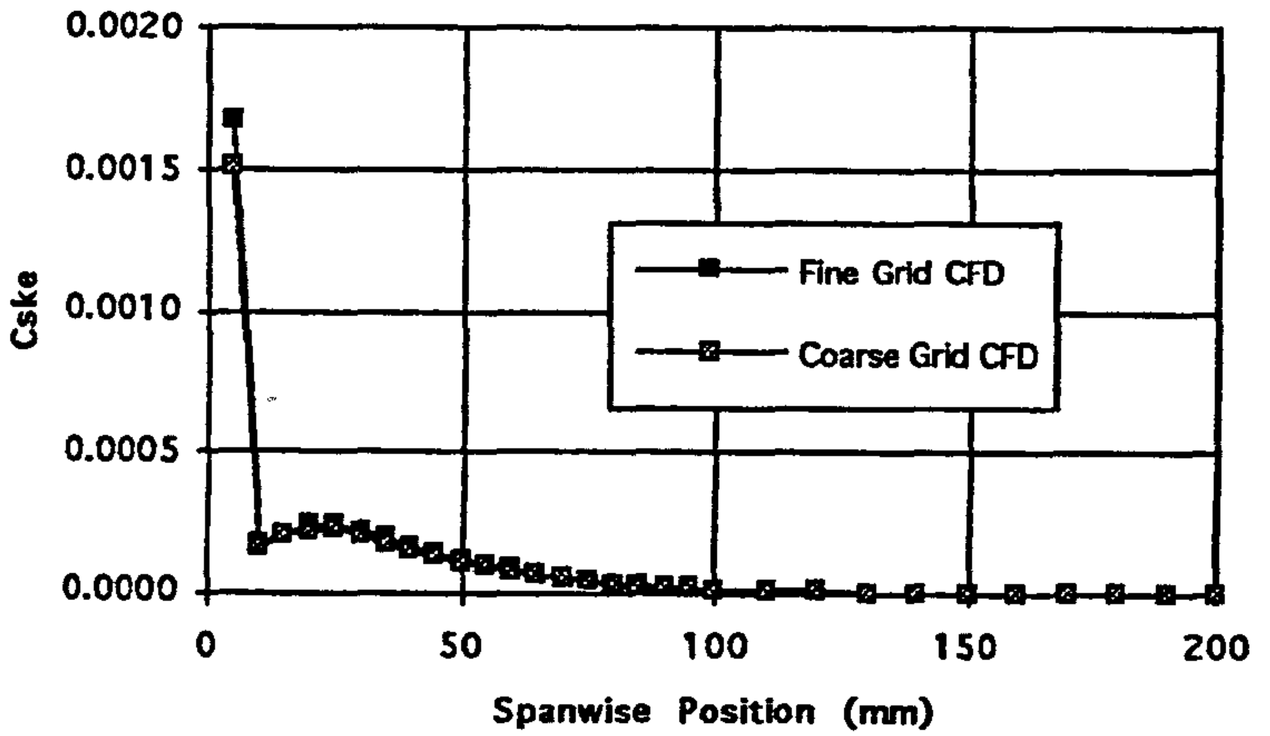

Figure 5.5 Pitch Averaged CFD Data at Slot 6 (Both Grids Shown).

a) Total Pressure Loss Coefficient.

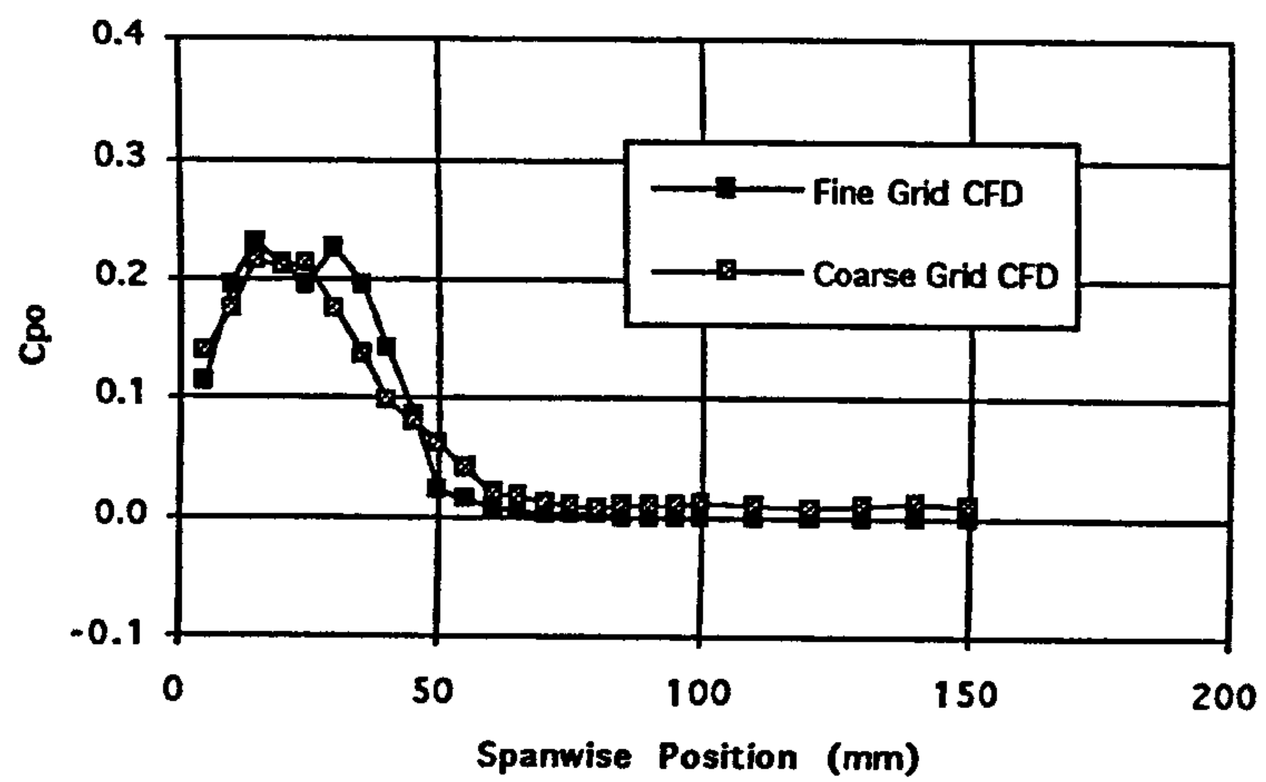

b) Yaw Angle.

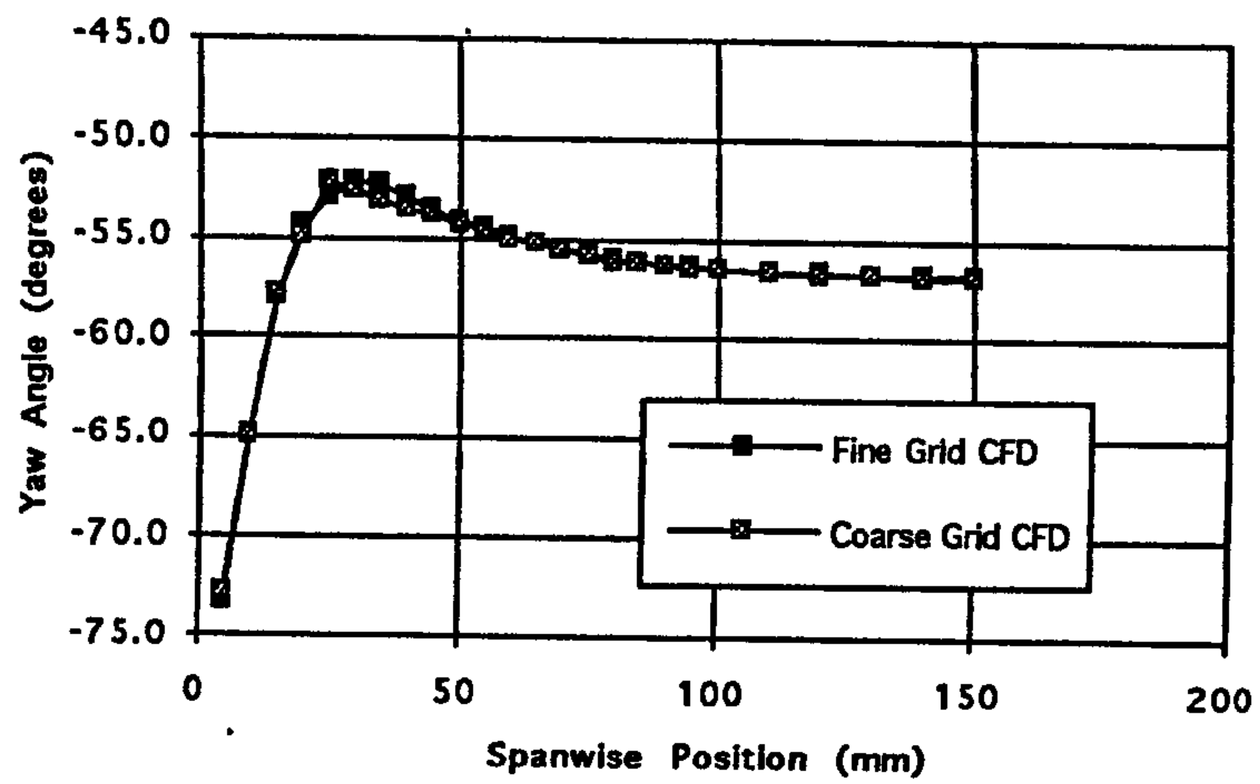

c) Pitch Angle.

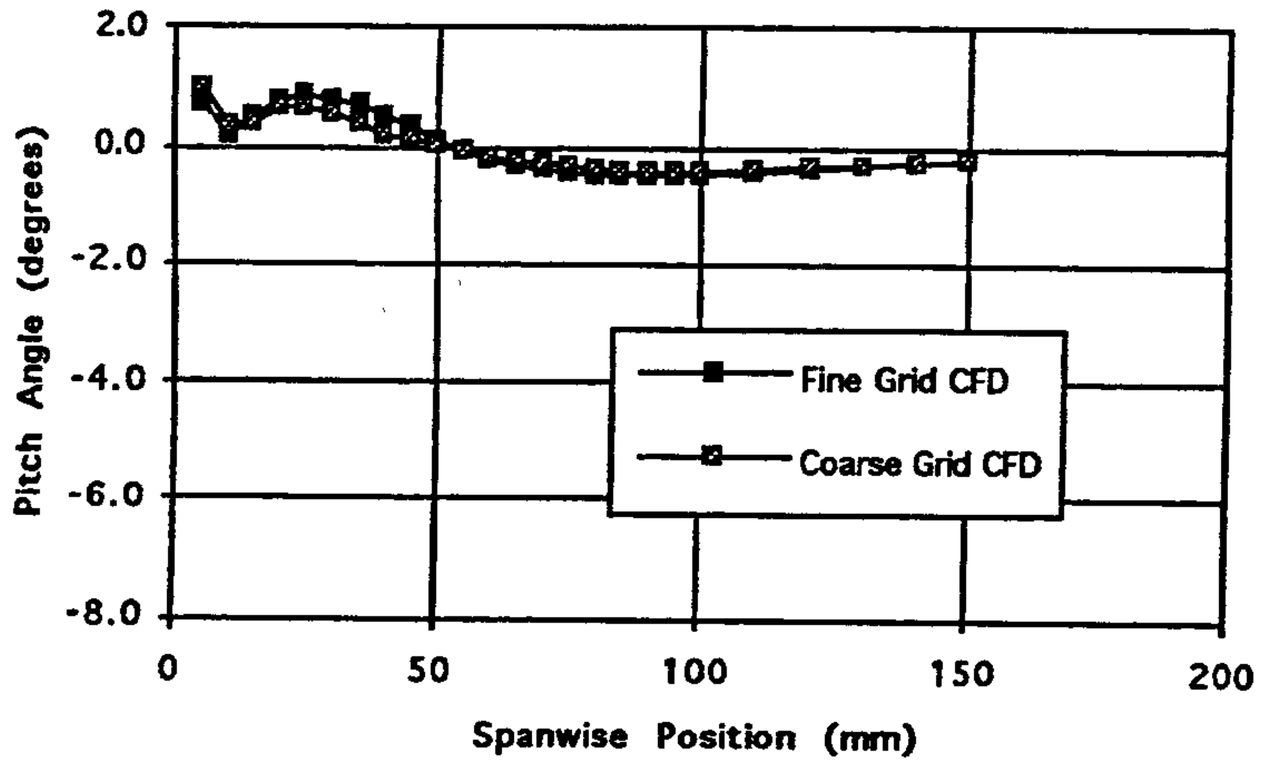

d) Secondary Kinetic Energy Coefficient.

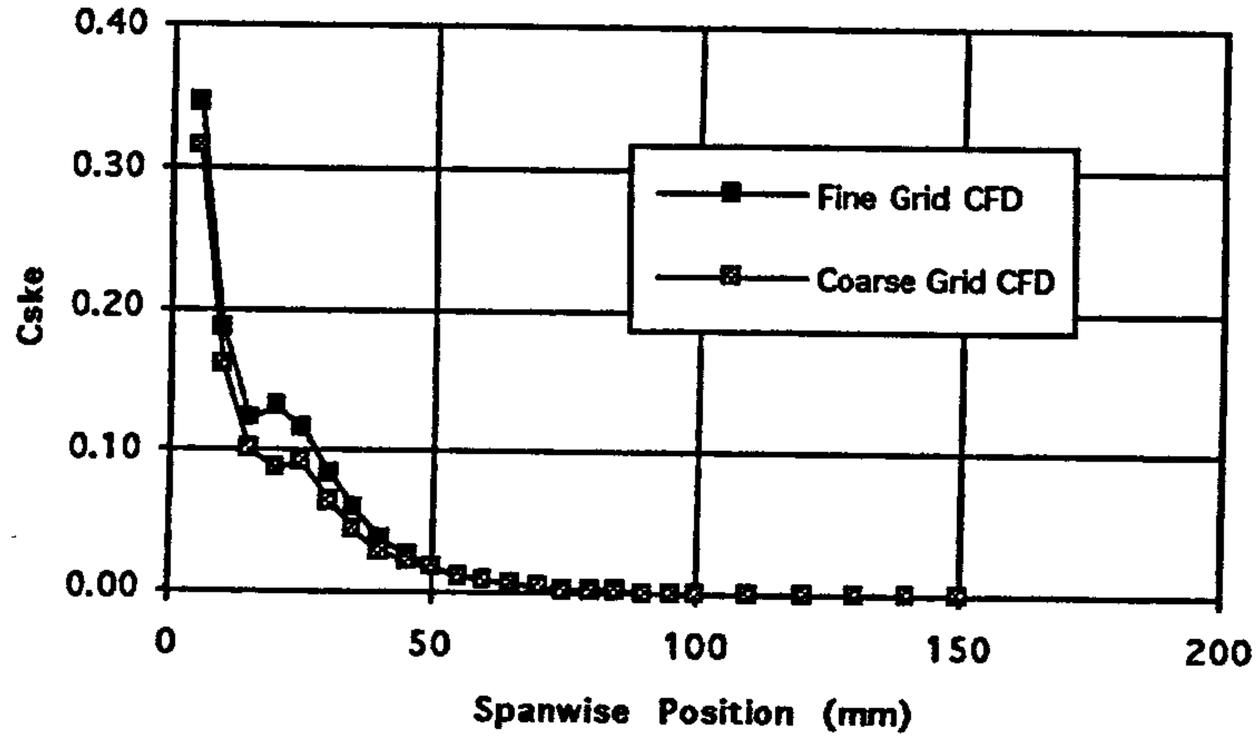

Figure 5.6 Pitch Averaged CFD Data at Slot 8 (Both Grids Shown).

a) Total Pressure Loss Coefficient.

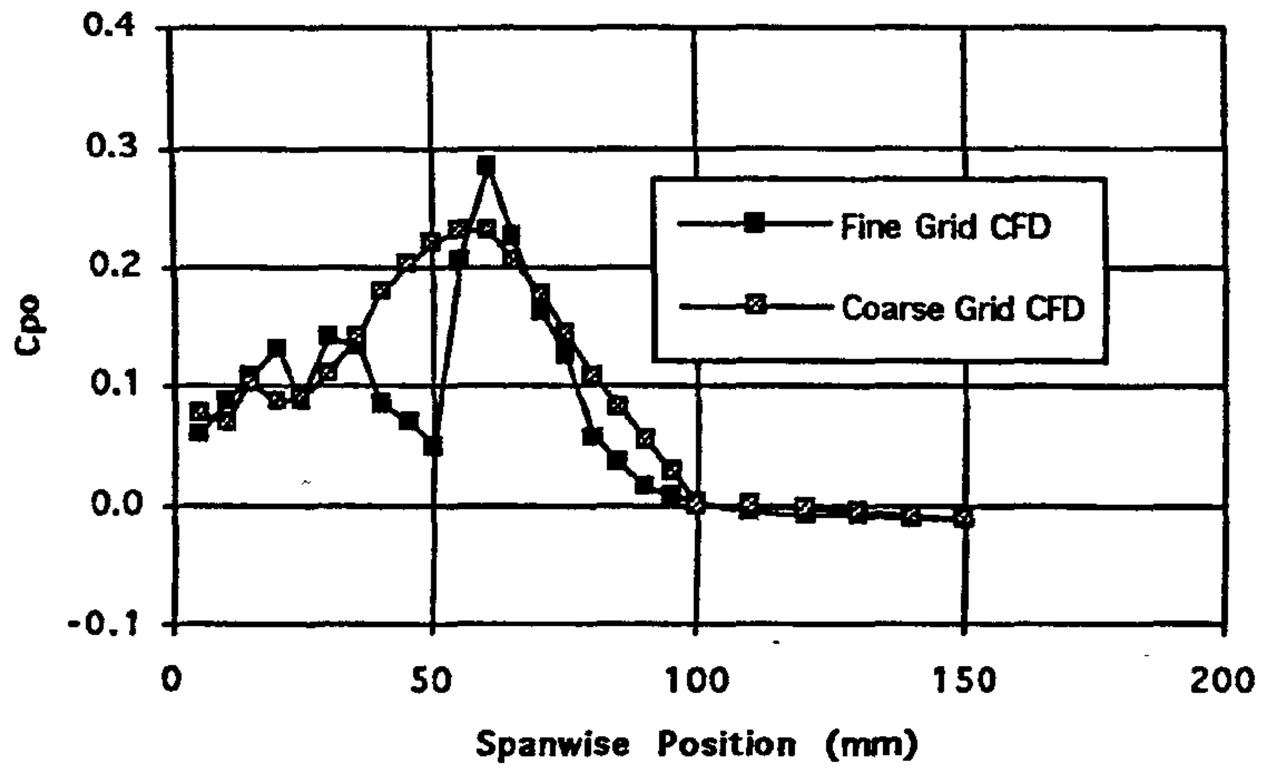

b) Yaw Angle.

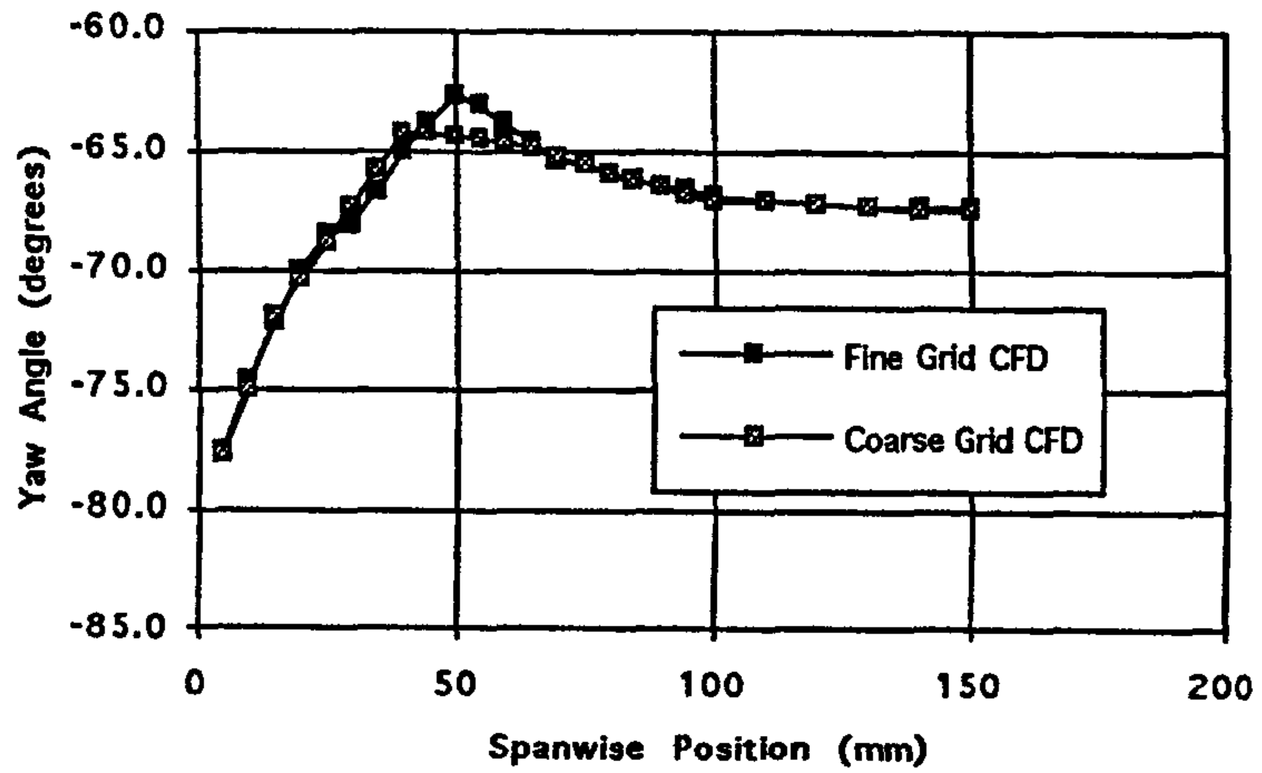

c) Pitch Angle.

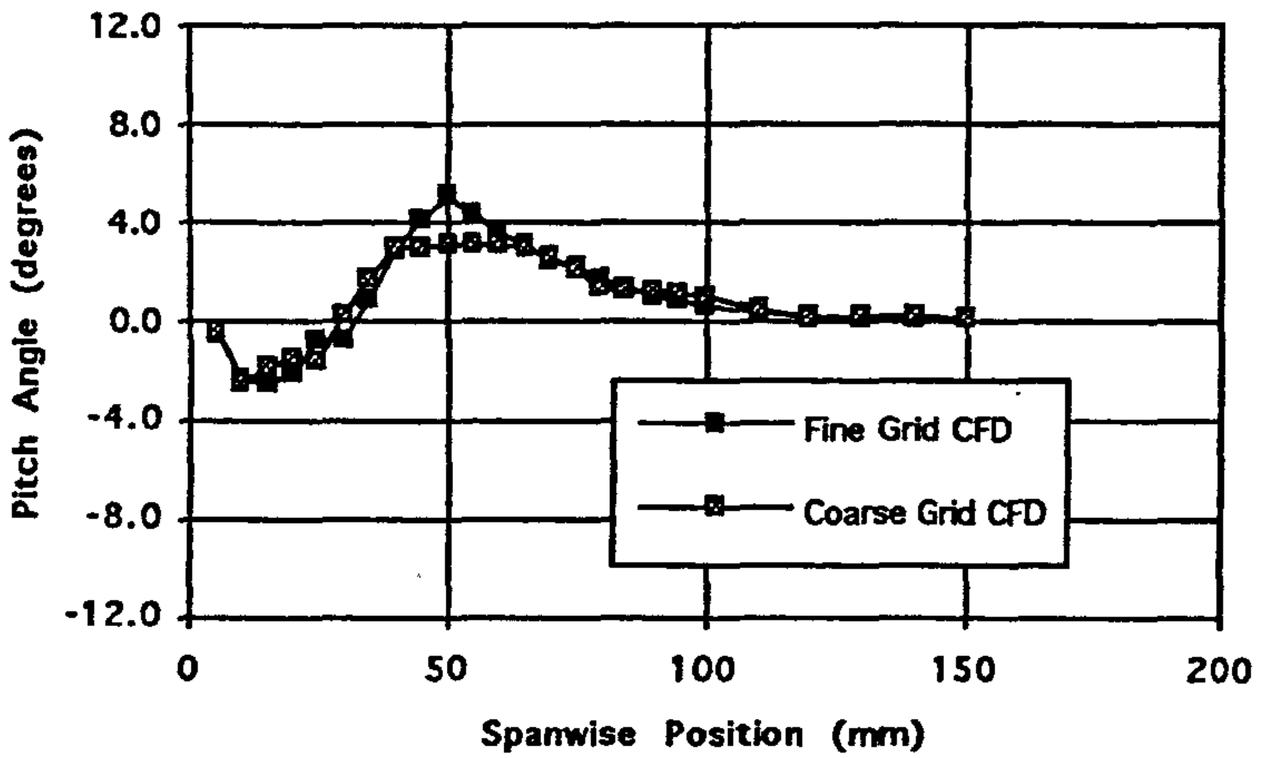

d) Secondary Kinetic Energy Coefficient.

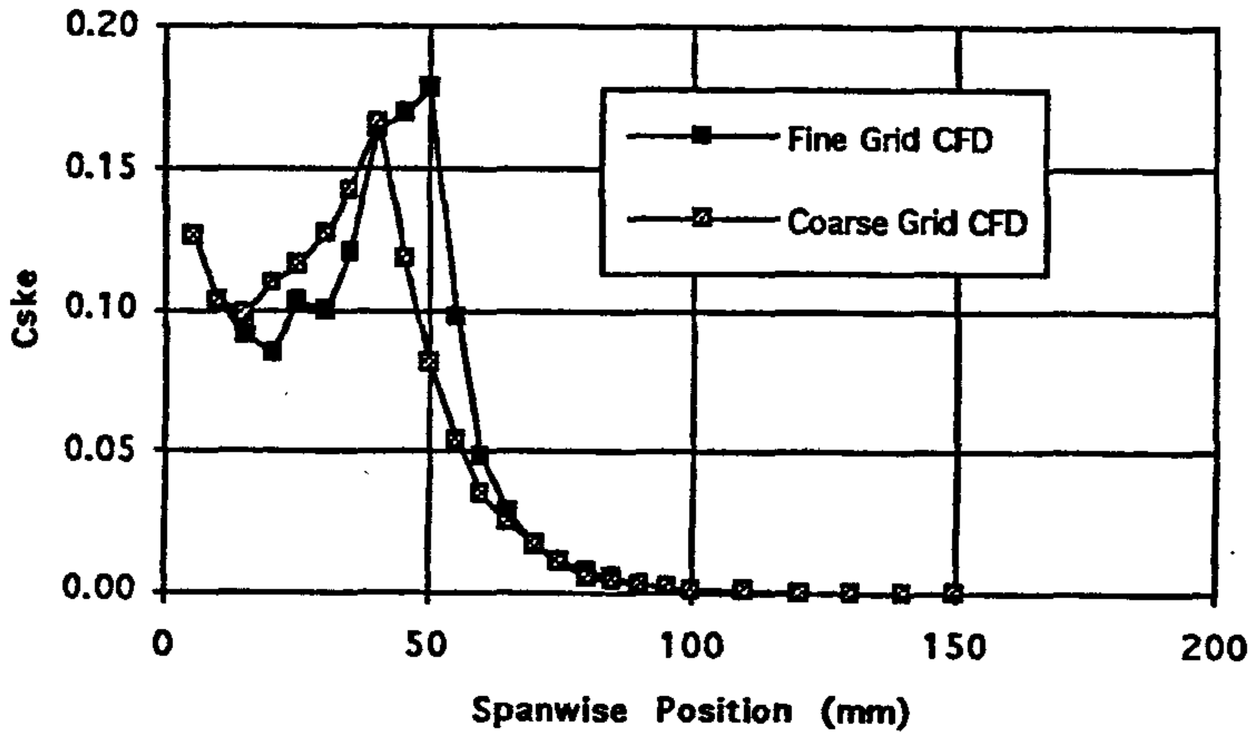

Figure 5.7 Pitch Averaged CFD Data at Slot 10 (Both Grids Shown).

a) Total Pressure Loss Coefficient.

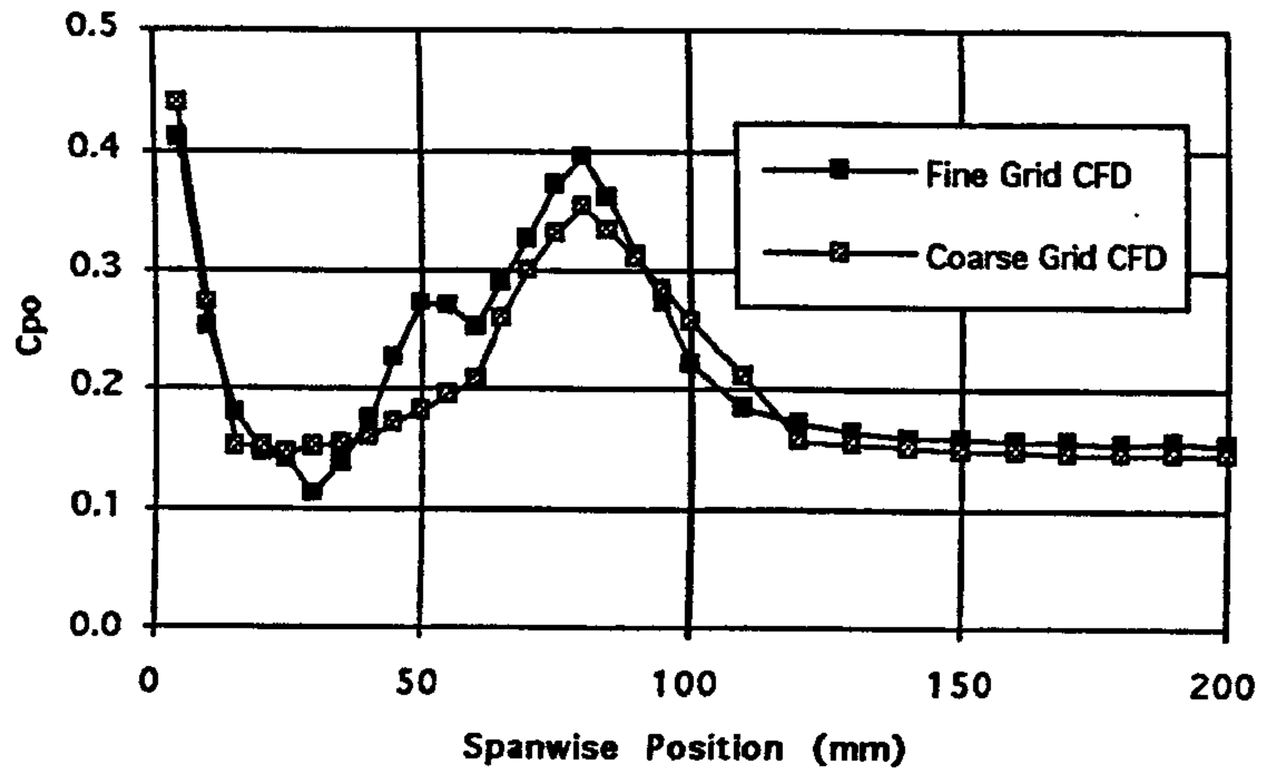

b) Yaw Angle.

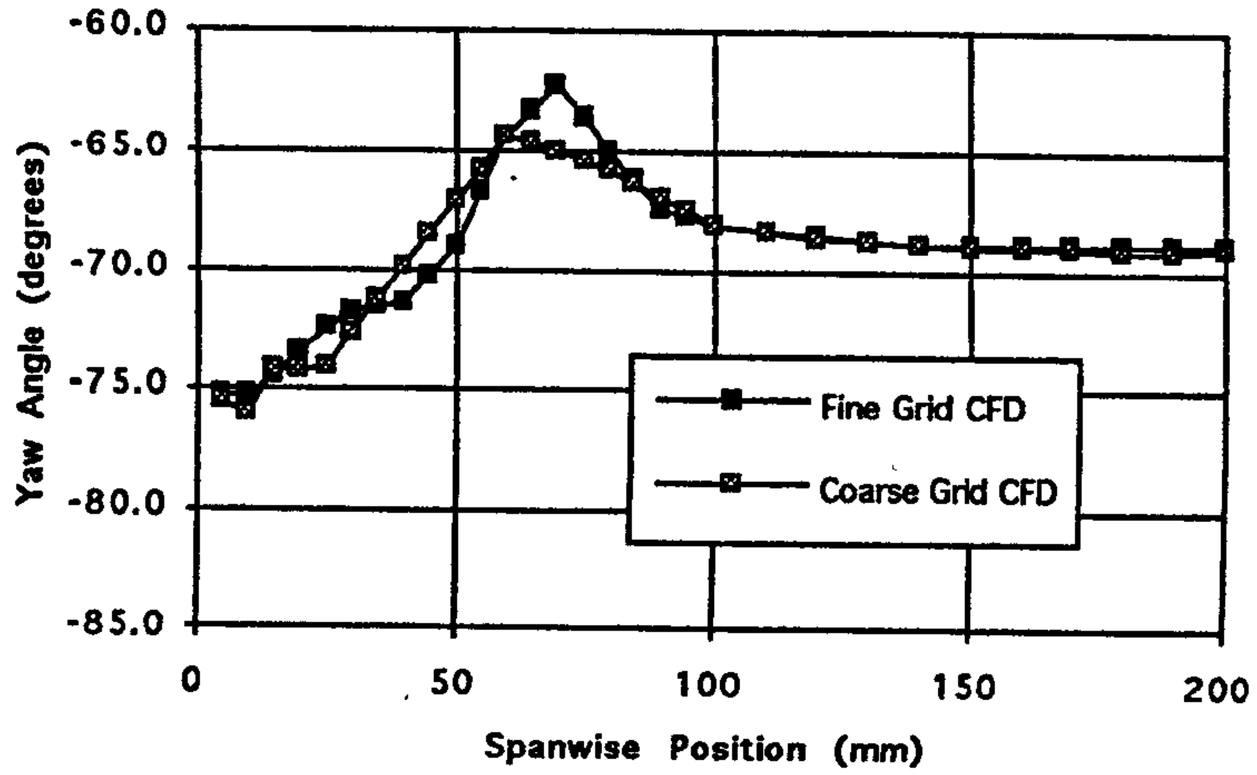

c) Pitch Angle.

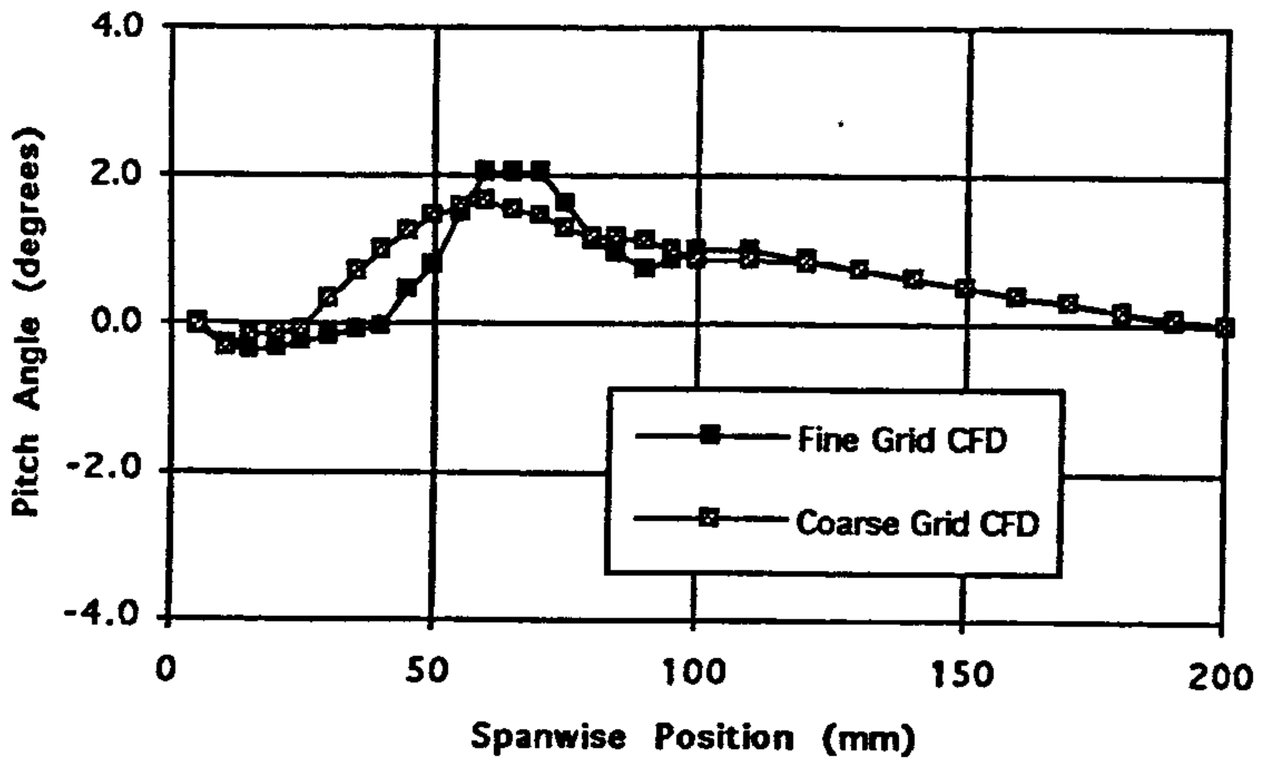

d) Secondary Kinetic Energy Coefficient.

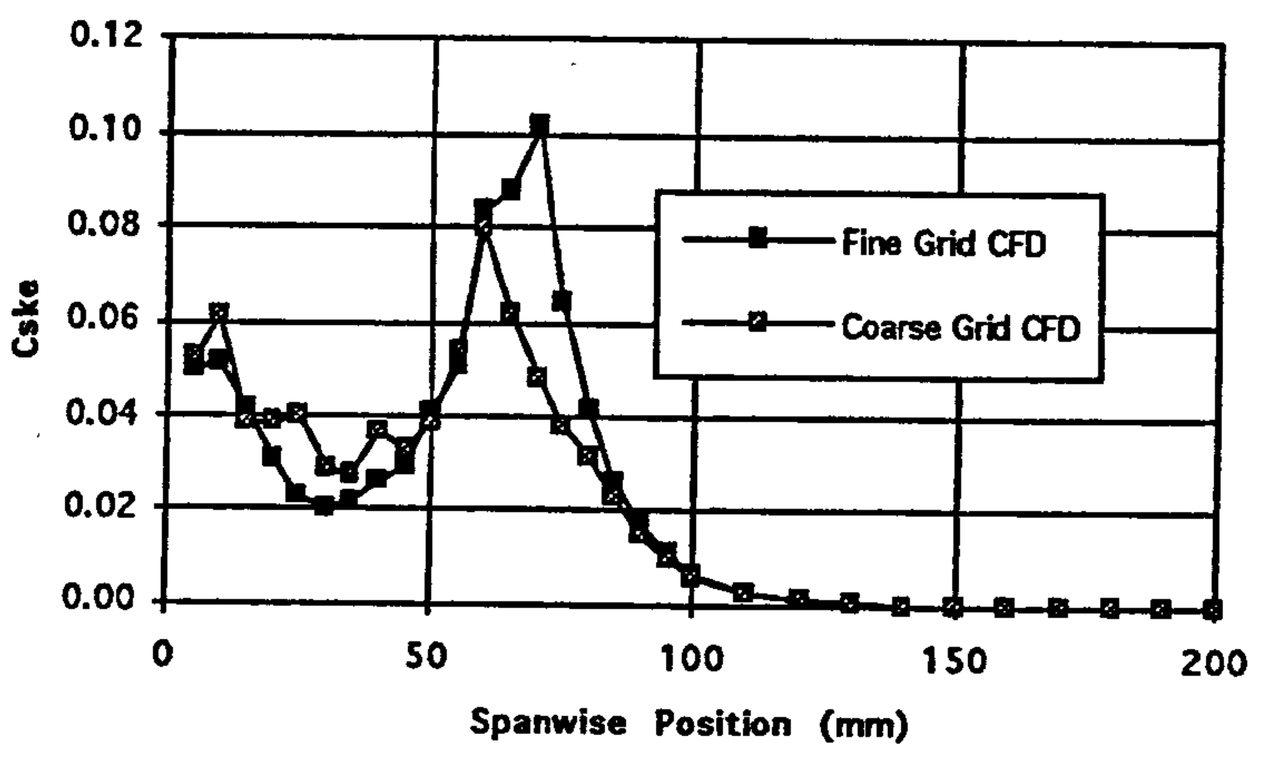

Figure 5.8 Fine Grid CFD Data at Slot 1.

a) Secondary Velocity Vectors.

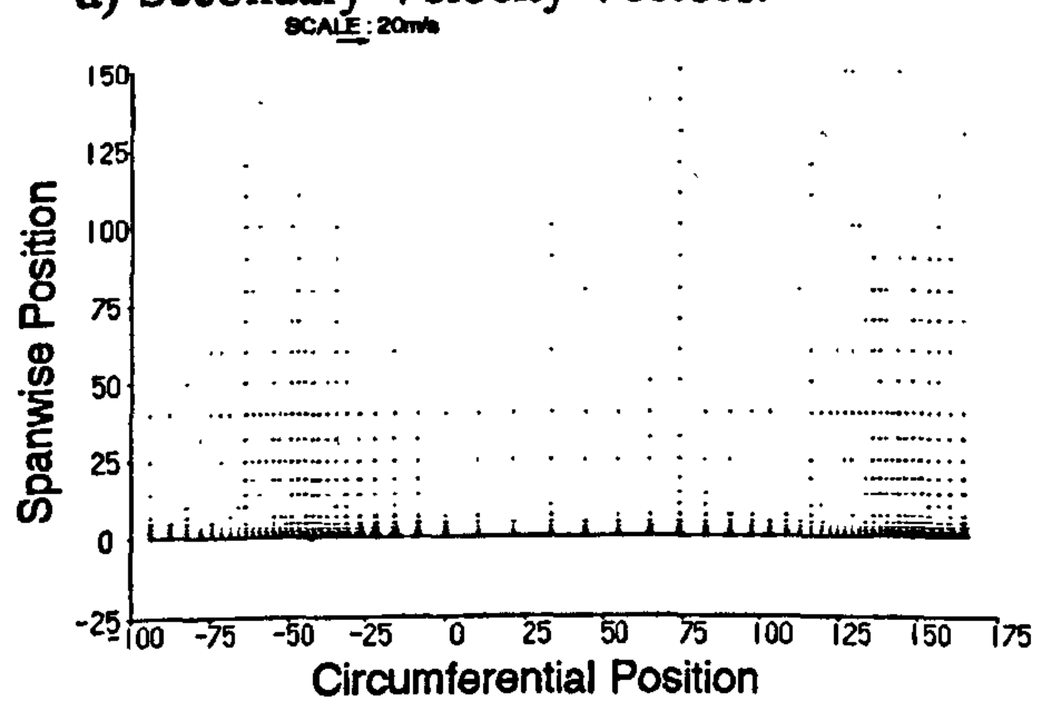

b) Total Pressure Loss Coefficient.

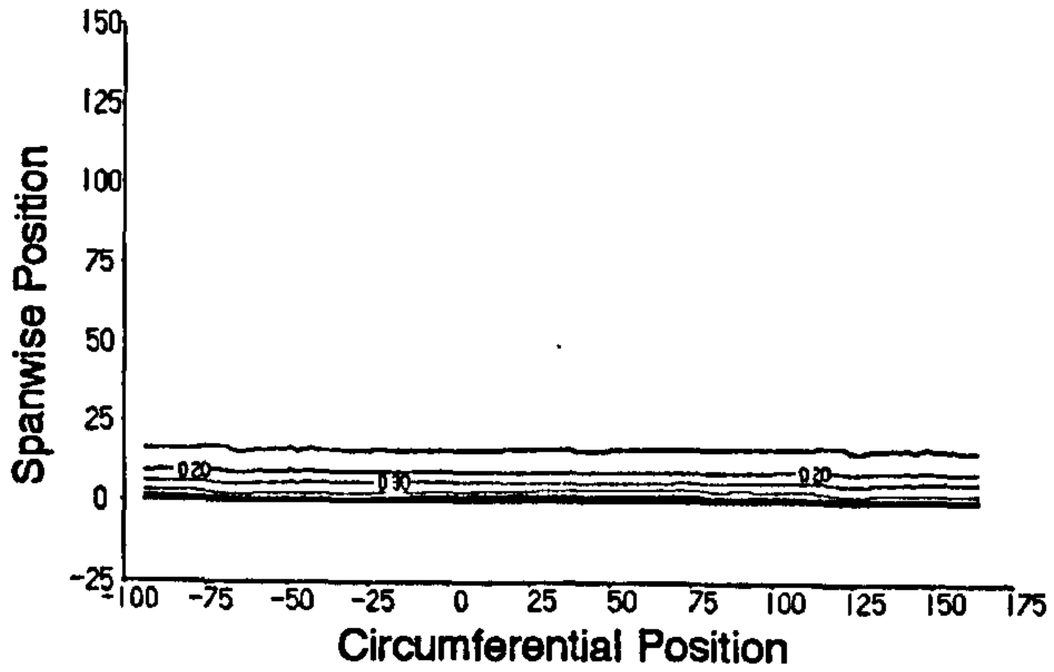

c) Yaw Angle.

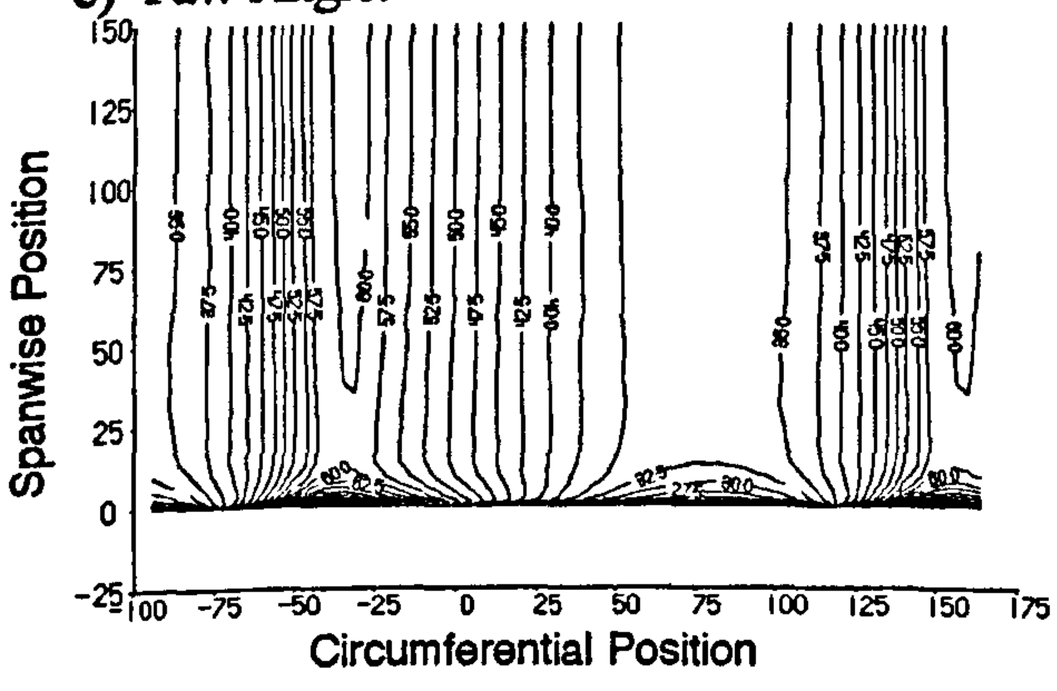

d) Secondary Kinetic Energy Coefficient.

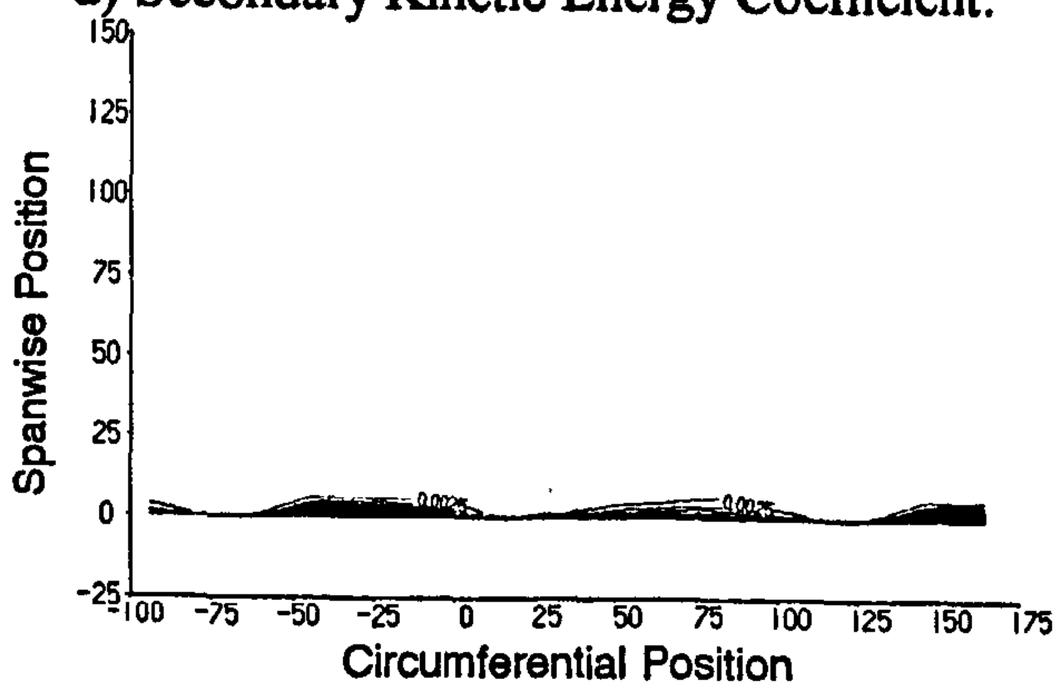

Figure 5.9 Fine Grid CFD Data at Slot 6.

a) Secondary Velocity Vectors.

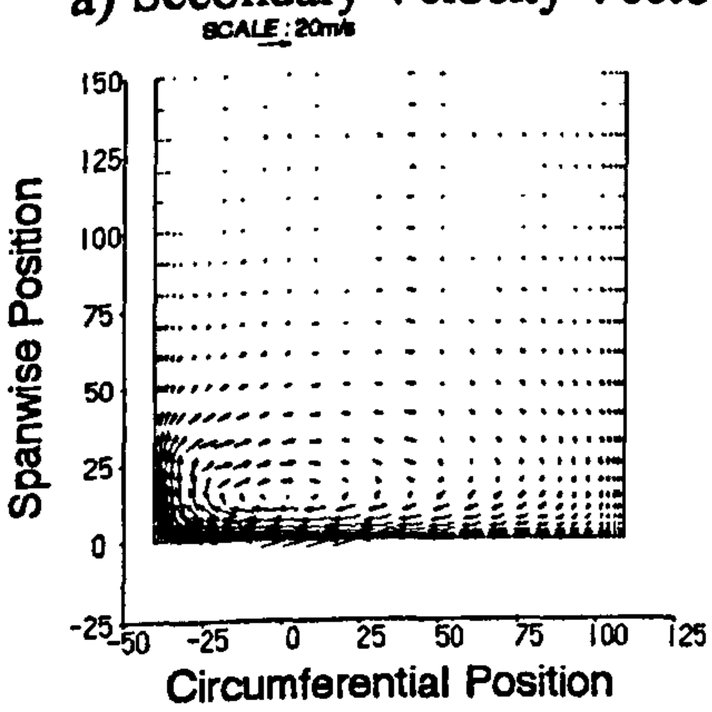

b) Total Pressure Loss Coefficient.

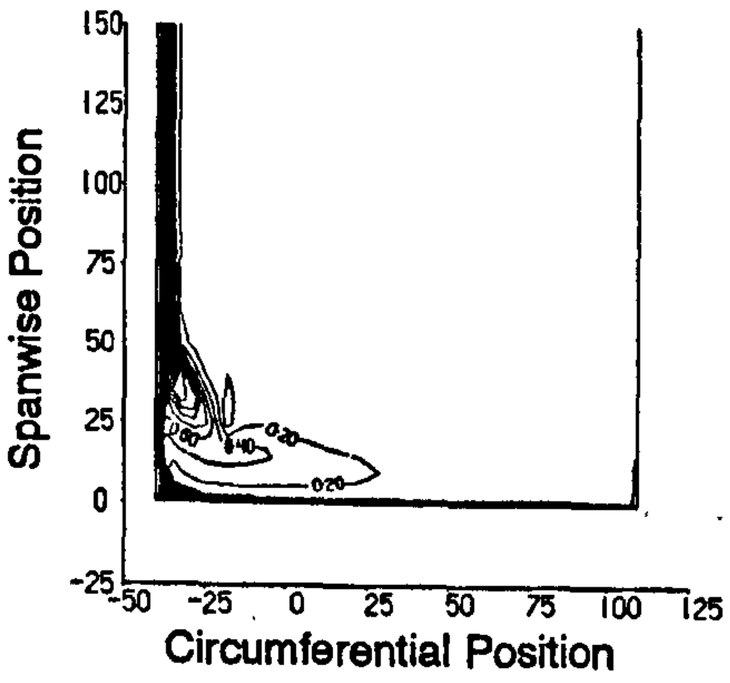

c) Yaw Angle.

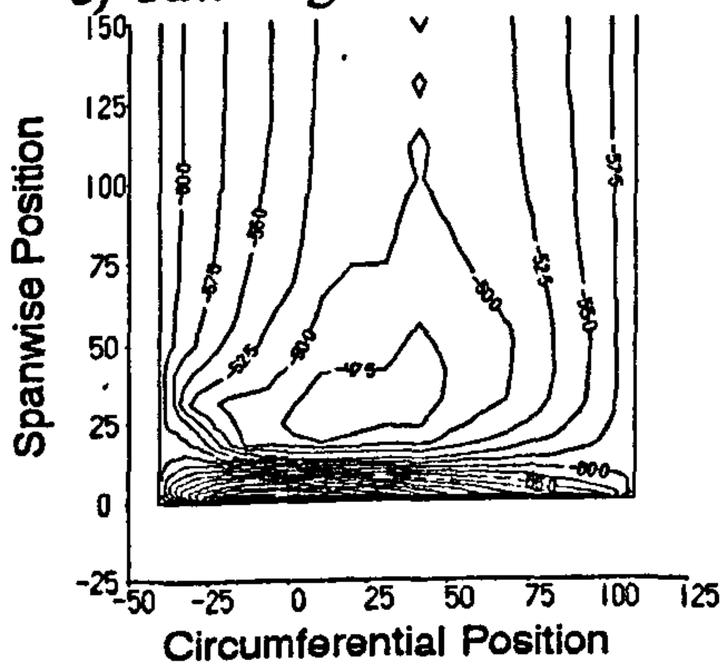

d) Secondary Kinetic Energy Coefficient.

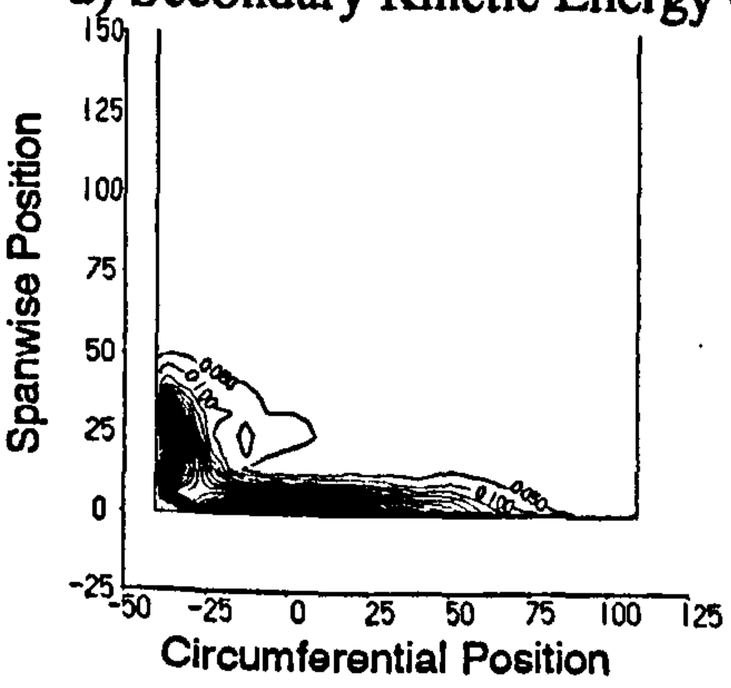

Figure 5.10 Fine Grid CFD Data at Slot 8.

a) Secondary Velocity Vectors.

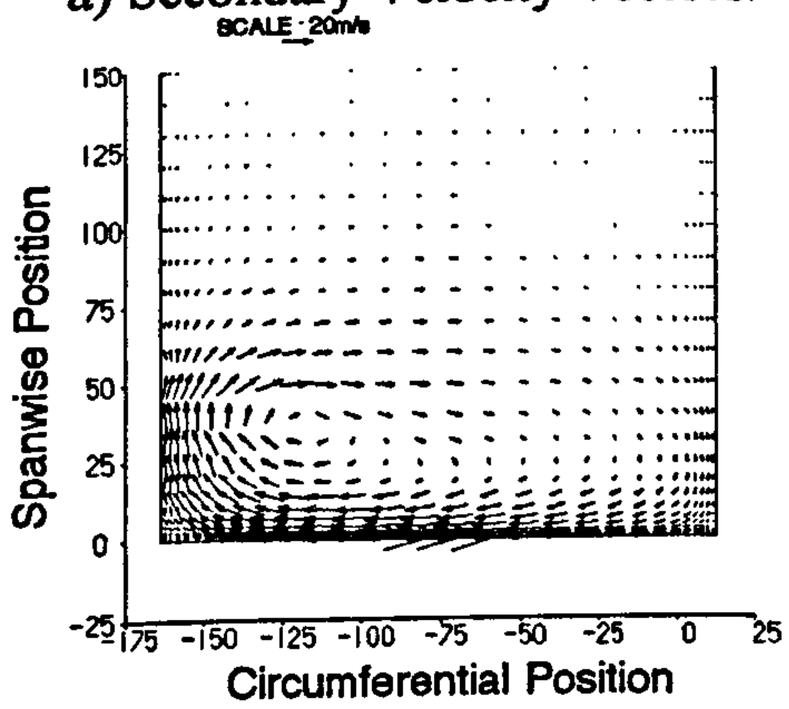

b) Total Pressure Loss Coefficient.

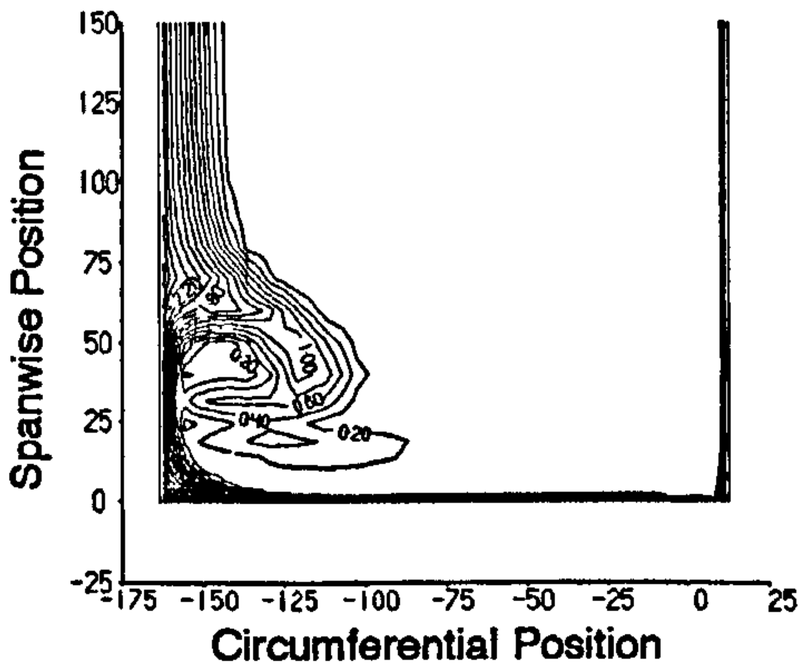

c) Yaw Angle.

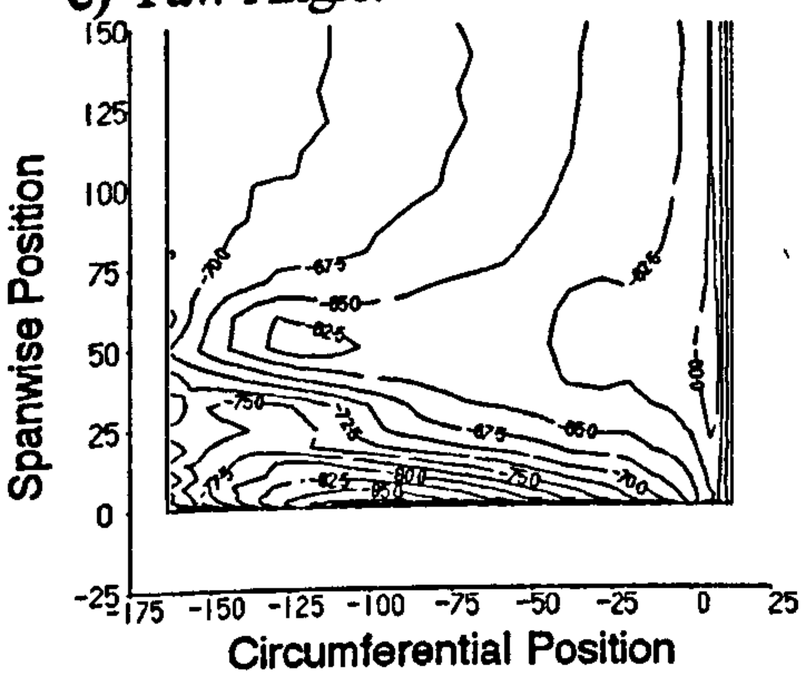

d) Secondary Kinetic Energy Coefficient.

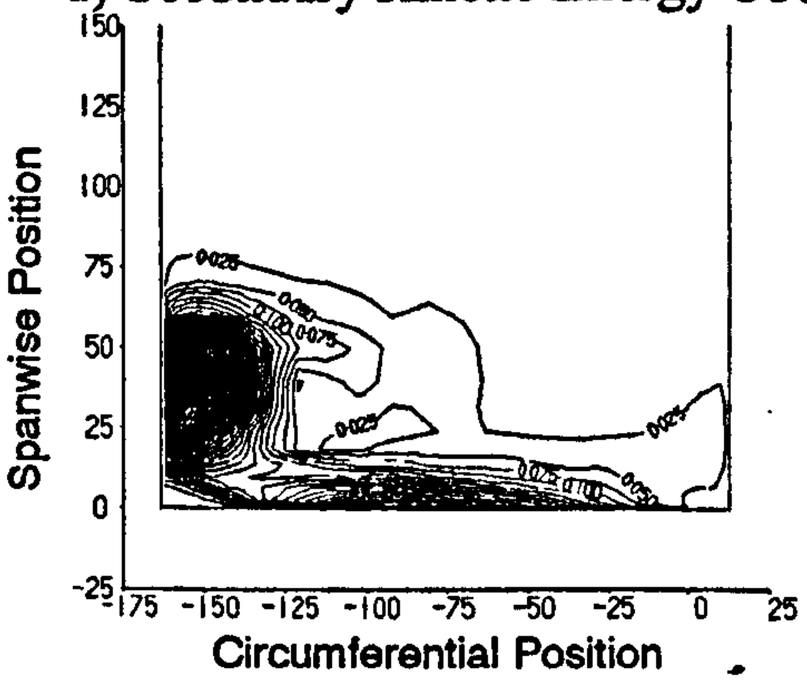

Figure 5.11 Fine Grid CFD Data at Slot 10.

a) Secondary Velocity Vectors.

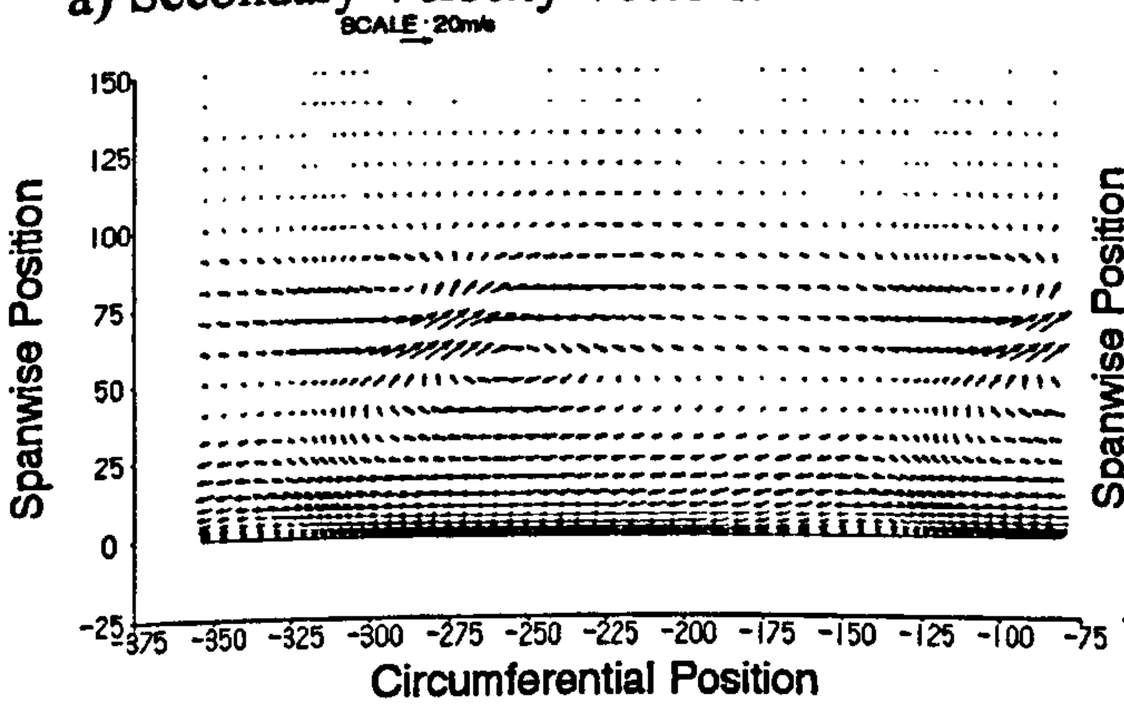

b) Total Pressure Loss Coefficient.

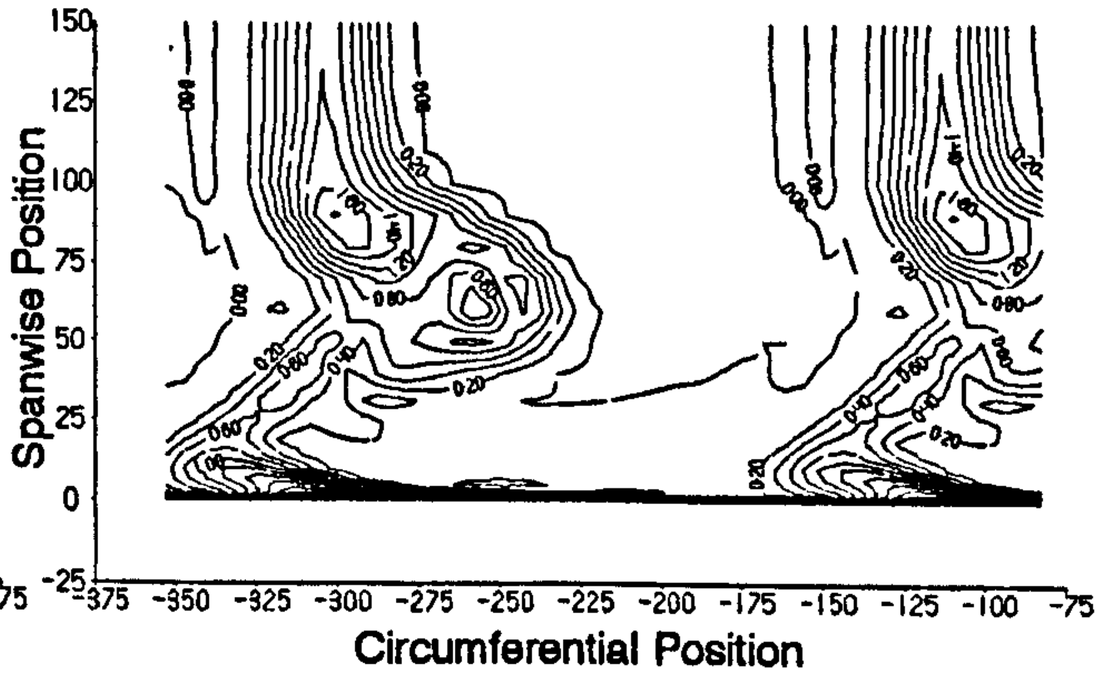

c) Yaw Angle.

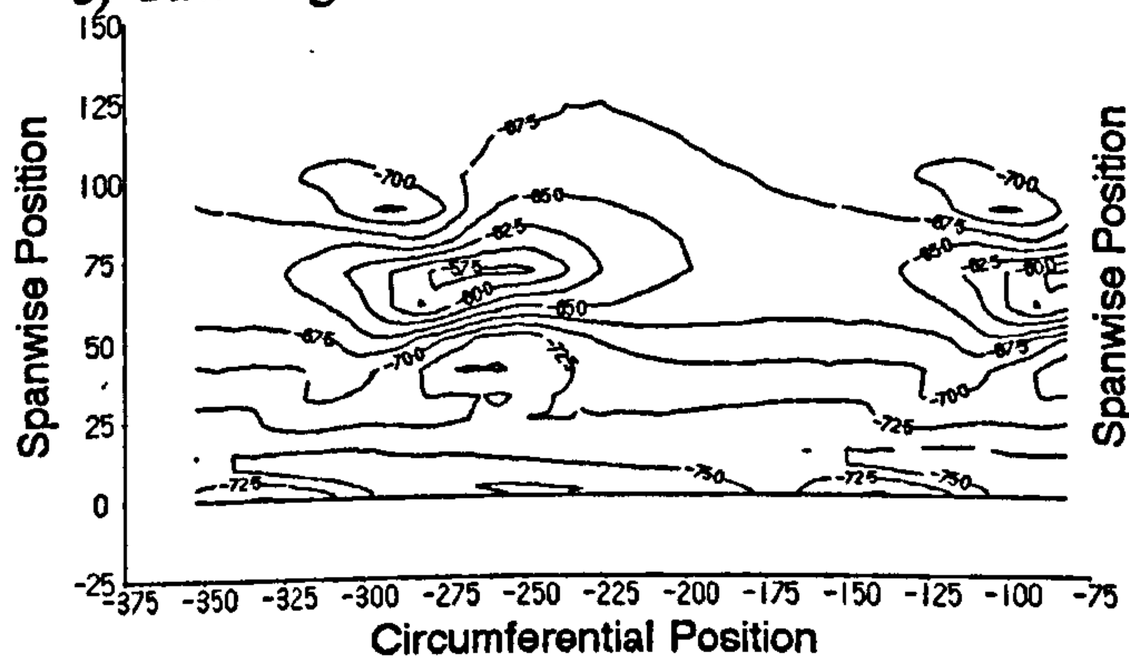

d) Secondary Kinetic Energy Coefficient.

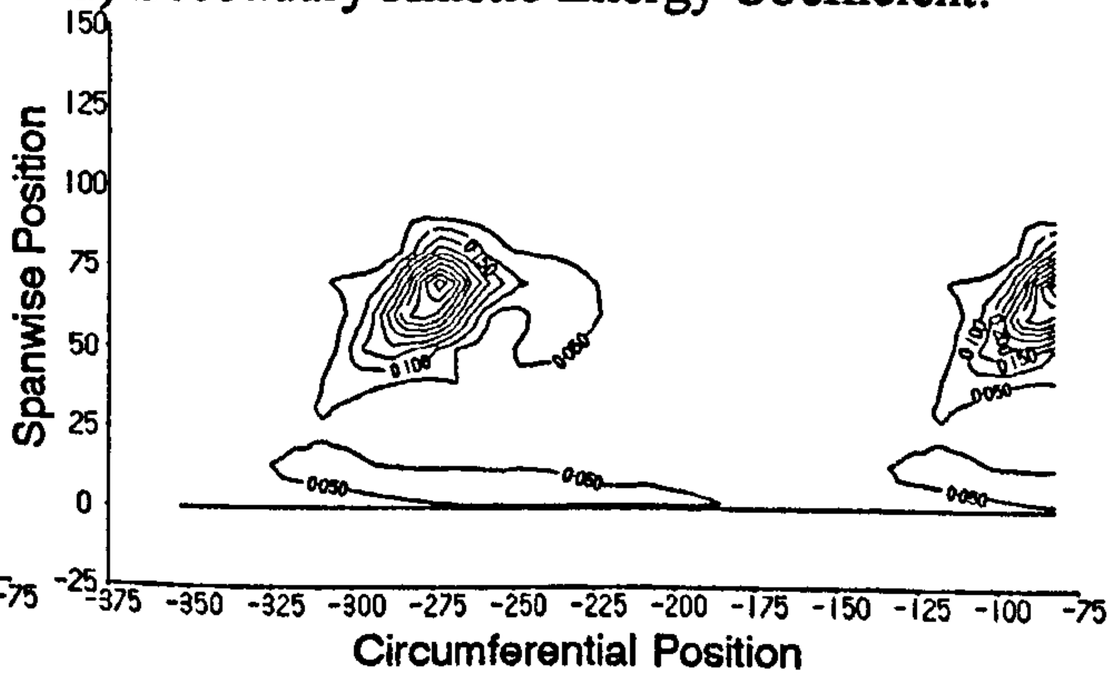

Figure 5.12 Coarse Grid CFD Data at Slot 10.

a) Secondary Velocity Vectors.

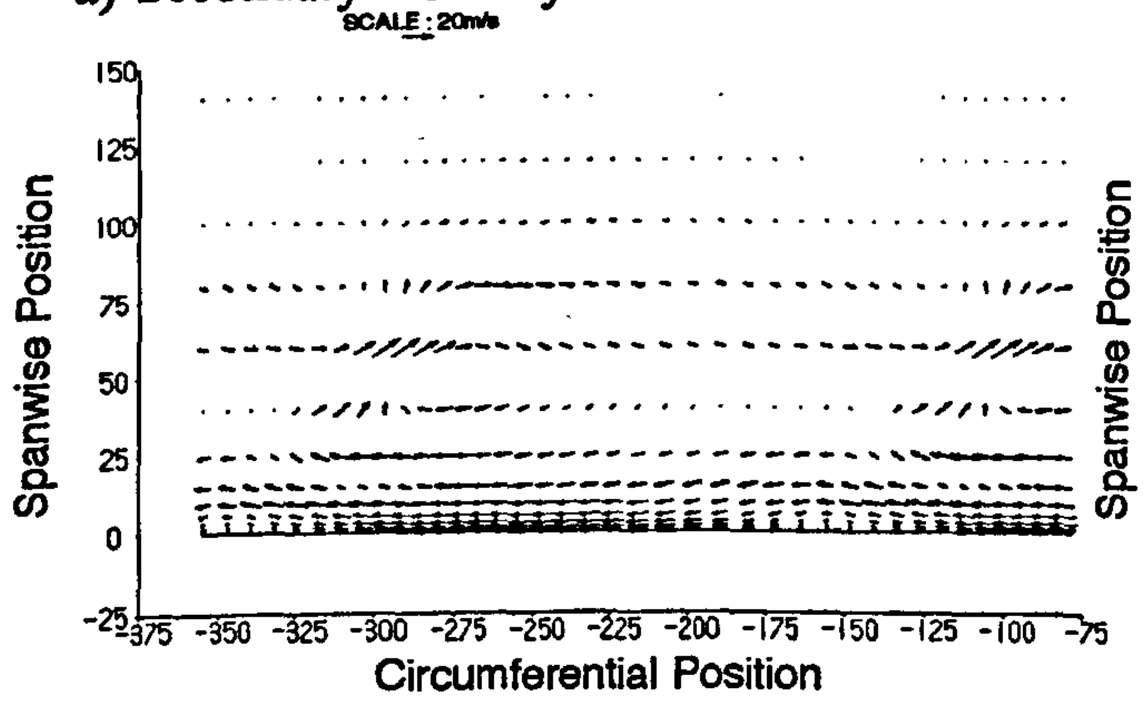

b) Total Pressure Loss Coefficient.

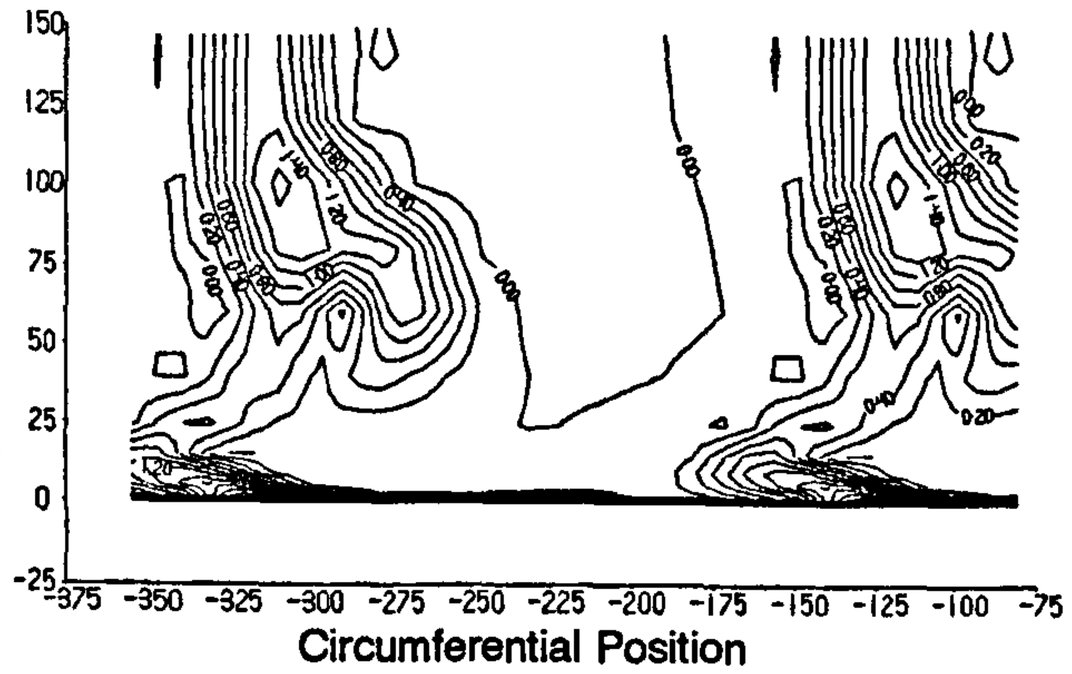

c) Yaw Angle.

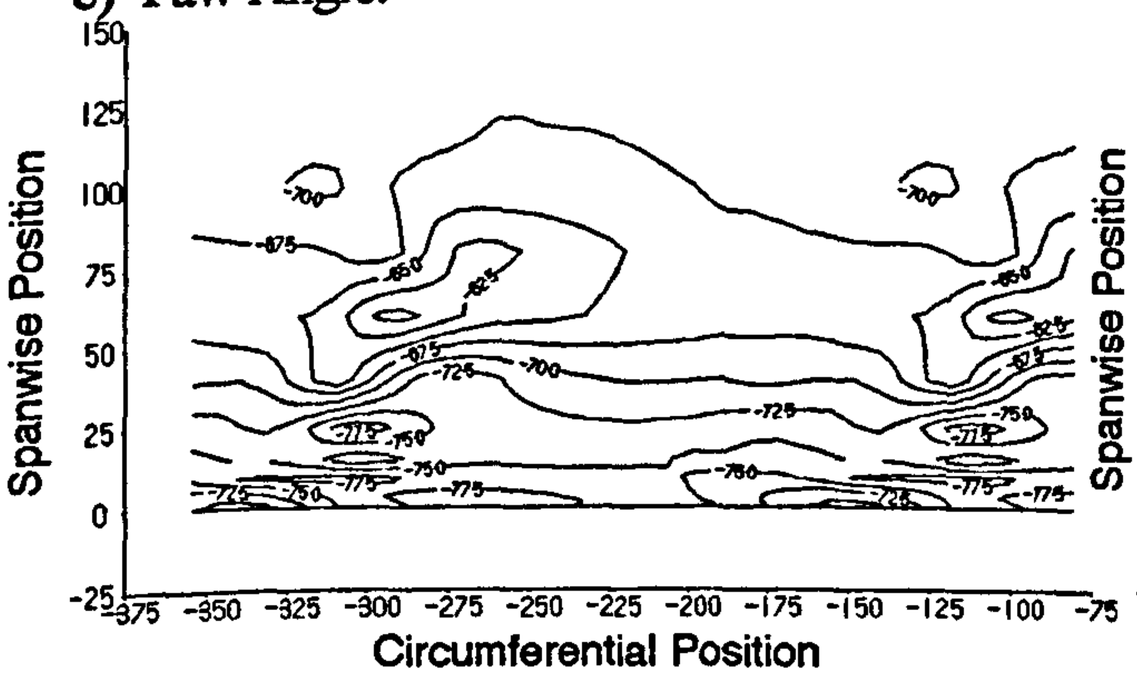

d) Secondary Kinetic Energy Coefficient.

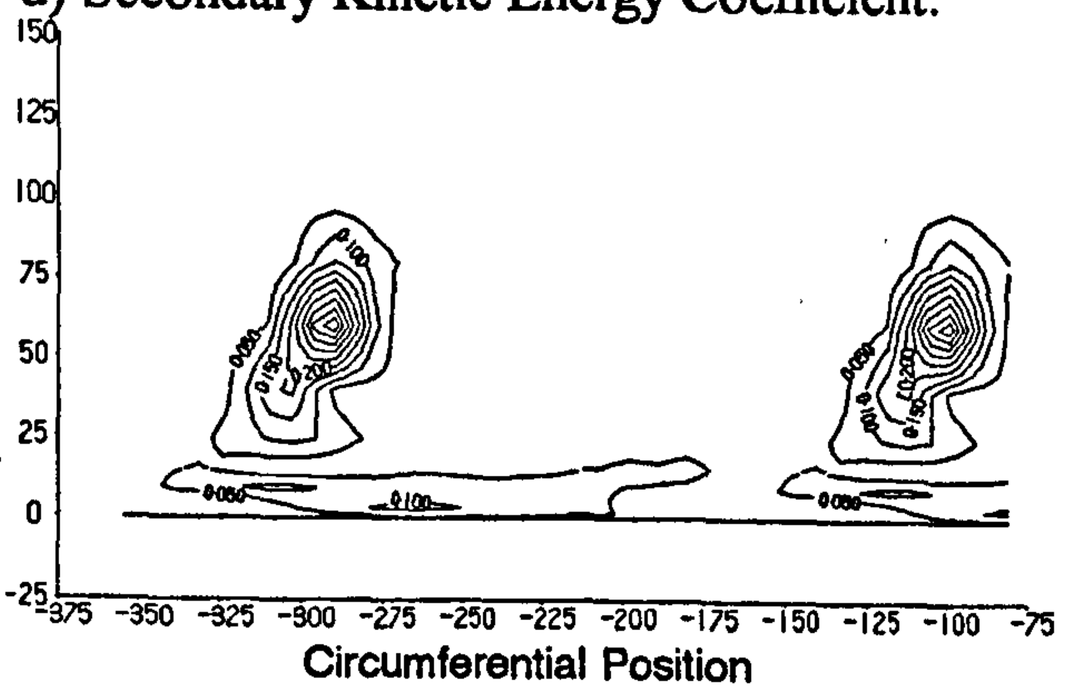

Figure 5.13 Experimental and Fine Grid CFD End-wall C_p Contours.

a) Experiment.

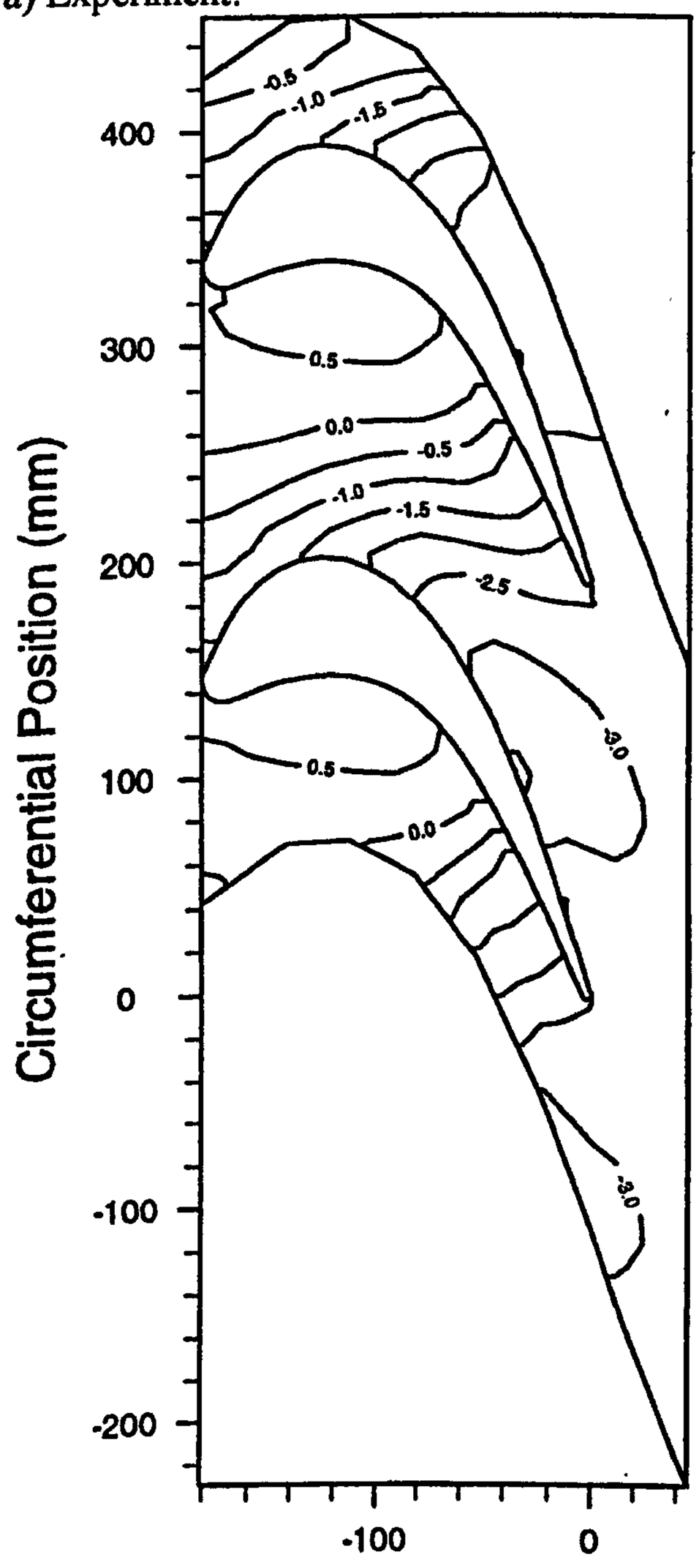

b) Fine Grid CFD.

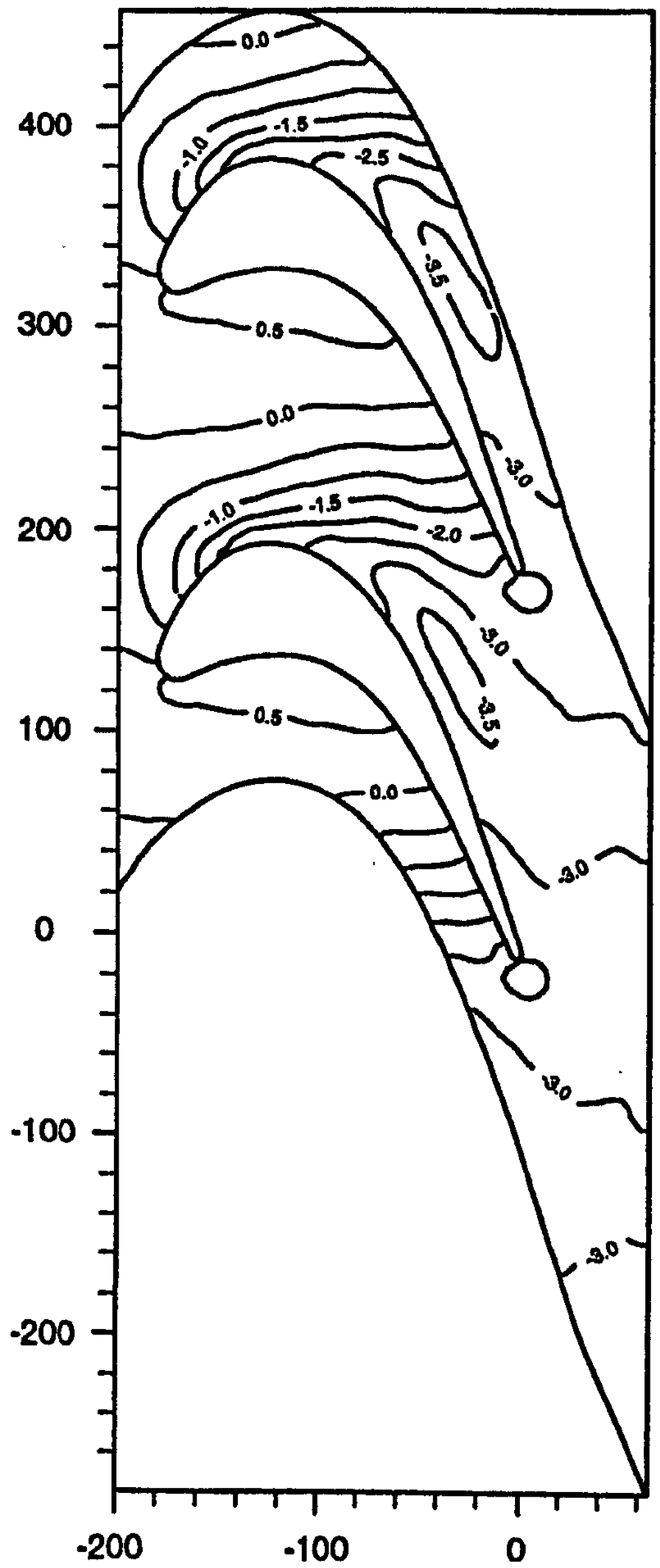

Figure 5.14 Measured Total Pressure Coefficient 100% C_{ax} Upstream.

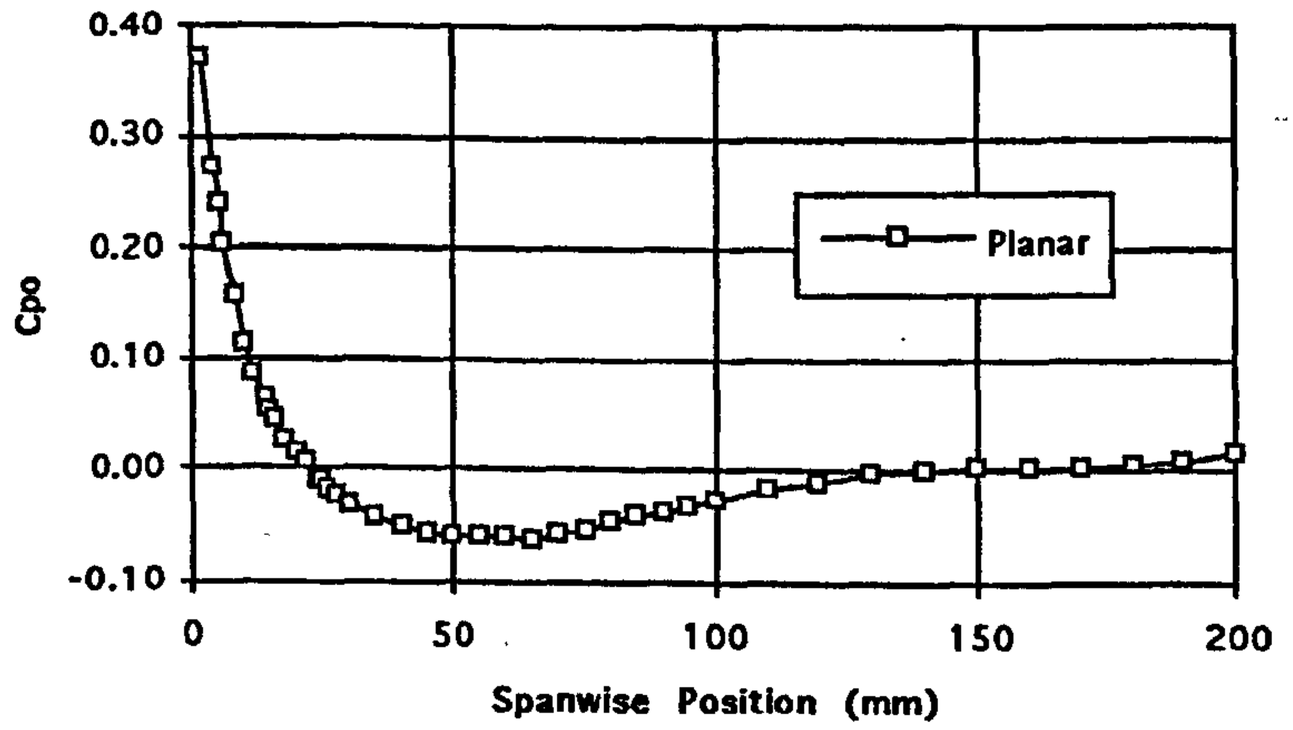

Figure 5.15 Pitch Averaged Experimental and CFD Data at Slot 1 (Both Grids Shown).

a) Total Pressure Loss Coefficient.

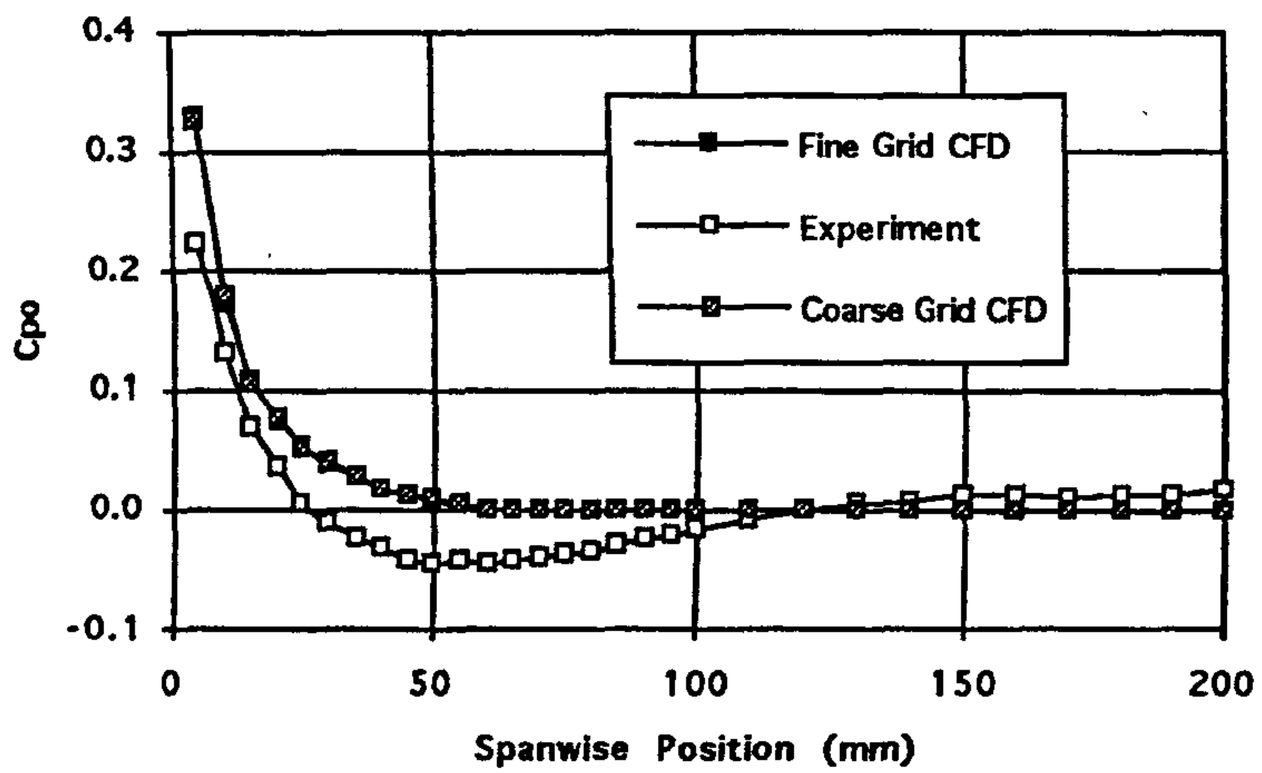

b) Yaw Angle.

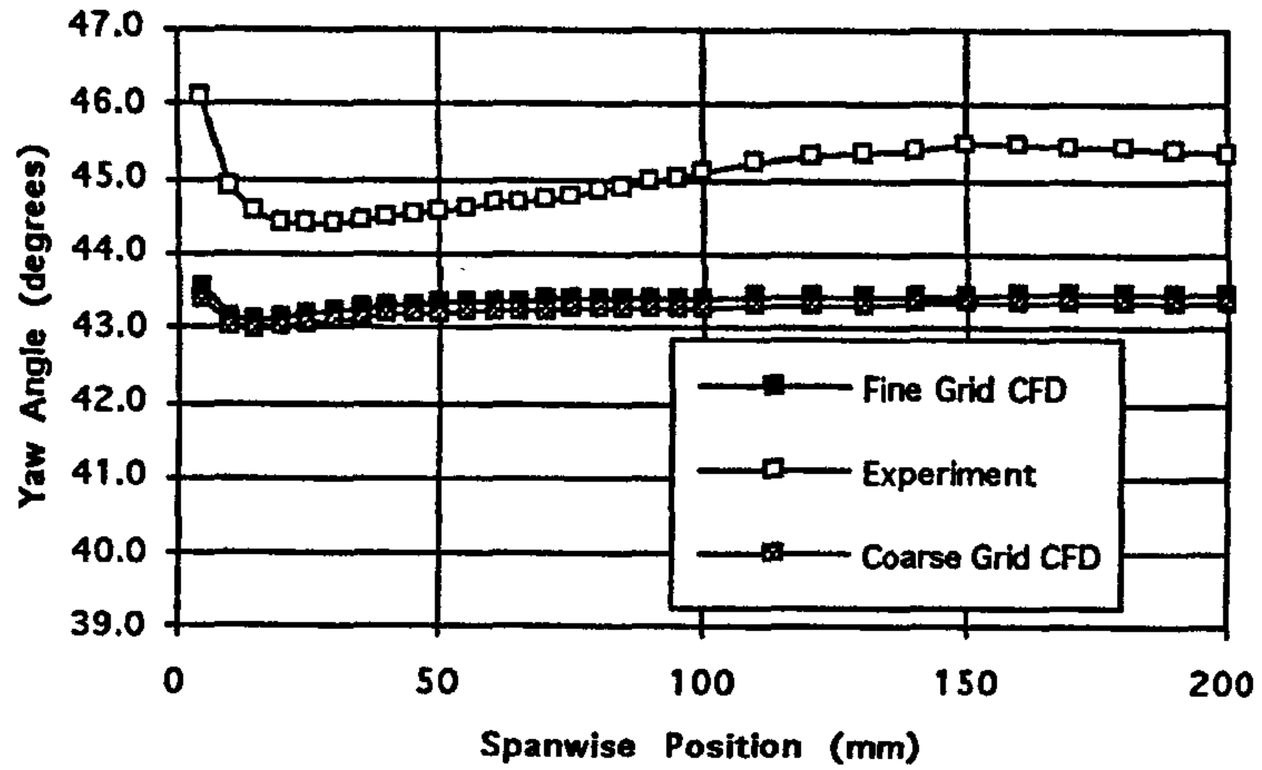

c) Pitch Angle.

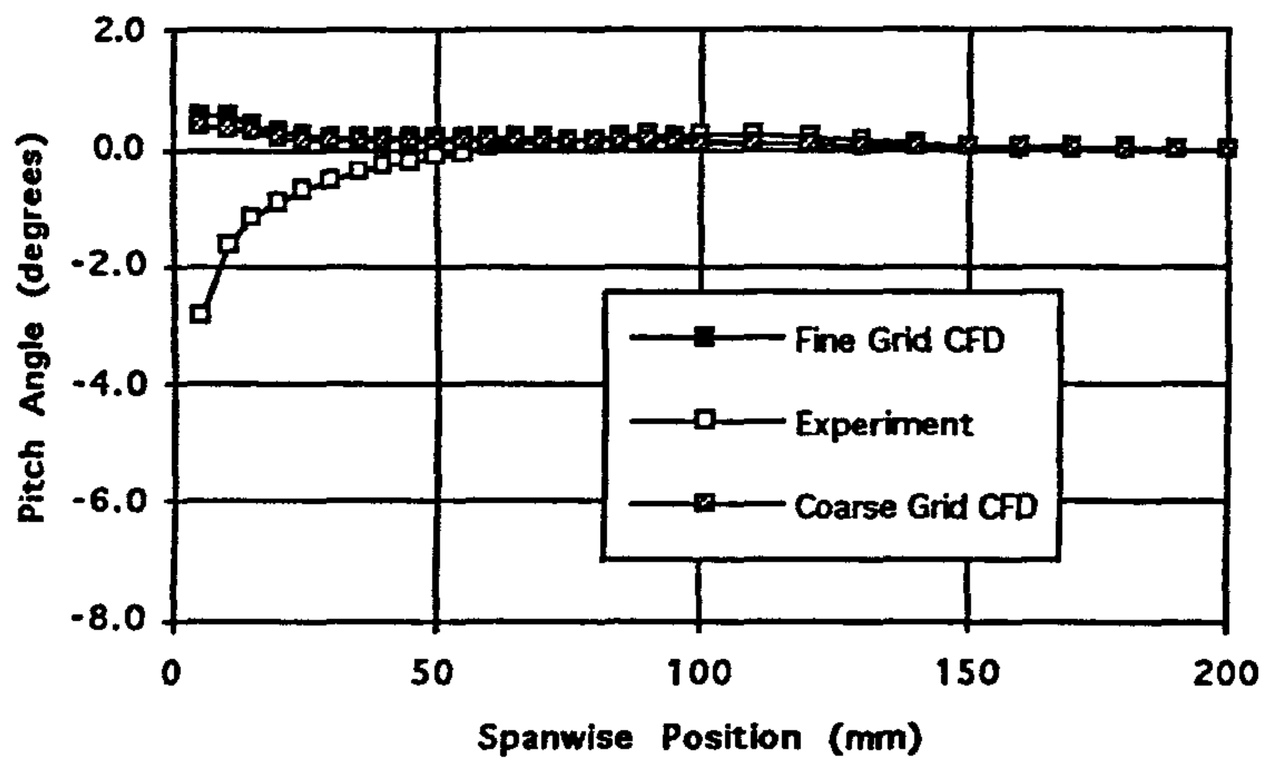

d) Secondary Kinetic Energy Coefficient.

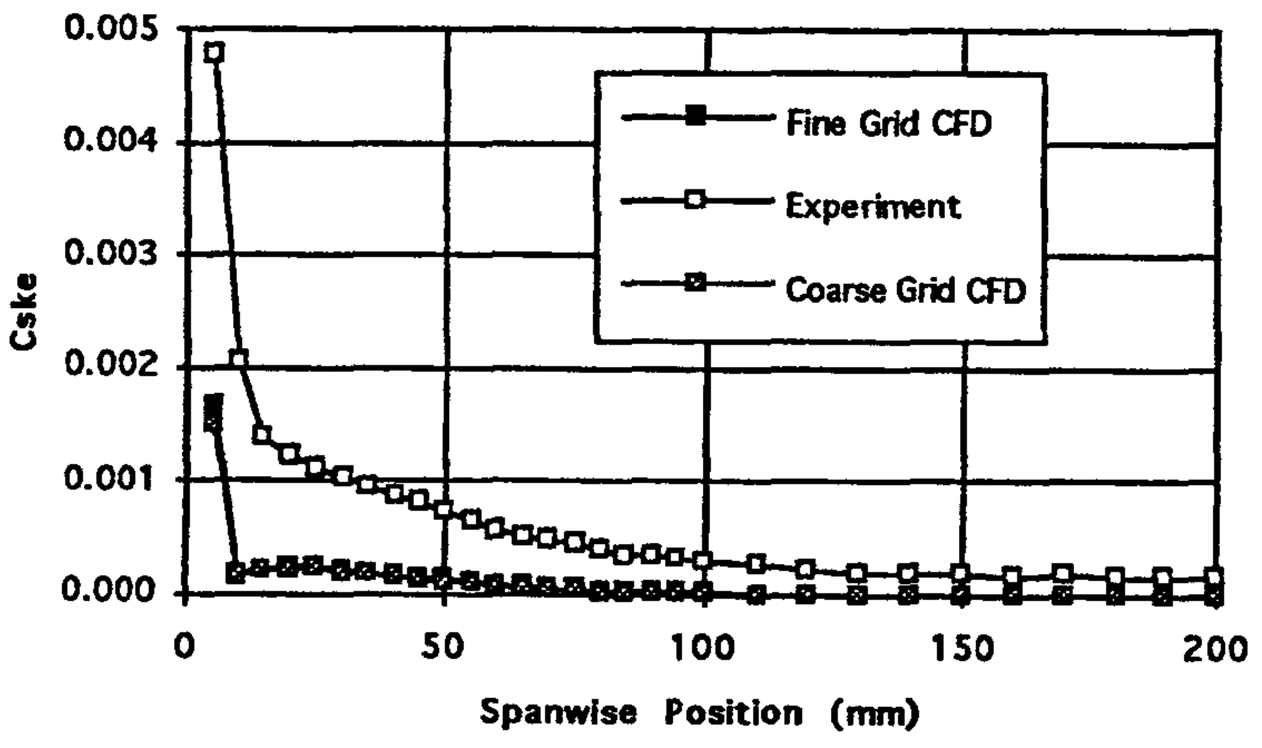

Figure 5.16 Pitch Averaged Experimental and CFD Data at Slot 6 (Both Grids Shown).

a) Total Pressure Loss Coefficient.

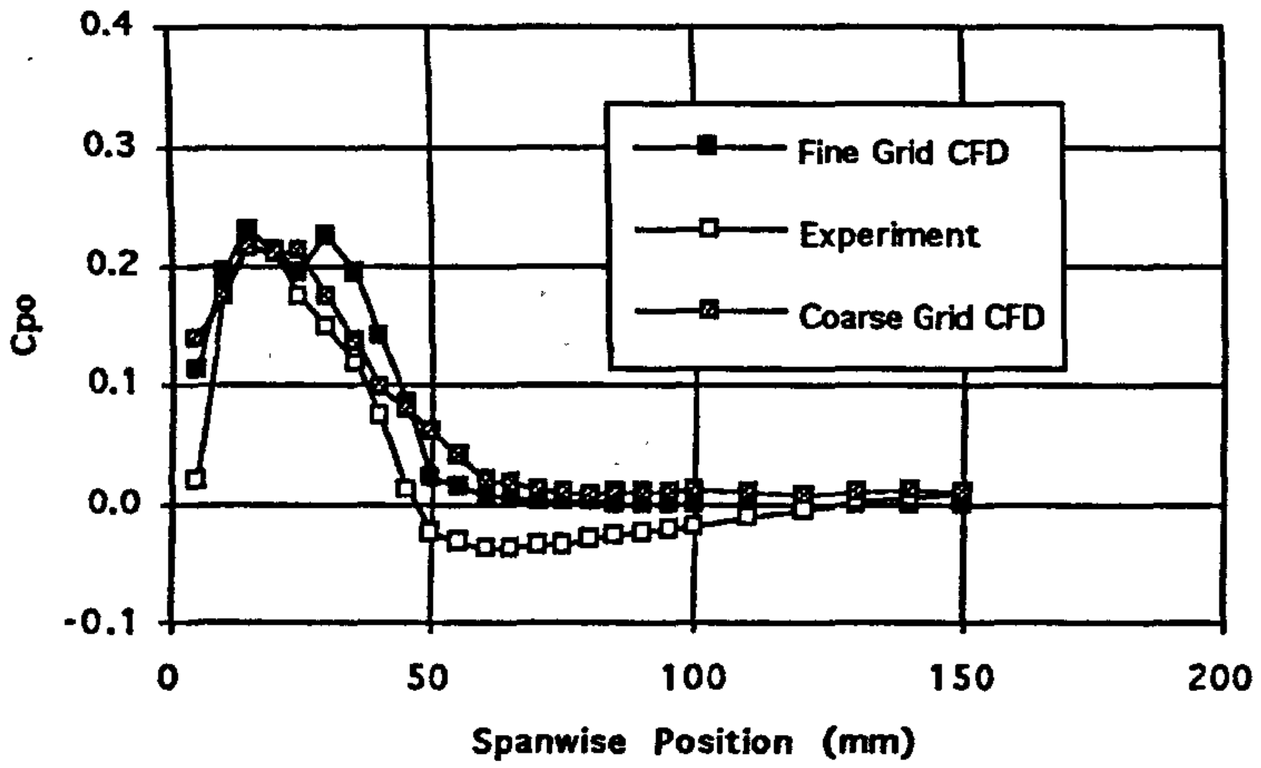

b) Yaw Angle.

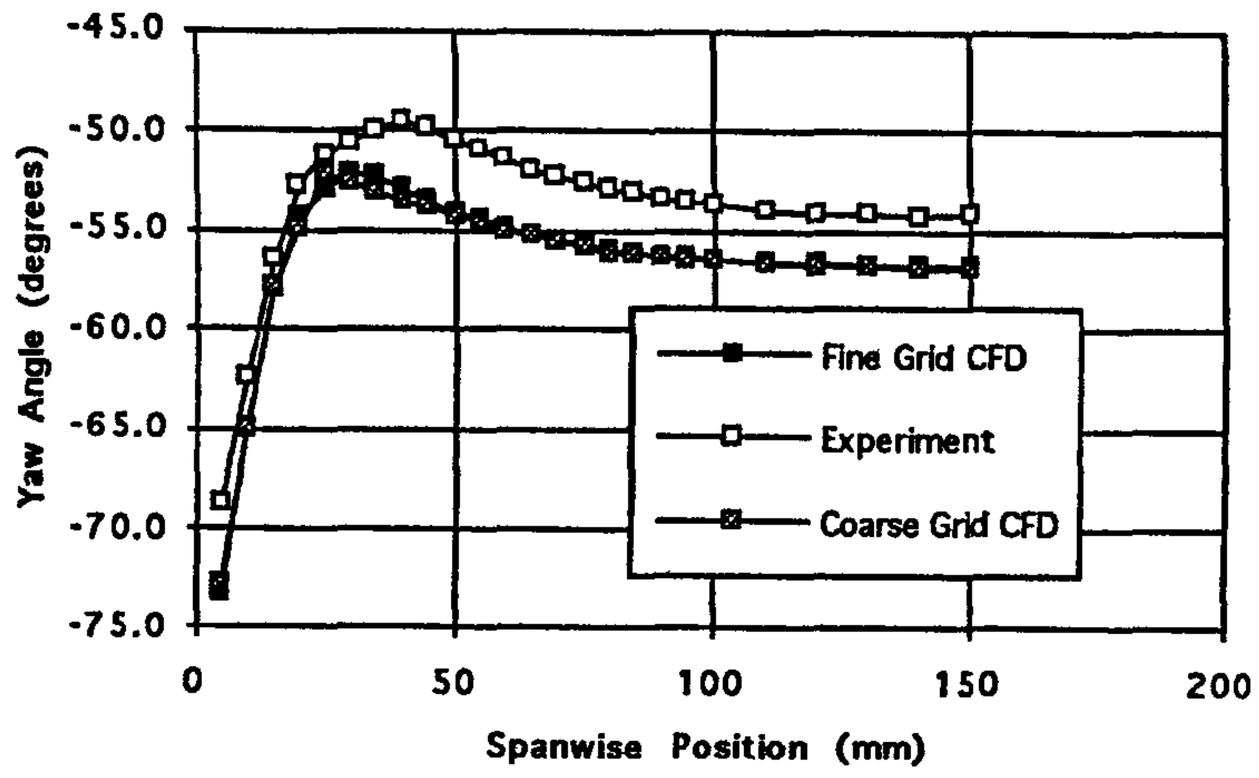

c) Pitch Angle.

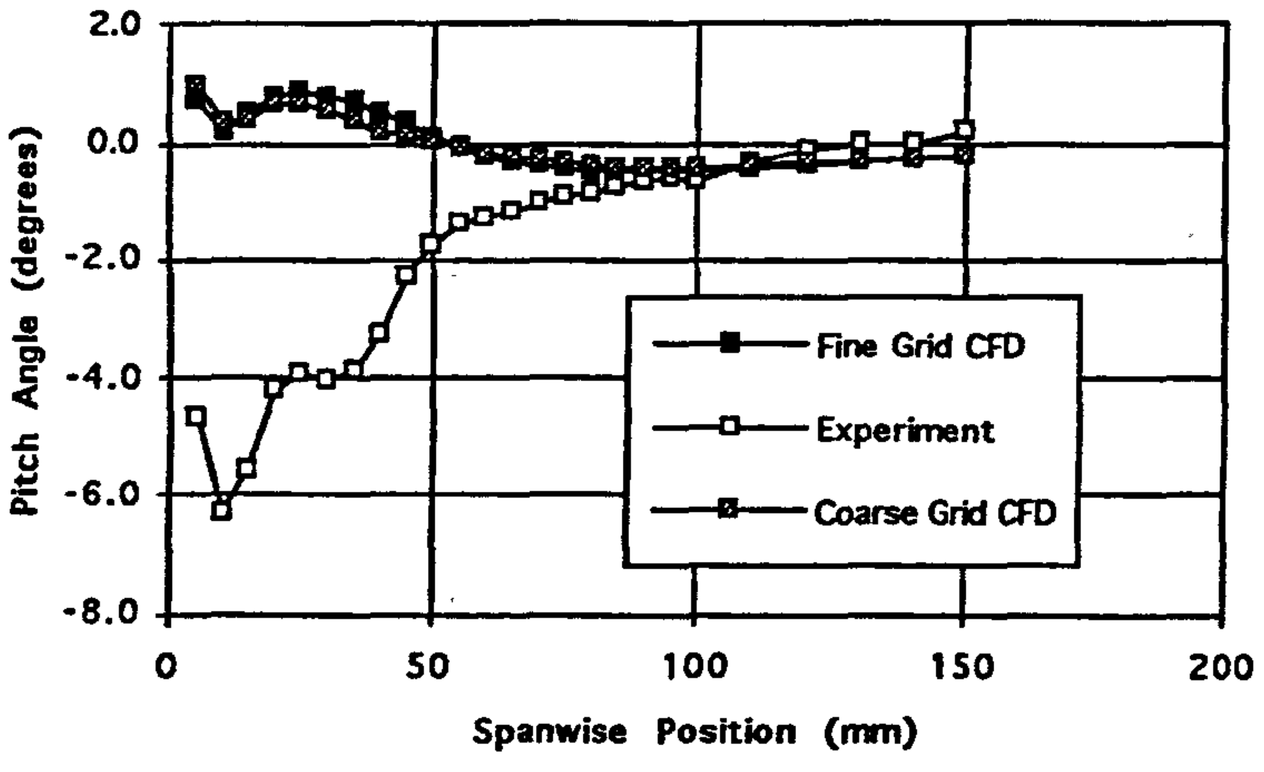

d) Secondary Kinetic Energy Coefficient.

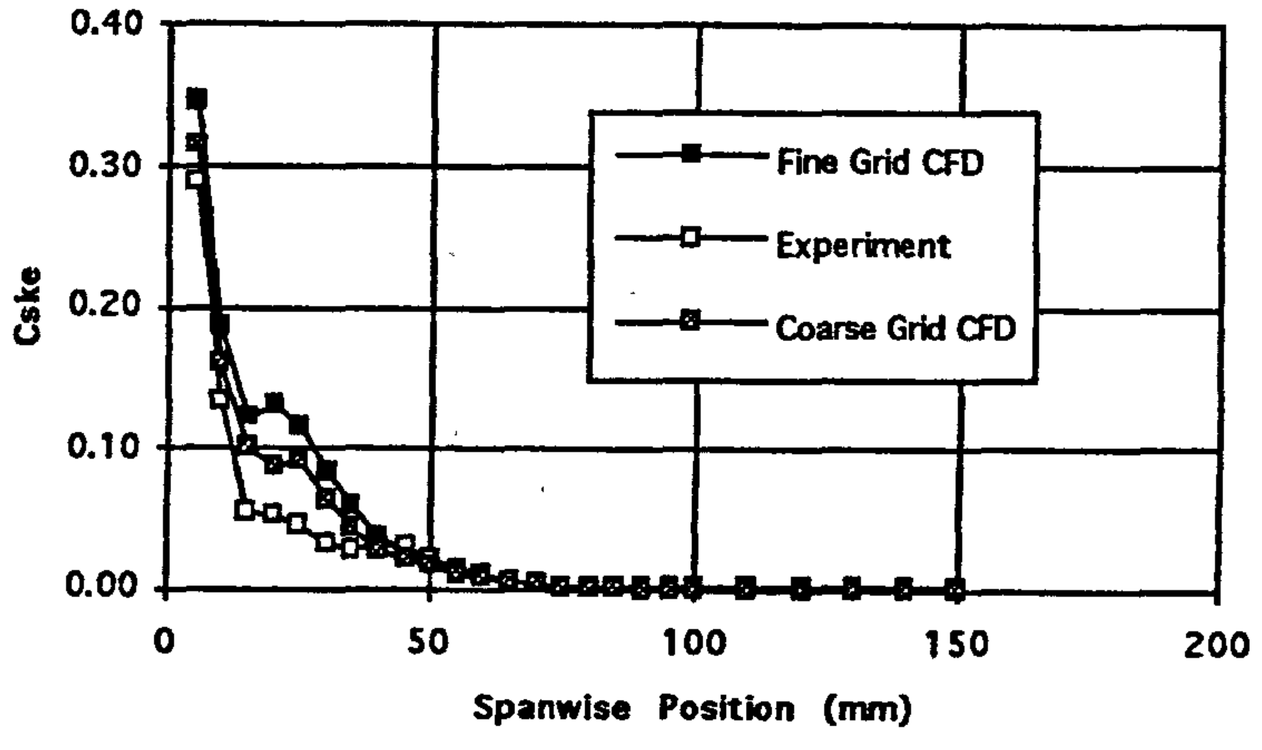

Figure 5.17 Pitch Averaged Experimental and CFD Data at Slot 8 (Both Grids Shown).

a) Total Pressure Loss Coefficient.

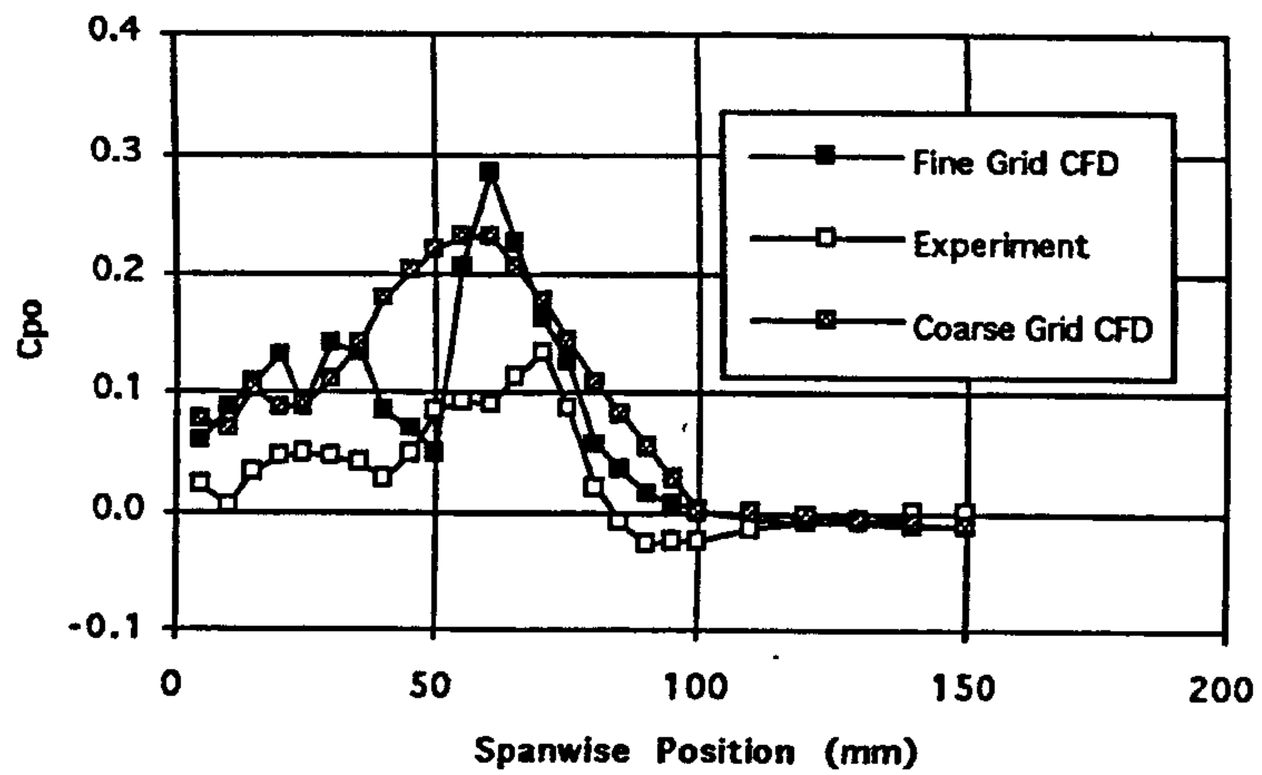

b) Yaw Angle.

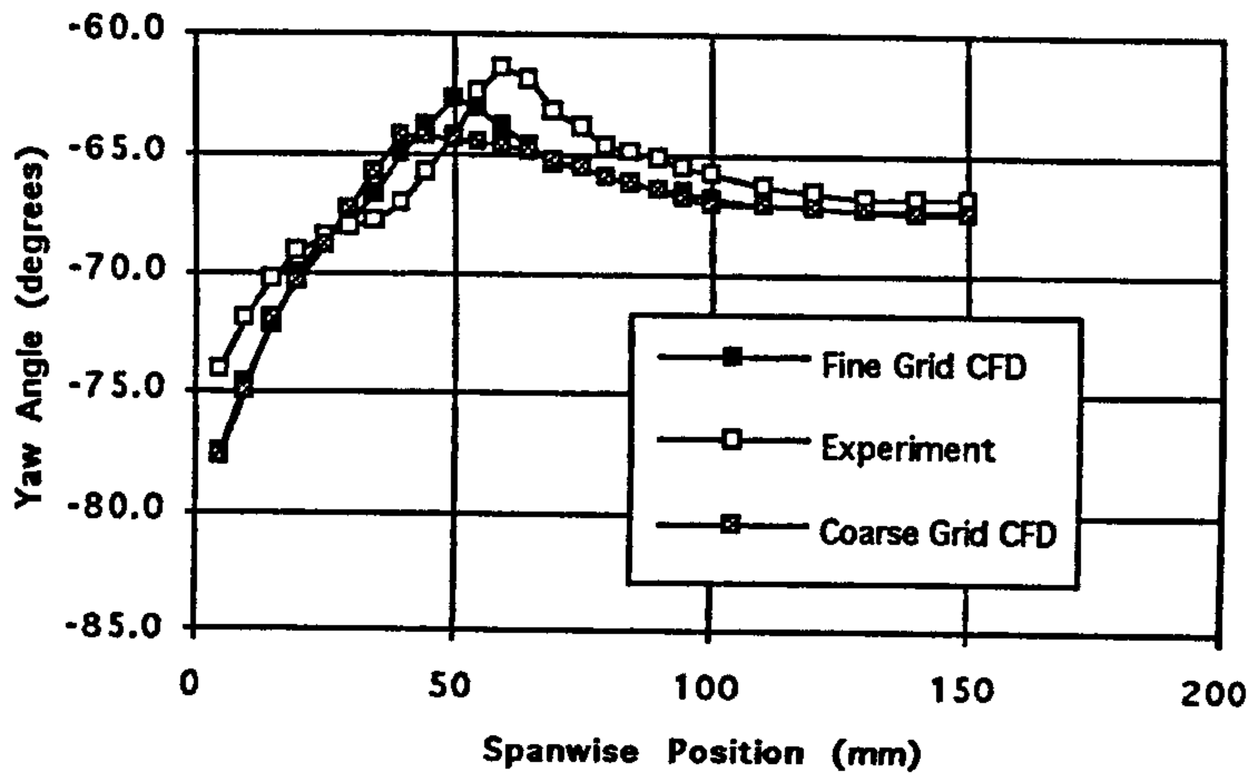

c) Pitch Angle.

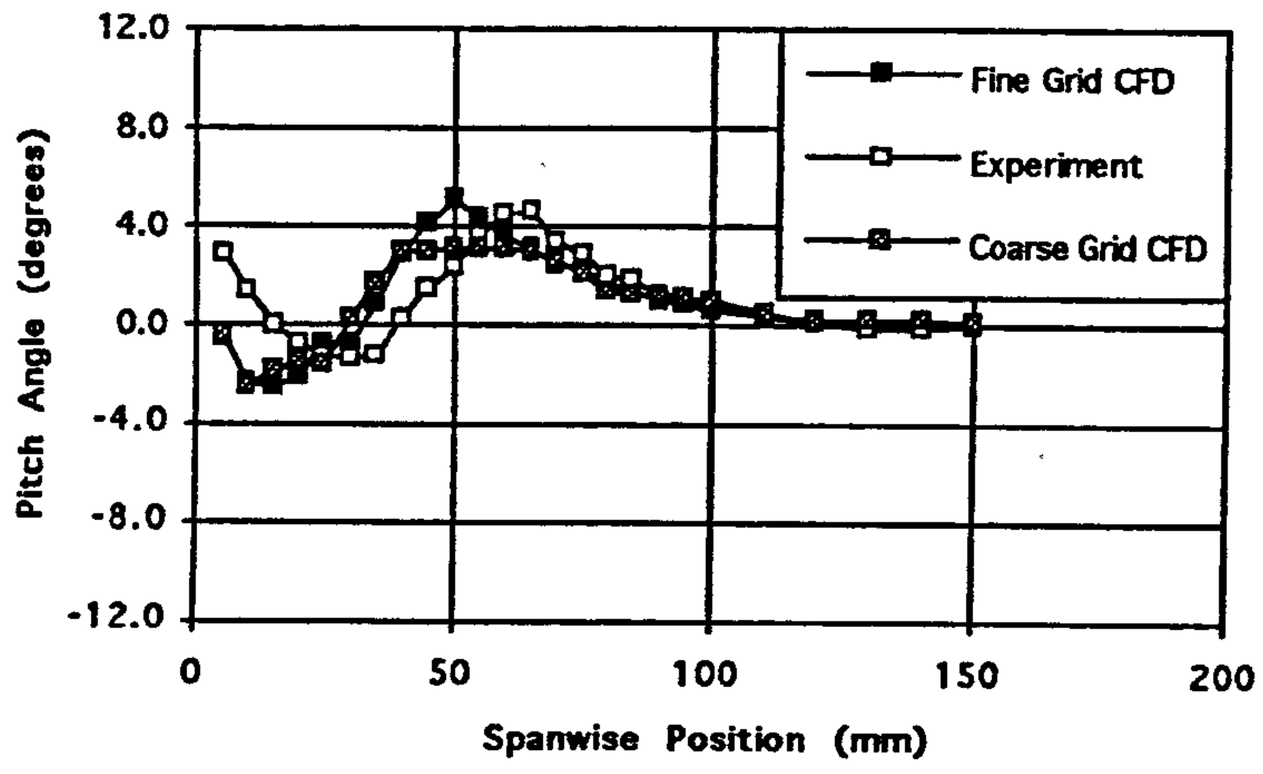

d) Secondary Kinetic Energy Coefficient.

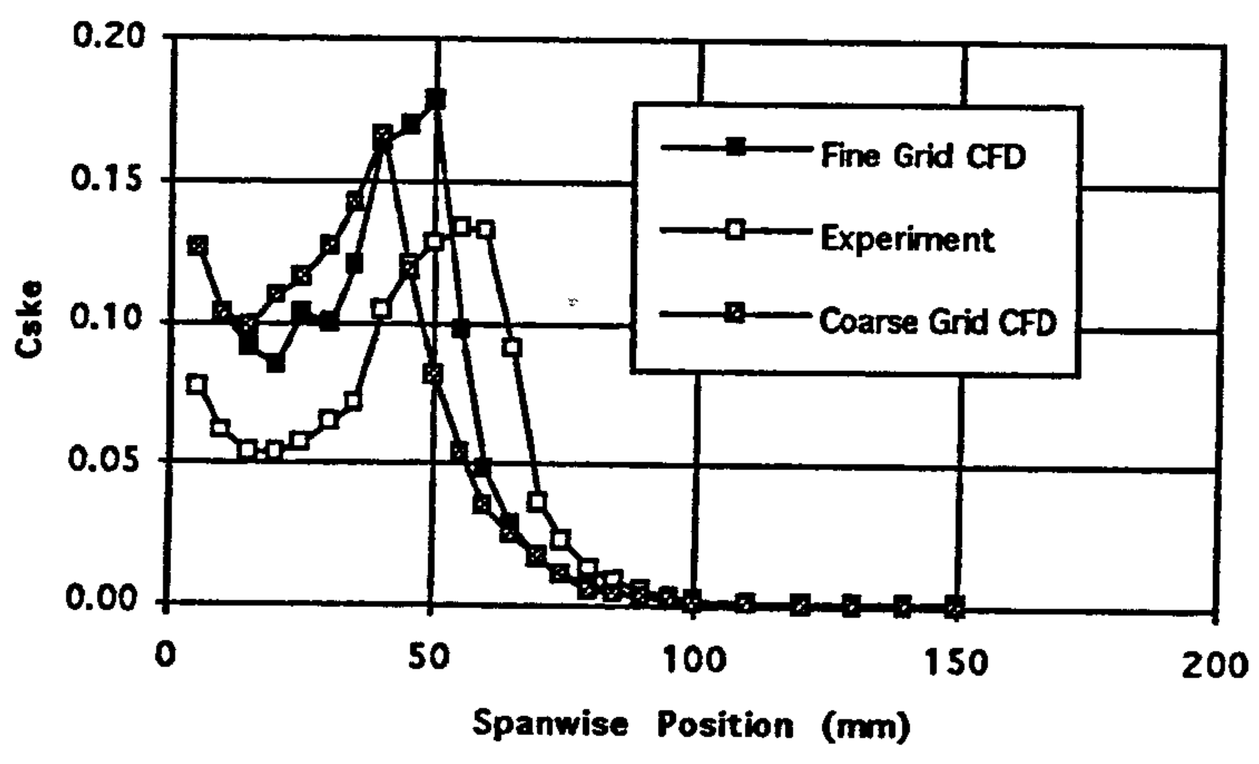

Figure 5.18 Pitch Averaged Experimental and CFD Data at Slot 10 (Both Grids Shown).

a) Total Pressure Loss Coefficient.

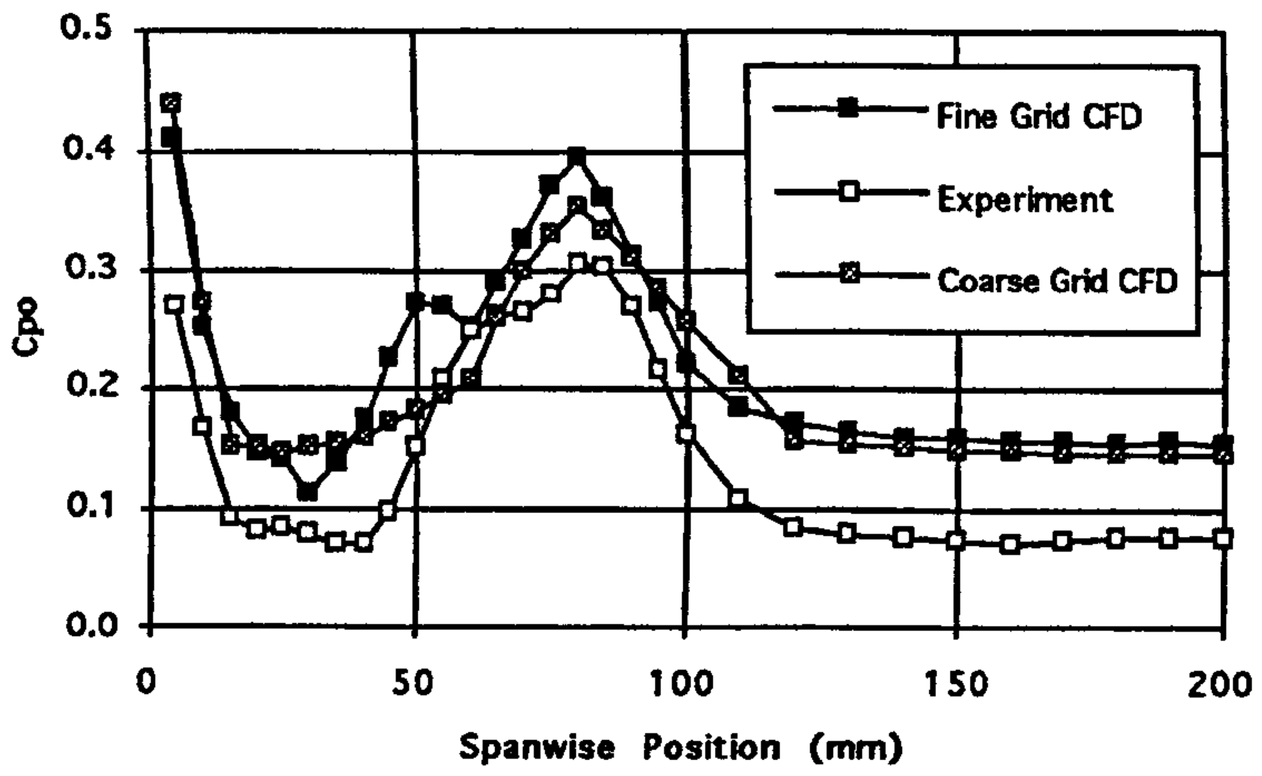

b) Yaw Angle.

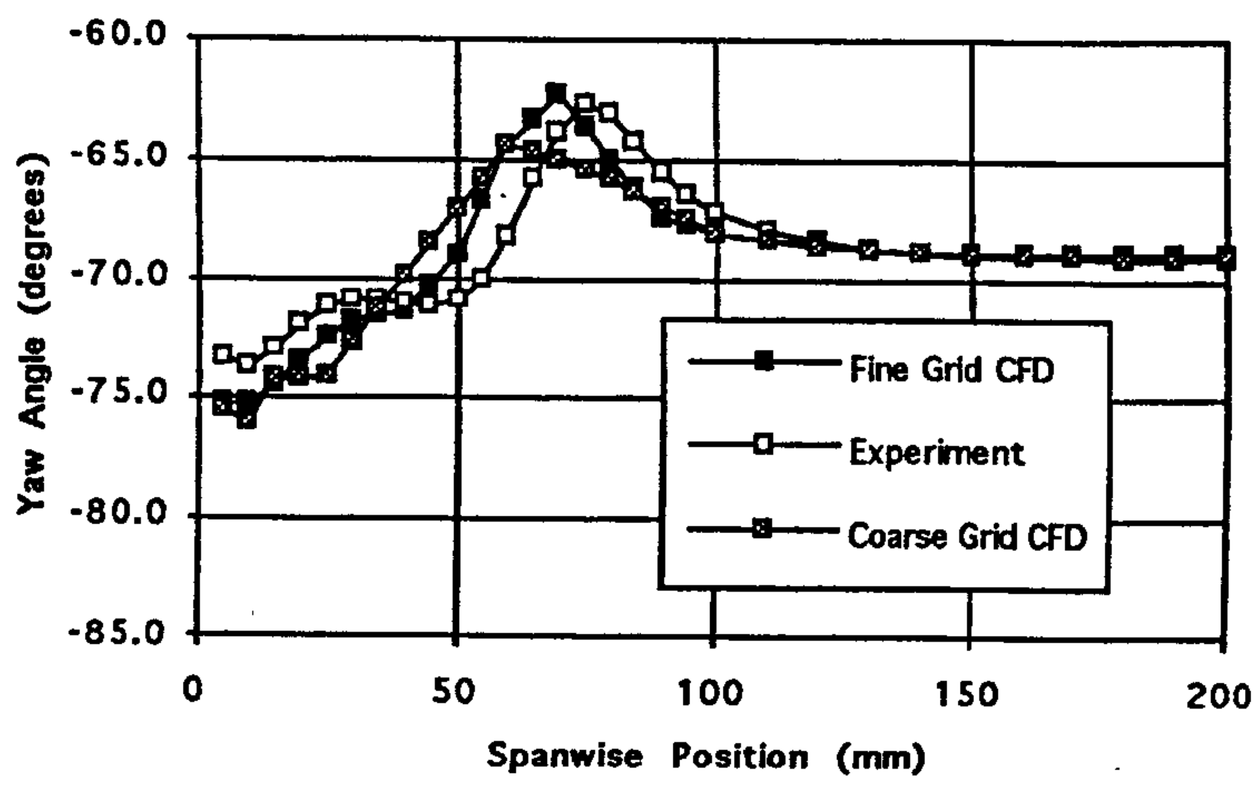

c) Pitch Angle.

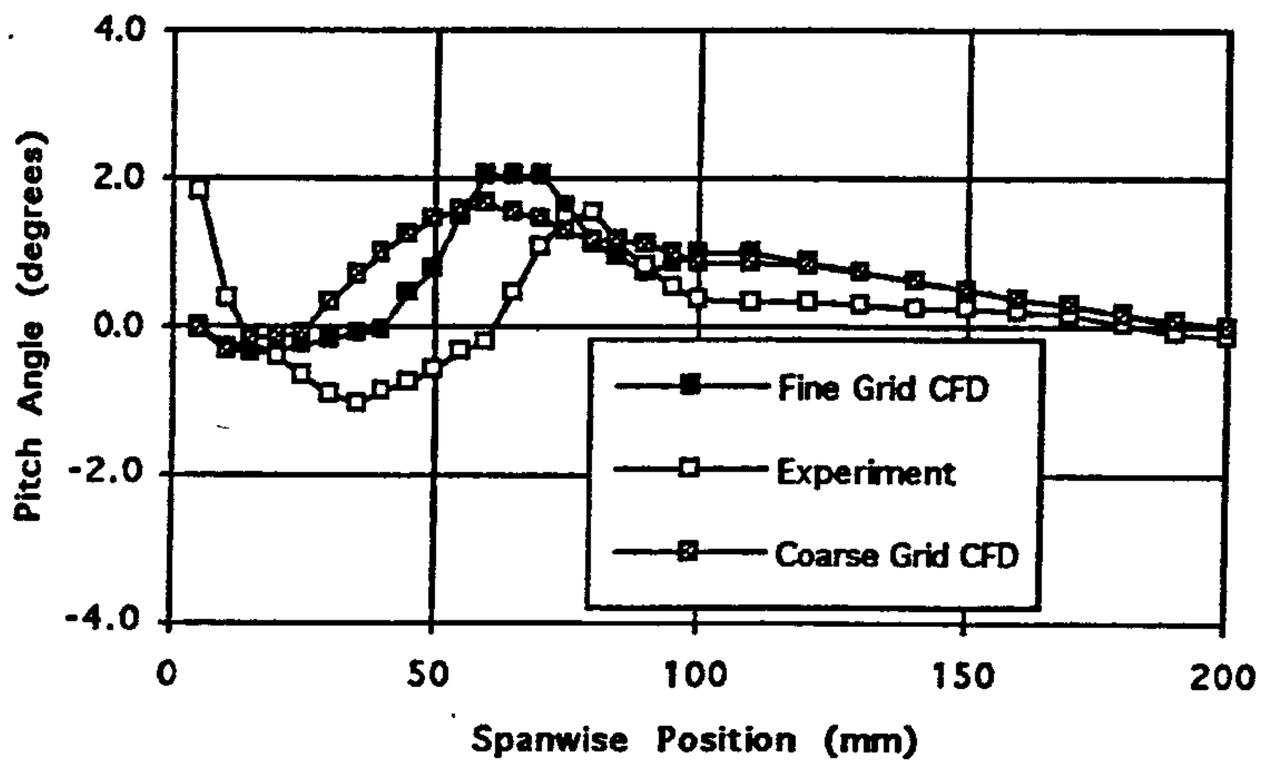

d) Secondary Kinetic Energy Coefficient.

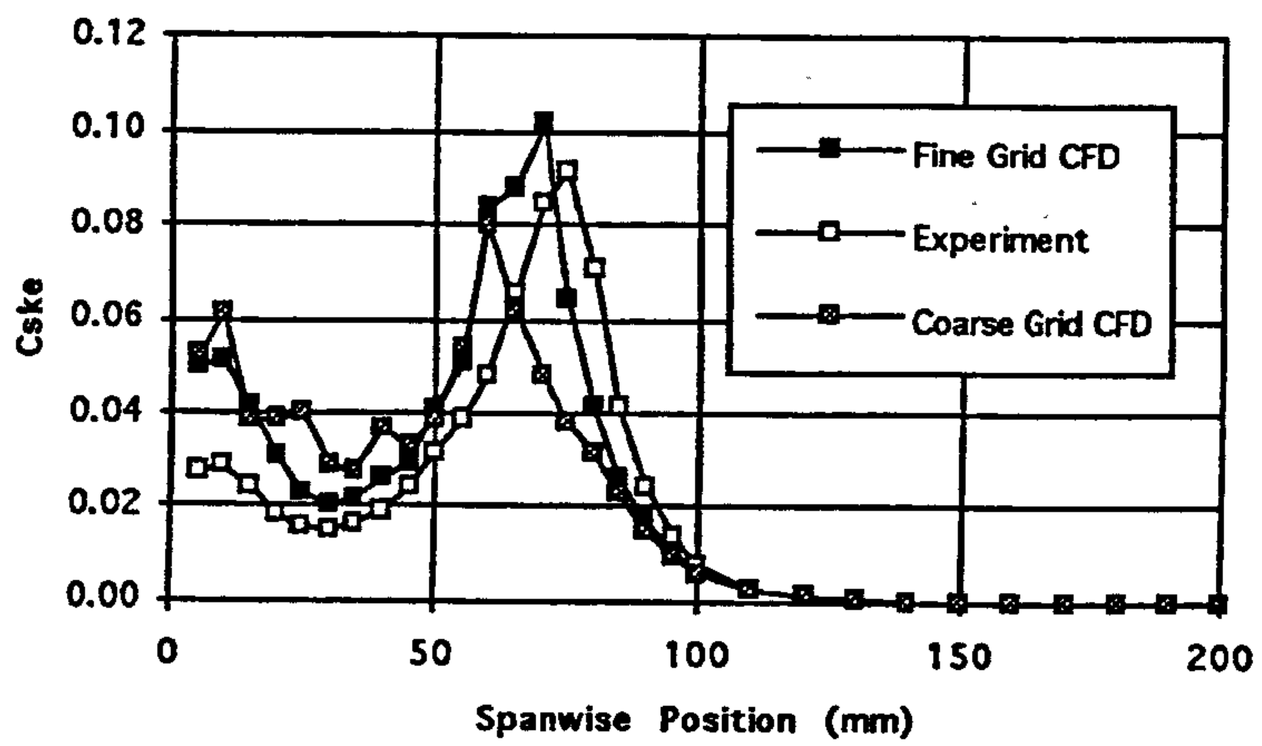

Figure 5.19 Comparison of Data with Previous Research.

a) Total Pressure Loss Coefficient.

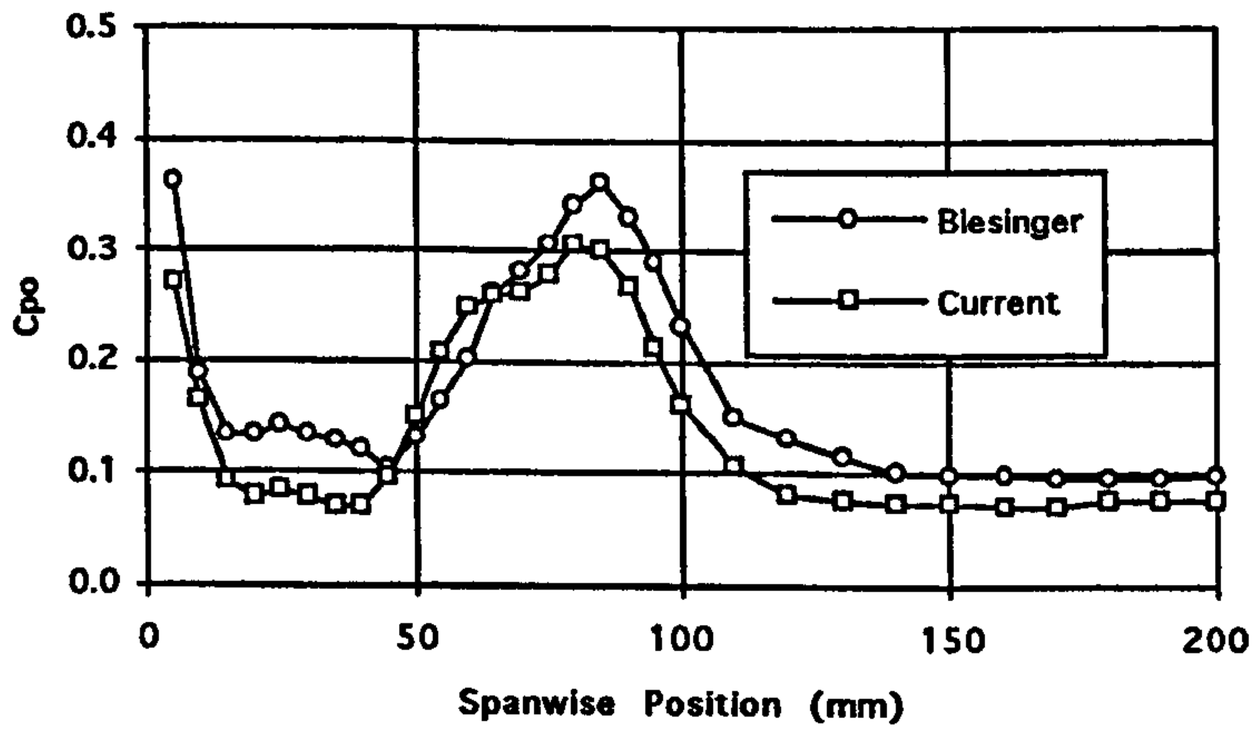

b) Yaw Angle.

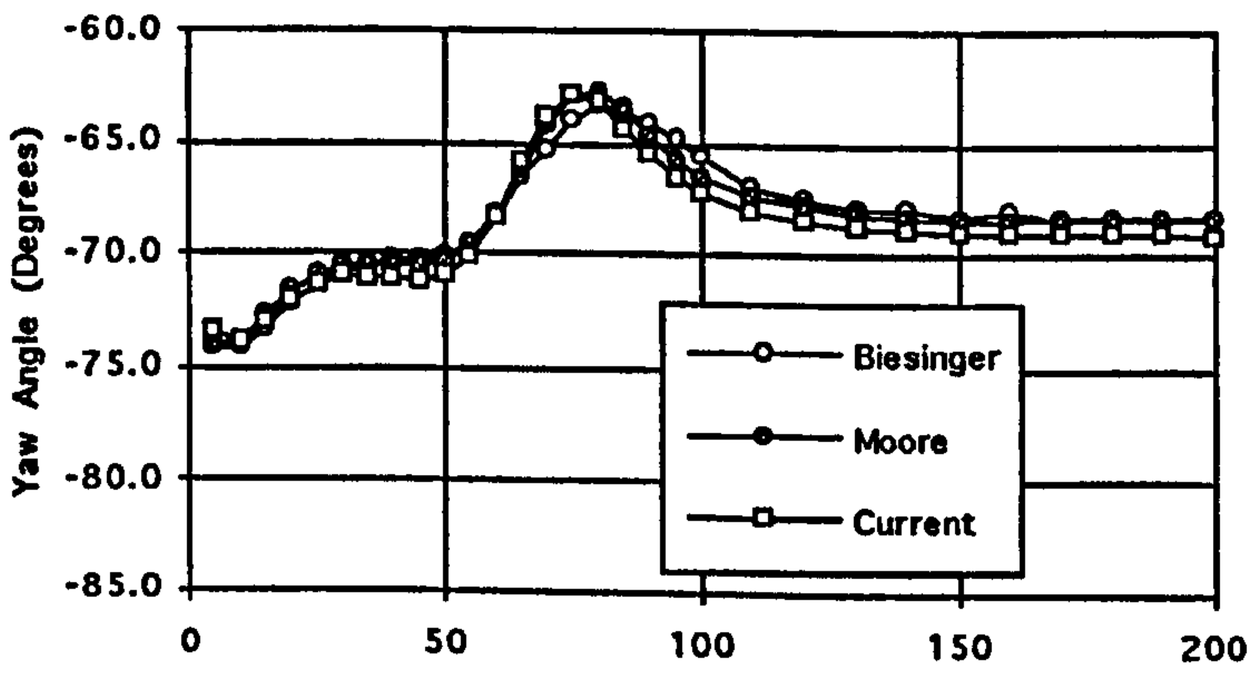

Figure 5.20 Growth of Secondary Kinetic Energy Through the Cascade.

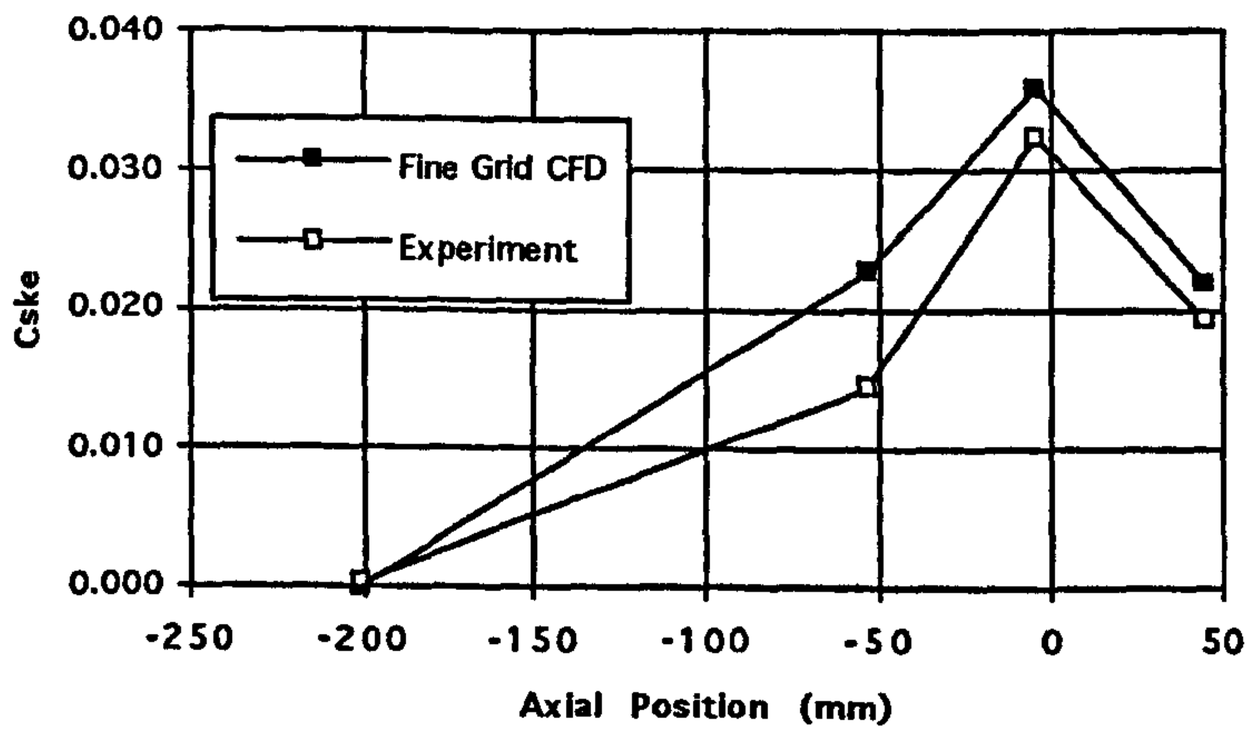

Figure 5.21 Experimental Data at Slot 1.

a) Secondary Velocity Vectors.

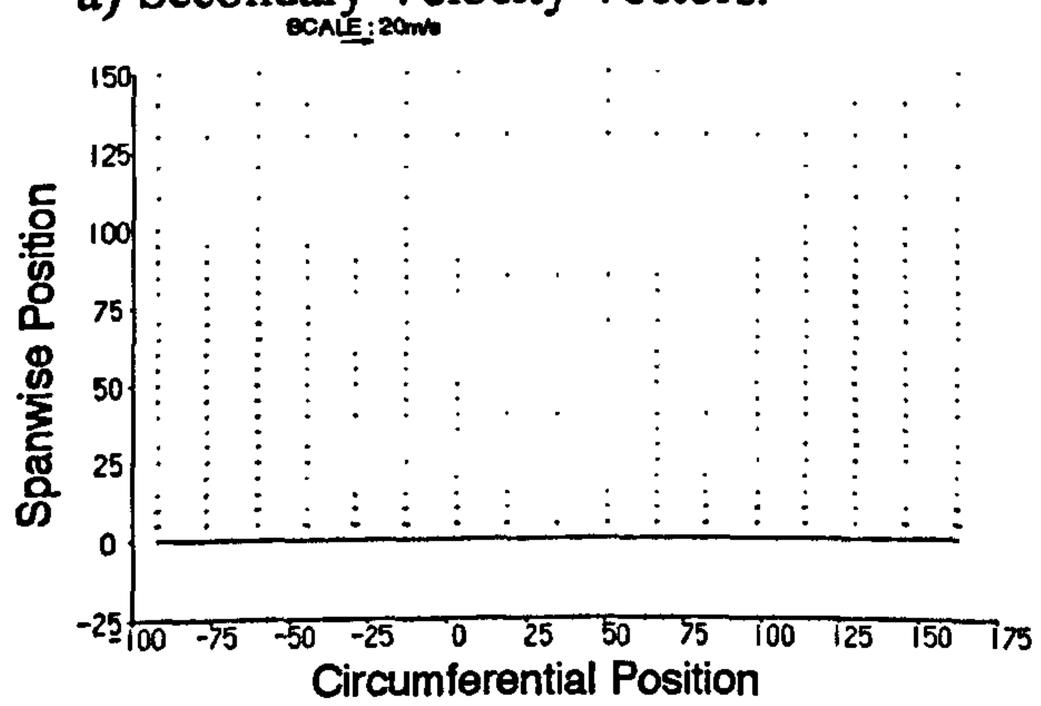

b) Total Pressure Loss Coefficient.

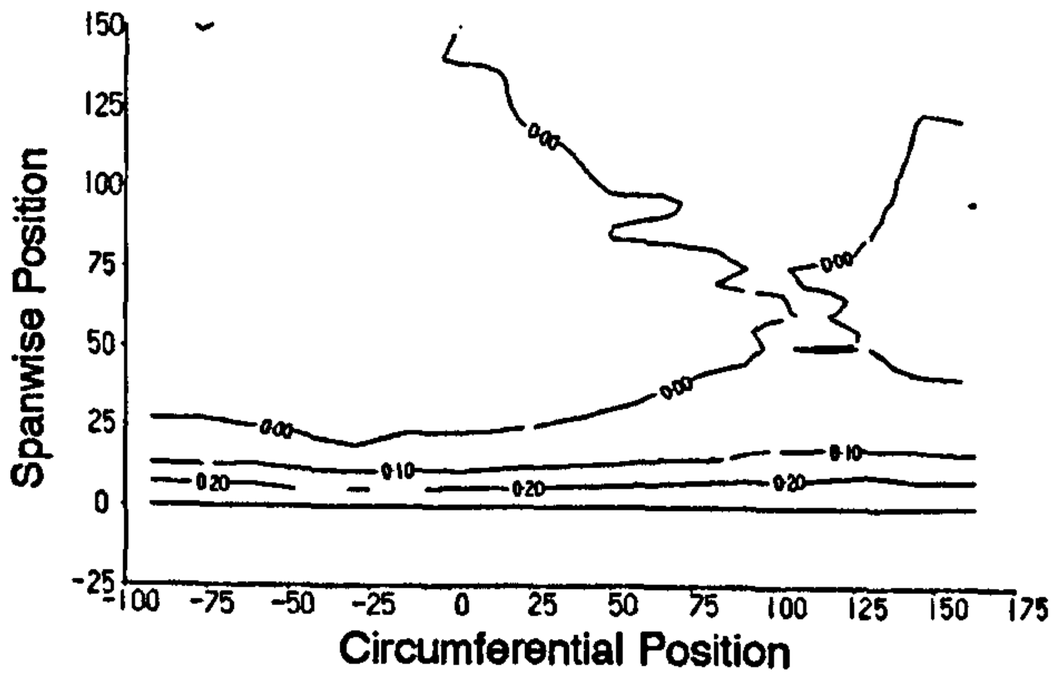

c) Yaw Angle.

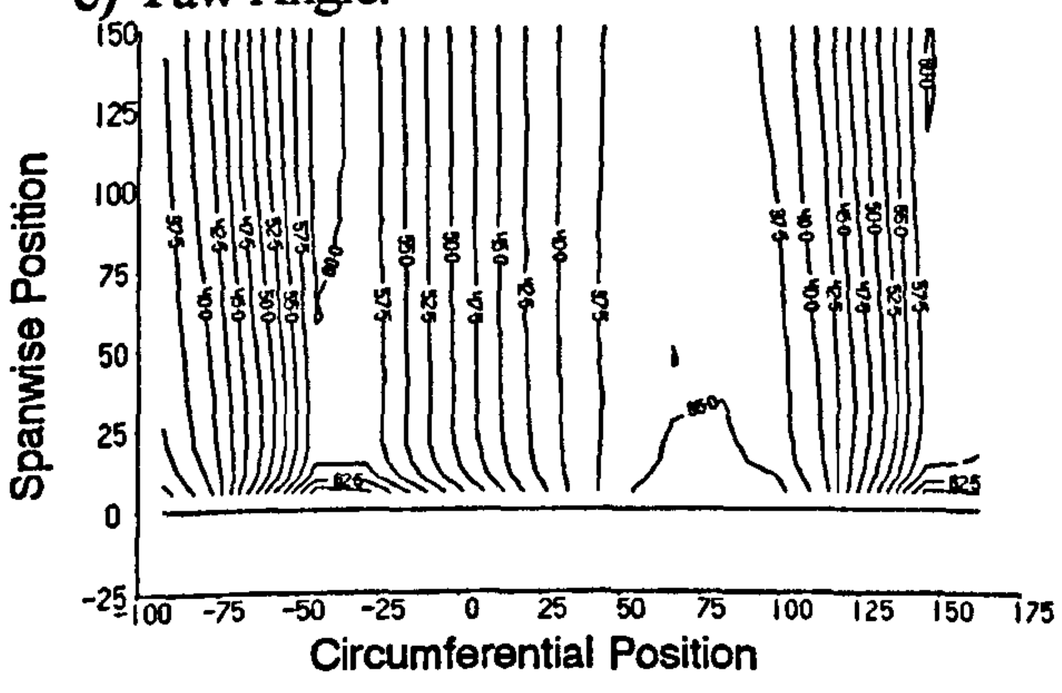

d) Secondary Kinetic Energy Coefficient.

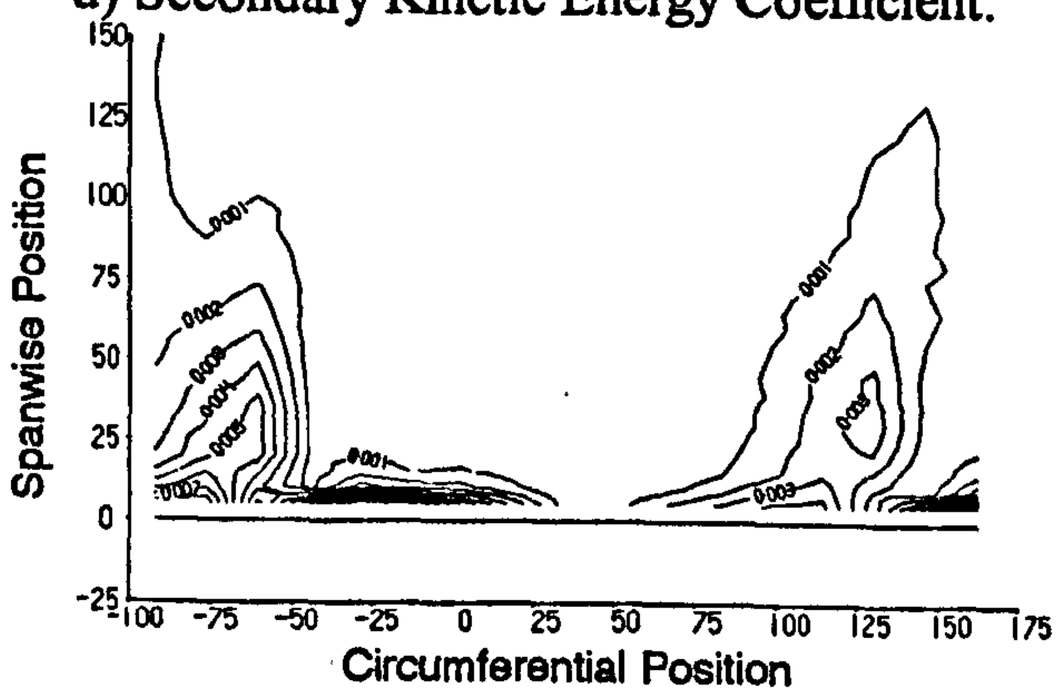

Figure 5.22 Experimental Data at Slot 6.

a) Secondary Velocity Vectors.

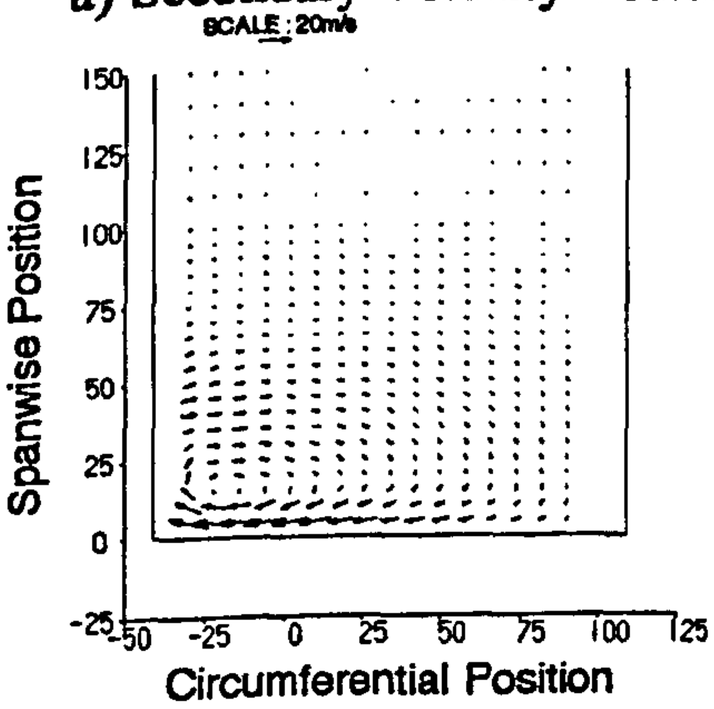

b) Total Pressure Loss Coefficient.

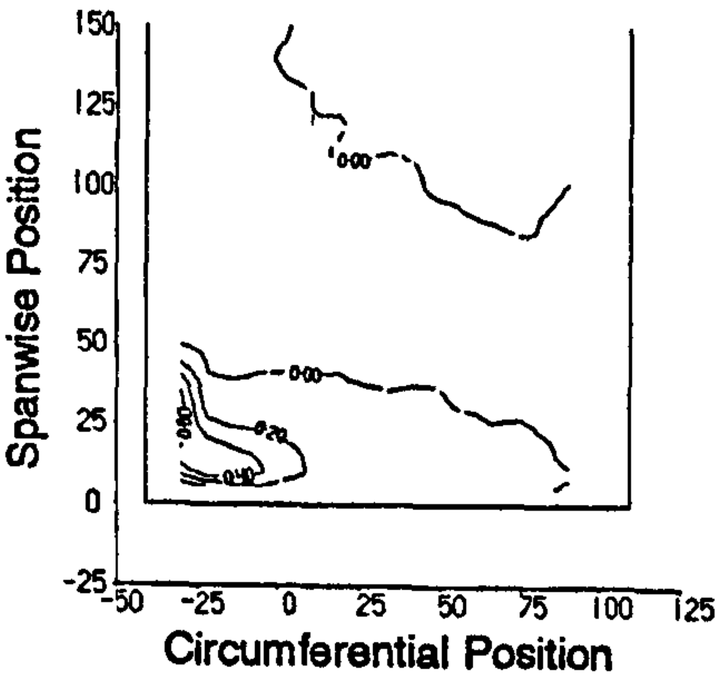

c) Yaw Angle.

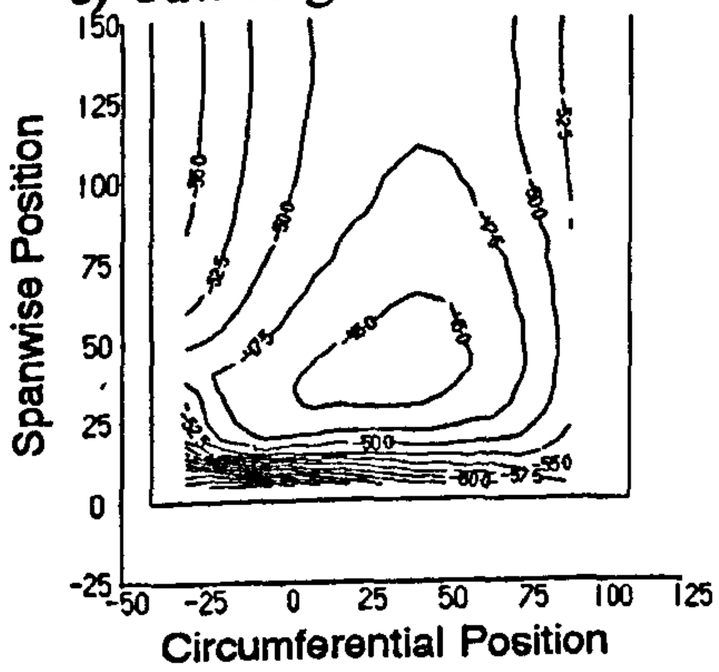

d) Secondary Kinetic Energy Coefficient.

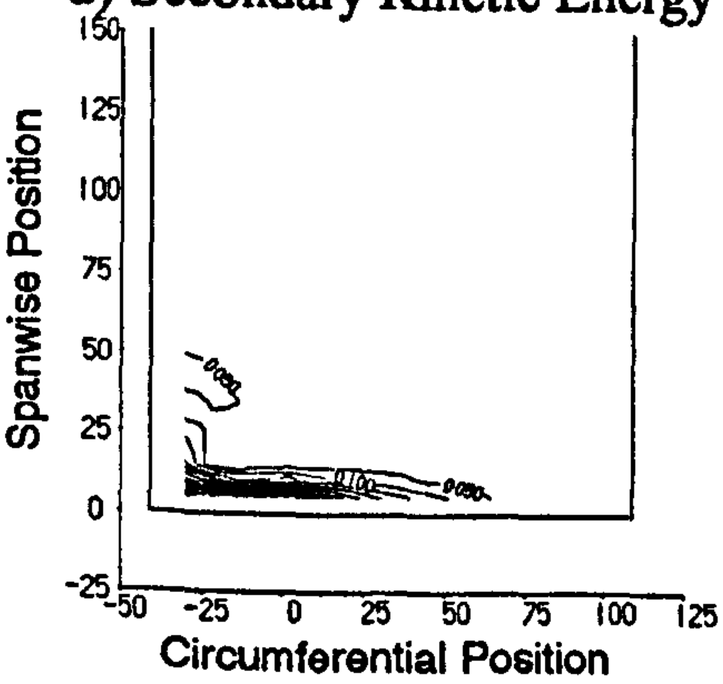

Figure 5.23 Experimental Data at Slot 8.

a) Secondary Velocity Vectors.

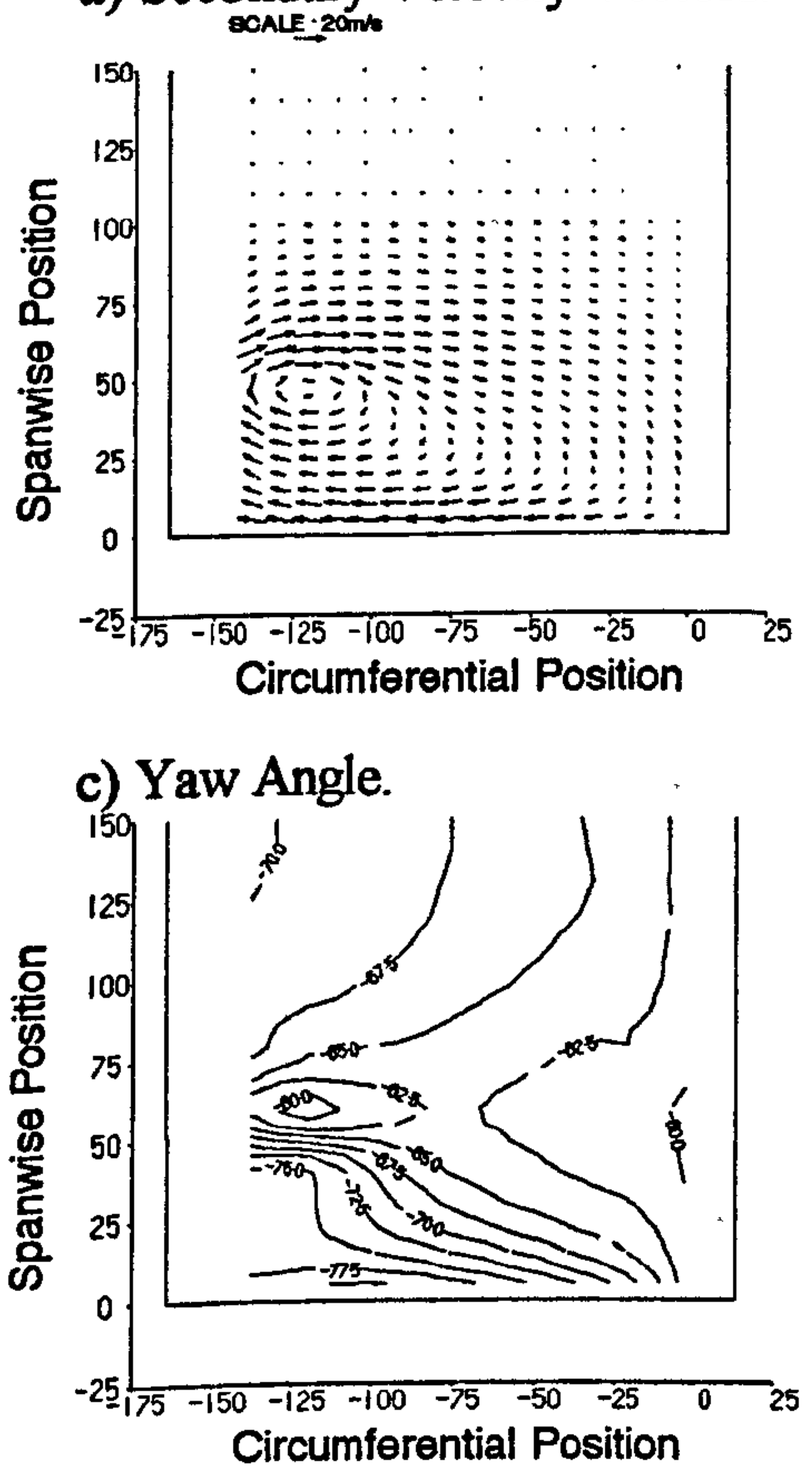

b) Total Pressure Loss Coefficient.

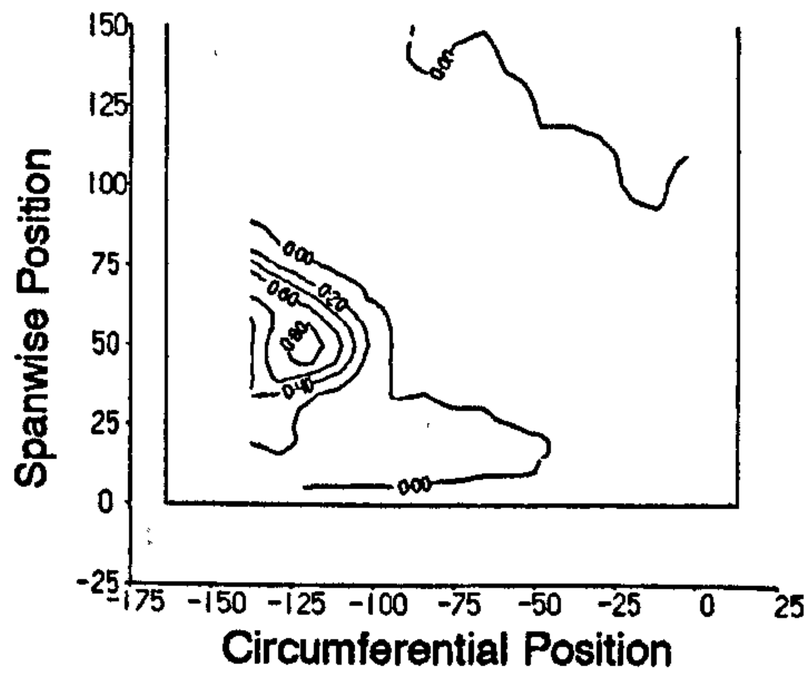

c) Yaw Angle.

d) Secondary Kinetic Energy Coefficient.

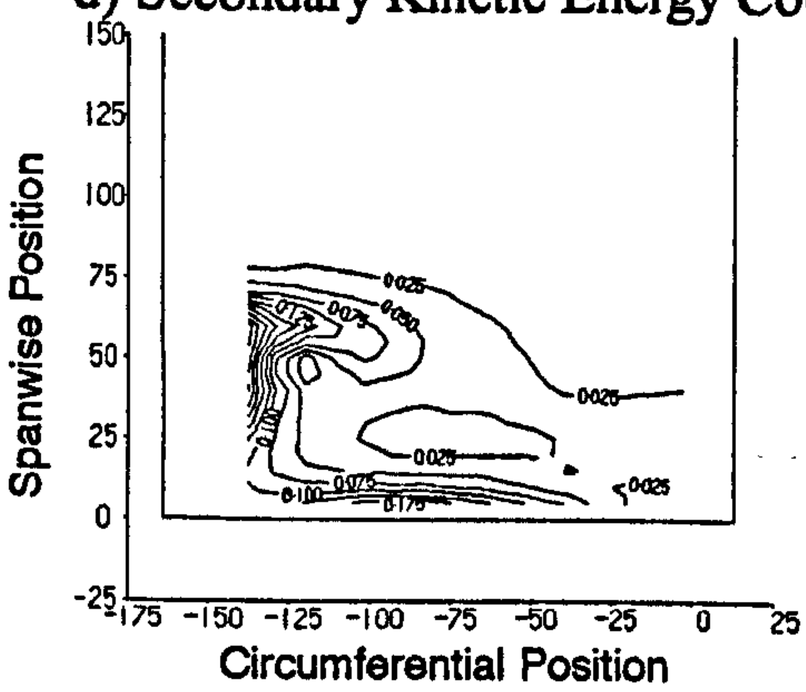

Figure 5.24 Experimental Data at Slot 10.

a) Secondary Velocity Vectors.

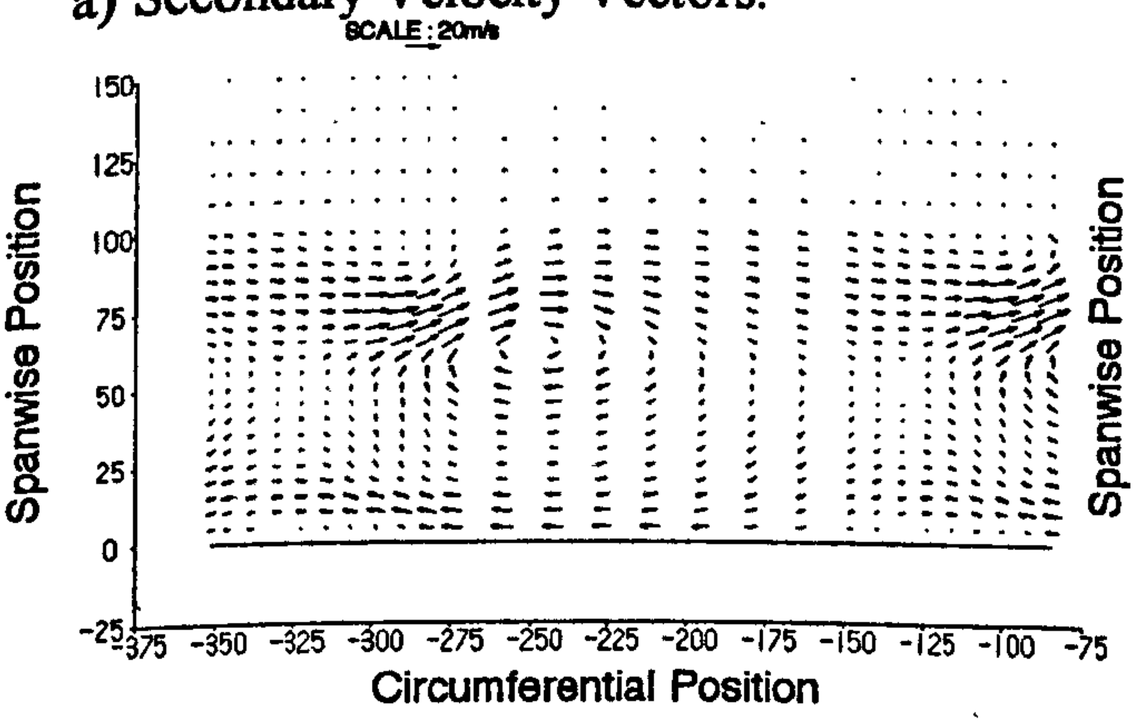

b) Total Pressure Loss Coefficient.

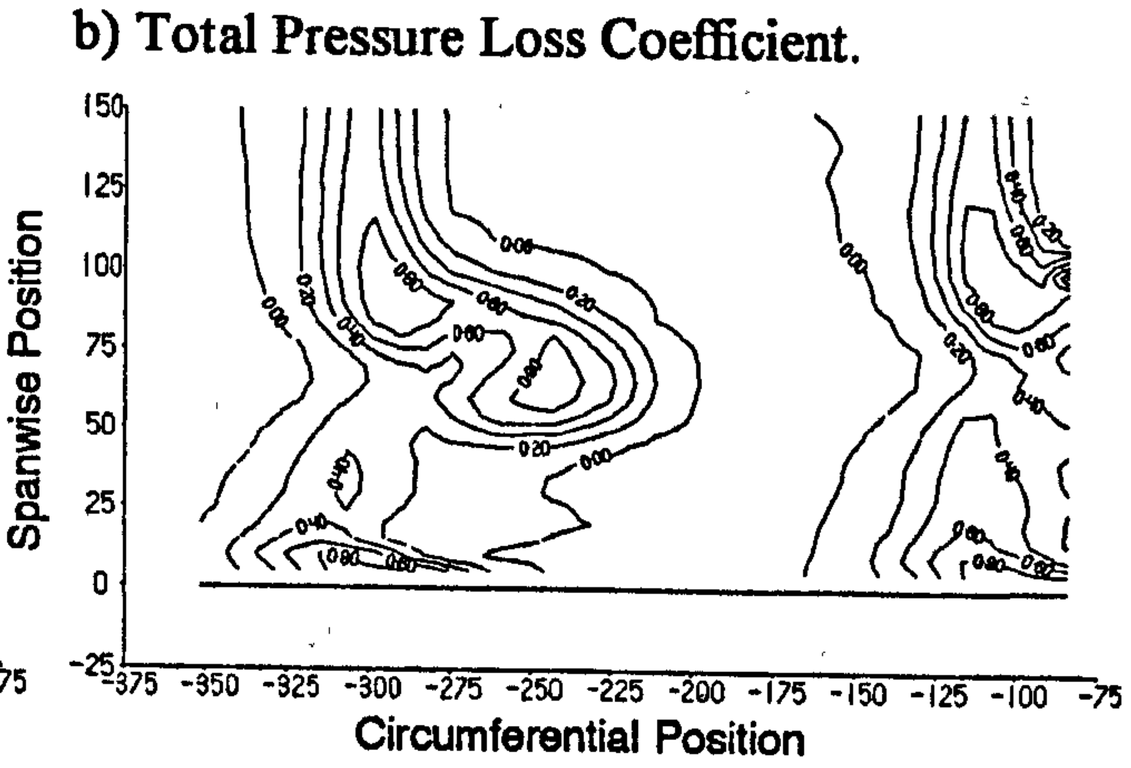

c) Yaw Angle.

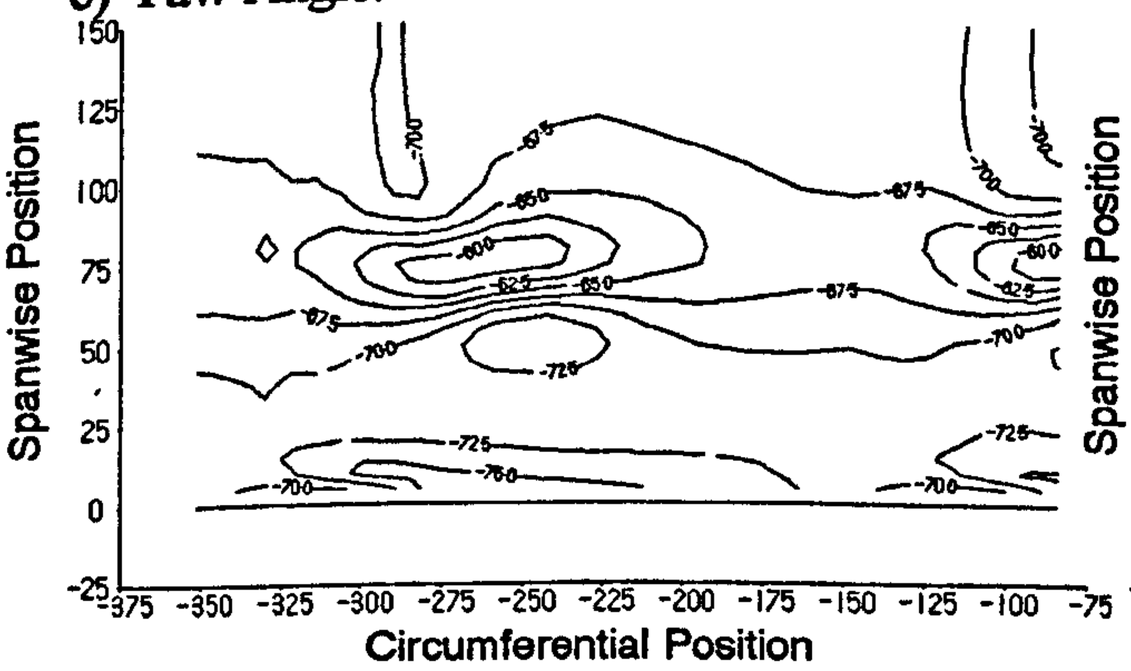

d) Secondary Kinetic Energy Coefficient.

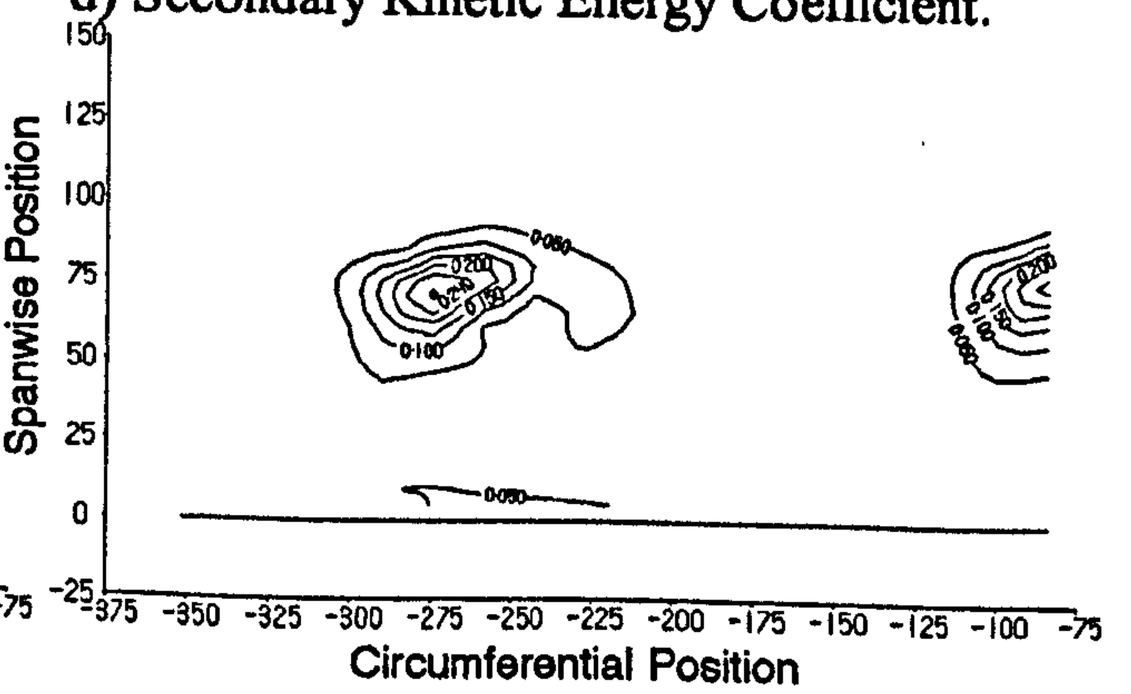

6 Reduction of Circumferential Pressure Non-uniformities at Exit from the Cascade.

6.1 Introduction.

The end-wall profile suggested by Rose[1994] has been redesigned for use in the Durham cascade (Rose used an annular nozzle row as opposed to a linear "rotor row", along with different blade profiles). Rose suggested that 15 - 23% of core flow in a large aeroengine is used as coolant, and each rim seal looses about 0.5%. As coolant flow contributes an approximate 1% increase in SFC, then rim seal leakage contributes a possible 0.1% SFC. The design philosophy and calculations are discussed in Section 6.2.

As can be seen from Figures 5.2 and 5.13 a high pressure region propagates downstream from the blade trailing edge at approximately 90° to the flow direction. This pressure field is shown schematically in Figure 6.1. Any hub coolant flow must be designed for the highest end-wall pressure to prevent ingestion of hot fluid into the hub. Where the end-wall pressure is low however, coolant will tend to leak out. To reduce coolant leakage, it is therefore necessary to reduce this pressure non-uniformity at the axial position of the seal.

CFDS has been used for these design calculations. The resulting profiled wall was manufactured as described in Chapter 4 and tested experimentally to verify the accuracy of the CFD prediction. The results of the design analysis, and the CFD and experimental results are discussed, and compared with the planar wall results from Chapter 5, in Sections 6.3 and 6.4 respectively.

6.2 CFD Design.

The profile design was based on the assumption that the end-wall static pressure could be locally raised by applying a concave curvature to the end-wall. Likewise it was assumed that the surface pressure could be lowered by convex curvature. The resulting profile is the product of an axial profile giving curvature at the platform trailing edge, and a pitchwise profile to vary the magnitude of that curvature tangentially to match the pressure non-uniformity.

The axial profile is parabolic starting at the blade leading edge, feathering into a sine wave which ends at the platform trailing edge. The downstream axial profile is such that the maximum curvature is achieved at the platform trailing edge. The equations of the axial profiles are given in Equations 6.1 and 6.2, and the maximum axial curvature which is at the rim seal location is given by Equation 6.3.

$$\delta r = \alpha(z - z_{le})^2 \qquad \text{Equation 6.1}$$

$$z \le z_i$$

$$\delta r = \frac{\delta r_m}{2}\left(1 + \sin\pi\left(\frac{3}{2} - \frac{(z - z_{pte})}{(z_m - z_{pte})}\right)\right) \qquad \text{Equation 6.2}$$

$$z_i \le z \le z_{pte}$$

$$\rho_{pte} = \frac{\delta r_m}{2(z_{pte} - z)^2} \qquad \text{Equation 6.3}$$

The tangential component of the profile is sinusoidal and is given by Equation 6.4. In Equation 6.5, phase is used to set the maximum convex curvature to match the expected maximum pressure, and ADBIT is used for fine tuning.

$$Fc = \sin\left(\frac{2\pi(y - y_{mean})}{pitch} + phase + \frac{3\pi}{2} + ADBIT\right) \qquad \text{Equation 6.4}$$

Where

$$phase = \frac{2\pi(z - z_{pte})}{pitch}\left(\tan(\beta) + \frac{1}{\tan(\beta)}\right)$$

Figure 6.2 shows a schematic view of the axial shape of the profile.

Calculations have been made using CFDS to model the flow in the cascade. Initially the coarse grid was used (75 axial, 27 pitchwise and 35 spanwise points). Figures 5.2 and 6.3, show the platform trailing edge pressure non uniformity clearly.

The initial profile, "Profile 1" was based on Rose's most successful design, which was non-dimensionalised by blade pitch. Initially ADBIT was taken to be 0. The position of the effective platform trailing edge was assumed to be 20mm (≈10% Cax) downstream, based on typical blades. The resulting change in pressure coefficient, seen in Figure 6.4 (C_{Pt} here is based on average platform trailing edge pressure rather than inlet static pressure) is almost sinusoidal, it was therefore assumed that the final pressure change would be a sine wave, linearly linked to the profile curvature. The curvature of profile 1 at the platform trailing edge is also shown in Figure 6.4, but the scale has been reduced so that its amplitude is the same as that of the sine fit to the change in C_{Pt}. A best fit sine wave was applied to the change in pressure distribution, for the calculation of parameters (amplitude and phase). The best fit sine wave appears to be off-set circumferentially from the experimental data, which is a result of an offset in the ΔC_{Pt} data above the circumferential axis. This stems from the method of calculating ΔC_{Pt} from C_{Pt}, which is itself not sinusoidal. An optimised theoretical sinusoidal pressure change was also derived by adding an arbitrary sine wave to the planar pressure distribution and varying the amplitude and phase of the sine wave to minimise the RMS C_{Pt} along the platform trailing edge. This gave the target pressure distribution shown in Figure 6.4. Based on the assumption that all changes in the

trailing edge pressure distribution generated by this family of end-wall profiles would be sinusoidal (as was the case with profile 1), this sine wave should be the change in trailing edge pressure distribution that would result from the optimum end-wall profile.

The amplitude of the target pressure modification was 68.5% of that due to profile 1, and the error in phase is 0.475 radians. The curvature was therefore reduced to 68.5% by moving Zm, and ADBIT was assumed to be 0.475 radians. This iteration gave profile 2.

From Figure 6.5 it can be seen that shifting the curvature tangentially does not give an equal shift in pressure. As mentioned previously, ADBIT was 0.475 radians, but the change in phase of the pressure modification ΔC_{Pt} was only 0.22 radians. ADBIT was therefore assumed to have only a 46.4% effect, so the next value chosen was 0.475/0.464 = 1.024 radians. Also, the curvature was reduced to 68.4% of profile 1 but the pressure modification only reduced to 84%. Curvature however was again reduced linearly.

From Figure 6.6 it can be seen that when a best sine fit is used, the target pressure modification has been achieved. Table 6.1 shows the position of maximum curvature and ADBIT for the three profiles and target, along with their effects on the pressure distribution.

Table 6.1 Changes in Profile and Flow Parameters.

	Profile		Pressure Change		
	Z_m (mm)	ADBIT (rad)	RMS C_{Pt} (% Planar)	Amplitude of ΔC_{Pt} ()	Phase of ΔC_{Pt} (rad from wake)
Profile 1	-5	0	0.7737	0.3040	-2.8674
Profile 2	-10	0.475	0.4122	0.2470	-2.6469
Profile 3	-13	1.024	0.2872	0.2021	-2.3227
Target	-	-	0.4473	0.2080	-2.3921

Figures 6.7 show the platform trailing edge pressure distributions for the planar end-wall and profile 3. As can be seen, the effect of the profiling is not an exact sinusoidal change in pressure and this gives rise to the improvement in RMS pressure in table 6.1 being better than the target distribution. Figures 6.8 show the end-wall pressure distributions for the planar end-wall and profile 3. Figures 6.9 show the change in end-wall pressure distribution and the end-

wall height of profile 3. Figures 6.9 show that the change in end-wall pressure is proportional to the profile height which would be expected as for a sinusoidal profile, where curvature is approximately proportional to height.

6.3 CFD Results.

After the design phase, the fine grid (89 axial x 38 pitchwise x 29 half span points) was used to investigate the effects of the profile on the flow-field with better resolution of the flow features.

6.3.1 End-Wall Height and Cp Values.

From Figures 6.10 and 6.11, the reduction in the downstream end-wall pressure non-uniformity can be seen clearly, with little difference between the fine and coarse grid calculations.

The blade C_P plots shown in Figures 6.12 a to f show that the effect of profiling in this case is limited to very close to the end-wall as by 10% span there is hardly any difference between the planar and profiled blade pressure distributions. Looking at Figure 6.9 a, it is also clear that the effect of profiling is limited to the latter 20% of the blade. This is as expected as the end-wall profile is very gentle in the upstream part of the passage, as seen in Figure 6.9 b. It is surprising to note that the planar and profiled C_P curves cross over between 60% and 80% C_{ax} whereas the main profile curvature only starts at about 90% C_{ax}.

6.3.2 Area and Pitch Averaged Results.

Figures 6.13 to 6.16 show pitch averaged C_{Po}, Yaw and Pitch angle and C_{SKE} and at Slots 1, 6, 8 and 10. Upstream and within the passage, there is very little change in the flow, and at Slot 10 there are only slight changes to the flow-field. The most notable change is the large increase in loss on the end-wall side of the passage vortex. Also, near the end-wall a slight decrease in the overturning and an increase in loss is seen. It can also be seen that the passage vortex has moved towards the end-wall slightly. Figure 6.16 d would also indicate a slight reduction in C_{SKE} up to 30mm and between 60 and 100mm from the end-wall.

Tables 6.2 and 6.3 show area averaged C_{Po}, C_{SKE} and Yaw Angle through the cascade for both planar and profiled CFD. Table 6.4 shows net losses at Slot 10. The net loss for Profile 3

(see Table 6.3) is slightly higher than for the planar wall, and this is possibly due to the increase in loss near the end-wall, although this may be due to errors in the CFD solutions. The apparent reduction in the passage vortex seen in the C_{SKE} values with profile 3 would suggest a decrease in secondary loss, although this is not the case.

Table 6.2 Area Averaged Values for the Profile 3 CFD.

	C_{Po}			Mixed out			
	Full	Mid-Span	Secondary	Full	Mid-Span	Secondary	C_{SKE}
Slot 1	0.016	0.000	0.016	0.016	0.000	0.016	0.0001
Slot 6	0.037	-0.005	0.042	-	-	-	0.0219
Slot 8	0.049	-0.012	0.061	-	-	-	0.0317
Slot 10	0.215	0.152	0.063	0.245	0.162	0.083	0.0180

Table 6.3 Area Averaged Values for the Planar Wall CFD.

	C_{Po}			Mixed out			
	Full	Mid-Span	Secondary	Full	Mid-Span	Secondary	C_{SKE}
Slot 1	0.015	0.000	0.016	0.016	0.000	0.016	0.0001
Slot 6	0.039	-0.002	0.041	-	-	-	0.0227
Slot 8	0.048	-0.010	0.059	-	-	-	0.0359
Slot 10	0.211	0.153	0.058	0.244	0.163	0.081	0.0218

Table 6.4 Net Area Averaged C_{Po} at Slot 10 for Planar and Profile 3 CFD.

	C_{Po}			Mixed out		
	Full	Mid-Span	Secondary	Full	Mid-Span	Secondary
Profile 3	0.200	0.152	0.047	0.229	0.162	0.067
Planar	0.195	0.153	0.042	0.228	0.163	0.065

6.3.3 Contour Maps and Secondary Velocity Vectors.

Figures 6.17 to 6.20 show contour maps of C_{Po}, C_{SKE}, Yaw angle and secondary velocity vectors at Slots 1, 6, 8 and 10. From these figures, there are no significant changes in the flow in the upstream part of the passage, and this is as would be expected from the gentle nature of the profiling in this part of the passage. The decrease in overturning and slight increase in loss near the end-wall seen in Figures 6.16 are probably due to the counter-vortex (Figures 6.20 a at approximately -150mm and -350mm tangential location) which has increased in size in the

profiled case. Again, the movement of the passage vortex towards the end-wall, and the significant increase in loss from the end-wall side of the passage vortex is seen in the profiled case. It is possible that the passage vortex develops in the trough in the profile along the blade suction surface and then does not fully recover its distance from the end-wall after the sharp curvature at the trailing edge. This is supported by the data at Slots 6 and 8, where the passage vortex appears to maintain a fixed distance from the end-wall when comparing the profiled and planar walls. When comparing Slots 8 and 10, the passage vortex retains its absolute radial location, that is in both the planar and profiled cases the vortex moves away from the end-wall radially by about 20 mm. The vortex in the profiled case does not move a greater distance as would be expected from the increase in end-wall height between Slots 8 and 10 where the trough ends and the end-wall resumes zero height.

6.4 Experimental Results.

6.4.1 End-Wall Cp Values.

Figures 6.21 show the profiled end-wall static pressure coefficient, the planar end-wall being included for comparison. The reduction in the downstream pressure non-uniformity can clearly be seen and, comparing with Figure 6.9, the CFD predictions agree very well with the experimental results. Figure 6.22 shows the CFD and experimental non-dimensional pressure non-uniformities at the platform trailing edge for both profiled and planar end-walls. From this, the quantitative agreement can clearly be seen. From the experimental data, the reduction in Profile 3 RMS pressure non-uniformity to 30.1% of the planar case, agrees well with the reduction to 28.7% shown in Table 6.1.

6.4.2 Area and Pitch Averaged Results.

From Figures 6.23 and 6.24 a (upstream boundary layer and Slot 1) the region of high total pressure (seen previously in Figure 5.14 and 5.15 a) can still be seen in the inlet boundary layer. The errors in yaw angles at Slot 1 (Figure 6.24 b) are possibly due to the proximity of the probe to the blade leading edge. The high flow angles relative to the probe, and high pressure gradients in this region, could significantly effect the accuracy of the results at this location.

Figures 6.25 and 6.26 show a significant increase in the size of the loss core at Slots 6 and 8. This is also seen in the secondary loss in Tables 6.5 and 6.6, although it is not apparent from the total loss due to slight errors in the inlet loss and mid-span losses. It is interesting to note that while the secondary loss is increased at Slots 6 and 8, C_{SKE} is reduced. These effects on the flow are unexpected as they are well upstream of where the main profile curvature starts. The increase in the loss core shown by the experimental data is significantly greater than in the CFD data. This is possibly due to the poor loss prediction of the CFD code, discussed in Section 5.4

The gradients in Yaw angle are much less at Slots 6 and 8 (Figures 6.27 and 6.28) in the profiled case, which emphasises the reduction in C_{SKE}.

Tables 6.5 and 6.6 show area averaged C_{Po}, C_{SKE} and Yaw Angle through the cascade for both planar and profiled CFD. Table 6.7 shows net losses at Slot 10. Again, the loss increase is greater in the experimental data than in the CFD data.

Table 6.5 Area Averaged Experimental Values for the Profile 3 Wall.

	C_{Po}			Mixed out			C_{SKE}
	Full	Mid-Span	Secondary	Full	Mid-Span	Secondary	
Slot 1	0.001	0.007	-0.006	0.003	0.017	-0.013	0.0006
Slot 6	0.024	0.000	0.024	-	-	-	0.0173
Slot 8	0.032	-0.012	0.044	-	-	-	0.0332
Slot 10	0.159	0.077	0.082	0.180	0.081	0.099	0.0182

Table 6.6 Area Averaged Experimental Values for the Planar Wall.

	C_{Po}			Mixed out			C_{SKE}
	Full	Mid-Span	Secondary	Full	Mid-Span	Secondary	
Slot 1	-0.002	0.017	-0.019	-0.002	0.016	-0.018	0.0005
Slot 6	0.022	0.008	0.013	-	-	-	0.0145
Slot 8	0.020	-0.001	0.022	-	-	-	0.0323
Slot 10	0.136	0.076	0.060	0.157	0.079	0.079	0.0194

Table 6.7 Net Area Averaged Experimental C_{Po} for the Planar and Profile 3 Walls at Slot 10.

	C_{Po}			Mixed out		
	Full	Mid-Span	Secondary	Full	Mid-Span	Secondary
Profile 3	0.174	0.070	0.104	0.195	0.074	0.121
Planar	0.148	0.068	0.080	0.169	0.071	0.098

6.4.3 Contour Maps and Secondary Velocity Vectors.

Figures 6.29 to 6.32 show contour maps of C_{Po}, C_{SKE}, Yaw angle and secondary velocity vectors at Slots 1, 6, 8 and 10. The conclusion reached from the CFD data that the passage vortex follows the bottom of the trough on the end-wall and then fails to recover fully after the end-wall returns to zero height is shown to be the case. The flow in the cascade shows a greater movement of the passage vortex toward the end-wall at Slot 10, indicating that the recovery is

over-predicted by the CFD. It can also be seen from the loss contours that the distortion of the wake is slightly less with the end-wall profiling.

The increase in loss seen in the experimental data is much larger than that seen in the CFD Data, as seen in the pitch averaged data. This could be due to the effects on loss of the recovery of the passage vortex downstream of the profile not being correctly resolved by the CFD, and hence the increase in loss being incorrectly predicted by the CFD. The increase in secondary loss is outside the limit of the experimental accuracy (estimated at +/- 0.01% dynamic head, see Section 4.3.2), and so is probably a truly physical phenomenon.

6.4.4 Flow Visualisation.

A mixture of Diesel oil and Fluorescent dye was injected through the end-wall pressure tappings, and this gave streak-lines across the end-wall. Figures 6.33 show this for both the planar and profiled case. When viewed with the secondary velocity vectors (Figure 6.29 a to 6.32 a) the change in flow angle near the end-wall is significant. Looking back to Figure 6.9 b This change in flow coincides with the bump on the end-wall. This could be due to acceleration of the flow over the crest of the bump, reducing the overturning effect of the end-wall pressure gradient by reducing the near wall velocity deficit.

6.5 Discussion.

6.5.1 C_{SKE} Compensation for End-Wall Slope.

It was thought that the definition of C_{SKE} was incorrect for a profiled end-wall. The existing definition outlined by Equation 6.5 does not account for any slope on the end-wall. In effect, flow that is parallel to the end-wall (which is itself sloped) will incorrectly contribute a radial velocity to C_{SKE}.

$$C_{SKE} = \frac{\left(U_1 \frac{\sin(\beta - \beta_{mid})}{\cos(\beta)}\right)^2 + U_3^2}{U_{inlet}^2} \qquad \text{Equation 6.5}$$

A more appropriate formulation would be that given in Equation 6.6 where α_{inv} and β_{inv} are the inviscid pitch and yaw angles respectively. These inviscid angles are obtained from an inviscid CFDS calculation with no inlet boundary layer. To resolve any problems with differences at mid-span the inviscid yaw angles are adjusted to give the same mid-span yaw angle.

$$C_{SKE} = \frac{\left(U_1 \frac{\sin(\beta - \beta_{inv})}{\cos(\beta)}\right)^2 + \left(U_1 \frac{\sin(\alpha - \alpha_{inv})}{\cos(\alpha)}\right)^2}{U_{inlet}^2} \qquad \text{Equation 6.6}$$

Figures 6.34 and 6.35 show the pitch averaged compensated C_{SKE} at Slots 1, 6, 8 and 10 for both CFD and experimental data.

At Slot 1, not much is happening, and as the wall is still planar, no changes would be expected here. At Slot 6, the compensated C_{SKE} follows the uncompensated curve away from the wall with a decrease to below the planar value near the wall. Again, not much has happened by this point. At Slot 8, however, the profile has begun to take effect, and the compensated C_{SKE} shows the effects of the profiling. Away from the end-wall, the compensated curve follows the uncompensated one closely. Closer to the wall there is a significant decrease in the C_{SKE}, by more than the difference between profiled and planar data. Near to the wall, the compensated data tends towards the planar case, showing that the effects of localised

acceleration over the bump and deceleration in the trough has been cancelled out. At Slot 10, this effect is demonstrated very well in the CFD data as the compensated data follows the uncompensated data except in the region within about 25mm from the end-wall where the compensated data follows the planar data. In the experimental data, the compensated data actually shows an increase in C_{SKE} near the end-wall. This is probably due to effects of the end-wall curvature on the inviscid flow at the trailing edge propagating downstream to Slot 10, also seen in the CFD case very close to the end-wall. The compensation has not affected the flow effects away from the wall, such as the squeezing of the passage vortex due to the rapid recovery of end-wall height, but has reduced the immediate effects of the curvature of the wall.

The initial idea behind this compensation was to remove the effect of the radial velocity component of flow parallel to the end-wall. Initially, the angle between the profiled and flat end-walls in the direction of the local end-wall flow was calculated, and this was then assumed to decay over the secondary flow region. This resulted in a decaying stream-wise pitch angle which the flow could be resolved onto to give the radial component of C_{SKE}. However, differences between the local yaw angle and the end-wall yaw angle, used to generate the assumed decaying end-wall pitch angle, led to uncertainty over the physical accuracy of this model. It was therefore decided to carry out inviscid CFD calculations with no inlet boundary layer to obtain a baseline flow-field with no "secondary" flow. However, this introduces yaw angle effects from an inverse "secondary" flow caused by the action of the reduced blade loading near the end-wall on the high momentum flow which replaced the inlet boundary layer along the end-wall. These yaw angle effects act to increase the compensated C_{SKE} partially or completely negating the effect of the radial velocities (seen later in Chapter 7). It is still believed that this approach is physically more accurate than the assumption that the radial velocity near the end-wall is zero.

6.6 Conclusions.

This results presented in this chapter have proved that it is possible to design an end-wall profile using CFD methods to control directly the end-wall pressure distribution to reduce the platform trailing edge pressure non-uniformity for the purpose of reducing rim seal leakage. The changes in end-wall pressure resulting from profiling have been shown to be directly related to the curvature of the end-wall profiling. The profile generated in this work only aimed to reduce the 1st harmonic of the platform trailing edge pressure non-uniformity, and further iterations using the same procedure could potentially eliminate the pressure non-uniformity altogether. The experimental testing of the profile has confirmed the results of the CFD design used to control the pressure distribution on the end-wall. The end-wall profiling in this case does not have a significant effect on the secondary flow, although the loss is increased slightly, and slight reduction in C_{SKE} is predicted. The C_{SKE} reduction in the experimental data is slightly higher than predicted by the CFD. This is thought to be due to the sharp curvature at the trailing edge, and the resulting reduction in size of the passage vortex as it fails to recover its radial location as the end-wall returns to zero height.

Figure 6.1 Schematic Pressure Field Downstream of a Blade Row.

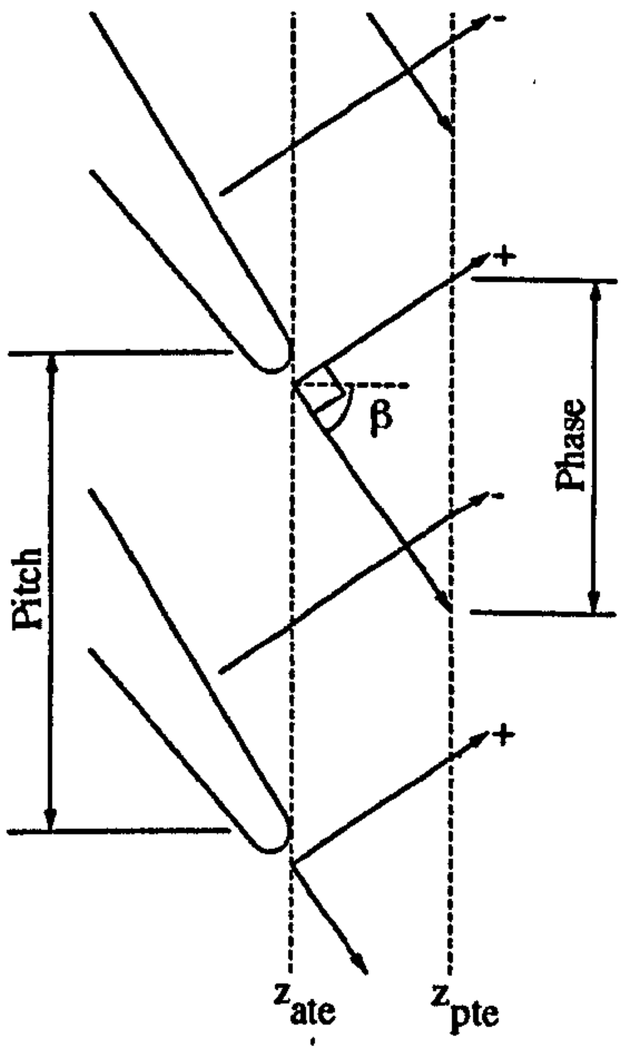

Figure 6.2 Schematic View of the Axial Shape of the Profile.

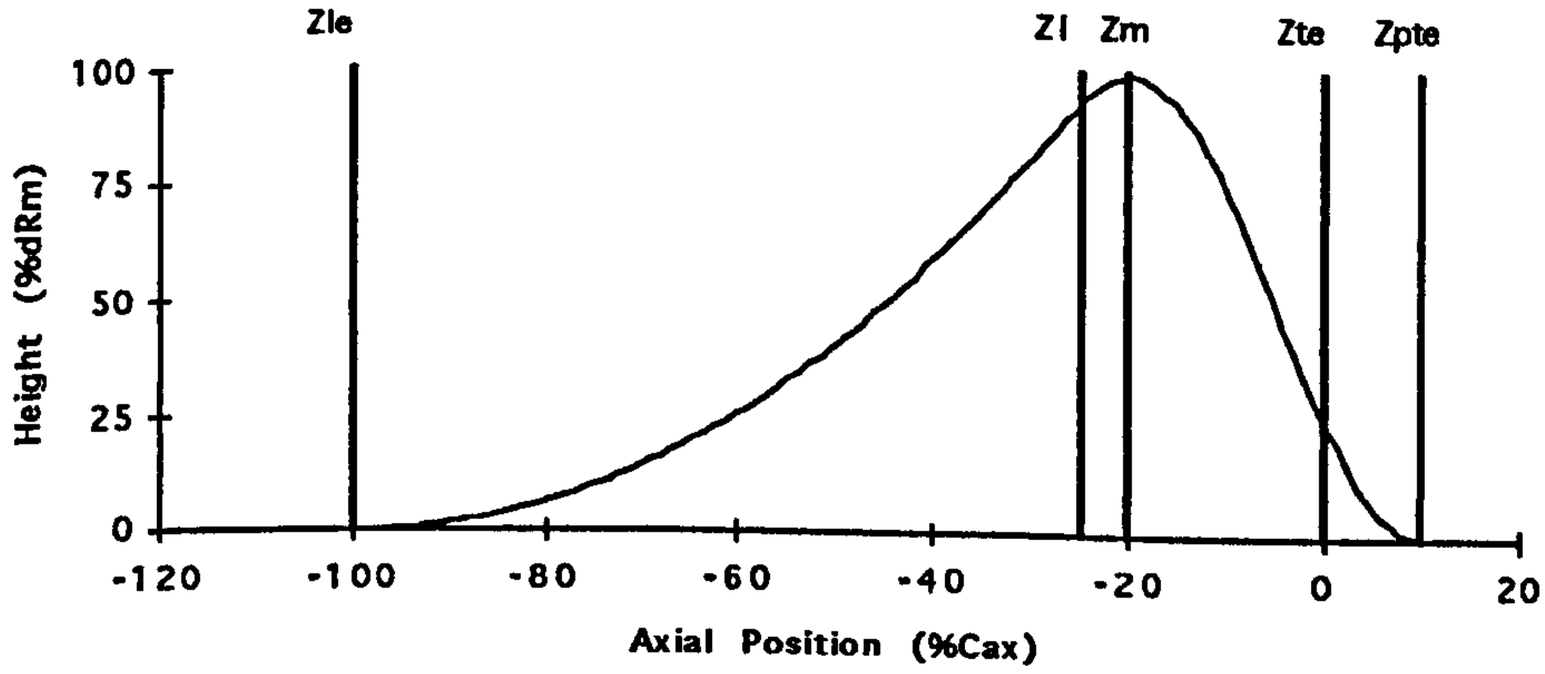

Figure 6.3 Non-Dimensional Pressure at Platform Trailing Edge (Coarse Grid CFD).

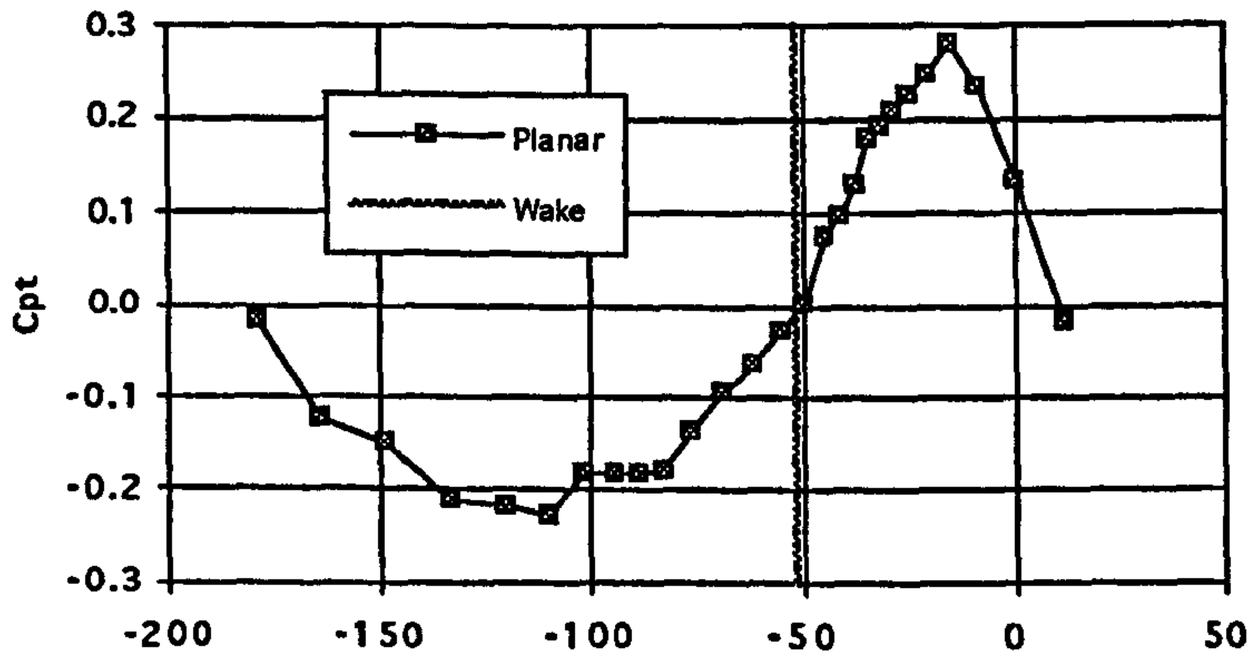

Figure 6.4 Change in Non-Dimensional Pressure at Platform Trailing Edge (Profile1 - Planar).

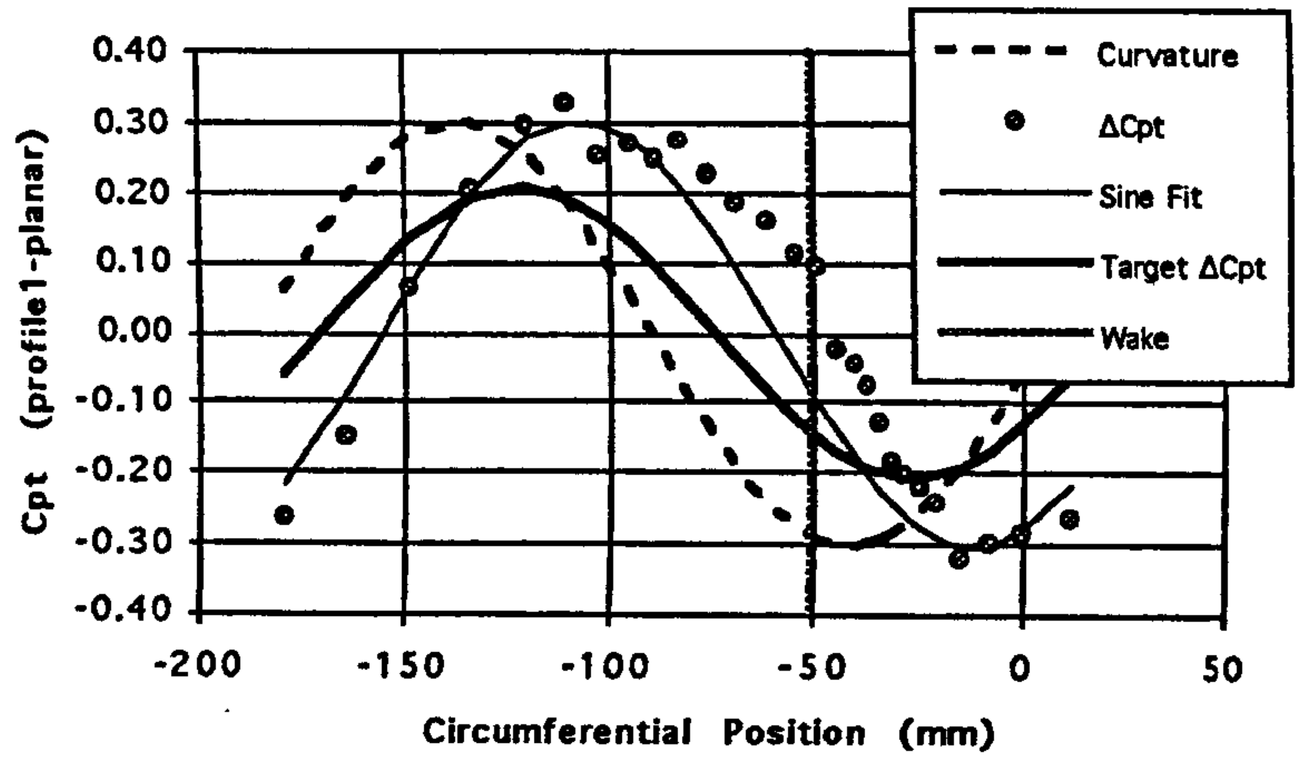

Figure 6.5 Change in Non-Dimensional Pressure at Platform Trailing Edge (Profile2 - Planar).

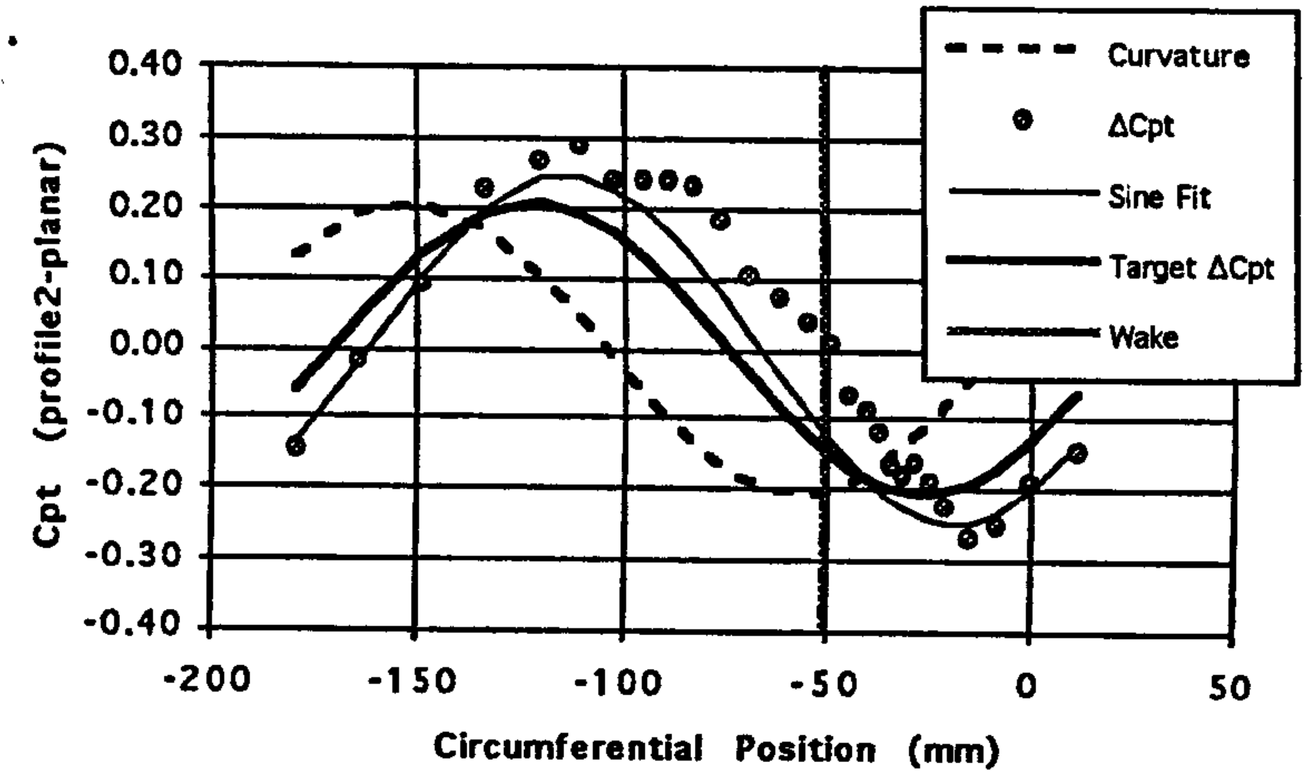

Figure 6.6 Change in Non-Dimensional Pressure at Platform Trailing Edge (Profile3 - Planar).

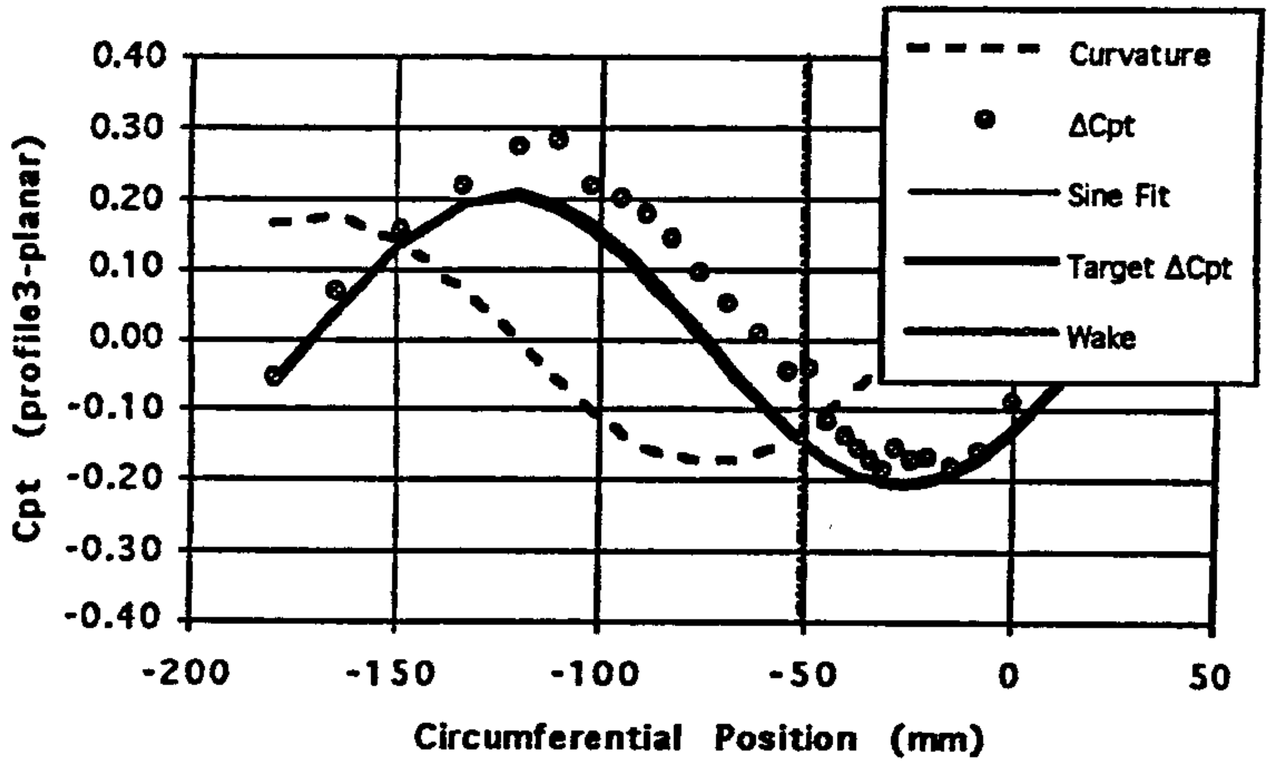

Figure 6.7 Designed Non-Dimensional Pressure at Platform Trailing Edge (Coarse Grid CFD).

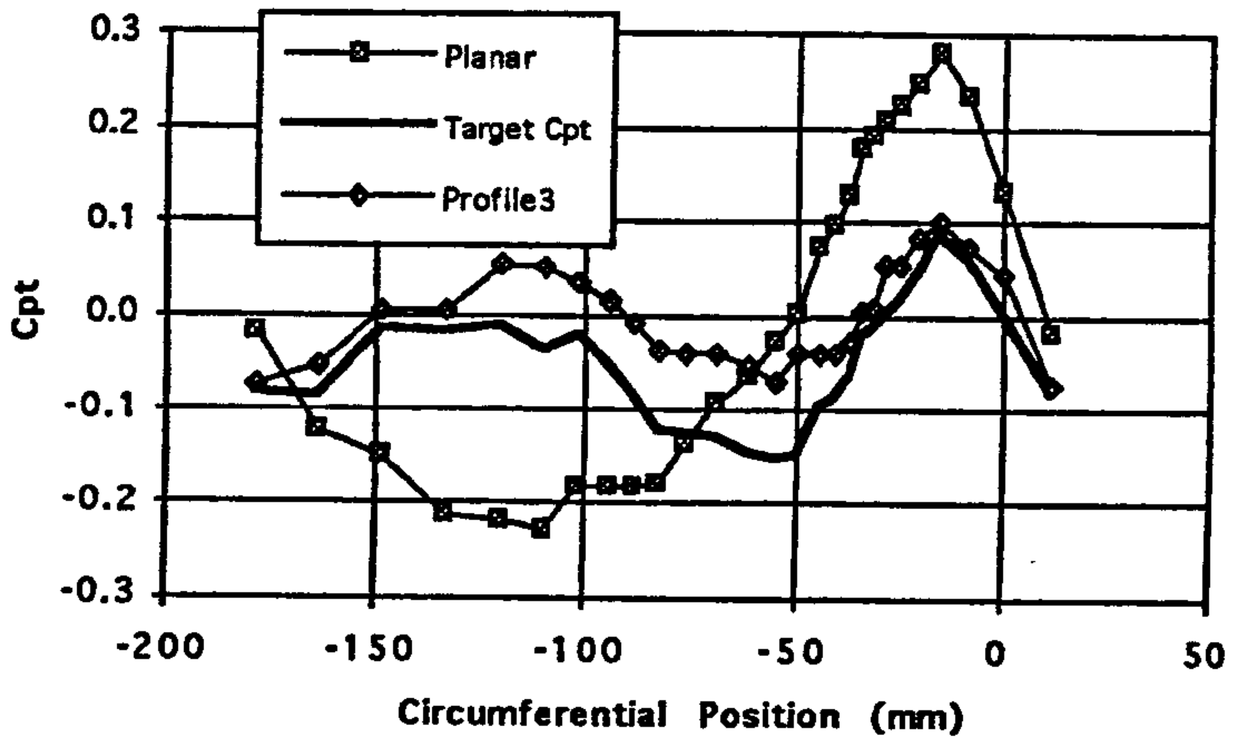

Figure 6.8 End-wall Pressure Coefficients (Coarse Grid CFD).

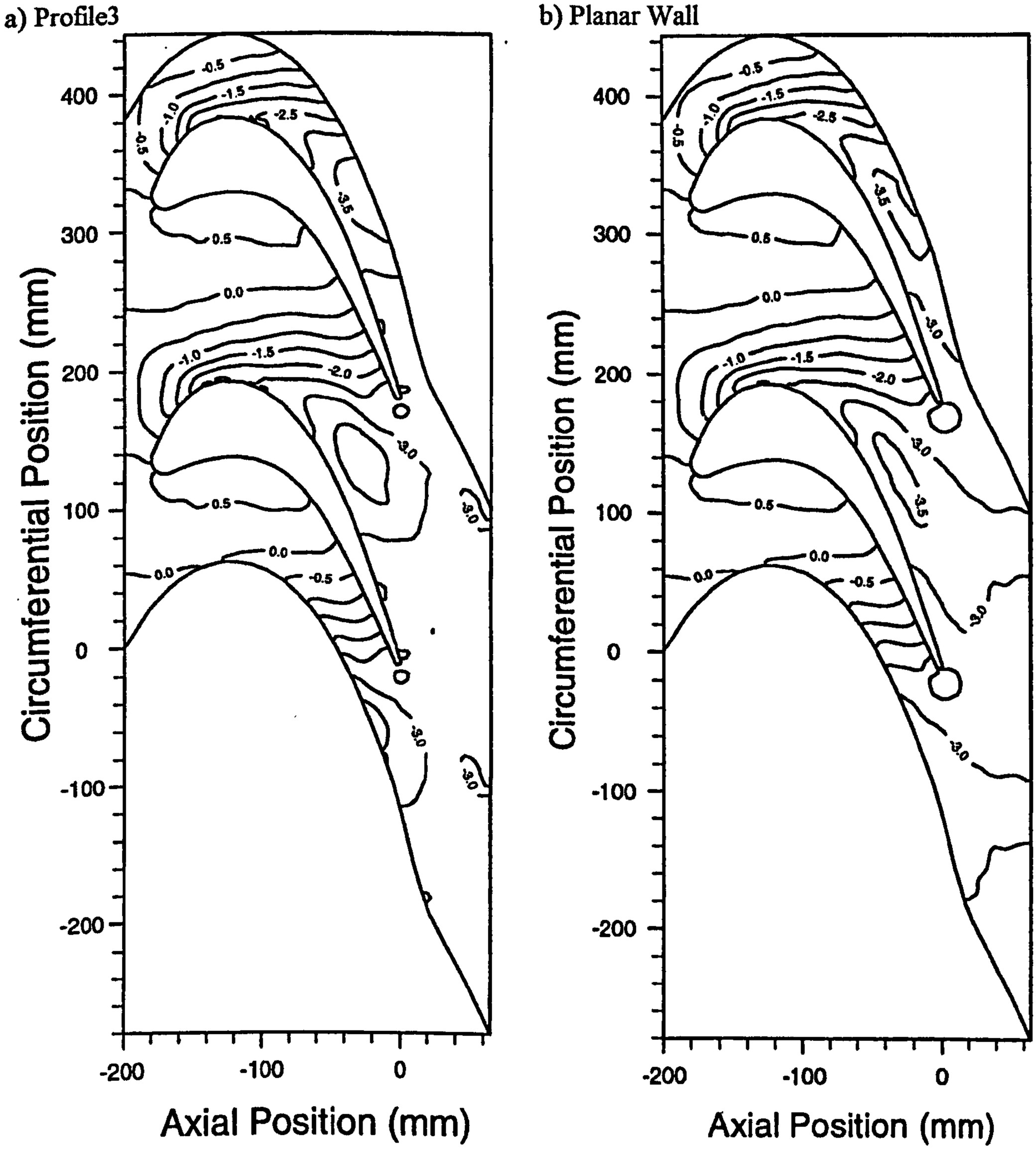

Figure 6.9 Change in End-wall Pressure Coefficient (Profile 3 - Planar) and End-wall Height (Profile 3).

a) ΔC_{pt} (Profile 3 - Planar)

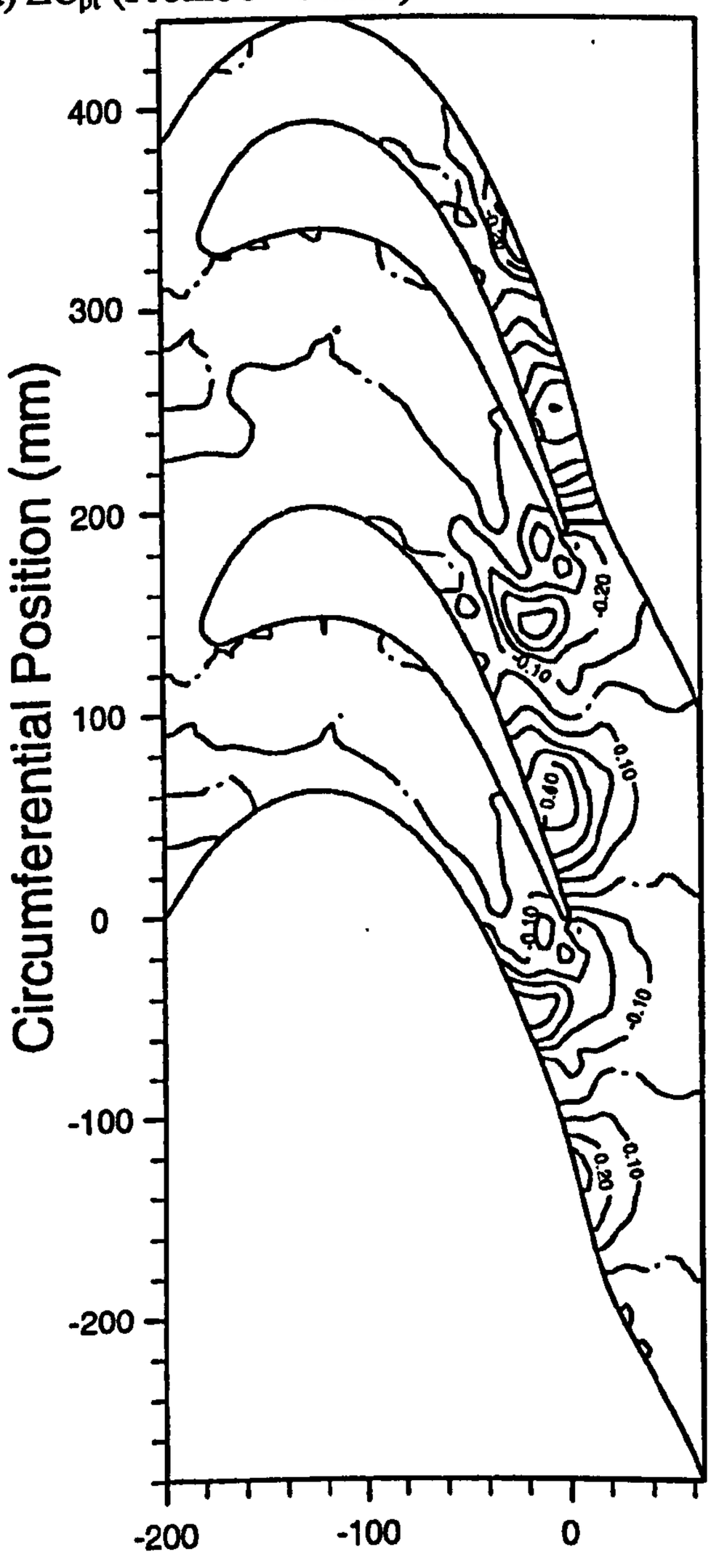

b) End-wall Height (mm)

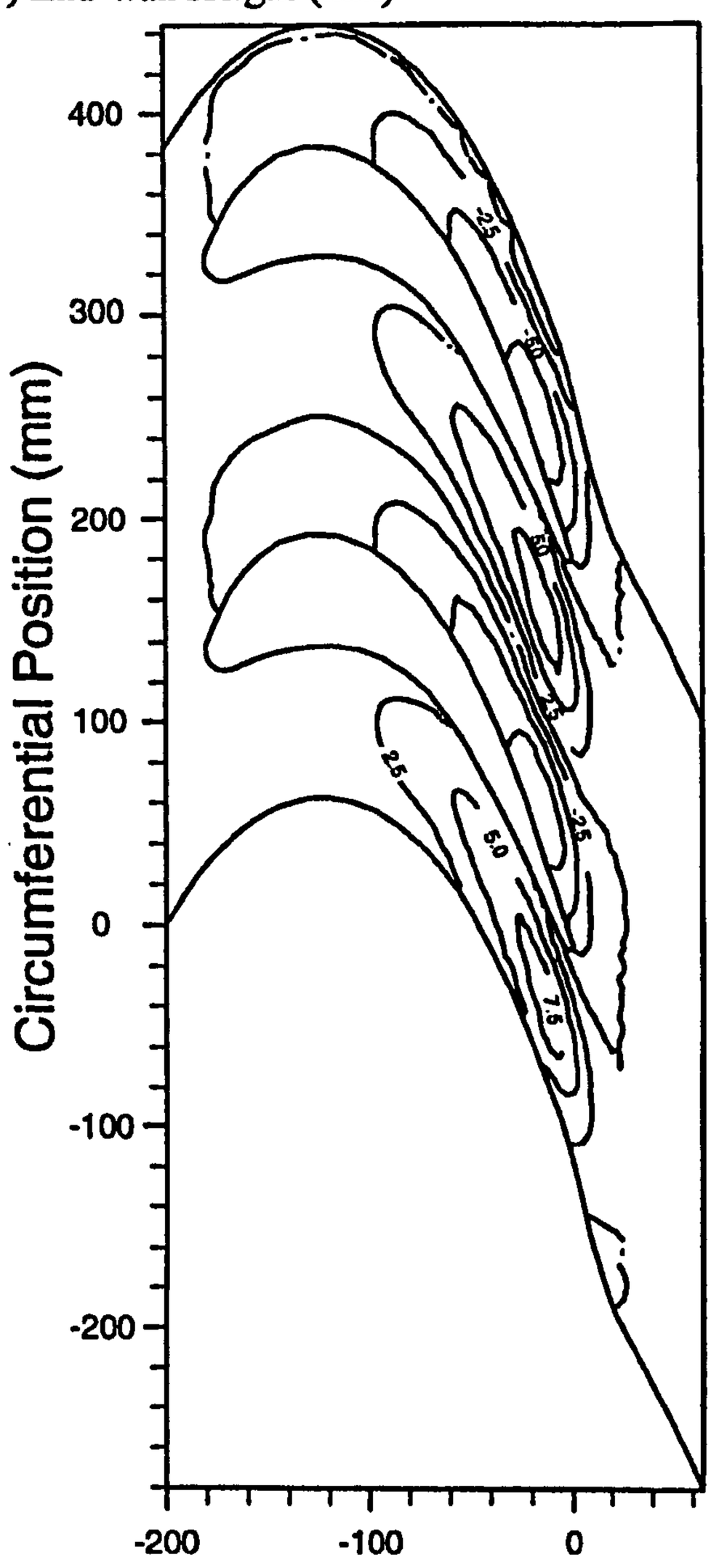

Figure 6.10 CFD Non-Dimensional Pressures at Platform Trailing Edge.

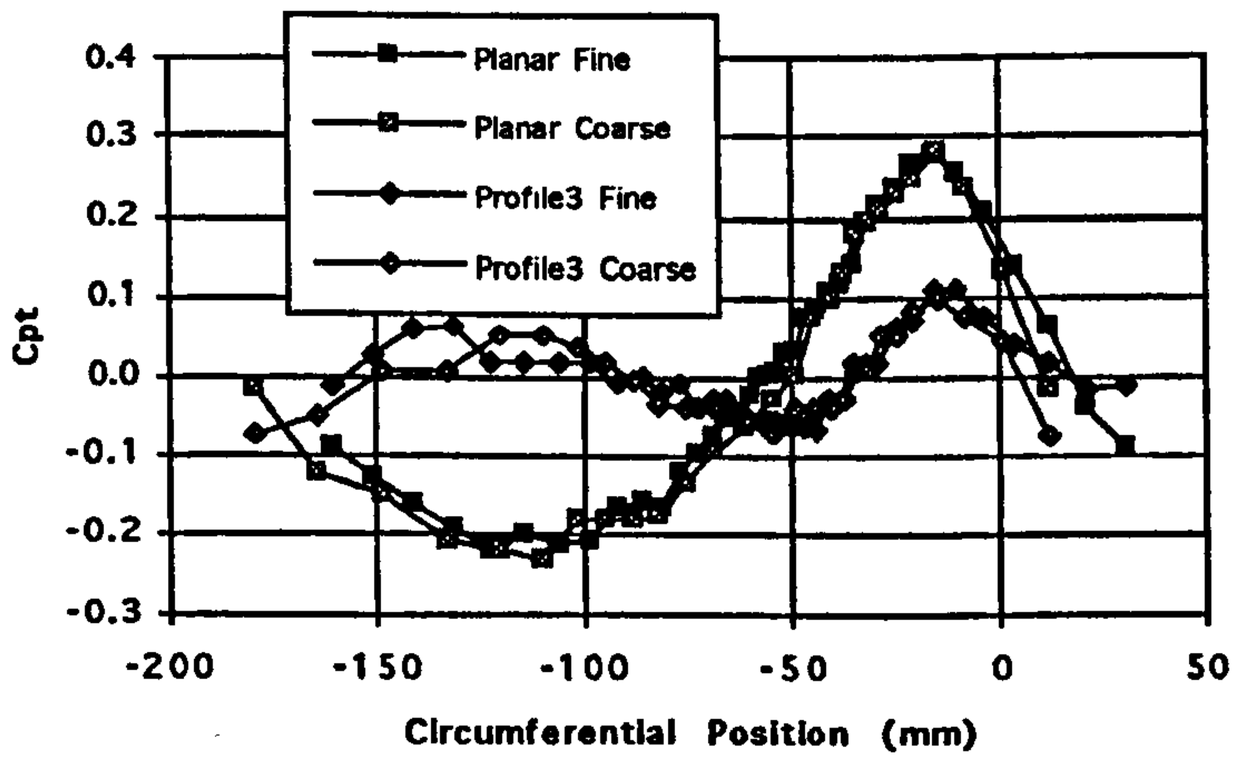

Figure 6.11 End-wall Pressure Coefficients (Fine Grid CFD).

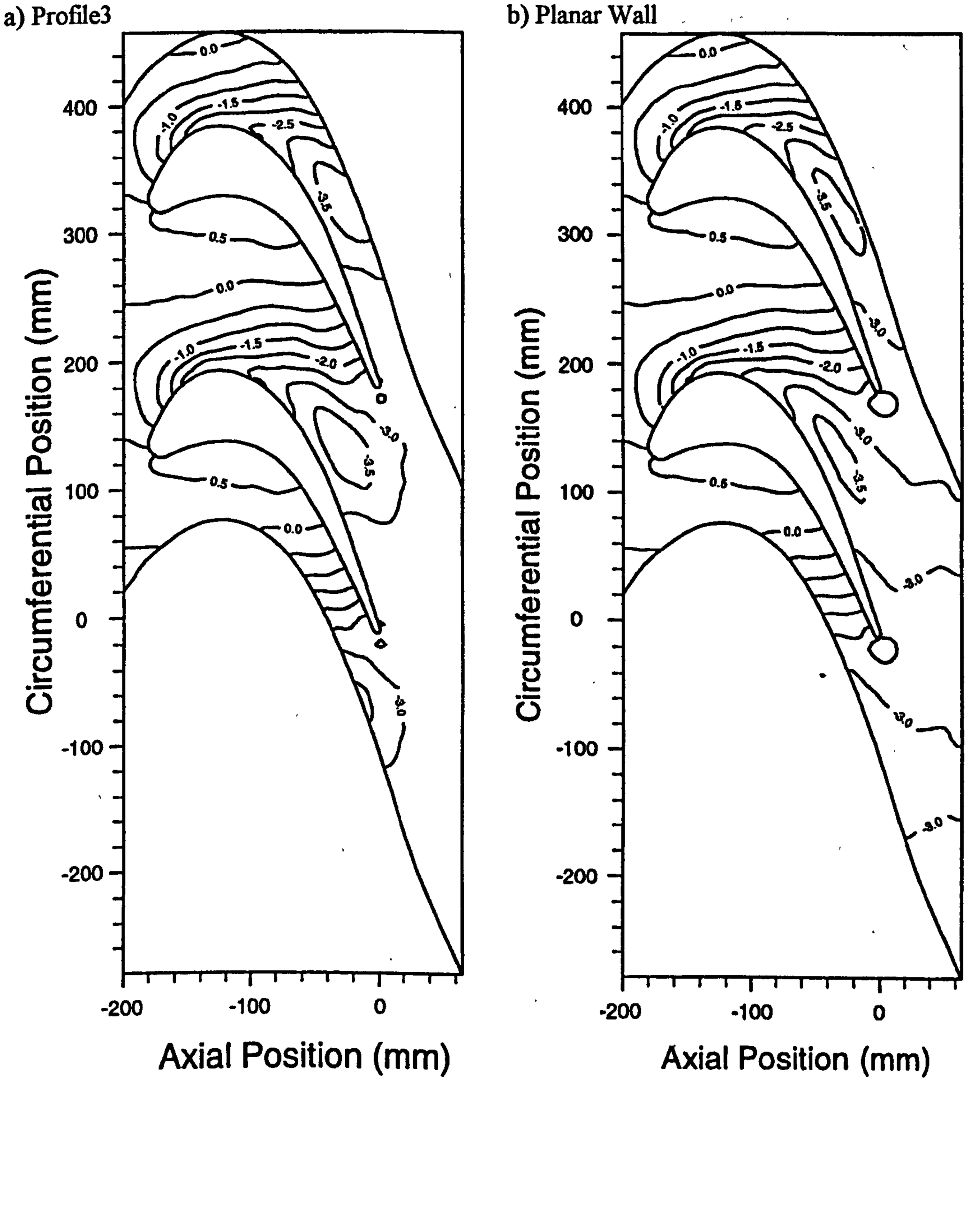

Figure 6.12 CFD Blade Cp Plots for Profile 3 and the Planar End-wall.

a) 0% Height.

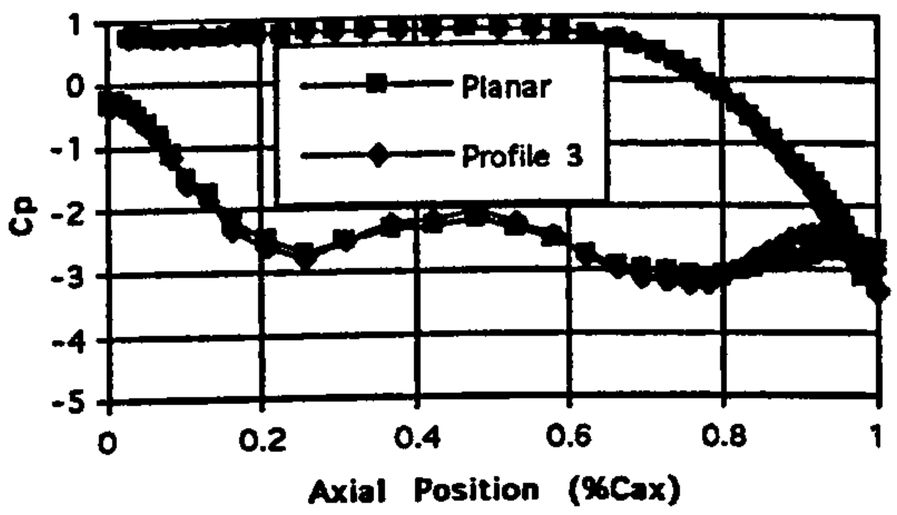

b) 4.65% Height.

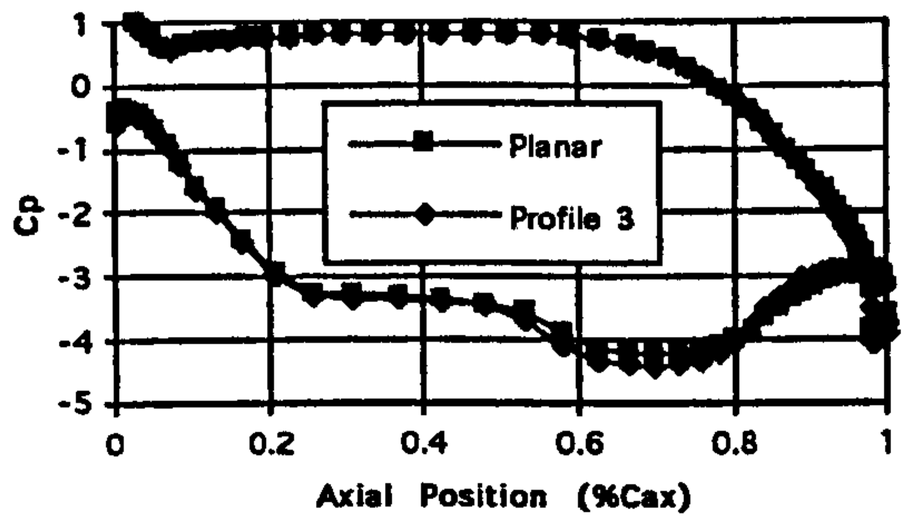

c) 10% Height.

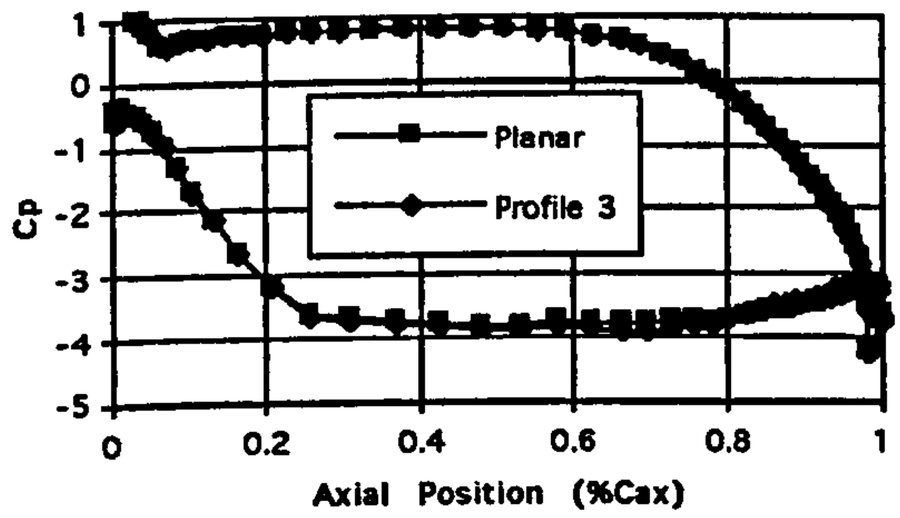

d) 15% Height.

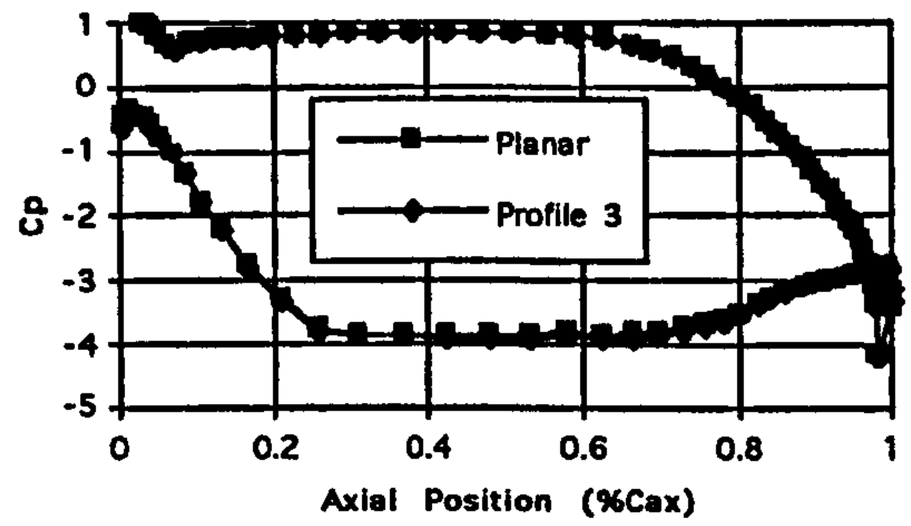

e) 20% Height.

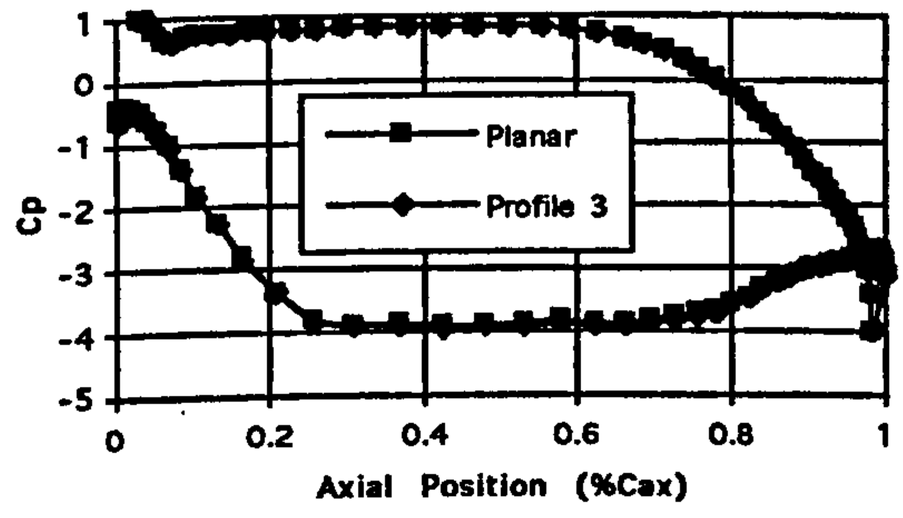

f) 50% Height.

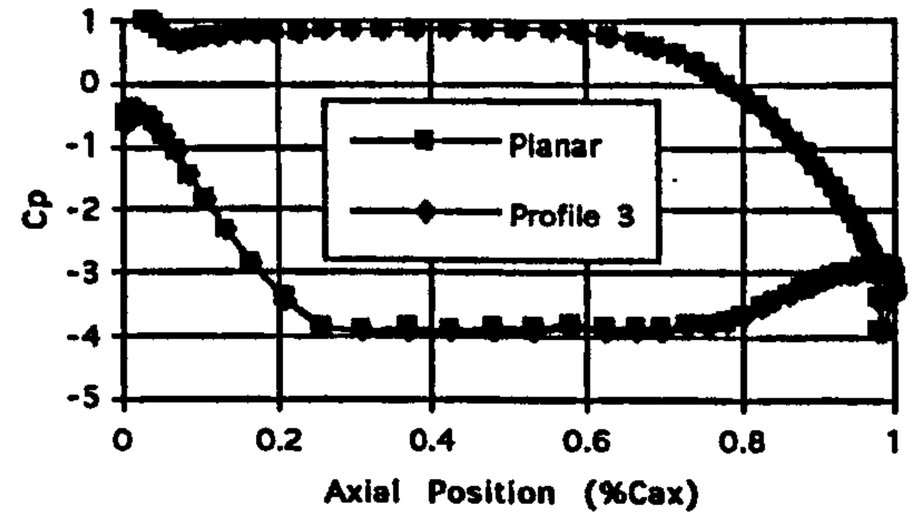

Figure 6.13 Pitch Averaged CFD Data at Slot 1 (Planar Wall Included for Comparison).

a) Total Pressure Loss Coefficient.

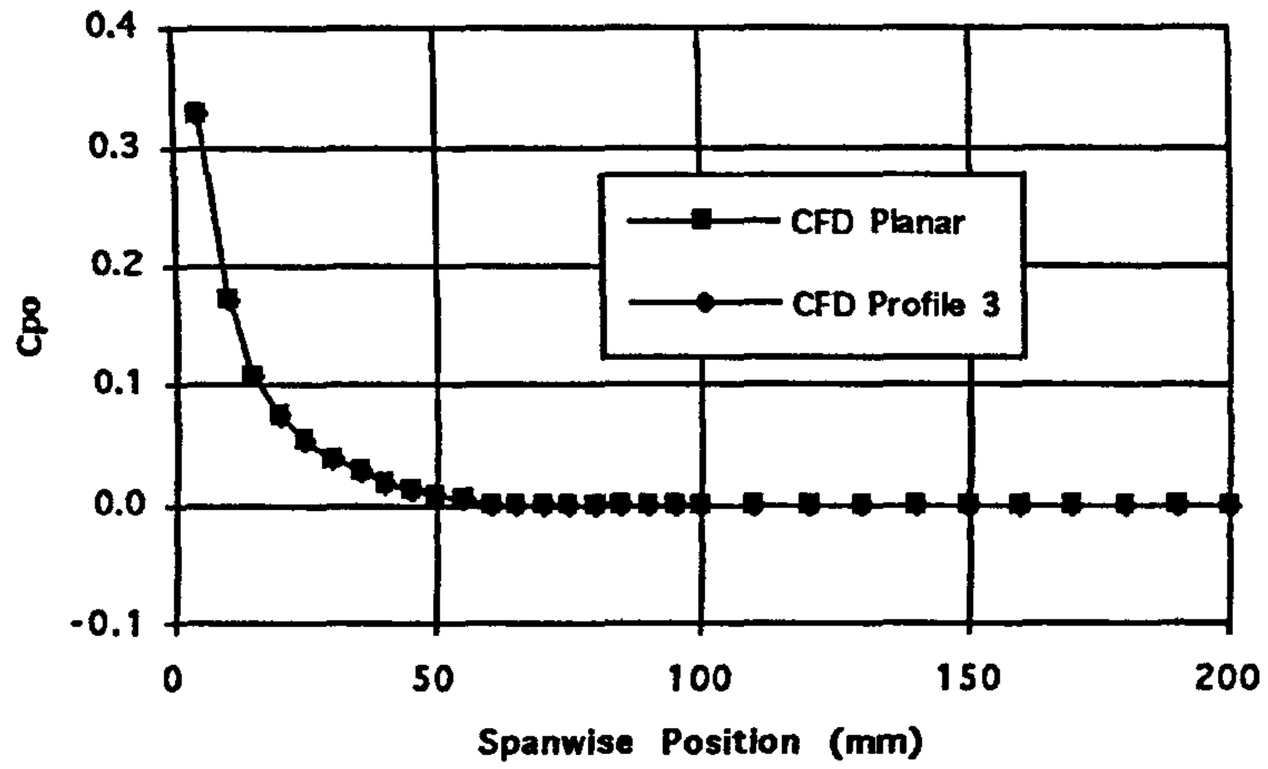

b) Yaw Angle.

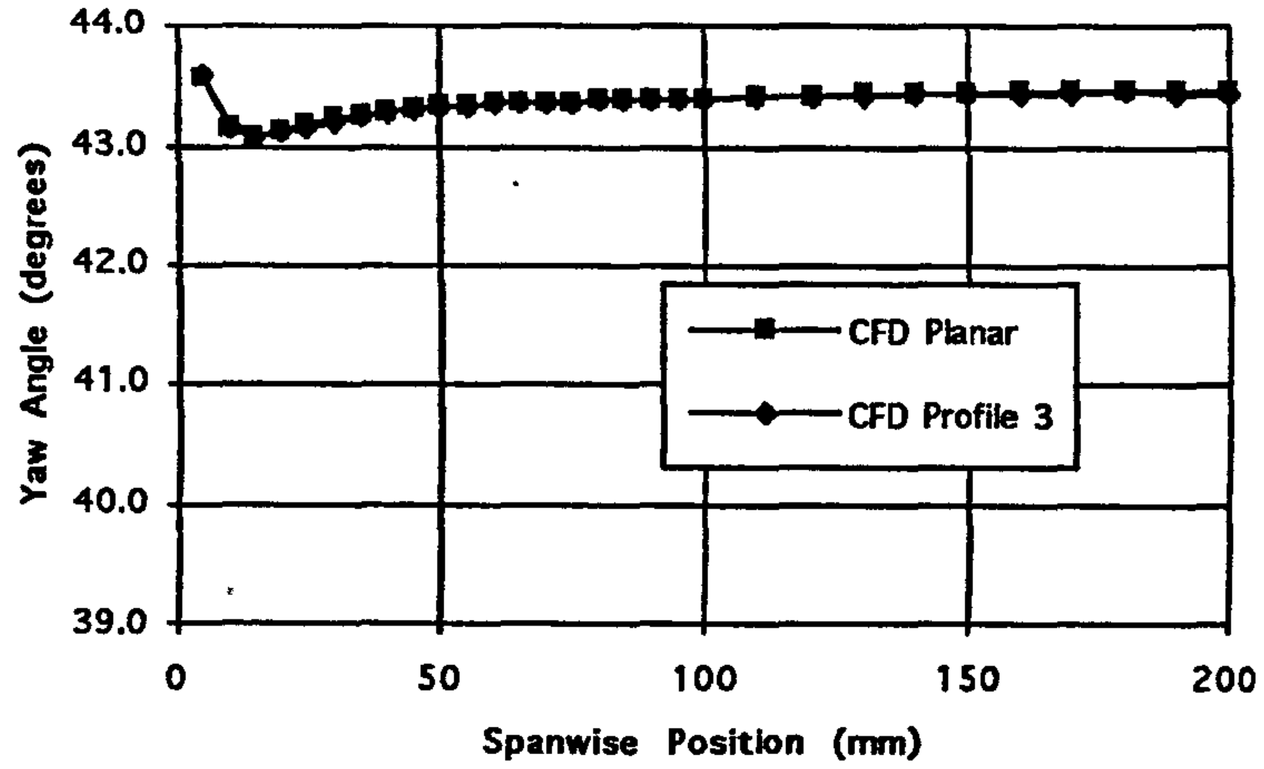

c) Pitch Angle.

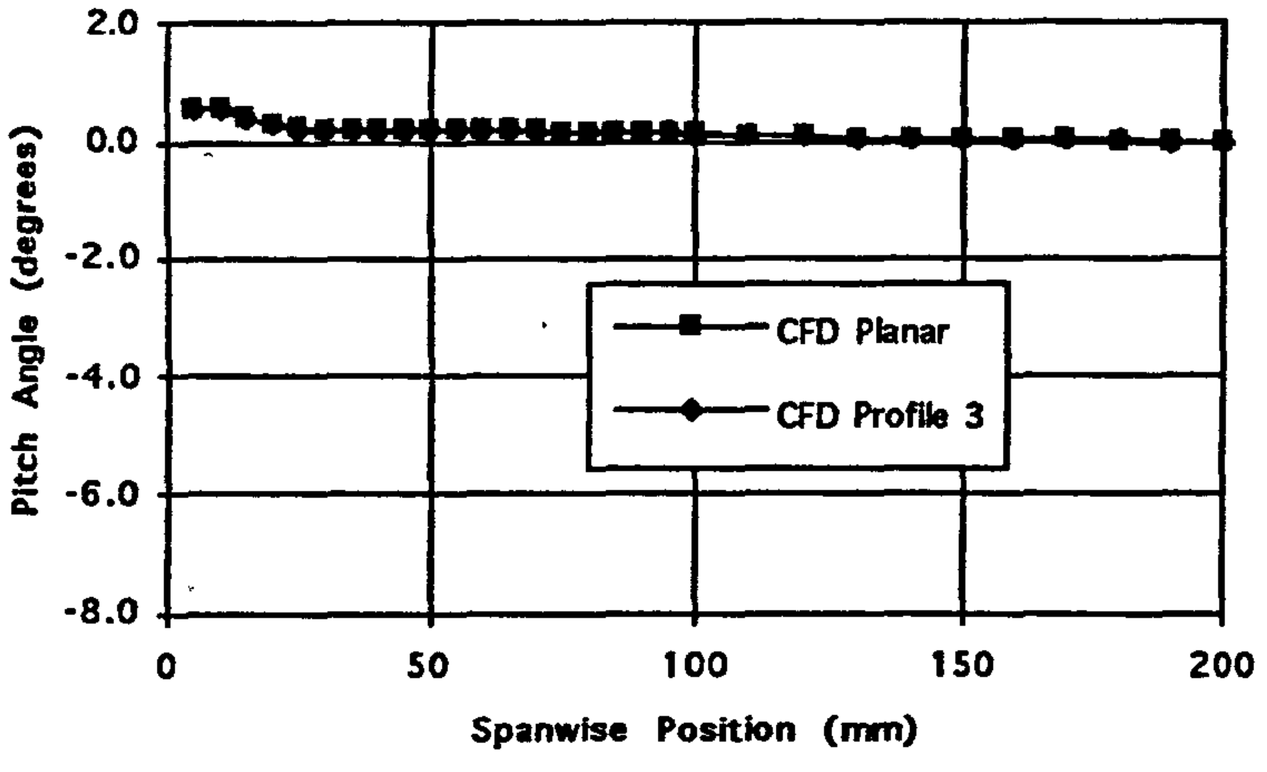

d) Secondary Kinetic Energy Coefficient.

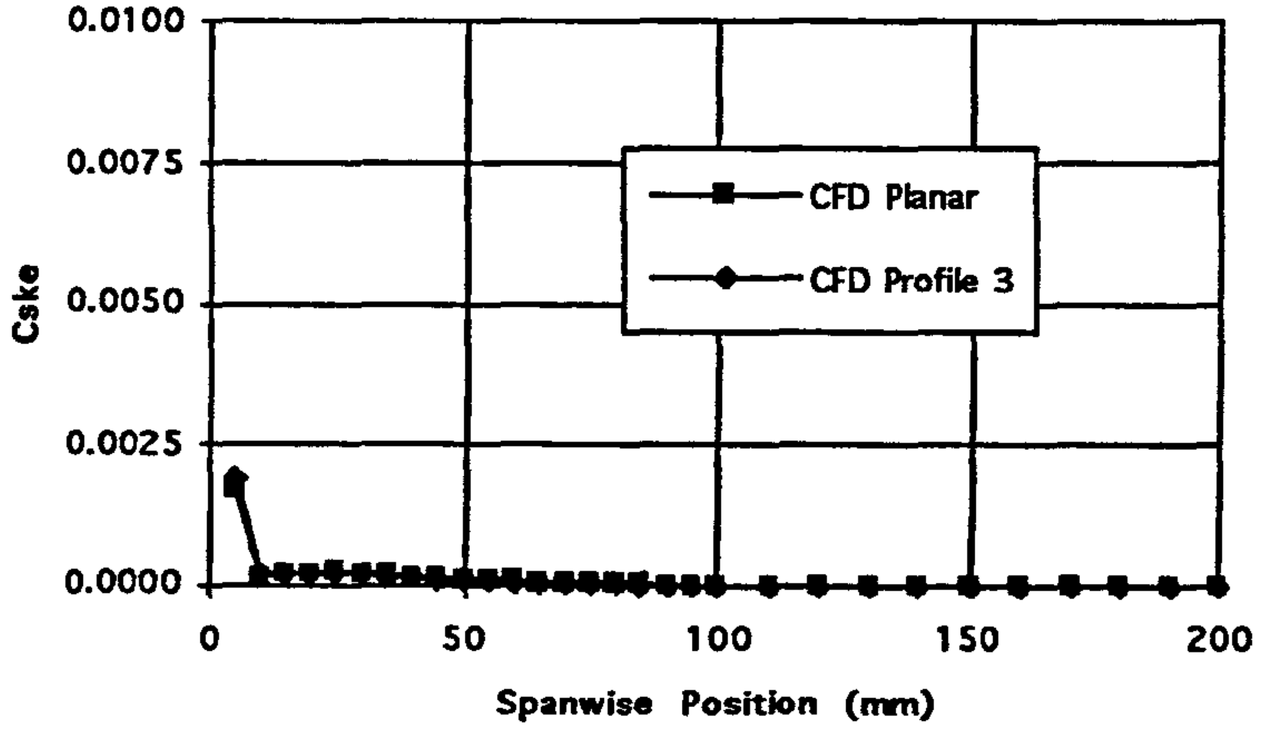

Figure 6.14 Pitch Averaged CFD Data at Slot 6 (Planar Wall Included for Comparison).

a) Total Pressure Loss Coefficient.

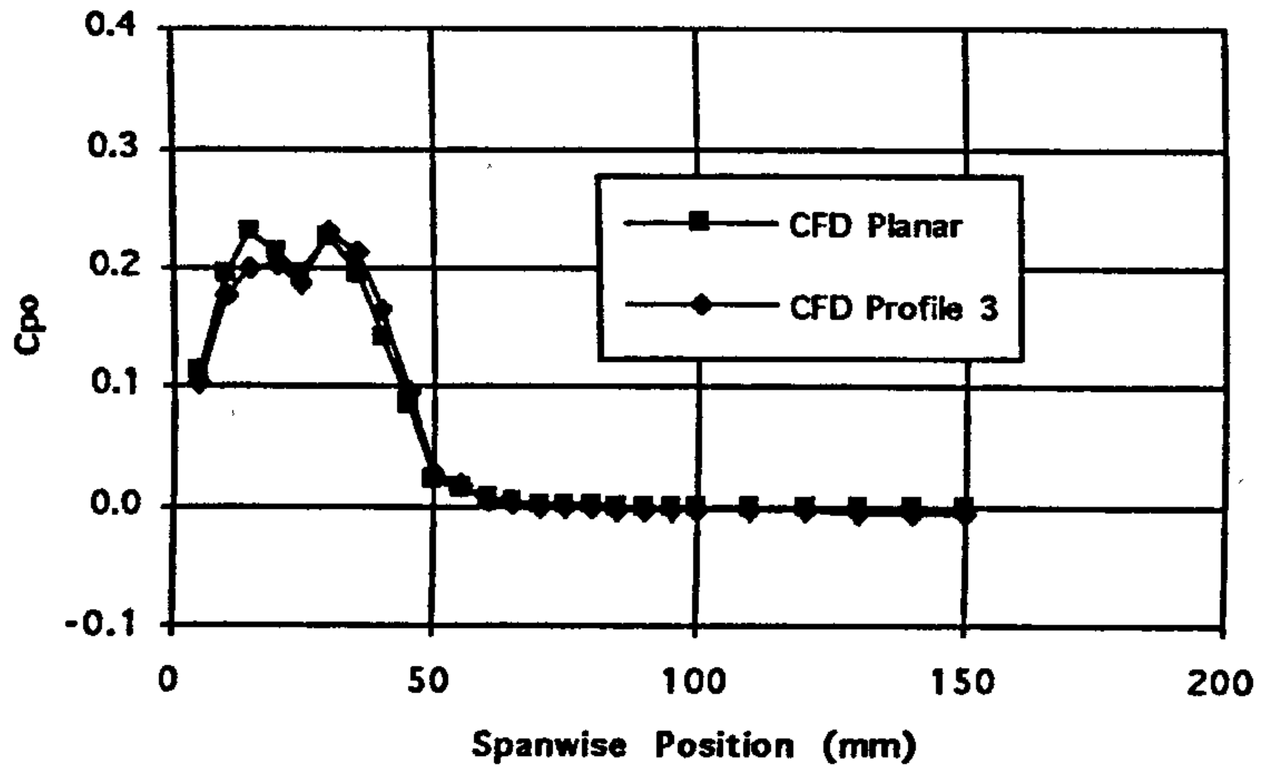

b) Yaw Angle.

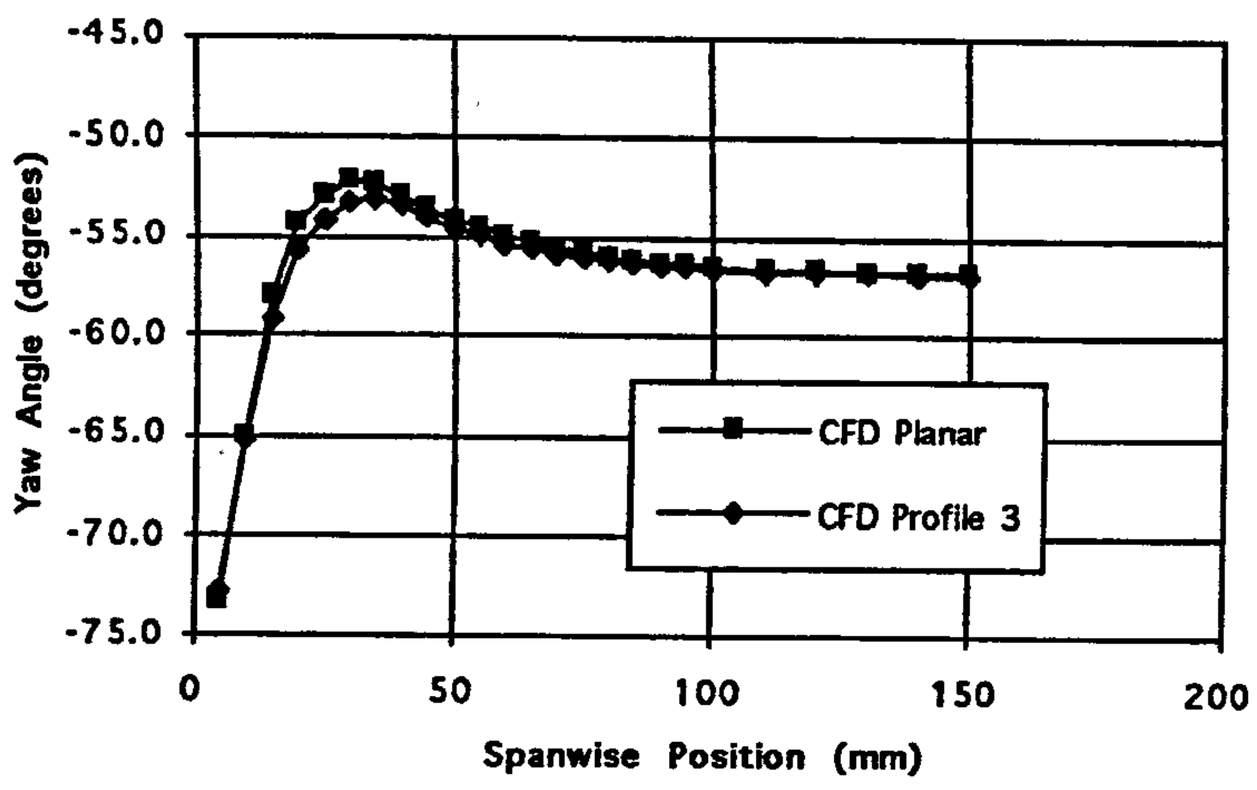

c) Pitch Angle.

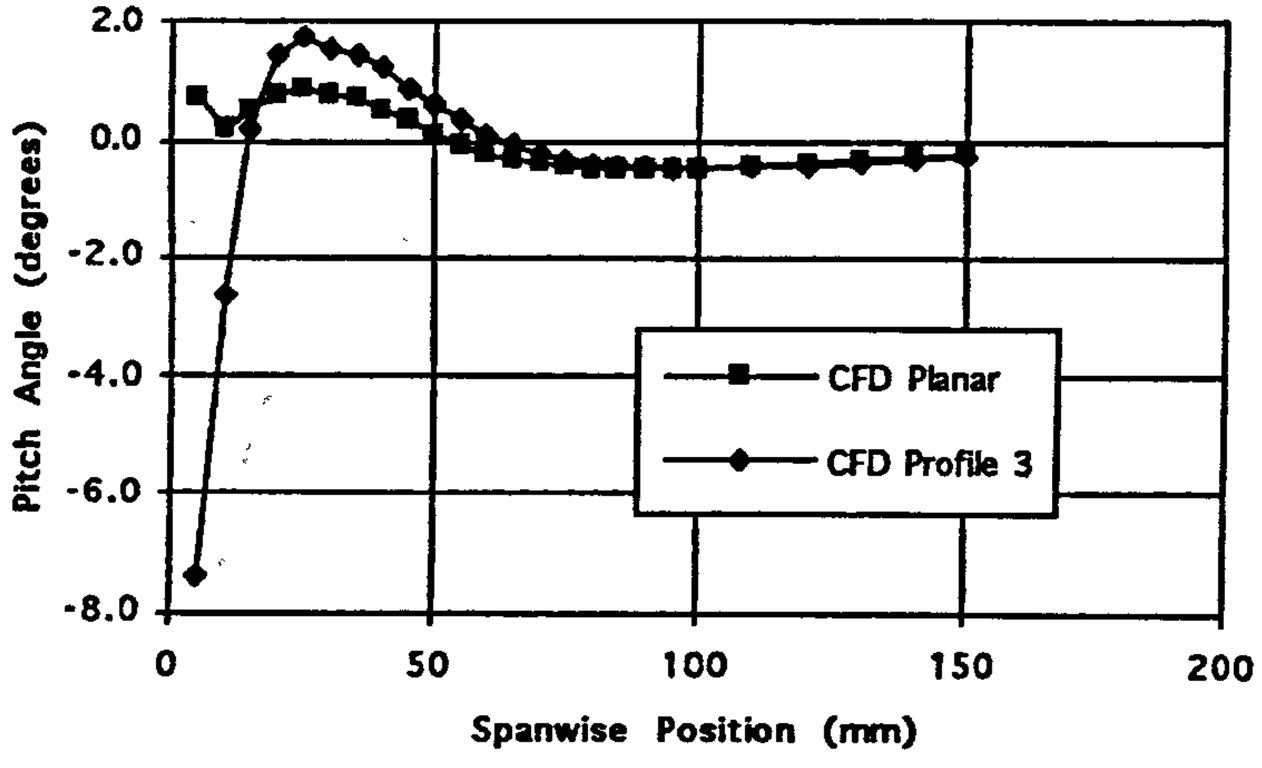

d) Secondary Kinetic Energy Coefficient.

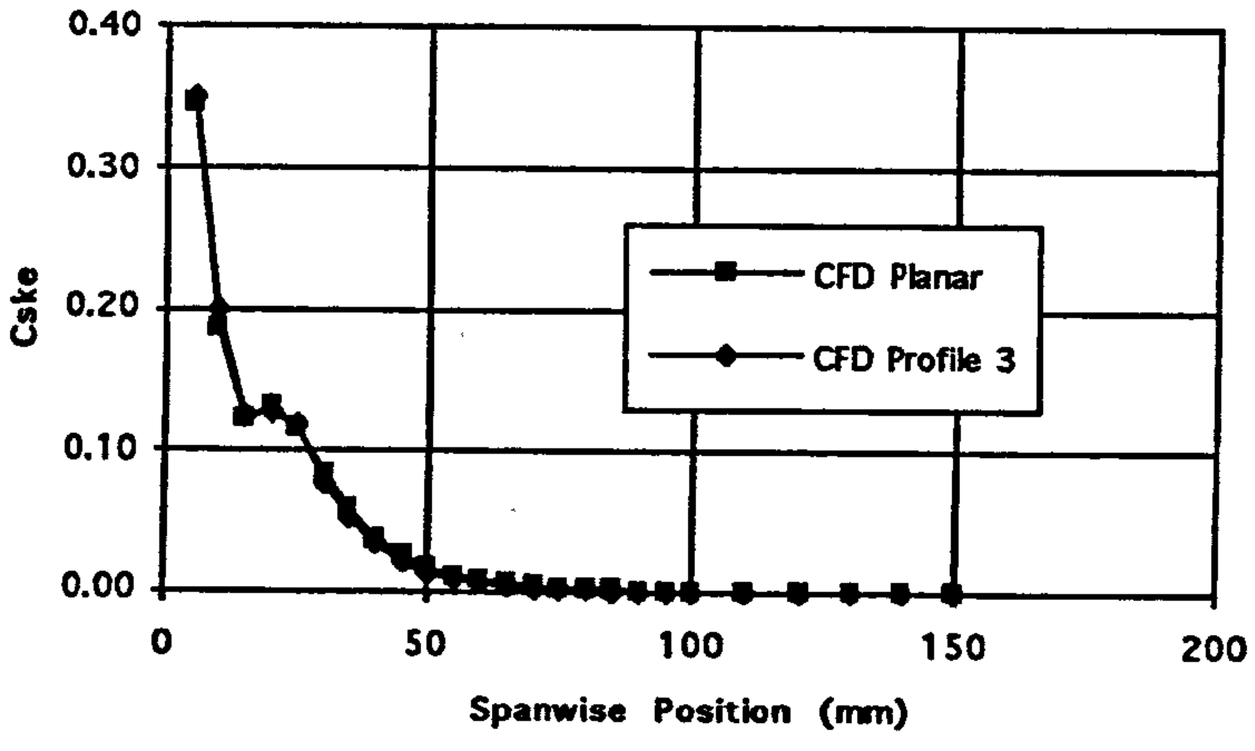

Figure 6.15 Pitch Averaged CFD Data at Slot 8 (Planar Wall Included for Comparison).

a) Total Pressure Loss Coefficient.

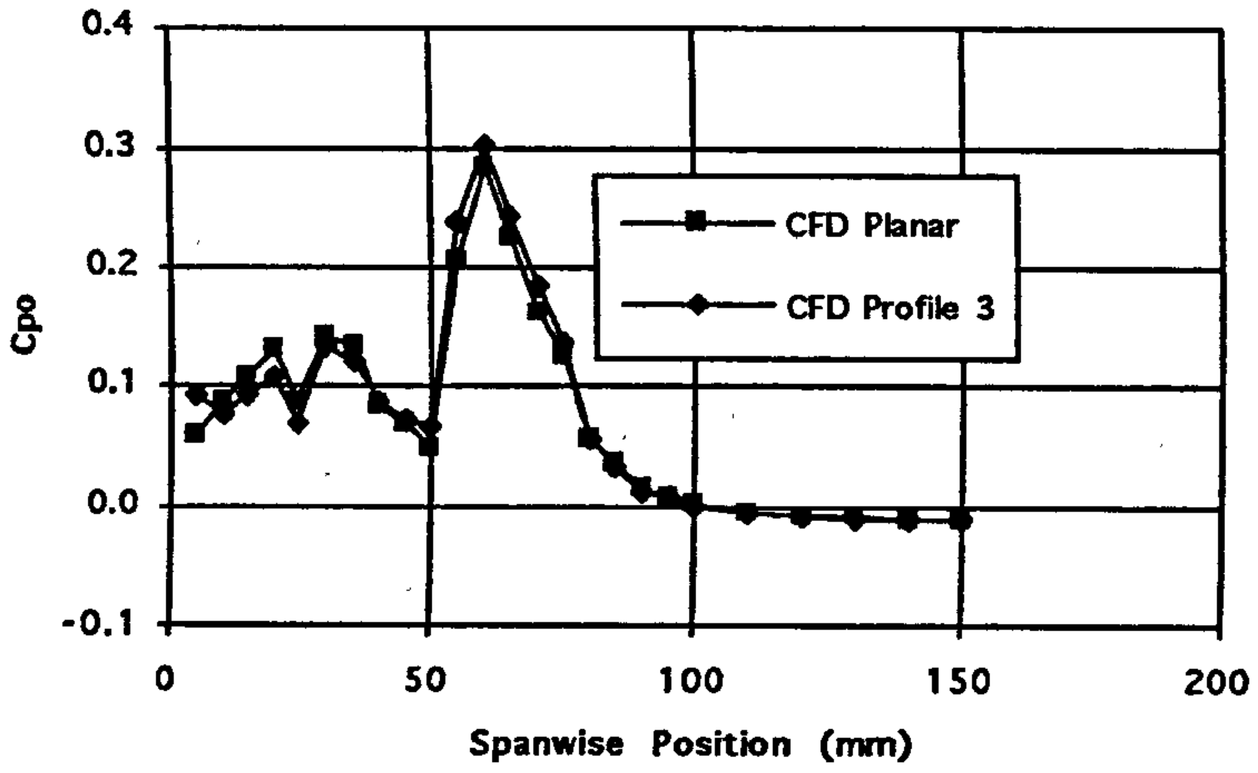

b) Yaw Angle.

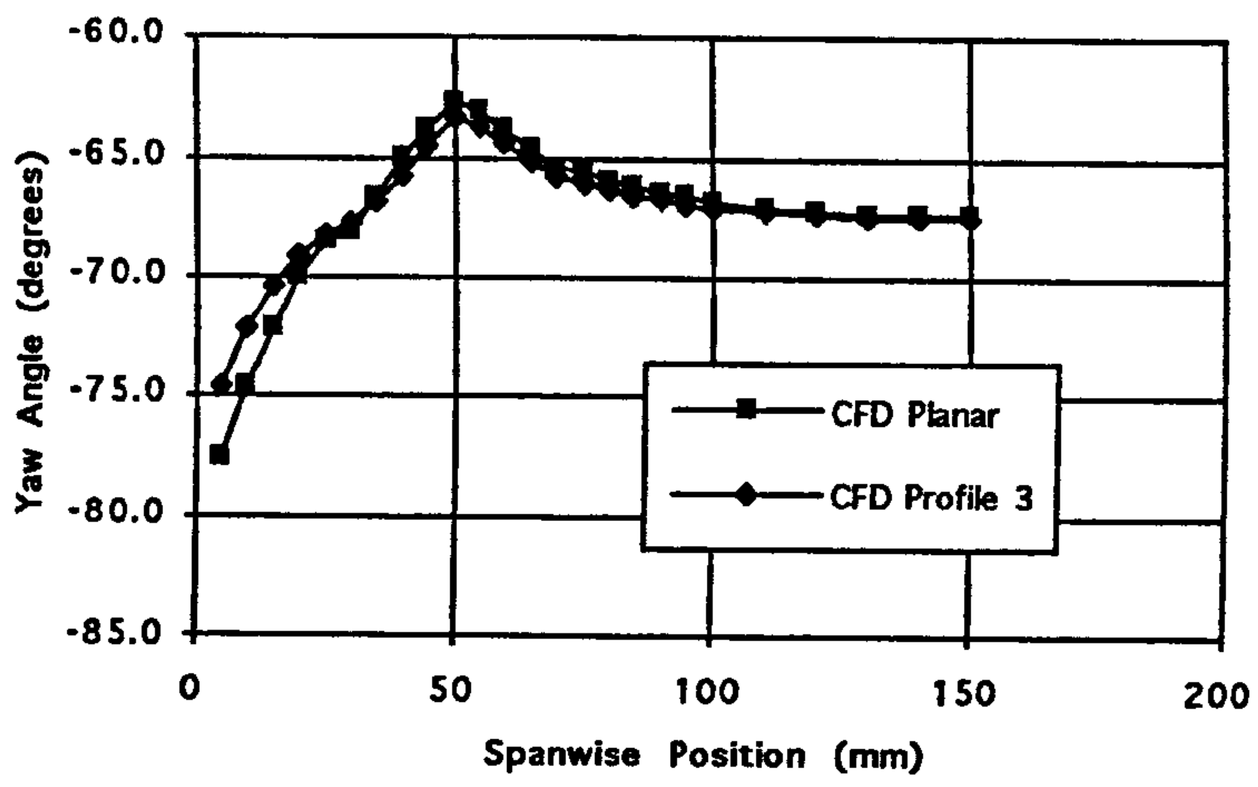

c) Pitch Angle.

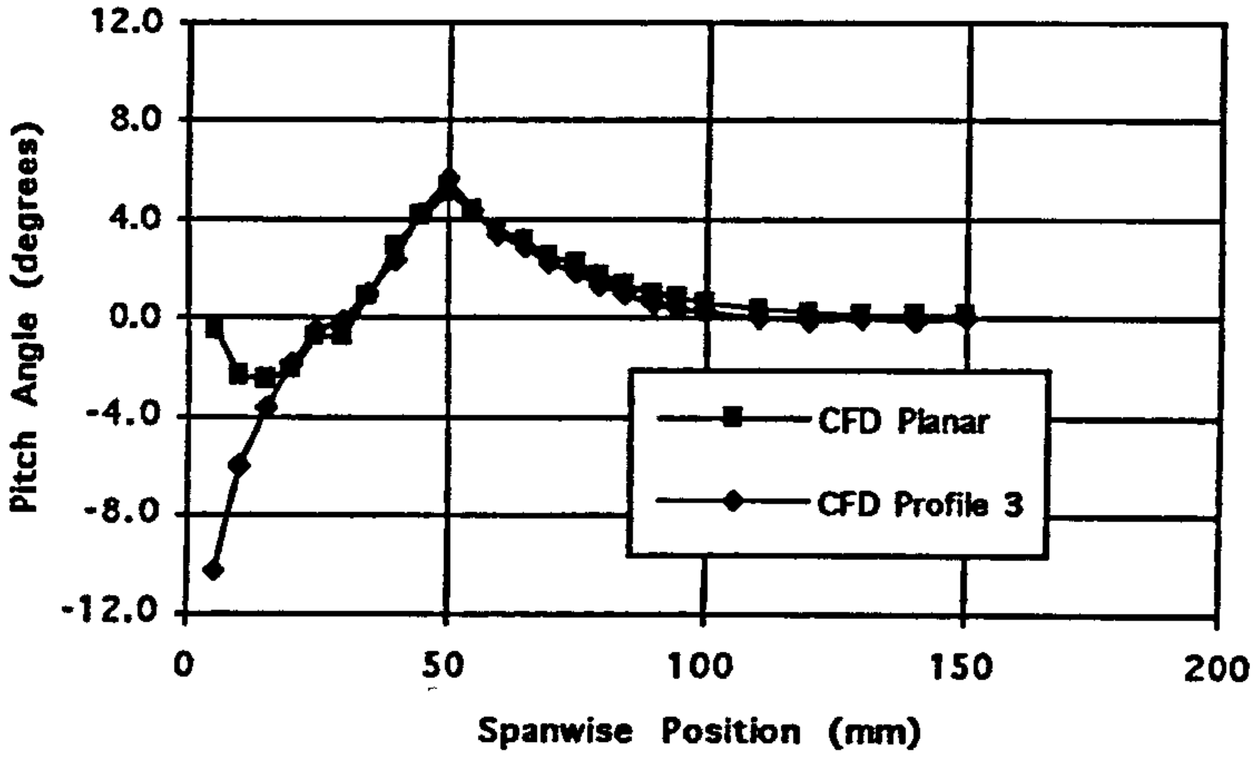

d) Secondary Kinetic Energy Coefficient.

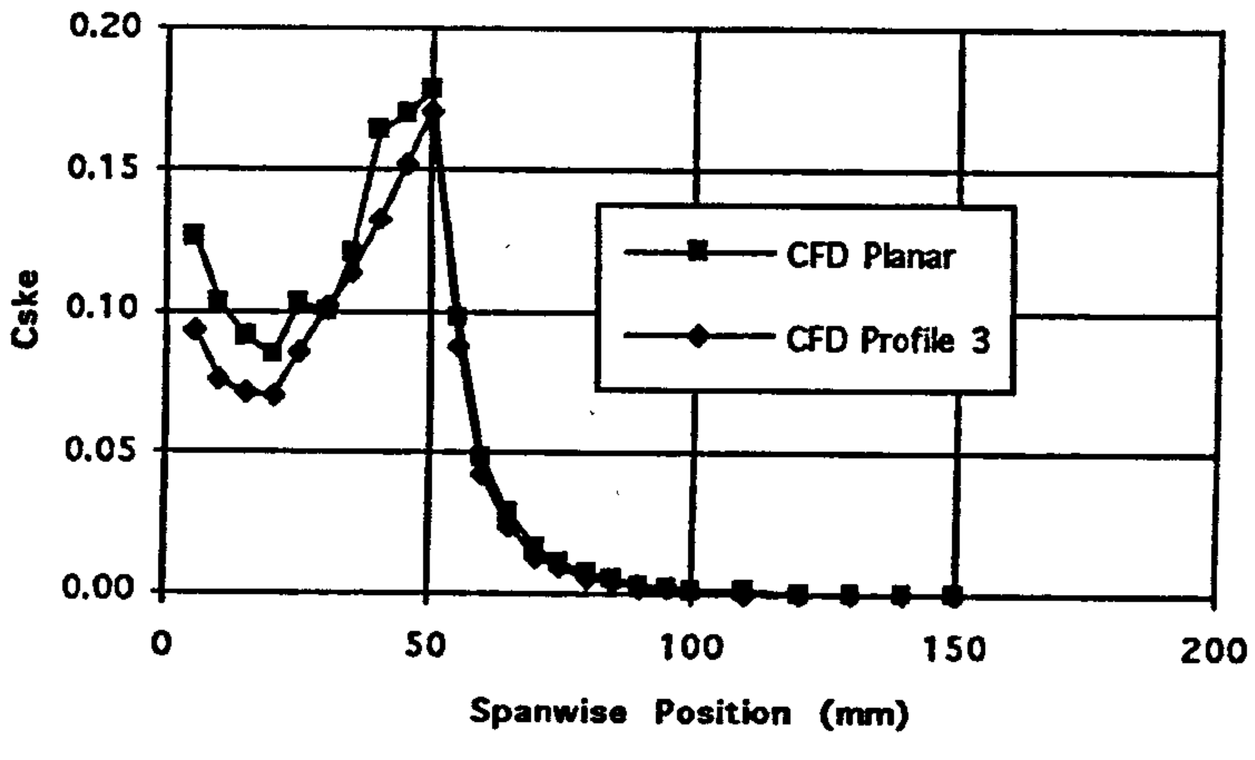

Figure 6.16 Pitch Averaged CFD Data at Slot 10 (Planar Wall Included for Comparison).

a) Total Pressure Loss Coefficient.

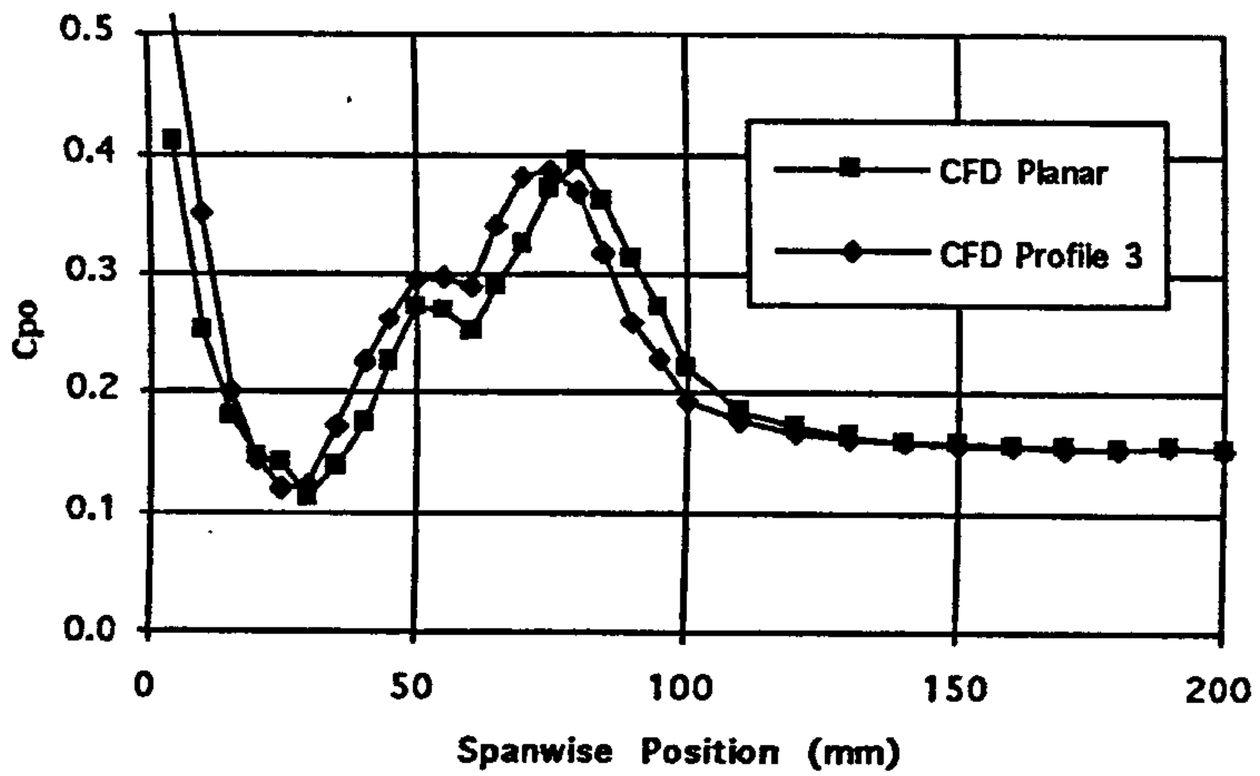

b) Yaw Angle.

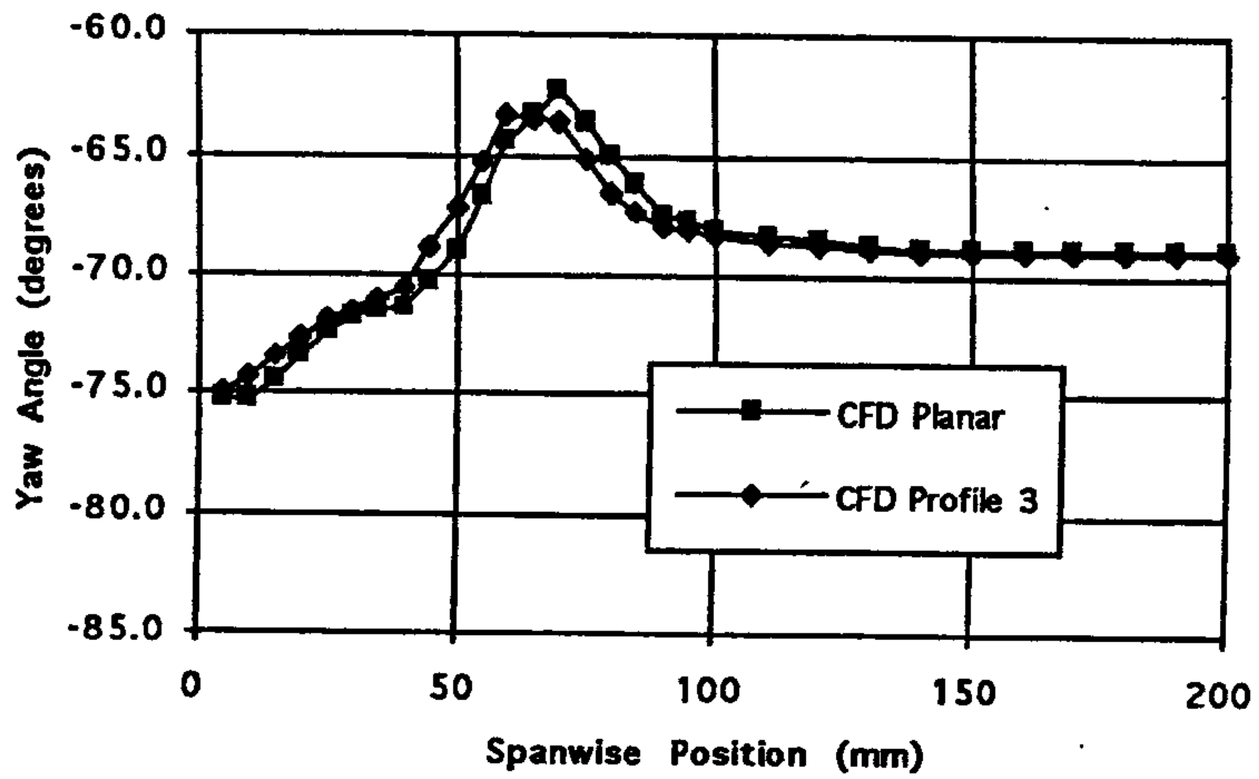

c) Pitch Angle.

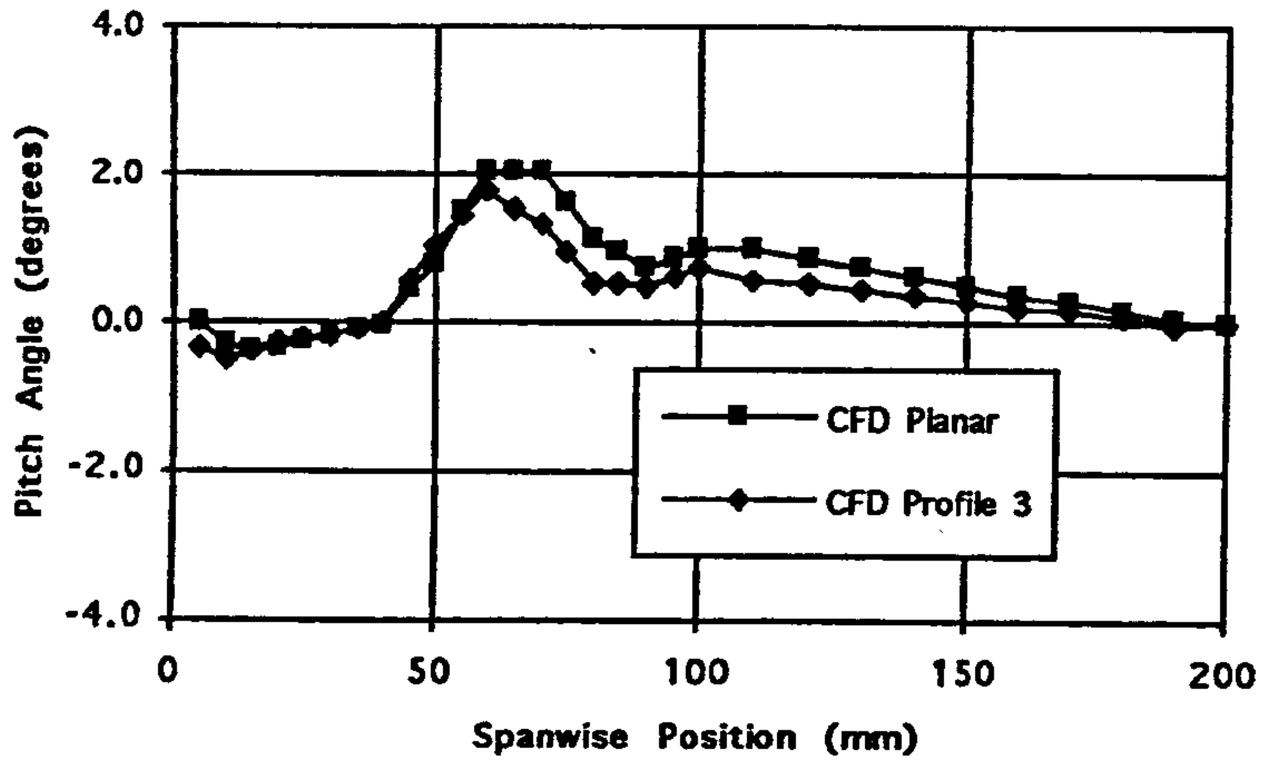

d) Secondary Kinetic Energy Coefficient.

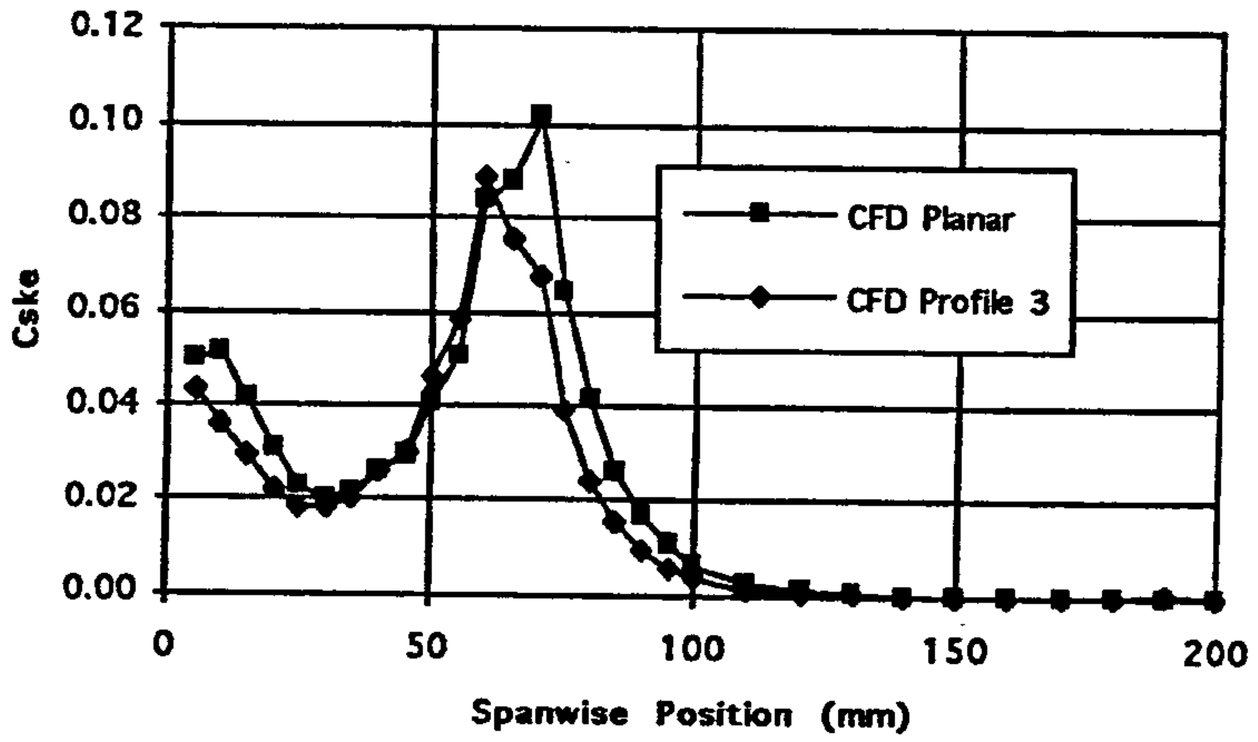

Figure 6.17 CFD Data at Slot 1.

a) Secondary Velocity Vectors.

Profile 3

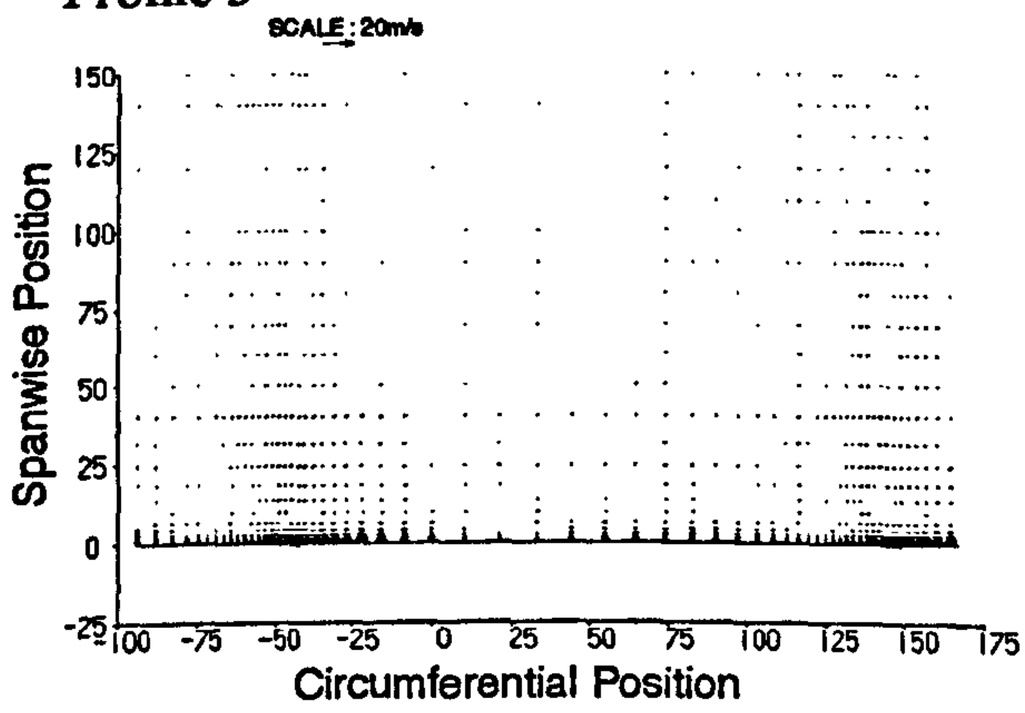

Planar Wall

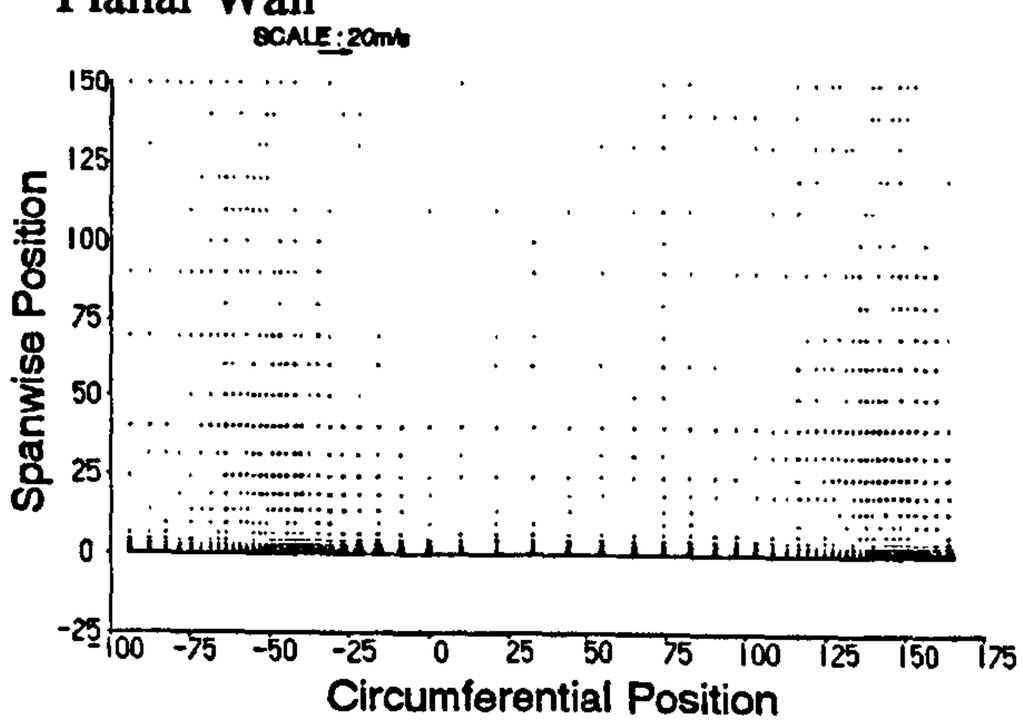

b) Total Pressure Loss Coefficient.

Profile 3

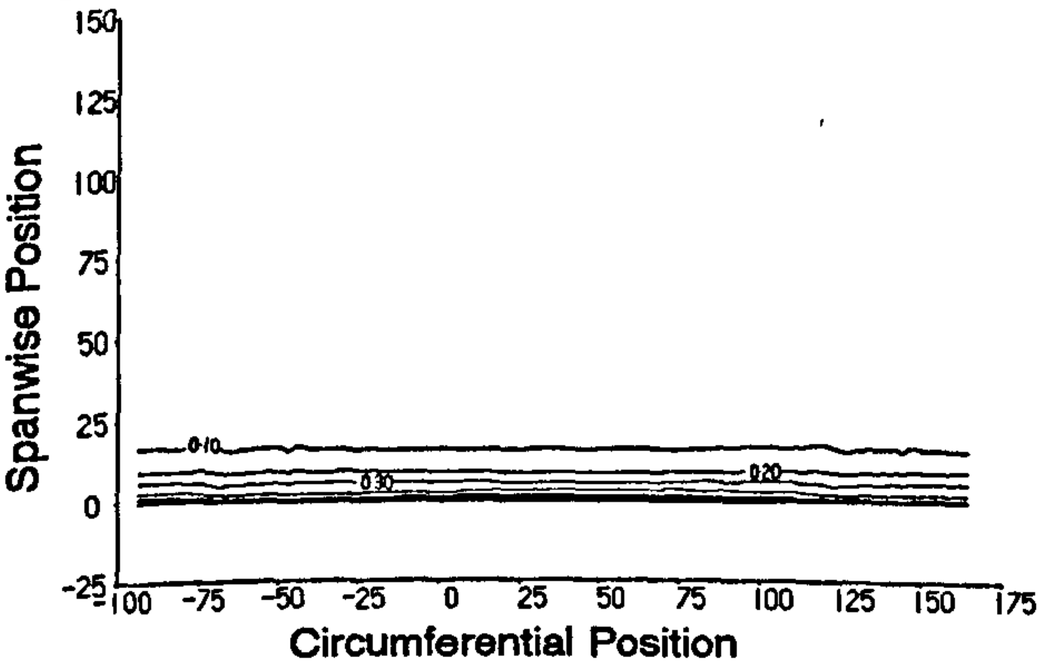

Planar Wall

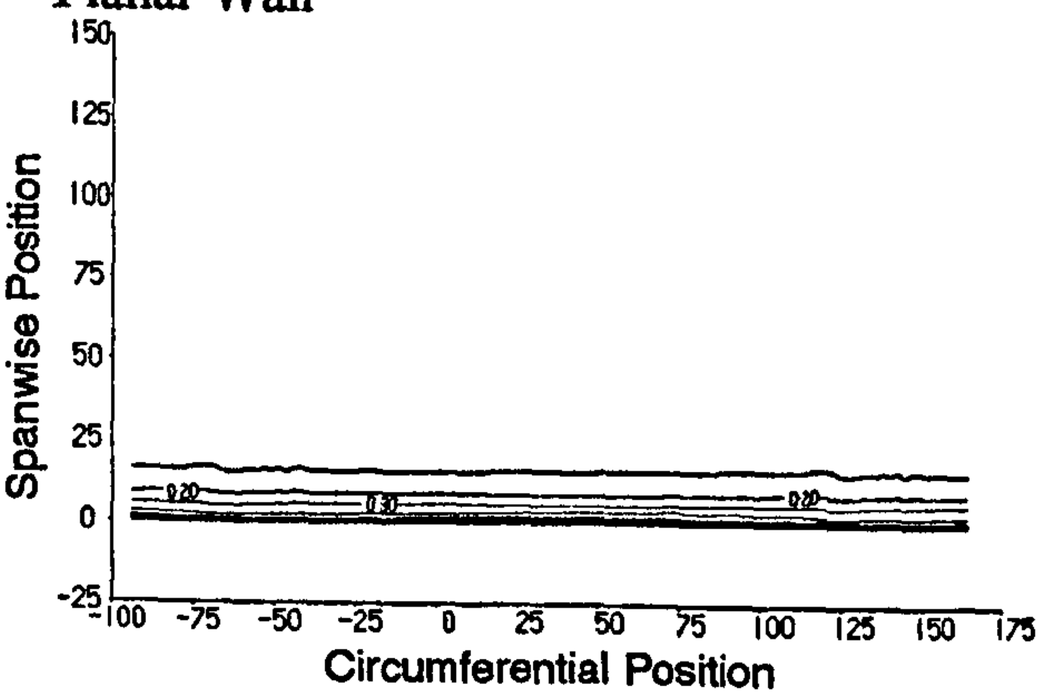

c) Yaw Angle.

Profile 3

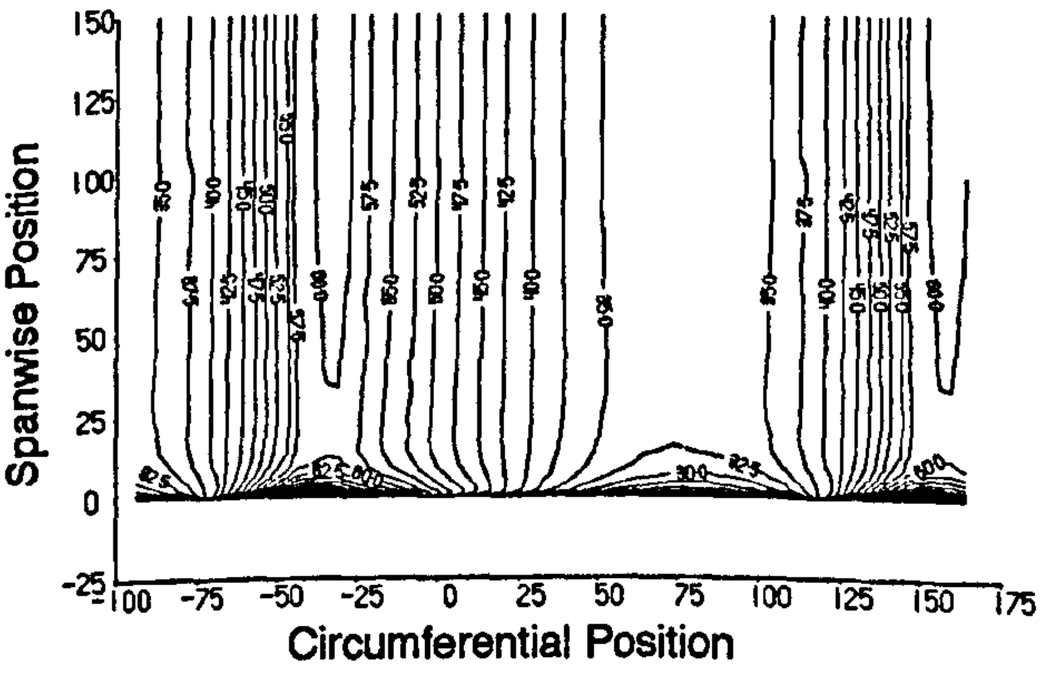

Planar Wall

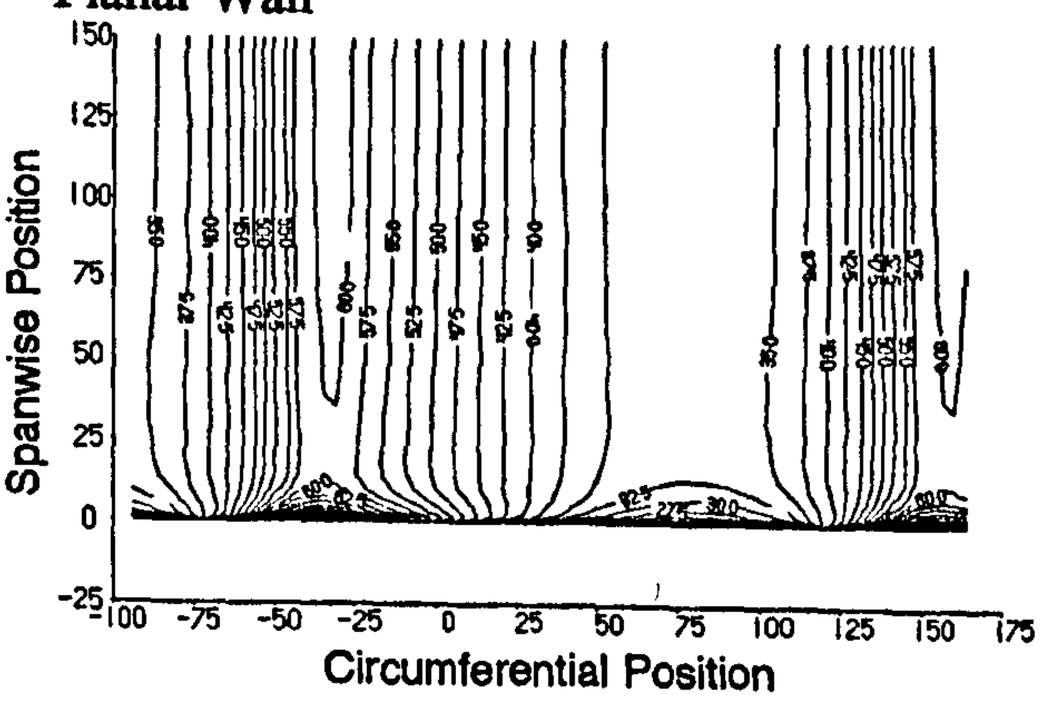

d) Secondary Kinetic Energy Coefficient.

Profile 3

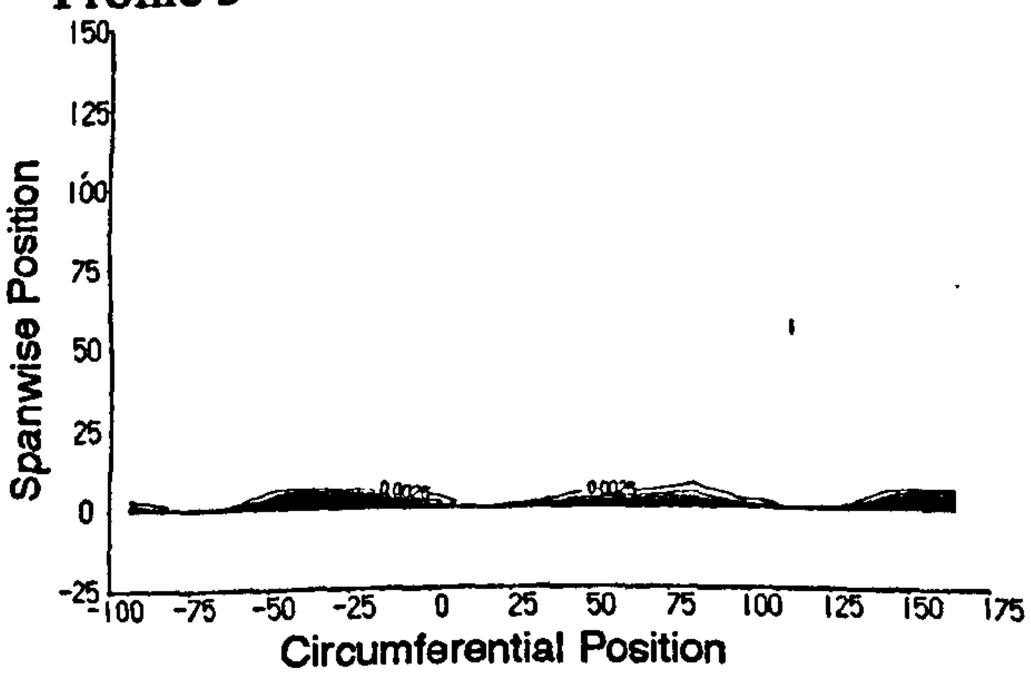

Planar Wall

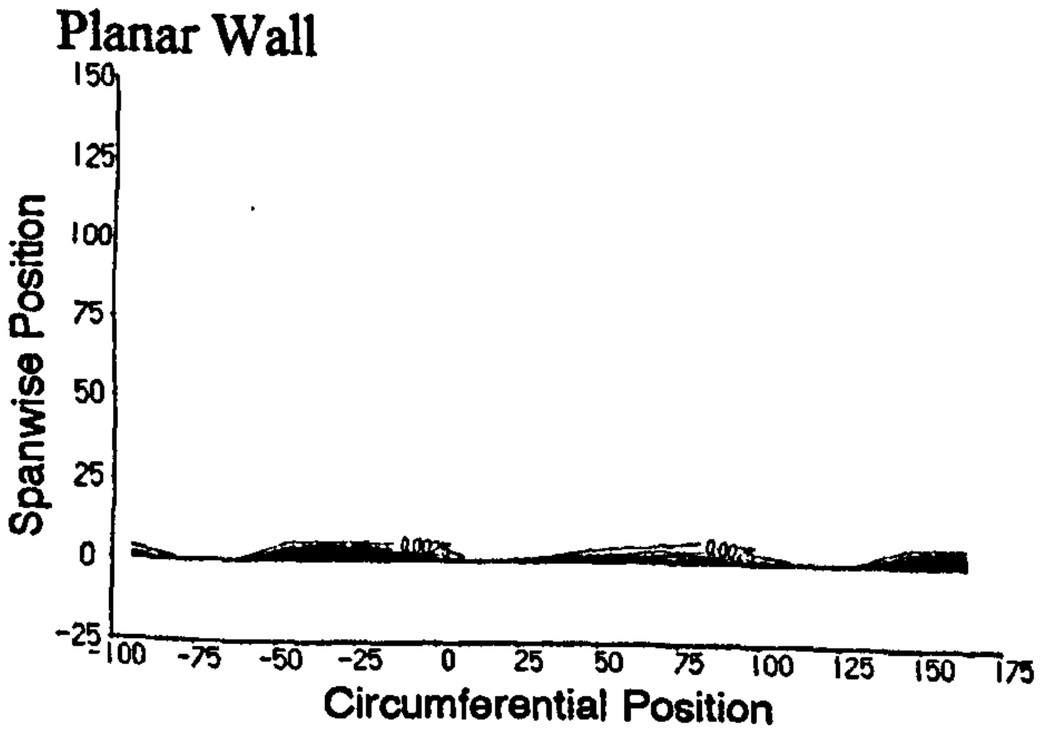

Figure 6.18 CFD Data at Slot 6.

a) Secondary Velocity Vectors.

Profile 3

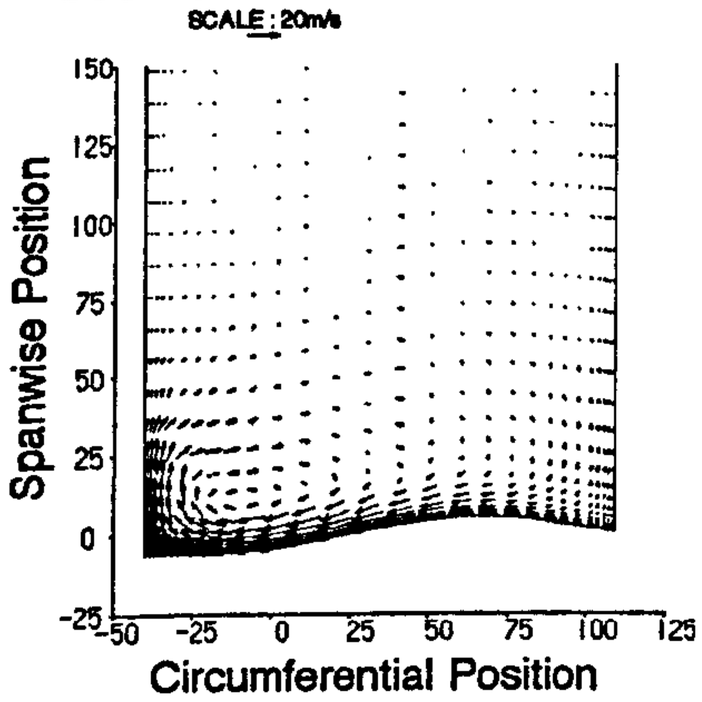

Planar Wall

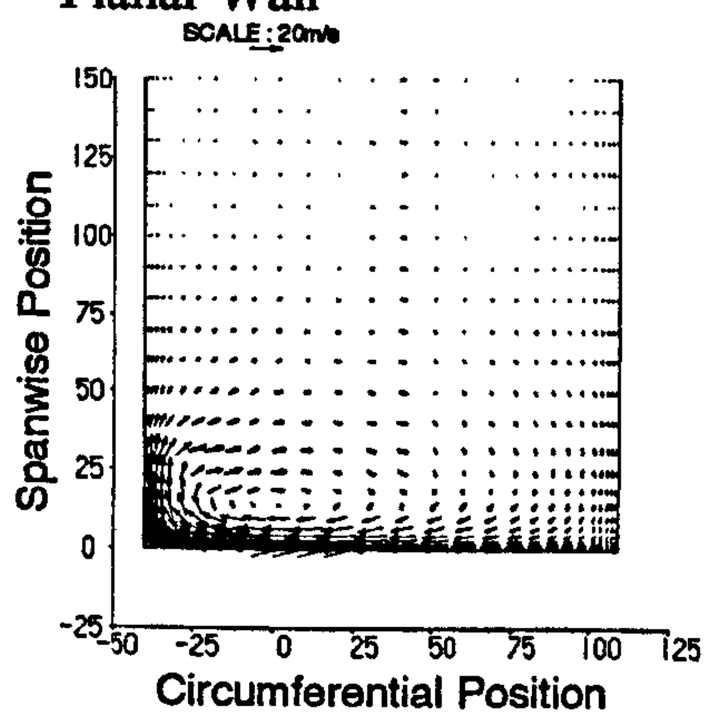

b) Total Pressure Loss Coefficient.

Profile 3

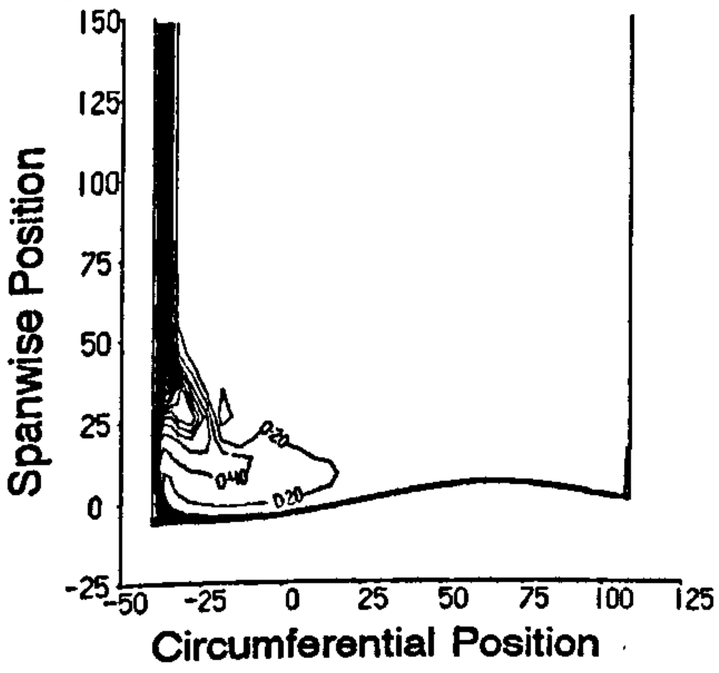

Planar Wall

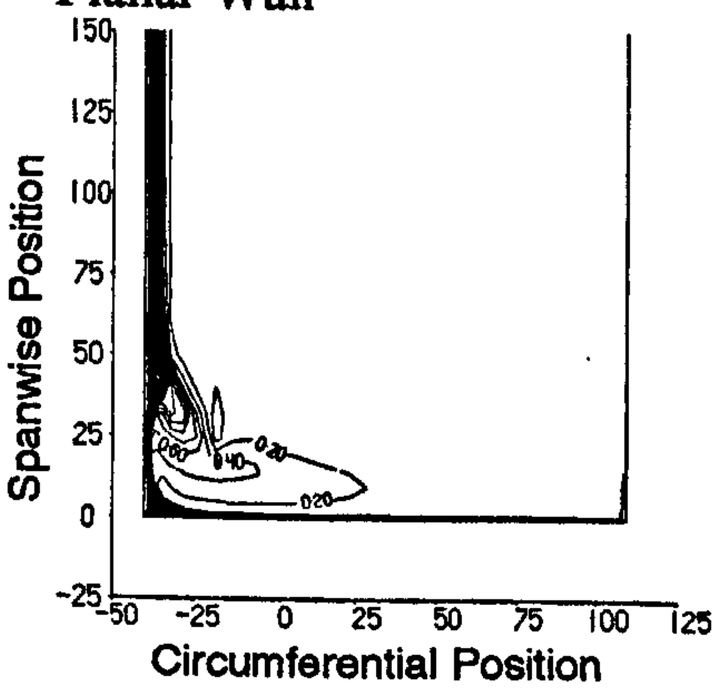

c) Yaw Angle.

Profile 3

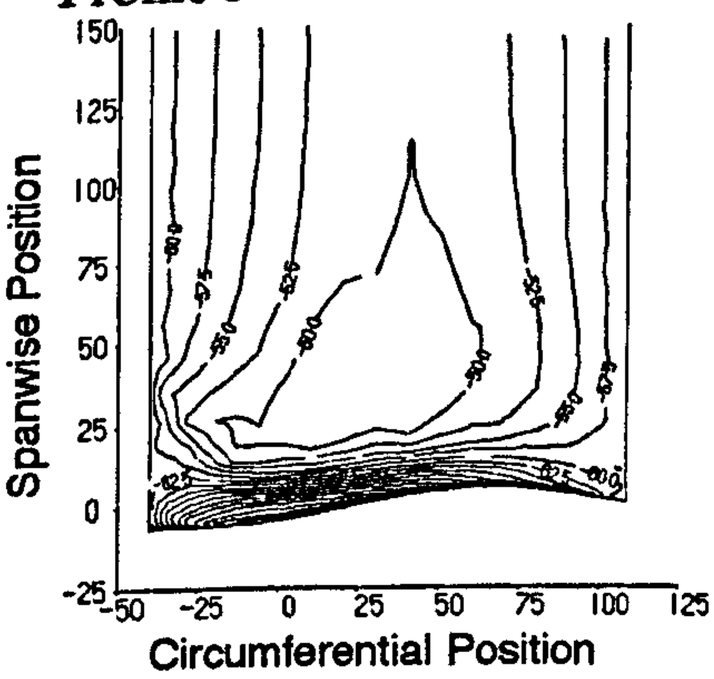

Planar Wall

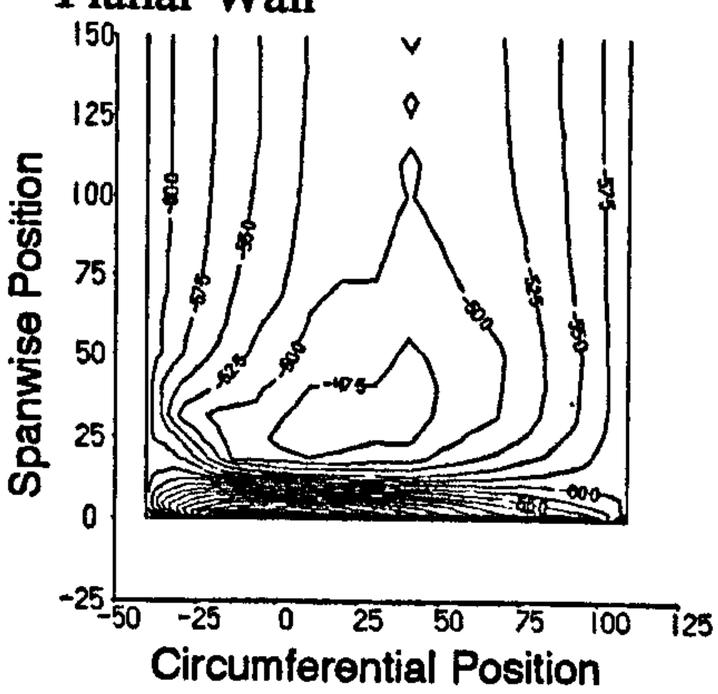

d) Secondary Kinetic Energy Coefficient.

Profile 3

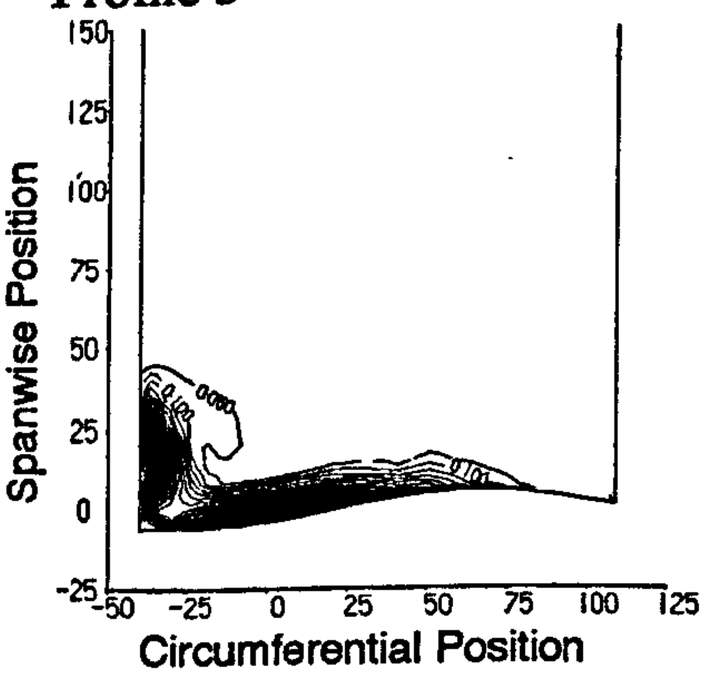

Planar Wall

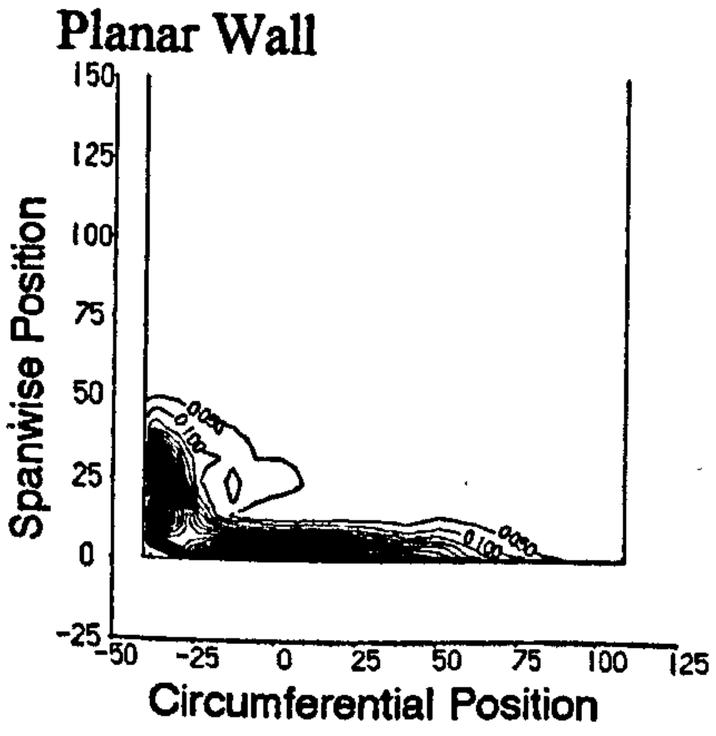

Figure 6.19 CFD Data at Slot 8.

a) Secondary Velocity Vectors.

Profile 3

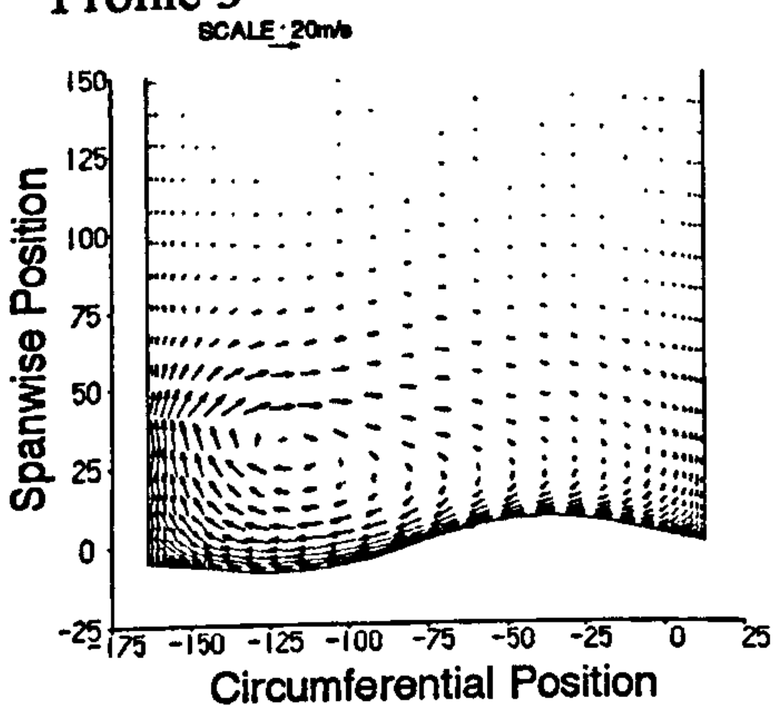

Planar Wall

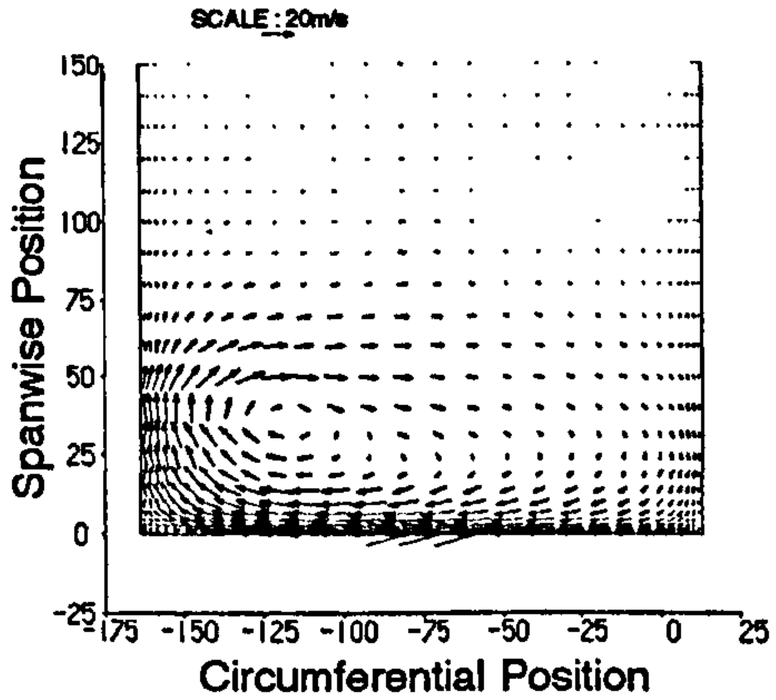

b) Total Pressure Loss Coefficient.

Profile 3

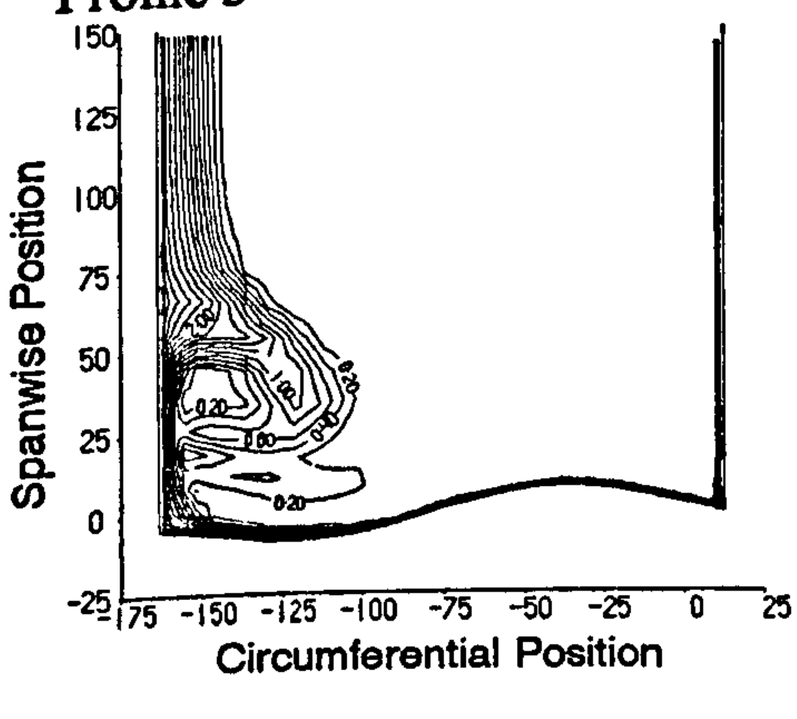

Planar Wall

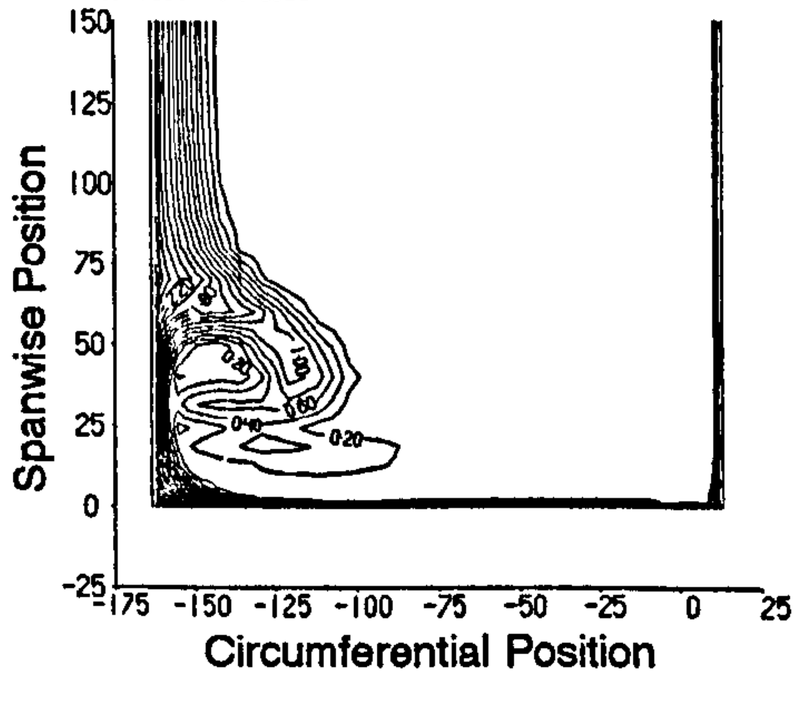

c) Yaw Angle.

Profile 3

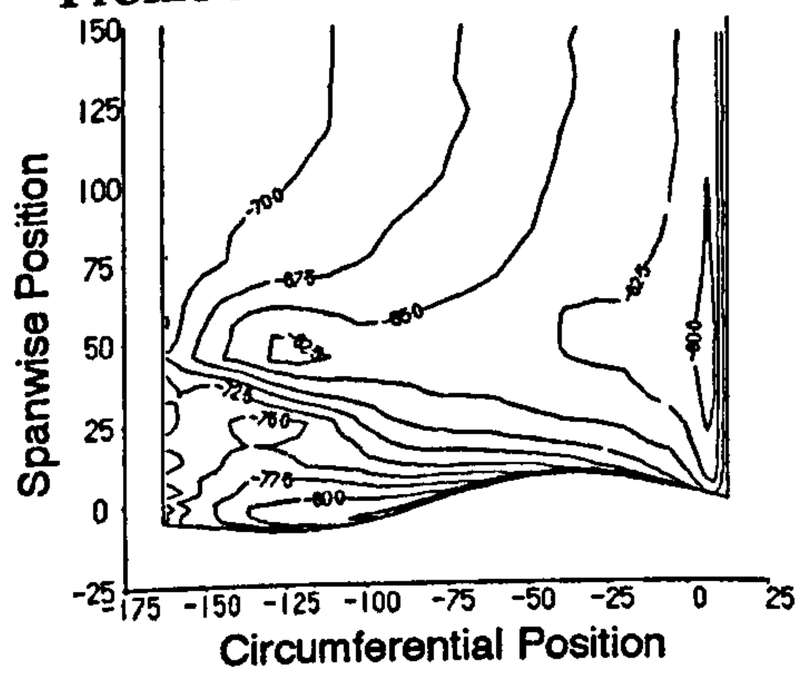

Planar Wall

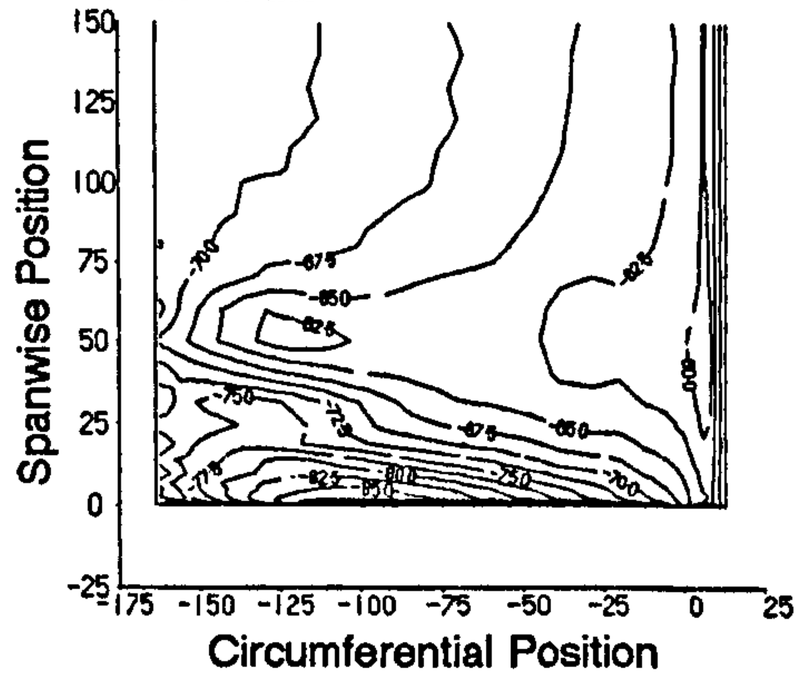

d) Secondary Kinetic Energy Coefficient.

Profile 3

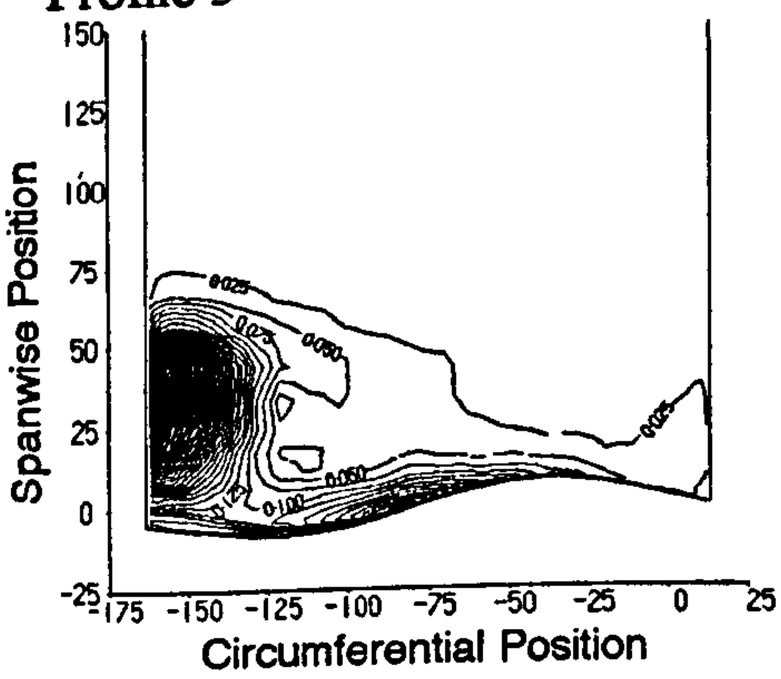

Planar Wall

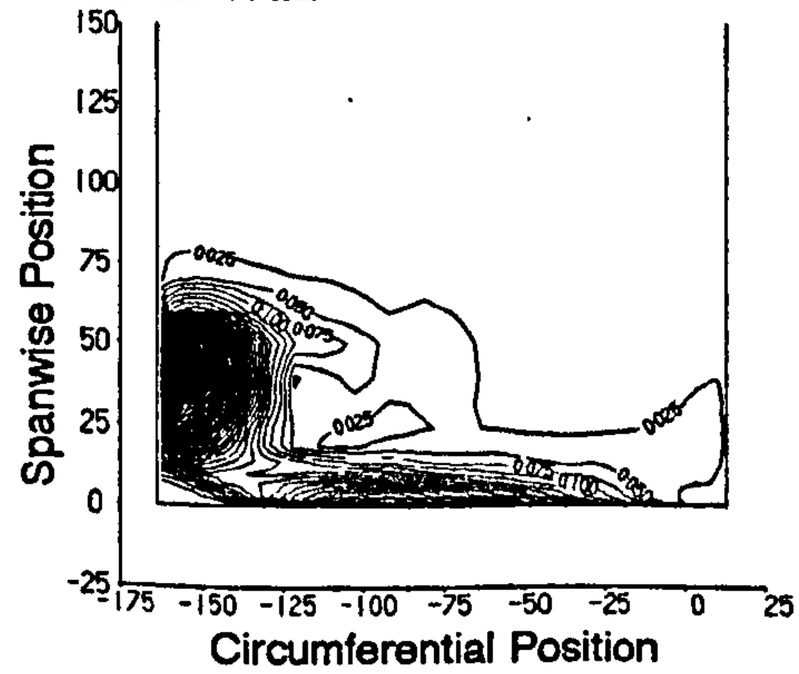

Figure 6.20 CFD Data at Slot 10.

a) Secondary Velocity Vectors.

Profile 3

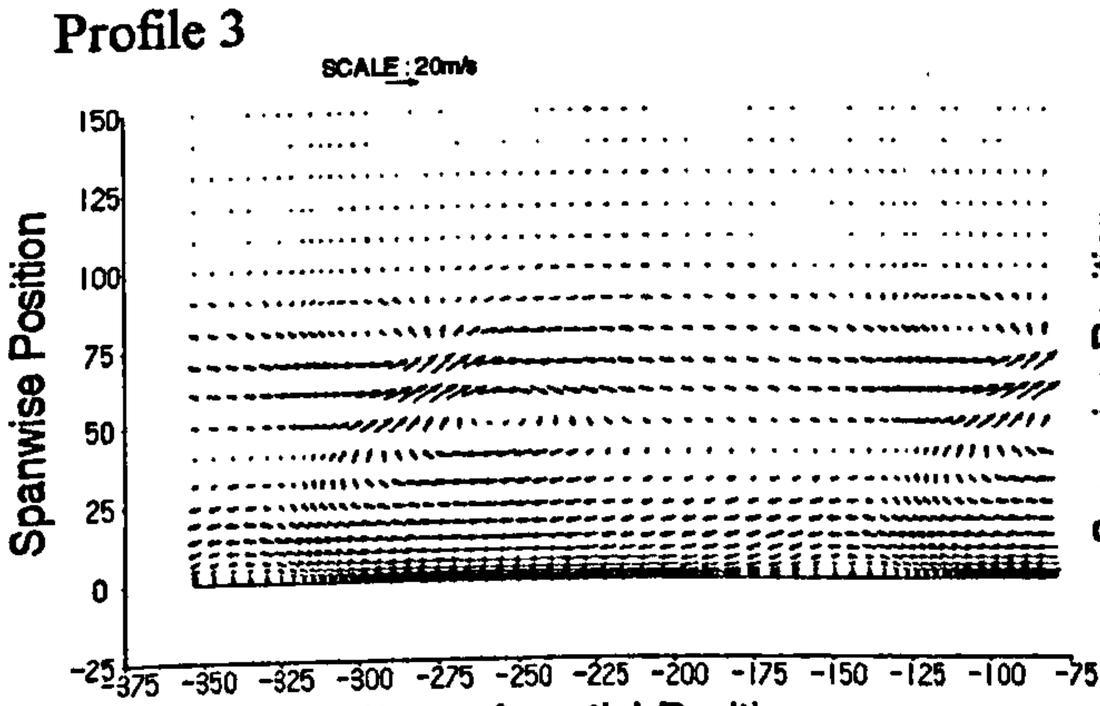

Planar Wall

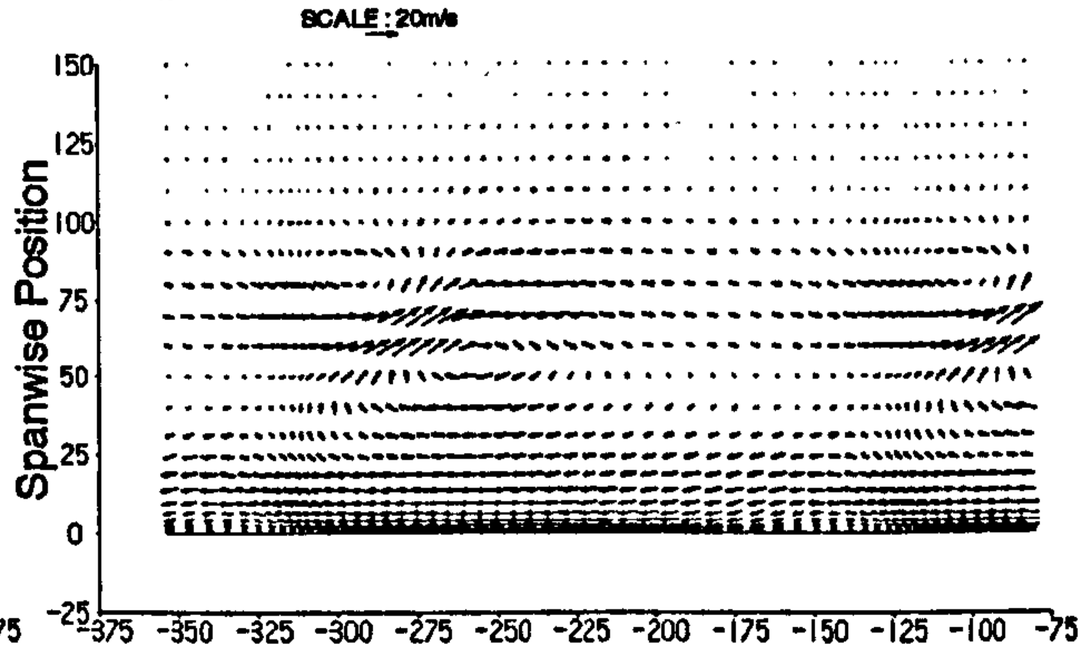

b) Total Pressure Loss Coefficient.

Profile 3

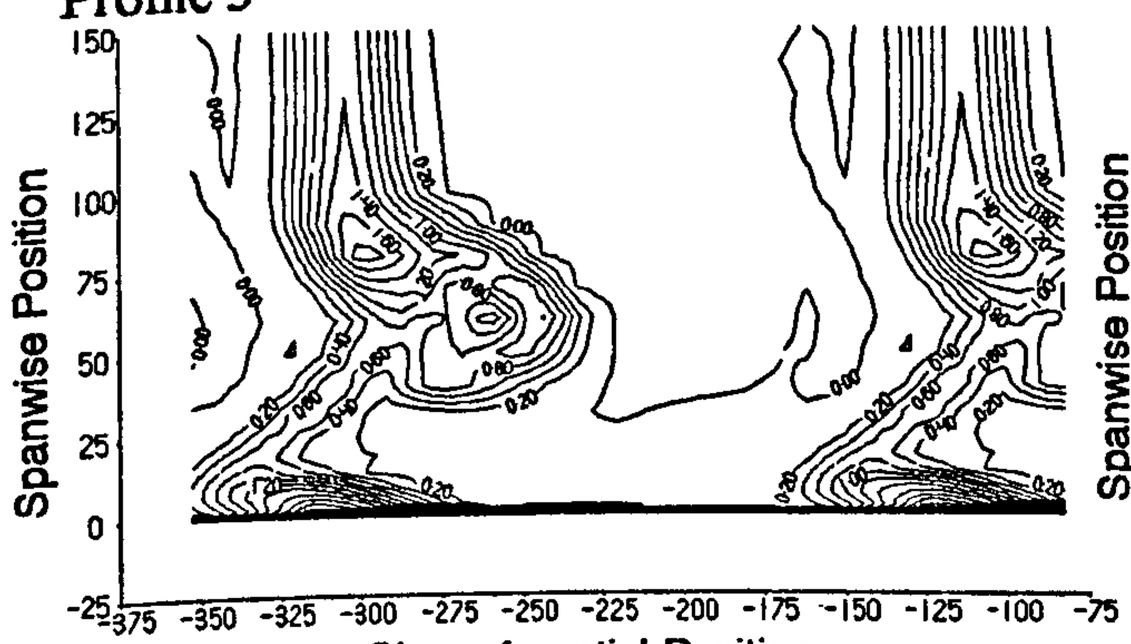

Planar Wall

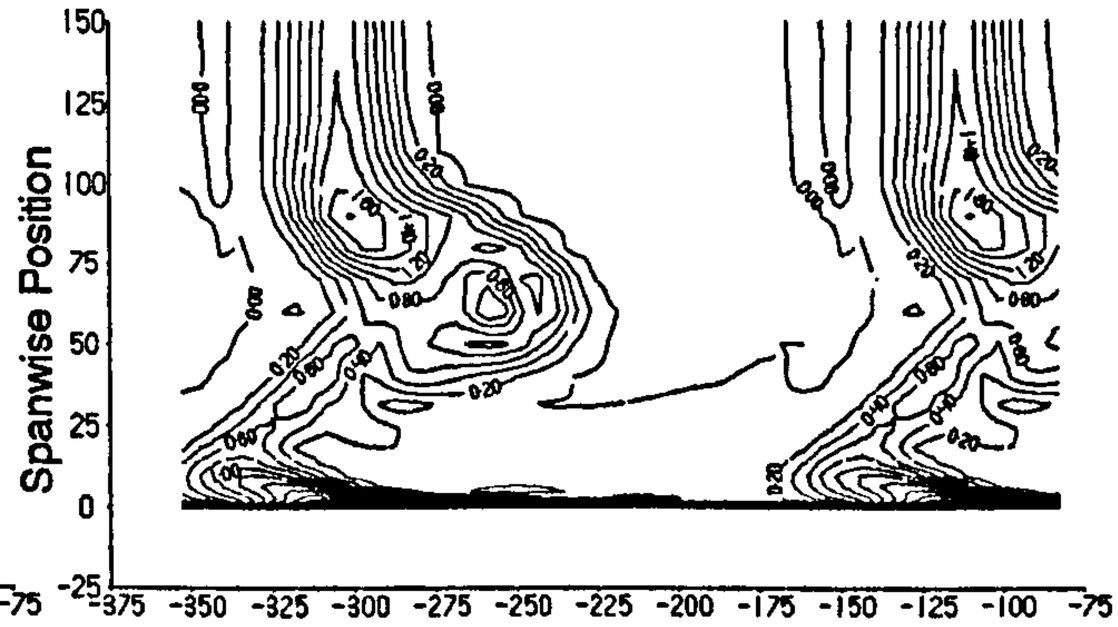

c) Yaw Angle.

Profile 3

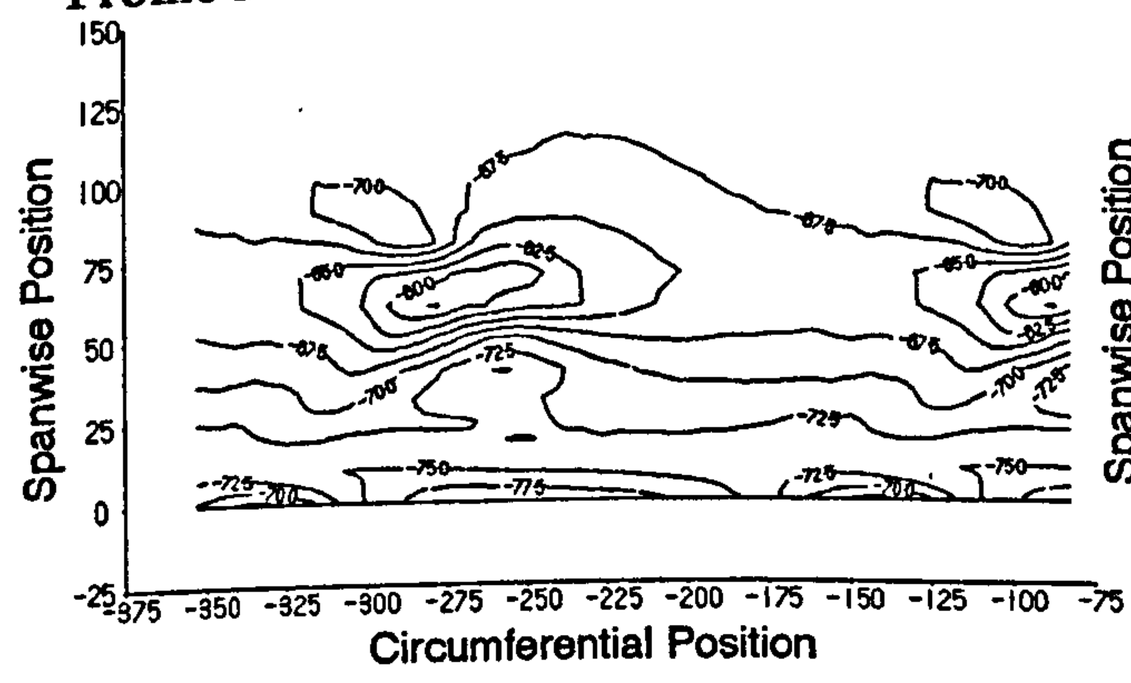

Planar Wall

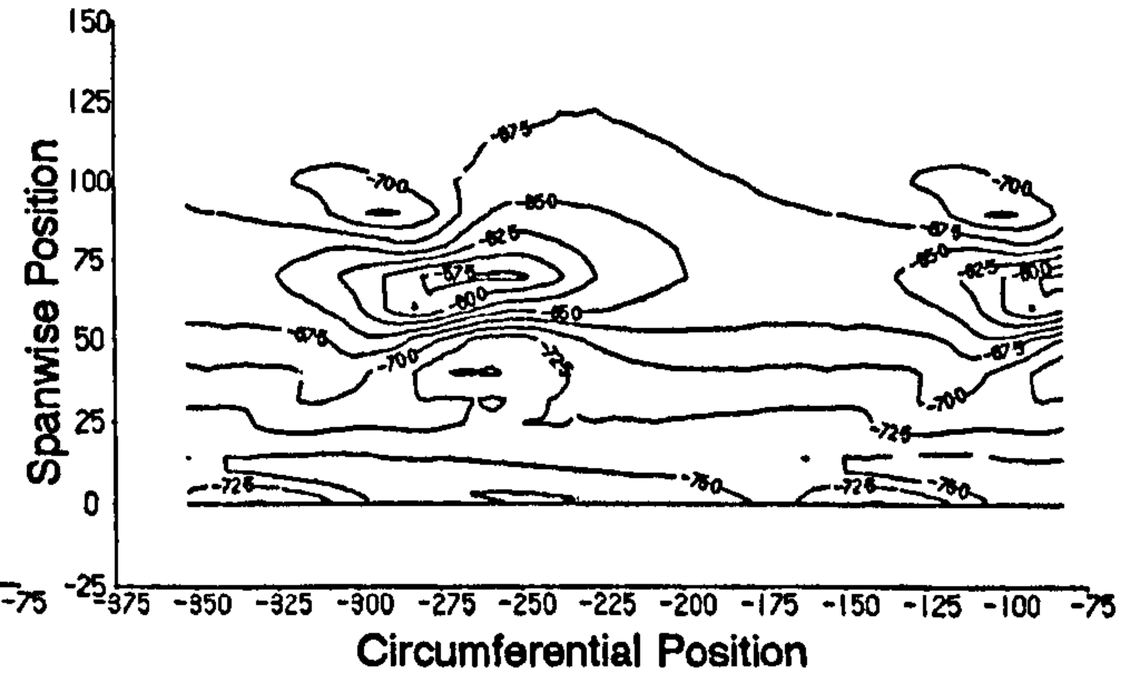

d) Secondary Kinetic Energy Coefficient.

Profile 3

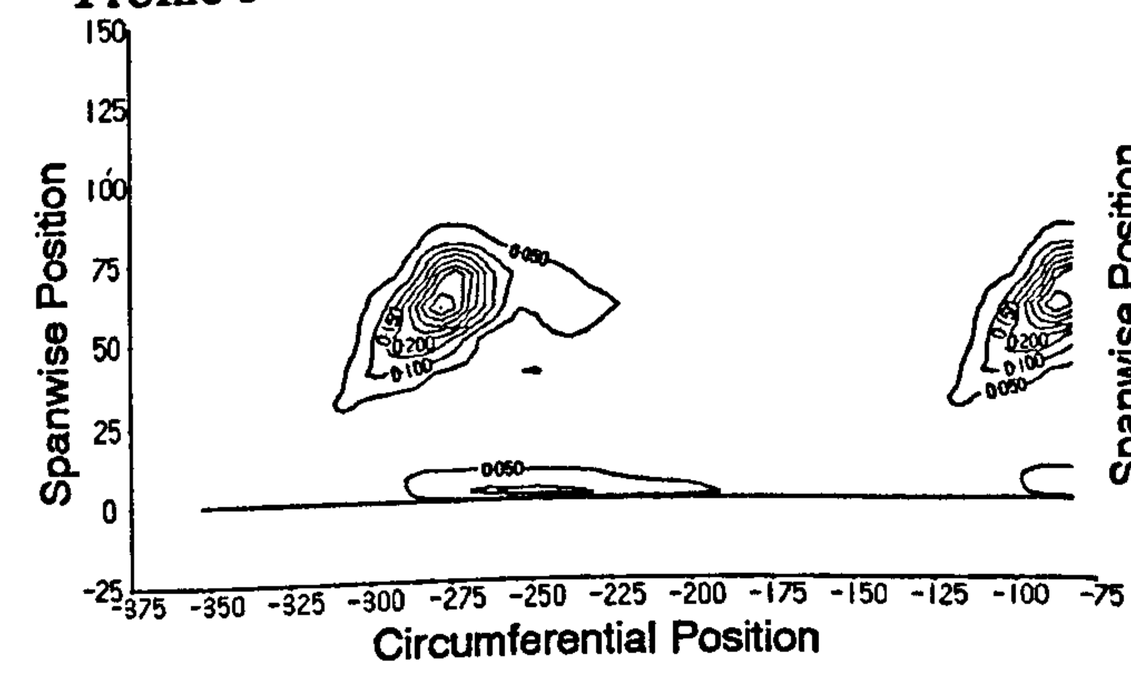

Planar Wall

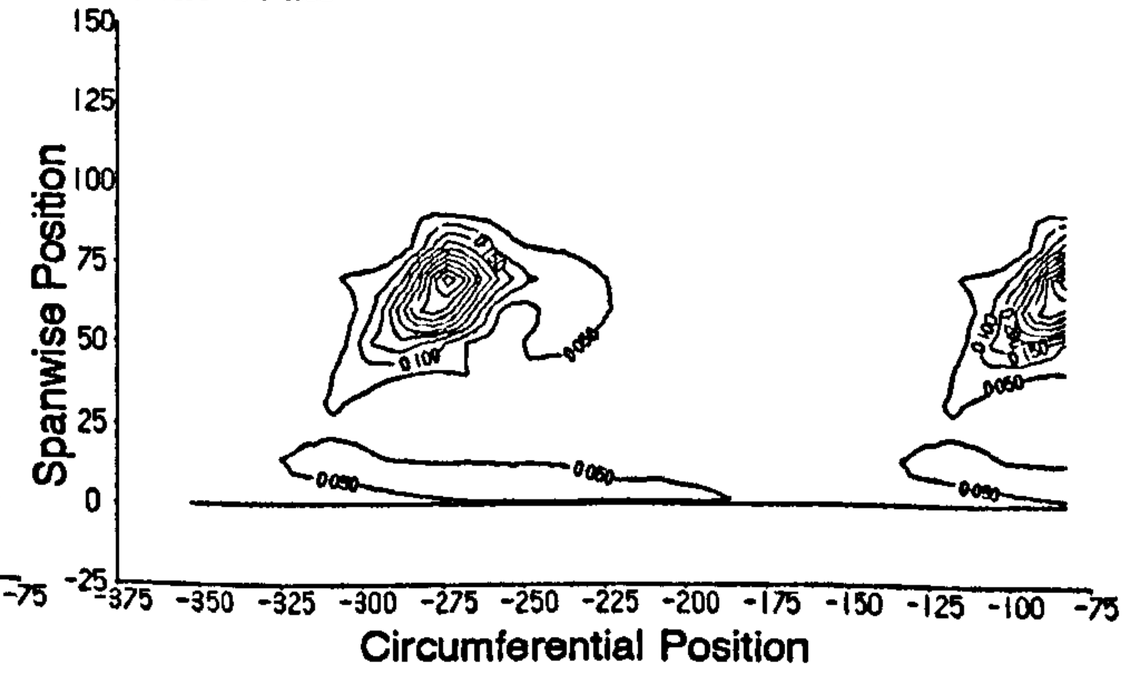

Figure 6.21 Experimental End-wall Pressure Coefficients.

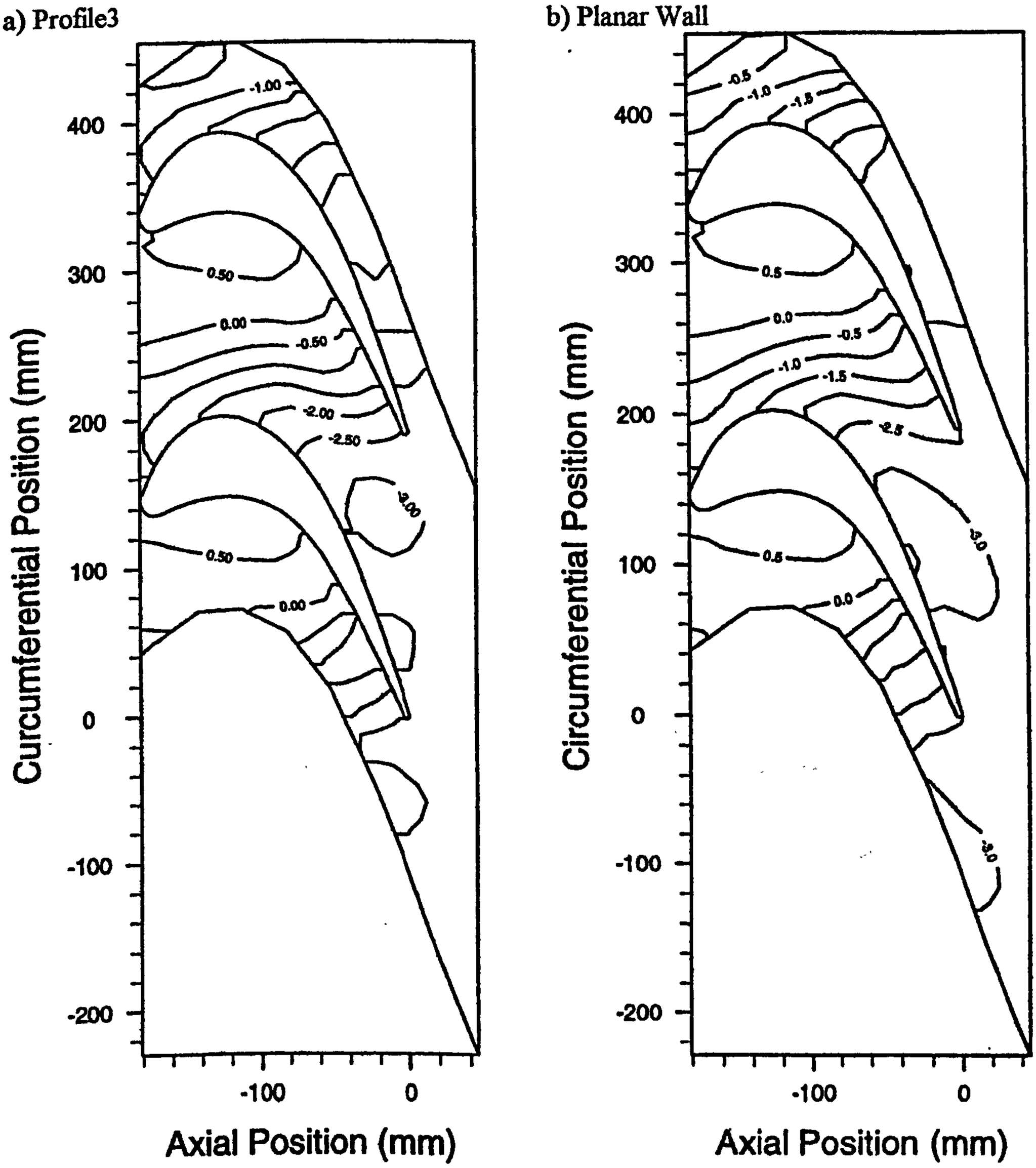

Figure 6.22 Experimental Non-Dimensional Pressures at Platform Trailing Edge (Fine Grid CFD and Planar Wall Data Included for Comparison).

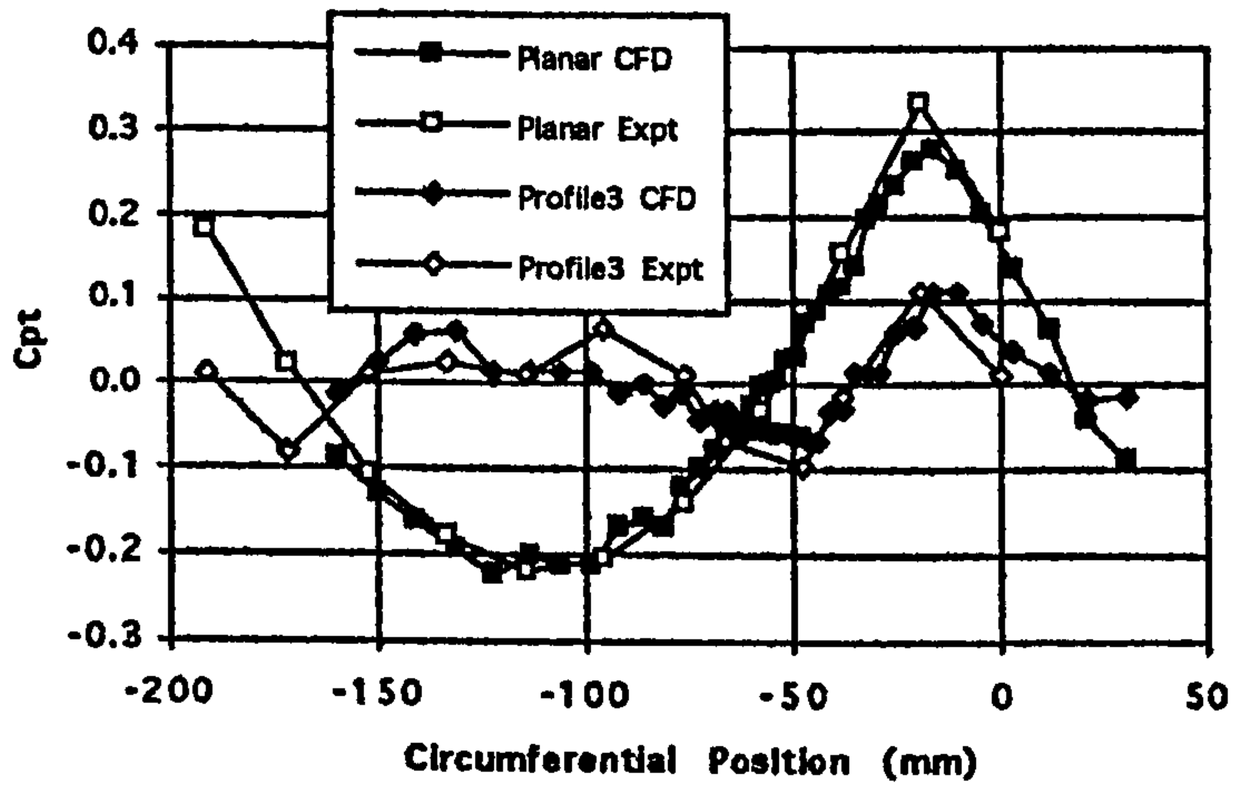

Figure 6.23 Measured Total Pressure Coefficient 100% C_{ax} Upstream.

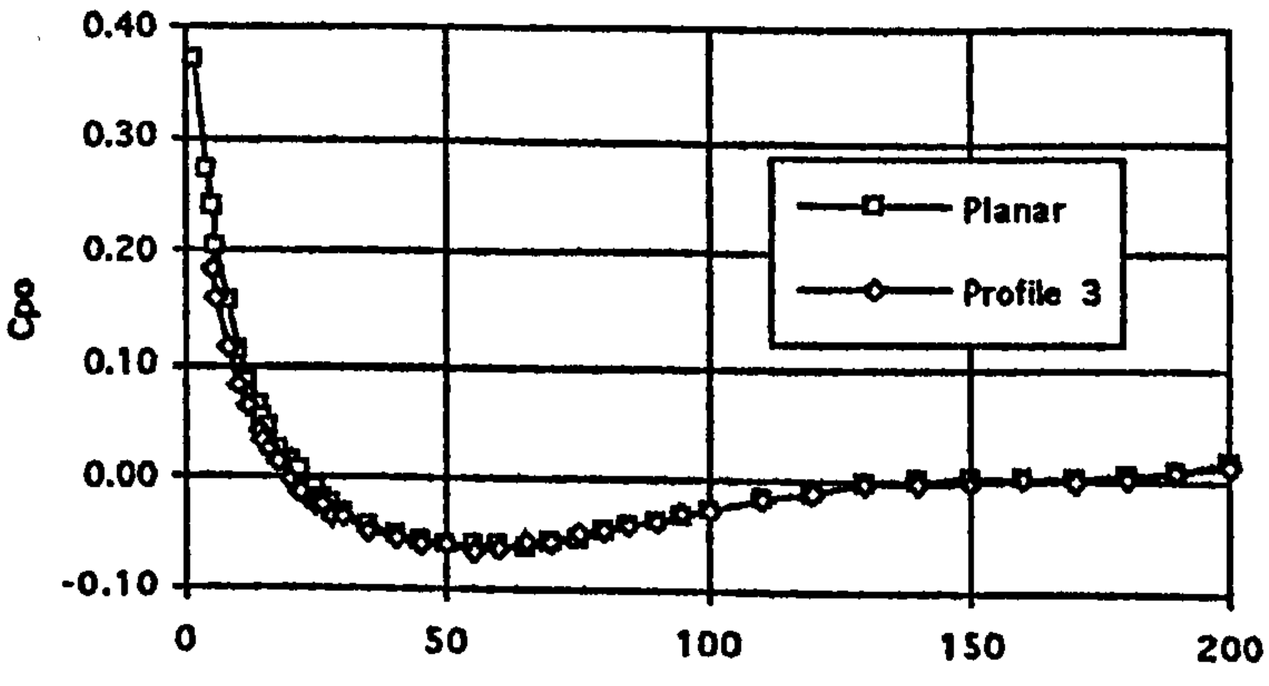

Figure 6.24 Pitch Averaged Experimental Data at Slot 1 (Planar Wall and CFD Data Included for Comparison).

a) Total Pressure Loss Coefficient.

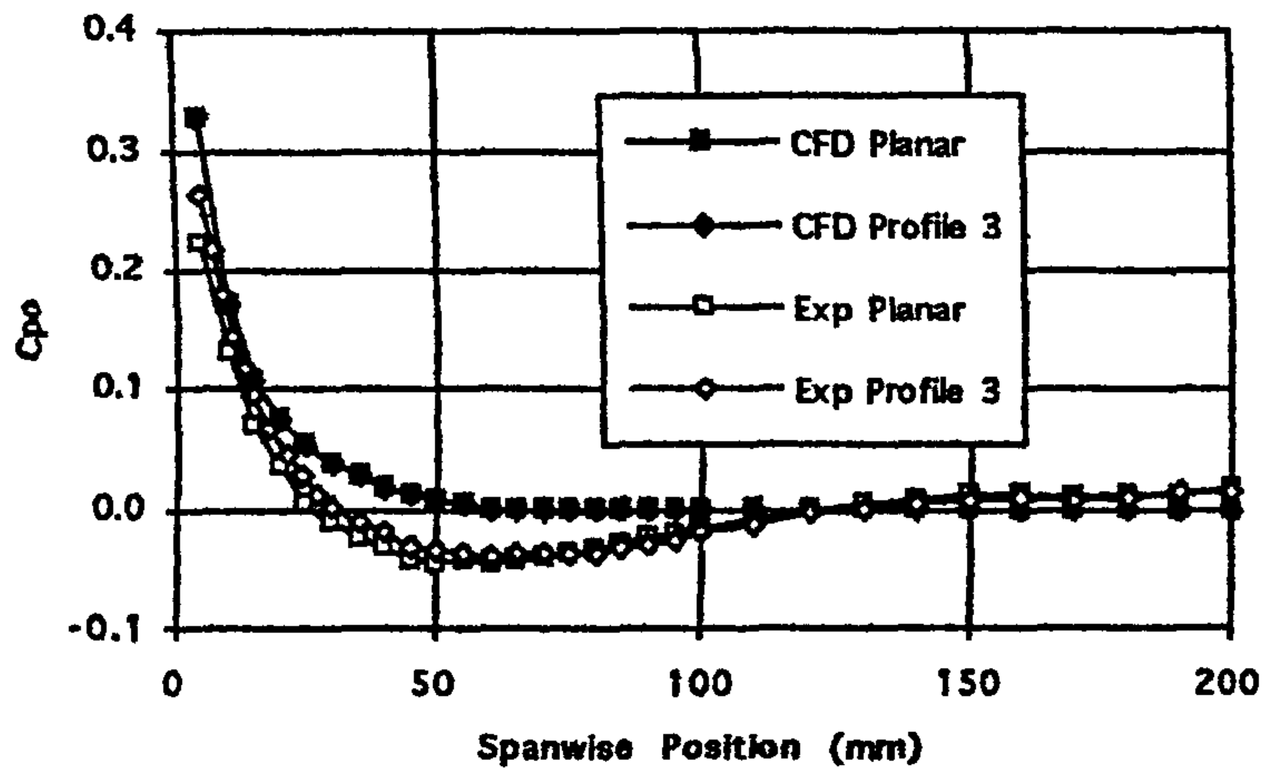

b) Yaw Angle.

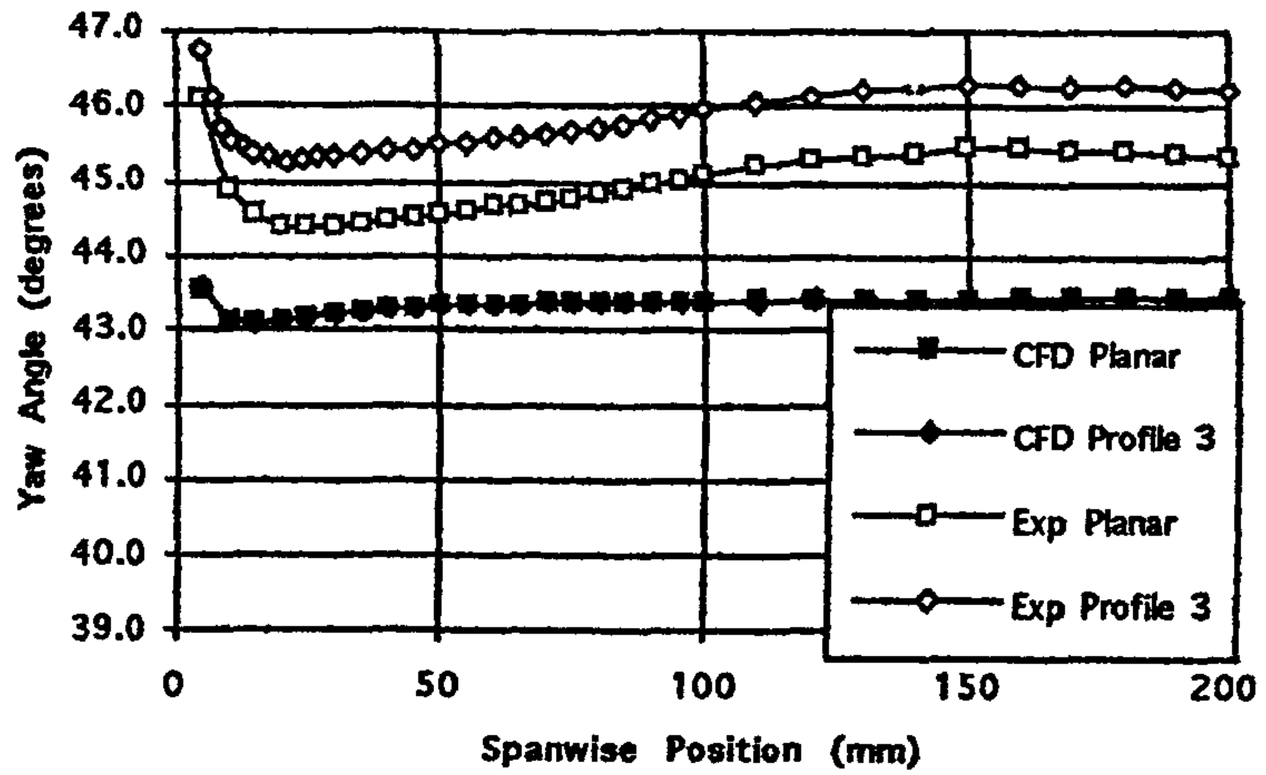

c) Pitch Angle.

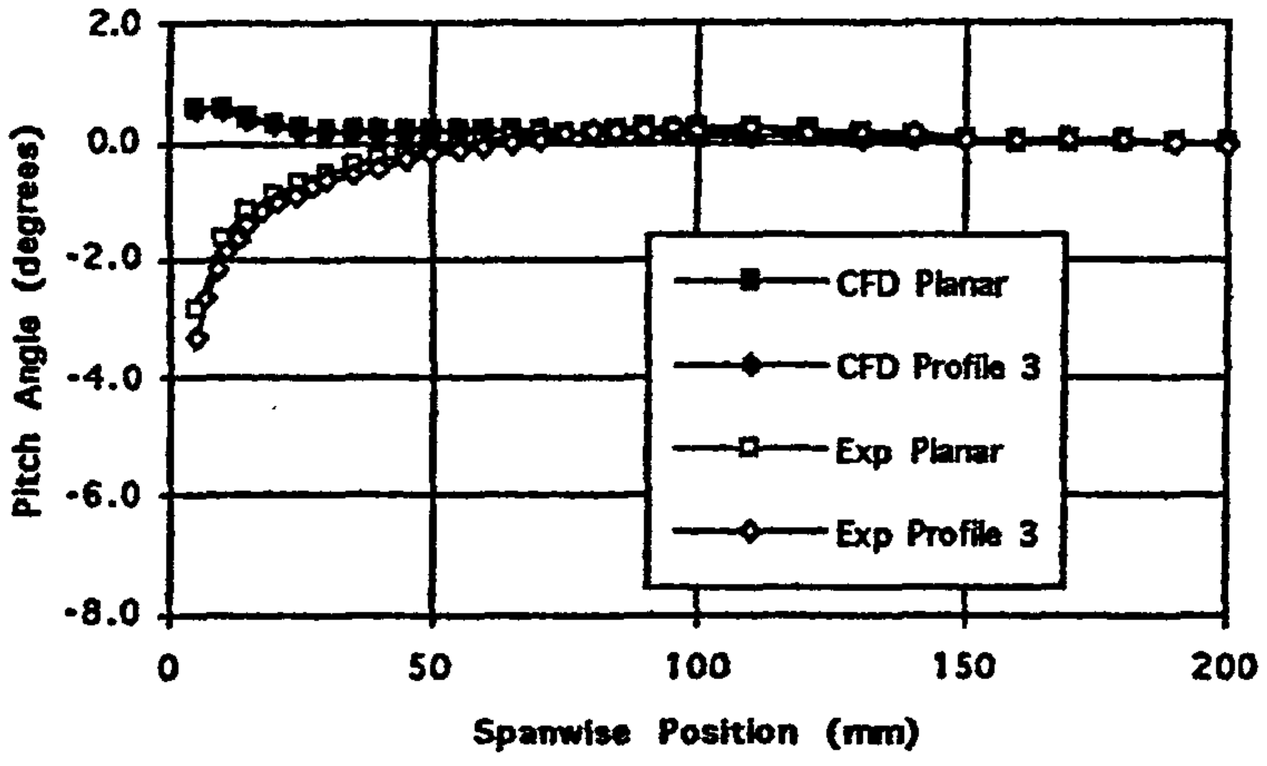

d) Secondary Kinetic Energy Coefficient.

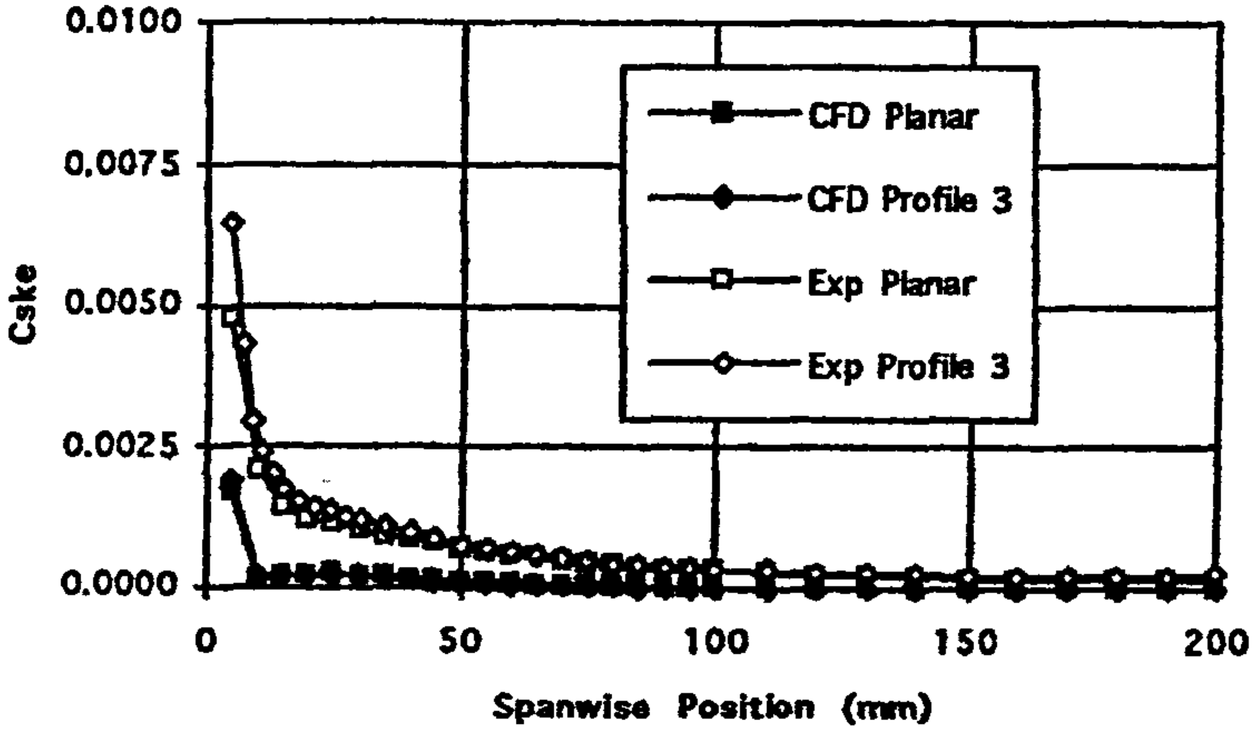

Figure 6.25 Pitch Averaged Experimental Data at Slot 6 (Planar Wall and CFD Data Included for Comparison).

a) Total Pressure Loss Coefficient.

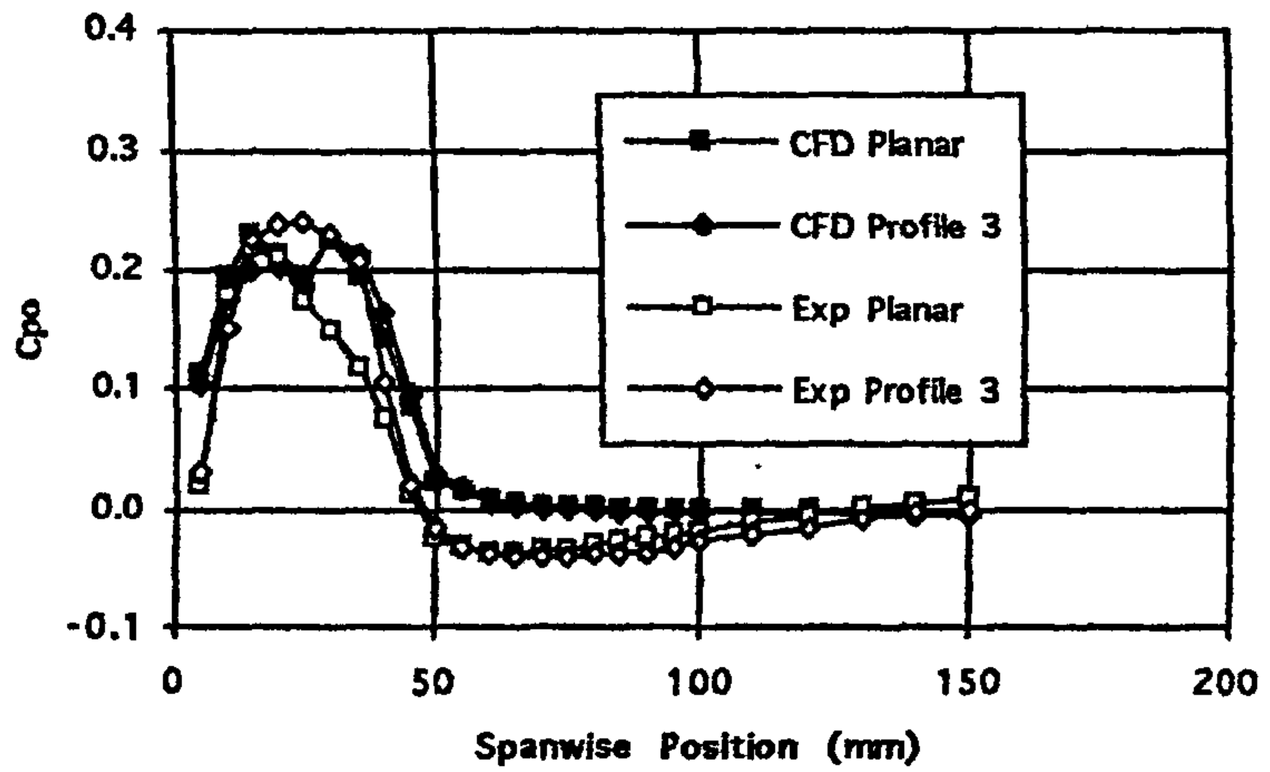

b) Yaw Angle.

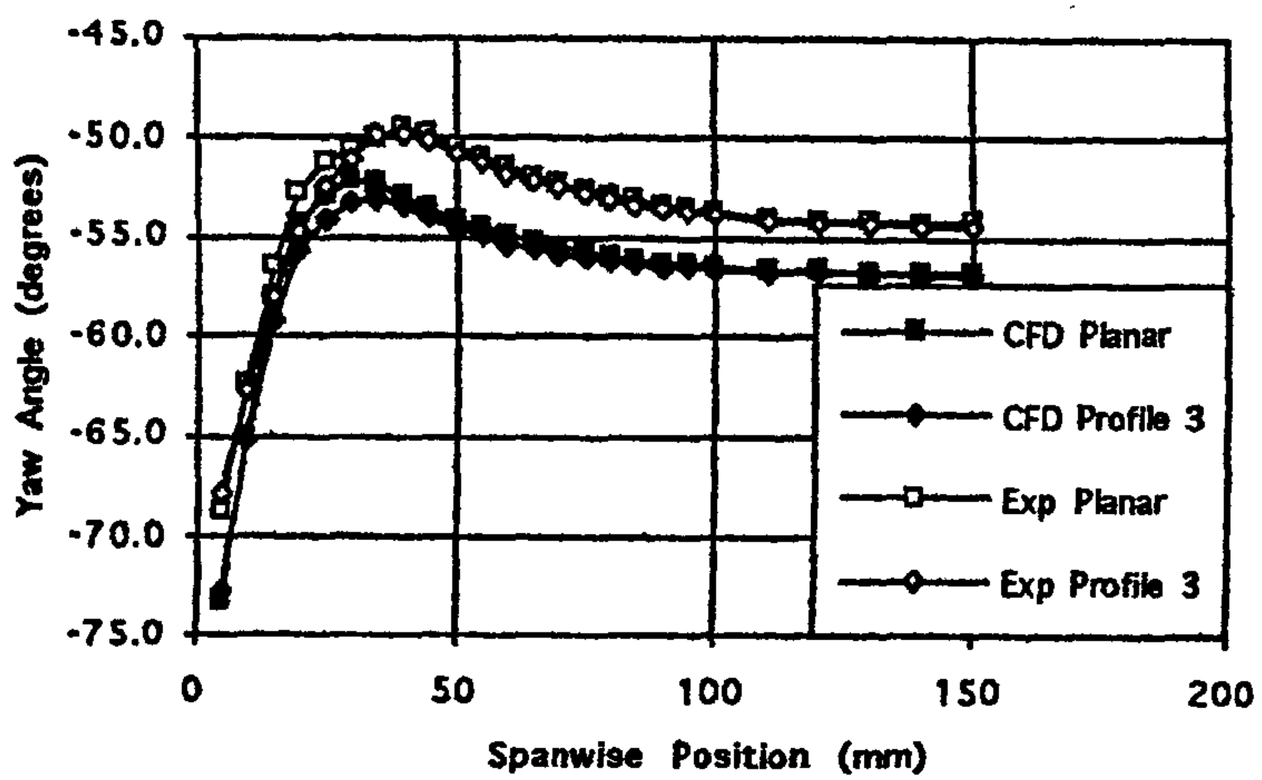

c) Pitch Angle.

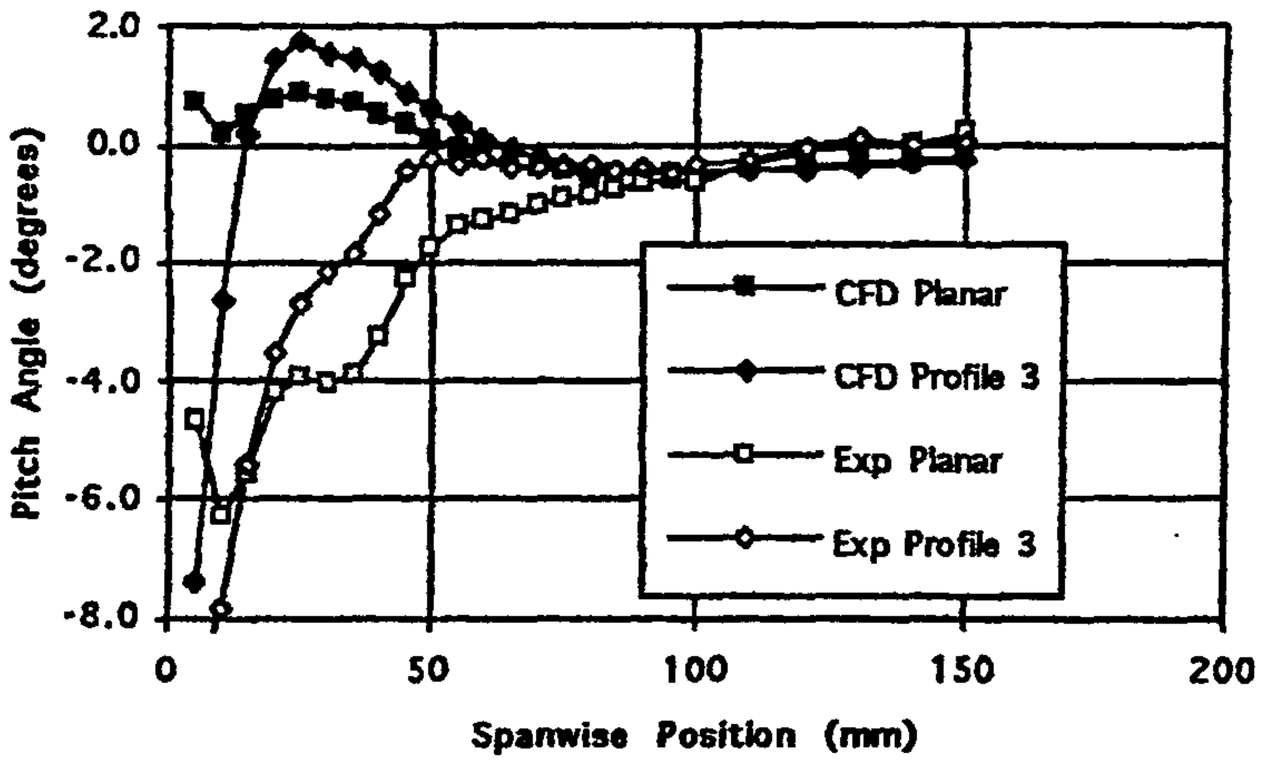

d) Secondary Kinetic Energy Coefficient.

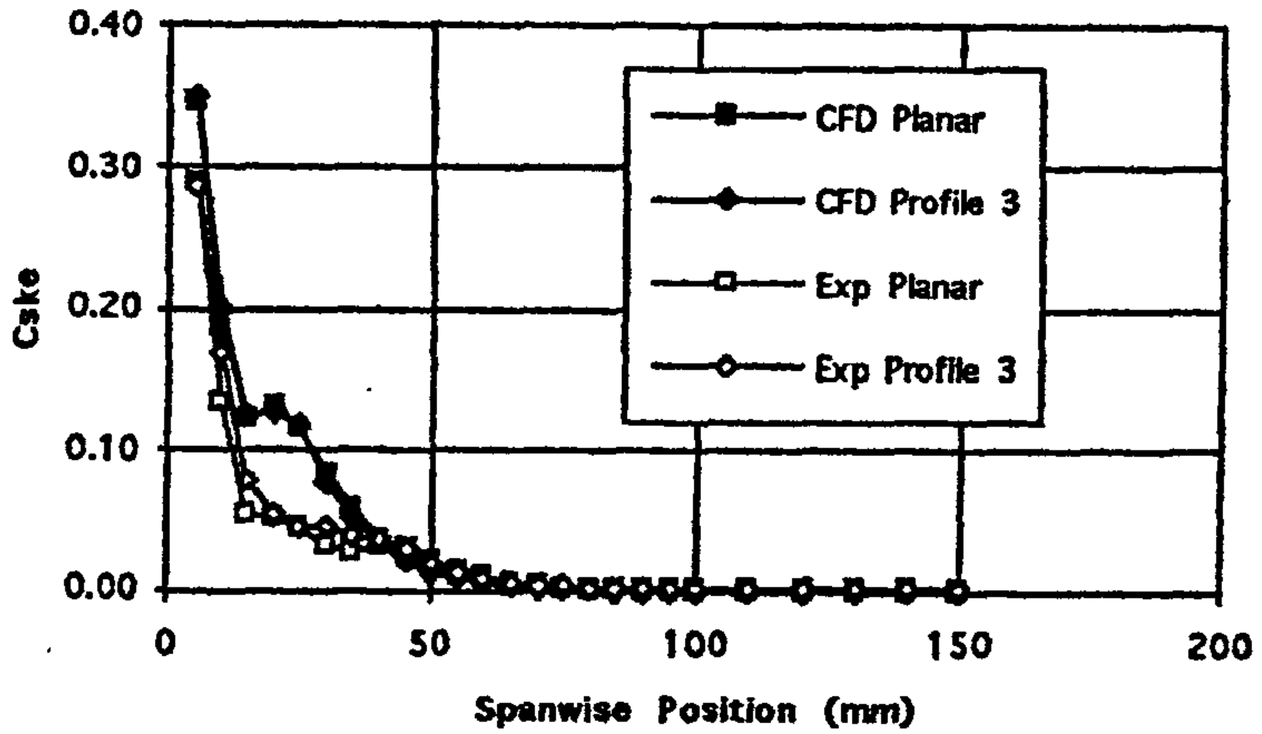

Figure 6.26 Pitch Averaged Experimental Data at Slot 8 (Planar Wall and CFD Data Included for Comparison).

a) Total Pressure Loss Coefficient.

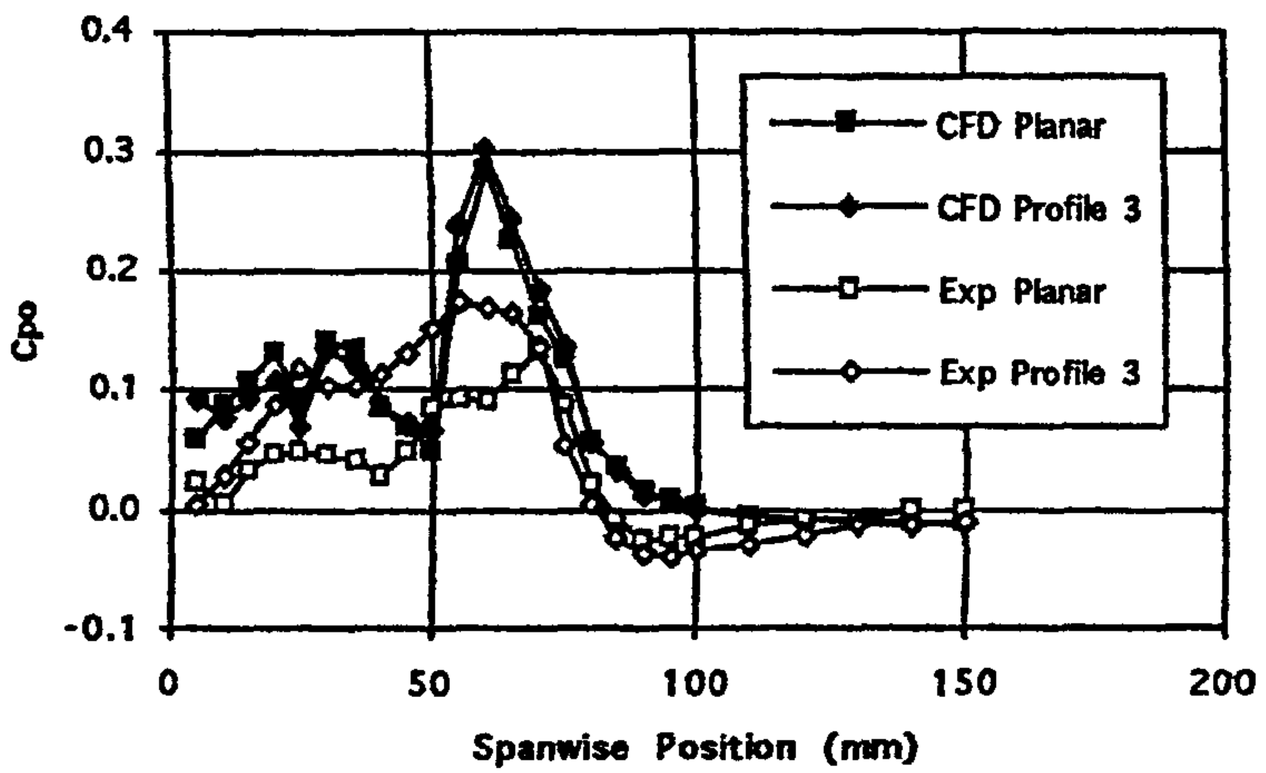

b) Yaw Angle.

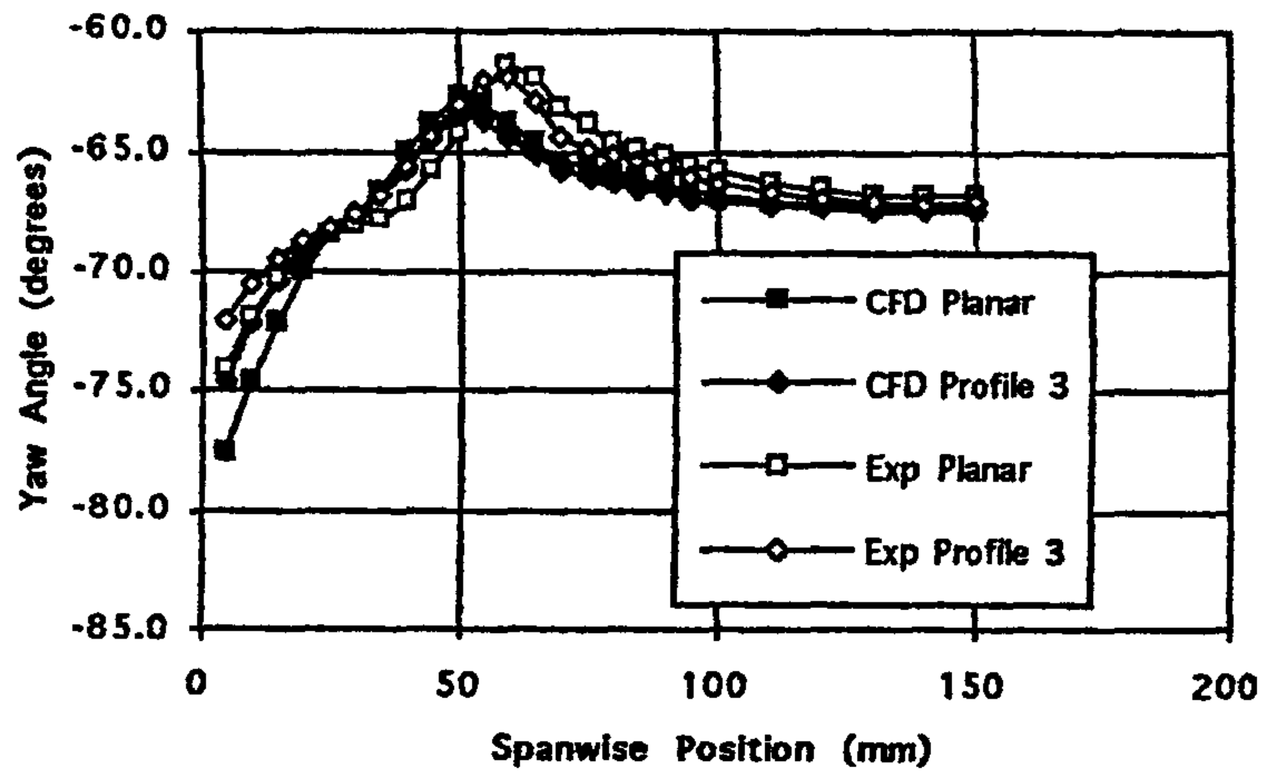

c) Pitch Angle.

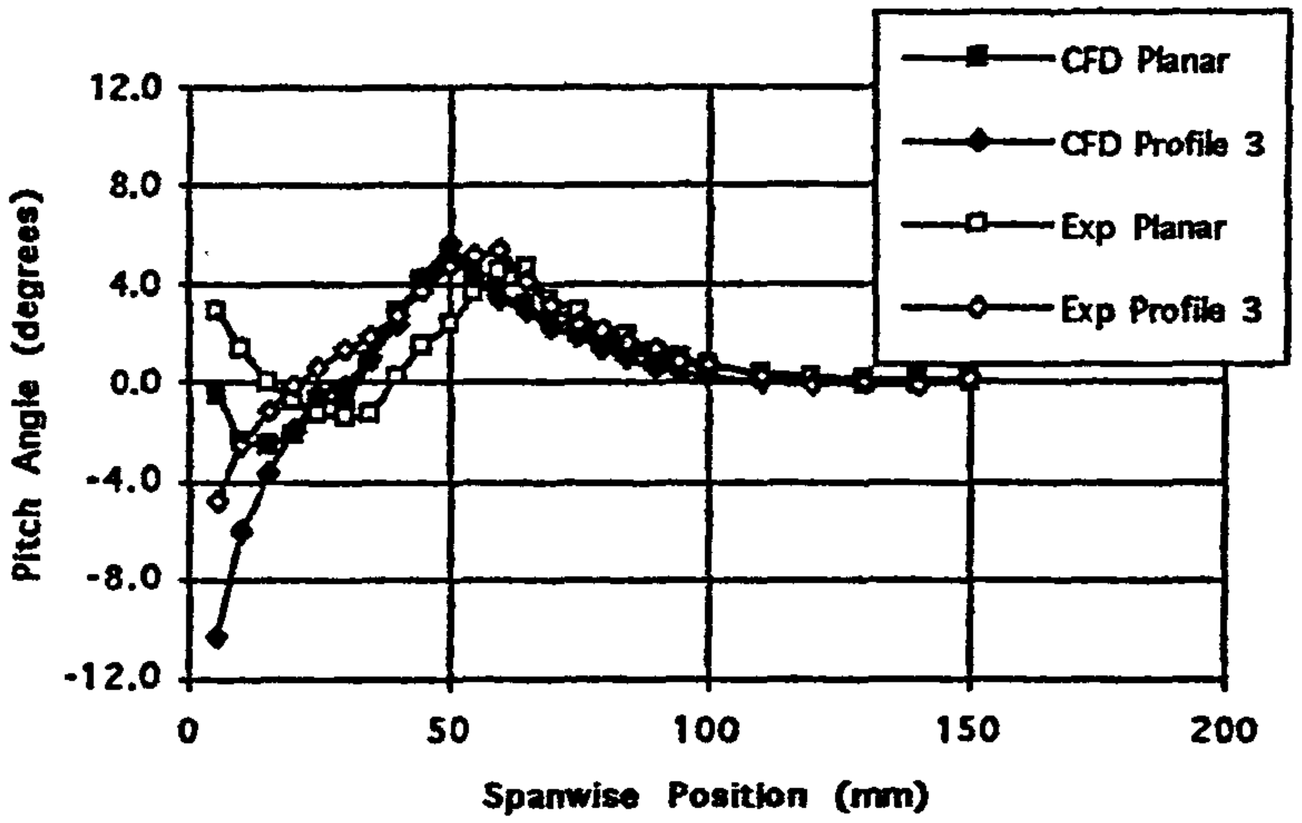

d) Secondary Kinetic Energy Coefficient.

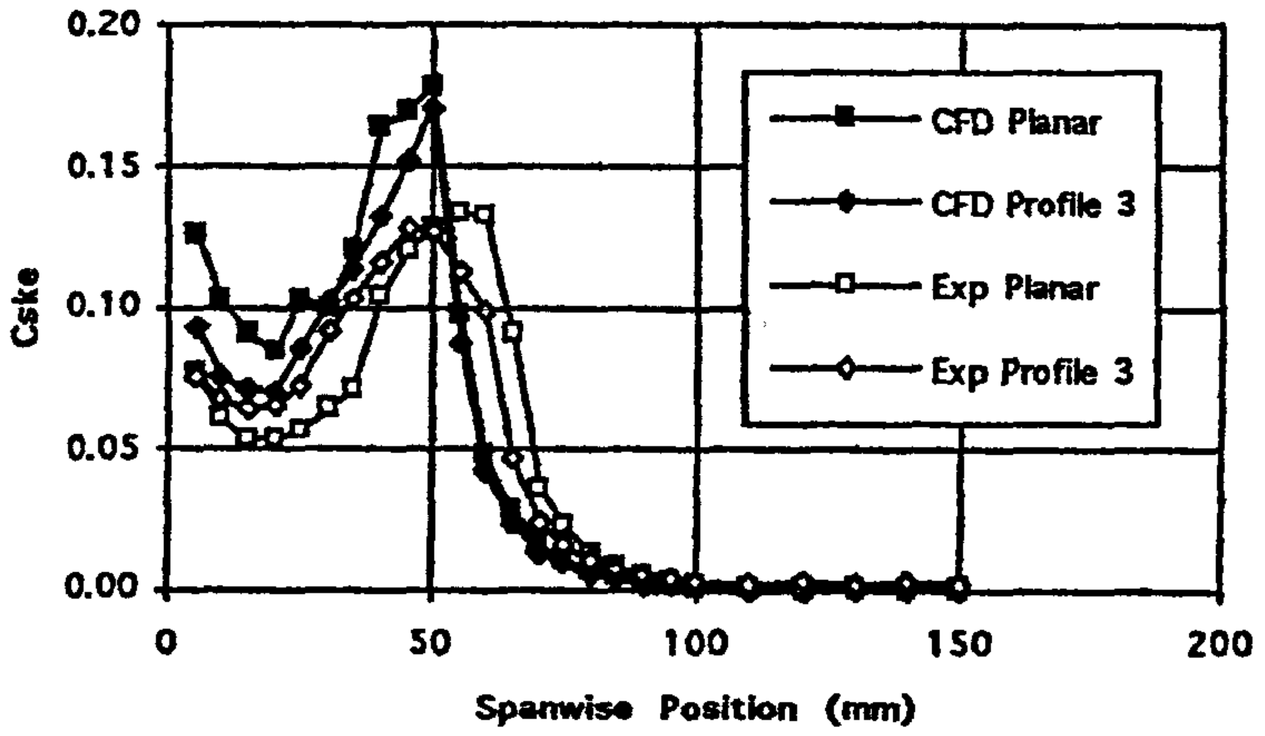

Figure 6.27 Pitch Averaged Experimental Data at Slot 10 (Planar Wall and CFD Data Included for Comparison).

a) Total Pressure Loss Coefficient.

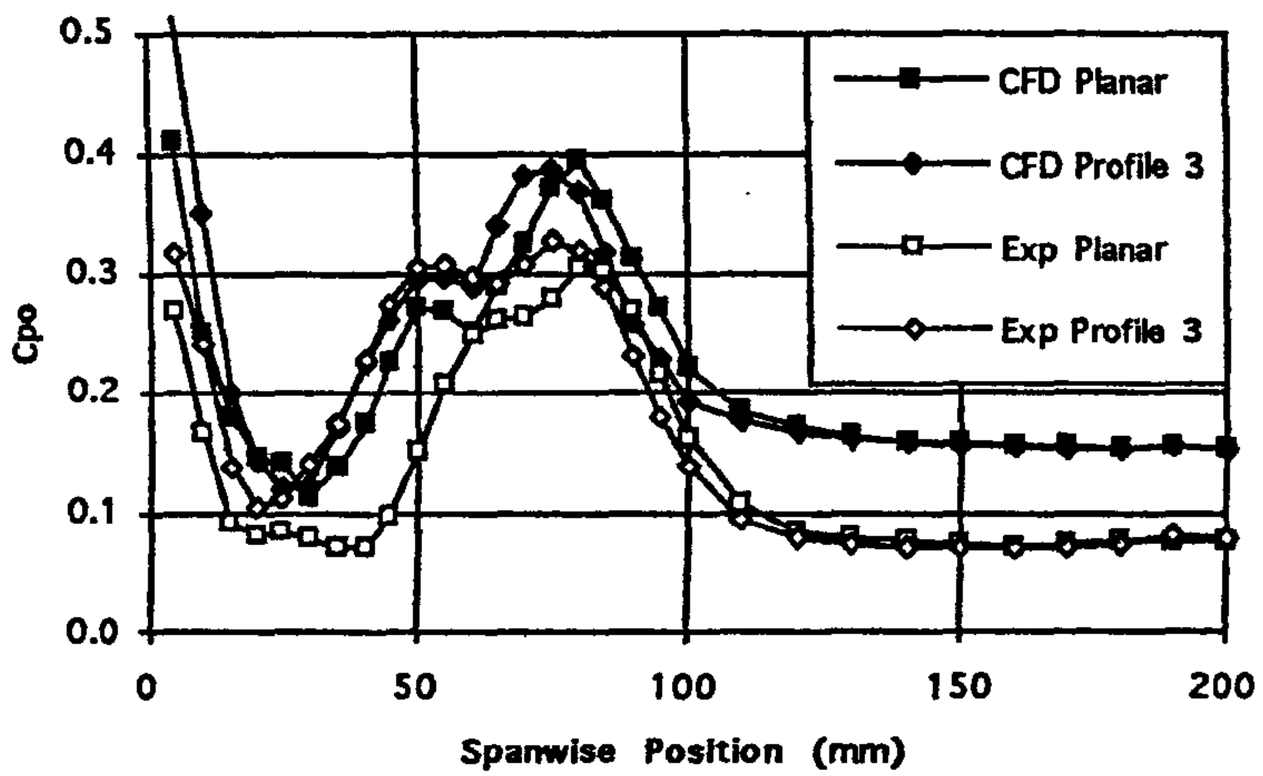

b) Yaw Angle.

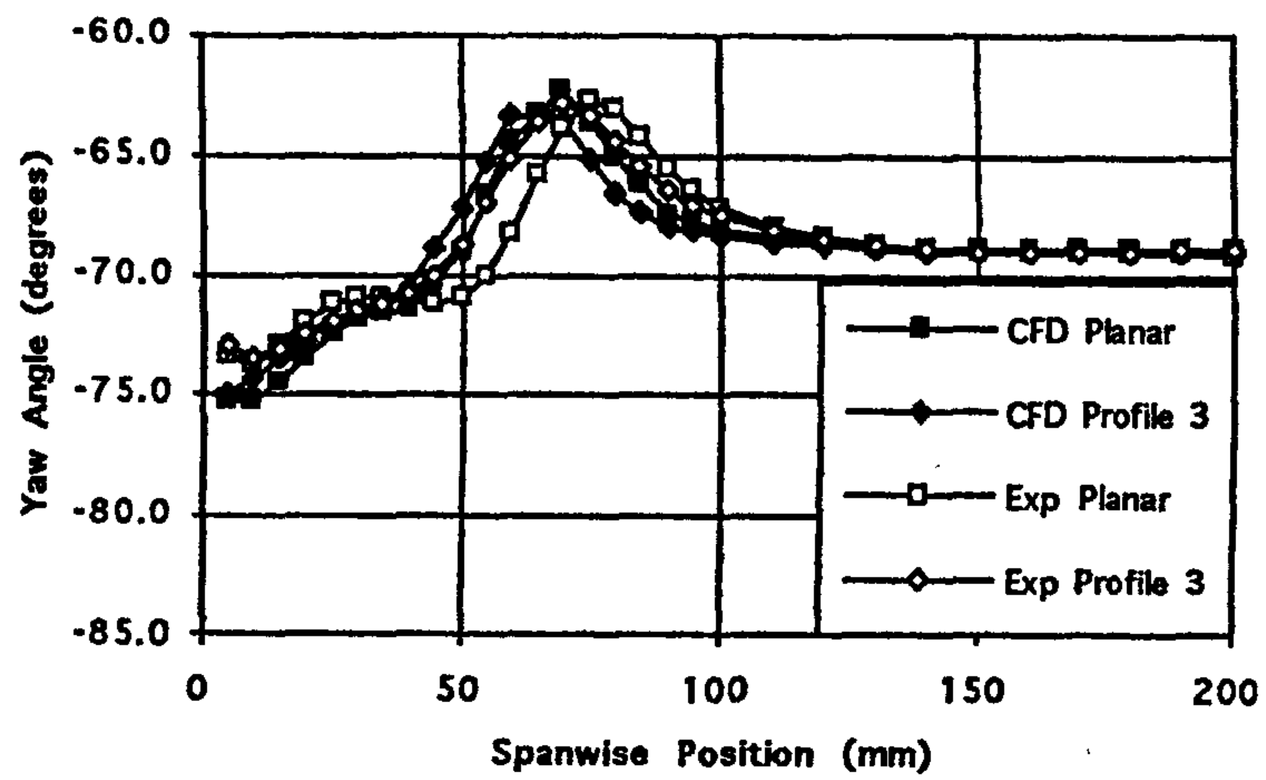

c) Pitch Angle.

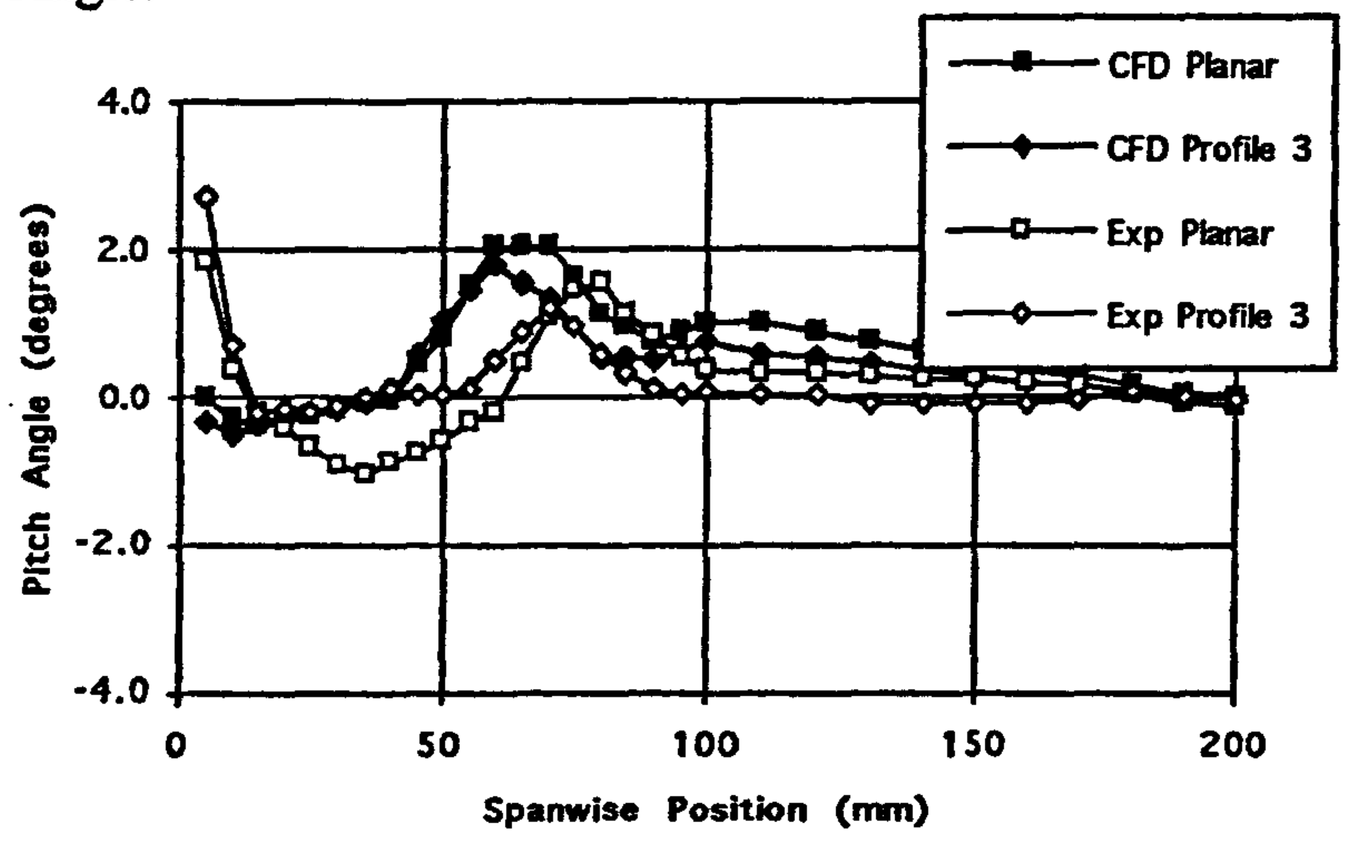

d) Secondary Kinetic Energy Coefficient.

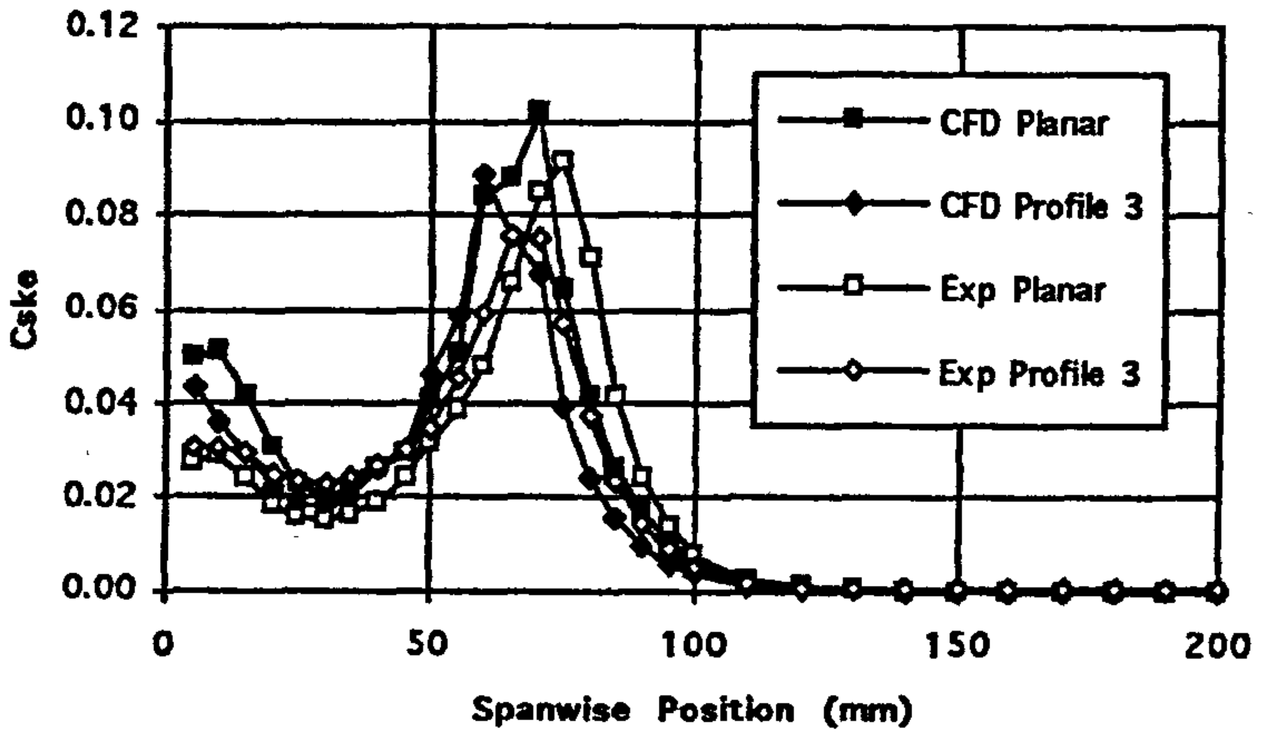

Figure 6.28 Growth of C_{SKE} Through the Cascade.

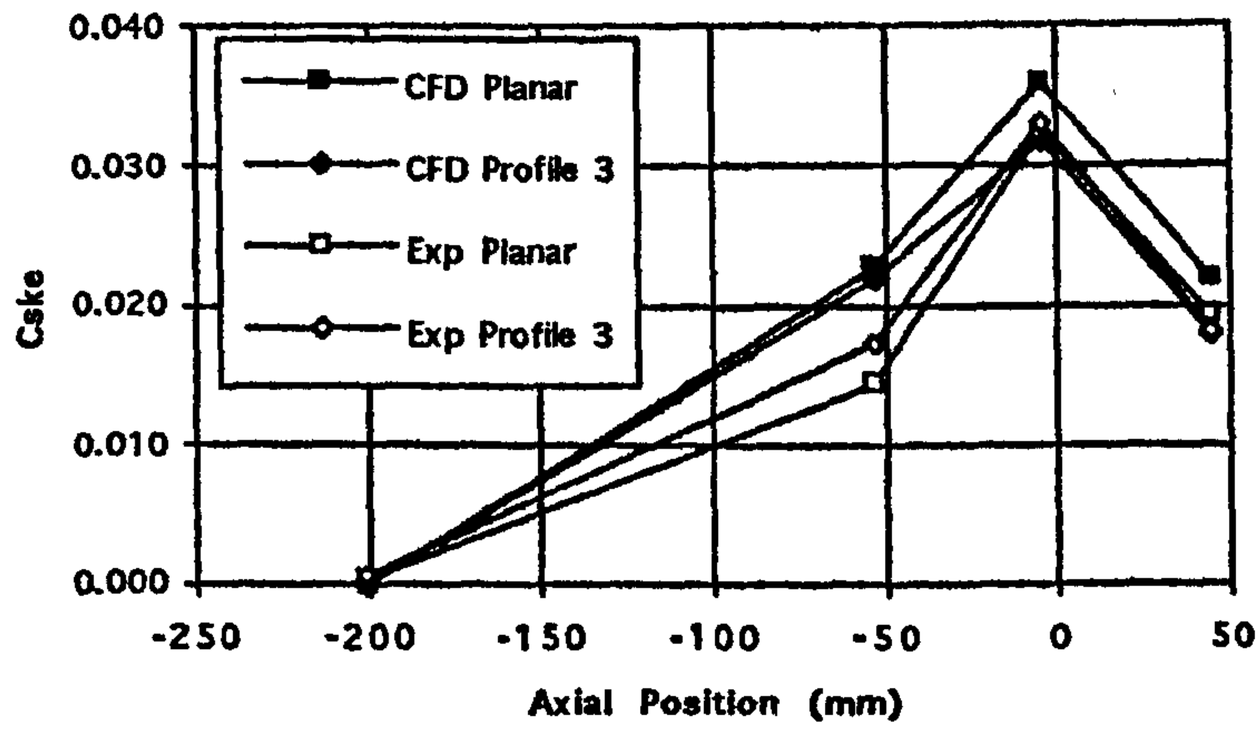

Figure 6.29 Experimental Data at Slot 1.

a) Secondary Velocity Vectors.

Profile 3

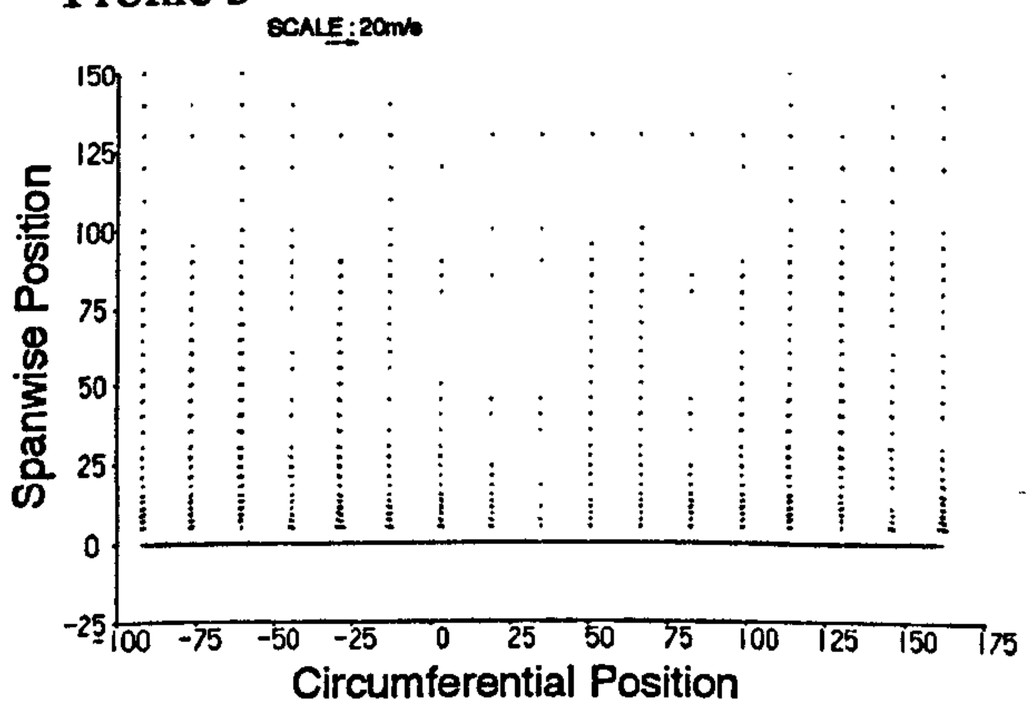

Planar Wall

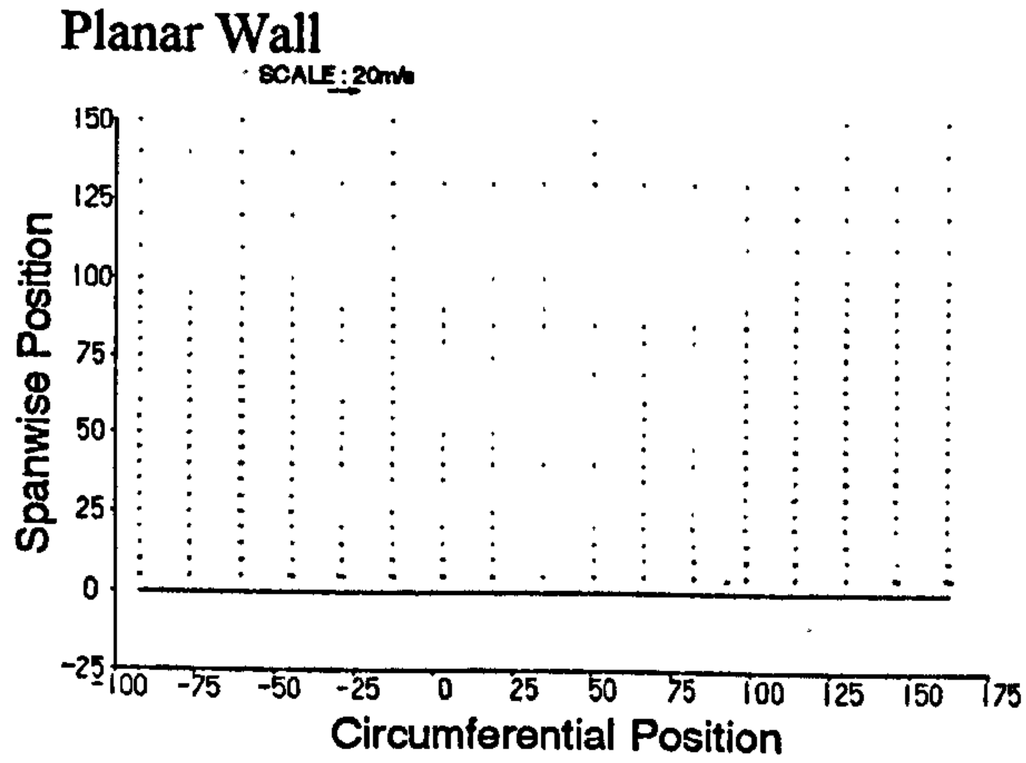

b) Total Pressure Loss Coefficient.

Profile 3

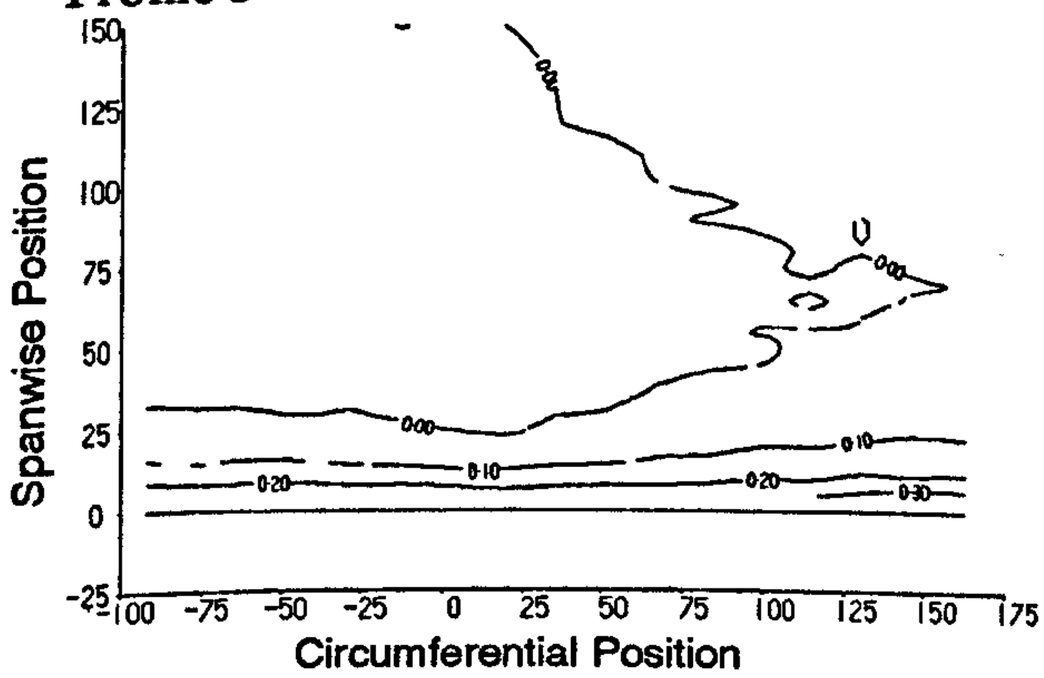

Planar Wall

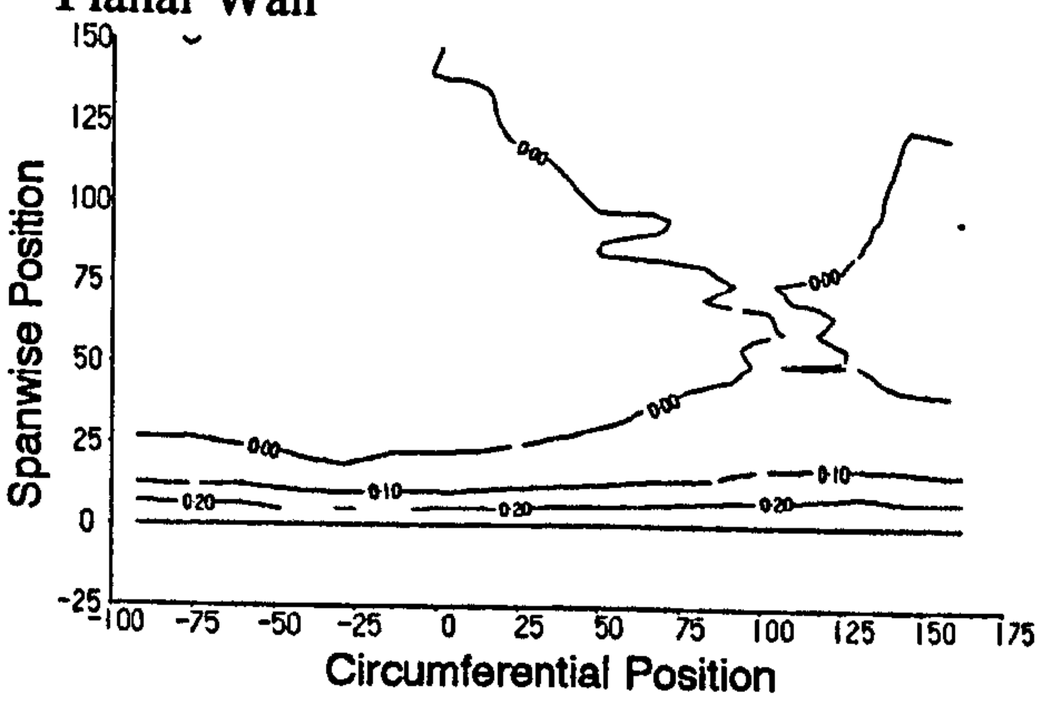

c) Yaw Angle.

Profile 3

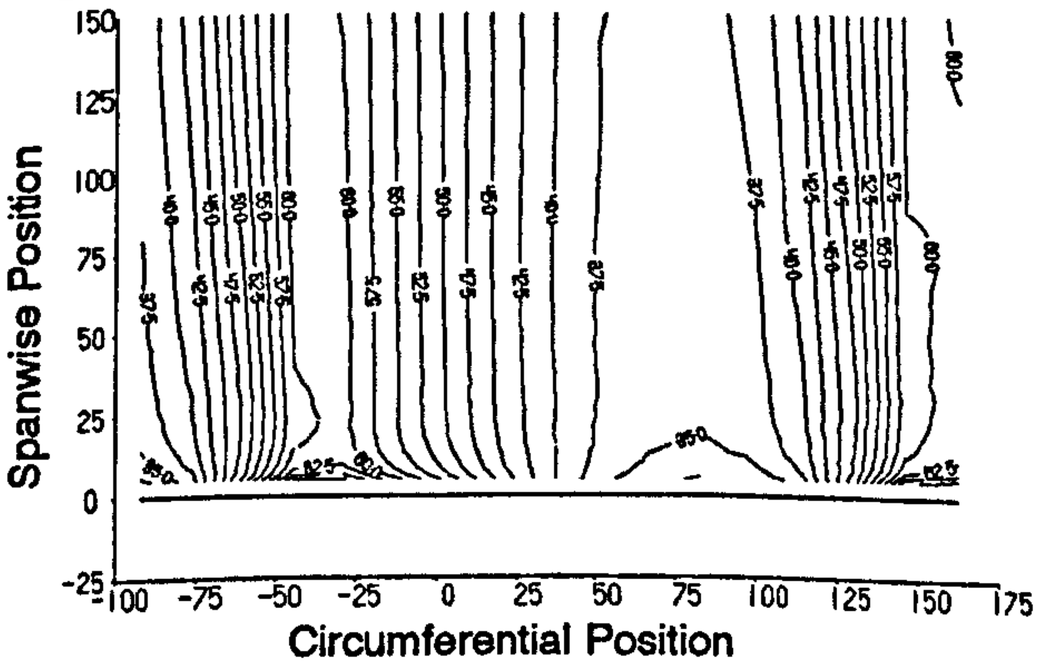

Planar Wall

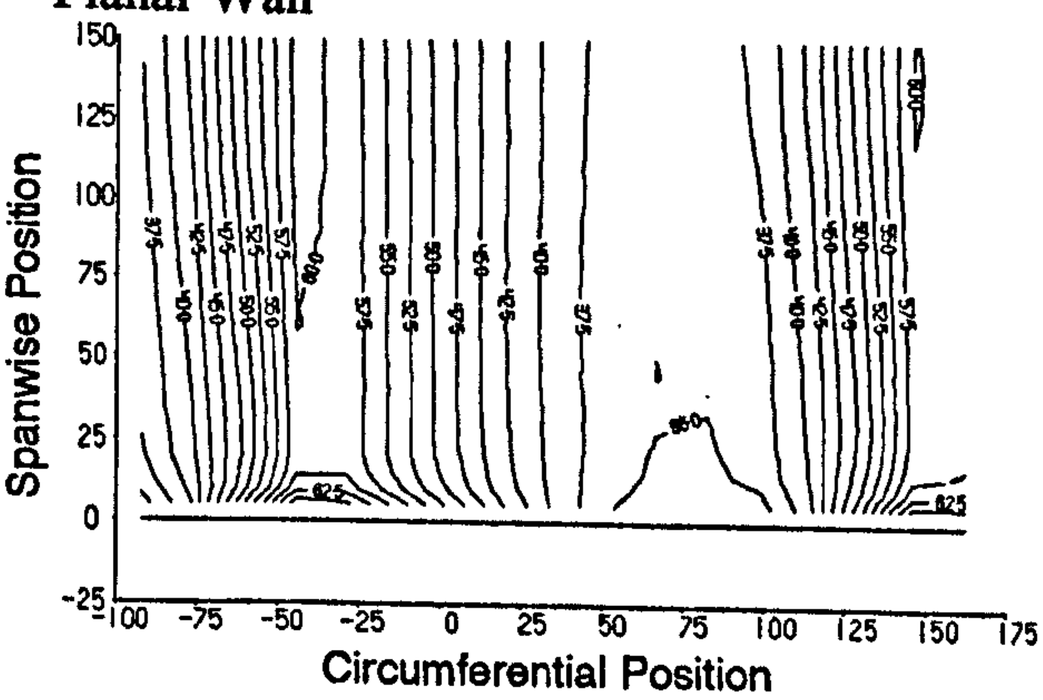

d) Secondary Kinetic Energy Coefficient.

Profile 3

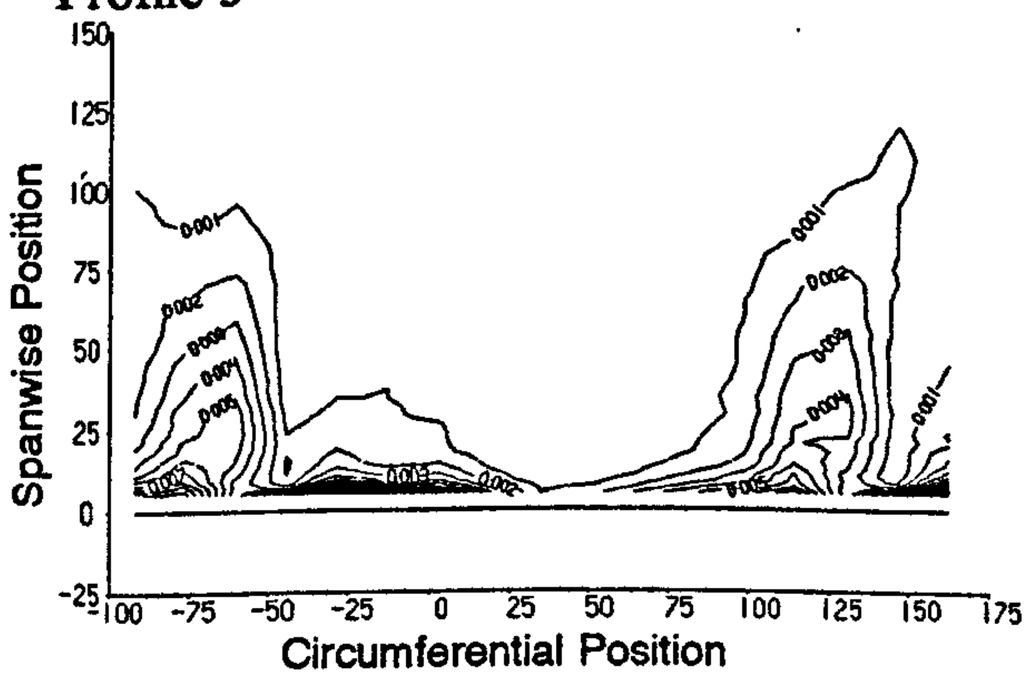

Planar Wall

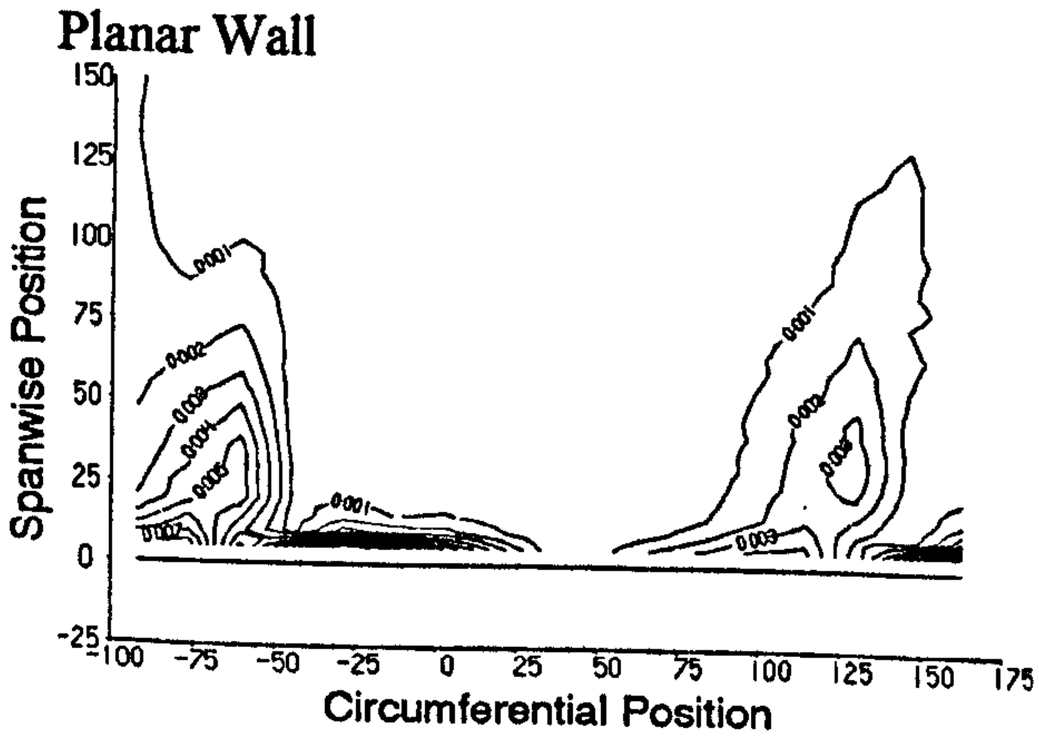

Figure 6.30 Experimental Data at Slot 6.

a) Secondary Velocity Vectors.

Profile 3

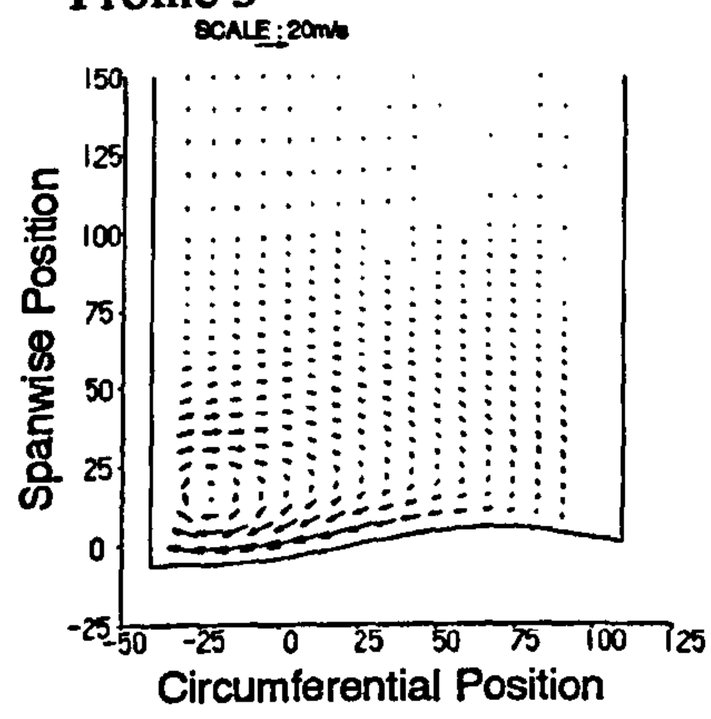

Planar Wall

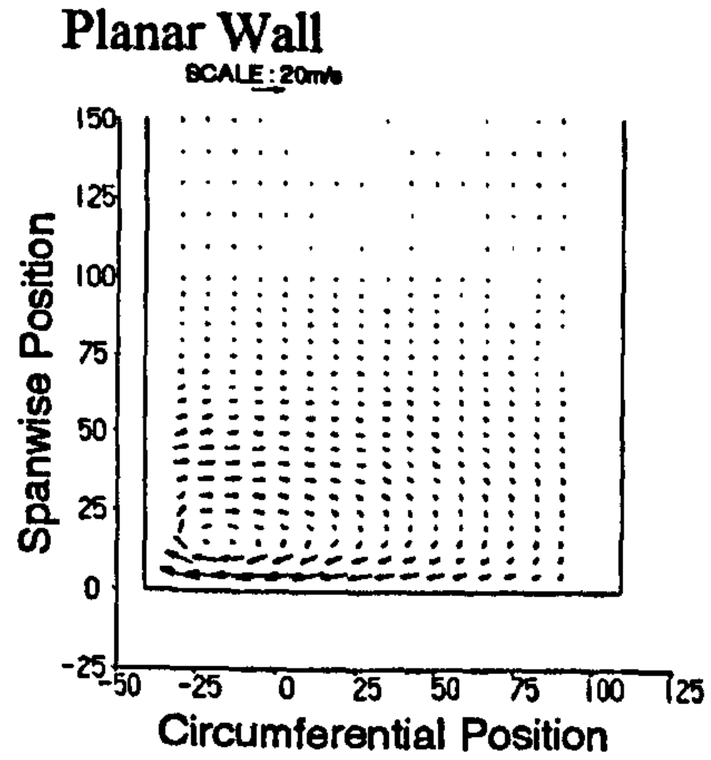

b) Total Pressure Loss Coefficient.

Profile 3

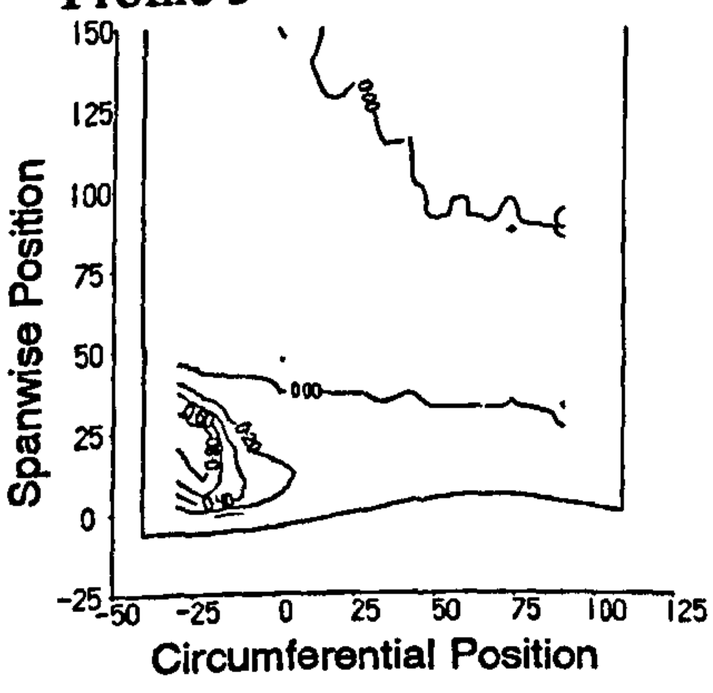

Planar Wall

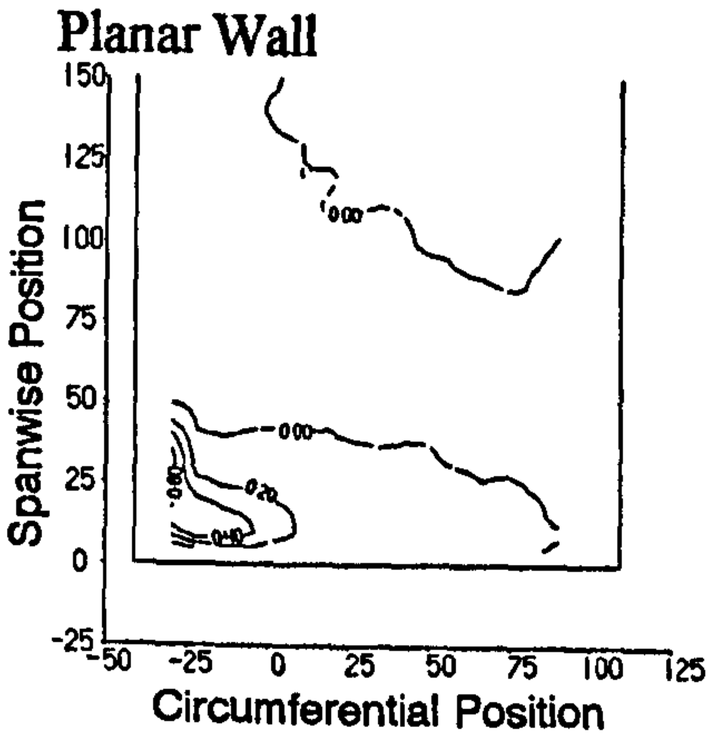

c) Yaw Angle.

Profile 3

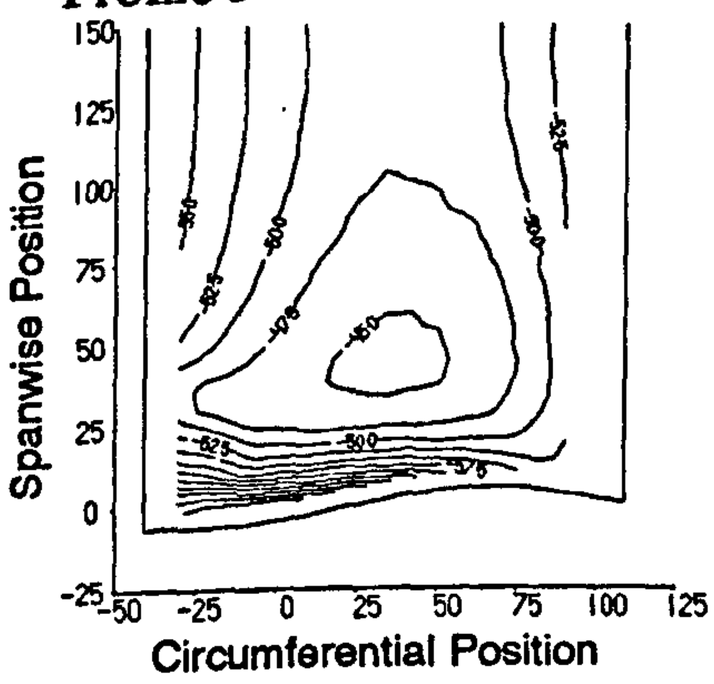

Planar Wall

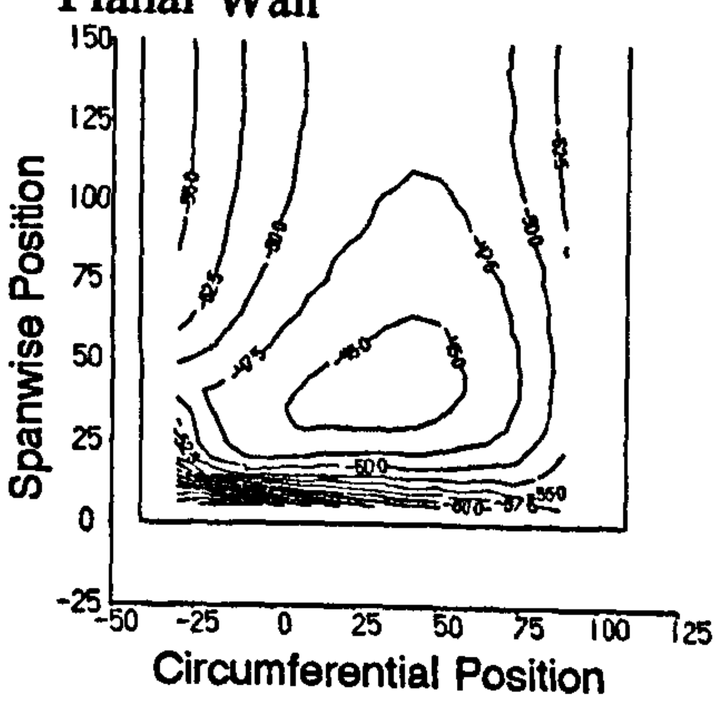

d) Secondary Kinetic Energy Coefficient.

Profile 3

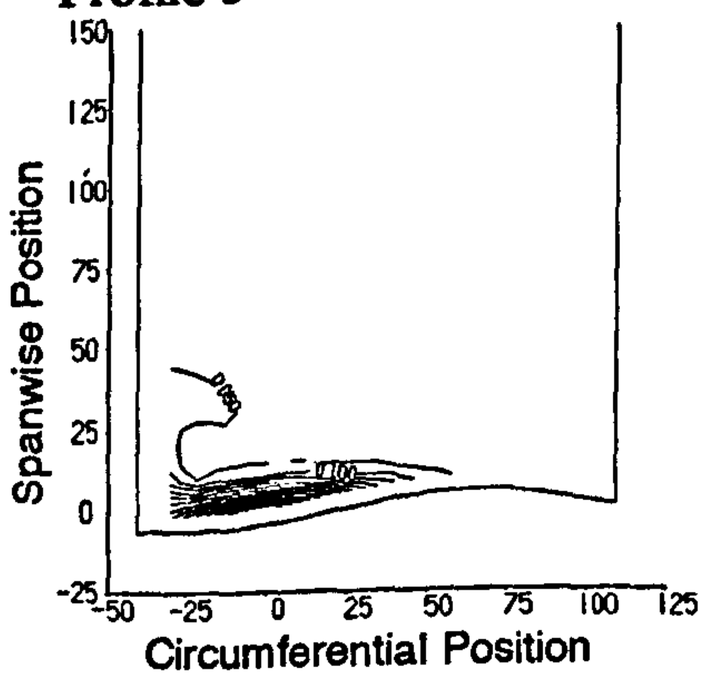

Planar Wall

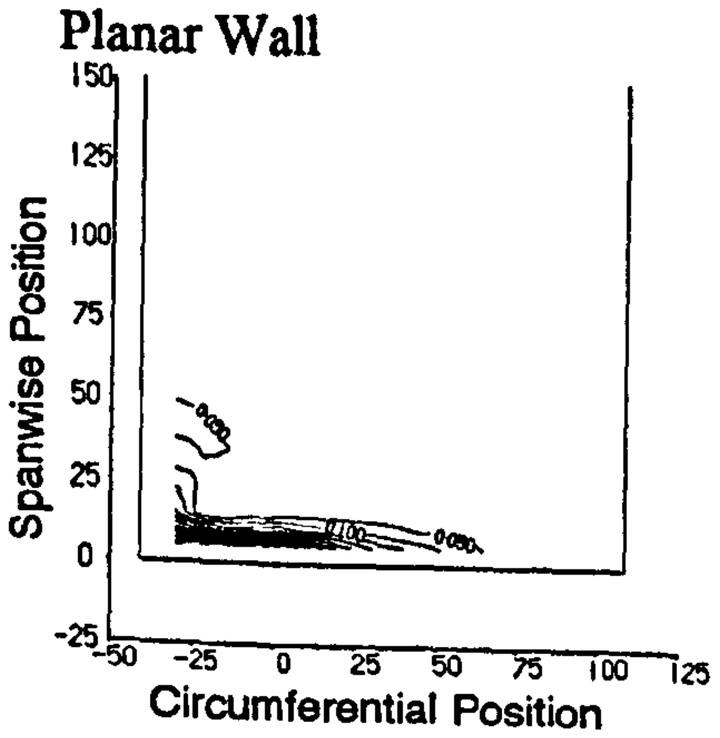

Figure 6.31 Experimental Data at Slot 8.

a) Secondary Velocity Vectors.

Profile 3

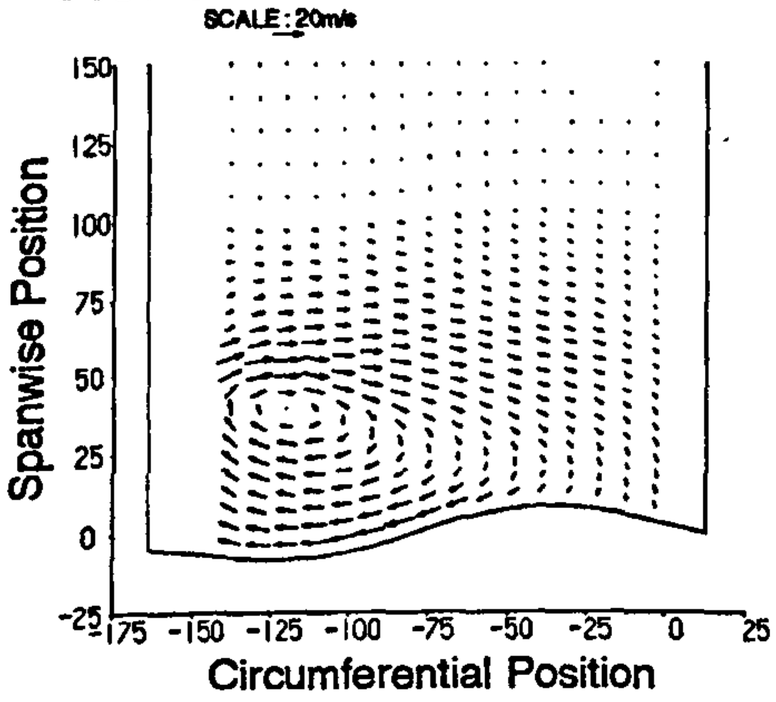

Planar Wall

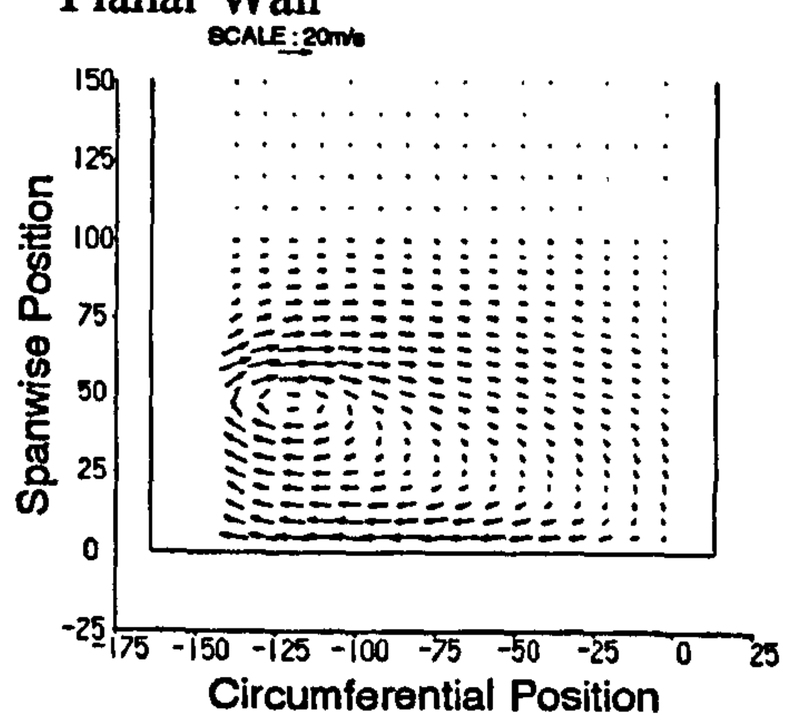

b) Total Pressure Loss Coefficient.

Profile 3

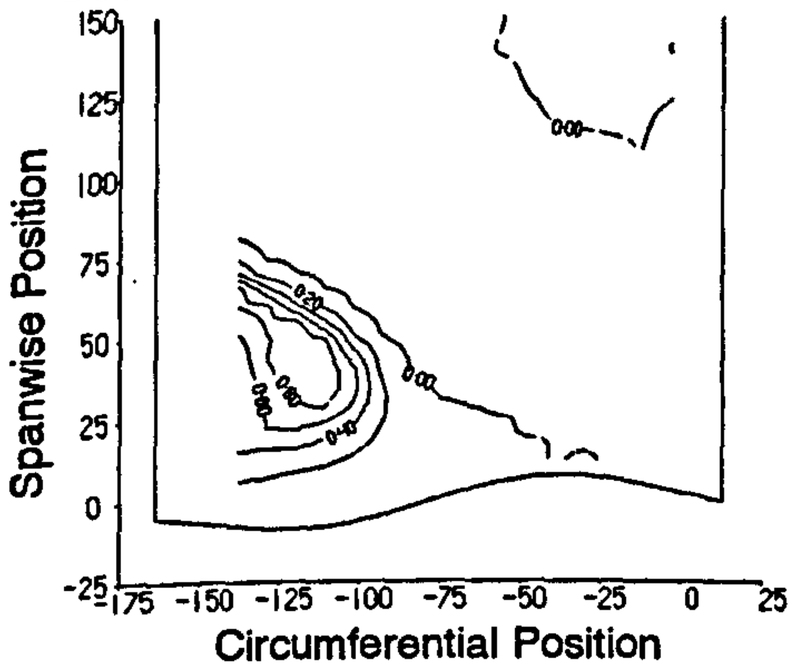

Planar Wall

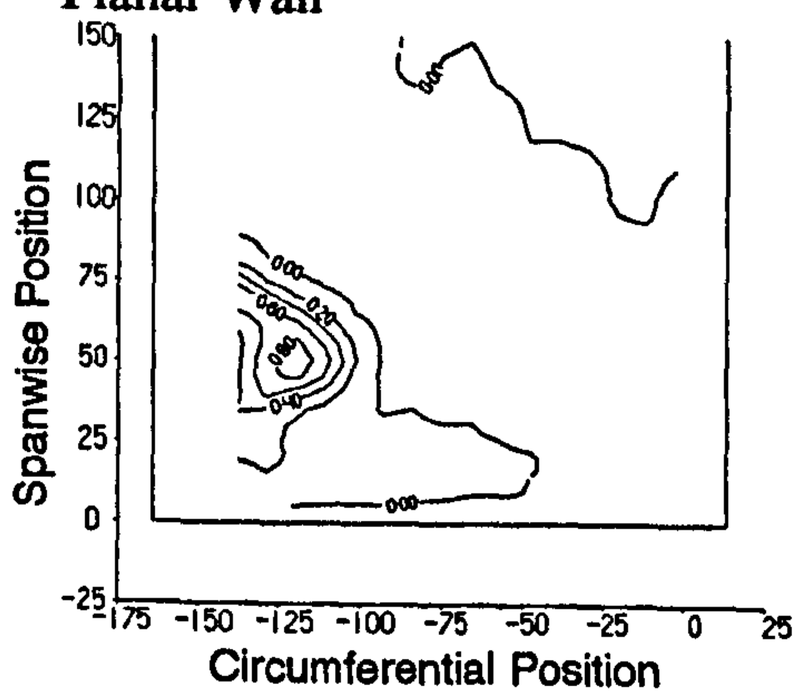

c) Yaw Angle.

Profile 3

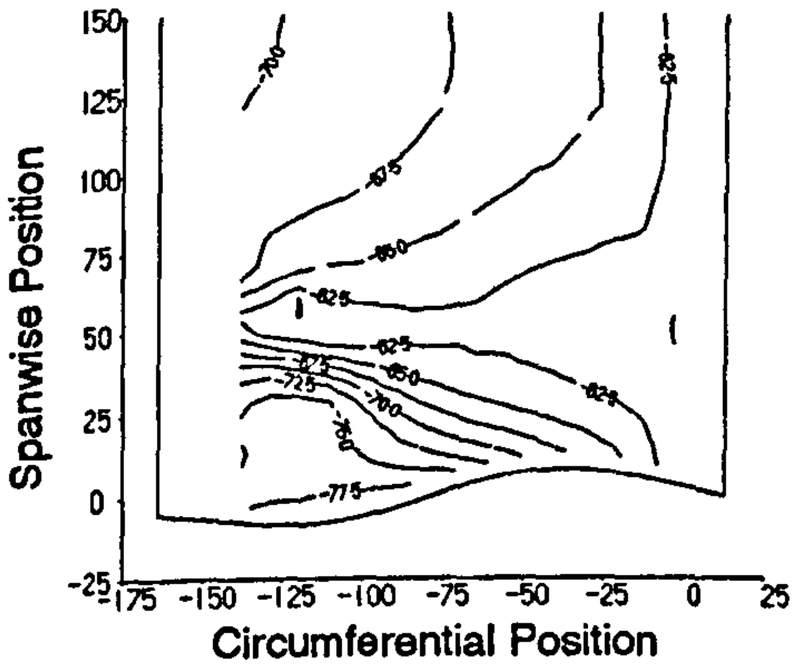

Planar Wall

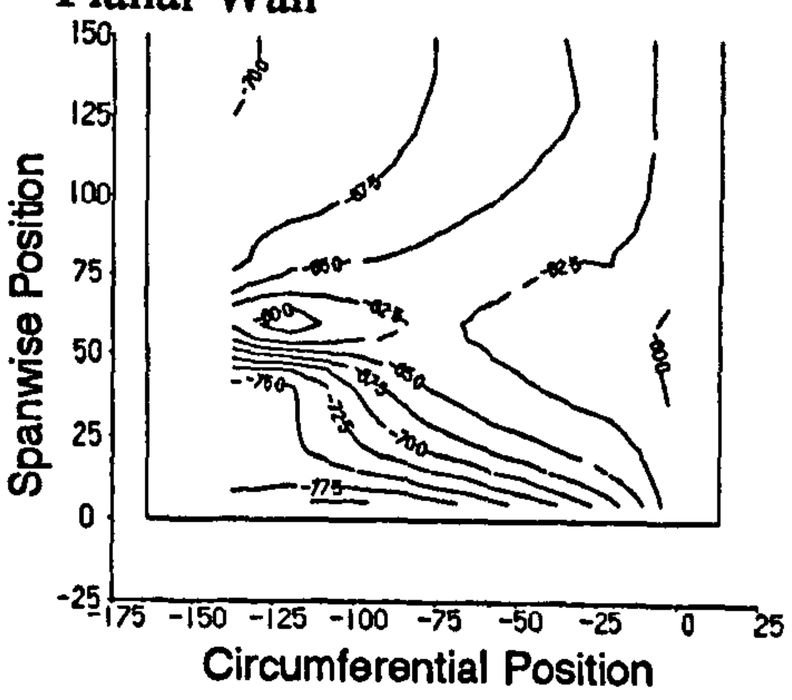

d) Secondary Kinetic Energy Coefficient.

Profile 3

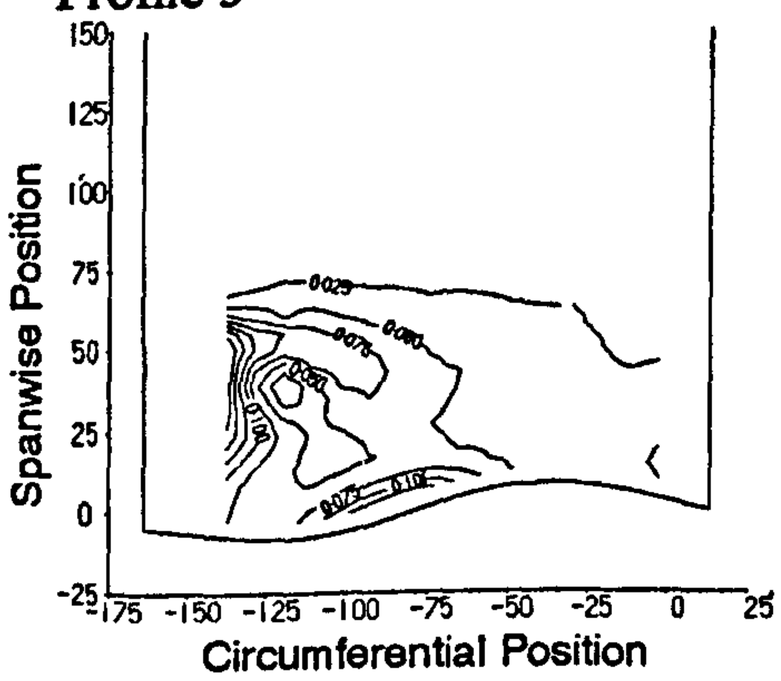

Planar Wall

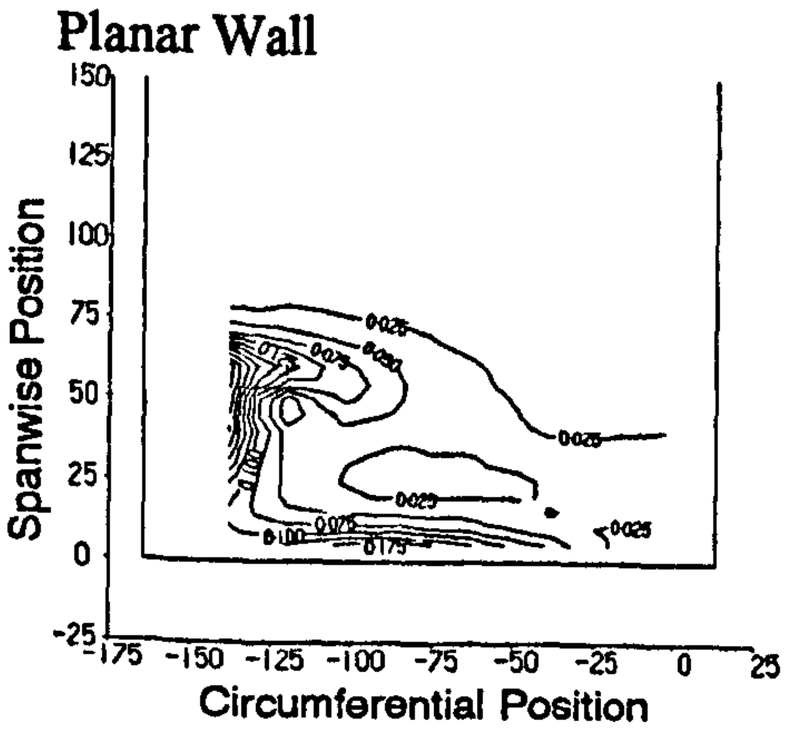

Figure 6.32 Experimental Data at Slot 10.

a) Secondary Velocity Vectors.

Profile 3

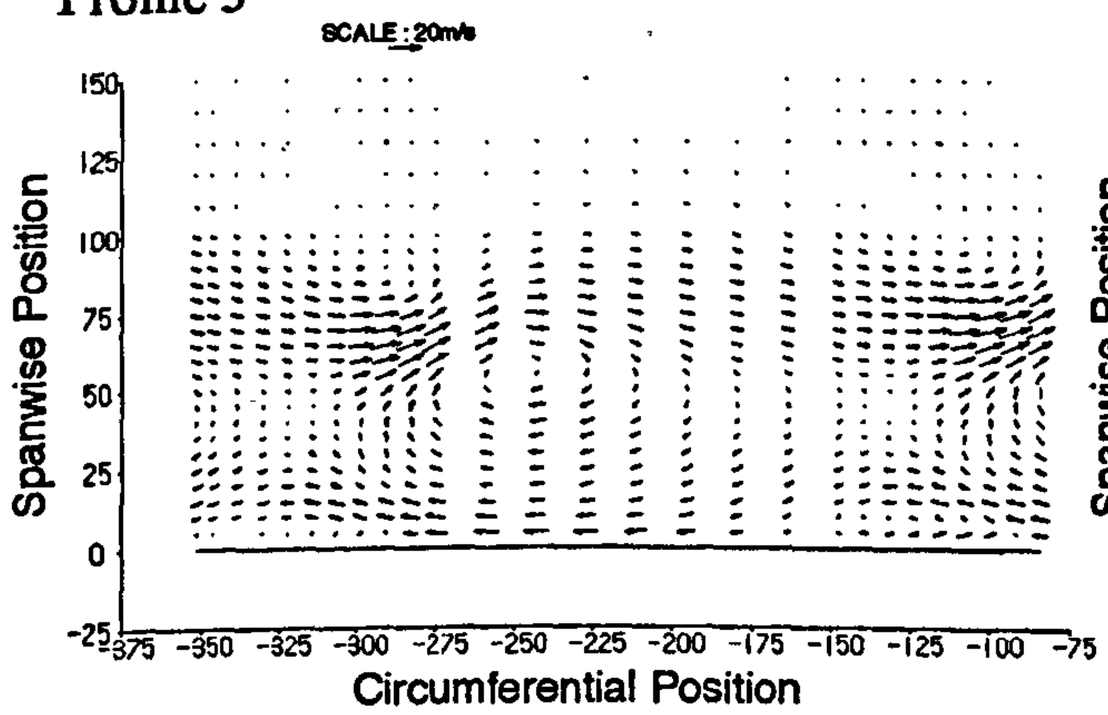

Planar Wall

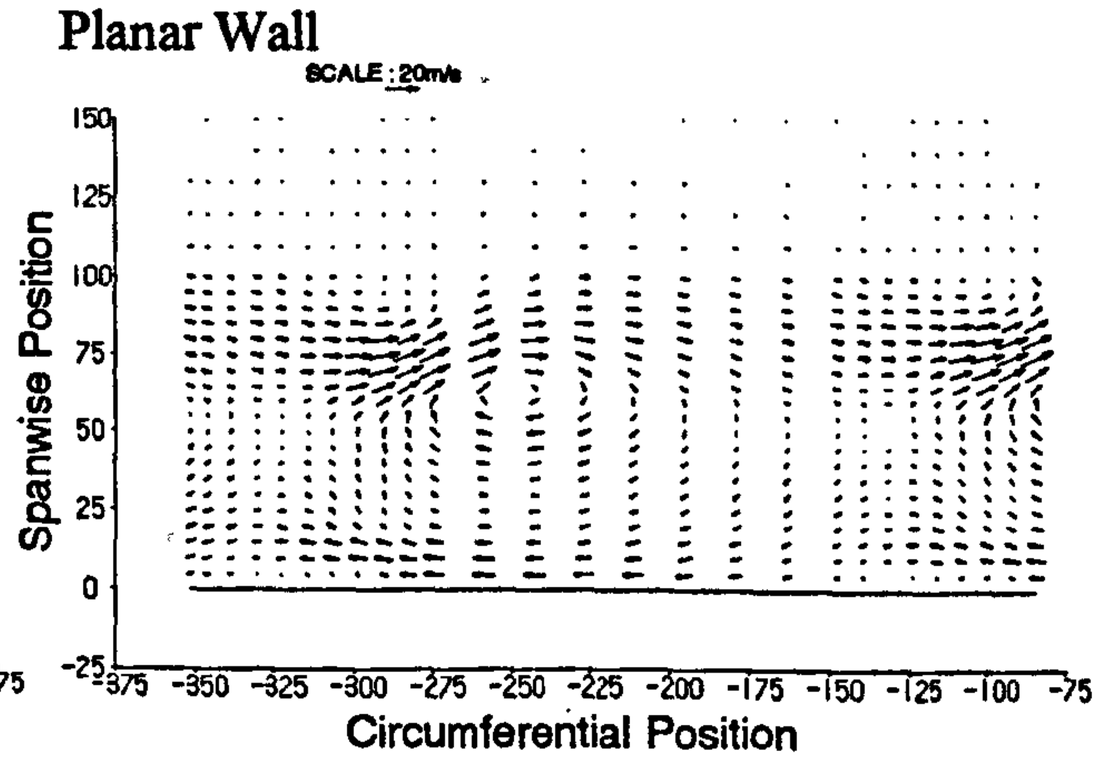

b) Total Pressure Loss Coefficient.

Profile 3

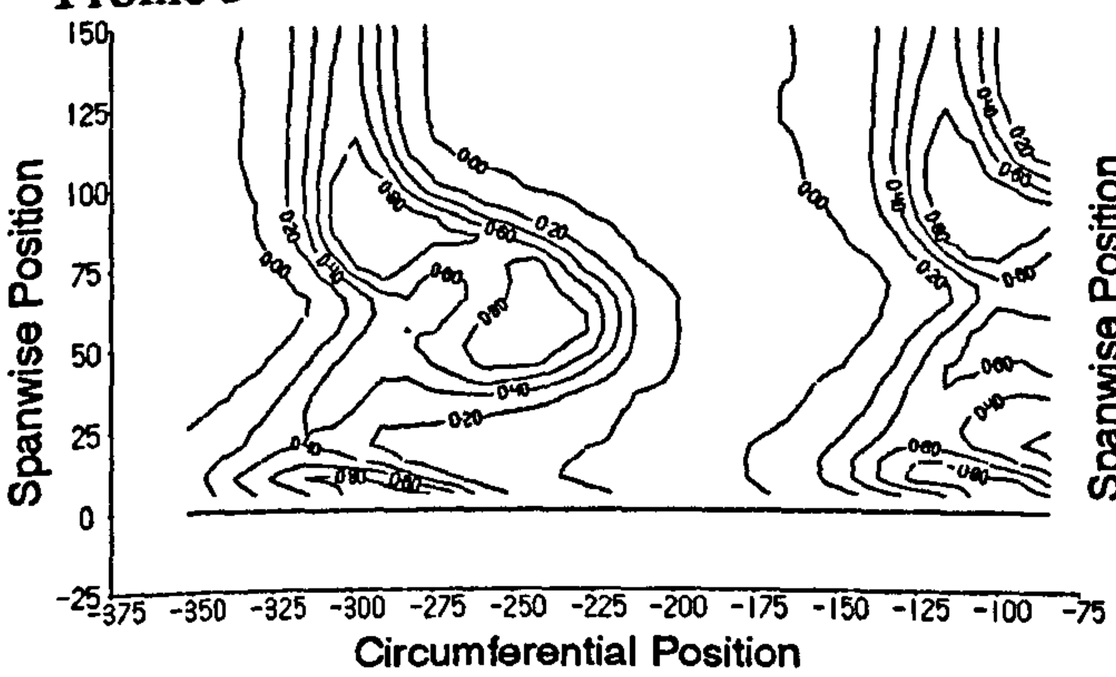

Planar Wall

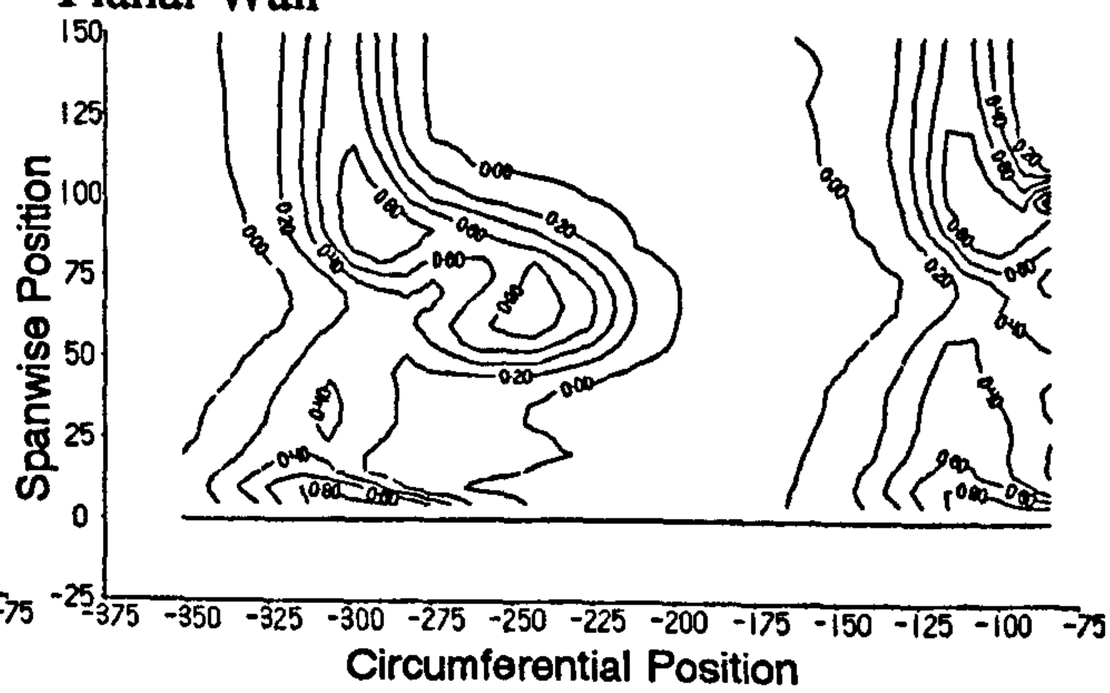

c) Yaw Angle.

Profile 3

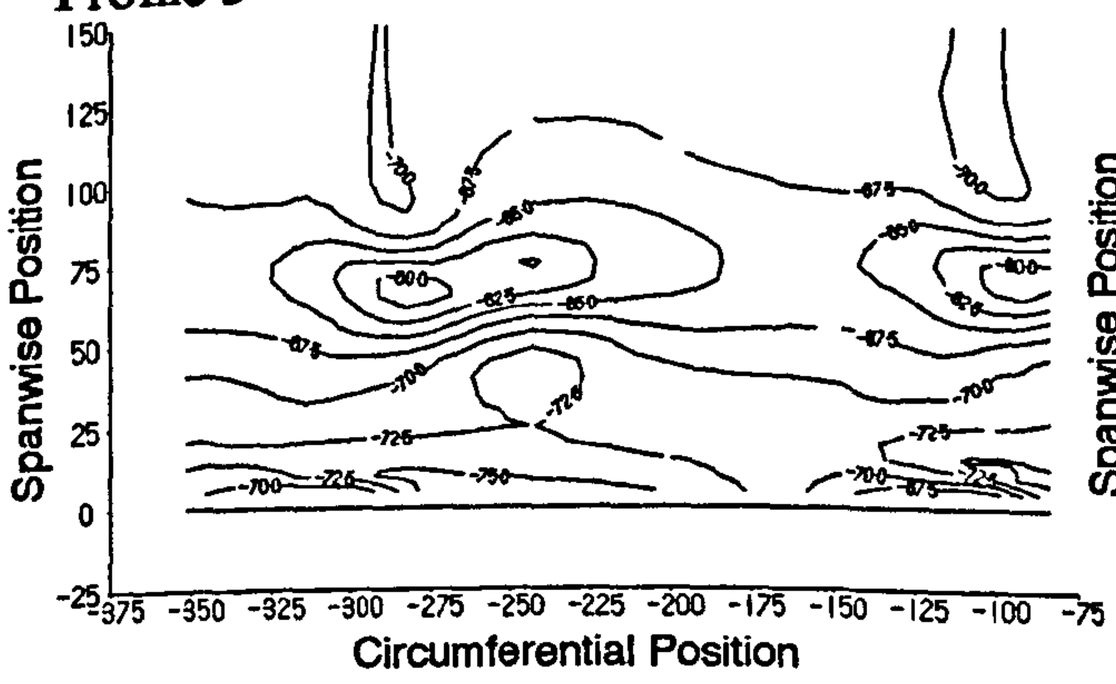

Planar Wall

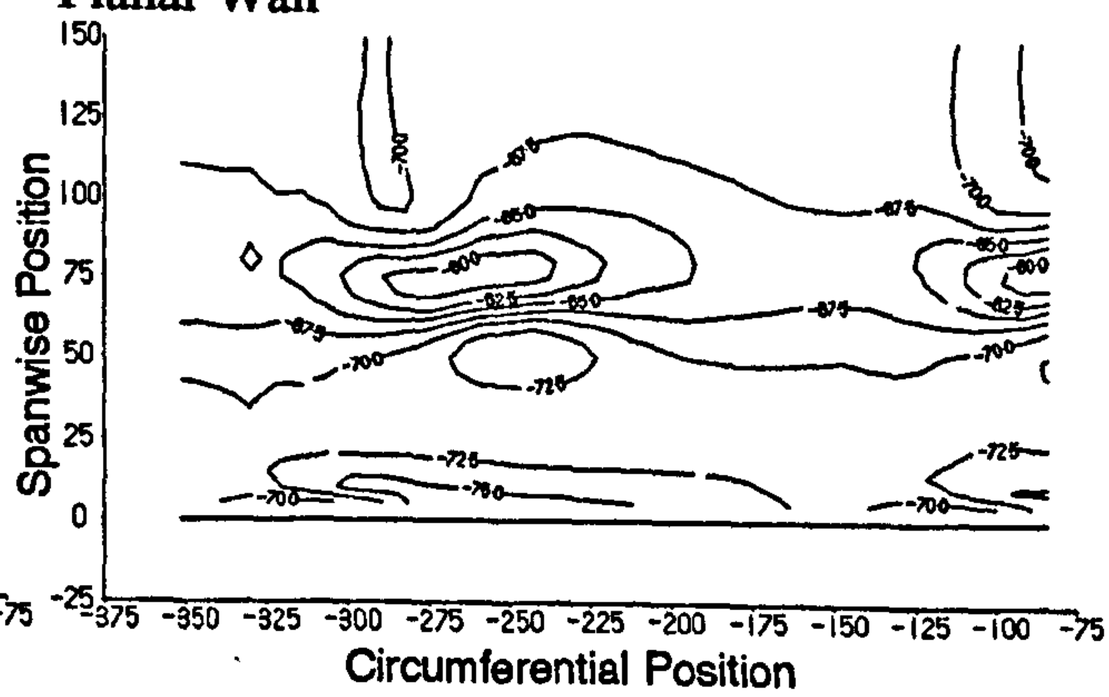

d) Secondary Kinetic Energy Coefficient.

Profile 3

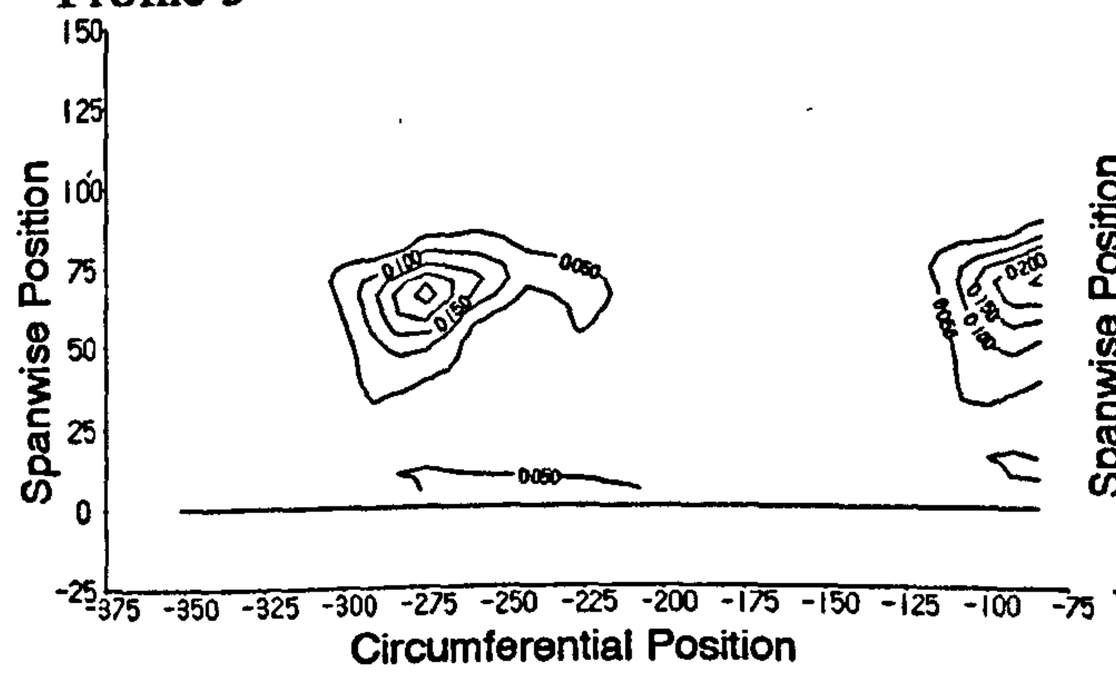

Planar Wall

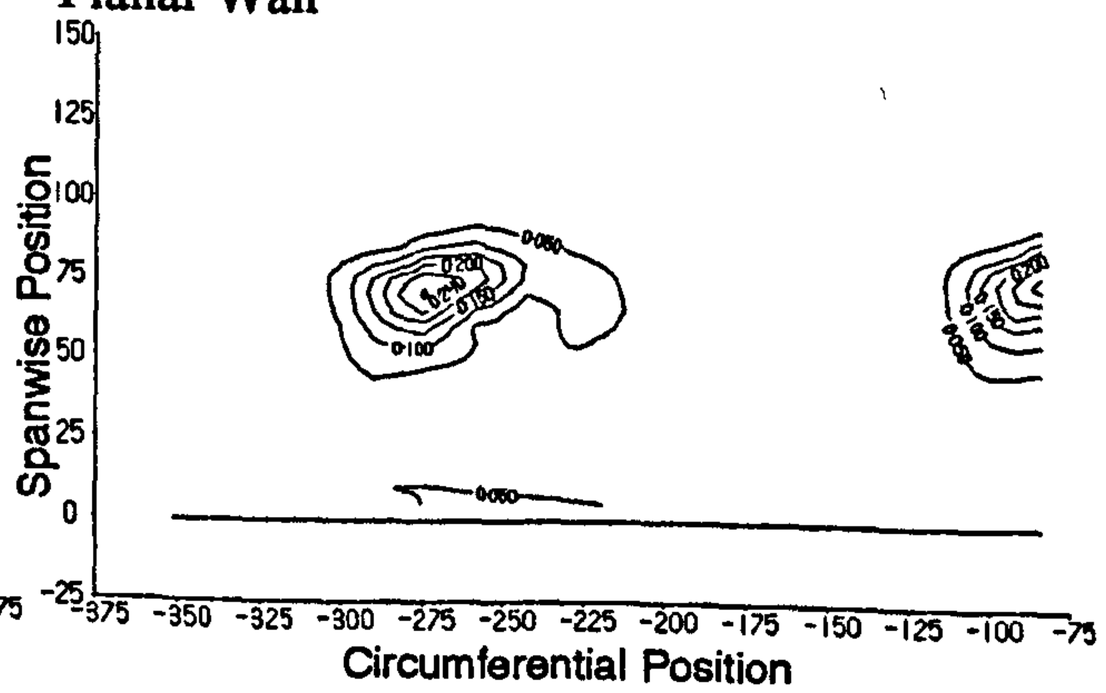

Figure 6.33 End-wall Flow Visualisation.

a) Profile 3

b) Planar Wall

Figure 6.34 Compensated CFD C_{SKE} Throughout the Cascade (Uncompensated and Planar Data Included for Comparison).

a) Slot 1

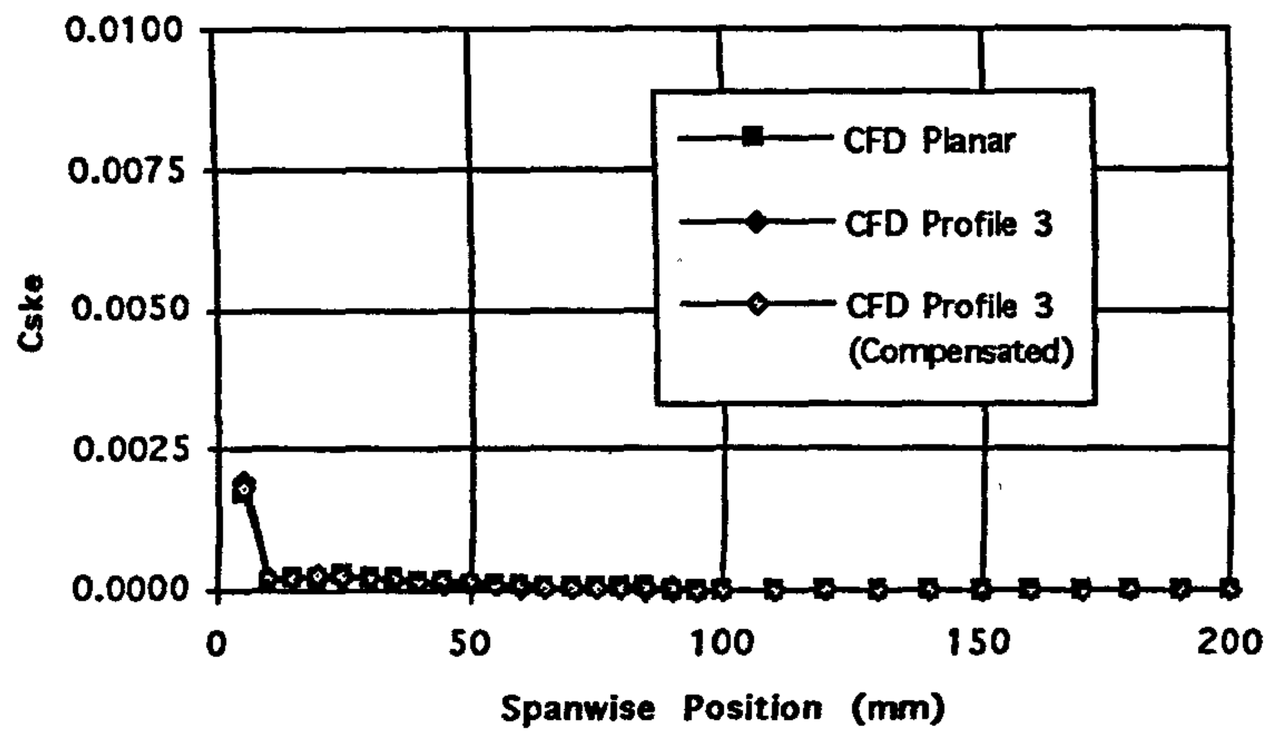

b) Slot 6

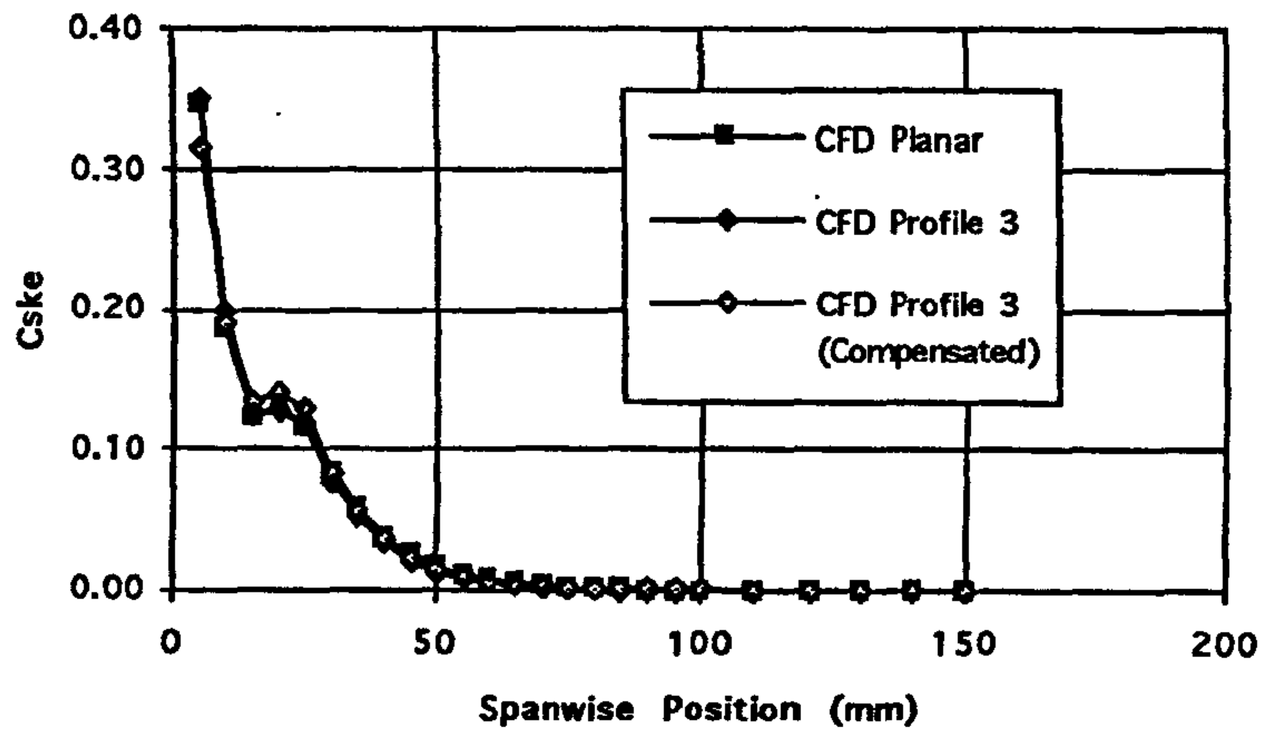

c) Slot 8

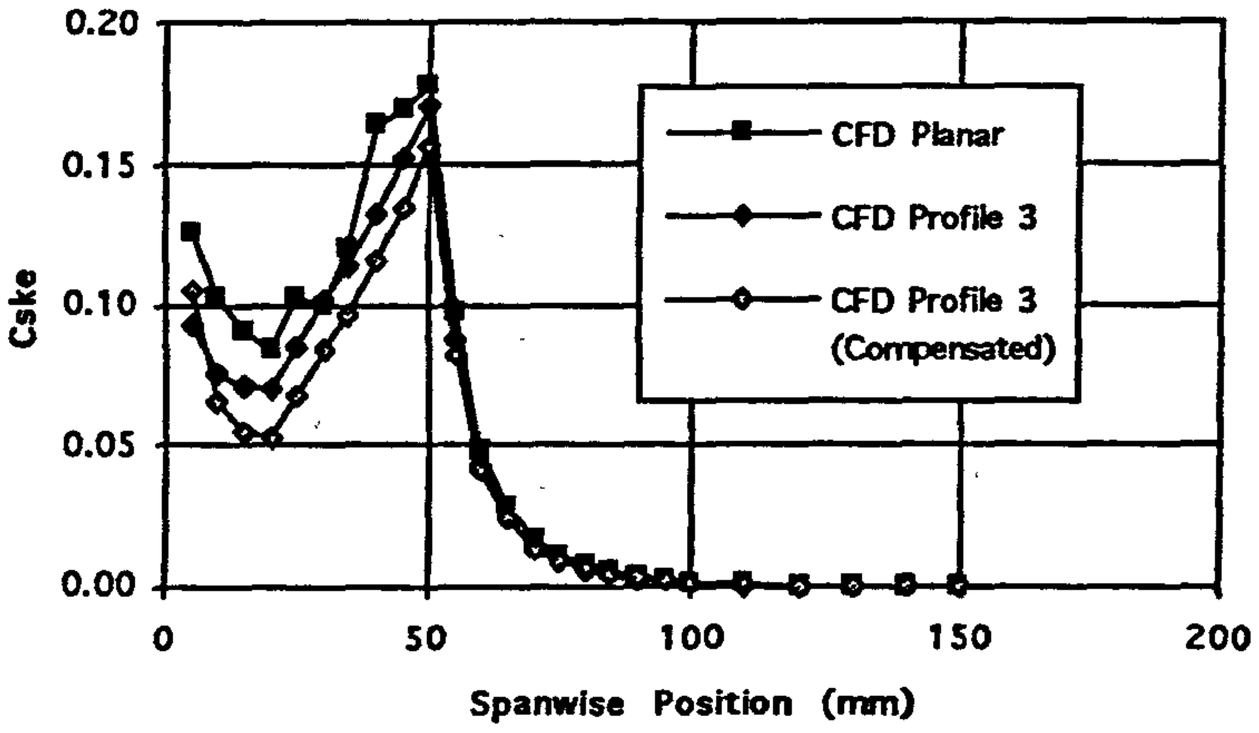

d) Slot 10

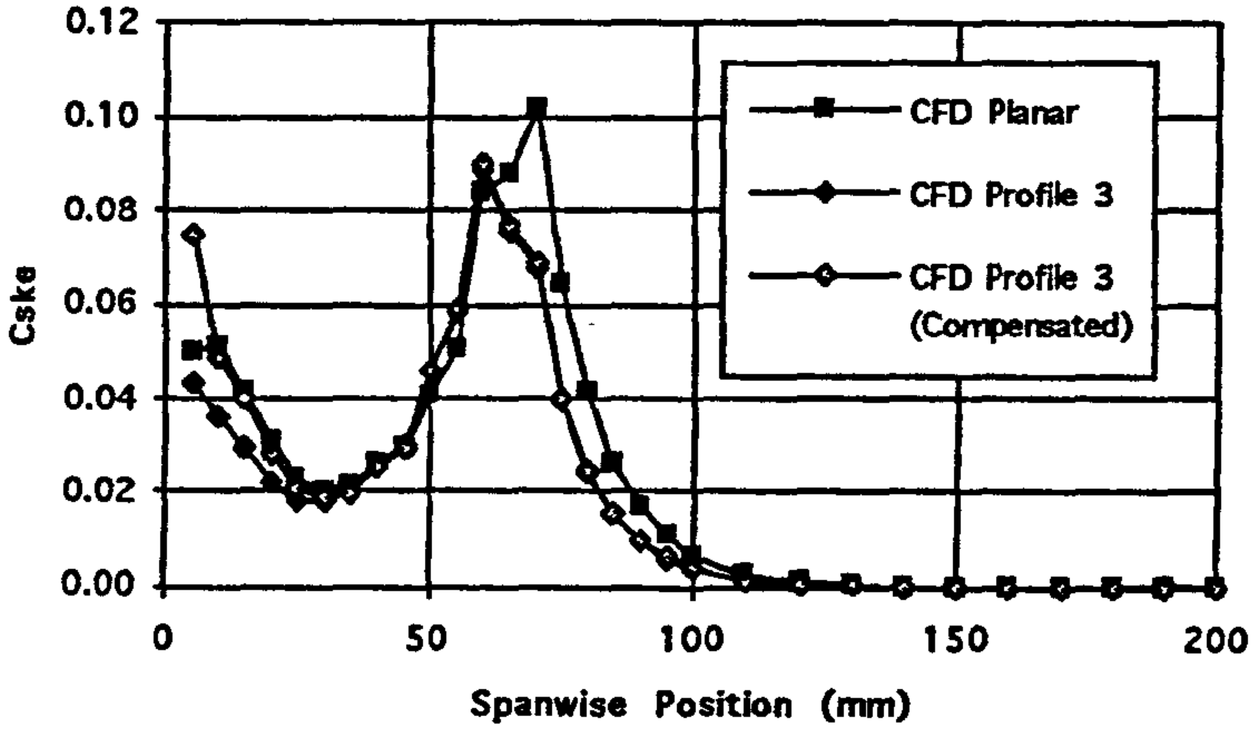

Figure 6.35 Compensated Experimental C_{SKE} Throughout the Cascade (Uncompensated and Planar Data Included for Comparison).

a) Slot 1

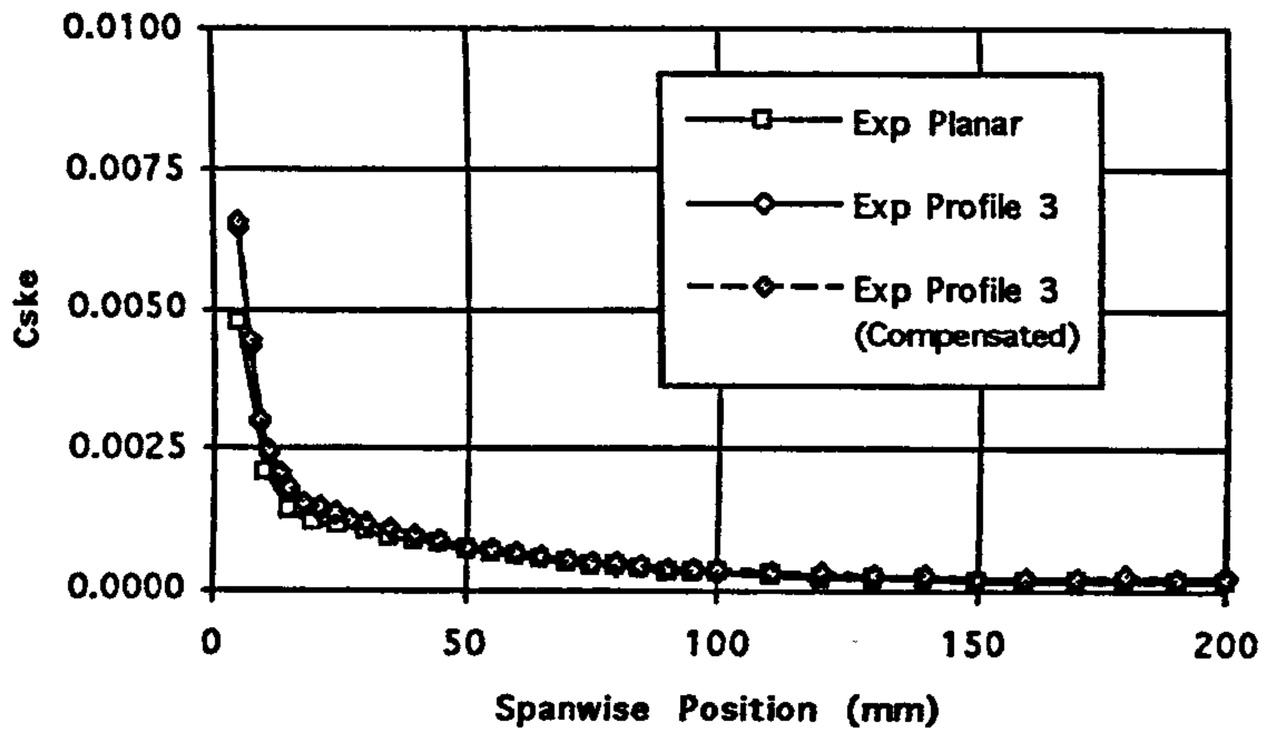

b) Slot 6

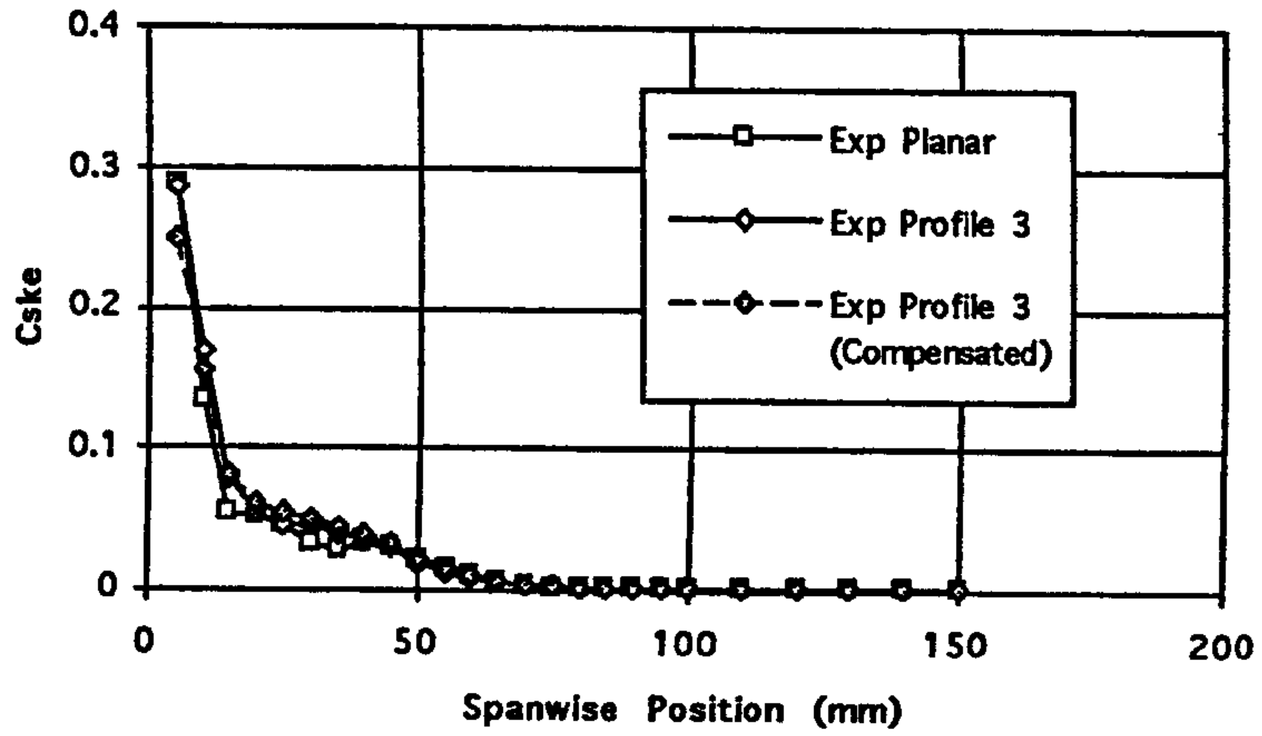

c) Slot 8

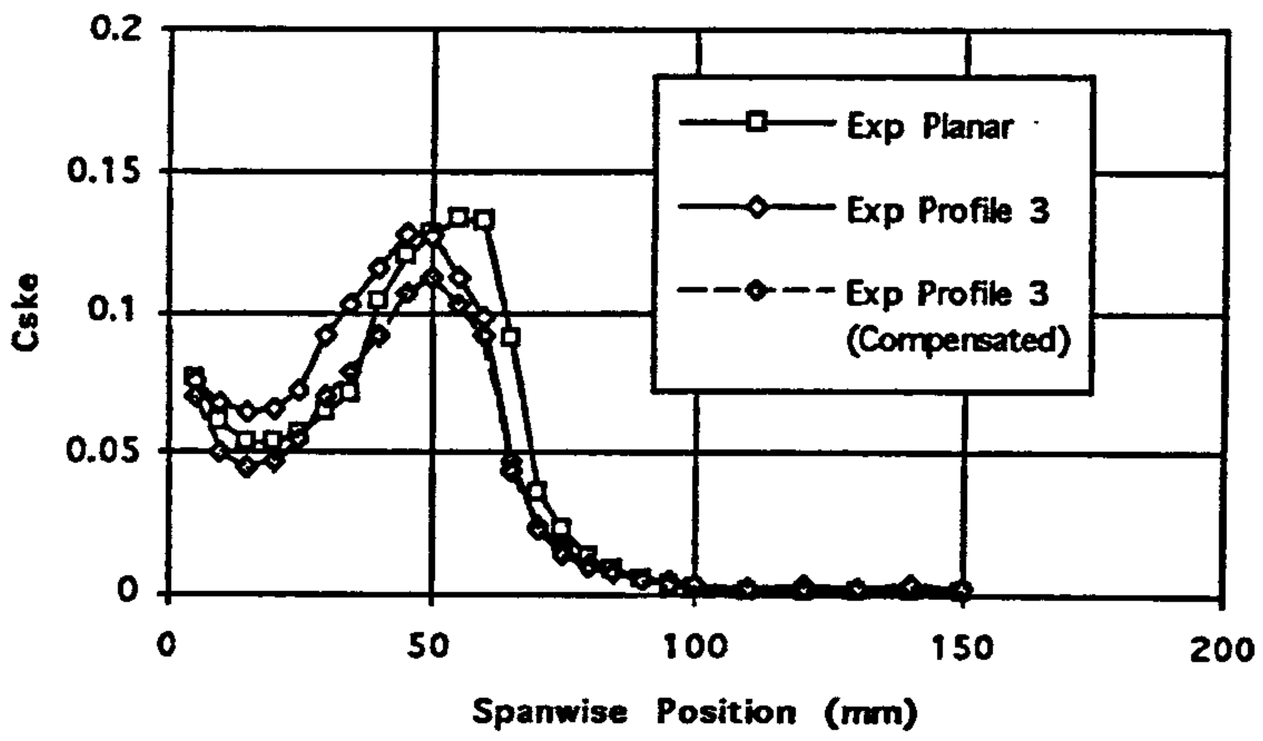

d) Slot 10

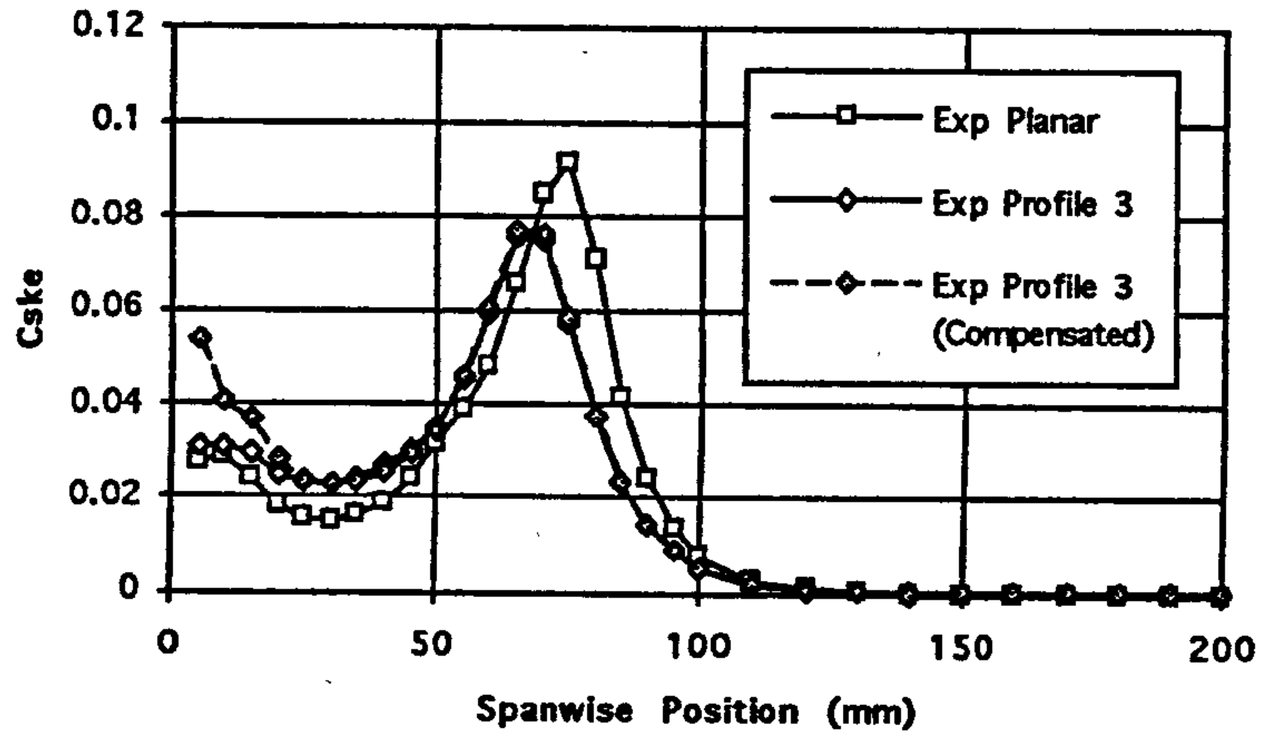

7 End-wall Profiling to Reduce Secondary Loss.

7.1 Introduction.

In this Chapter, the results of the end-wall profile designed using the Rolls-Royce inverse design code, FAITH, are discussed. Before using FAITH to design the end-wall, it was first necessary to decide on an end-wall pressure distribution to aim towards. The philosophy behind the target end-wall pressure distribution is discussed first in section 7.2. Once the design code had generated a geometry, this was used to calculate the flow-field using the version of CFDS in Durham and results of these calculations are presented in Section 7.3. The geometry generated by the FAITH code was manufactured in poly-urethane foam as described in Chapter 4 and pressure tappings were placed in the same locations as with the planar wall and the previous profiled wall (Chapter 5). Due to this profile extending further upstream than the blade leading edge, the window in which the end-wall segments are mounted had to be extended upstream. The wind tunnel was dismantled and the upstream mounting was moved 150mm upstream. A scale drawing of the modified end-wall window is shown in Figure 7.1. The pressure tappings on the new end-wall segments extend upstream by an extra 150mm to capture the end-wall static pressures around the profiled leading edge better. Slot traverses were carried out at slots 1, 6, 8 and 10 and the inlet boundary layer was measured using a 5-hole pressure probe as before. These experimental results are presented in Section 7.4. In Section 7.5, the computational and experimental results presented in Sections 7.3 and 7.4 are discussed in relation to the planar wall results and the conclusions that can be drawn from the results presented in this chapter are stated in Section 7.6.

7.2 Design Philosophy and FAITH Design Code.

Two blade lean calculations were initially carried out in Durham to investigate the effect of compound blade lean on the cascade end-wall pressure gradient. A parabolic variation of the stacking of the blade was introduced in such a way as to produce lean angles of 15 and 30° at the end-wall. The end-wall pressure distributions from this CFD blade lean investigation were examined during discussion of the goals for the design of the new profile with Rolls-Royce in Derby. The end-wall pressure distributions can be seen in Figures 7.2 along with their effect on pitch averaged yaw, C_{SKE} and C_{Po} and pitch (Figures 7.3). The blade lean calculations both show a reduction in the cross passage pressure gradient in the upstream part of the passage. Comparing the pitch averaged loss at Slot 10, both lean angles show a reduction in loss near the end-wall, although this is coupled to an increase in loss at mid-span. The lean appears to result in higher turning at mid-span, along with a reduction of overturning near the end-wall. However, taking into account the increased mid-span yaw angle, an increase in under-turning is seen in both cases. C_{SKE} is also reduced near the end-wall, although this also increases further from the end-wall. From this brief investigation of blade lean, it can be concluded that the lean does reduce the cross passage pressure gradient, and also reduces overturning near the end-wall.

It was decided that the design would concentrate initially on two end-wall pressure distribution modifications, both intended to unload the blades in the region of maximum turning to reduce the driving force of the secondary flow. The first modification suggested was to increase the pressure on the suction surface, and the second to attempt to reduce the pressure on the pressure surface. During the discussion it was agreed that the first of these would probably be easier, and as such, would be tried first.

The FAITH code used for the design is a forward and inverse three-dimensional linear design system used for turbomachinery aerofoils and recently extended for the design of non-axisymmetric end-walls. The approach used by the FAITH code is as follows.

a) Generate a systematic set of perturbations of the end-wall. This is achieved by the combination of two curves in axial and circumferential directions. An axial component of the

profile is defined by a B-spline curve, controlled at up to 6 axial locations. The circumferential component of the end-wall perturbation is defined by the first three terms of a Fourier series given in Equation 7.1.

$$\delta r(\theta) = \frac{1}{C}\sum_{i=1}^{3}\left(a_i \sin\left(\frac{2\pi\theta}{p}\right) + b_i \cos\left(\frac{2\pi\theta}{p}\right)\right) \qquad \text{Equation 7.1}$$

where p is the blade pitch, a_i and b_i are related to the amplitude and phase of each harmonic and C is a normalising coefficient. Since there are six terms in each circumferential curve and six axial locations, 36 control points are available for the end-wall perturbation.

b) Compute the viscous flow-field for all of these perturbations.

c) Construct a linear sensitivity matrix using numerical differentiation

d) Use linear superposition to construct new geometries and flow-fields.

e) Apply inverse design through matrix inversion and quasi-Newton techniques to generate geometries to satisfy chosen design criteria.

Further details of the FAITH code and the design philosophy are given by Harvey et al [1999].

7.3 CFD Results.

7.3.1 End-Wall Height and Cp Values.

Figures 7.4 a and b show the end-wall height and a CFD static pressure coefficient contour plot for the FAITH profile. From Figure 7.4 a, it can be seen that the profiling extends upstream such that by the blade leading edge there is a significant pitchwise height variation. Within the upstream region of the passage a region of concave curvature gives a trough along the suction surface and a region of convex curvature gives a bump along the pressure surface. The maximum height along the pressure surface is between 20 and 25mm and the minimum height along the suction surface is between -10 and -15mm. The end-wall perturbation was limited to 45mm (25% C_{ax}) in the design process.

Comparing Figure 7.4 b with Figure 5.2, it can be seen that the pressure has been increased close to the suction surface and reduced near the pressure surface at the point of maximum turning. Following the -2.0 contour, this leaves the pressure surface near the trailing edge at approximately the same location for both cases, but whereas it attaches to the suction surface at about -150mm in the planar case, this contour contacts the suction surface at about -130mm with the FAITH profile. This decreases the loading and results in a decrease in the driving force of the secondary flow. The profile has however produced an increase in loading later in the blade passage which can be seen from the size of the -3.5 suction peak and the intercepts between the -3.0 contour and suction surface, which would be expected to have a detrimental effect on the generation of secondary flow. The effects of the profiling are greater near the suction surface than near the pressure surface, as would be expected from the higher dynamic pressure along the suction surface.

Figures 7.5 show the CFD Blade C_p plots for the FAITH profile, and the planar data is included for comparison. From these, the decrease in loading on the upstream part of the suction surface can be clearly seen, along with the increase in loading further downstream. These changes in end-wall pressure distribution are similar to those resulting from the blade lean calculations.

7.3.2 Area and Pitch Averaged Results.

Table 7.1 shows area averaged and mid-span total pressure loss and C_{SKE} (calculated using the traditional method) at slots 1,6,8 and 10 along with mixed out loss calculations at Slot 10. Table 7.2 shows the planar wall data for comparison. Table 7.3 shows the net losses (i.e. Slot 10 relative to Slot 1). The calculation of net loss is important for comparison with the experimental results where there is a region of negative loss at inlet which must be accounted for.

Figures 7.6 to 7.9 show mass weighted pitch averaged loss, yaw and pitch angles and secondary kinetic energy coefficient at Slots 1, 6, 8 and 10.

At Slot 1 (Figures 7.6), a small increase in loss is apparent near the end-wall, and this is probably due to the combined effect of the increased yaw angle (probably caused by the profiling extending up-stream) and the slope of the end-wall as it approaches the blade leading edge. It is possible that the ridge seen exiting the upstream boundary of the plot area as 260mm pitch exerts lift on the boundary layer causing it to deflect.

At Slots 6 and 8 (Figures 7.7 and 7.8), a decrease in overturning is seen near the end-wall which indicates a reduction in the secondary flow, although at Slot 6 the decrease in secondary flow is not as significant as at Slots 8 and 10. A decrease is seen in C_{SKE} even though (as mentioned above) no compensation has been carried out, demonstrating the reduction in overturning with the profiled end-wall.

At Slot 10 (Figures 7.9), the CFD predicts a slight (almost negligible) increase in overall loss, and movement of the passage vortex towards the end-wall. A large reduction in secondary kinetic energy due to the reduction in the passage vortex is predicted, although near the end-wall an increase in loss, due to a large counter-vortex described later, is predicted by the CFD. This peak in C_{Po}, and the associated counter-vortex, shown by the FAITH profile at 10mm height in Figure 7.9 a (also seen in Figure 7.9 d) is thought to be due to an enhanced counter vortex caused by the sharp re-entrant corner between the end-wall / suction surface corner which generates the counter-vortex. It is thought that by filling this corner the counter-vortex could be reduced,

although the counter-vortex contributes to the reduction in over-turning which is discussed in more detail in Section 7.3.3.

From the area averaged data (Tables 7.1 to 7.3), it would seem that the loss is increased by the profile. However, the significant (49% at Slot 10) reductions in C_{SKE} throughout the cascade show that the profile is reducing the secondary flow, if not the loss. The 6% reduction in mixed out secondary loss at Slot 10 demonstrates this point.

Table 7.1 Area Averaged Values for the FAITH Profiled Wall CFD.

	C_{Po}			Mixed out Loss			C_{SKE}
	Full	Mid-Span	Secondary	Full	Mid-Span	Secondary	
Slot 1	0.018	0.000	0.019	0.022	0.000	0.022	0.0014
Slot 6	0.037	-0.001	0.038	-	-	-	0.0144
Slot 8	0.057	-0.009	0.066	-	-	-	0.0181
Slot 10	0.213	0.151	0.062	0.237	0.161	0.077	0.0108

Table 7.2 Area Averaged Values for the Planar Wall CFD.

	C_{Po}			Mixed out			C_{SKE}
	Full	Mid-Span	Secondary	Full	Mid-Span	Secondary	
Slot 1	0.015	0.000	0.016	0.016	0.000	0.016	0.0001
Slot 6	0.039	-0.002	0.041	-	-	-	0.0227
Slot 8	0.048	-0.010	0.059	-	-	-	0.0359
Slot 10	0.211	0.153	0.058	0.244	0.163	0.081	0.0218

Table 7.3 Net Area Averaged C_{Po} at Slot 10 for Planar and FAITH Profiled Wall CFD.

	C_{Po}			Mixed out		
	Full	Mid-Span	Secondary	Full	Mid-Span	Secondary
FAITH	0.197	0.151	0.046	0.221	0.161	0.060
Planar	0.195	0.153	0.042	0.228	0.163	0.065

7.3.3 Contour Maps and Secondary Velocity Vectors.

Figures 7.10 to 7.13 show Secondary Vectors and contour maps of C_{Po}, Yaw Angle and uncompensated C_{SKE} at Slots 1, 6, 8 and 10. As with the pitch averaged results, the slight increase in secondary flow at Slot 1, and the increasing reduction in secondary flow through the rest of the cascade is seen in these results.

At Slot 6 there is a significant decrease in the secondary kinetic energy, which contrasts with the apparent increase at Slot 1. The end-wall appears to be almost flat at this point, and with reference to Figure 7.4 a this can also be seen. It is believed that the large concentration of C_{SKE} contours near the end-wall in Figure 7.11 d are caused by the definition of secondary flow. As mentioned in Chapter 6, when the end-wall is profiled, flow near the wall may be parallel to it but still have a radial component. This is treated as secondary flow, but is an ideal flow effect. Unlike in the planar wall case where most of the boundary layer has been convected to the suction surface by slot 6, the profiling has reduced the cross flow, and thus reduced the concentration of loss near the suction surface corner.

At Slot 8 (Figures 7.12), it appears that the secondary flow is made up of two distinct vortices, and it is possible that these are the horseshoe vortex from the pressure surface and a secondary vortex caused by the increased cross passage pressure gradient in the latter part of the cascade, although these separate vortices are not seen at Slot 6. The loss within the passage vortex is also reduced by the profiling.

A large counter vortex is also seen at Slot 10 (Figures 7.13 a). However the secondary flow due to the passage vortex is significantly reduced. In Figure 7.13 b the reduction in the loss peak due to the reduction in the passage vortex can clearly be seen, along with the increased loss peak due to the counter-vortex. The reduction in passage vortex and the counter-vortex can also be seen in the C_{SKE} contours in Figure 7.13 d.

7.3.4 Compensated C_{SKE}.

As mentioned before in Section 6.5, the high C_{SKE} near the end-wall in the profiled case is probably due to the slope of the end-wall and inviscid flow effects. The same compensation has been carried out for this case as in Chapter 6. Pitch averaged compensated C_{SKE} curves are shown for all four slots in Figure 7.14, along with planar data and uncompensated data. In the legend here, the "i" denotes the inviscid flow compensated data. The compensated C_{SKE} near the end-wall is lower than the uncompensated data at Slot 6, except for the data point nearest the end-wall. At Slot 8, the compensated data near the end-wall is actually closer to the planar data, i.e. higher than the uncompensated data, and slightly lower near the vortex core. At Slot 10 the compensated and uncompensated C_{SKE} curves are almost identical. The increase caused by the compensation at Slot 8 is possibly due to an effective reversed passage vortex in the inviscid CFD calculation, caused by the blade loading being reduced by the profiling in combination with the lack of a boundary layer velocity deficit as discussed in Section 6.5.1.

7.4 Experimental Results.

7.4.1 End-Wall Cp Values.

Referring back to Figures 7.4 b and 5.2 b, the CFD showed a slight reduction in the cross passage pressure gradient in the upstream half of the passage and an increase in the latter half of the passage. This is also seen in the experimental pressure maps (Figures 7.15) although the effects in the upstream half of the passage are greater than predicted by the CFD. On the suction surface the -1.0 contour meets the blade surface at approximately -140mm in the profiled case, whereas in the planar case, the -1.0 contour exits the upstream boundary of the plot area before returning to meet the suction surface near the leading edge. Also, the -0.5 contour meets the suction surface in the profiled case, whereas for the planar wall it is not seen to reattach. As in the CFD contour maps, the effects of the profiling are greater near the suction surface than near the pressure surface.

Overall, the CFD predictions of the static pressure field at the end-wall are quite good, although the effects of profiling are significantly greater in reality than predicted. It is not certain why the predictions should under-predict changes in static pressures for the FAITH profile in the light of the Profile 3 results.

7.4.2 Area and Pitch Averaged Results.

Area averaged total pressure loss coefficient and secondary kinetic energy coefficients at Slots 1, 6, 8 and 10 are presented in Tables 7.4 and 7.5 along with net loss at Slot 10 (Slot 10 - Slot 1) in Table 7.6. The nearly zero inlet loss in Tables 7.4 and 7.5 is due to the hump on the inlet profile and the new reference probe position giving negative loss. This is shown by the inlet boundary layer total pressure profile in Figure 7.16. At Slots 6 and 8 the experimental results have been adjusted to cover 200mm span in Table 7.4 and 7.5. Figures 7.17 to 7.20 show pitch averaged C_{Po}, yaw angle, pitch angle and C_{SKE} at slots 1, 6, 8 and 10 for both the planar and profiled walls.

Up to Slot 8, the FAITH profile shows an increase in loss, which could be due to adverse effects of the profiling before the benefits of profiling on the generation of secondary flow take effect. The net losses appear to show some variation at mid-span, although this is within the expected experimental accuracy discussed in Chapter 4. The yaw angles at slots 1 and 6 (Figures 7.17 b and 7.18 b) display some variation between the CFD and experimental data. This is around 1.5 to 2°, compared with the experimental accuracy outlined in Chapter 4 of 0.67° for yaw angle. It is possible that the adjustment of yaw angle to correct for slack in the dovetail slide is at fault. Due to measurements not being made within the boundary layers, the difference between the CFD mid-span mass flow rate when integrated over the experimental grid and the CFD mid-span inlet mass flow is used to approximate the mass flow rate across the experimental range. Whilst this gives an indication of the flow, it is not ideal. However, the yaw angles appear closer with this approximation than without. It is also possible that the pitch wise velocity distribution in the CFD calculations is incorrect, giving an error in the CFD yaw angle.

Table 7.4 Area Averaged Experimental Values for the FAITH Profiled Wall.

	C_{Po}			Mixed out			C_{SKE}
	Full	Mid-Span	Secondary	Full	Mid-Span	Secondary	
Slot 1	-0.016	0.006	-0.022	-0.017	0.003	-0.020	0.0014
Slot 6	0.015	0.002	0.013	-	-	-	0.0130
Slot 8	0.027	-0.003	0.030	-	-	-	0.0186
Slot 10	0.118	0.084	0.033	0.141	0.097	0.044	0.0100

Table 7.5 Area Averaged Experimental Values for the Planar Wall.

	C_{Po}			Mixed out			C_{SKE}
	Full	Mid-Span	Secondary	Full	Mid-Span	Secondary	
Slot 1	-0.002	0.017	-0.019	-0.002	0.016	-0.018	0.0005
Slot 6	0.022	0.008	0.013	-	-	-	0.0145
Slot 8	0.020	-0.001	0.022	-	-	-	0.0323
Slot 10	0.136	0.076	0.060	0.157	0.079	0.079	0.0194

Table 7.6 Net Area Averaged Experimental C_{Po} for the Planar and FAITH Profiled Walls at Slot 10.

	C_{Po}			Mixed out		
	Full	Mid-Span	Secondary	Full	Mid-Span	Secondary
FAITH	0.138	0.075	0.063	0.161	0.088	0.073
Planar	0.148	0.068	0.080	0.169	0.071	0.098

At Slot 1 (Figures 7.17), a small increase in C_{SKE} is evident near the end-wall, and this is probably due to the combined effect of the increased yaw angle and the slope of the end-wall as it approaches the blade leading edge. The region of negative loss due to the upstream total pressure non-uniformity is still seen with the profiled wall although it appears to be slightly more negative.

At Slots 6 and 8 (Figures 7.18 and 7.19), a decrease in overturning is seen near the end-wall which indicates a reduction in the secondary flow, although at Slot 6 the decrease in secondary flow is not as significant as at Slots 8 and 10. Figure 7.21 shows the growth of area averaged secondary kinetic energy through the cascade and this reinforces this point. The experimental data and CFD predictions agree very well when comparing the yaw angles, although the effects on profiling seem greater in the experimental results than predicted. As discussed above, the large offset in mid-span yaw angle between the CFD and experimental results is possibly due to errors in the CFD data, and the mass flow compensation of the experimental data, where the high velocity (high flow rate) region near the suction surface boundary layer, where the flow angles are greater, is incorrectly predicted by the CFD.

At Slot 10 (Figures 7.20), the CFD predictions generally agree well with the experimental results, and the trends in the loss were predicted. Where the CFD predicted a reduction in loss, and movement of the passage vortex towards the end-wall, the experimental results follow the same trend (Figures 7.20 a and b). Also, the predicted increase in the loss near the end-wall due to the counter-vortex is seen in the experimental data although to a lesser extent than in the CFD. The large reduction in secondary kinetic energy due to the reduction in the passage vortex is predicted very well, although near the end-wall the CFD predictions are not very good. This is

probably due to poor resolution of the size of the counter-vortex and its interaction with the passage vortex, possibly due to insufficient grid resolution or shortcomings in the turbulence model. It could also be that the experimental results are inaccurate so close to the wall as the probe is 3mm in diameter and the closest data point is only 5mm from the wall. The reduction in under-turning (Figures 7.20 b) due to the secondary flow has been predicted well, although the over-turning has not been predicted so well.

Generally, the flow has been predicted very well by the CFD, although the absolute levels of loss are not well predicted. The trends in loss from the pitch averaged data are however predicted quite well.

7.4.3 Contour Maps and Secondary Velocity Vectors.

Figures 7.22 to 7.25 show Secondary Vectors and contour maps of C_{Po}, Yaw Angle and uncompensated C_{SKE} at Slots 1, 6, 8 and 10. As with the pitch averaged results and the CFD, the slight increase in secondary flow at Slot 1, and the increasing reduction in secondary flow through the rest of the cascade is seen in these results.

At Slot 6 (Figure 7.23) again, there is a significant decrease in the secondary kinetic energy, which contrasts with the apparent increase at Slot 1. It is believed that the large concentration of C_{SKE} contours near the end-wall in Figure 7.23 d are caused by the definition of secondary flow. As mentioned in Section 6.5, when the end-wall is profiled, flow near the wall may be parallel to it but still have a radial component. This parallel component is treated as secondary flow, which is not the case.

At Slot 8 (Figures 7.24), the two distinct vortices predicted by the CFD within the secondary flow can clearly be seen. The significant reduction in the C_{SKE} peak, due to the passage vortex, predicted by the CFD is also seen.

The large counter vortex predicted at Slot 10 (Figures 7.13 a) is evident in the experimental results (Figure 7.25), although it appears to be smaller than predicted. This over-

prediction of the counter-vortex is also shown by the C_{SKE} contours. The reduction in secondary flow due to the passage vortex is predicted well, including the splitting of the passage vortex into two separate vortices. In Figure 7.25 b the loss reduction due to the reduction in the passage vortex can clearly be seen, along with the loss peak due to the counter-vortex although the loss peak due to the counter vortex is lower then predicted, mirroring the secondary vectors. Comparing with the CFD case where the movement of the passage vortex is only slight, the movement of the passage vortex towards the end-wall is much greater in the experimental data.

7.4.4 Compensated C_{SKE}.

Figures 7.26 show compensated C_{SKE} at Slots 1, 6, 8 and 10 (Compensated data denoted by "i"). At Slot 1, the compensation of the C_{SKE} shows a very similar curve to the planar data. At Slot 6, the compensation reduces C_{SKE} in comparison with both the planar and profiled results. At Slot 8, the compensation shows an increase in C_{SKE} towards the planar data, possibly due to the effects of the profiling on the inviscid flow as mentioned earlier (Section 7.3.4) where the increase in inviscid secondary flow complements the decrease in secondary flow seen in the experimental data. At Slot 10, the same trend is seen as at Slot 8, although to a lesser extent.

7.4.5 Flow Visualisation.

Flow visualisation was carried out using the same procedure as outlined in Chapter 6, and the results of this can be seen in Figure 7.27. At about 50% axial chord, the streak lines are displaced downstream on the profiled wall due to the lower cross-flow velocities. In the downstream part of the cascade, the cross-flow seems to be similar for both profiled and planar end-walls, and evidence of the counter-vortex in the end-wall suction surface corner is visible.

7.5 Conclusions.

The FAITH profile has been very successful in reducing the secondary flow and secondary losses. The experimental net secondary loss through the cascade has been reduced by over 21%, and the net mixed out secondary loss has been reduced by almost 26%. Although the CFD results gave a slight increase in loss, the trends displayed by the pitch averaged loss and loss contours are predicted correctly. The experimental secondary kinetic energy at Slot 10 has been reduced by 48%, and the CFD predicted this very well, giving a 49% reduction. The velocity vectors also show that the CFD predictions of flow features are very accurate. The ability of the CFD to predict secondary flow trends better than loss would be expected from the turbulence model, and the effect of the laminar flow regions within the cascade. CFD design based on secondary flow rather than secondary loss would appear to be an achievable goal.

Figure 7.1 Wind Tunnel Modifications to Allow Large End-wall Segments to be Mounted.

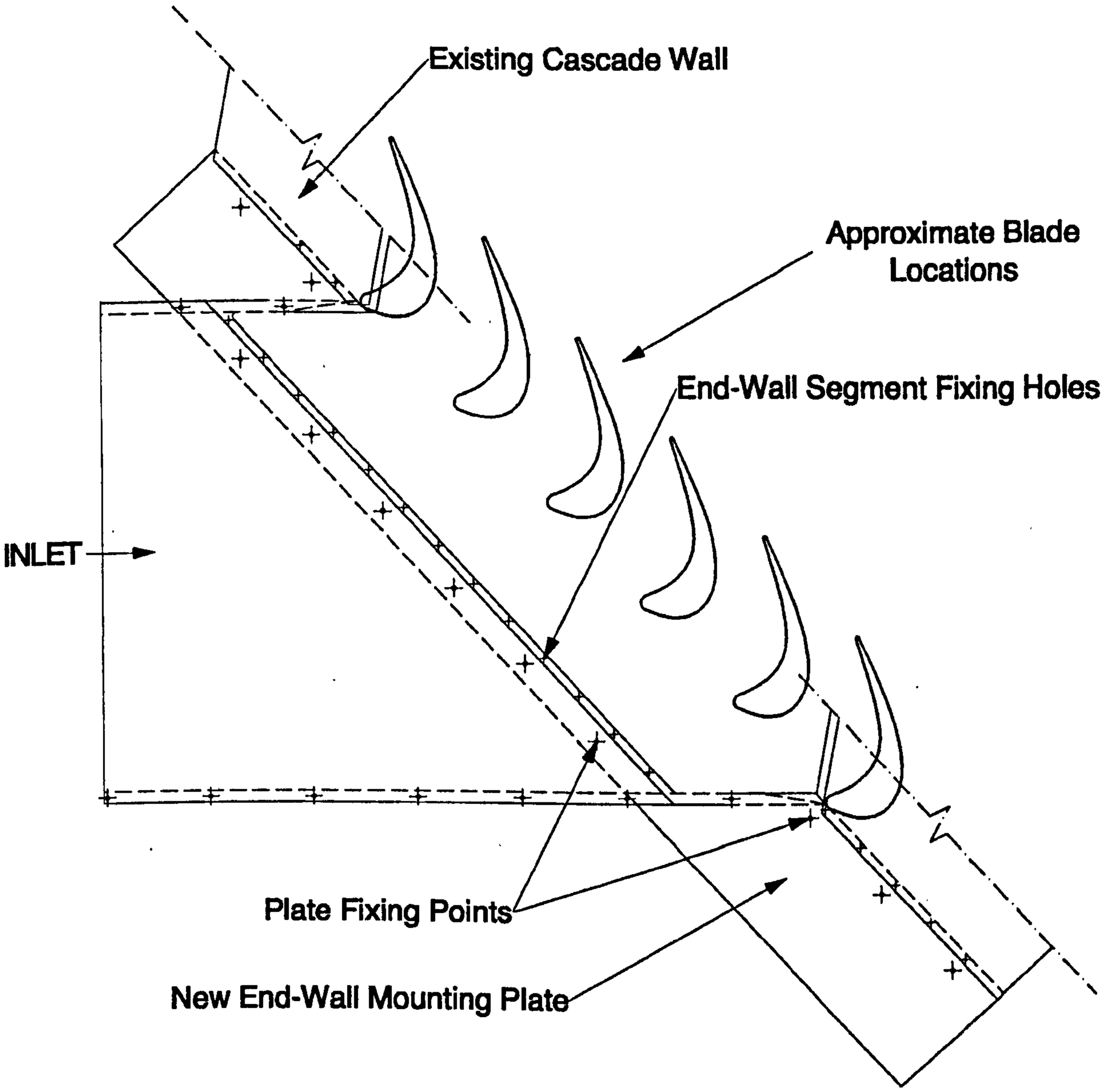

Figure 7.2 CFD End-wall Pressure Distributions with Compound Blade Lean.

a) +30 Degrees

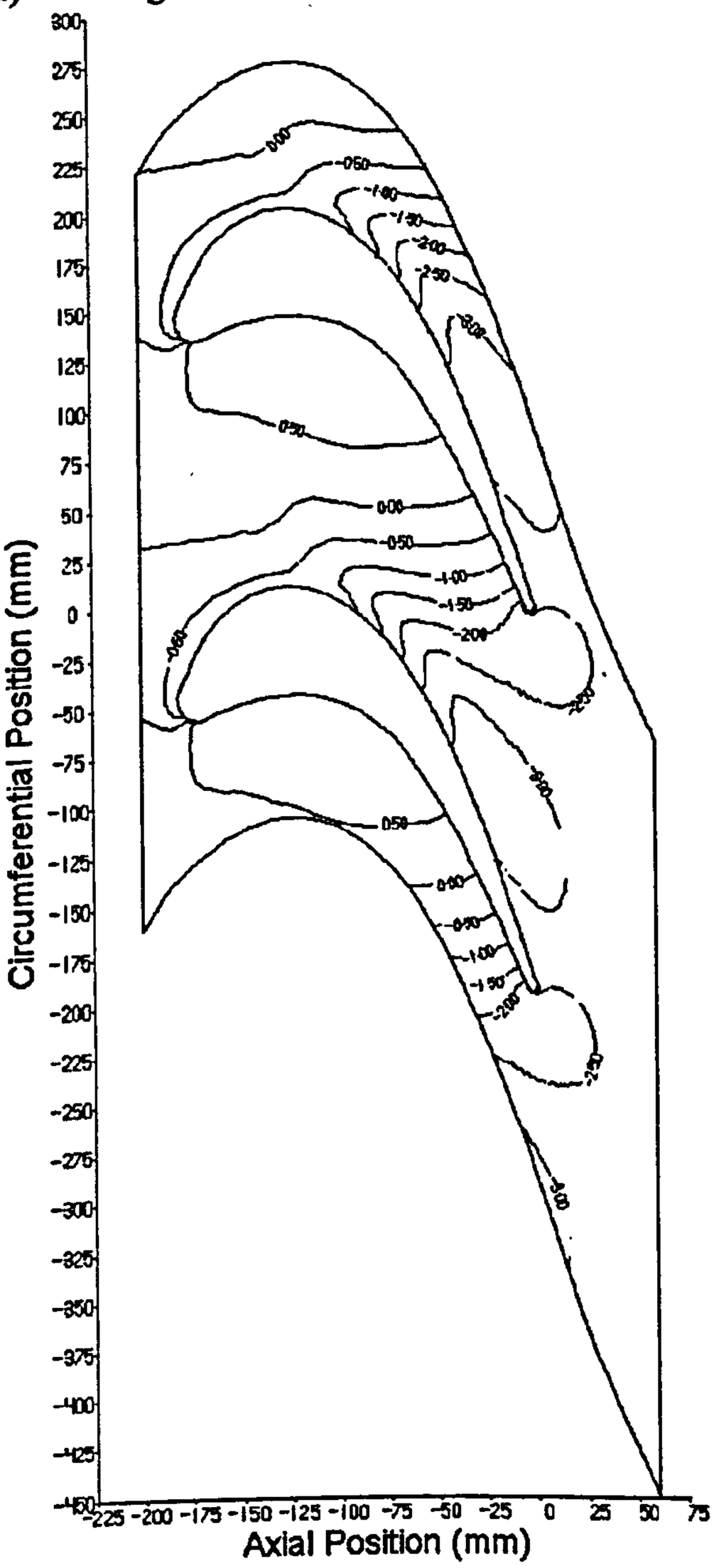

b) +15 Degrees

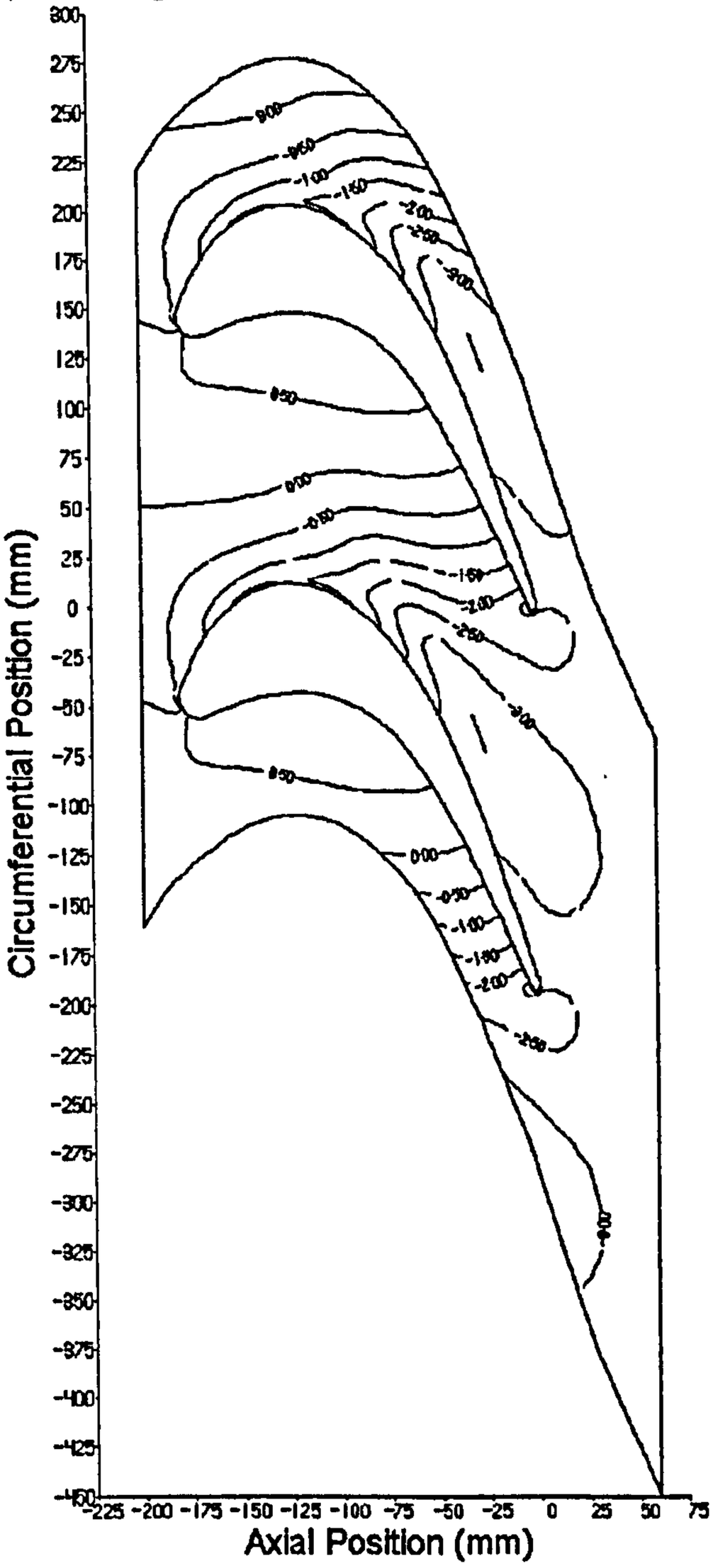

Figure 7.3 Pitch Averaged CFD Data for Compound Leant Blades at Slot 10.

a) Total Pressure Loss Coefficient.

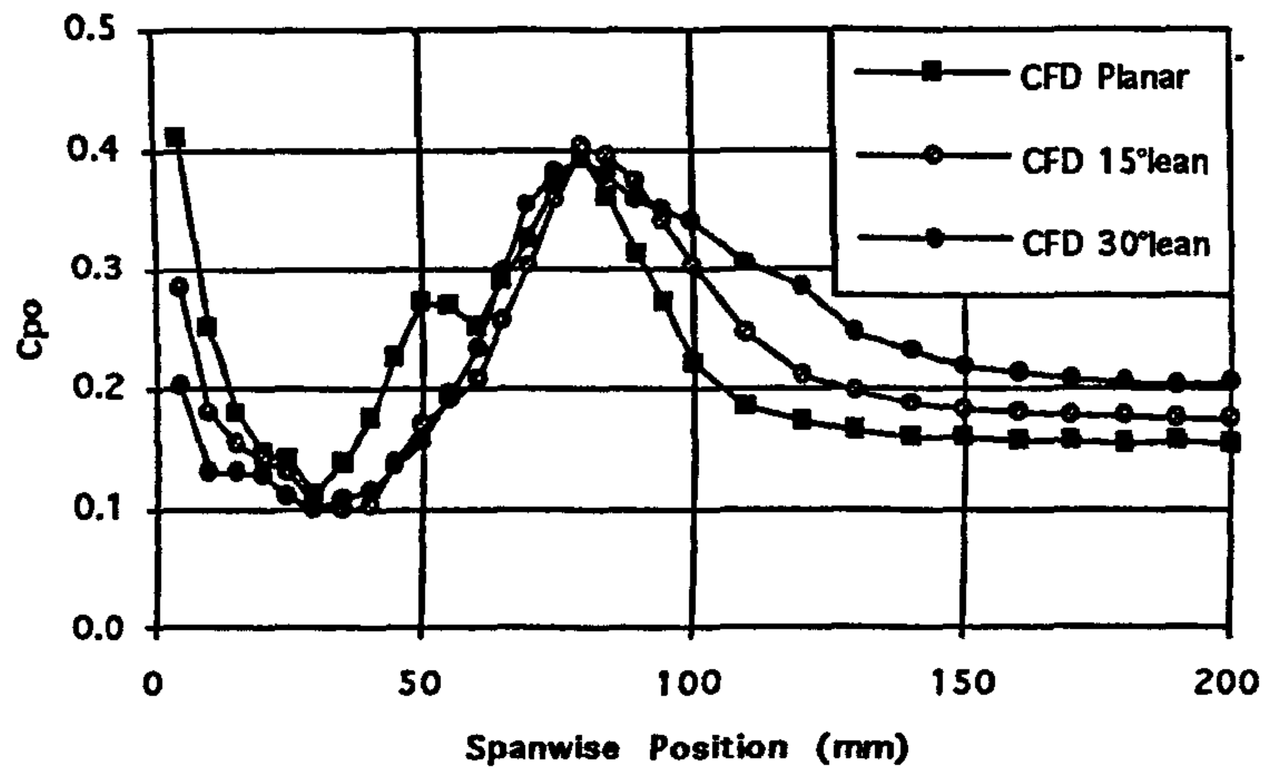

b) Yaw Angle.

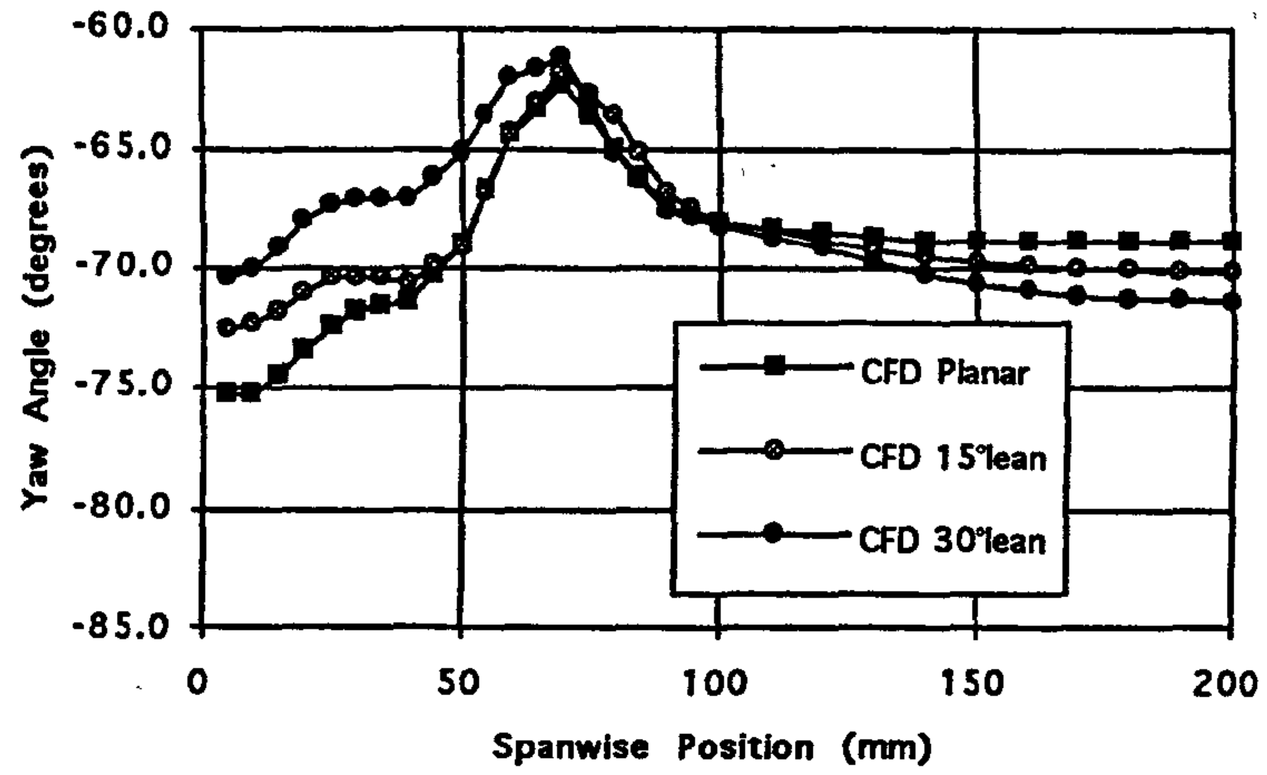

c) Pitch Angle.

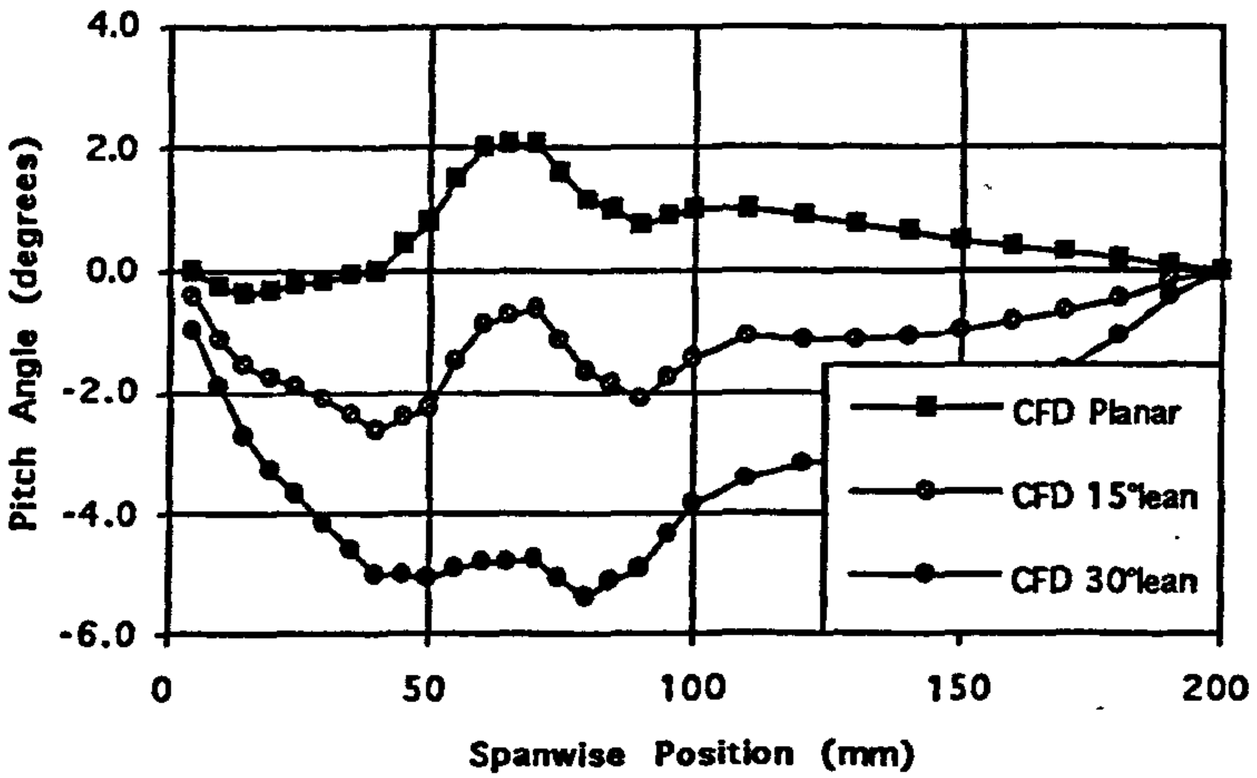

d) Secondary Kinetic Energy Coefficient.

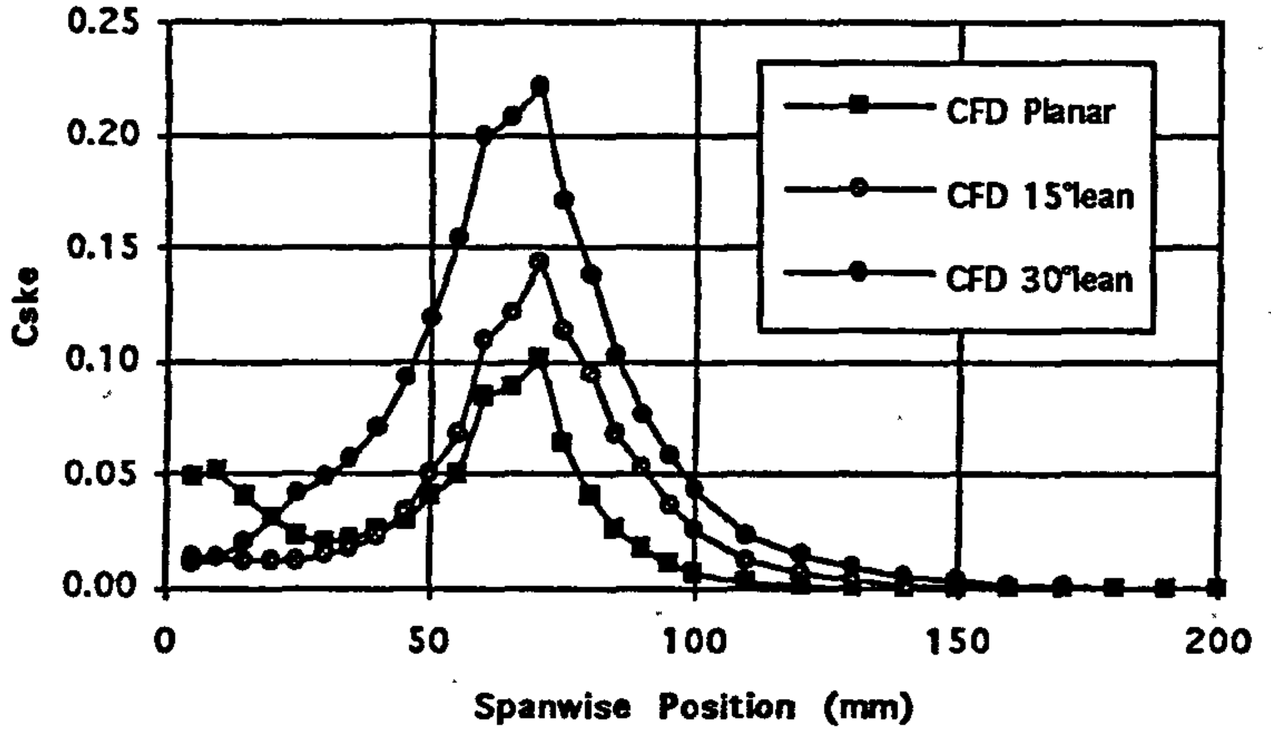

Figure 7.4 Contours of End-wall Height and CFD C_p Values.

a) End-wall Height (mm).

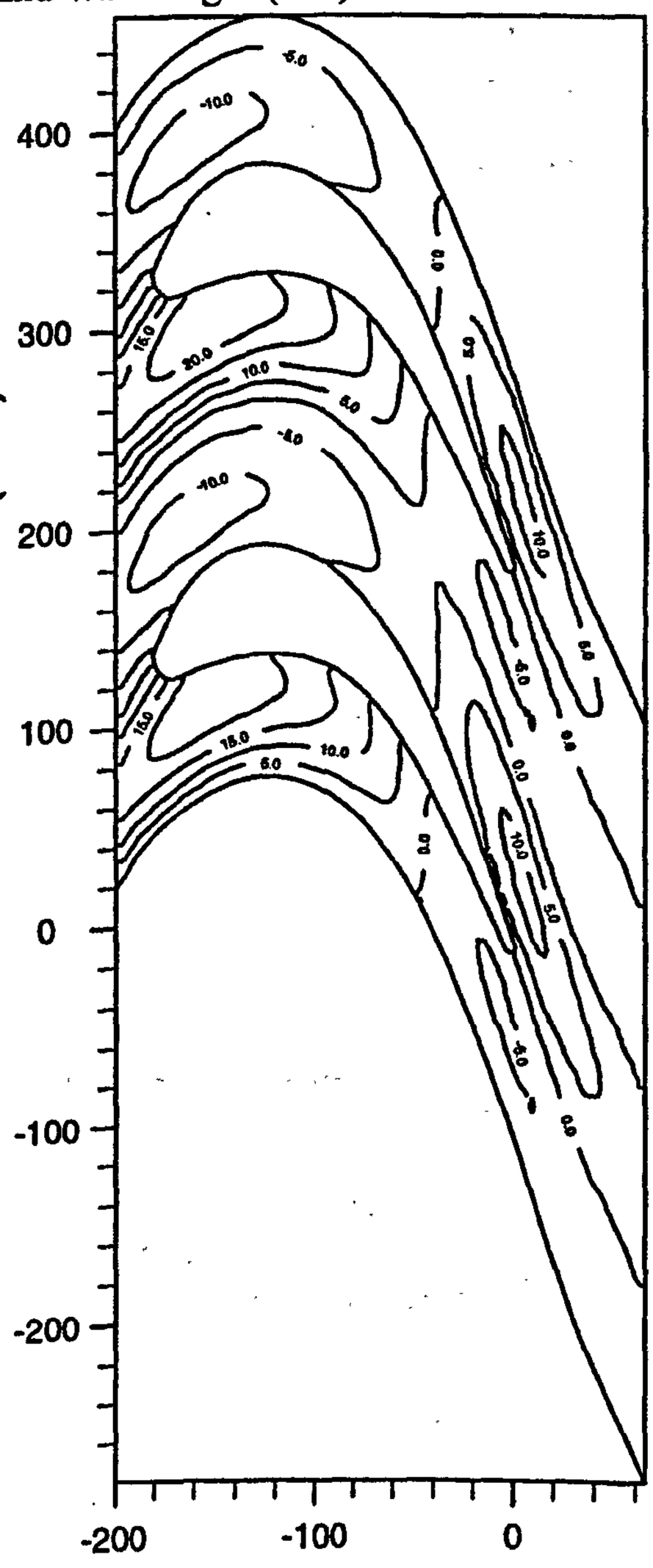

b) End-wall C_p (Fine Grid).

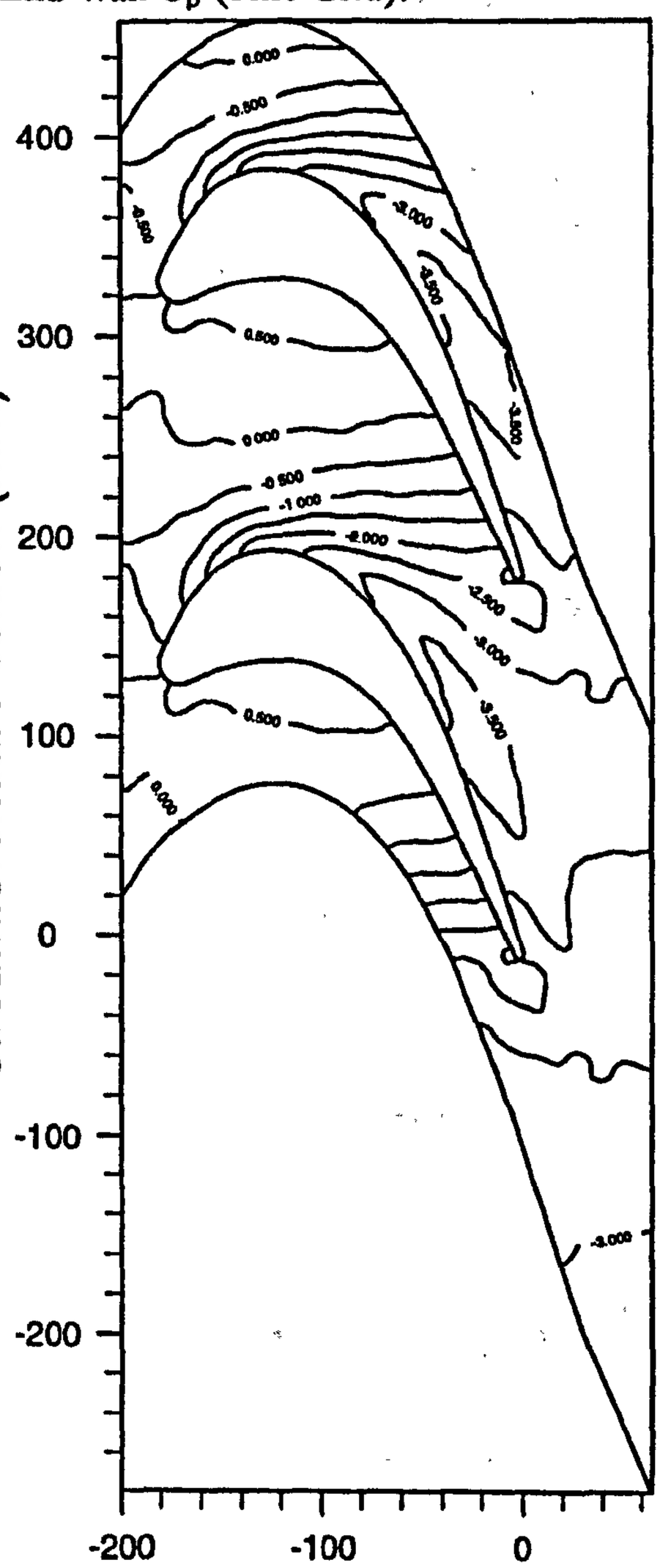

Figure 7.5 CFD Blade Cp Plots for the FAITH profile.

a) 0% Height.

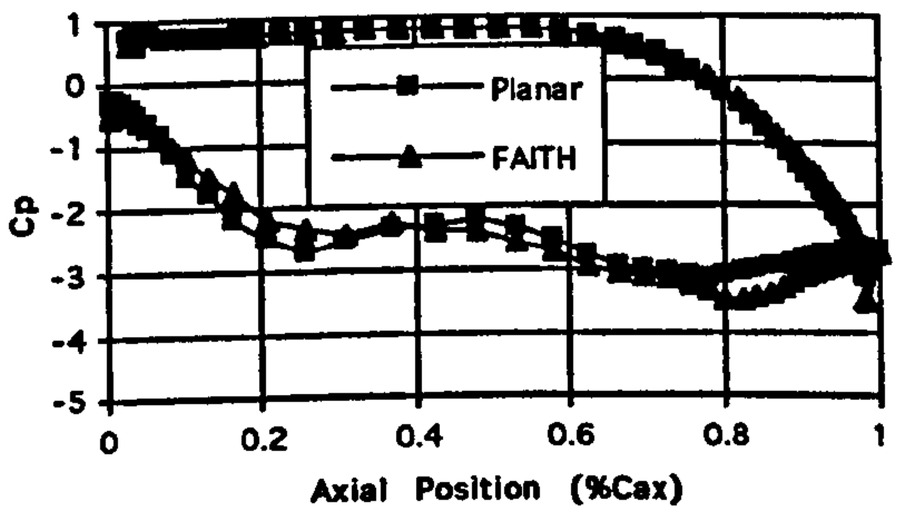

b) 4.65% Height.

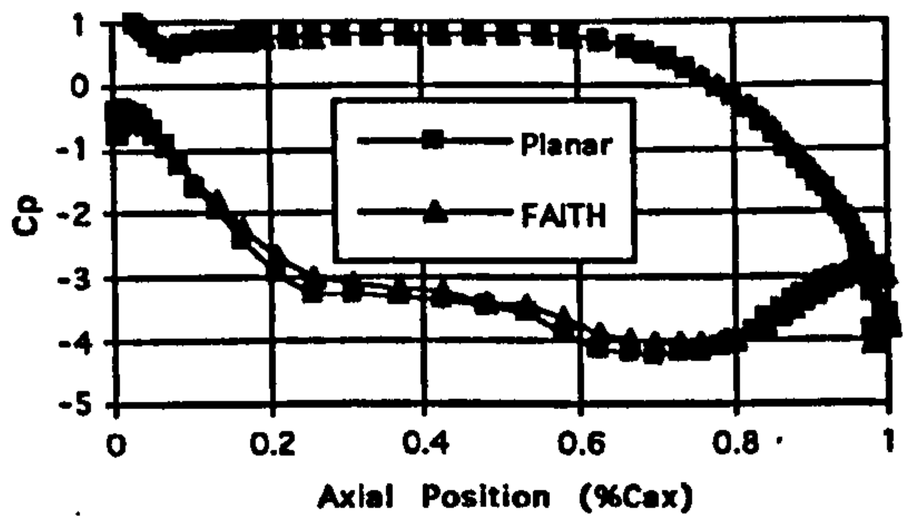

c) 10% Height.

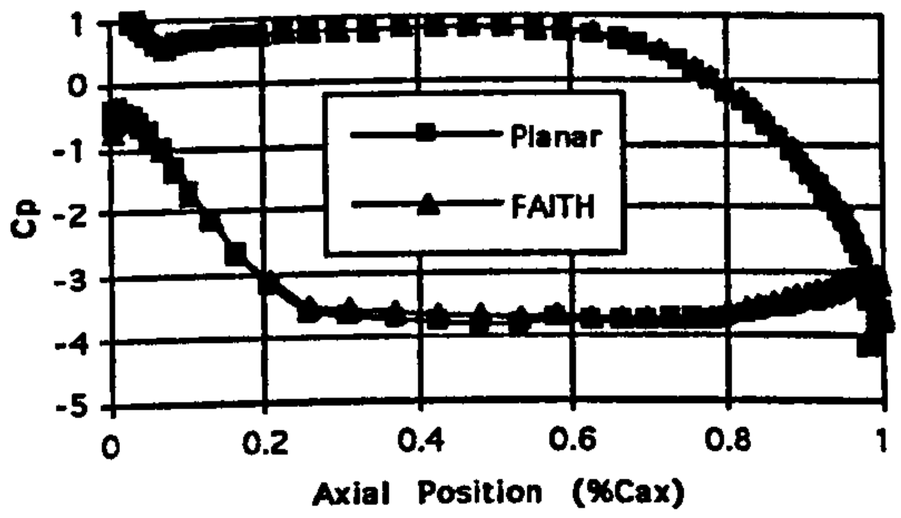

d) 15% Height.

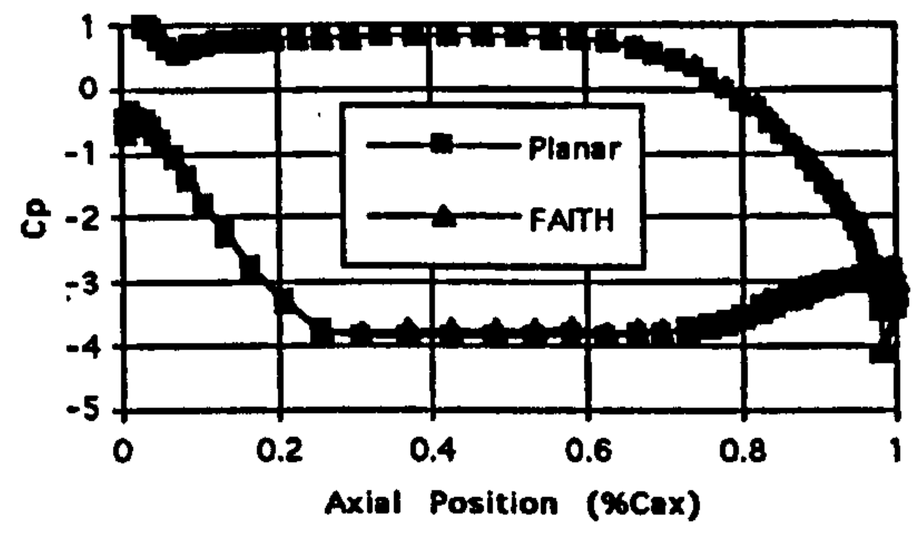

e) 20% Height.

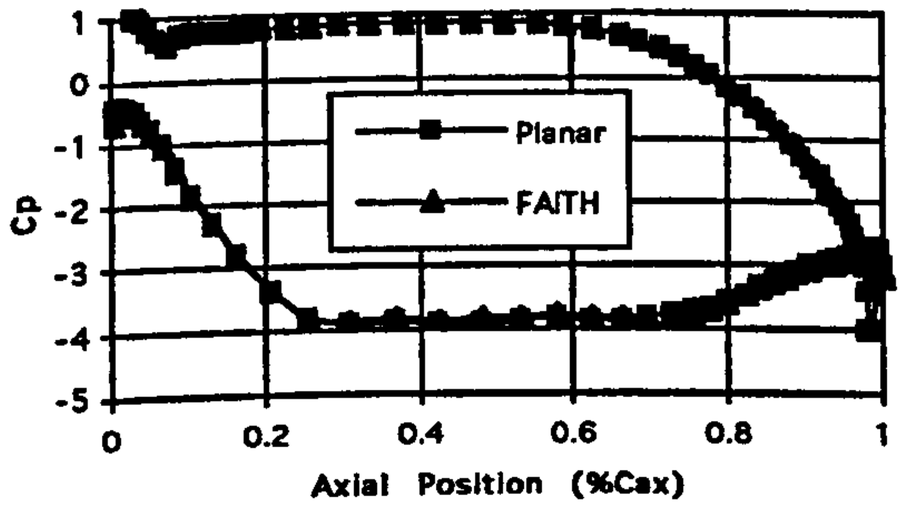

f) 50% Height.

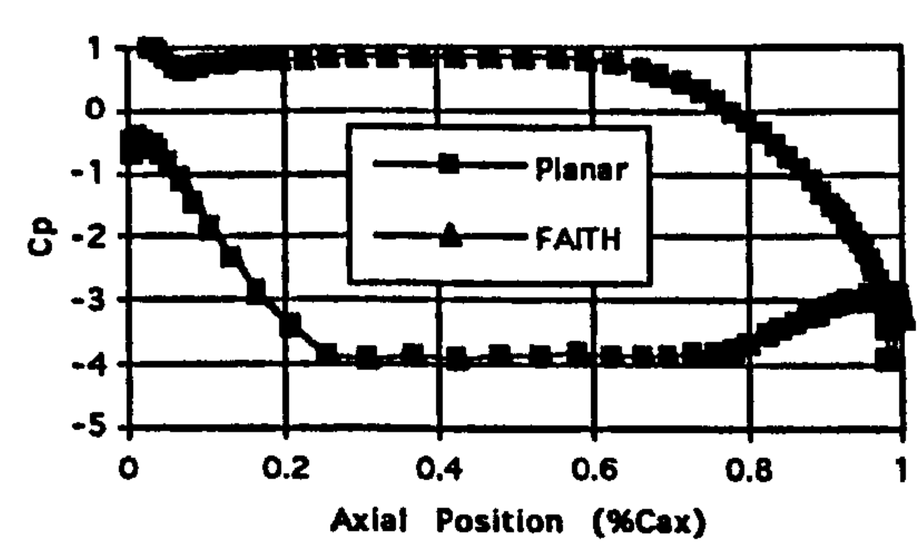

Figure 7.6 Pitch Averaged CFD Data at Slot 1 (Planar Wall Included for Comparison).

a) Total Pressure Loss Coefficient.

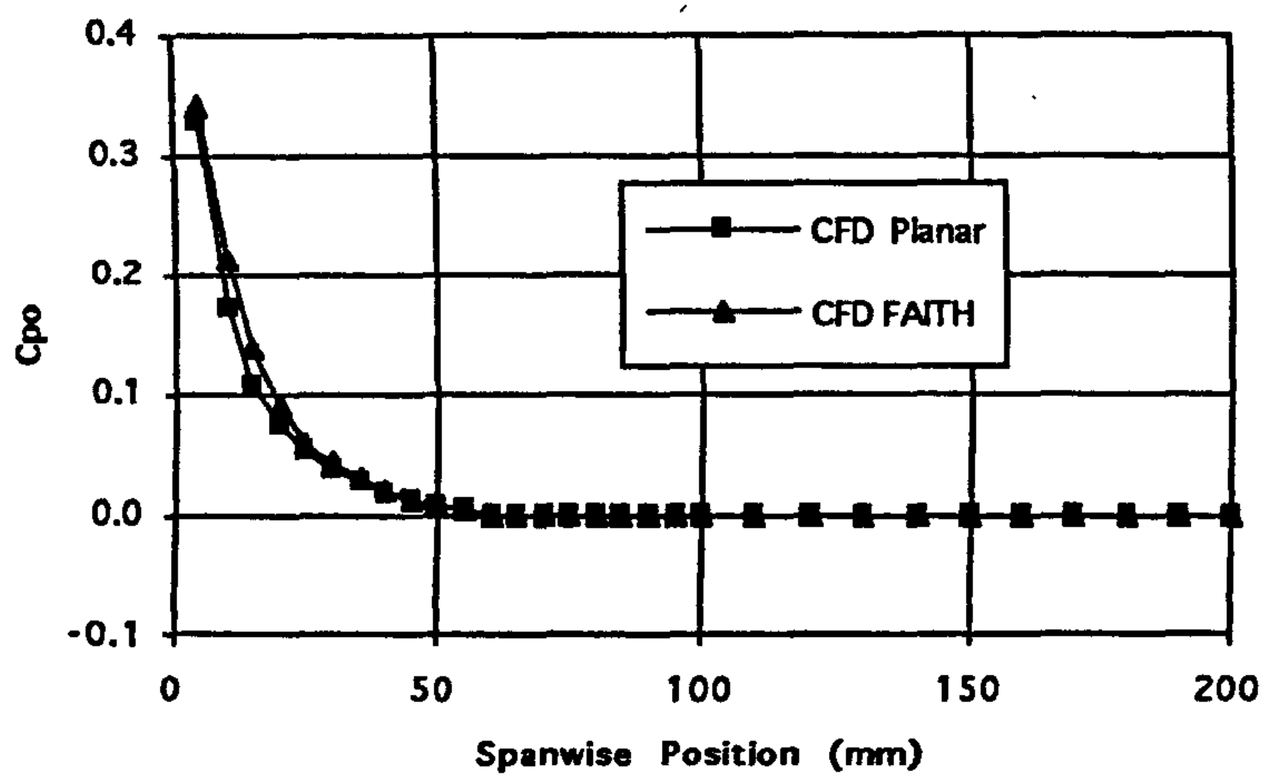

b) Yaw Angle.

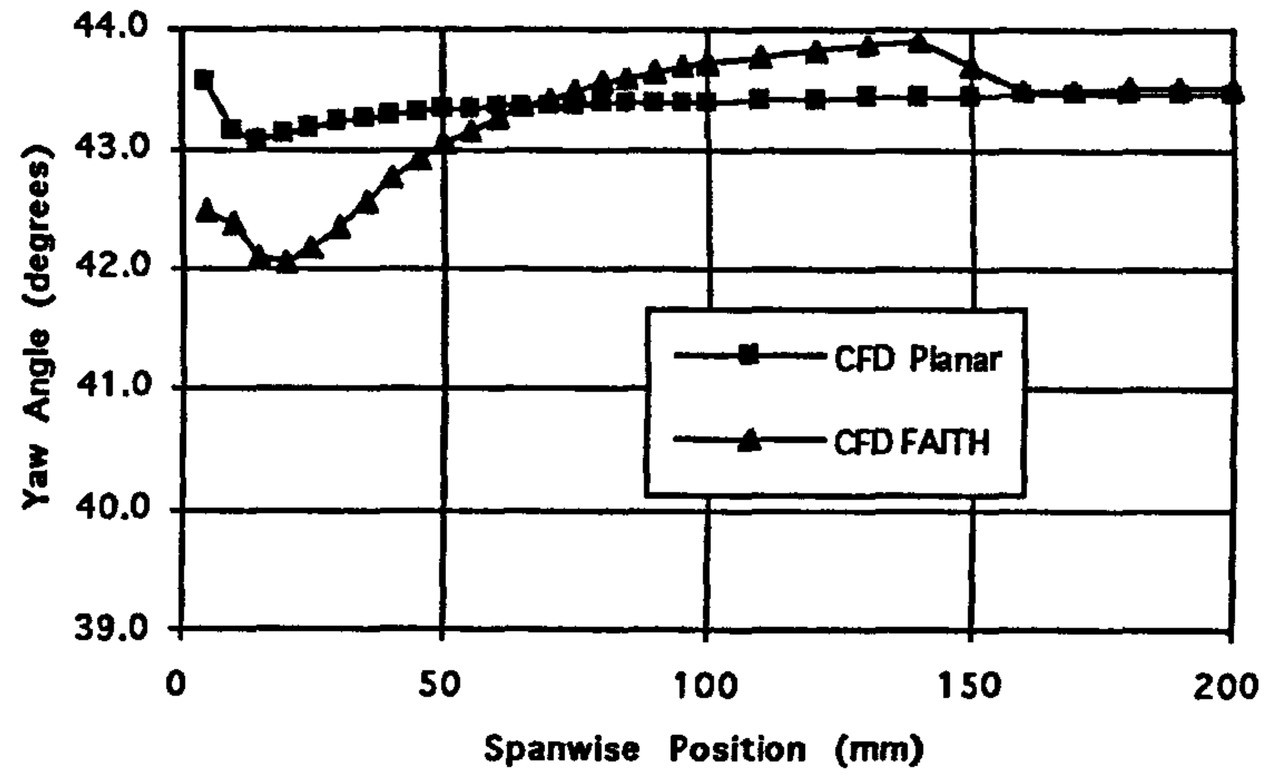

c) Pitch Angle.

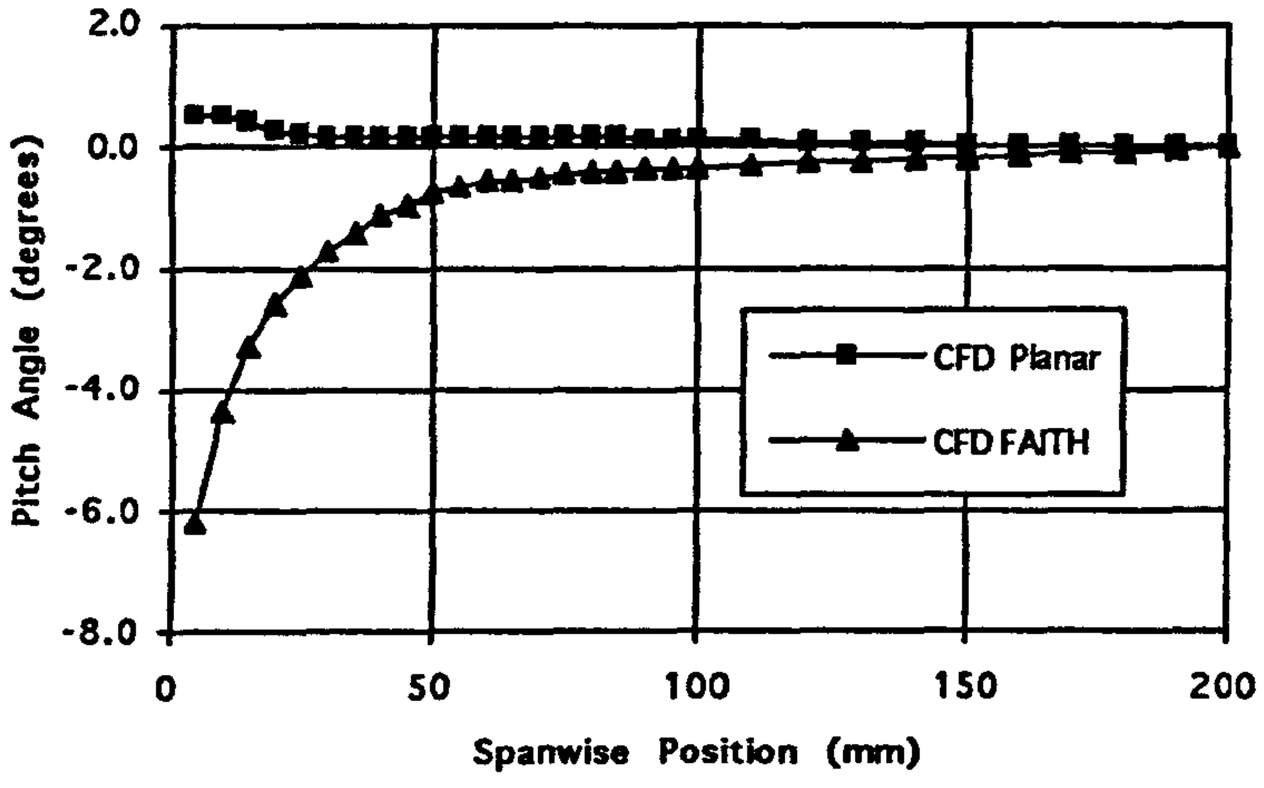

d) Secondary Kinetic Energy Coefficient.

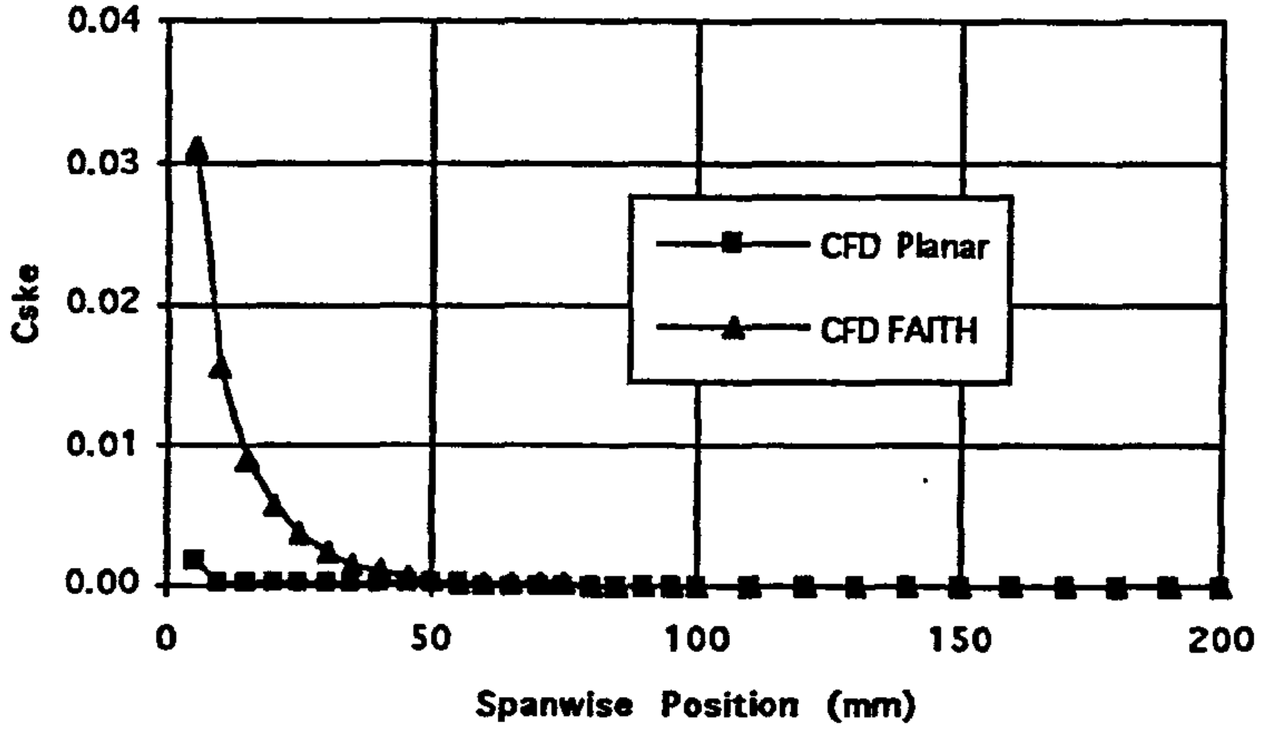

Figure 7.7 Pitch Averaged CFD Data at Slot 6 (Planar Wall Included for Comparison).

a) Total Pressure Loss Coefficient.

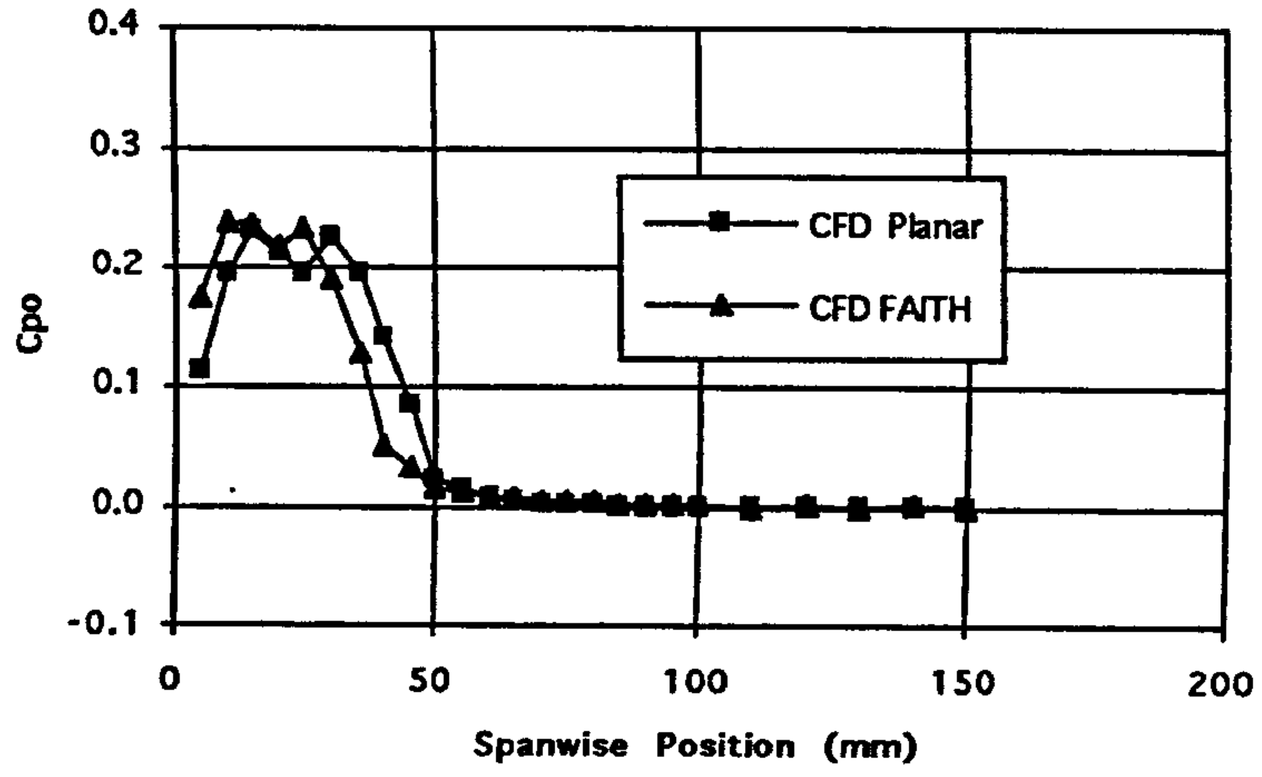

b) Yaw Angle.

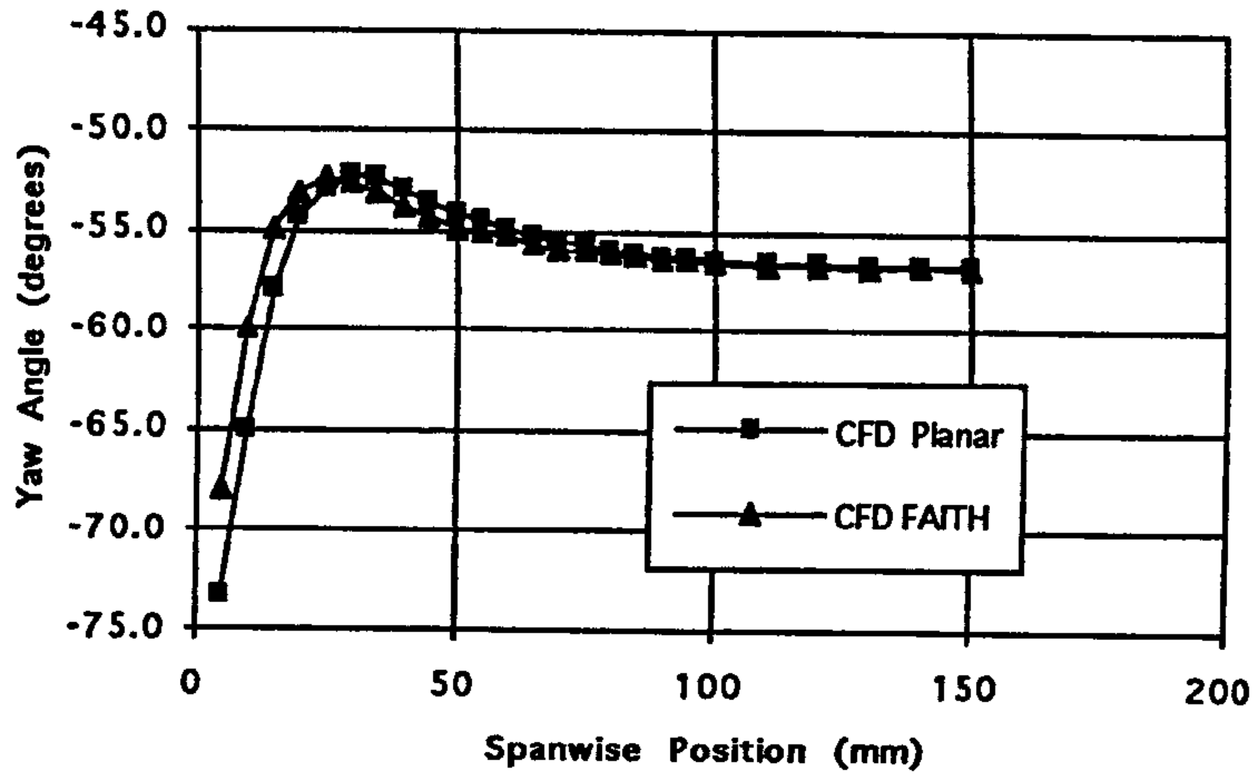

c) Pitch Angle.

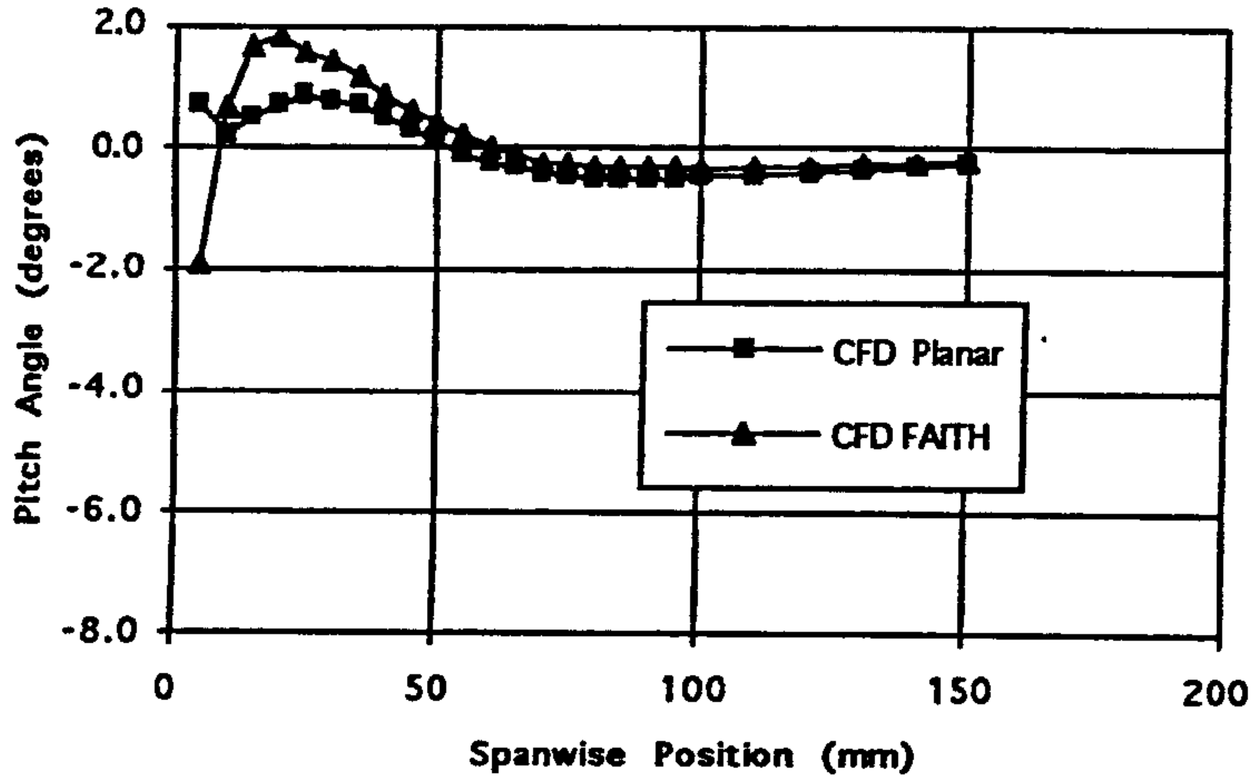

d) Secondary Kinetic Energy Coefficient.

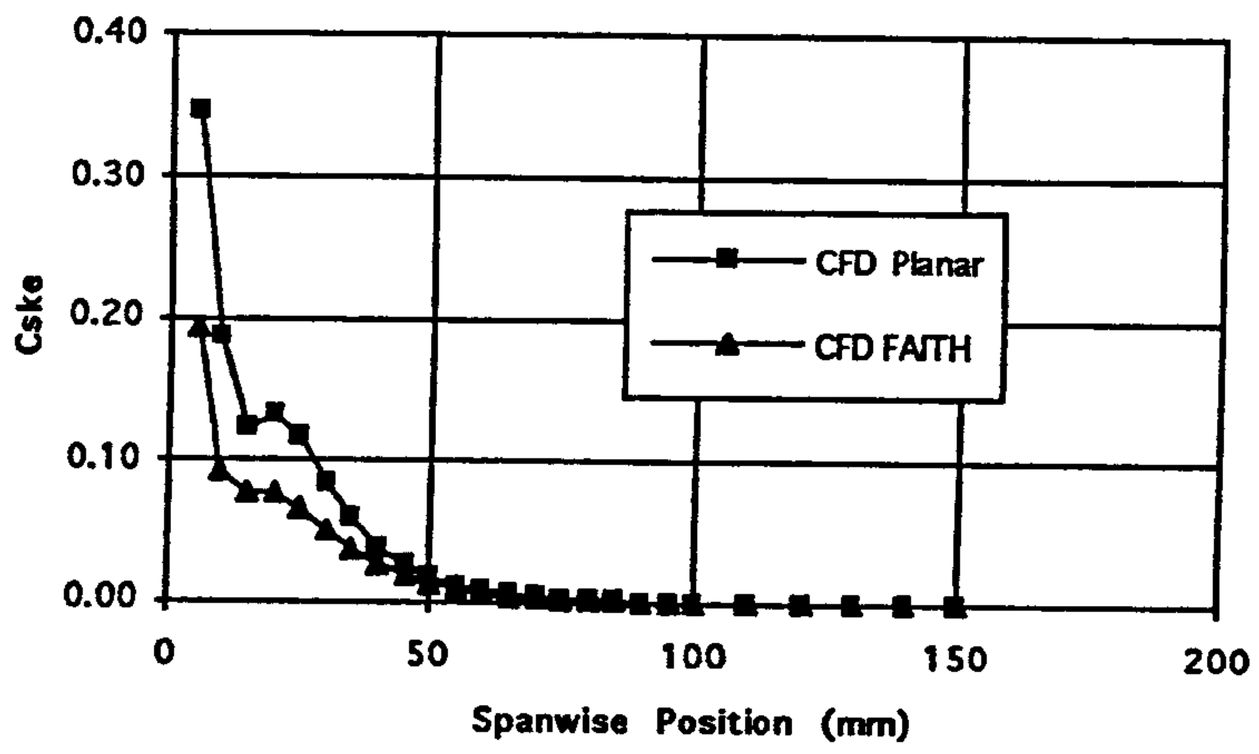

Figure 7.8 Pitch Averaged CFD Data at Slot 8 (Planar Wall Included for Comparison).

a) Total Pressure Loss Coefficient.

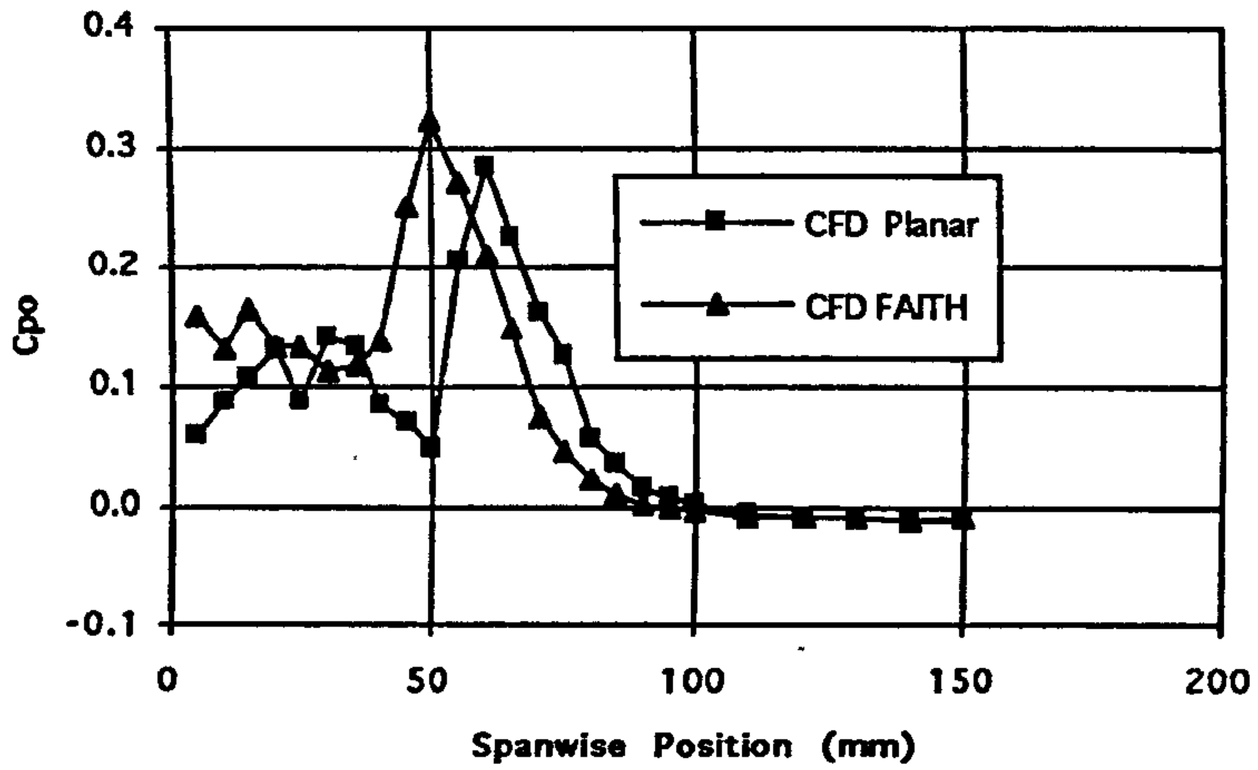

b) Yaw Angle.

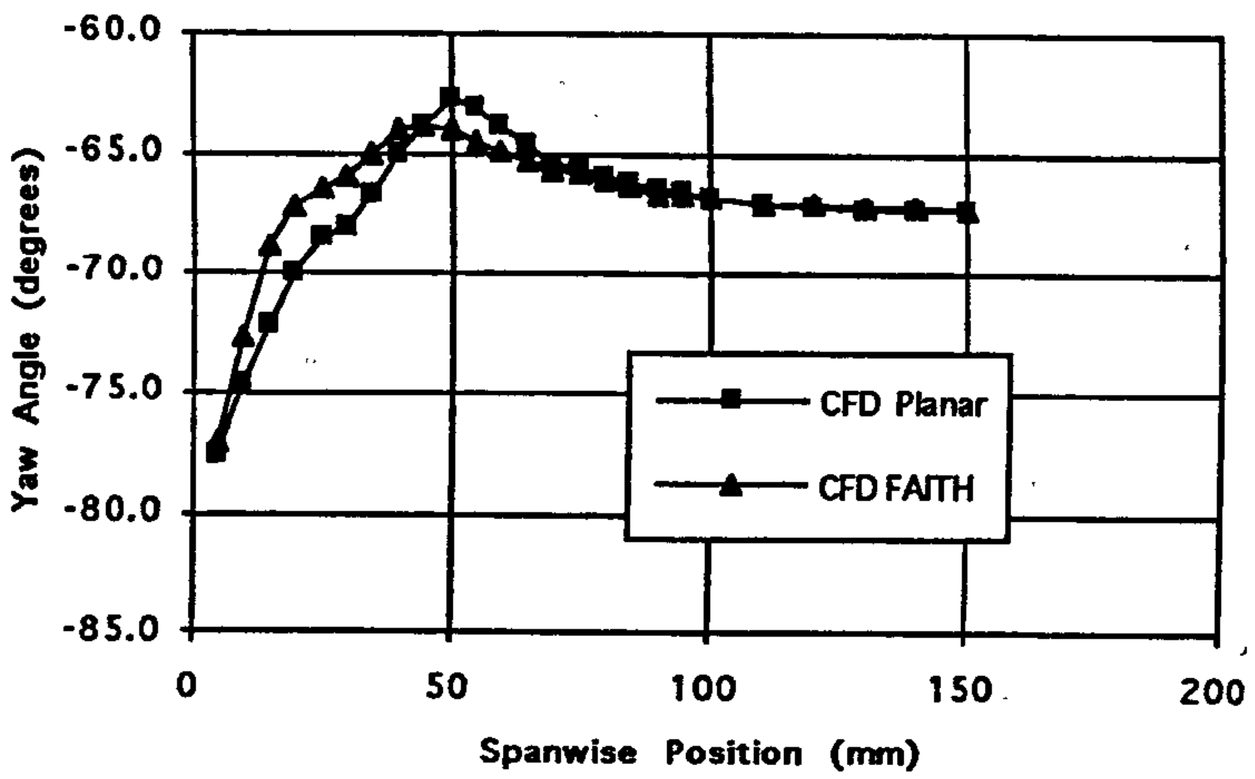

c) Pitch Angle.

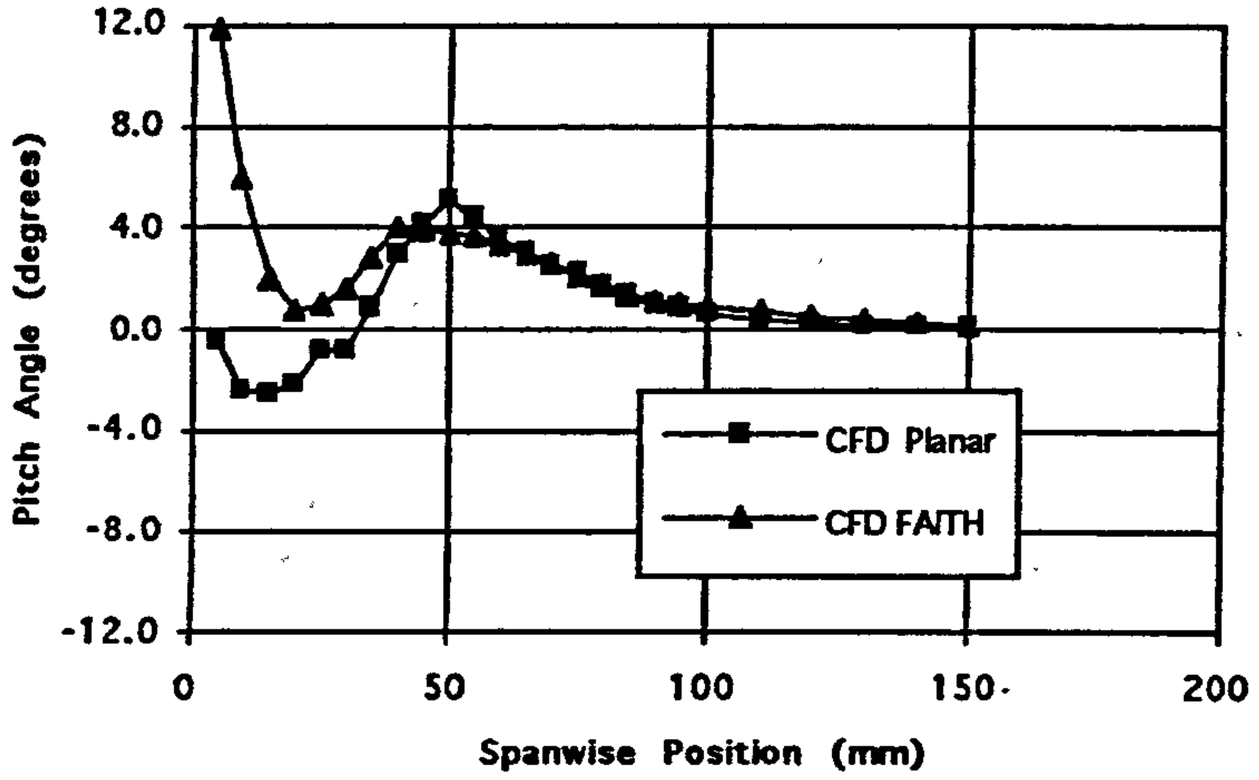

d) Secondary Kinetic Energy Coefficient.

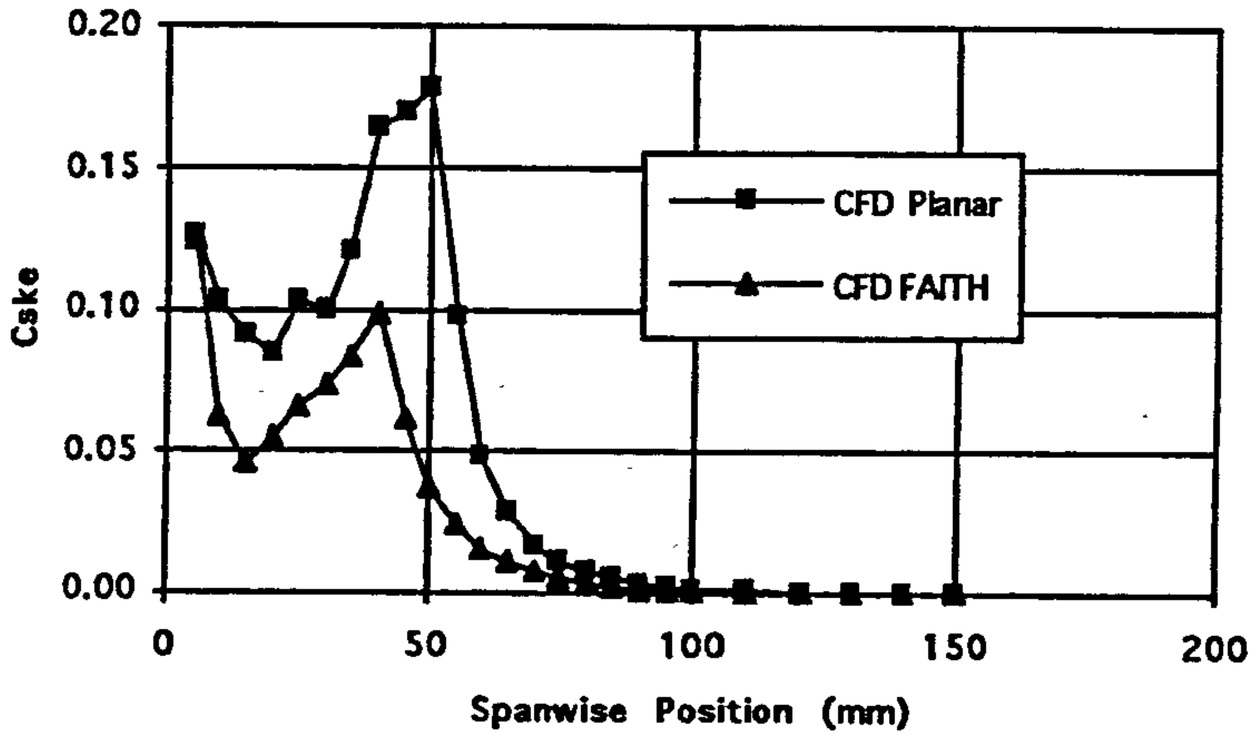

Figure 7.9 Pitch Averaged CFD Data at Slot 10 (Planar Wall Included for Comparison).

a) Total Pressure Loss Coefficient.

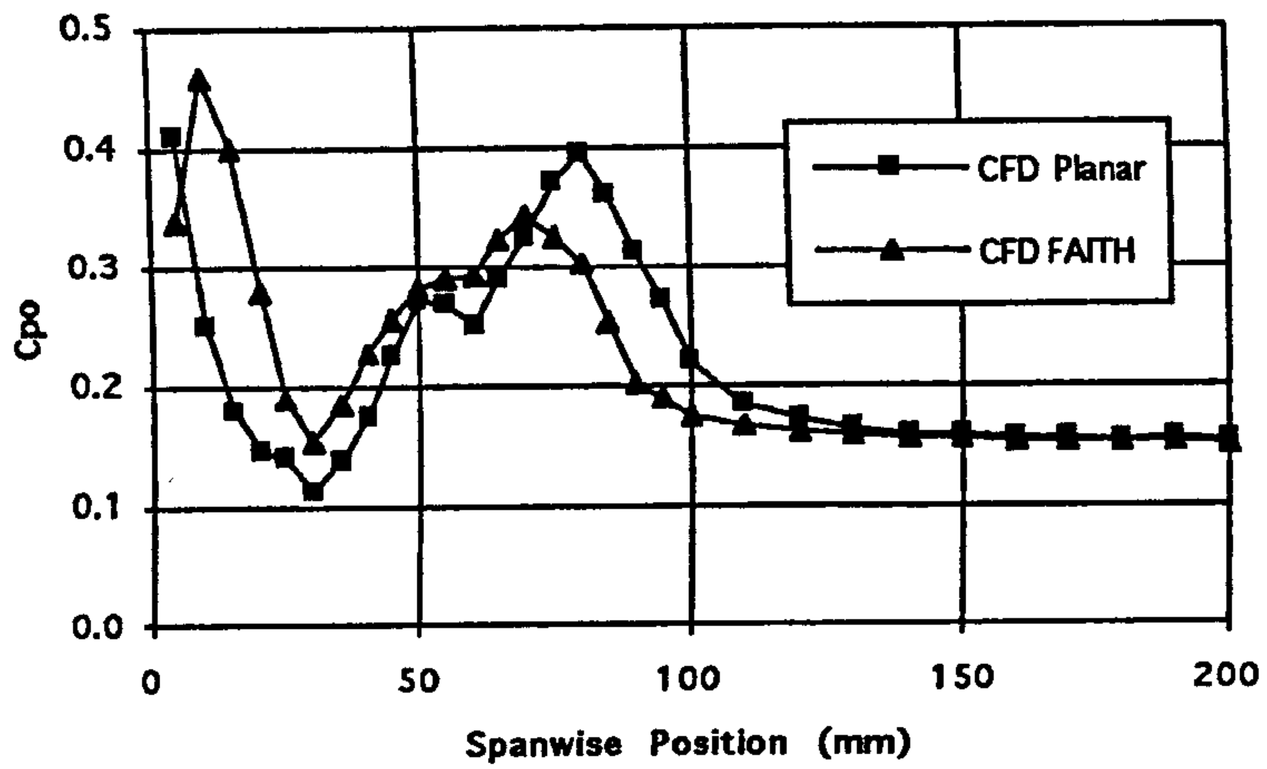

b) Yaw Angle.

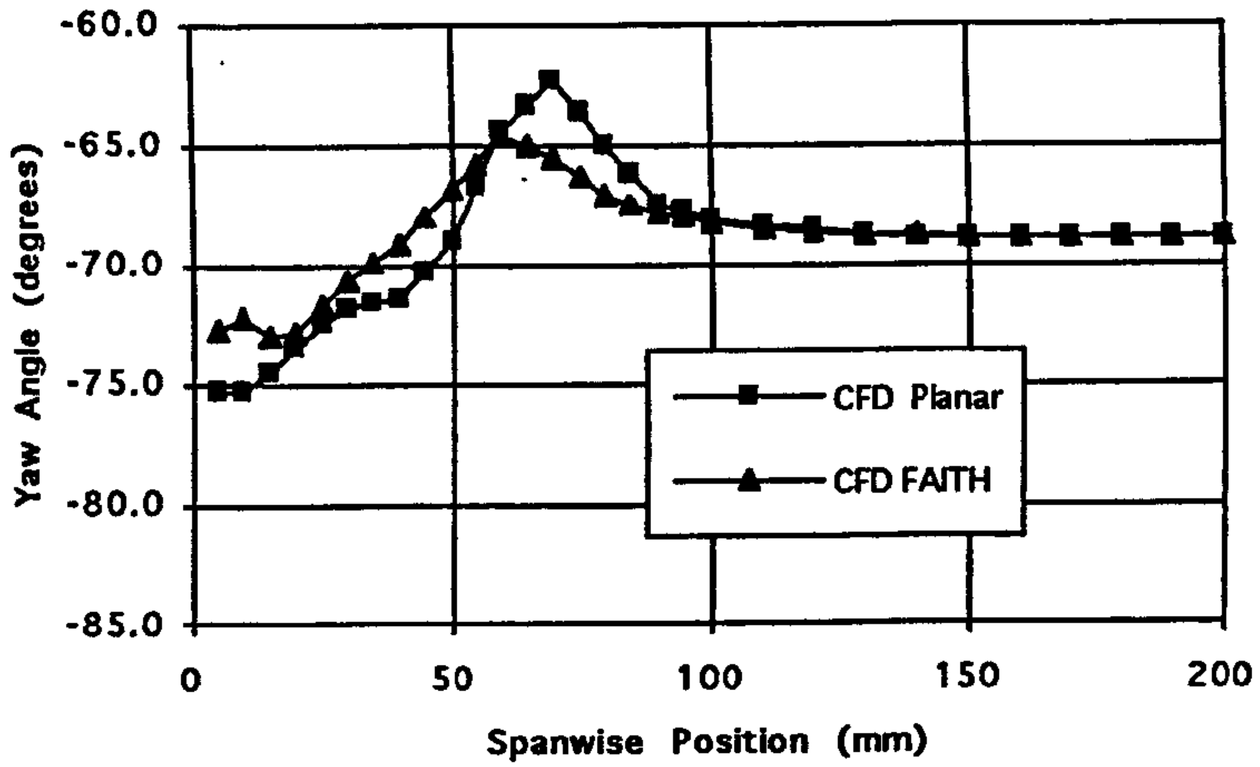

c) Pitch Angle.

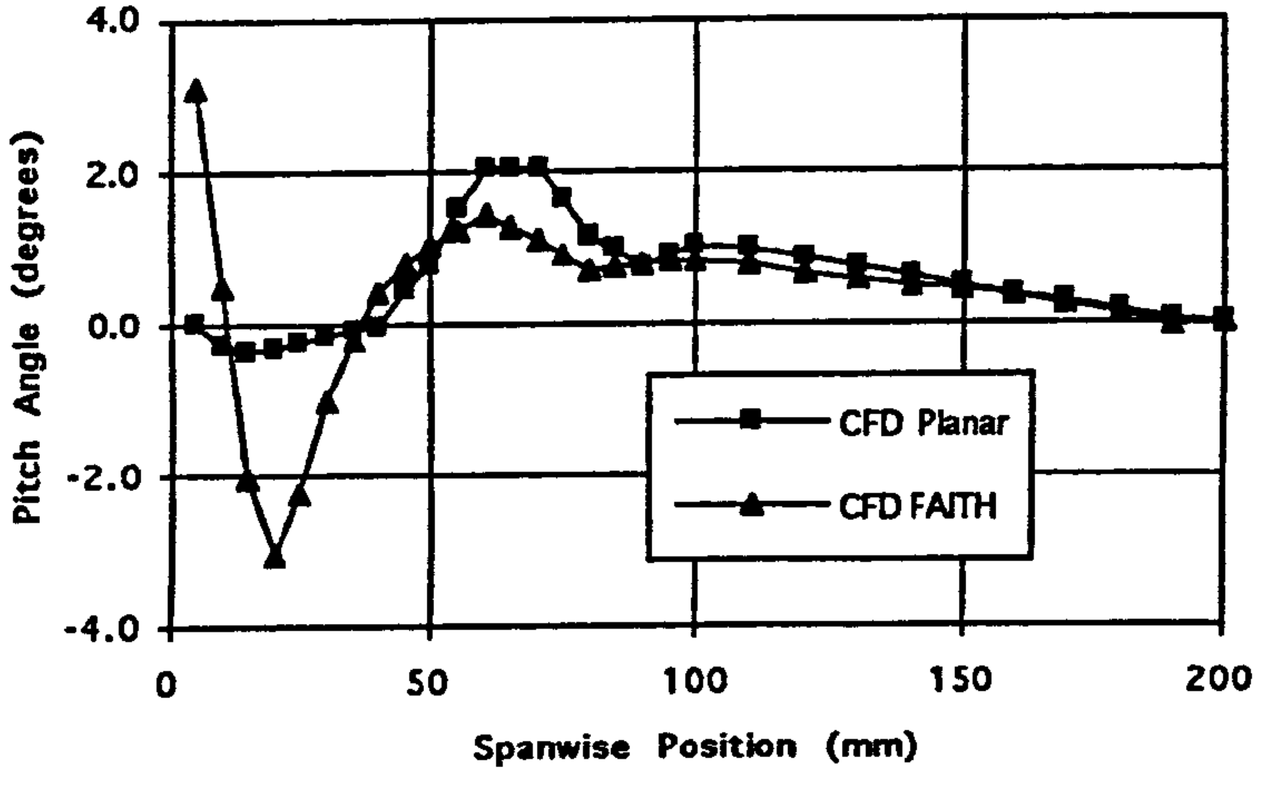

d) Secondary Kinetic Energy Coefficient.

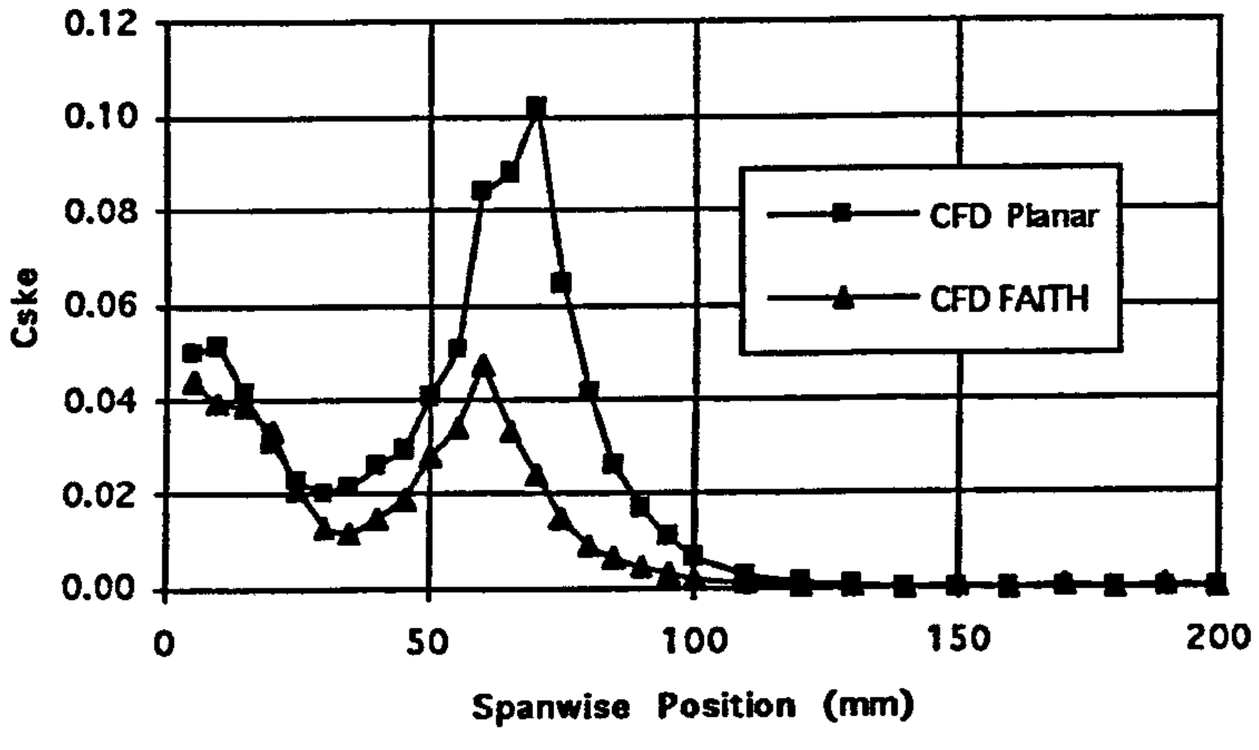

Figure 7.10 CFD Data at Slot 1.

a) Secondary Velocity Vectors.

FAITH Profile

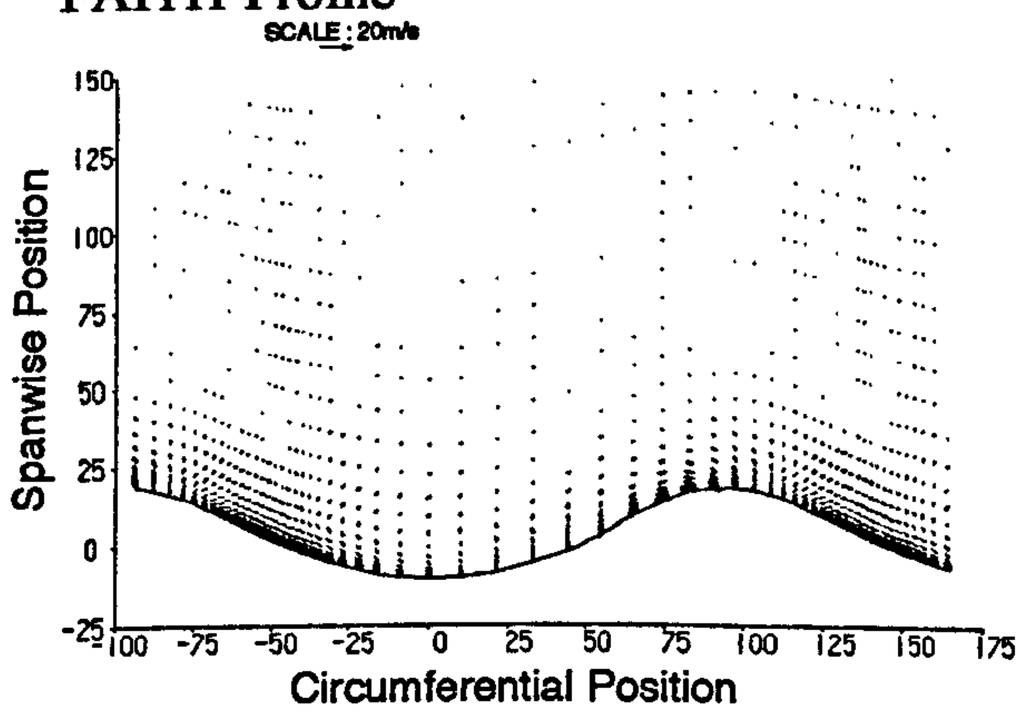

Planar Wall

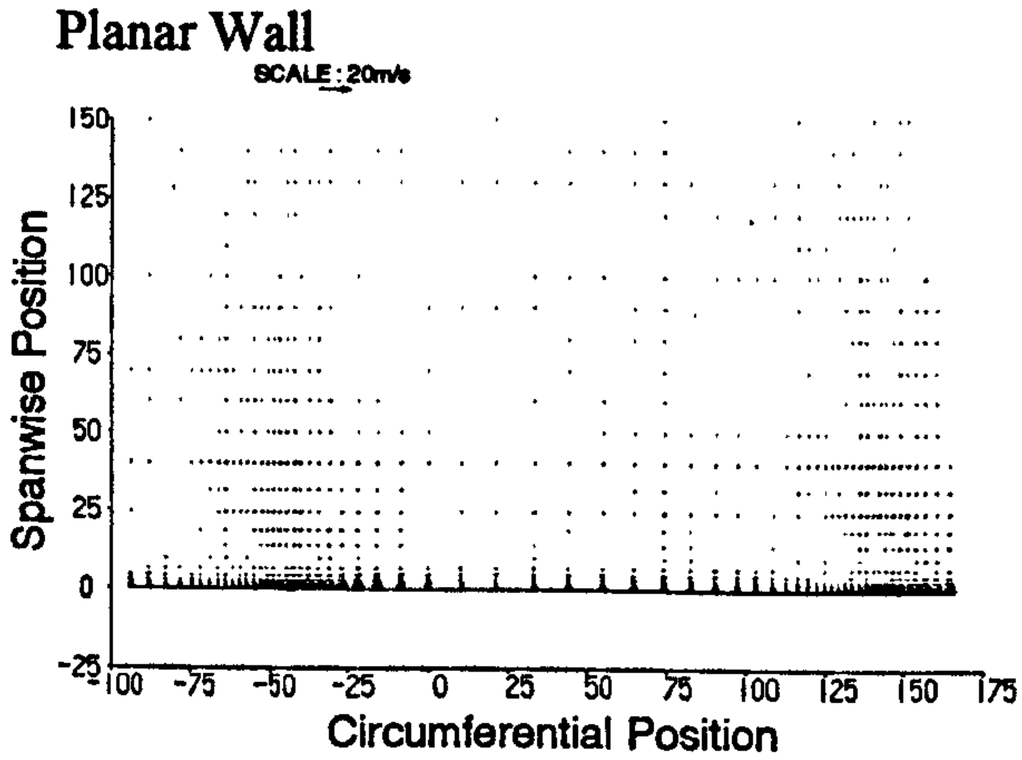

b) Total Pressure Loss Coefficient.

FAITH Profile

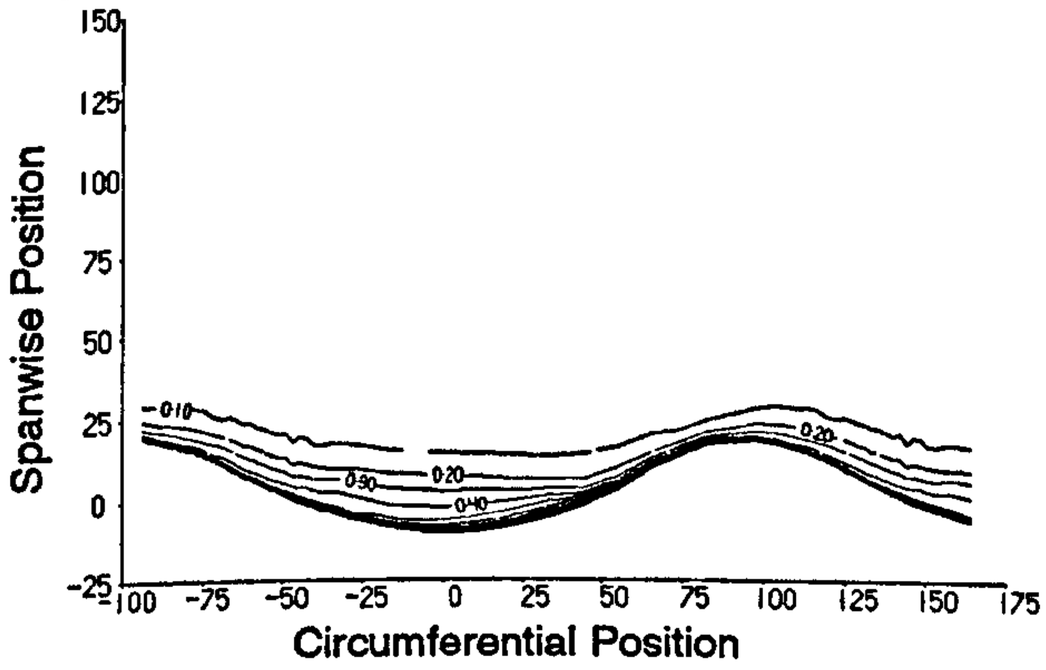

Planar Wall

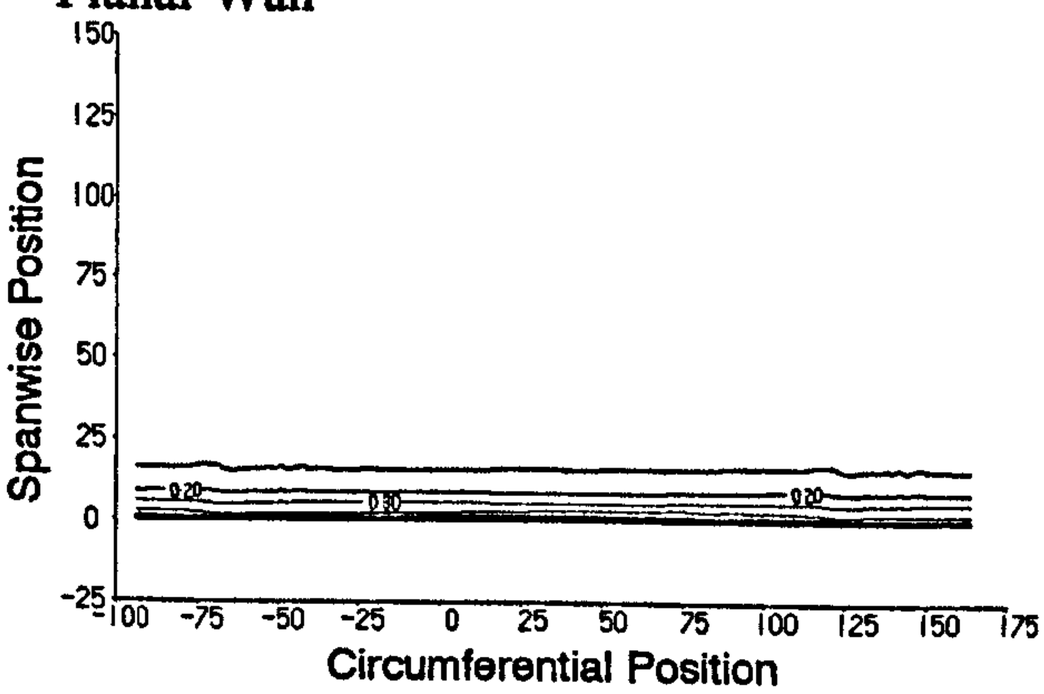

c) Yaw Angle.

FAITH Profile

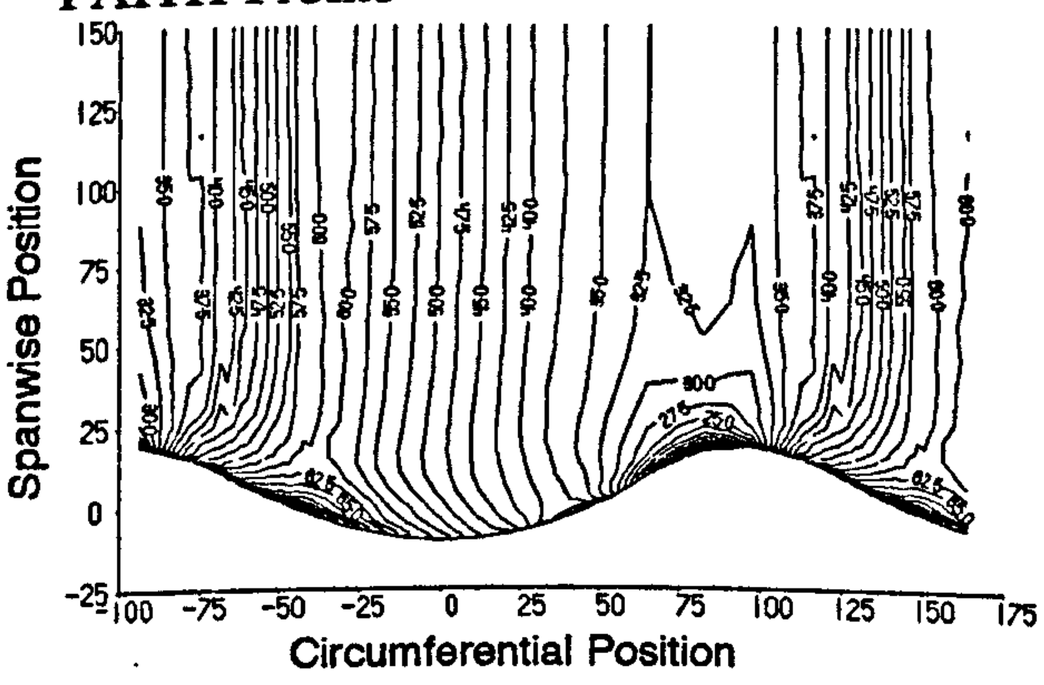

Planar Wall

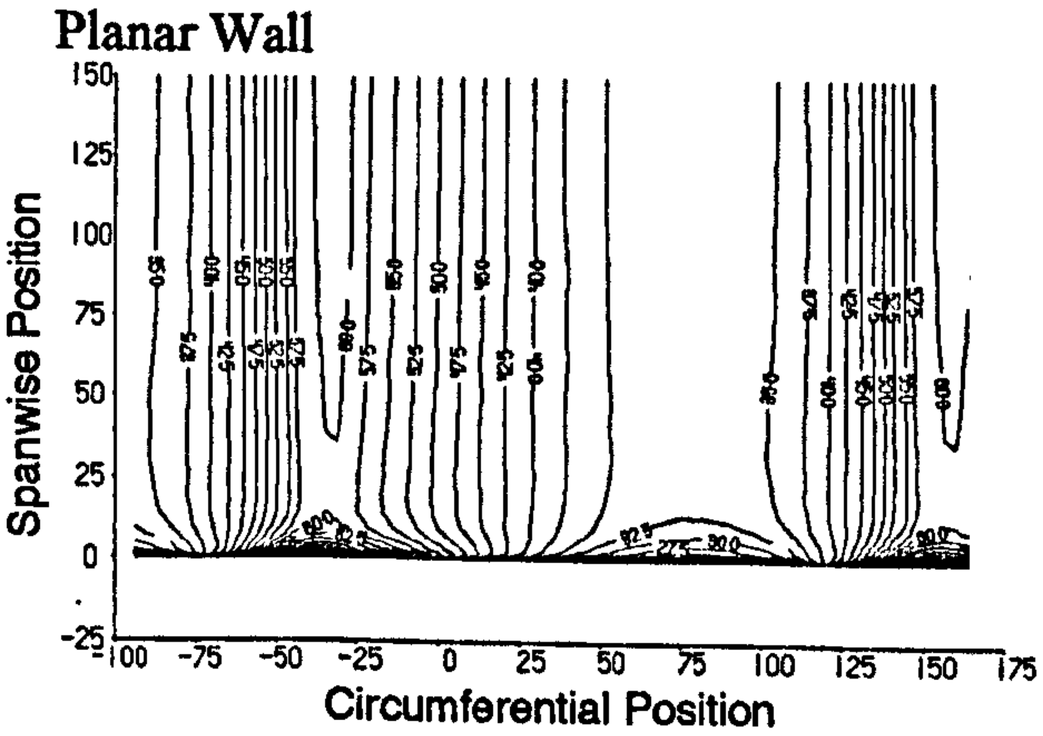

d) Secondary Kinetic Energy Coefficient.

FAITH Profile

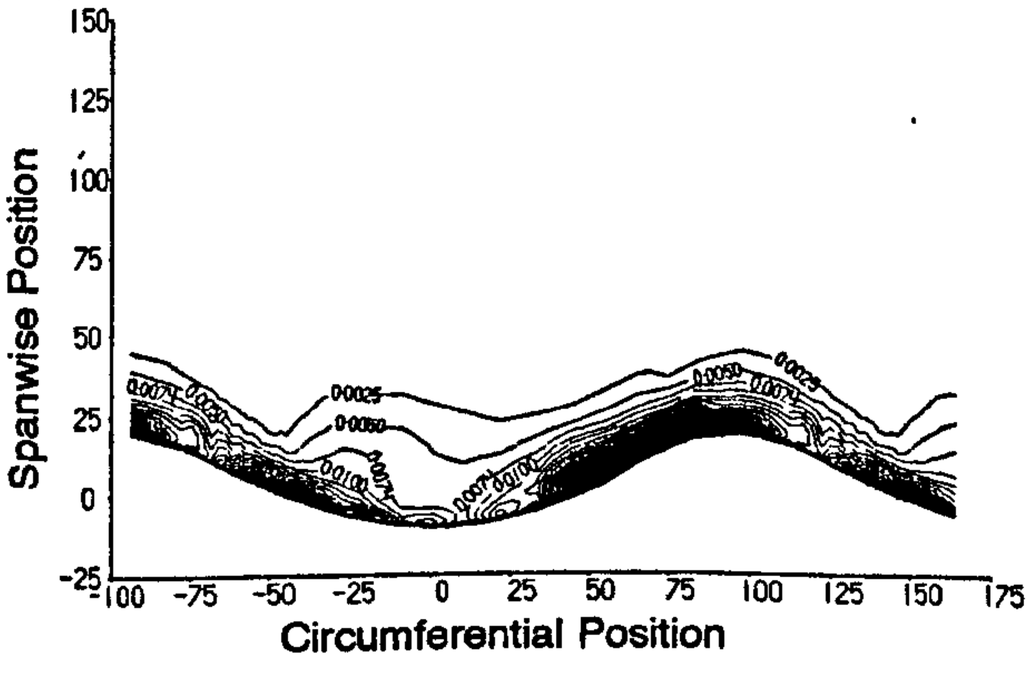

Planar Wall

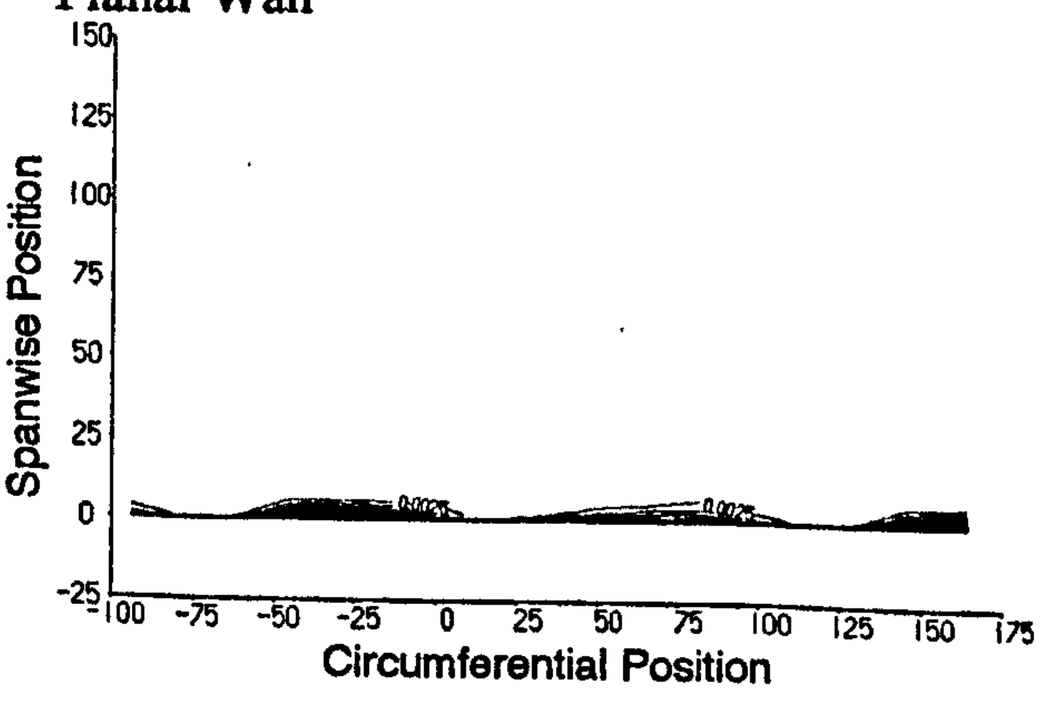

Figure 7.11 CFD Data at Slot 6.

a) Secondary Velocity Vectors.

FAITH Profile

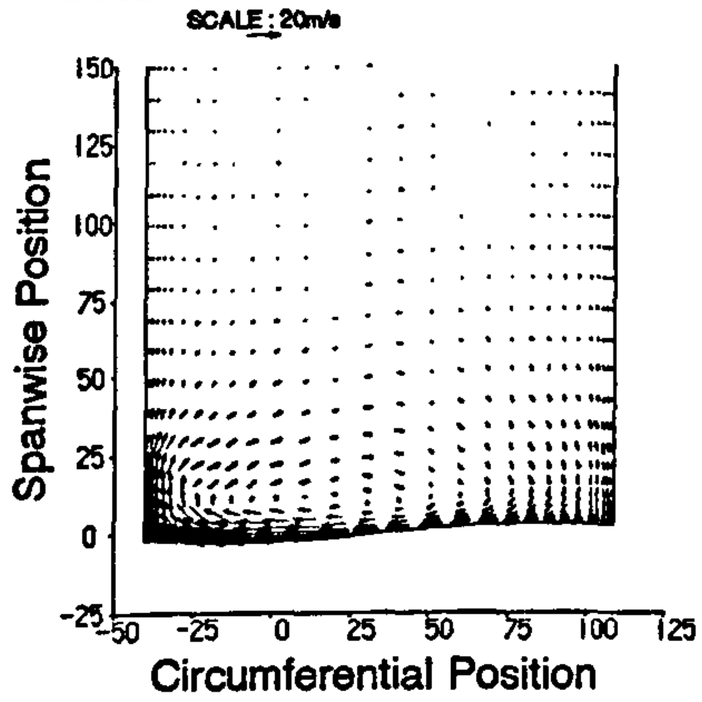

Planar Wall

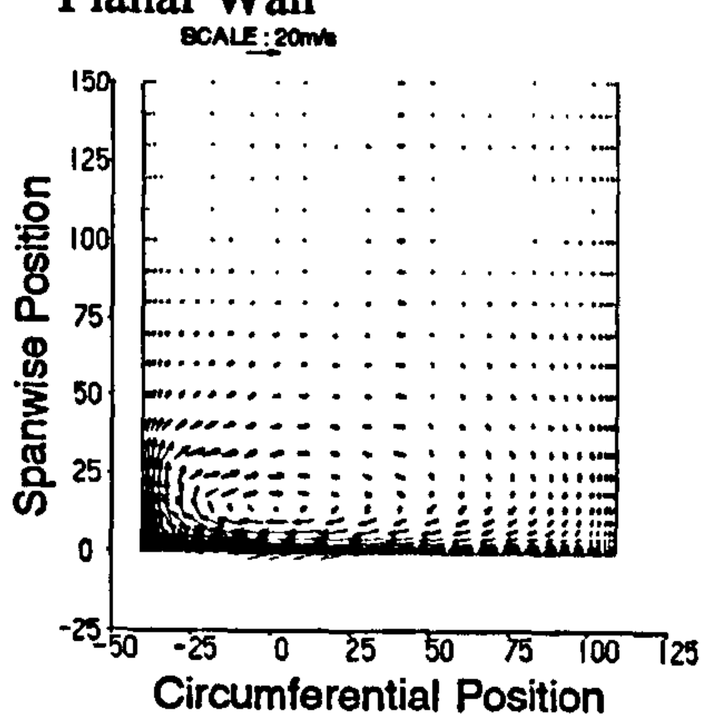

b) Total Pressure Loss Coefficient.

FAITH Profile

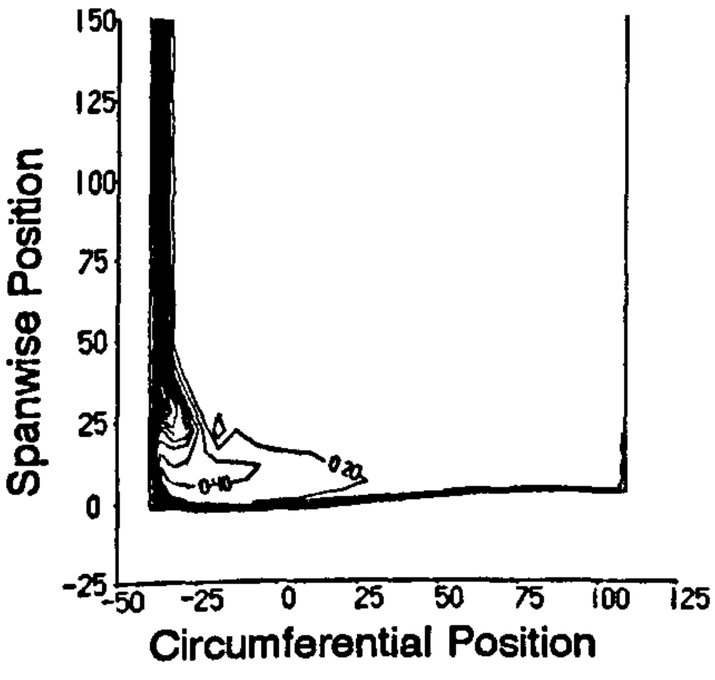

Planar Wall

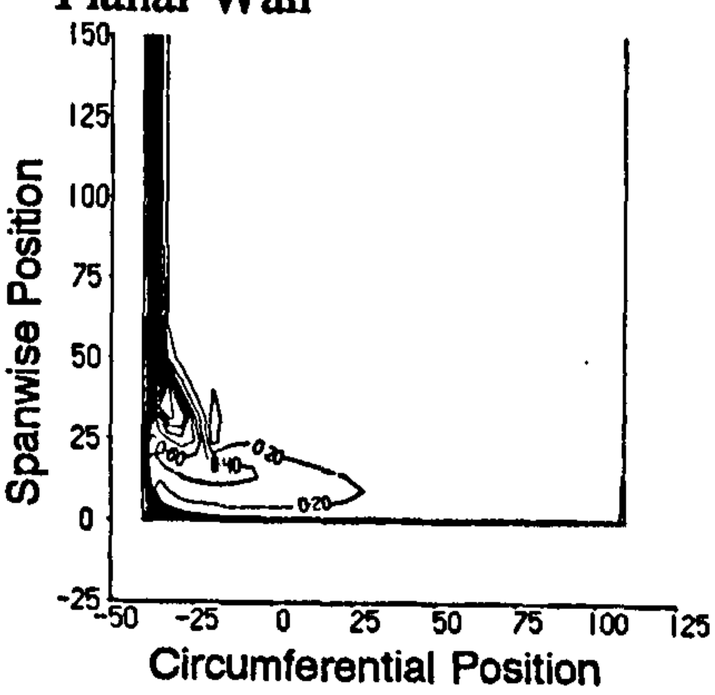

c) Yaw Angle.

FAITH Profile

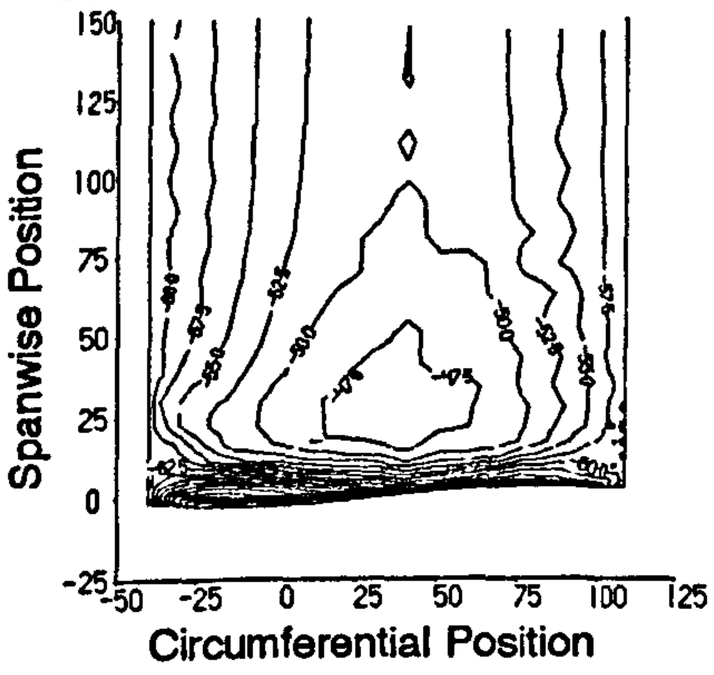

Planar Wall

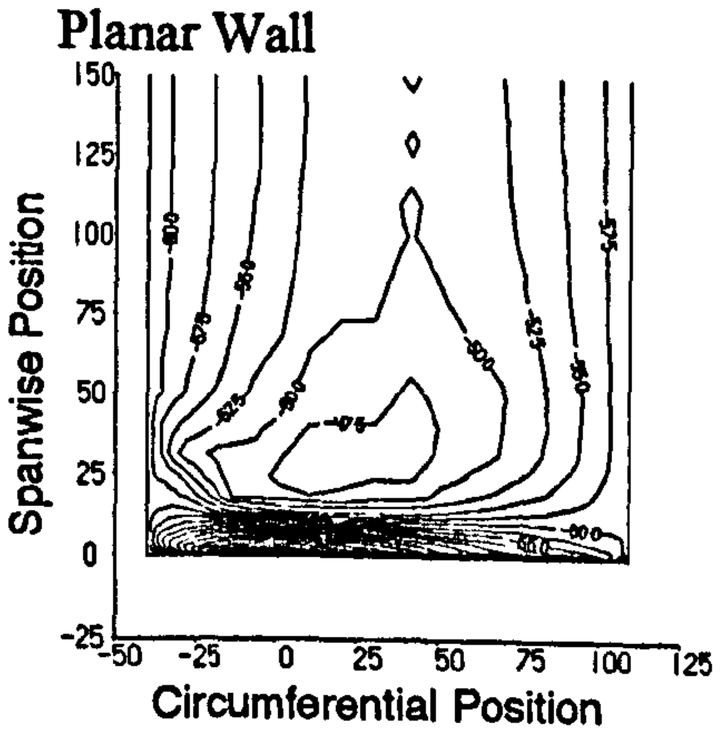

d) Secondary Kinetic Energy Coefficient.

FAITH Profile

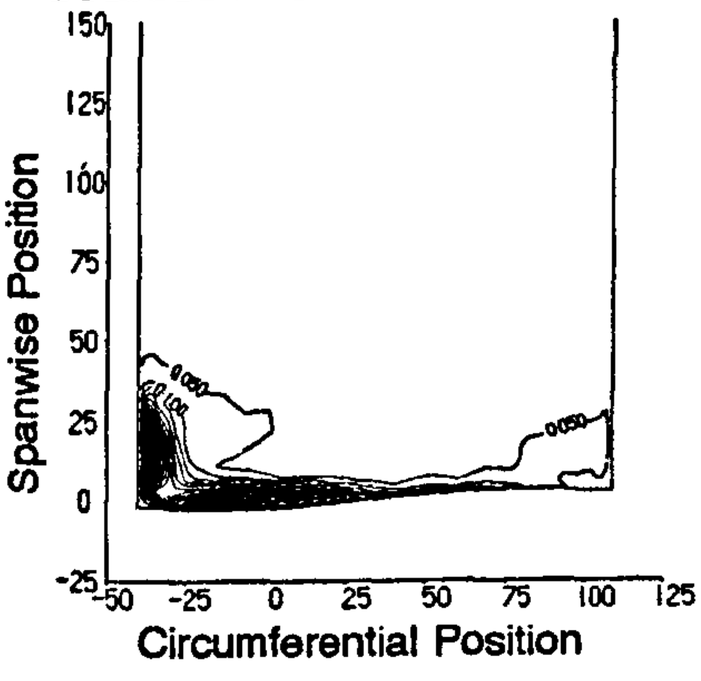

Planar Wall

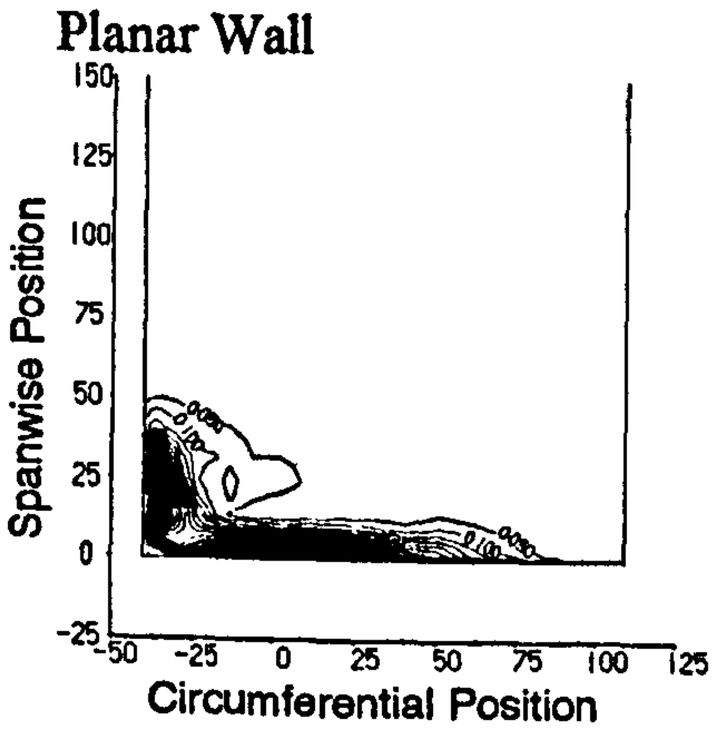

Figure 7.12 CFD Data at Slot 8.

a) Secondary Velocity Vectors.

FAITH Profile

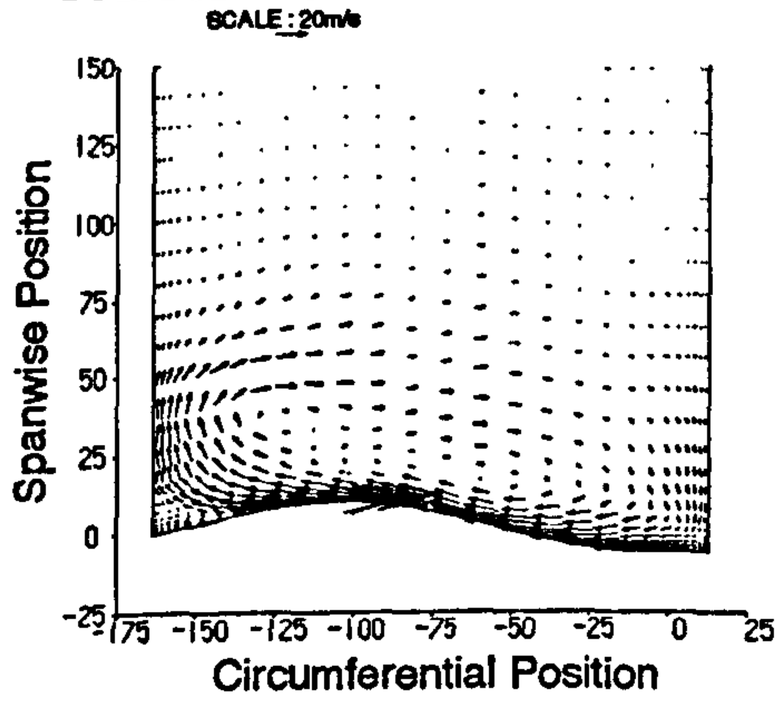

Planar Wall

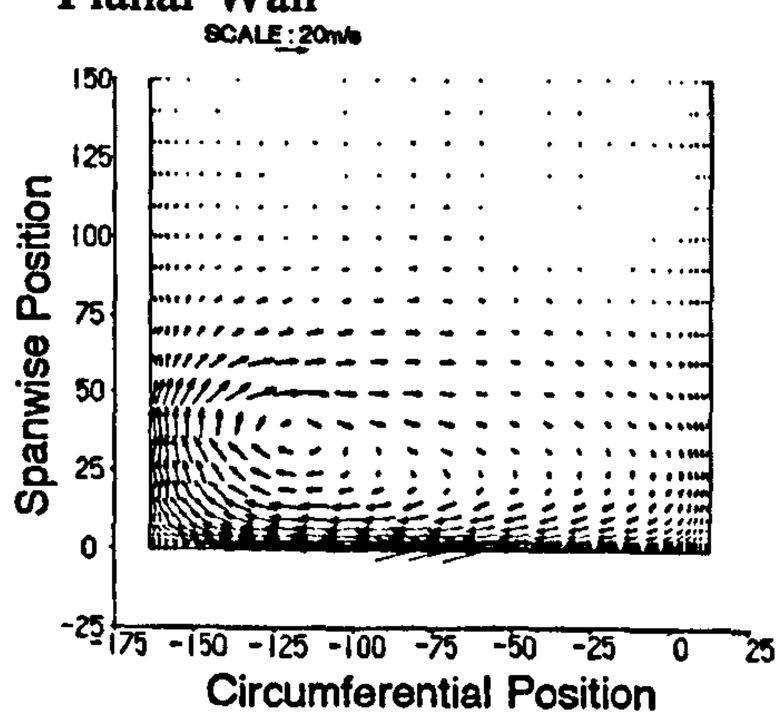

b) Total Pressure Loss Coefficient.

FAITH Profile

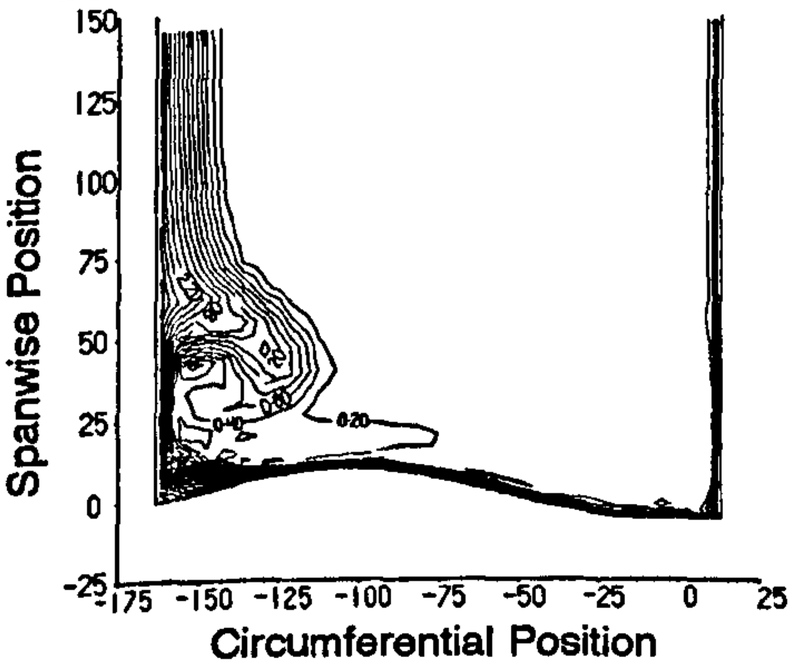

Planar Wall

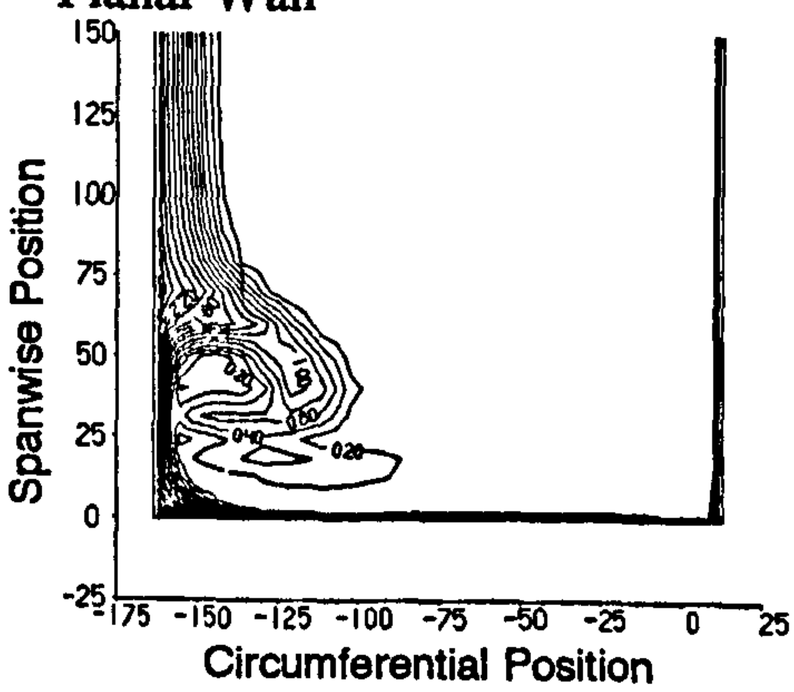

c) Yaw Angle.

FAITH Profile

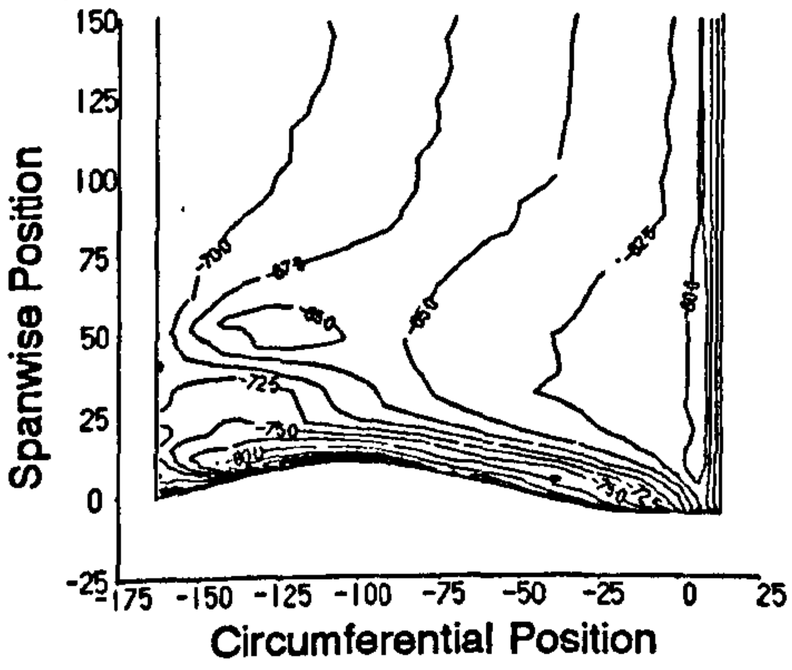

Planar Wall

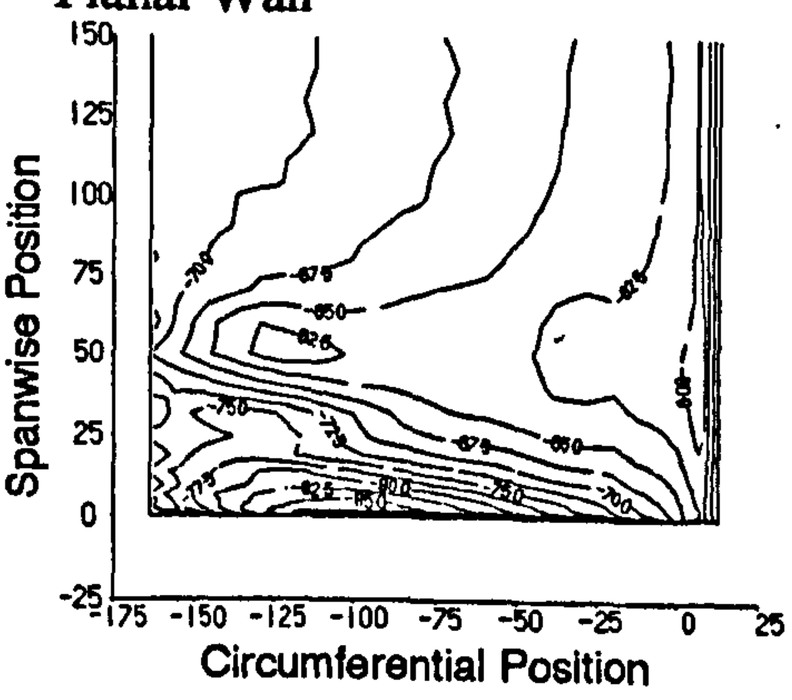

d) Secondary Kinetic Energy Coefficient.

FAITH Profile

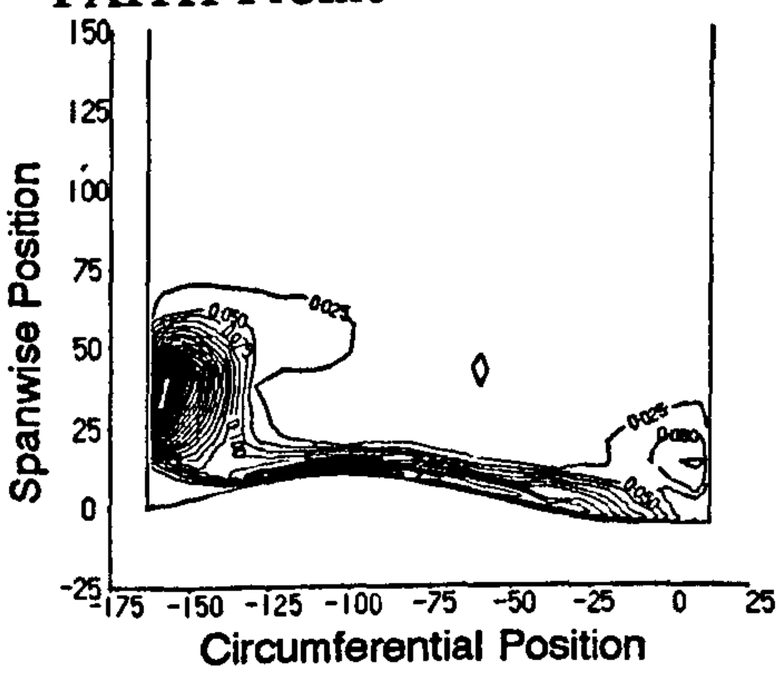

Planar Wall

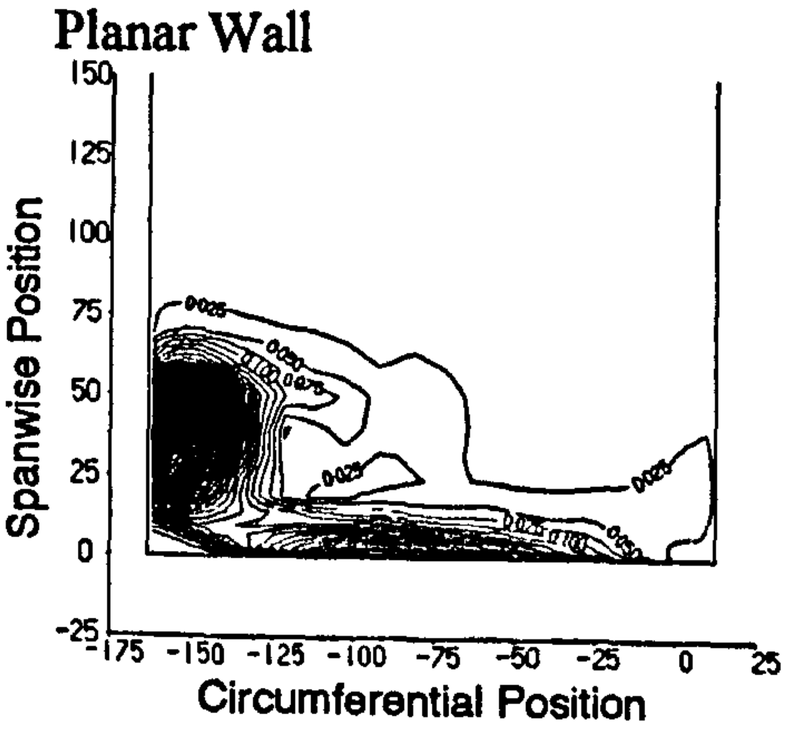

Figure 7.13 CFD Data at Slot 10.

a) Secondary Velocity Vectors.

FAITH Profile

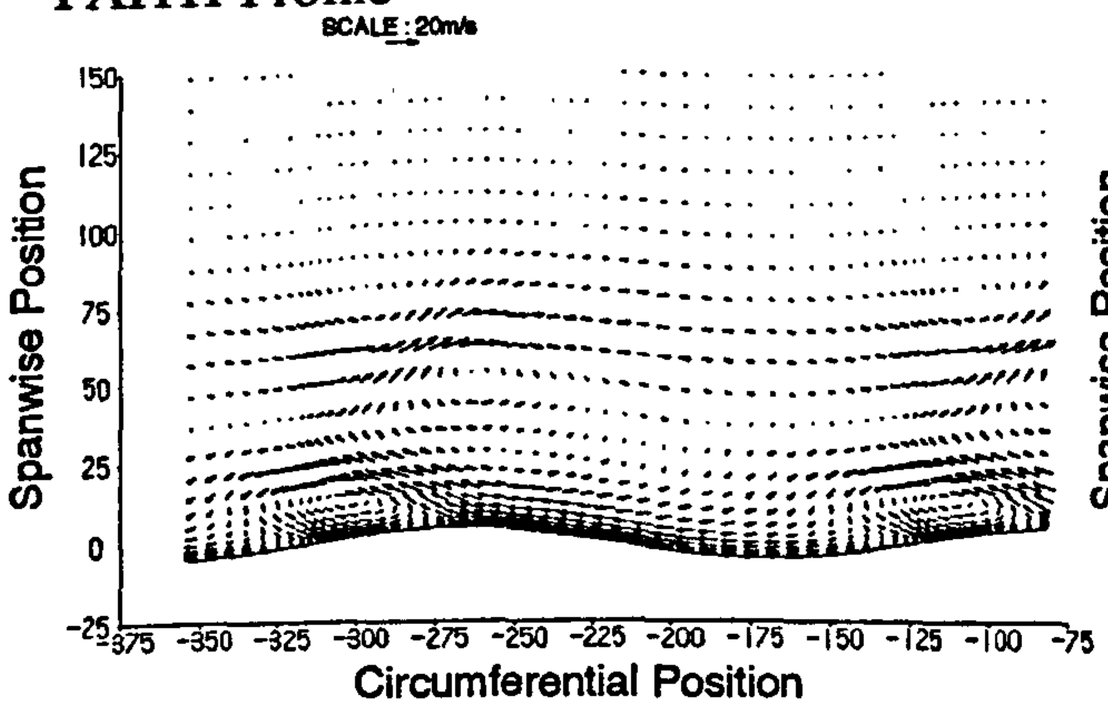

Planar Wall

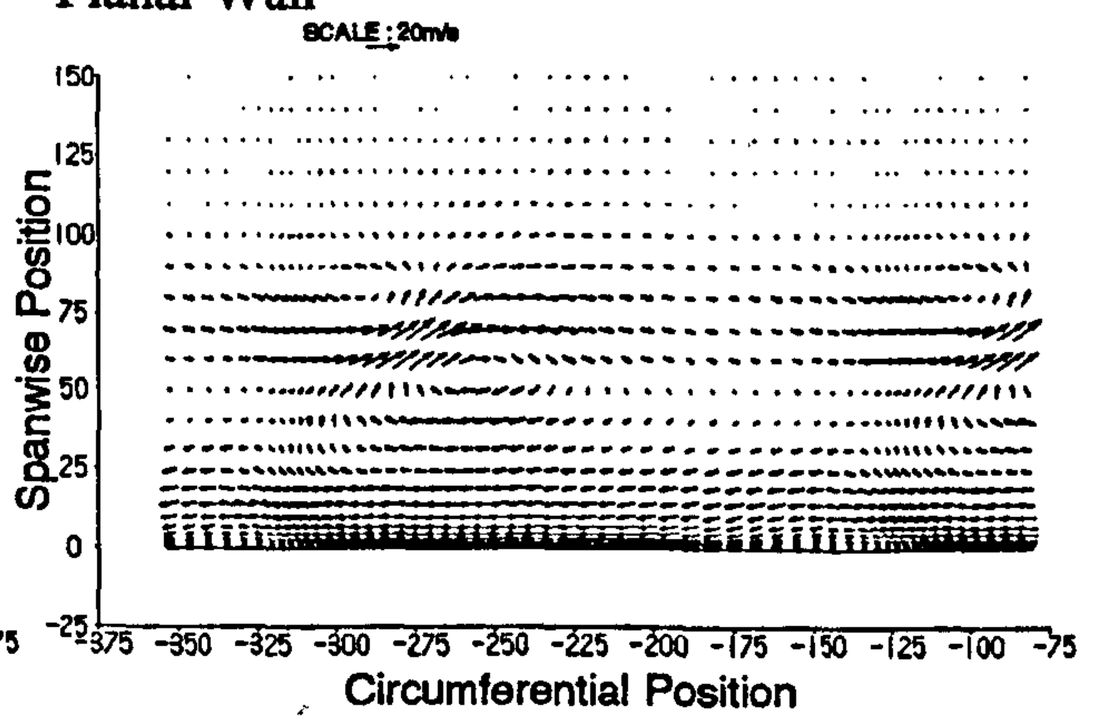

b) Total Pressure Loss Coefficient.

FAITH Profile

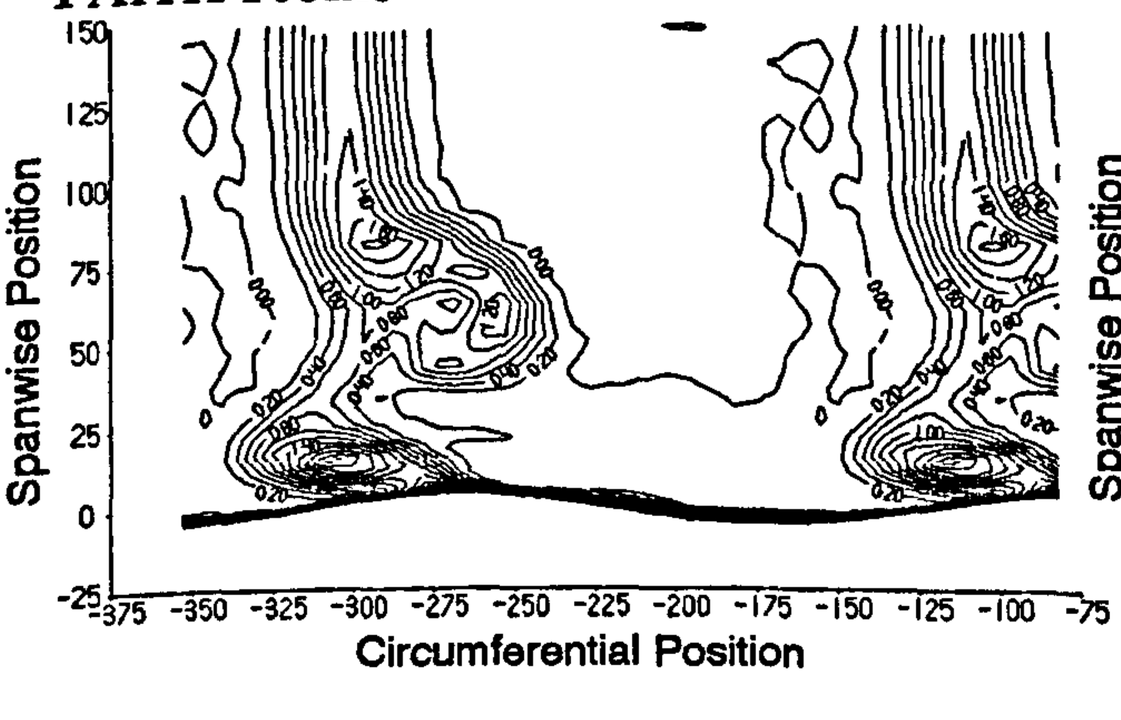

Planar Wall

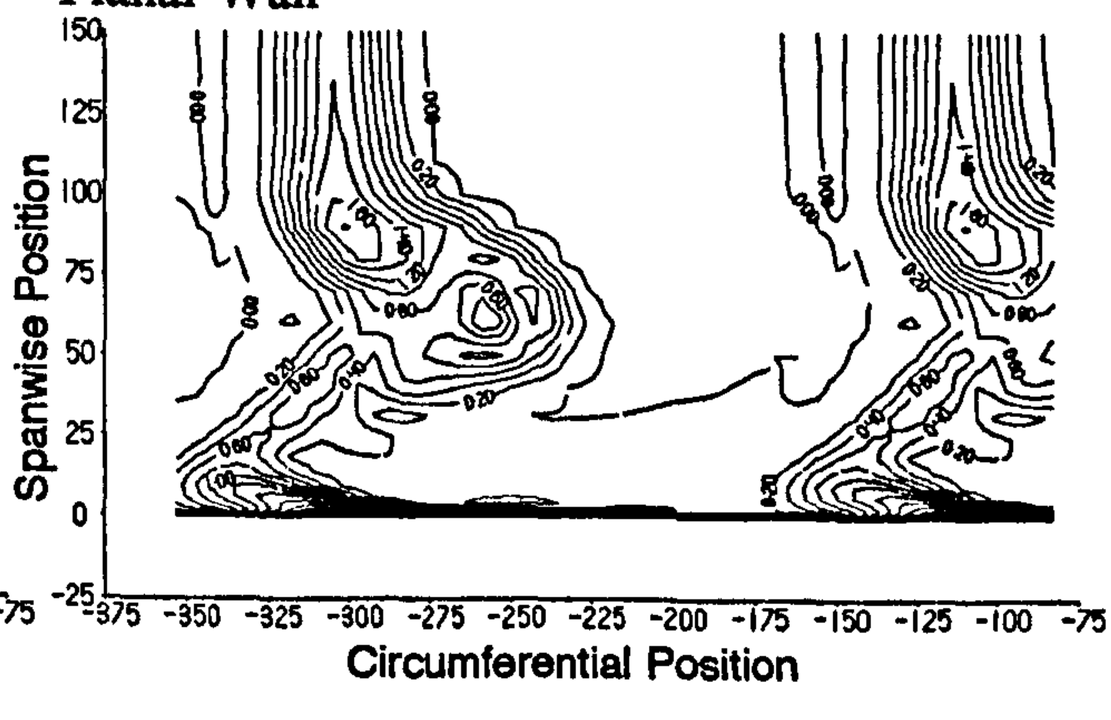

c) Yaw Angle.

FAITH Profile

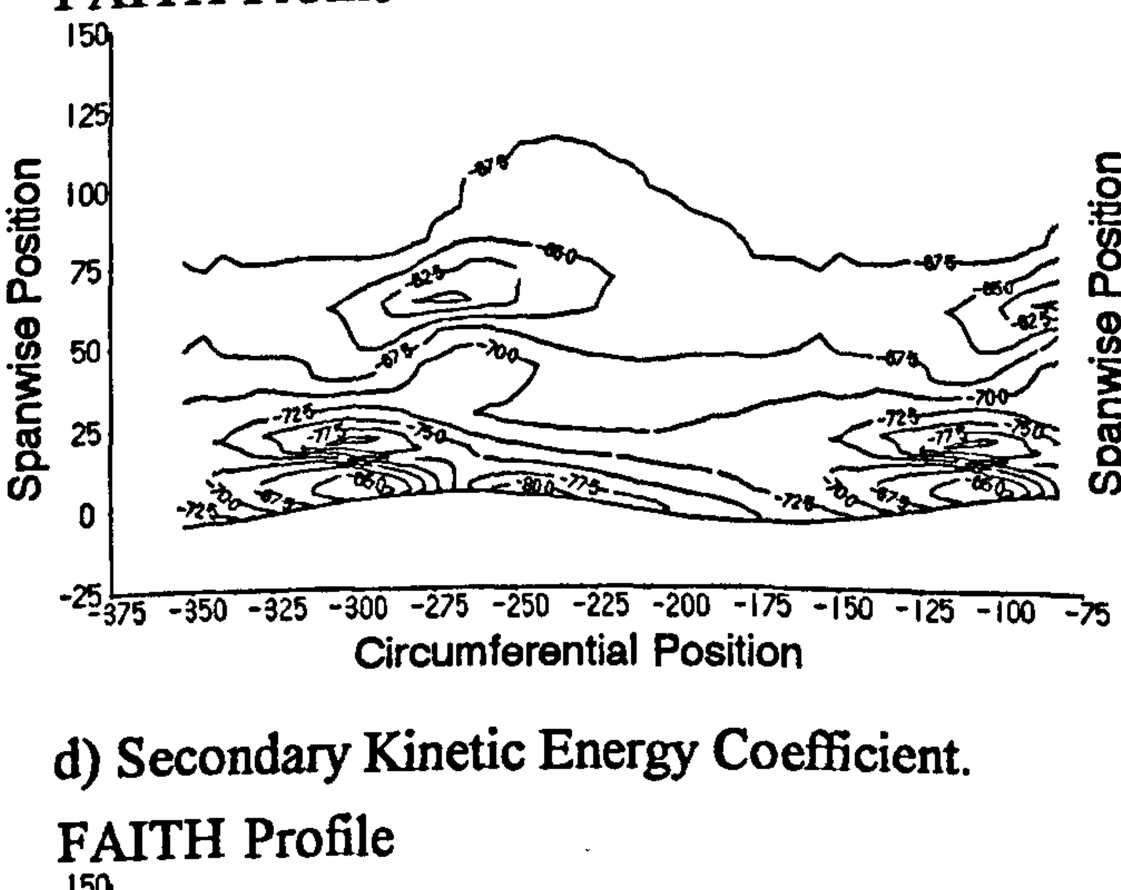

Planar Wall

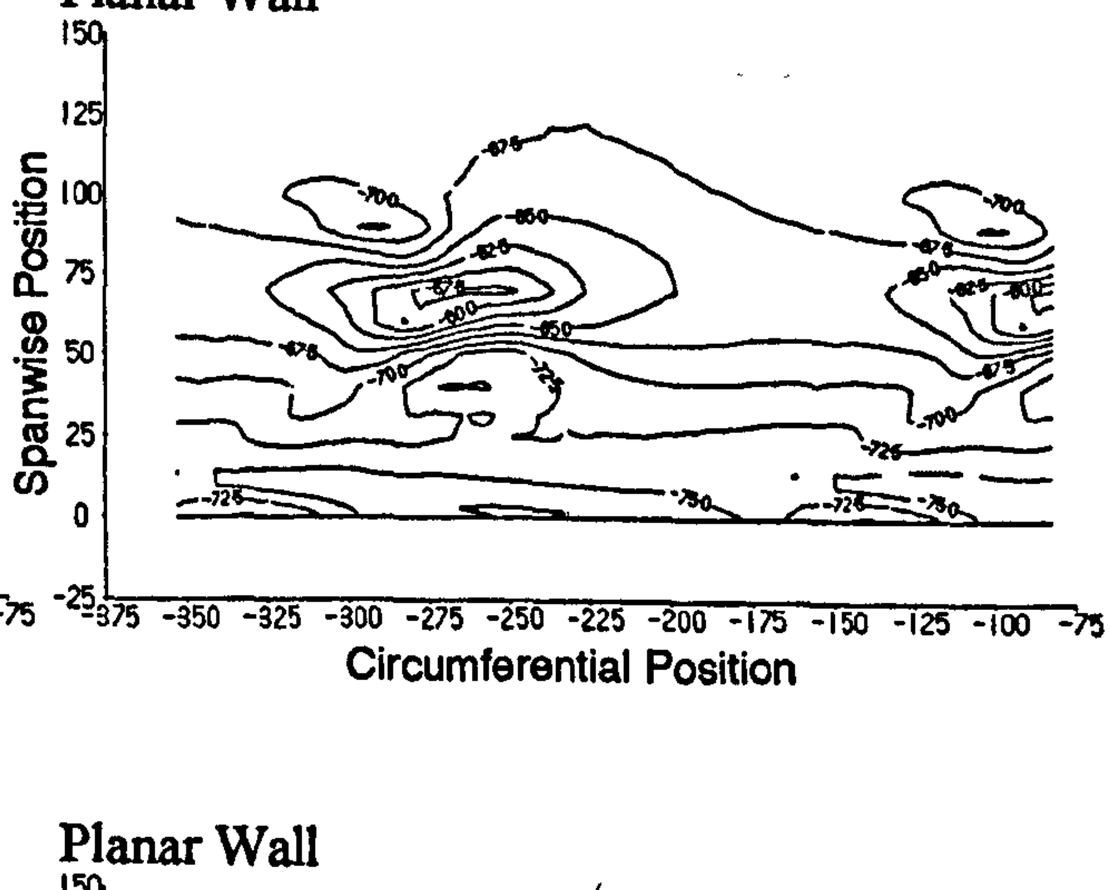

d) Secondary Kinetic Energy Coefficient.

FAITH Profile

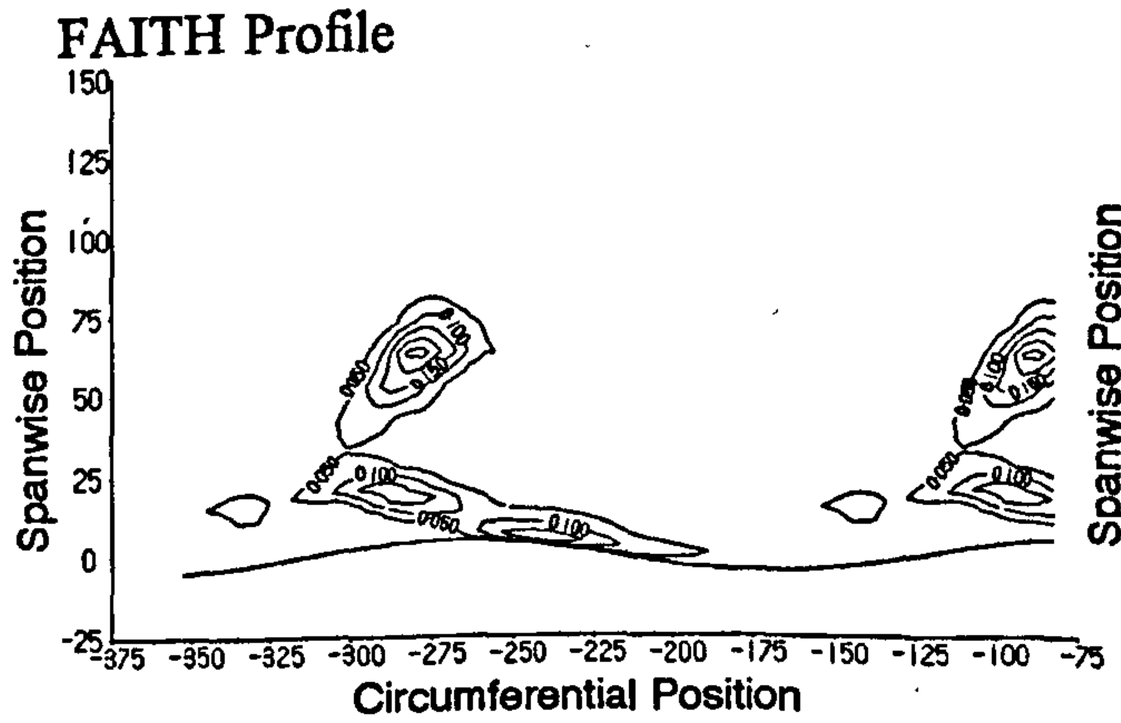

Planar Wall

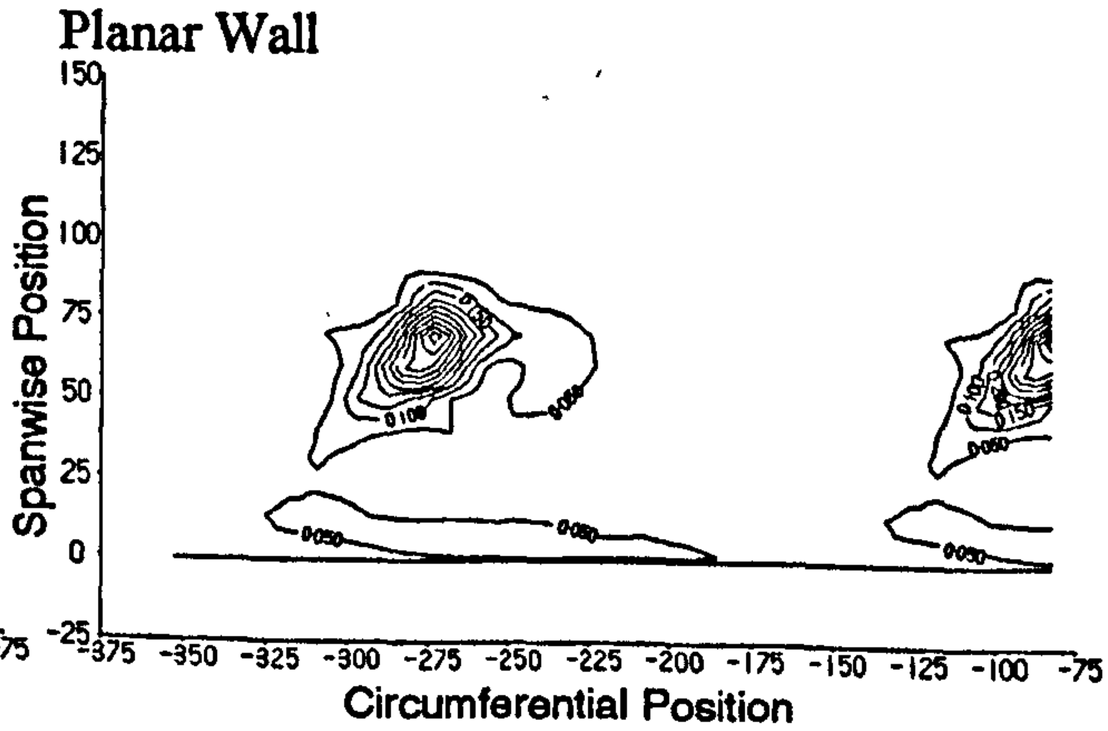

Figure 7.14 Pitch Averaged Compensated CFD C_{SKE} Through the Cascade.

Slot 1

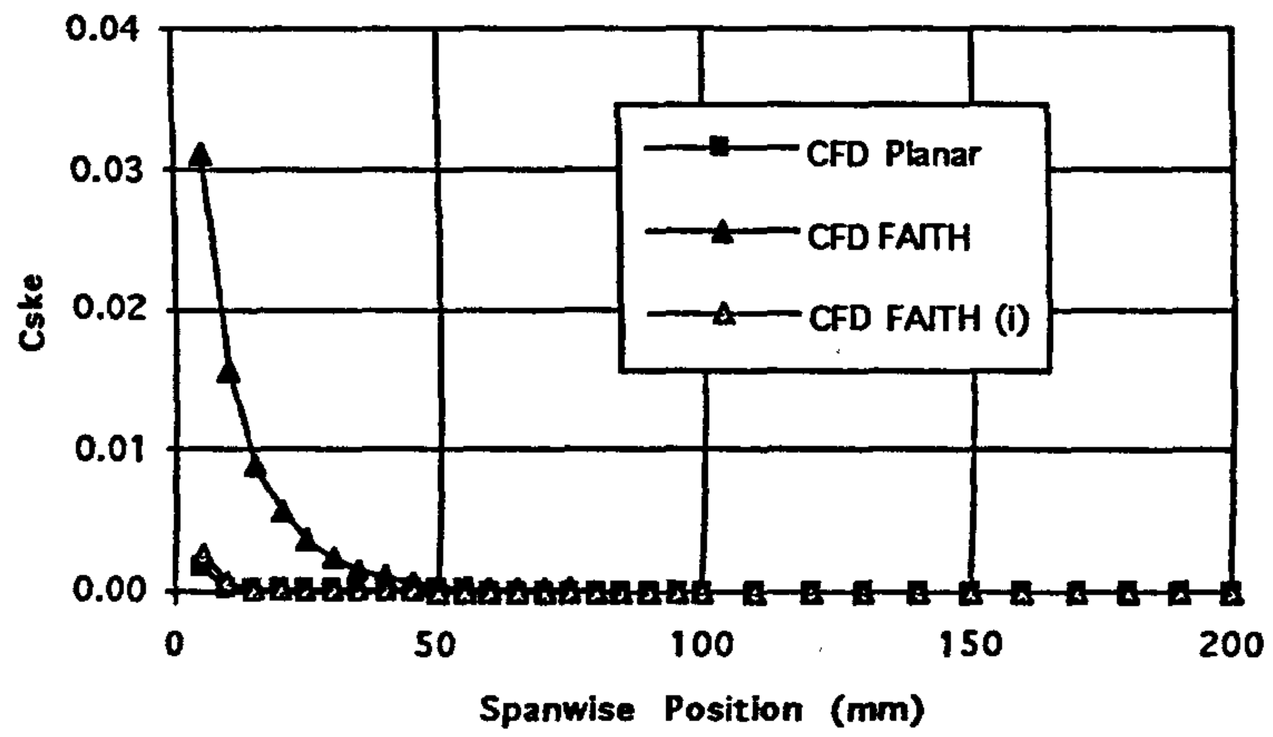

Slot 6

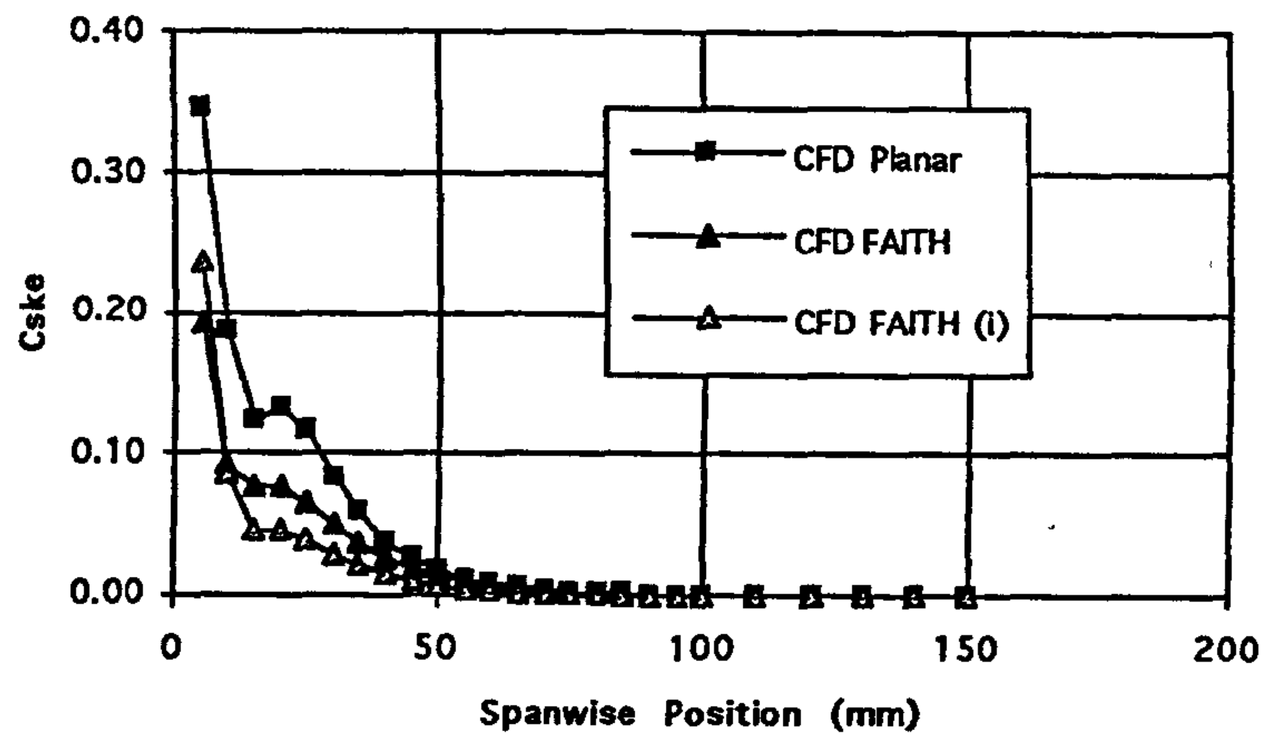

Slot 8

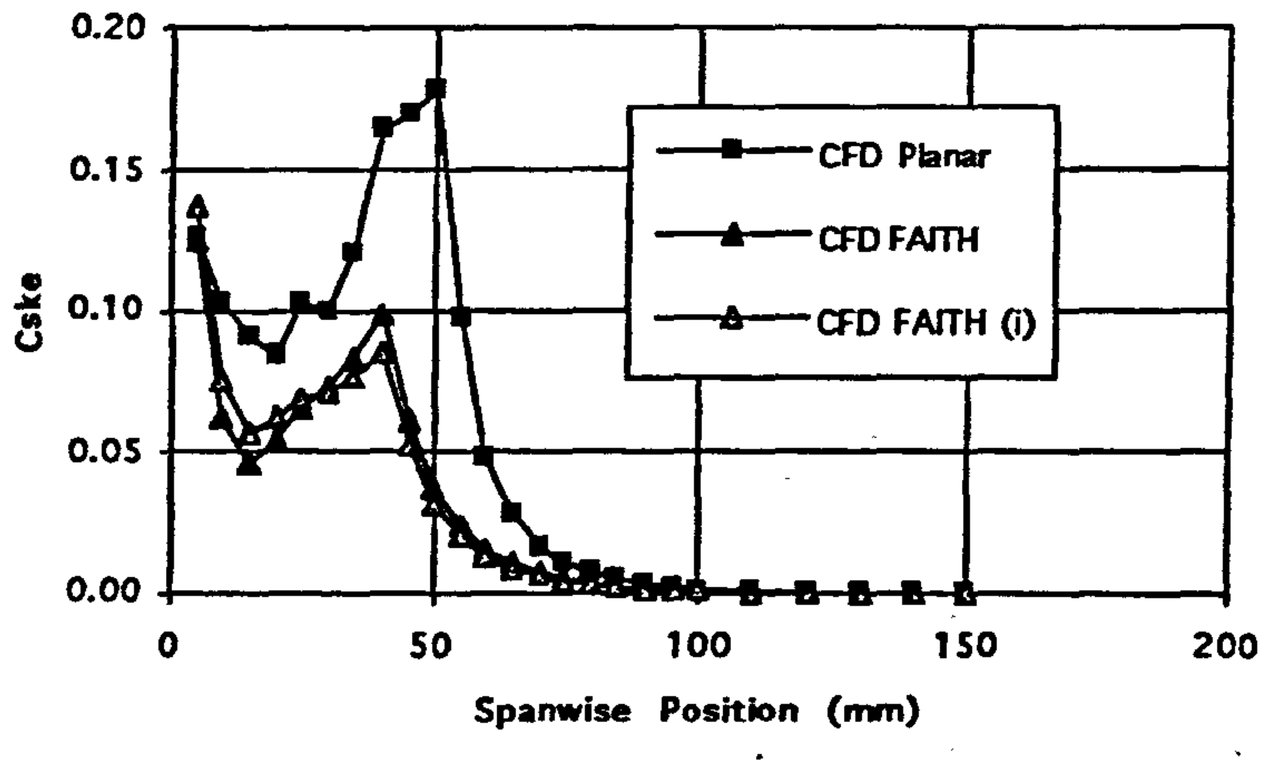

Slot 10

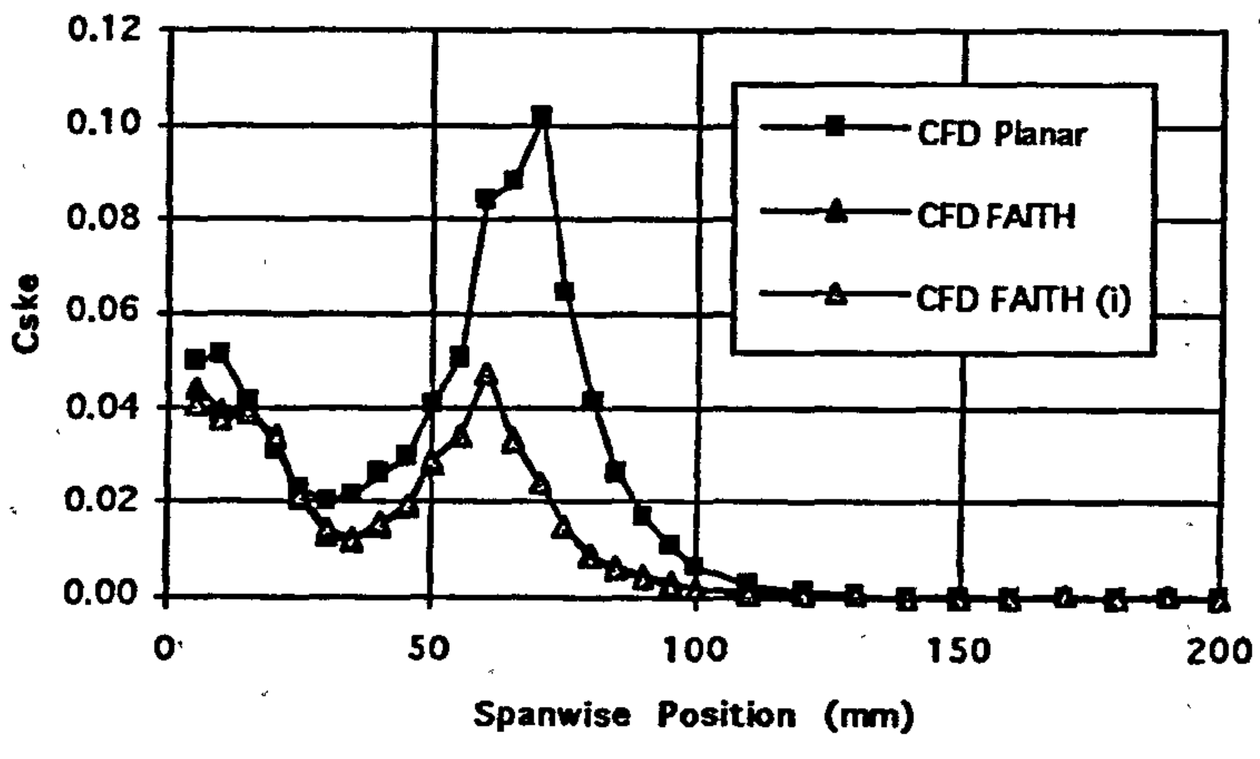

Figure 7.15 Experimental End-wall C_p Contours.

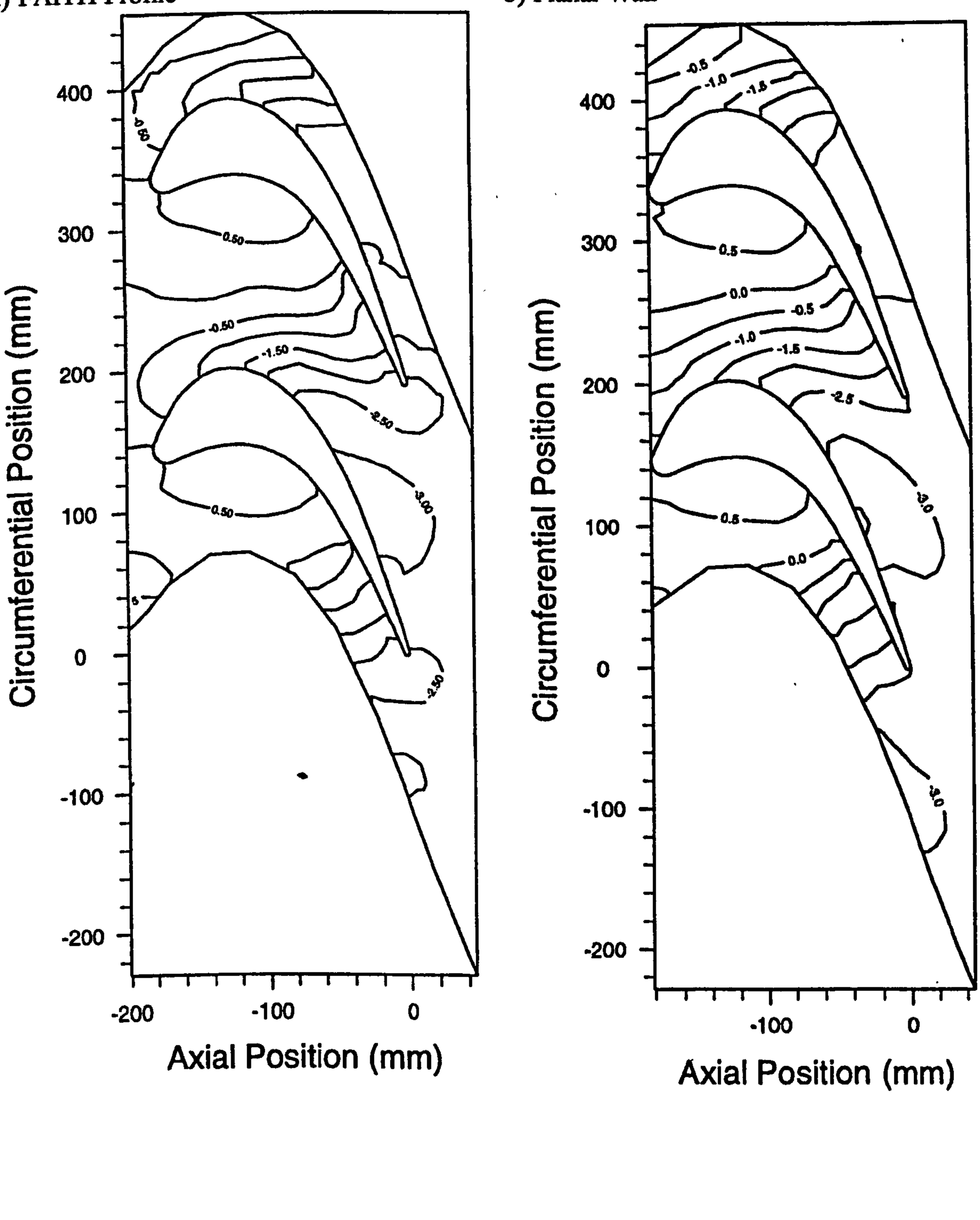

Figure 7.16 Measured Total Pressure Coefficient 100% C_{ax} Upstream.

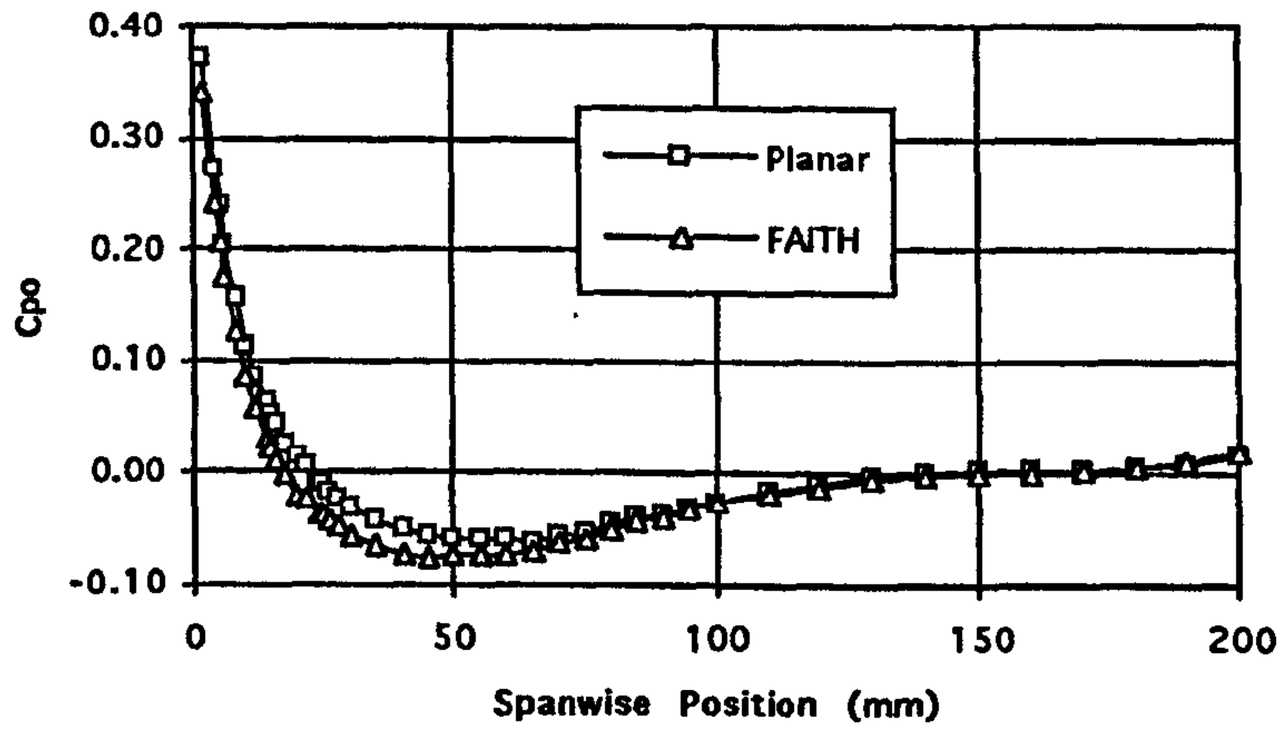

Figure 7.17 Pitch Averaged Experimental Data at Slot 1 (Planar Wall and CFD Data Included for Comparison).

a) Total Pressure Loss Coefficient.

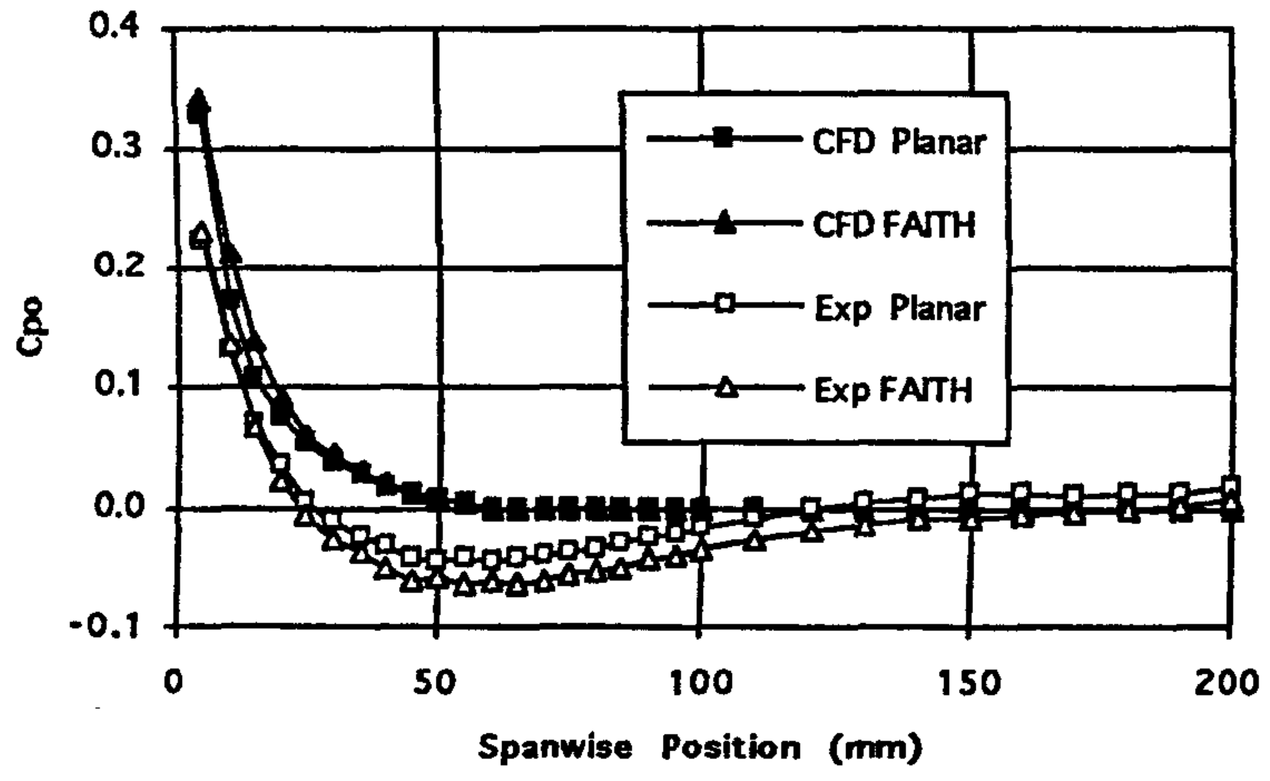

b) Yaw Angle.

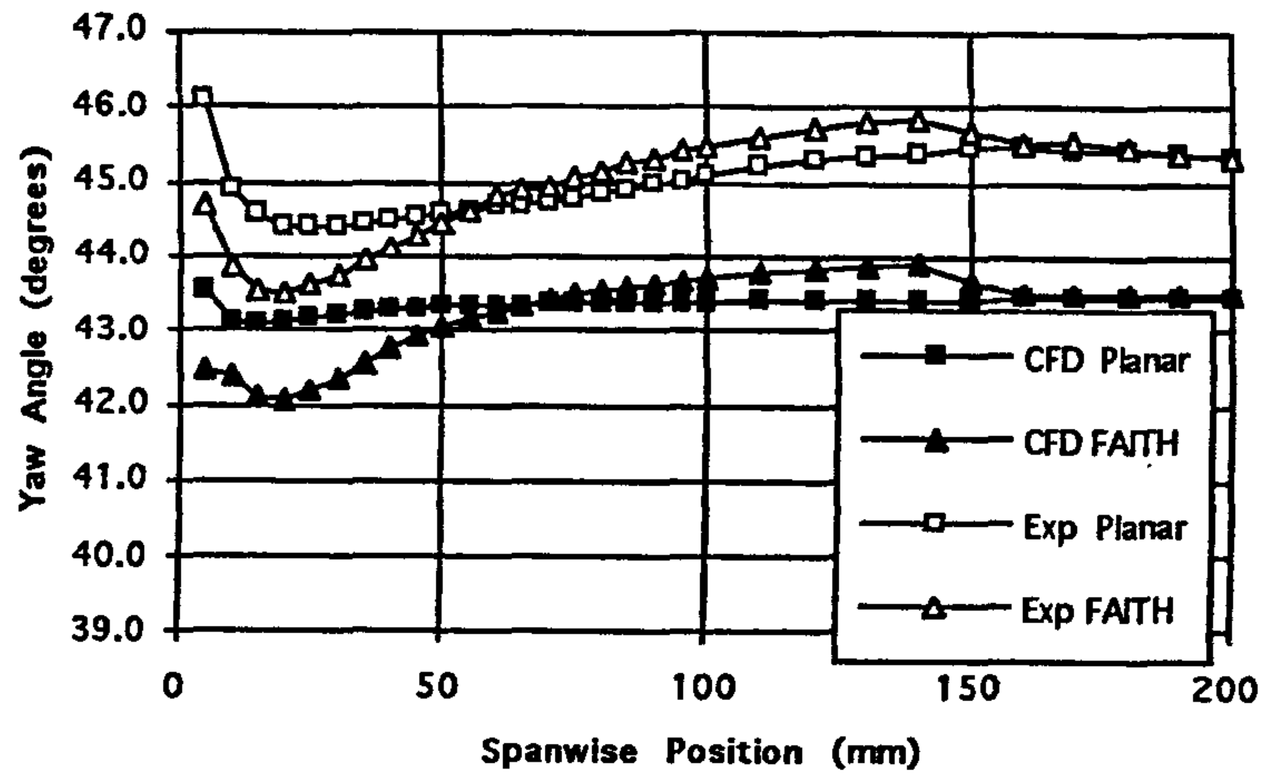

c) Pitch Angle.

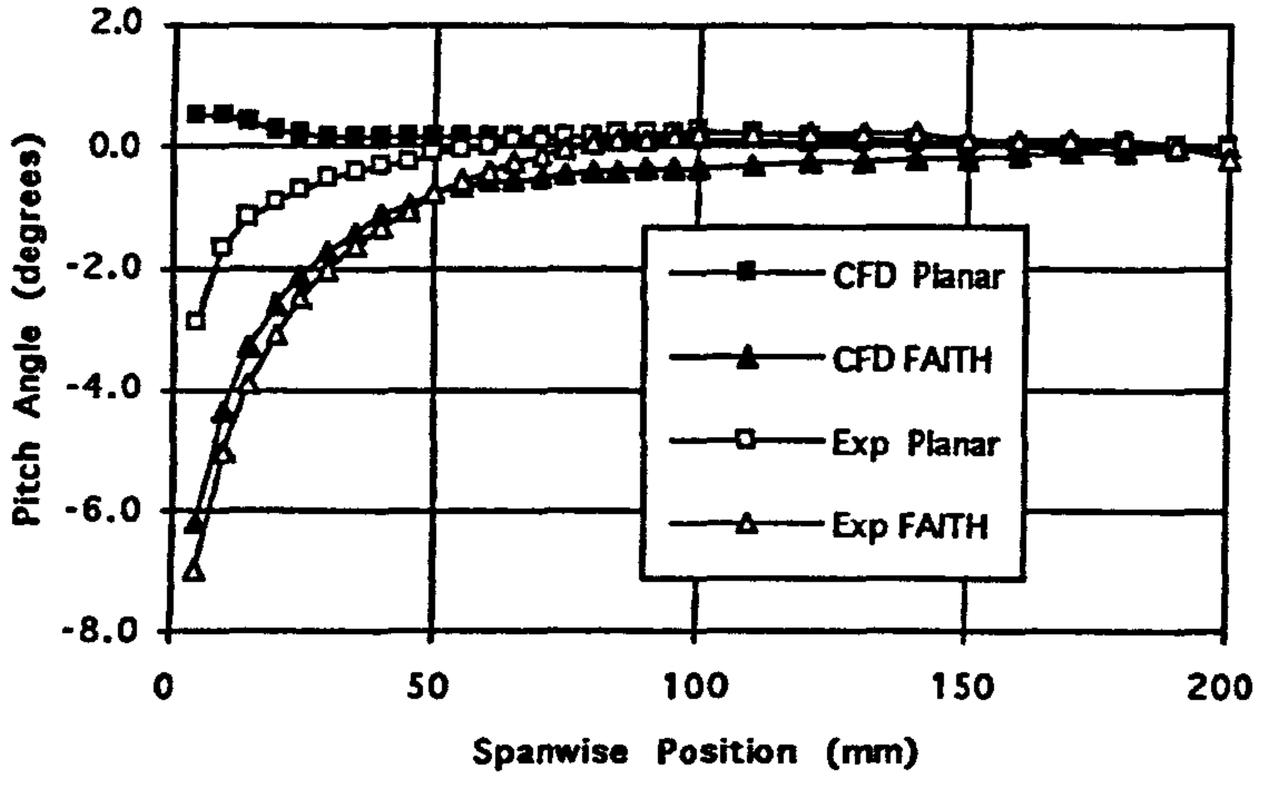

d) Secondary Kinetic Energy Coefficient.

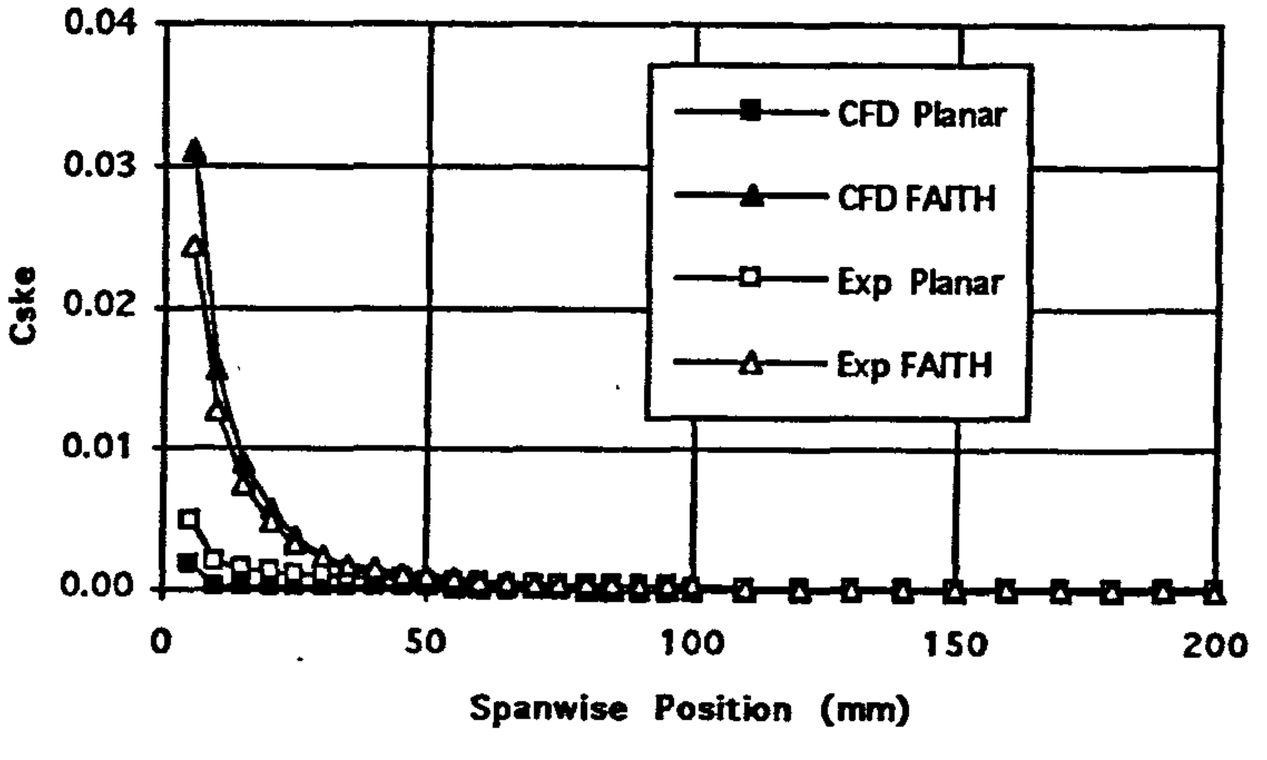

Figure 7.18 Pitch Averaged Experimental Data at Slot 6 (Planar Wall and CFD Data Included for Comparison).

a) Total Pressure Loss Coefficient.

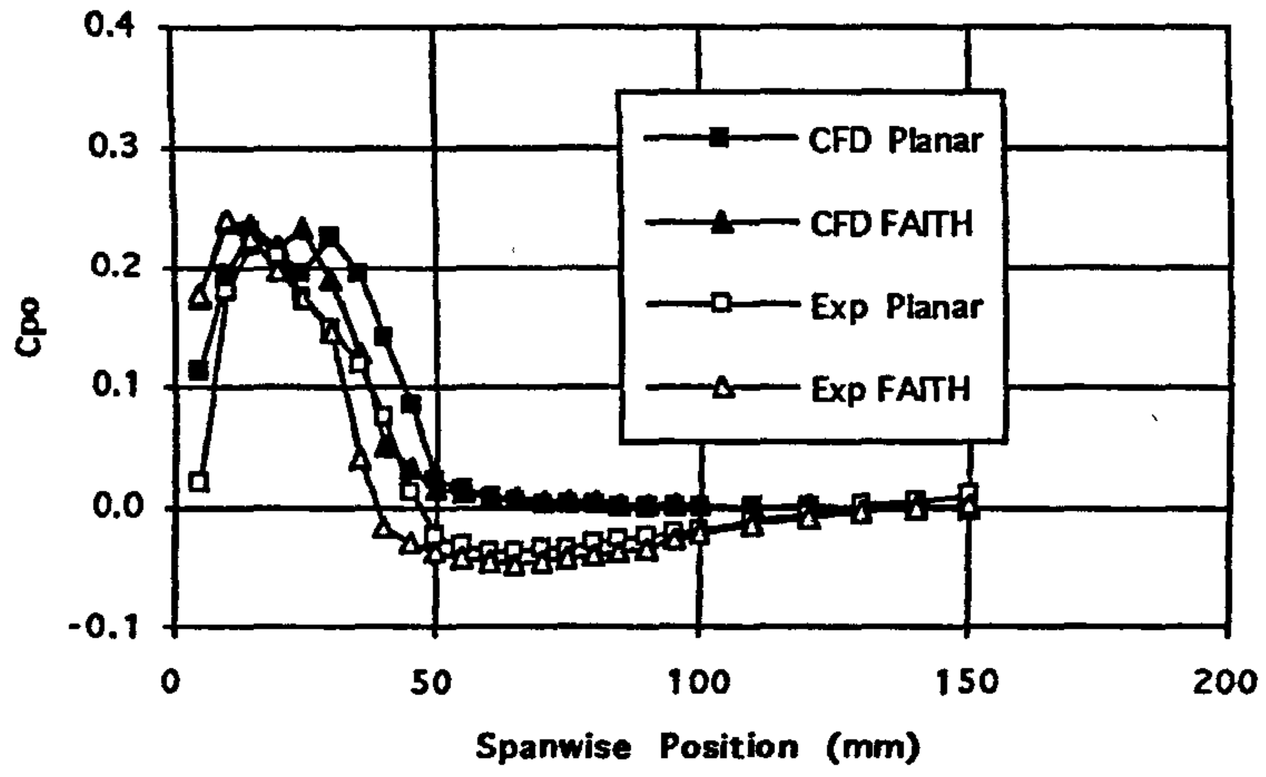

b) Yaw Angle.

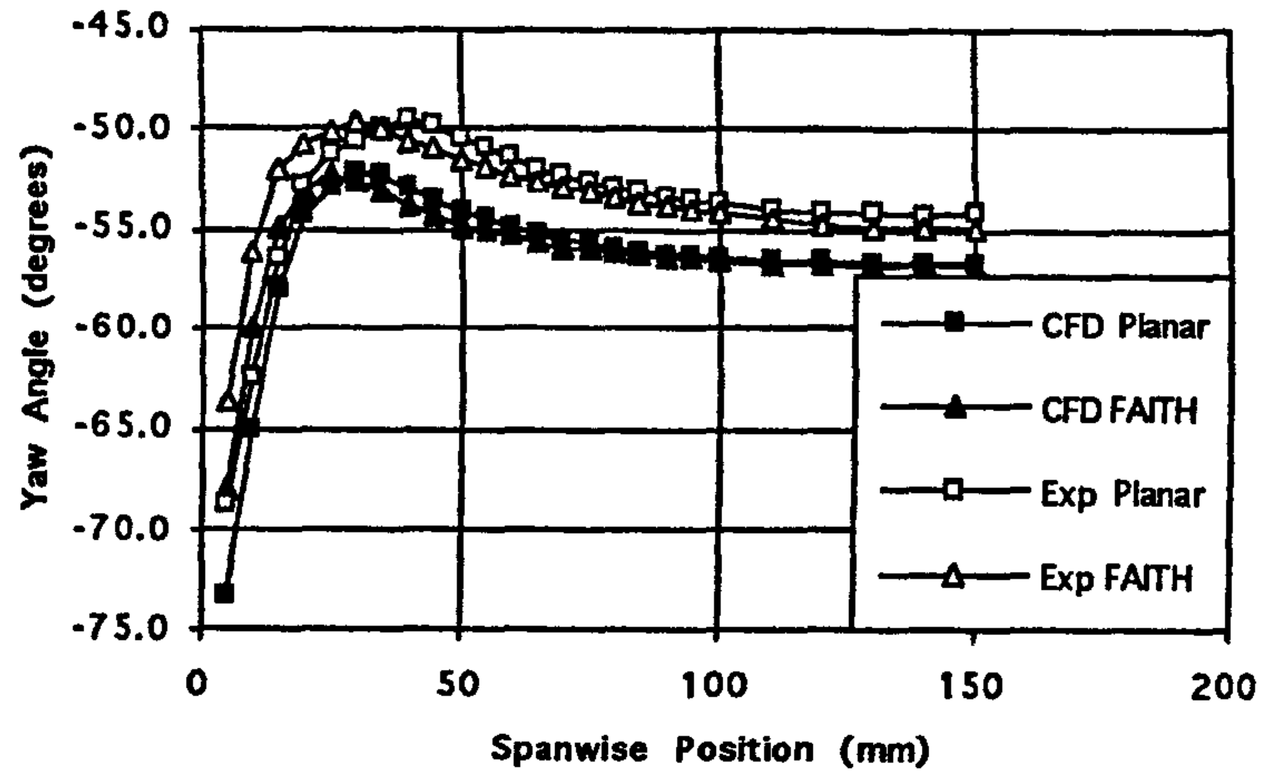

c) Pitch Angle.

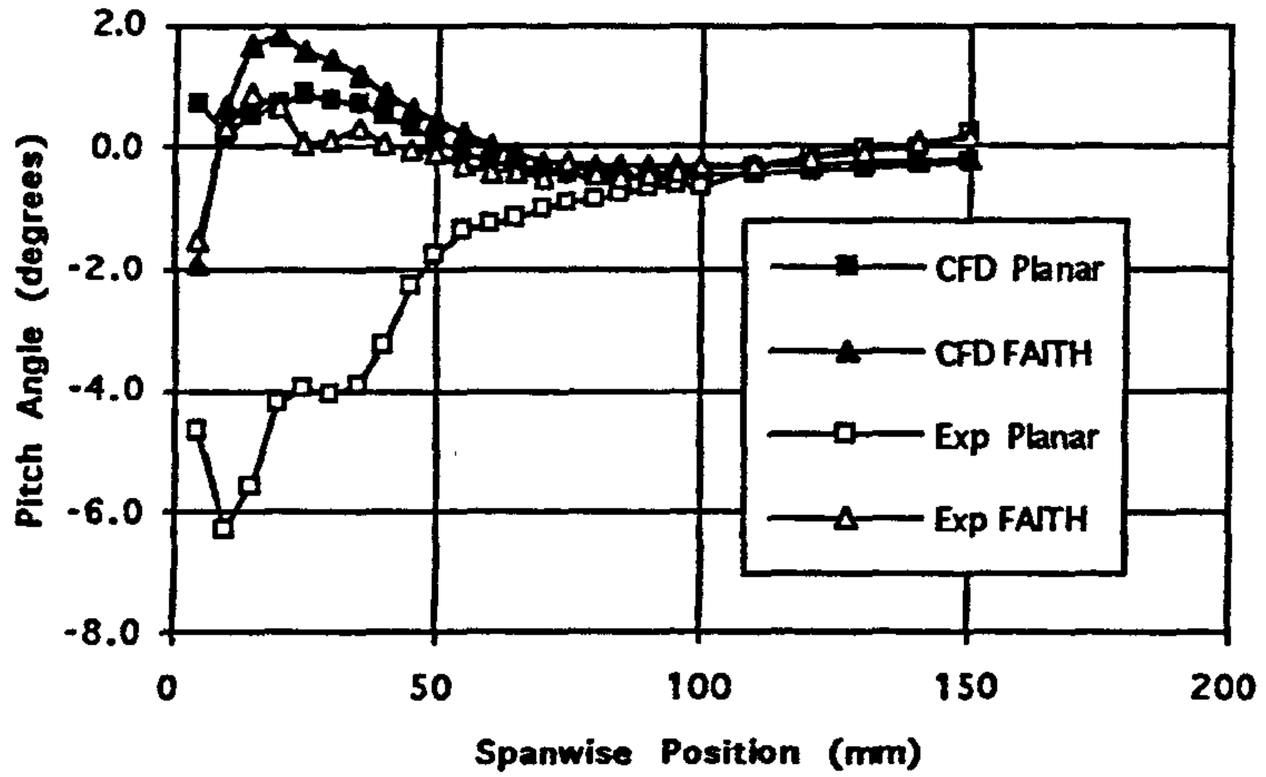

d) Secondary Kinetic Energy Coefficient.

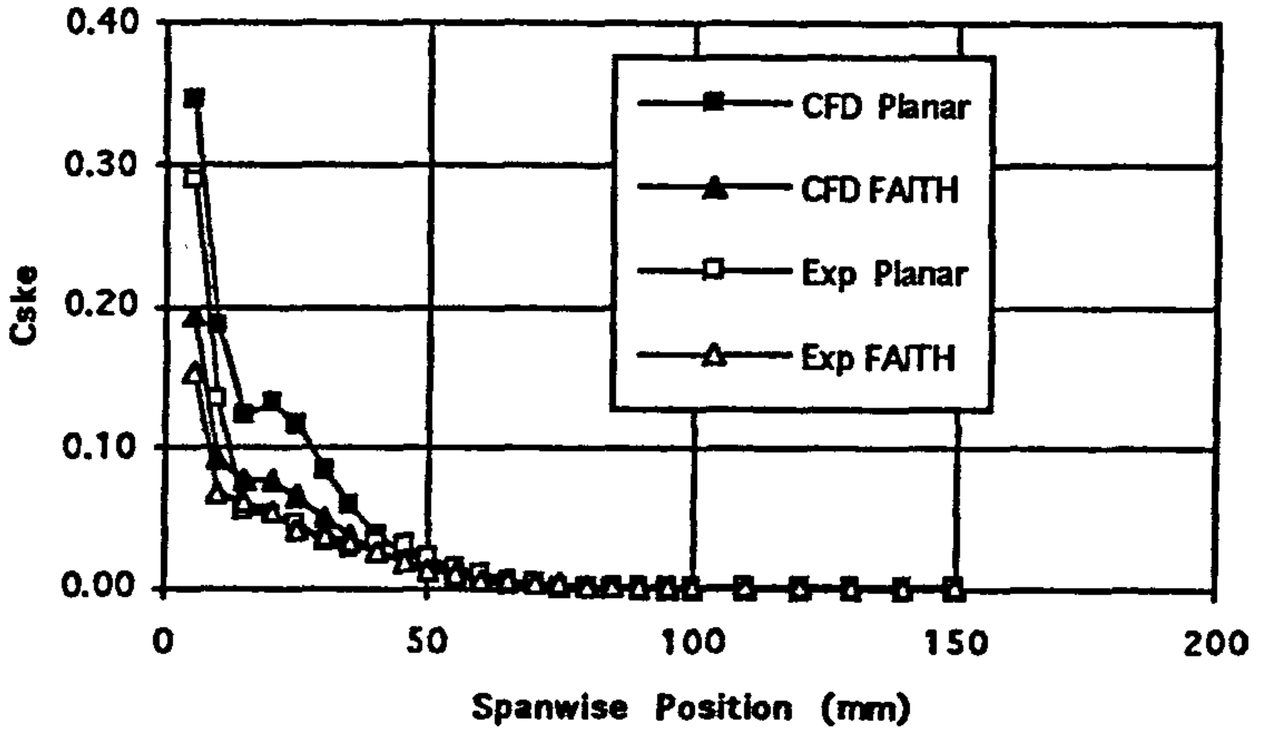

Figure 7.19 Pitch Averaged Experimental Data at Slot 8 (Planar Wall and CFD Data Included for Comparison).

a) Total Pressure Loss Coefficient.

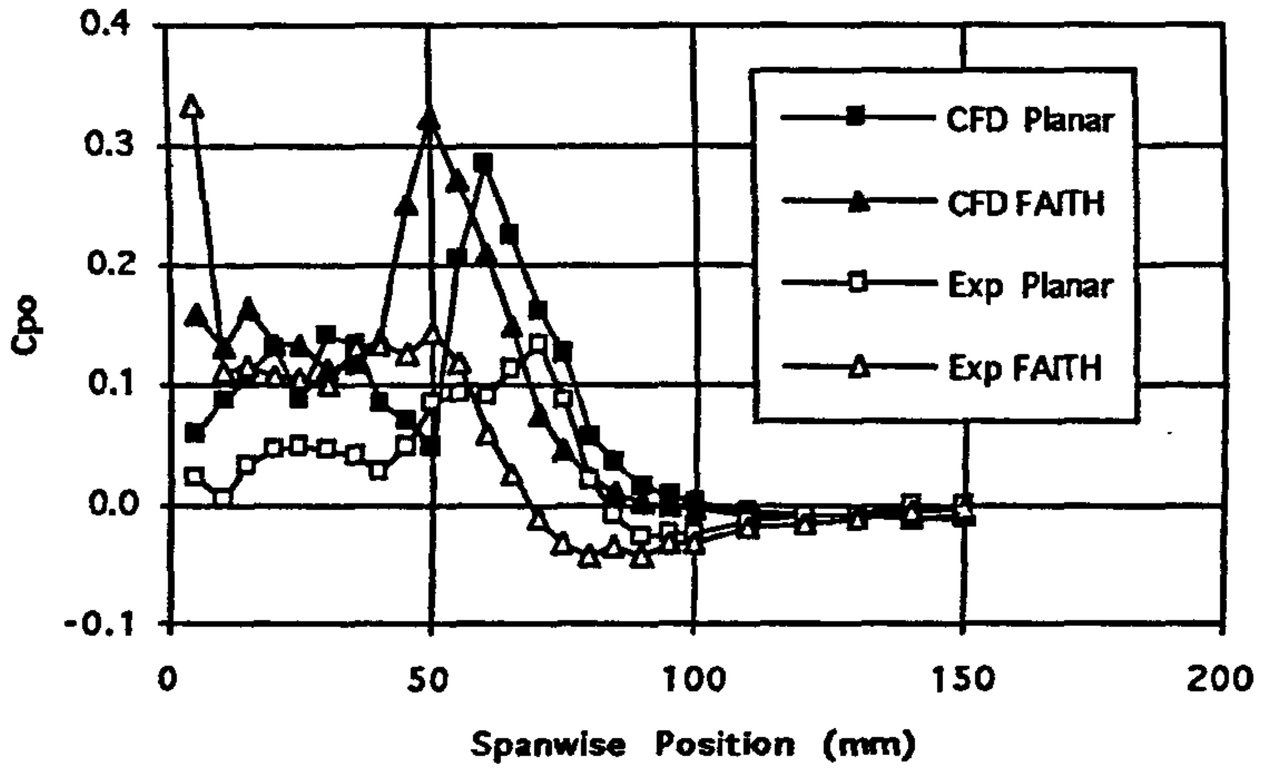

b) Yaw Angle.

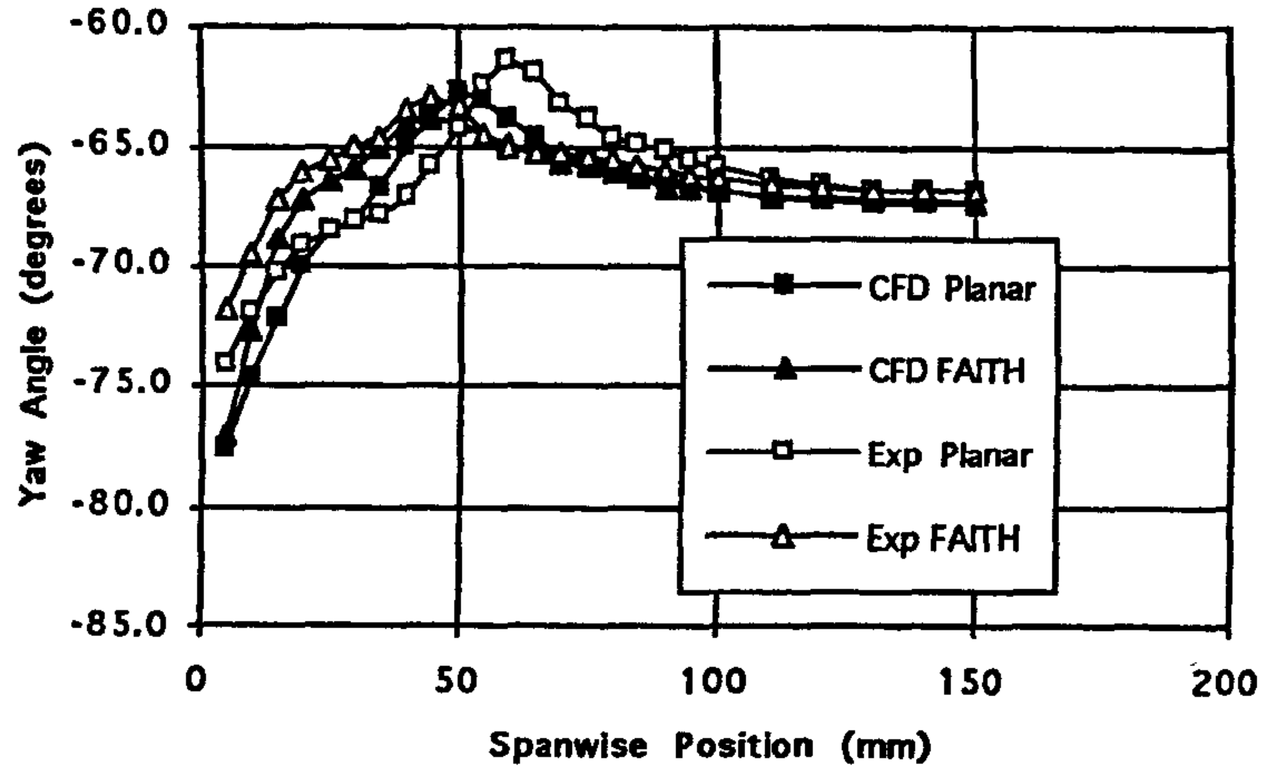

c) Pitch Angle.

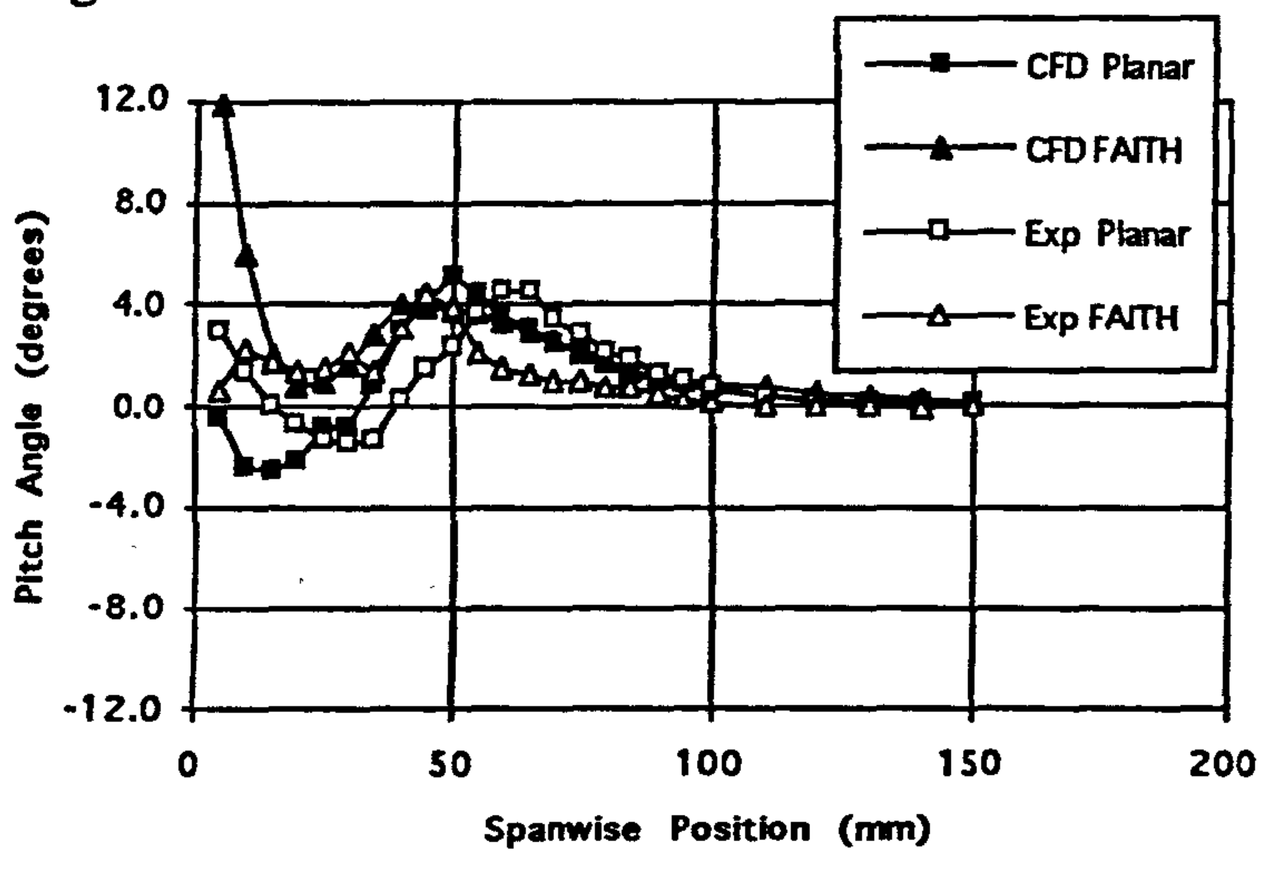

d) Secondary Kinetic Energy Coefficient.

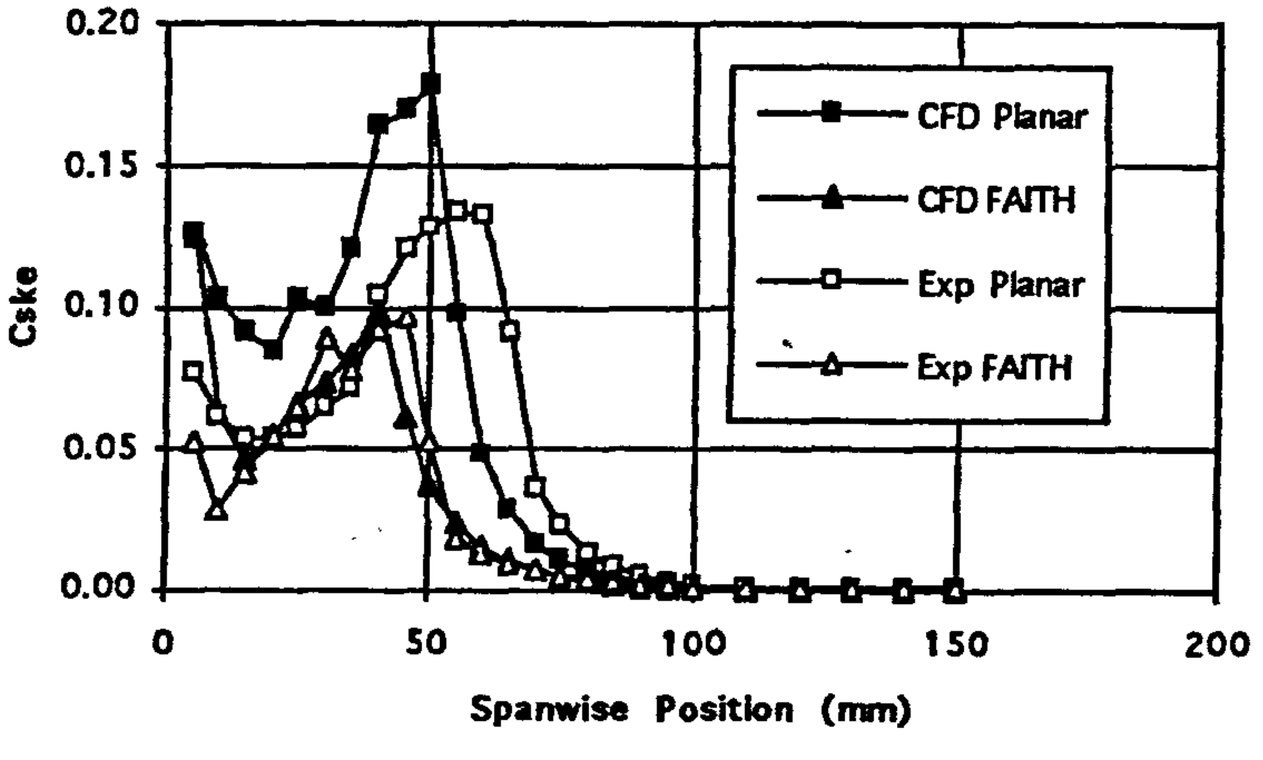

Figure 7.20 Pitch Averaged Experimental Data at Slot 10 (Planar Wall and CFD Data Included for Comparison).

a) Total Pressure Loss Coefficient.

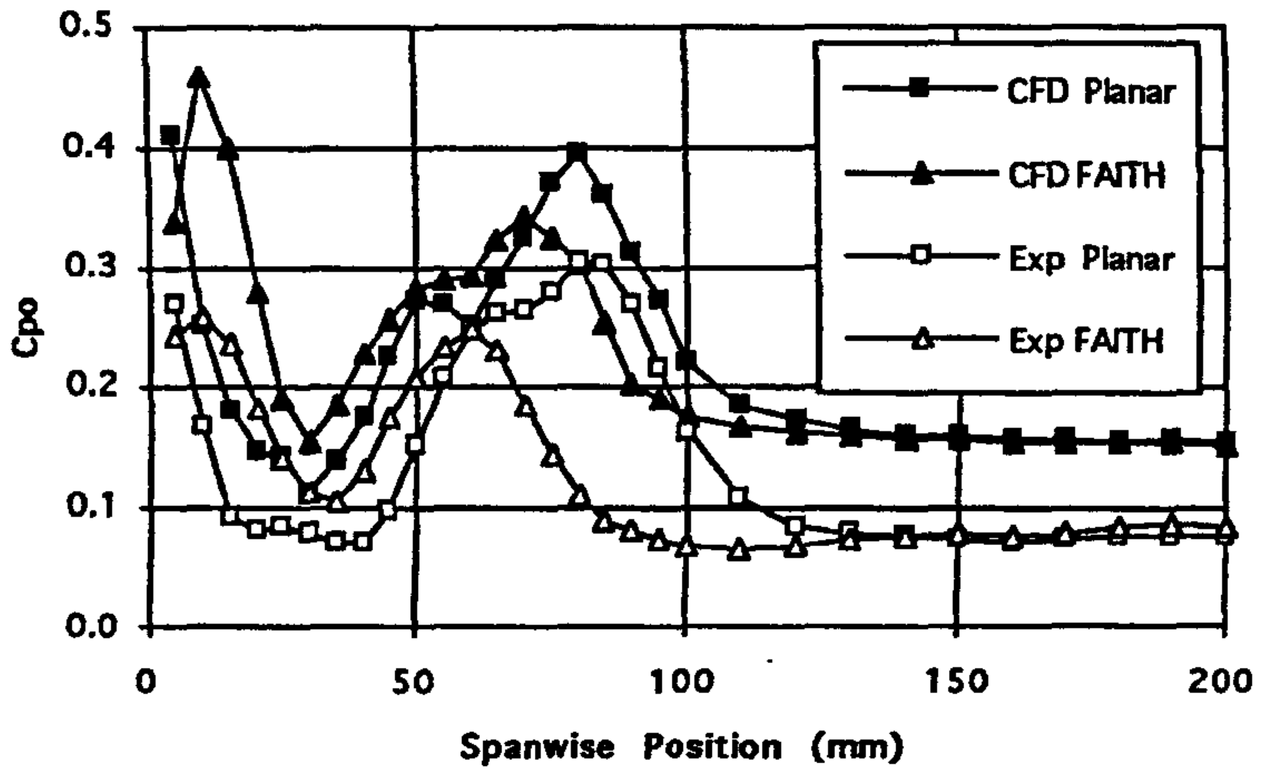

b) Yaw Angle.

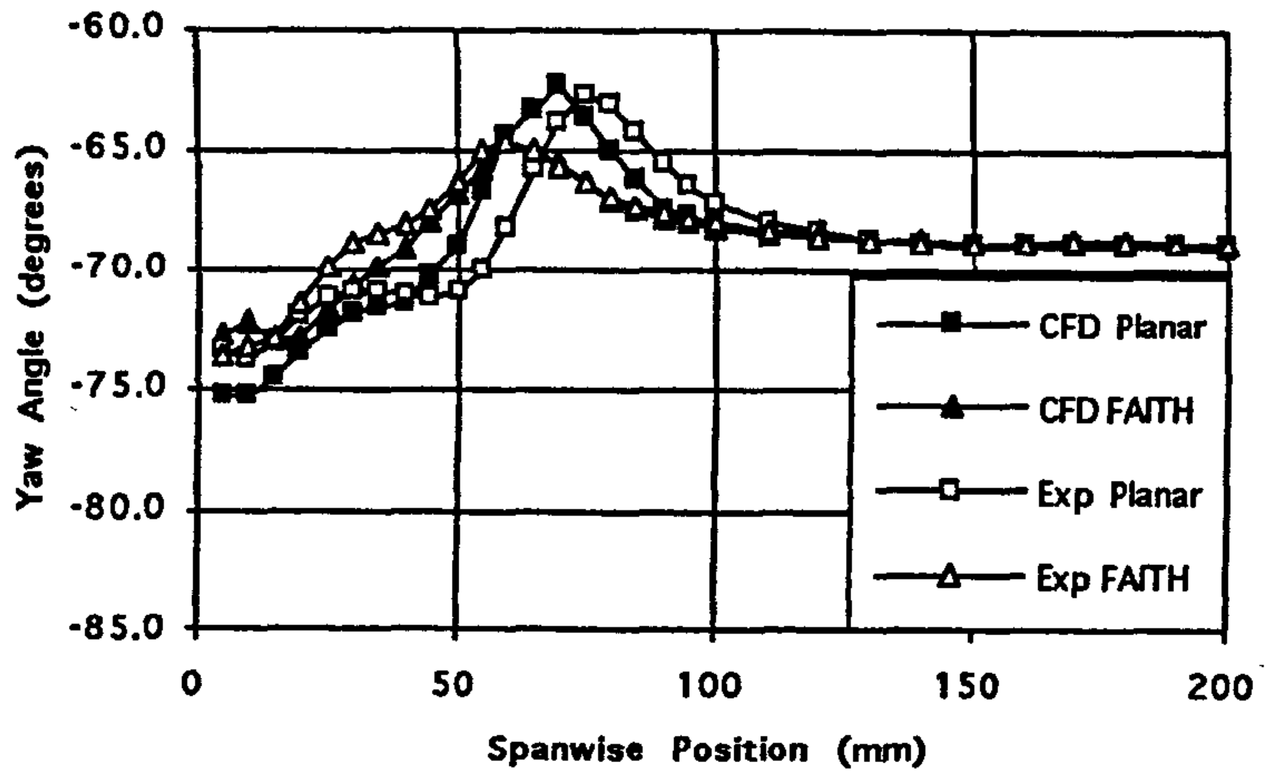

c) Pitch Angle.

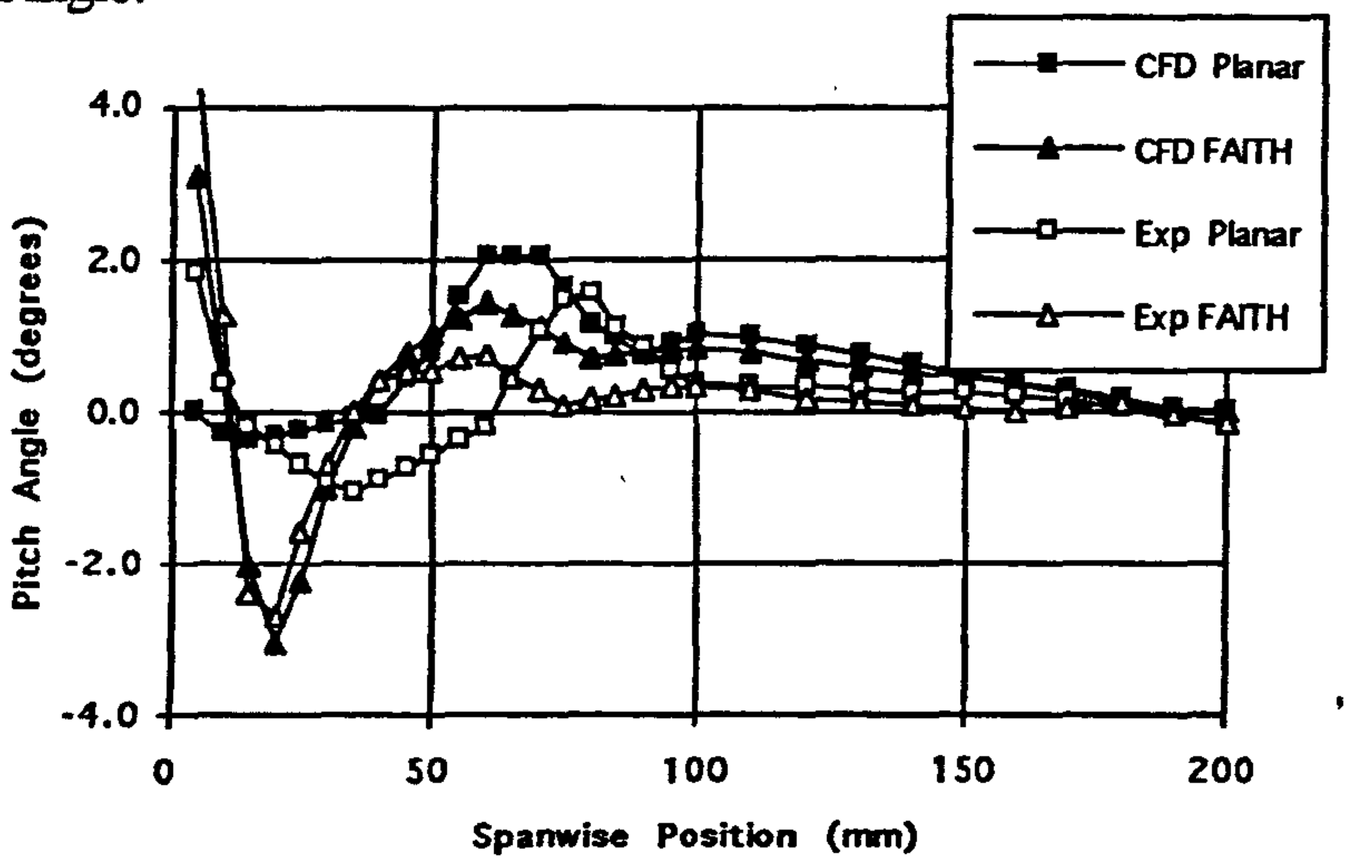

d) Secondary Kinetic Energy Coefficient.

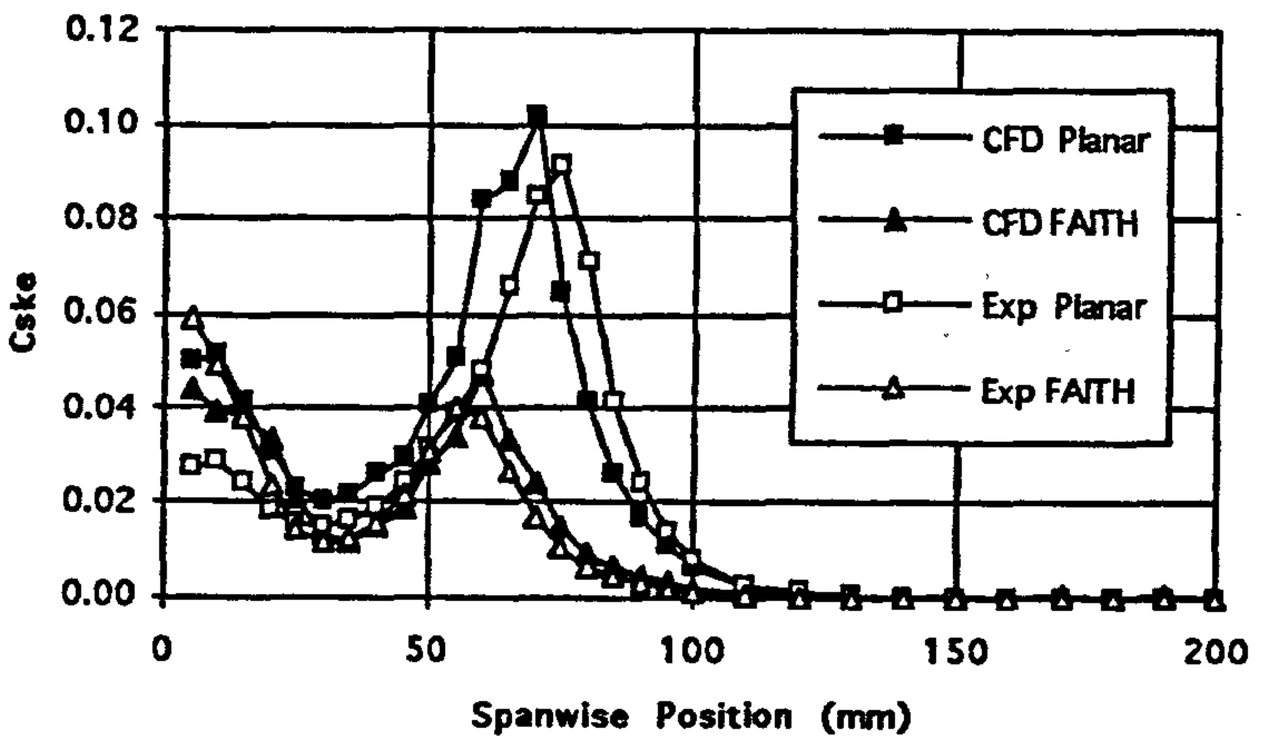

Figure 7.21 Growth of C_{SKE} Through the Cascade.

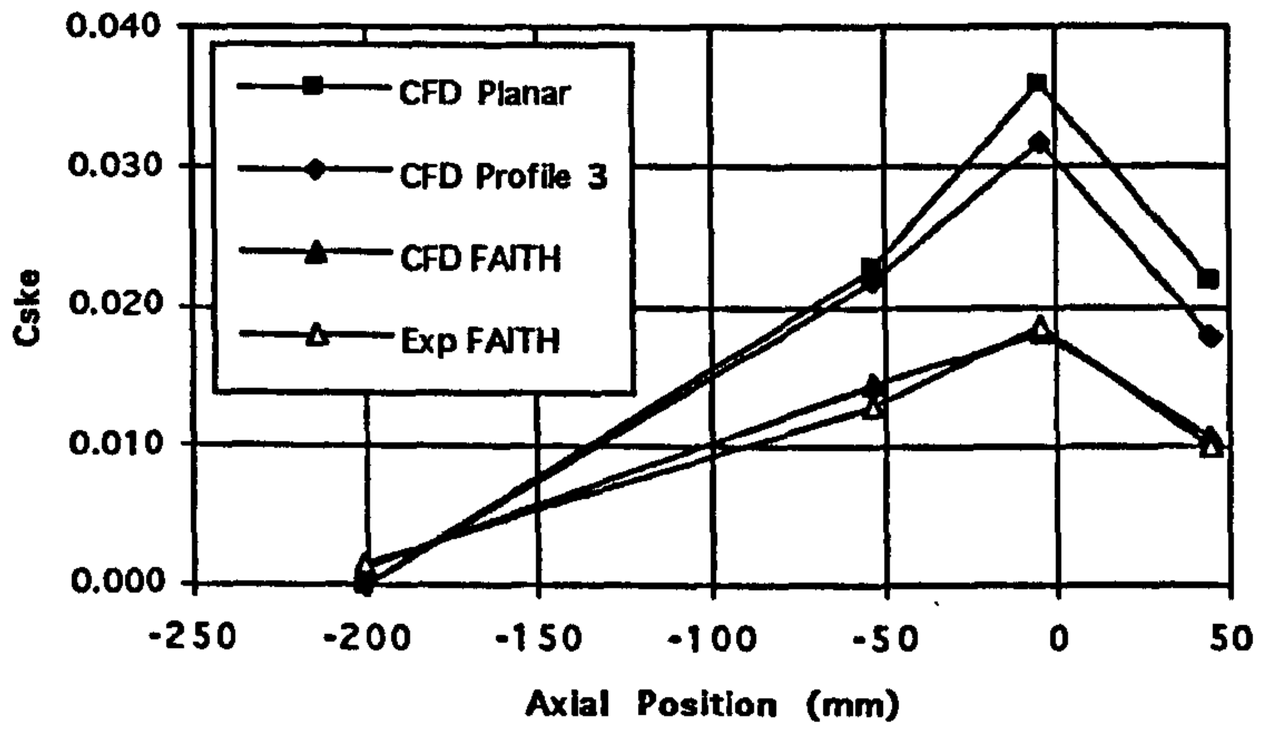

Figure 7.22 Experimental Data at Slot 1.

a) Secondary Velocity Vectors.

FAITH Profile

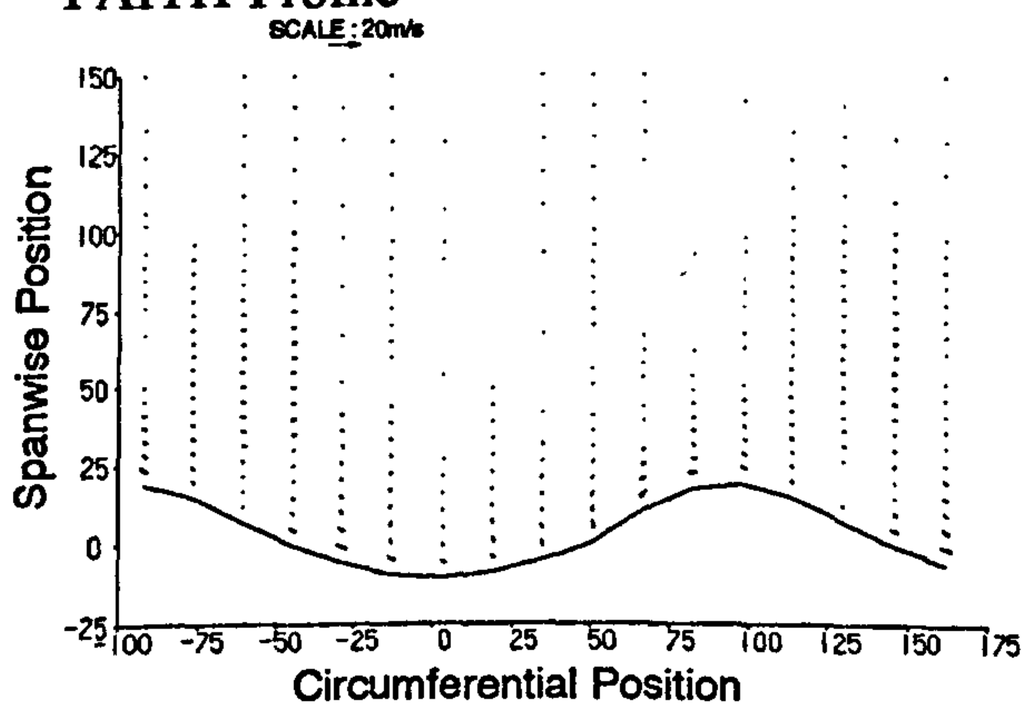

Planar Wall

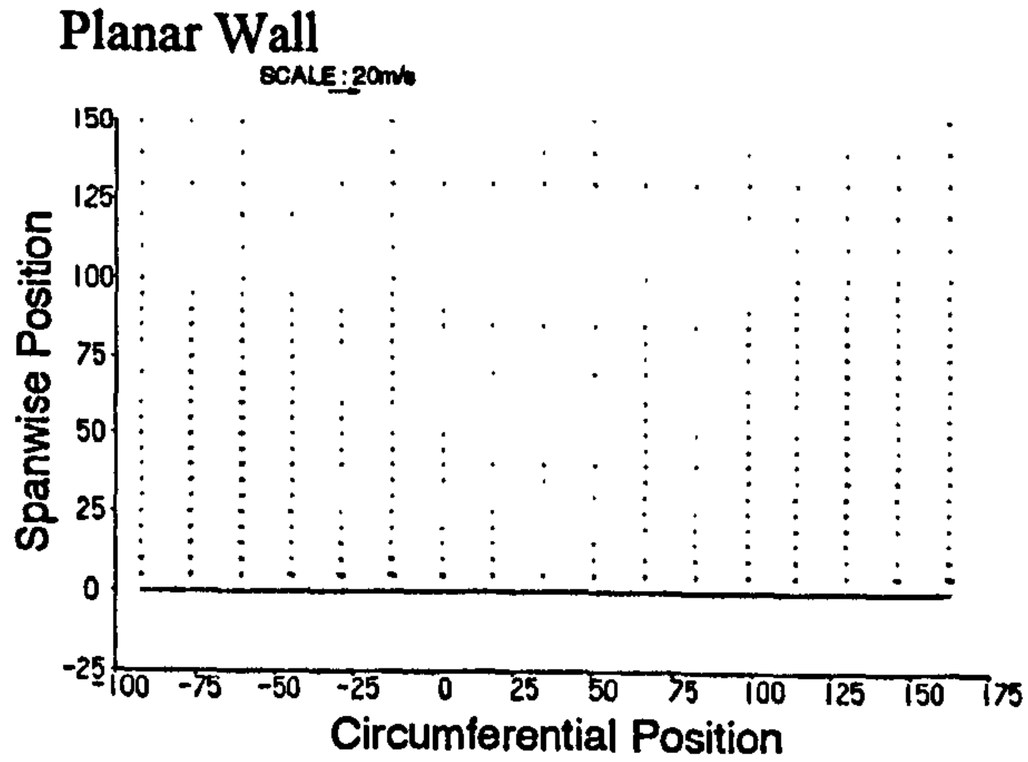

b) Total Pressure Loss Coefficient.

FAITH Profile

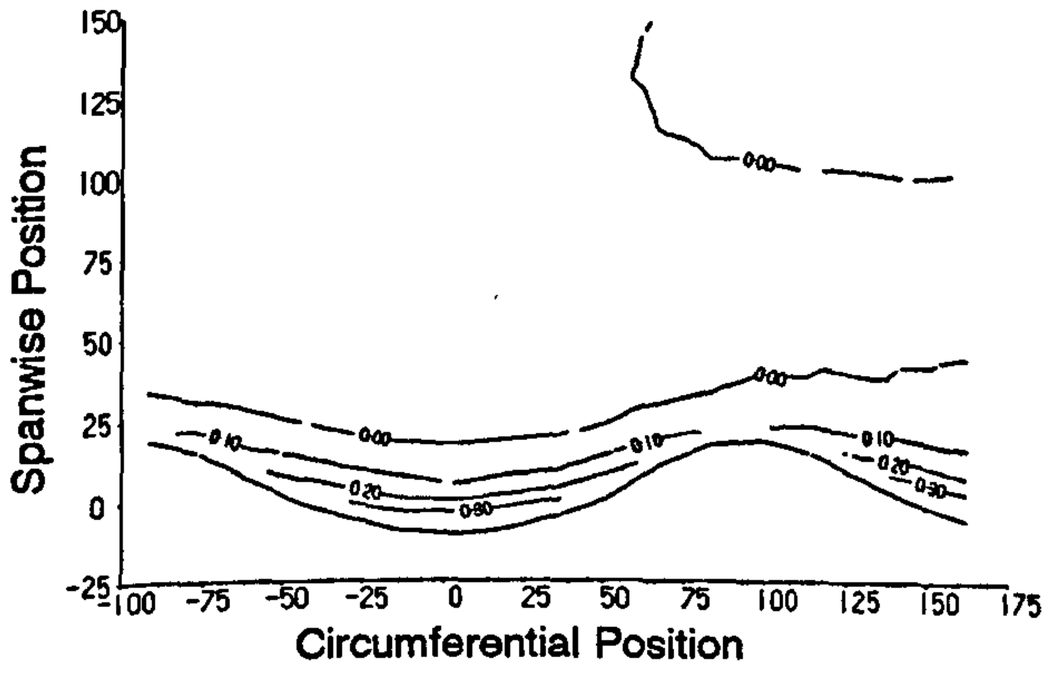

Planar Wall

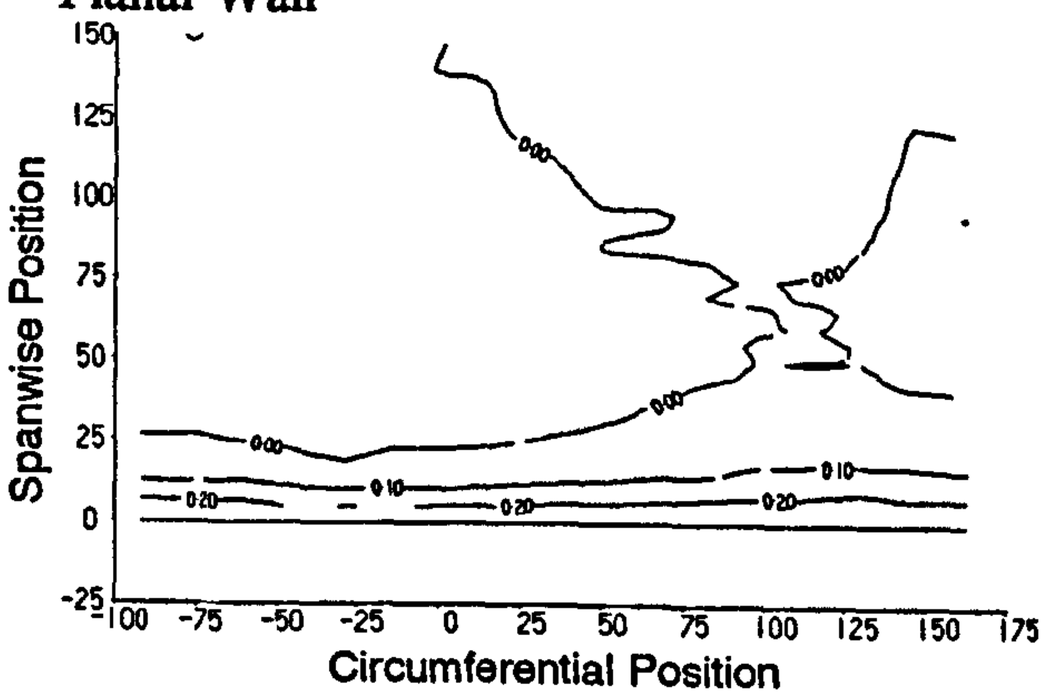

c) Yaw Angle.

FAITH Profile

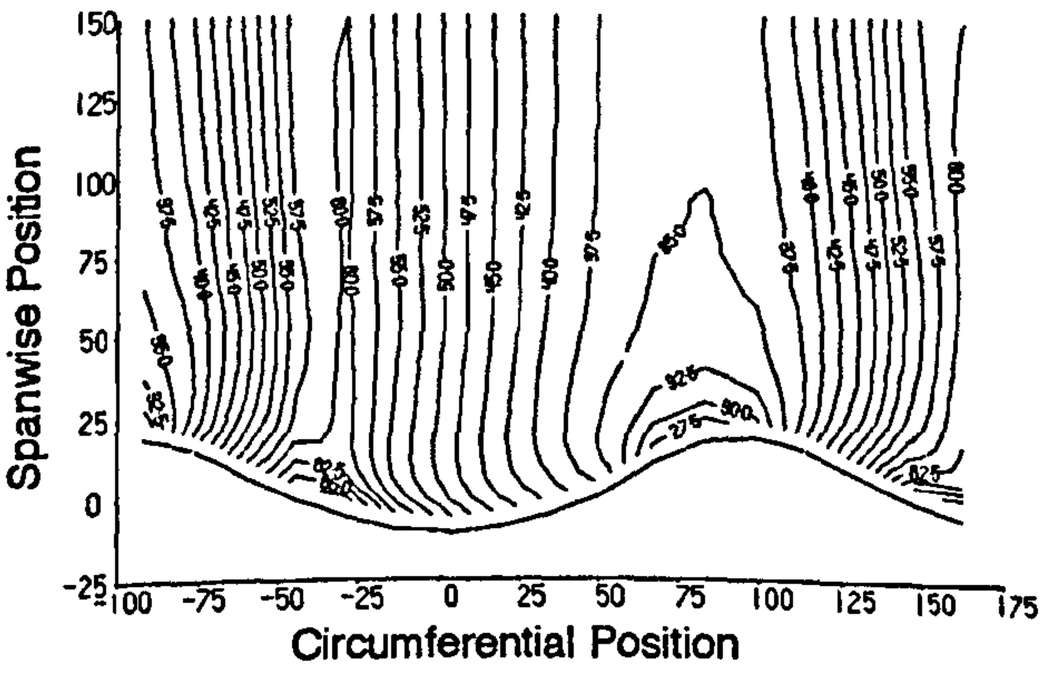

Planar Wall

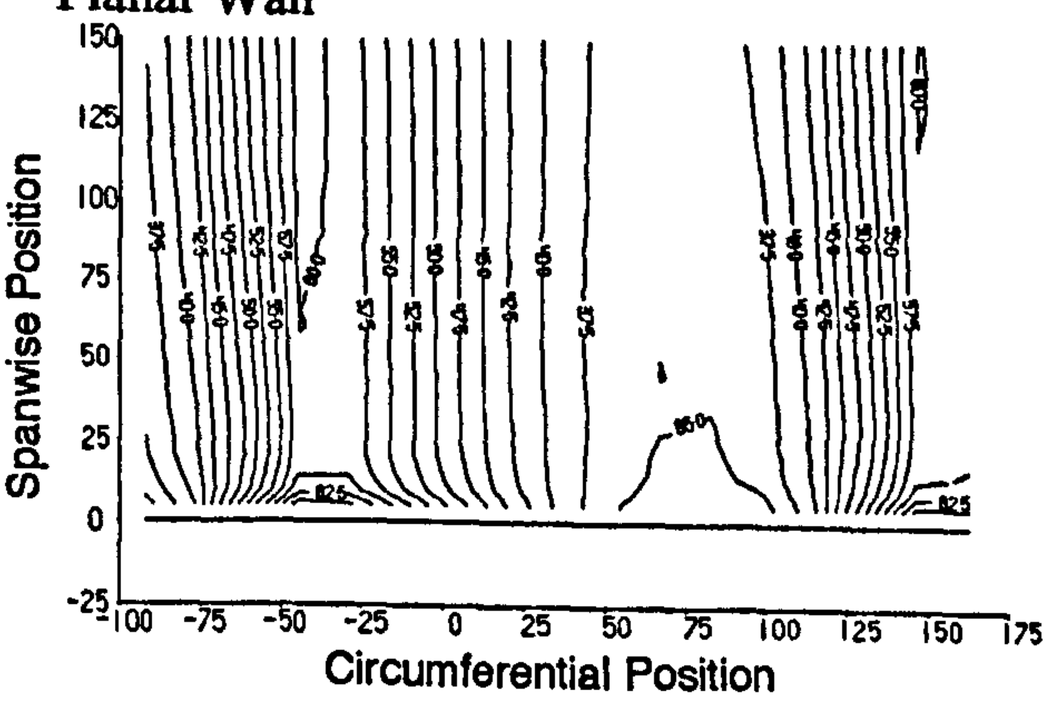

d) Secondary Kinetic Energy Coefficient.

FAITH Profile

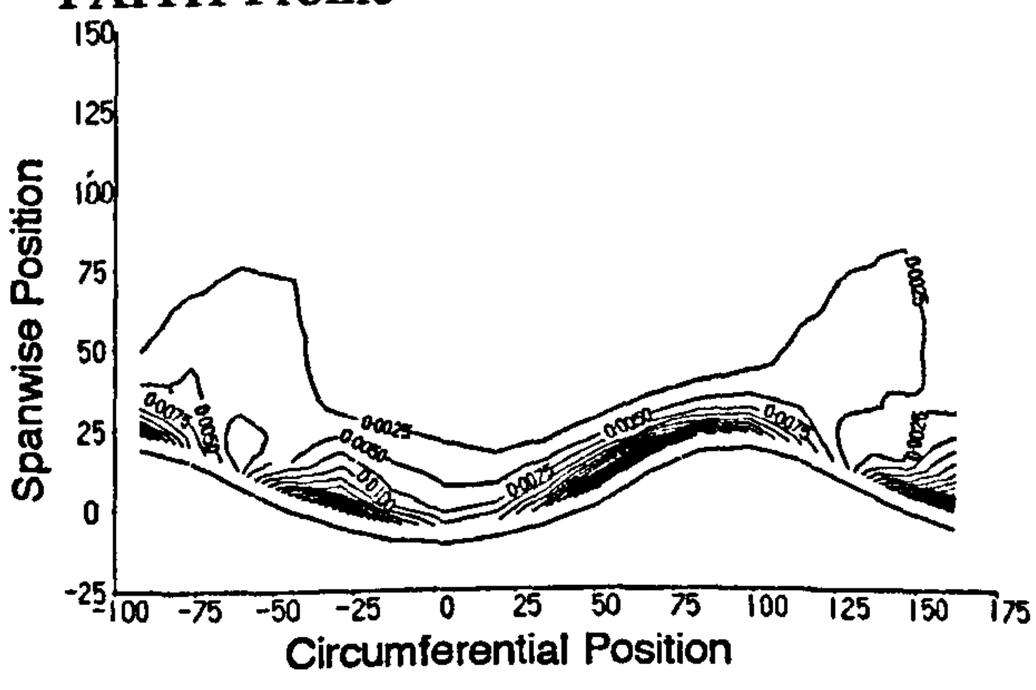

Planar Wall

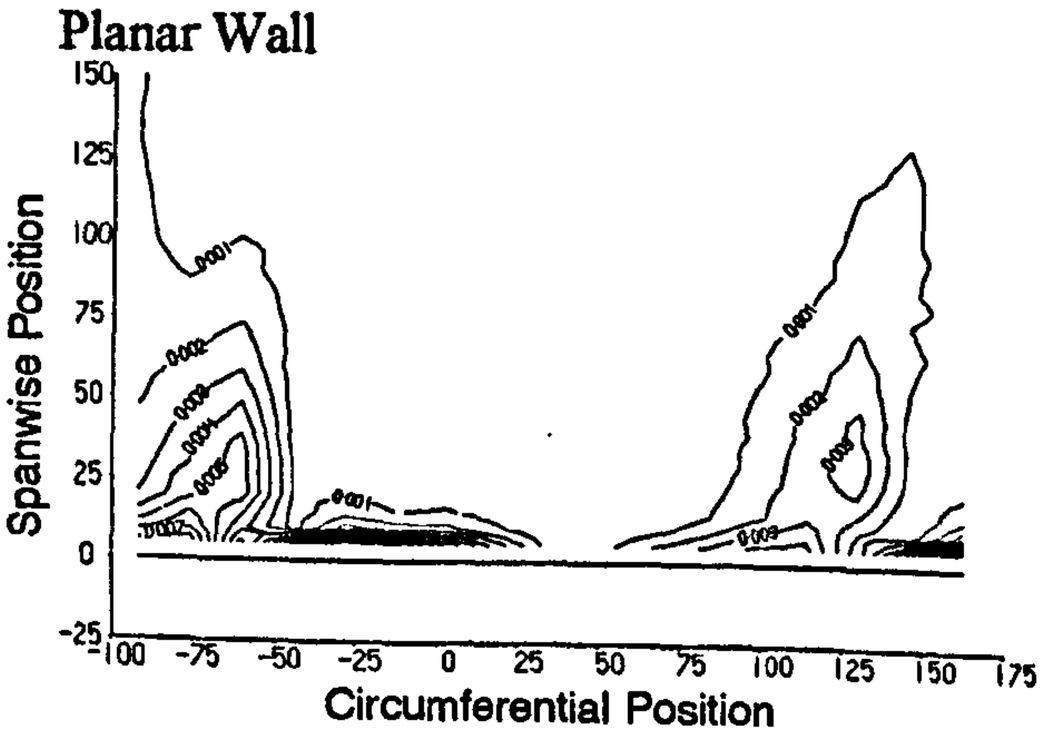

Figure 7.23 Experimental Data at Slot 6.

a) Secondary Velocity Vectors.

FAITH Profile

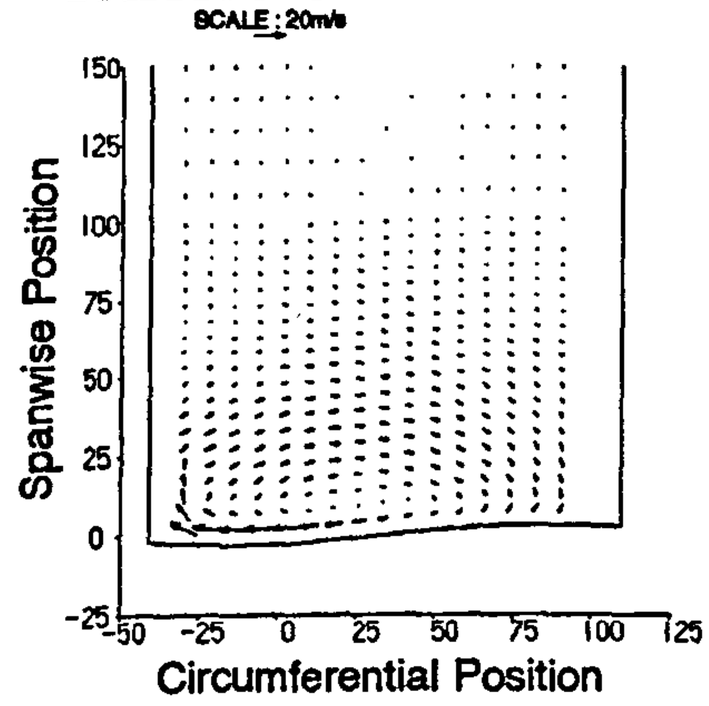

Planar Wall

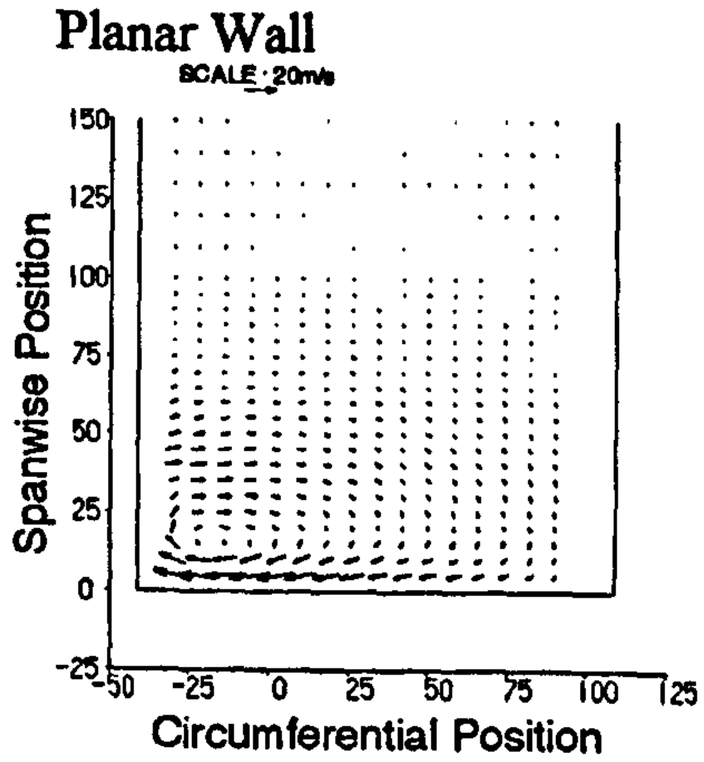

b) Total Pressure Loss Coefficient.

FAITH Profile

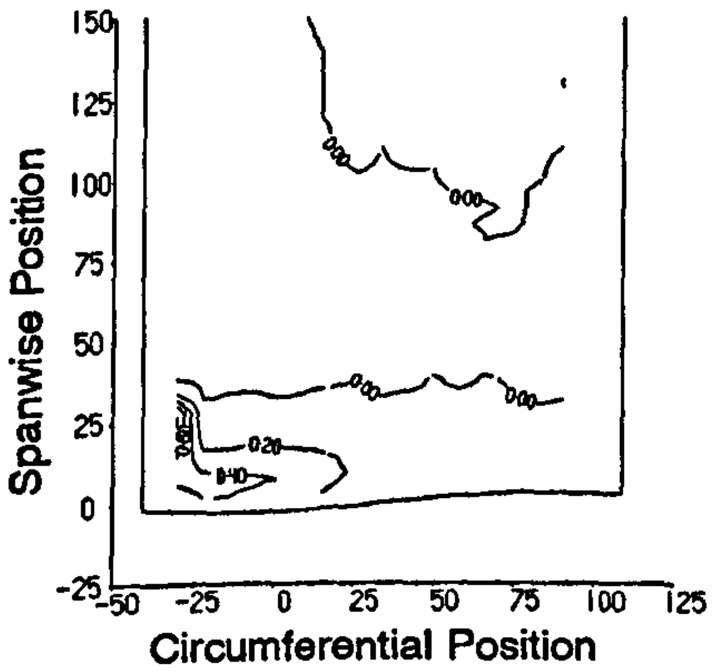

Planar Wall

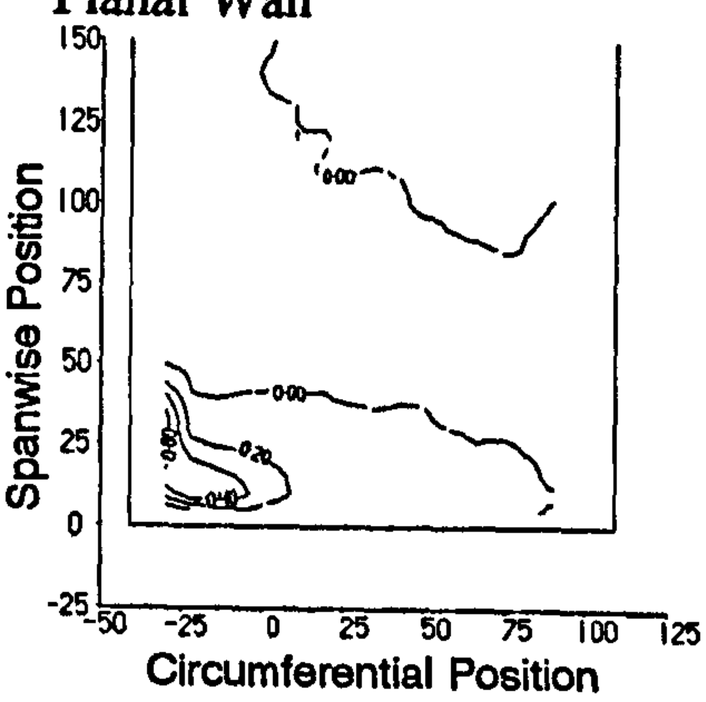

c) Yaw Angle.

FAITH Profile

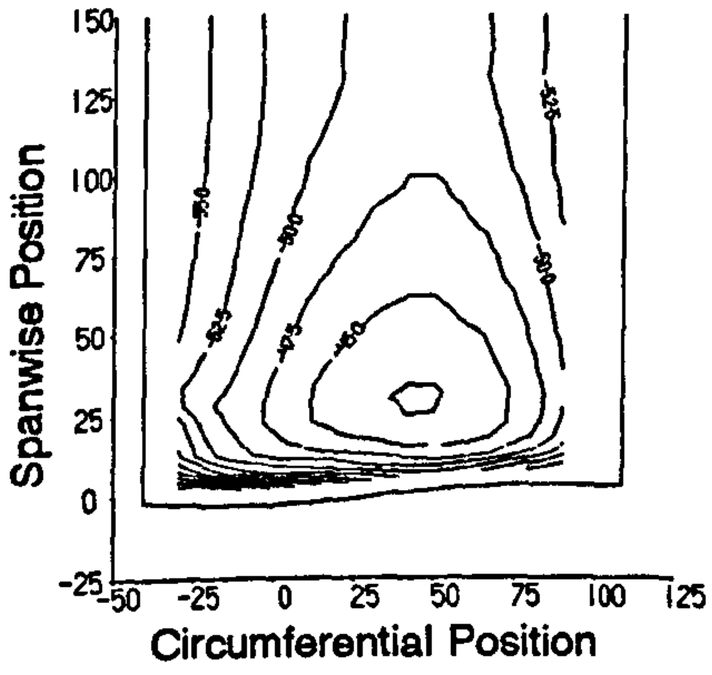

Planar Wall

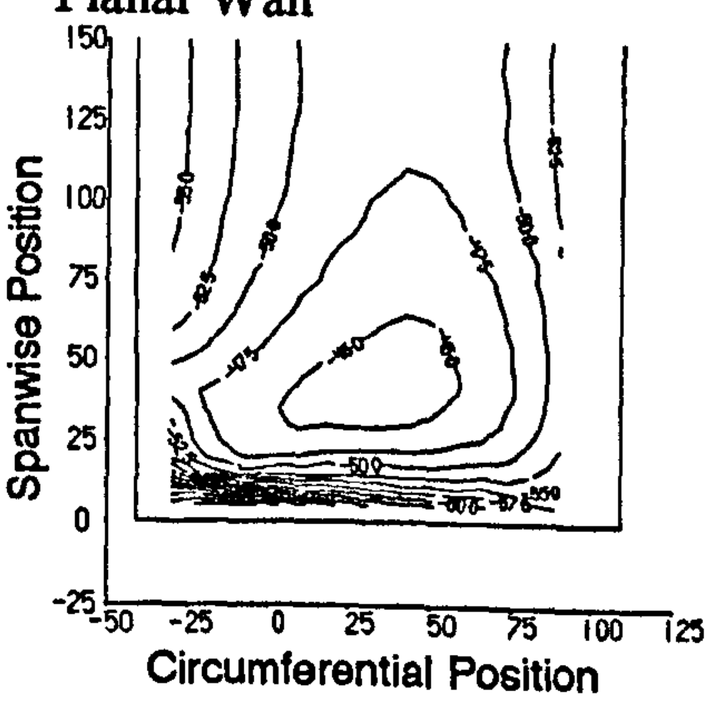

d) Secondary Kinetic Energy Coefficient.

FAITH Profile

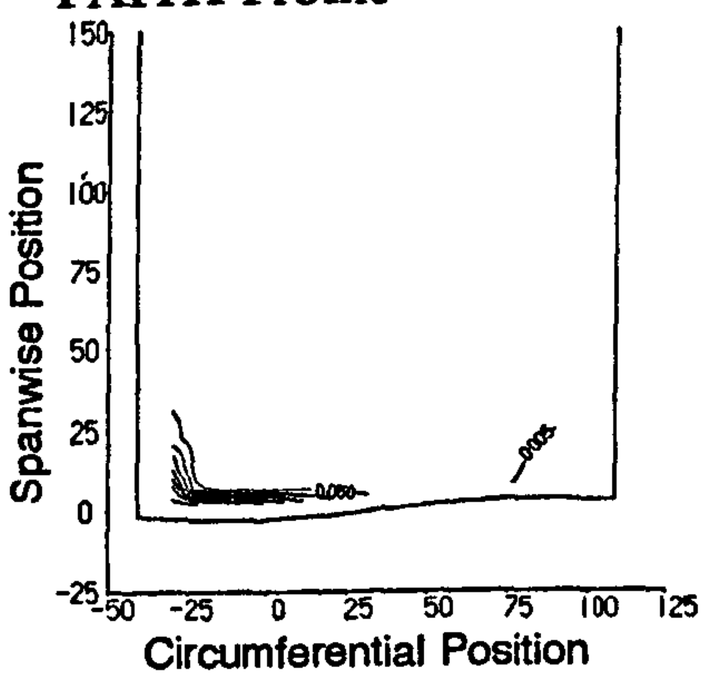

Planar Wall

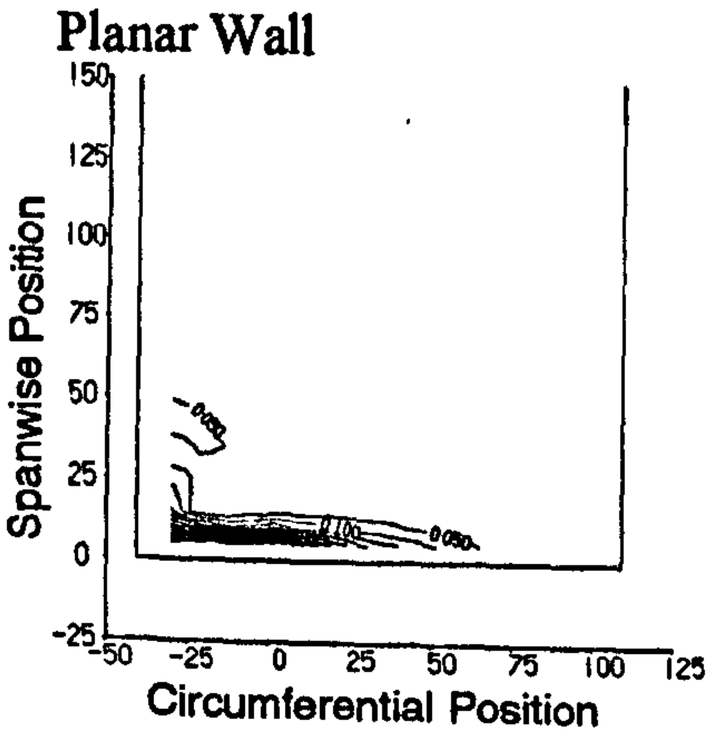

Figure 7.24 Experimental Data at Slot 8.

a) Secondary Velocity Vectors.

FAITH Profile

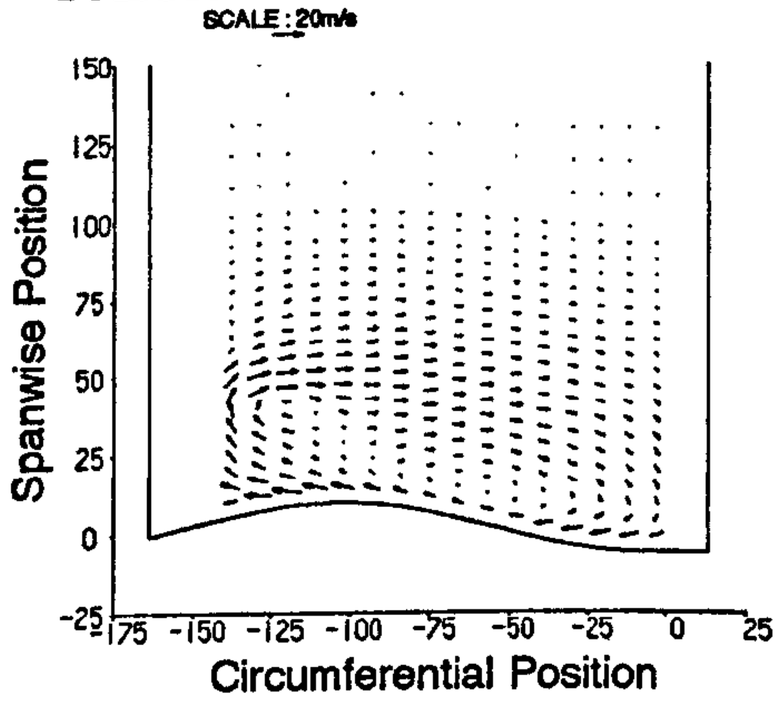

Planar Wall

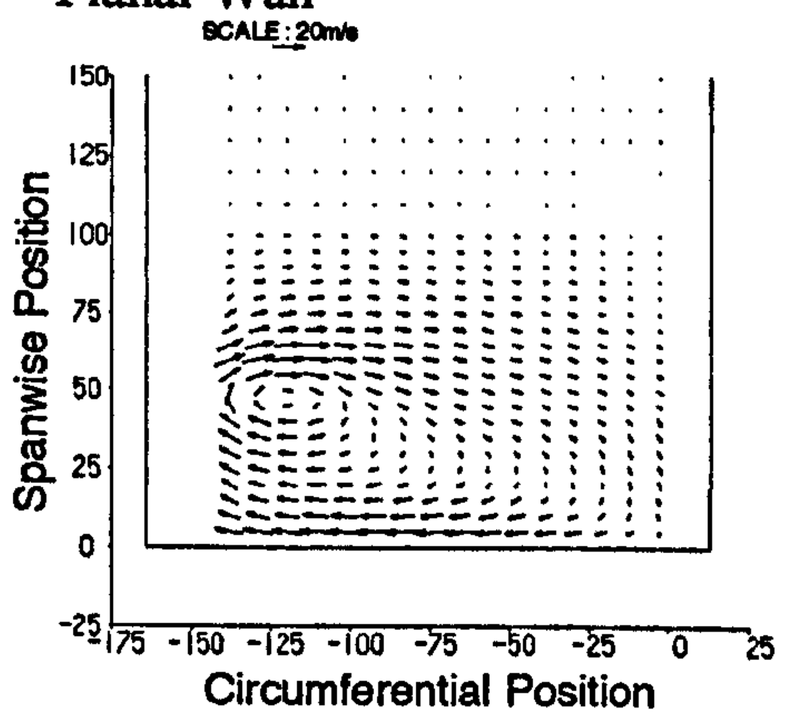

b) Total Pressure Loss Coefficient.

FAITH Profile

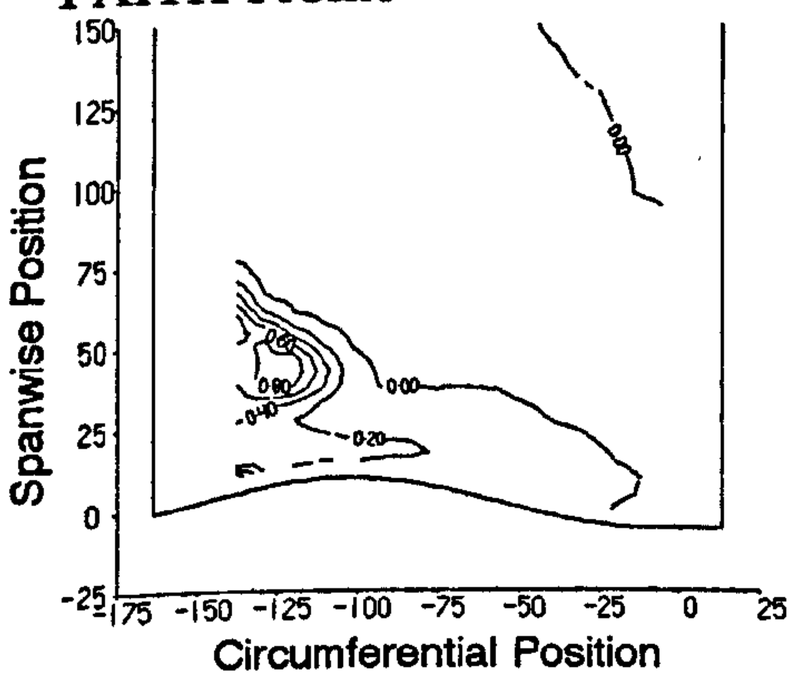

Planar Wall

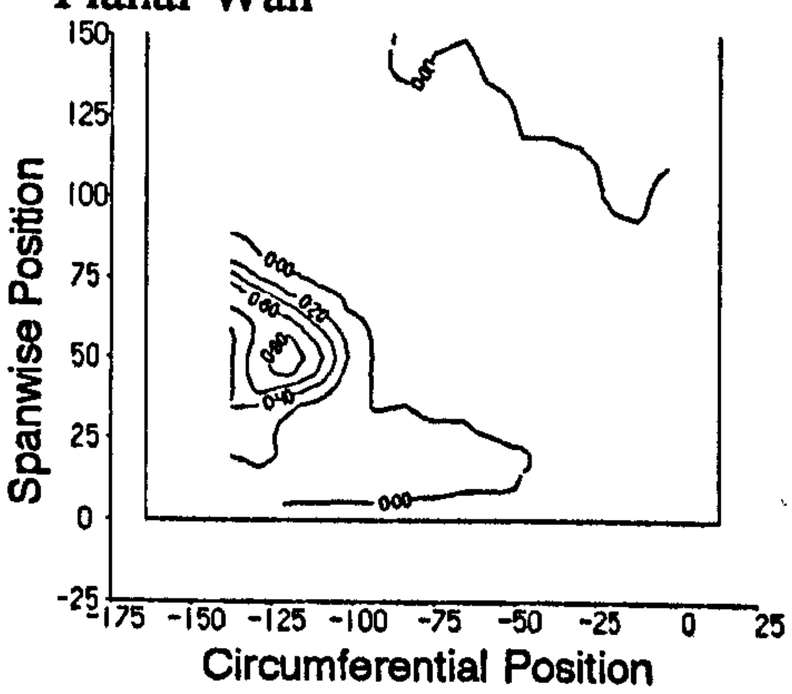

c) Yaw Angle.

FAITH Profile

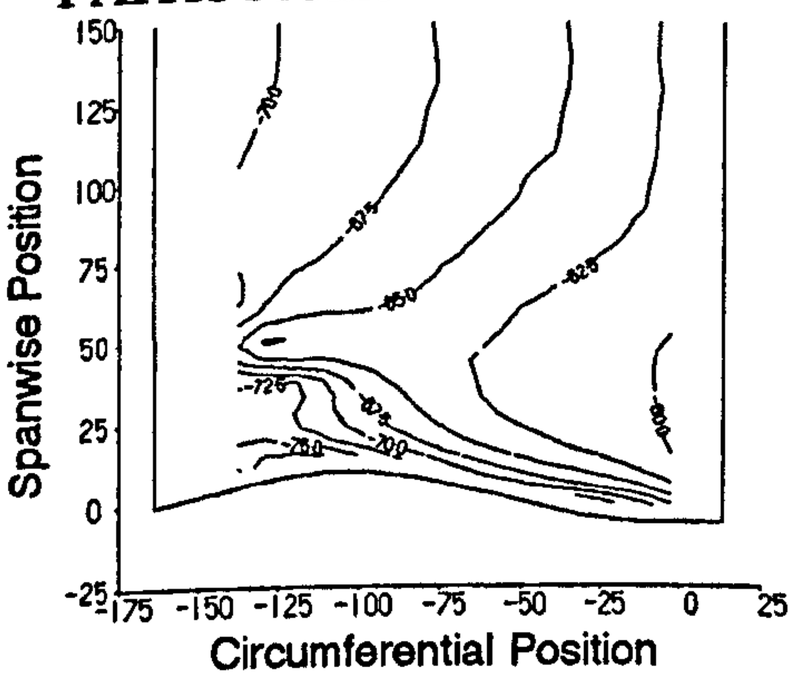

Planar Wall

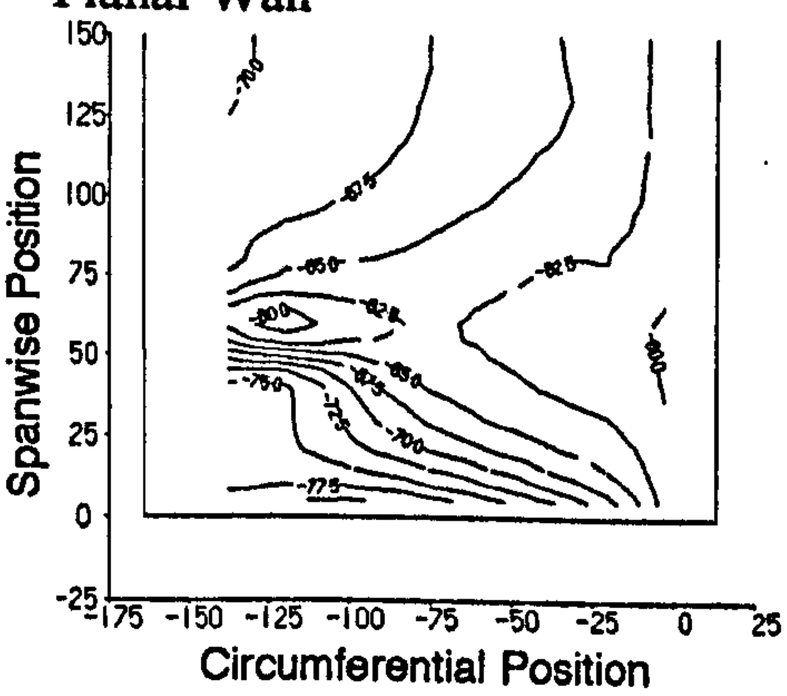

d) Secondary Kinetic Energy Coefficient.

FAITH Profile

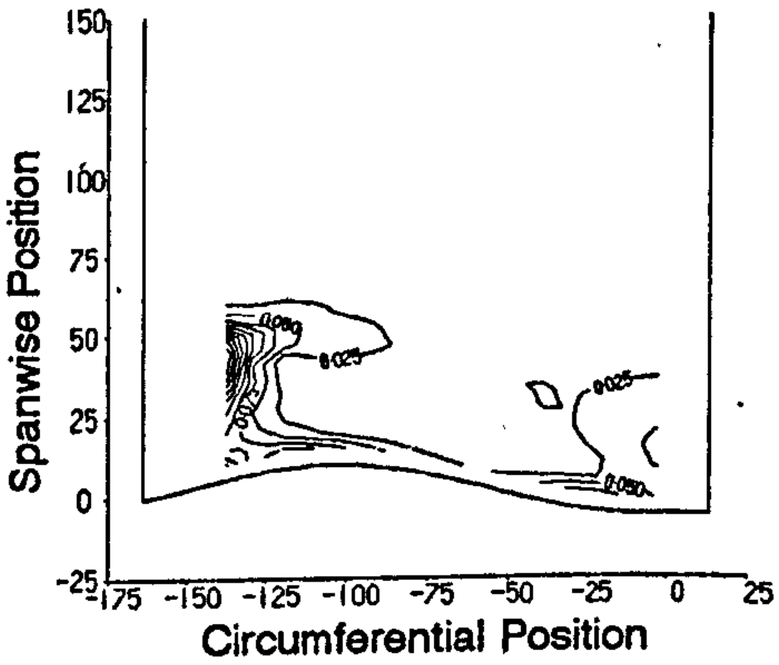

Planar Wall

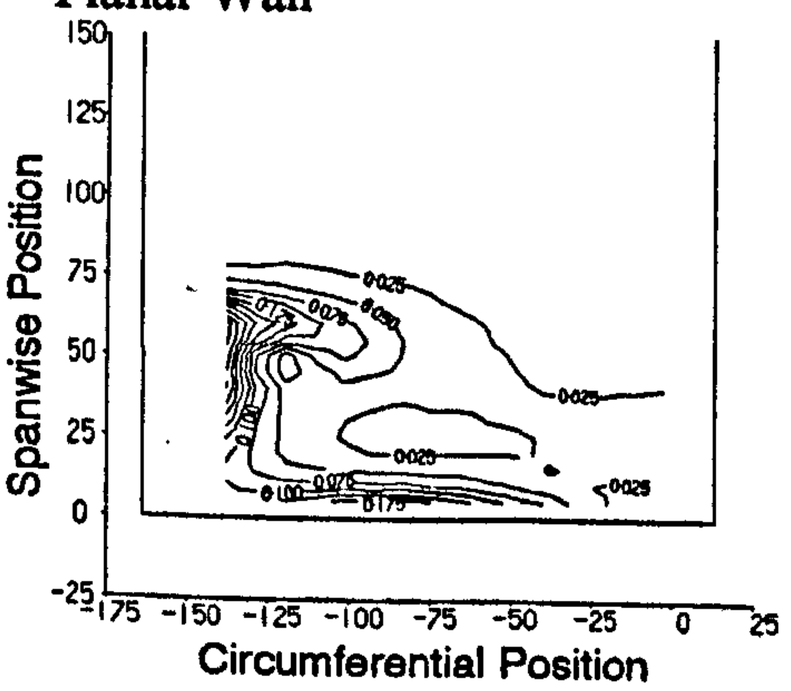

Figure 7.25 Experimental Data at Slot 10.

a) Secondary Velocity Vectors.

FAITH Profile

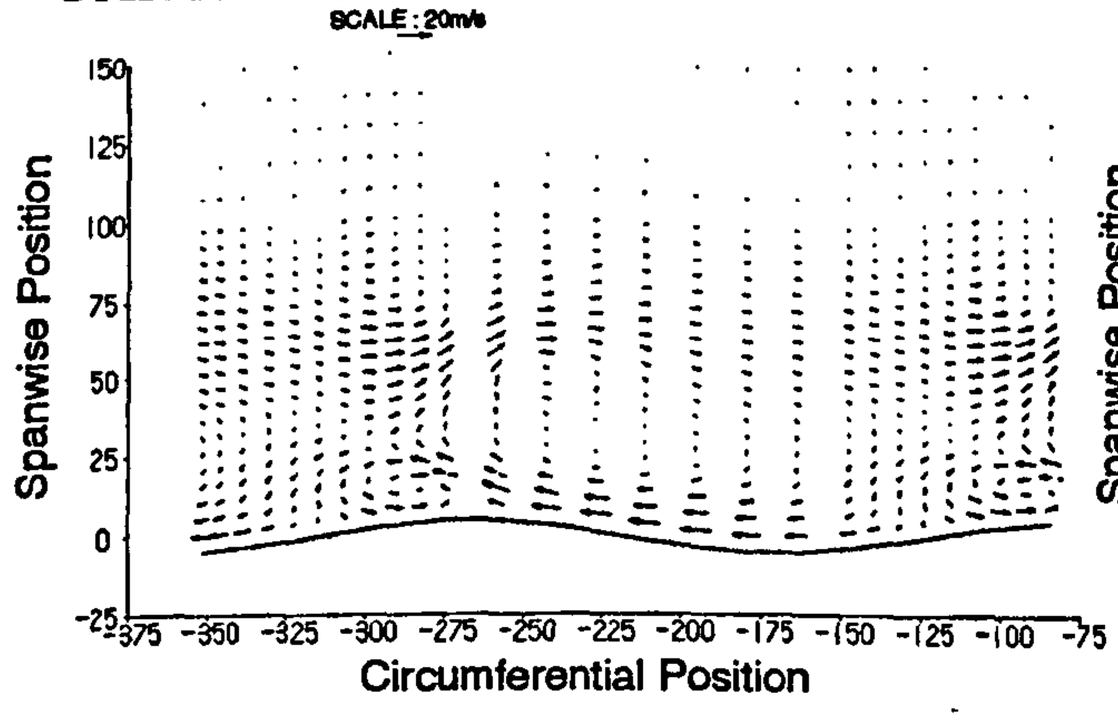

Planar Wall

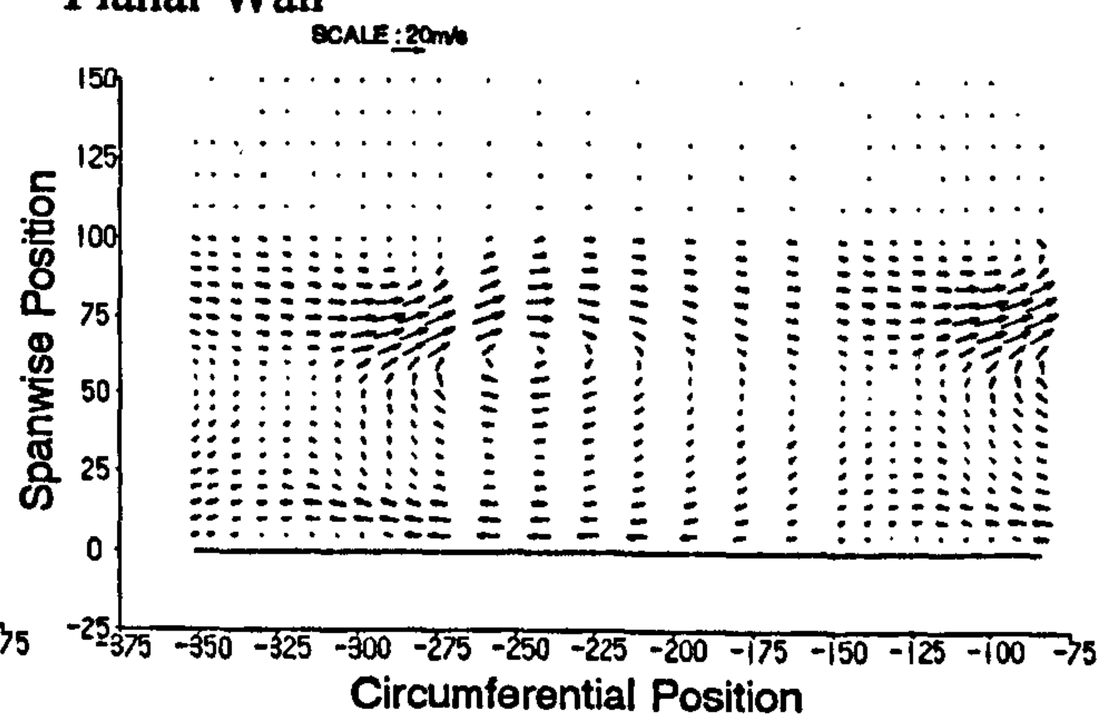

b) Total Pressure Loss Coefficient.

FAITH Profile

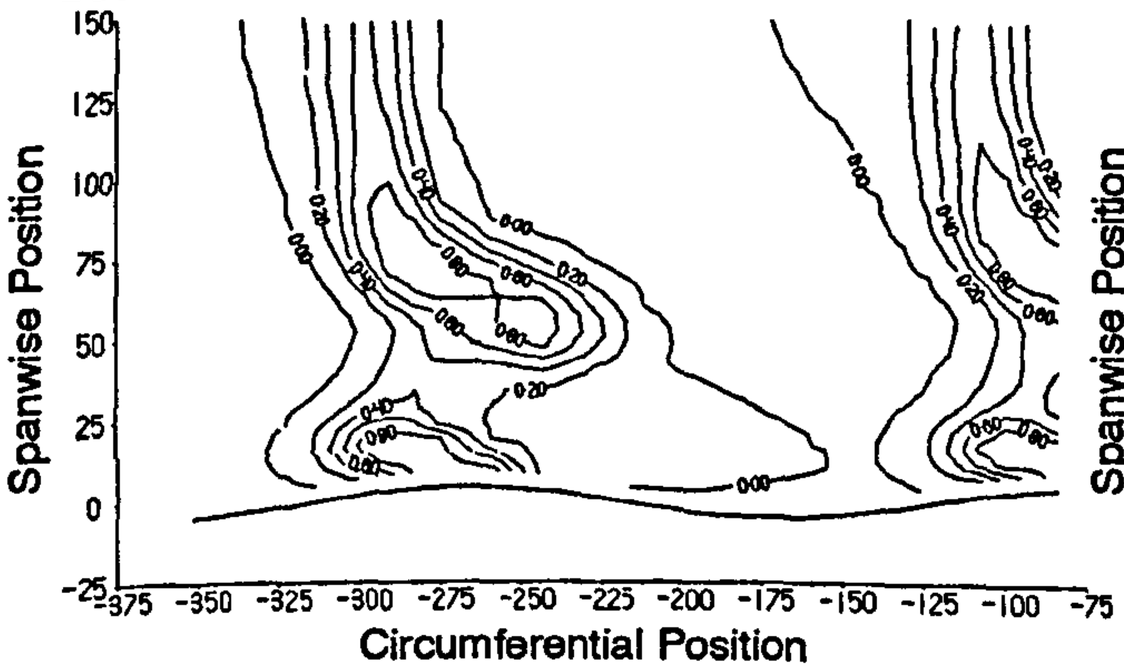

Planar Wall

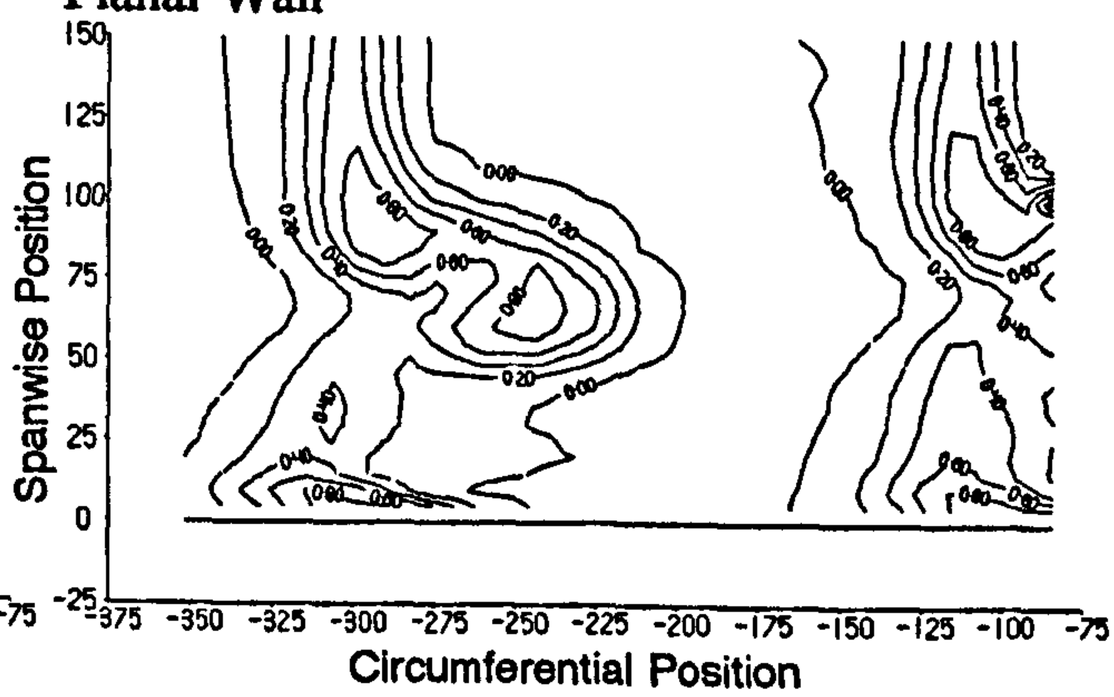

c) Yaw Angle.

FAITH Profile

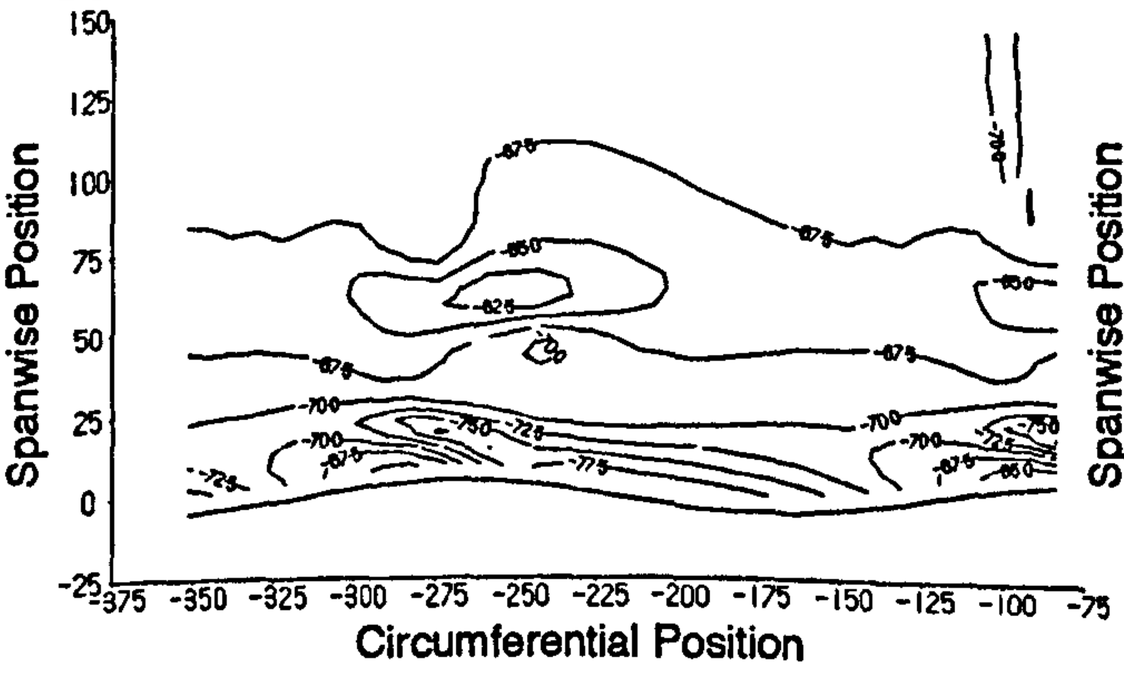

Planar Wall

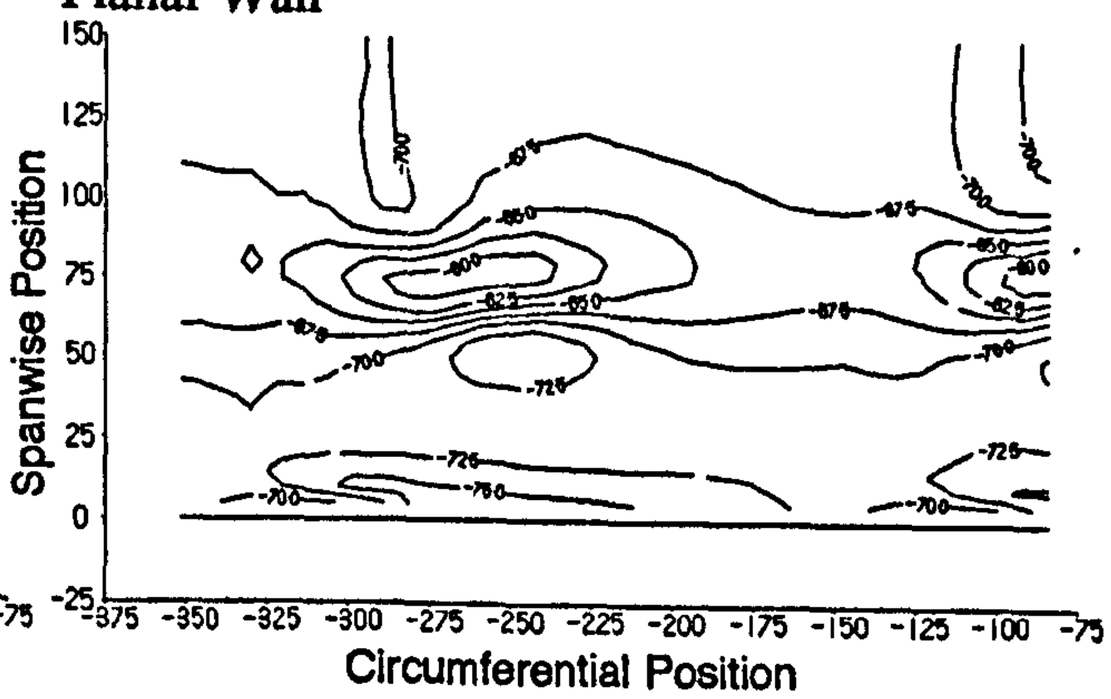

d) Secondary Kinetic Energy Coefficient.

FAITH Profile

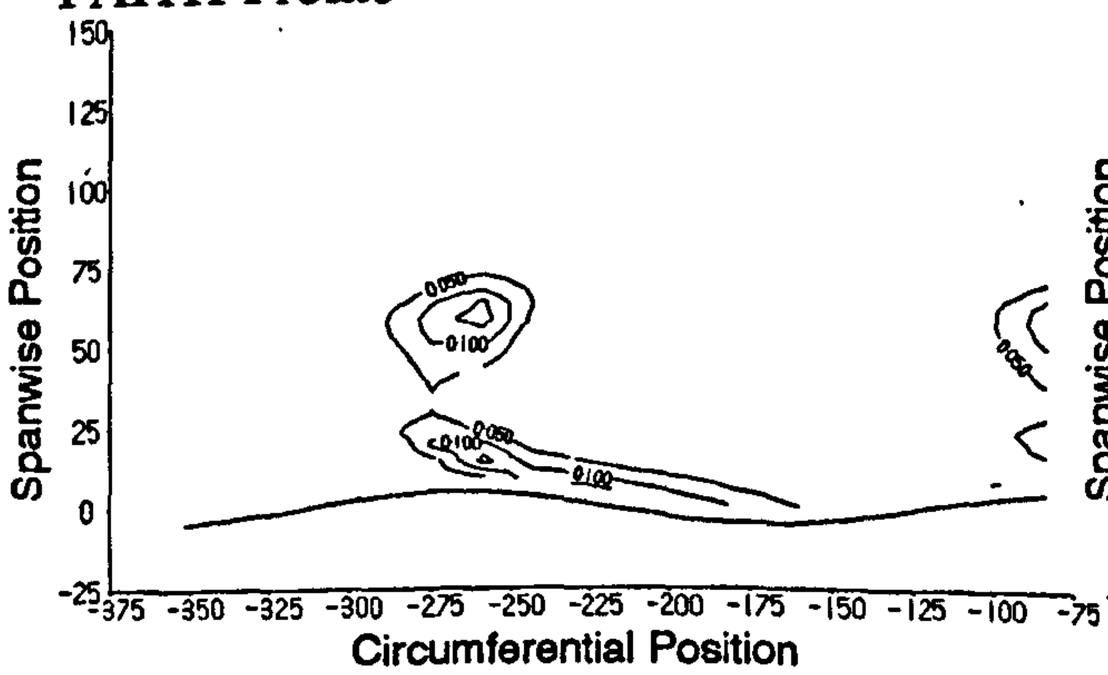

Planar Wall

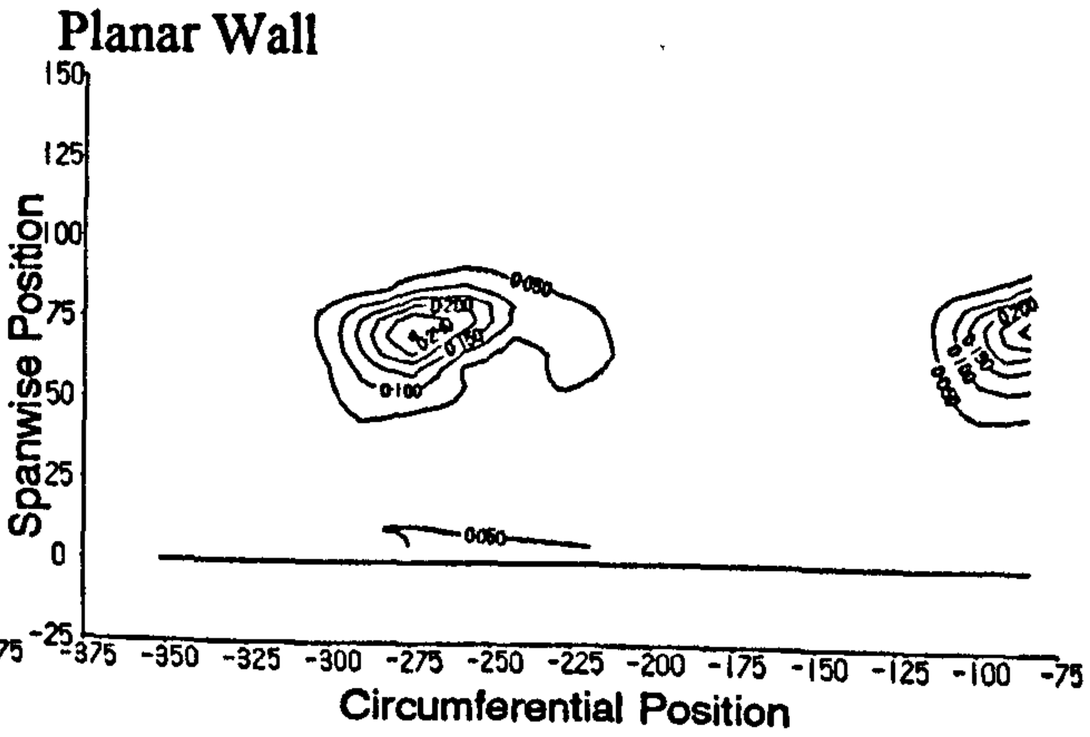

Figure 7.26 Pitch Averaged Compensated Experimental C_{SKE} Through the Cascade.

Slot 1

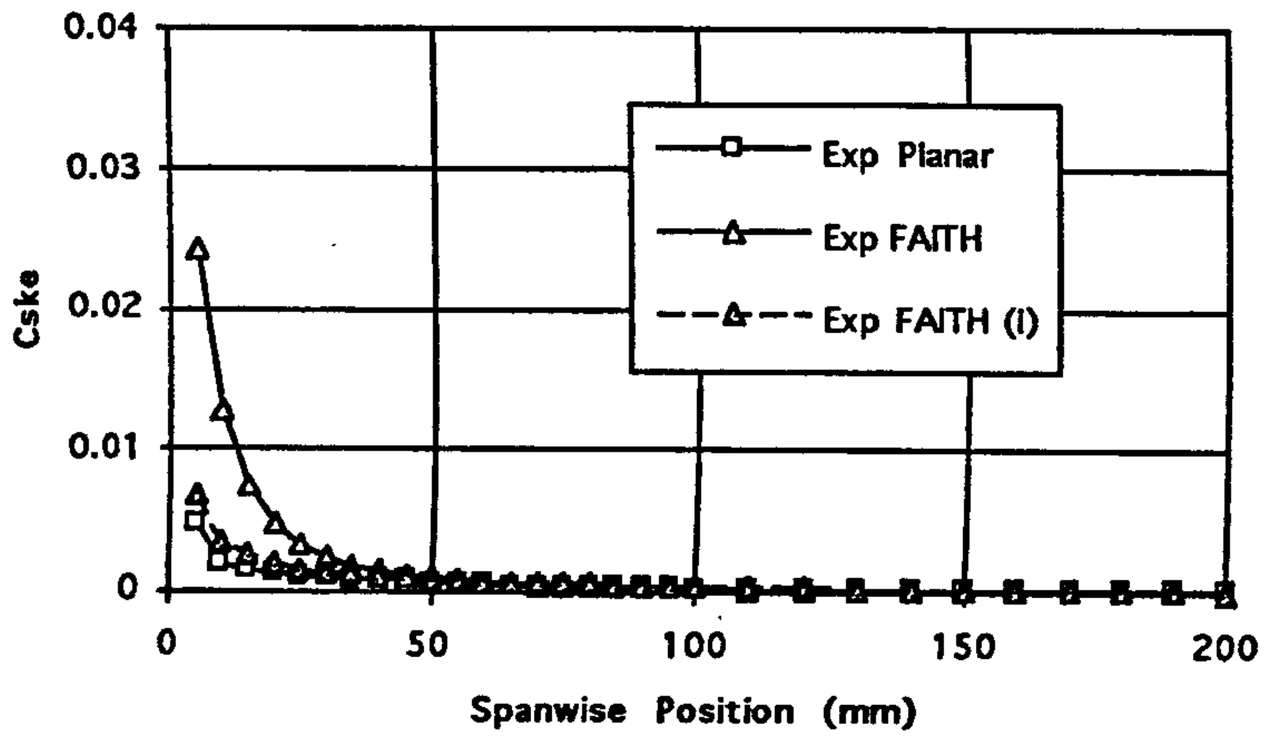

Slot 6

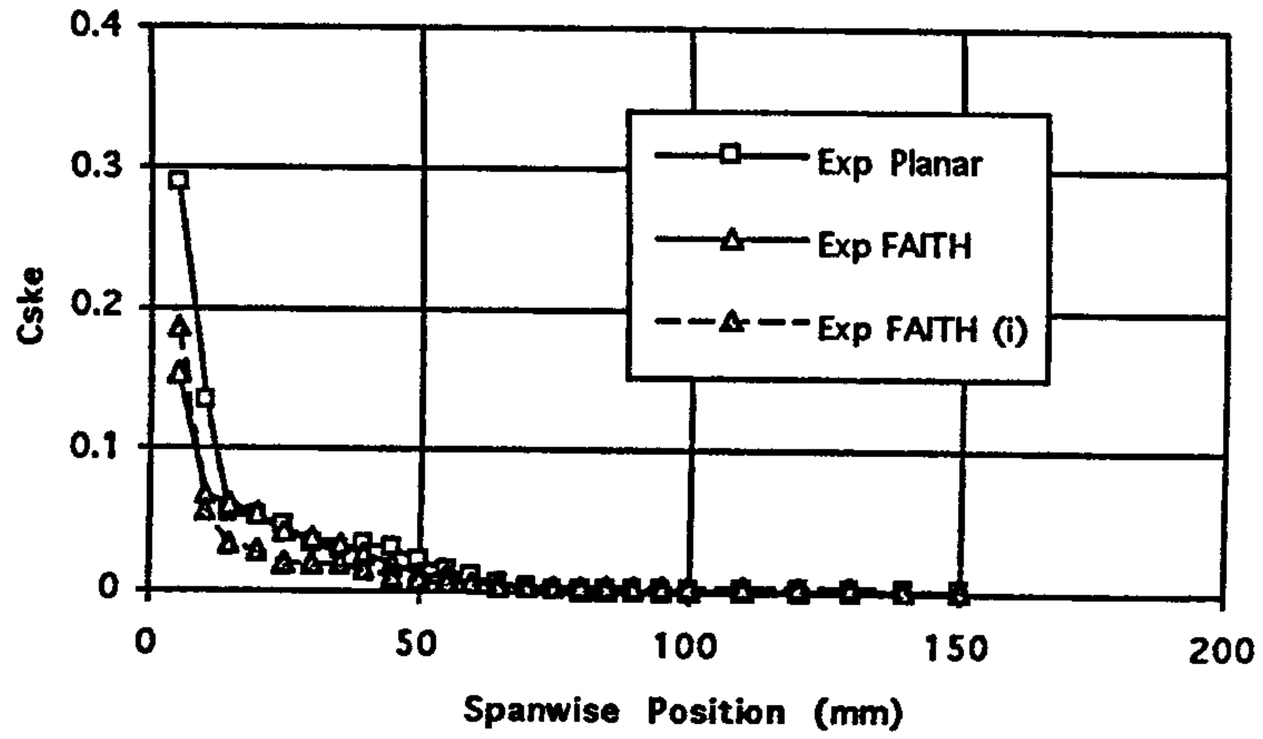

Slot 8

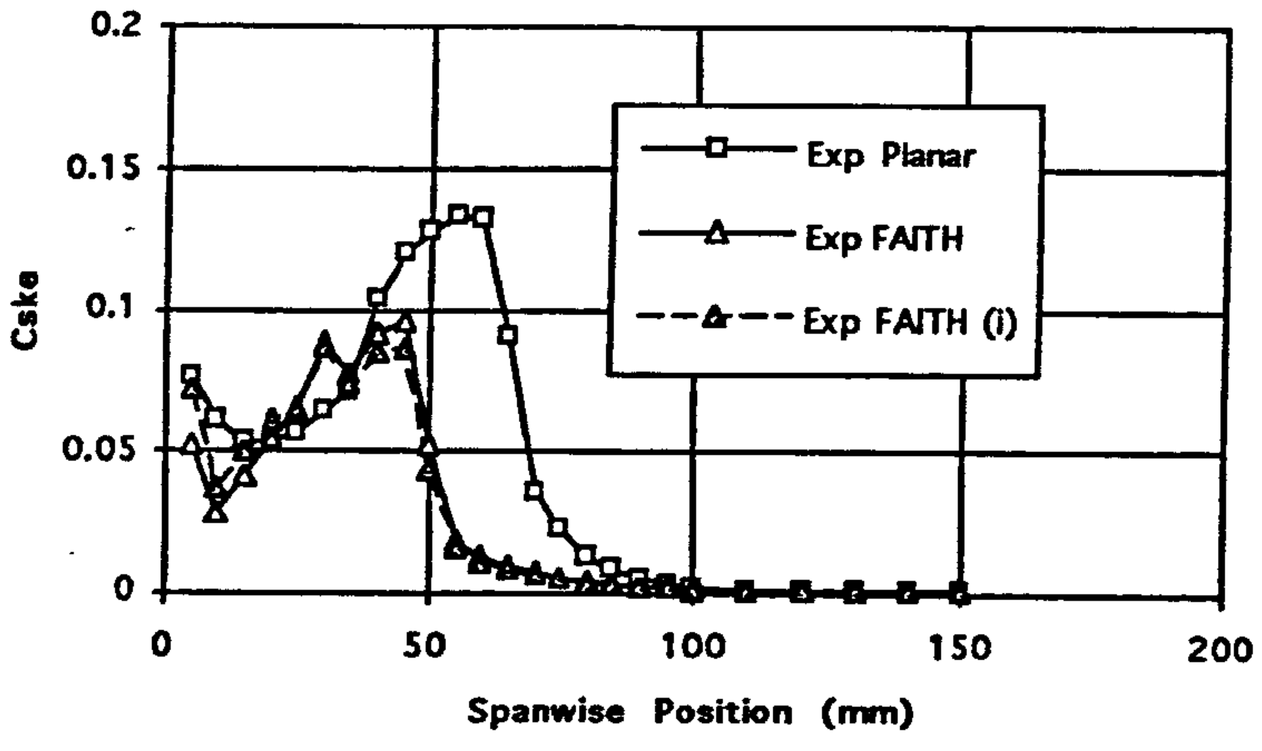

Slot 10

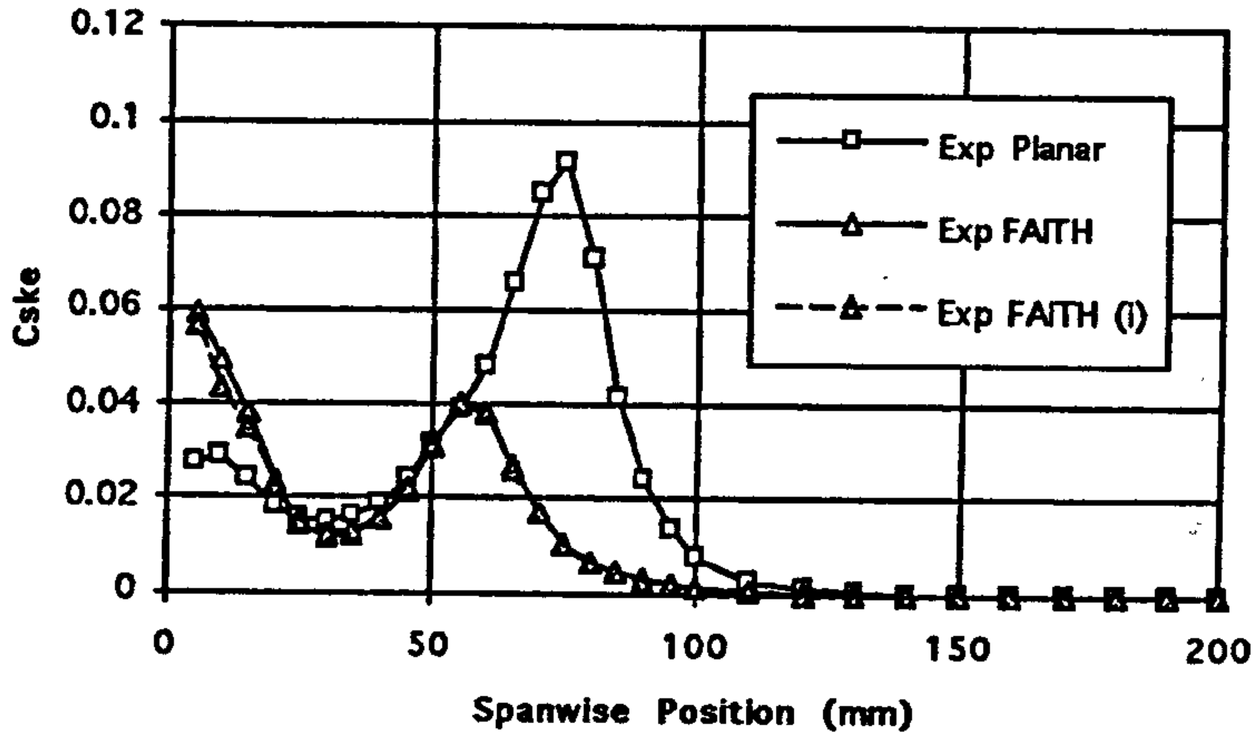

Figure 7.27 End-wall Flow Visualisation.

a) FAITH Profile

b) Planar Wall

8 Alternative End-wall Design Method.

8.1 Introduction.

An additional set of end-wall profiles for reducing secondary loss was briefly investigated using CFDS, and are covered in this chapter. The profiles tested, known as the Axial Mean Profiles (AXM) are based on the blade mean line. These were designed using philosophy that the blade (or rather flow) curvature causes the cross passage pressure gradient, so mirroring the blade curvature on the end-wall should assist in cancelling this effect.

8.2 Axial Mean Profile Design Philosophy.

Three profiles are presented here, all based on the mean line of the blade. The profile shape of the end-wall is defined by the product of an axial component based on the blade mean line, and a pitchwise component. The pitchwise component is a half cosine wave defined by Equation 8.1 giving minimum height (concave curvature) along the suction surface, maximum height (convex curvature) along the pressure surface and zero height at mid pitch.

$$z_y = -z_{axm}\cos\left(\pi\frac{y - y_{mean}}{s}\right) \qquad \text{Equation 8.1}$$

Where z_{axm} is the axial component at the current axial location, and

y_{mean} is the mean line at the current axial location.

The axial component is generated by rotating the blade mean line about the trailing edge and then axially rescaling the result to match the blade axial chord, as shown in Figure 8.1. This modified mean line is then smoothed onto the flat end-wall upstream and downstream by fitting a fillet between the profile and end-wall to give the axial component of the profile shown in Figure 8.2. The modified mean line is offset vertically and the angle of rotation is adjusted to give a smooth transition at inlet and exit.

The first two profiles presented use a circular fillet at the leading and trailing edge and the profiling is kept to within the axial limits of the blades. The first profile, referred to as AXM, uses a 10mm radius at the leading edge and a 171.6mm radius at the trailing edge (giving an additional rotation angle of 0°). A high suction peak was observed at the leading edge of the suction surface, so the second profile, AXM2 was designed using a 15mm radius at the leading edge and a 50mm radius at the trailing edge (giving an additional rotation angle of 10.3°) to reduce the curvature in this region. Figure 8.4 b shows that in fact, reducing the curvature increases the suction peak. The third profile, referred to as AXMe, uses a parabola to feather the profile in at the leading edge and out at the trailing edge. The parabola is calculated such that the profile has an axial run-in and run-out of 50mm upstream and downstream of the blade leading and trailing edges. Upstream and downstream of the blades, the pitchwise height discontinuity between the

positive height of the run-in/run-out of the pressure surface profile and the negative height of the run-in/run-out of the suction surface profile is smoothed by a pitchwise cubic spline. This matches the height and slope between pressure surface and suction surface profiles outside the passage. The profile is then smoothed slightly to ease the transition of the cubic spline. Contour plots of profile height for the three profiles are shown in Figures 8.3 a and b and c.

8.3 Discussion of Results.

8.3.1 End-wall Cp Contours.

Figures 8.4 a to d show contour plots of end-wall Cp for the three AXM profiles and the planar wall for comparison. The unloading of the blades at the point of maximum turning can clearly be seen with all the profiles. Following the -2.0 contour, this intercepts the suction surface at approximately -90mm for AXM and AXM2 and -110mm for AXMe, compared with -150mm for the planar wall. The reduction in pressure on the pressure surface is less significant, due to the lower flow velocities here. In the case of AXMe, the pressure even appears to have increased along the pressure surface. The loading further downstream has increased, as can be seen from the area encompassed by the -3.5 contour.

The large suction peak on just downstream of the leading edge can also be seen for profiles AXM and AXM2. It is uncertain why the suction peak increases in magnitude when the curvature is reduced. One possible explanation is that the flow separates at the leading edge of profile AXM, however, a close inspection of the flow in this area proved that this was not the case.

8.3.2 Area and Pitch Averaged Results.

Figures 8.5 a to d show pitch averaged C_{Po}, Yaw, Pitch and C_{SKE} for the three AXM profiles and the planar wall at Slot 10. Figures 8.6 a to d show the FAITH profile and planar wall data for comparison, and as AXMe performed best, it is also included. It should be noted that the pitch and area averaging has been carried out on the CFD grid, so direct comparisons with data from earlier Chapters may not be accurate. Table 8.1 shows area averages (calculated over the CFD grid) of C_{Po} and C_{SKE} for the three AXM profiles, planar wall and FAITH profile.

Table 8.1 Area Averaged CFD Data At Slot 10.

	Total Pressure Loss			
	Full	Mid-Span	Secondary	C_{SKE}
Planar	0.215	0.151	0.064	0.023
AXM	0.212	0.148	0.064	0.014
AXM2	0.214	0.151	0.062	0.013
AXMe	0.210	0.151	0.060	0.009
FAITH	0.219	0.151	0.068	0.012

The distributions of loss, shown in Figure 8.5a indicate that both AXM2 and AXMe result in a reduction in the size of the loss peak due to the passage vortex, and movement of this peak towards the end-wall. These effects are also shown in the area averaged losses in Table 8.1 where AXM2 results in 3% lower secondary loss and AXMe results in a 6% reduction in secondary loss. These area averaged values are, however, not reliable as demonstrated by the 6% increase in secondary loss predicted for the FAITH profile, compared with a 21% reduction from the experimental data (Chapter 7). The increase in loss seen in the region below the passage vortex (Figures 8.5a and 8.6a) with profile AXMe and to a lesser extent AXM2 is thought to be due to mixing of the opposing spanwise velocities generated by the secondary flow along the suction surface and the end-wall slope along the pressure surface. This is visible on close inspection of the CFD solution and is shown here by the significant reduction in pitch angle variation (Figure 8.5c). This acts to reduce the passage vortex and C_{SKE} at the Slot 10 plane at the expense of locally increased loss. Unfortunately mixed out loss calculations were not carried out for the AXM profiles.

Comparing the yaw angles shown in Figure 8.5b, all of the AXM profiles appear to reduce the under-turning. AXM seems to have the greatest effect on the under-turning, but does not appear to move the spanwise location towards the end-wall. AXM2 and AXMe both move the point of maximum under-turning towards the end-wall, AXMe having the greatest effect.

All three AXM profiles result in higher over-turning near the end-wall, to about the same extent, although from Figure 7.19 b, it is possible that this over-turning is an over-estimate. It is possible that over-turning near the end-wall may in fact be beneficial with respect to secondary flow in a downstream blade row as it will provide a beneficially skewed boundary layer (Walsh & Gregory-Smith [1989], Biesinger [1993]).

The C_{SKE} data shown in figure 8.5d indicates that AXM and AXM2 have the same effect on the magnitude of the C_{SKE} although the movement of the passage vortex towards the end-wall results in a lower area averaged value for AXM2. AXMe results in a further reduction in the magnitude of C_{SKE} and also further movement of the passage vortex towards the end-wall. All three AXM profiles result in a similar reduction in the extent, and increase in the magnitude of the C_{SKE} peak near the end-wall. The AXM profile does not reduce the extent of this peak by quite as much as AXM2 and AXMe and also results in a greater increase in peak C_{SKE}. Comparing the AXMe and FAITH profiles in Figure 8.6d, the AXMe profile gives a greater reduction in the peak C_{SKE} in the region of the passage vortex than the FAITH profile, and the peak is moved closer to the end-wall (also seen in Table 8.1).

8.3.3 Contour Maps and Secondary Velocity Vectors.

Figures 8.7 a to d show secondary velocity vectors, and contour maps of C_{Po}, yaw angle and C_{SKE} at Slot 10 for the three AXM profiles and the planar end-wall.

From the vector plots in Figure 8.7a, the reduction in the passage vortex can clearly be seen, along with its movement towards the end-wall with the AXM2 and AXMe profiles. With the AXM2 profile, the vortex centre is approximately 35mm from the end-wall and with the AXMe profile, the vortex centre, which is difficult to make out, is approximately 25mm from the end-wall. The passage vortex is centred approximately 60mm from the planar wall. The counter-vortex at approximately -325mm (circumferential location) is reduced, as would be expected with the reduction in passage vortex strength. It is interesting to note that AXM gives the largest reduction in counter-vortex size whereas AXMe gives the smallest reduction.

From the contours of C_{Po} , yaw and C_{SKE}, the reduction in peak loss can clearly be seen, along with the movement of the passage vortex towards the end-wall. The increase in C_{SKE} near the end-wall is probably due to the increased over-turning seen with all of the AXM profiles in Figure 8.5b and in the yaw angle contours in Figure 8.7c. This increased over-turning is probably due to the increased loading in the downstream part of the cascade. The thickening of the wake near the end-wall caused by the mixing or the spanwise velocities downstream of the trailing edge can clearly be seen in Figure 8.7b for the AXM2 and AXMe profiles.

8.4 Conclusions.

Three alternative end-wall profiles have been designed based on the mean line of the blades. From the brief CFD investigation into the effects of these profiles, they should all be effective in reducing the secondary flow within the cascade. The best profile was the AXMe profile which extended upstream and downstream of the blades to attempt to overcome the problems associated with the sharp curvature with the AXM and AXM2 profiles. Further study would result in the optimum method of gaining a smooth transition from the planar end-wall upstream to the profiled wall within the passage. The CFD predicts a 6% reduction in secondary loss and a 61% reduction in C_{SKE}. Whilst the loss predictions are not expected to be accurate, the reduction in C_{SKE} is likely to be similar to that achieved if the profile were tested experimentally. It is possible, considering the FAITH results presented in Chapter 7, that a significant reduction in loss should also result.

Figure 8.1 Modification of the Blade Mean Line.

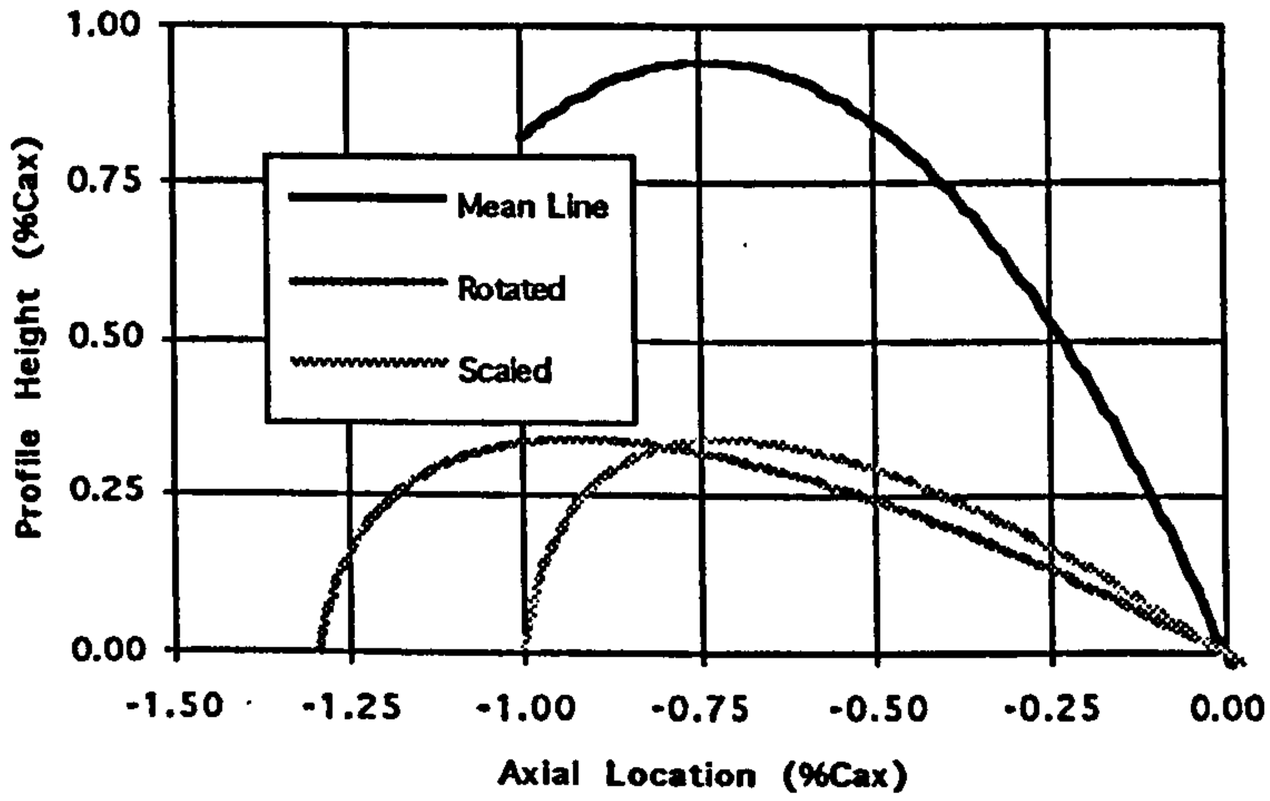

Figure 8.2 Axial Component of Profile AXM2

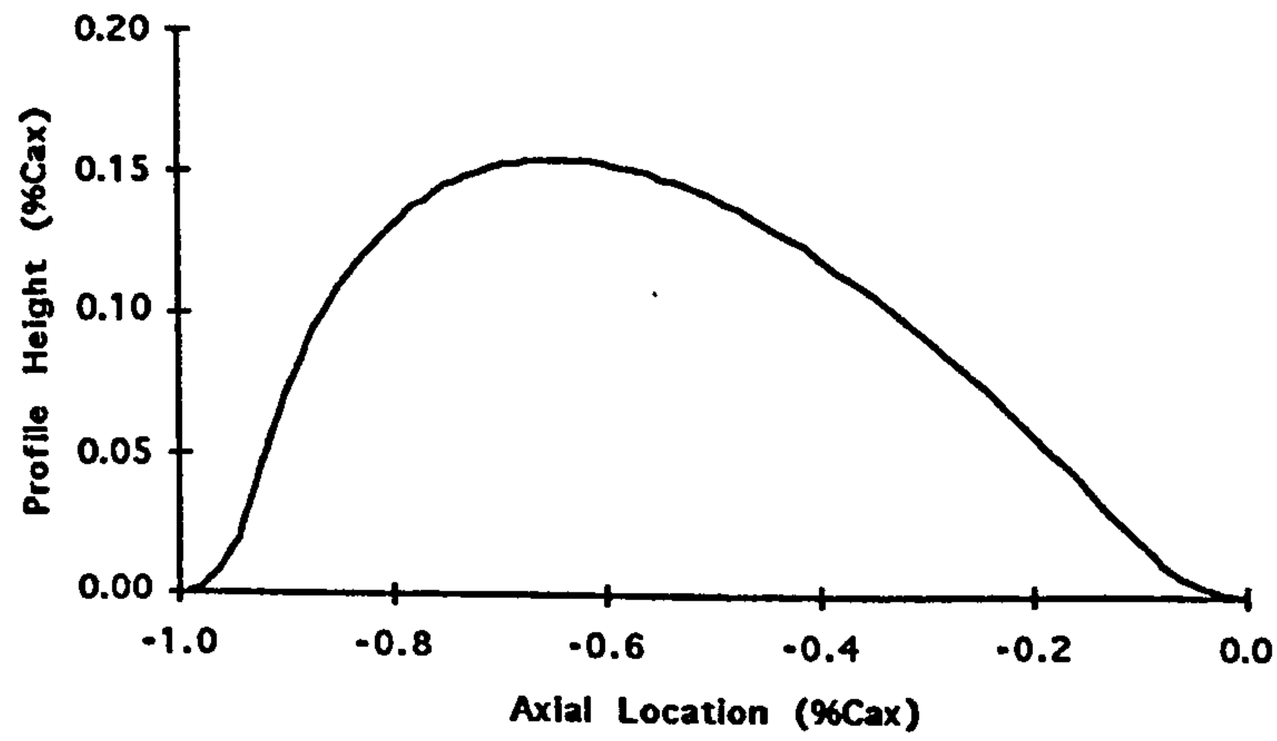

Figure 8.3 Contours of Profile Height (mm).

a) Profile AXM

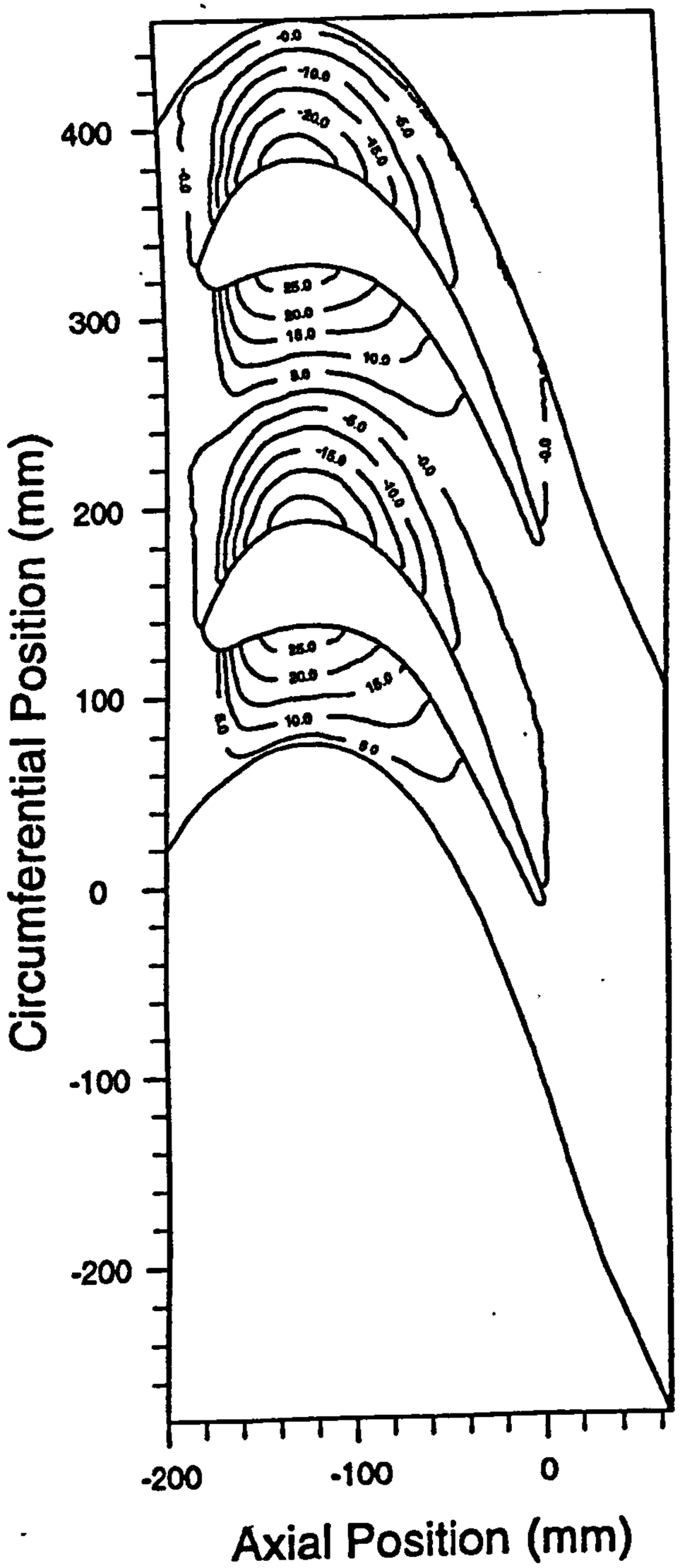

b) Profile AXM2

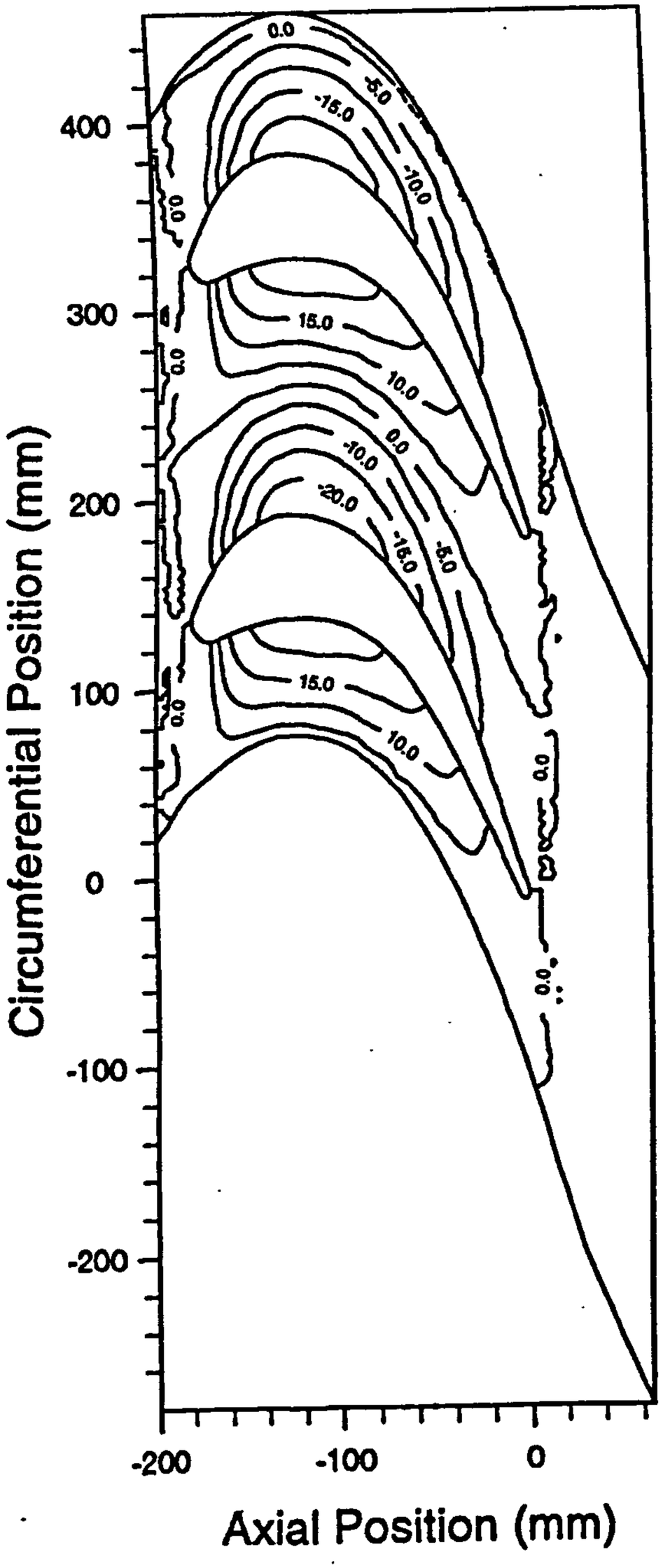

c) Profile AXMe

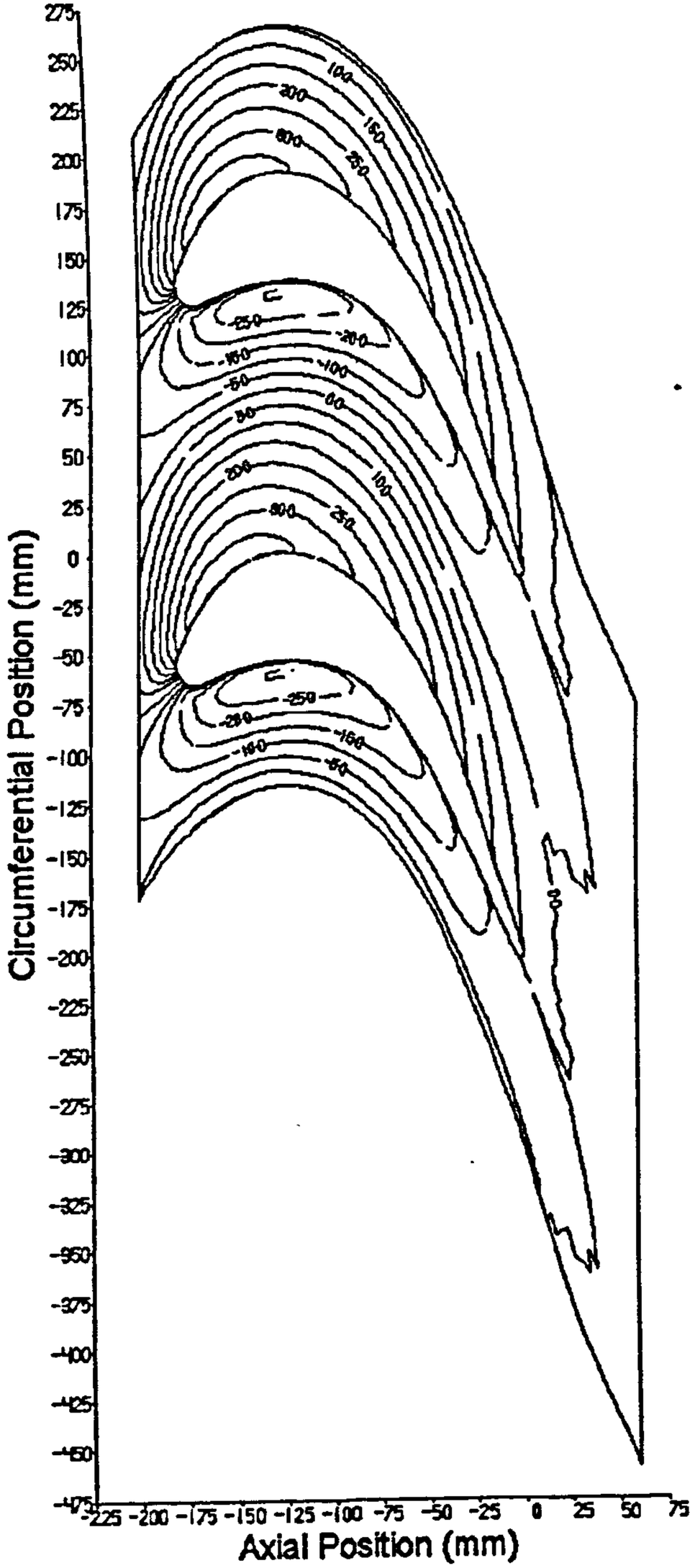

Figure 8.4 CFD End-wall Pressure Coefficients for the AXM, AXM2, AXMe Profiles and the Planar Wall.

a) Profile AXM

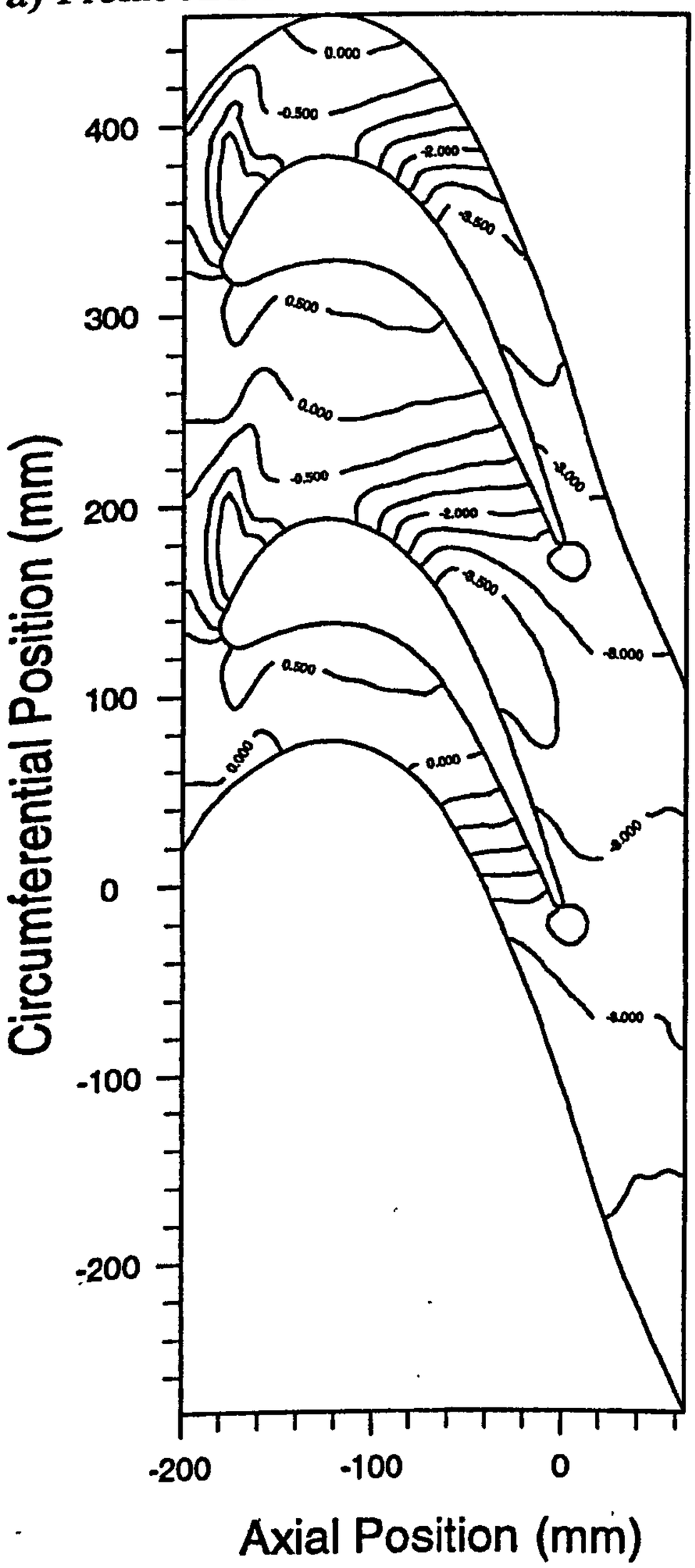

b) Profile AXM2

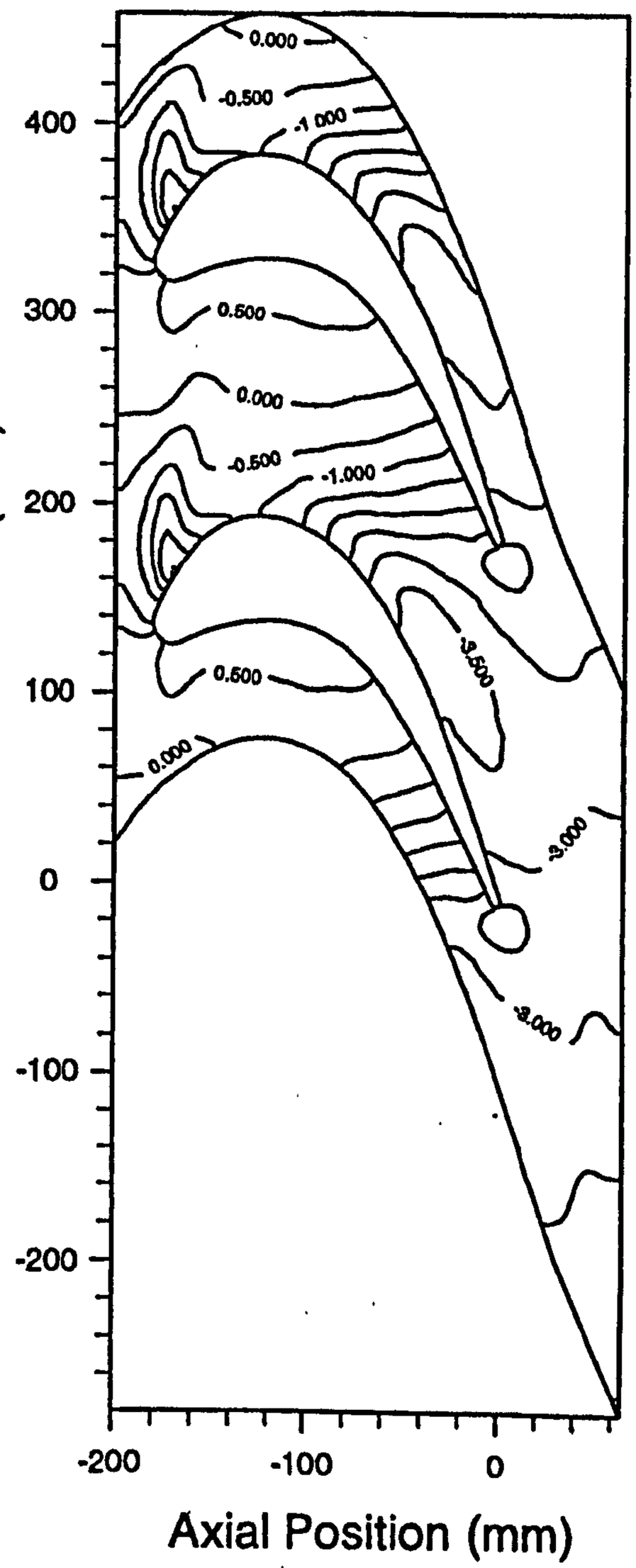

c) Profile AXMe

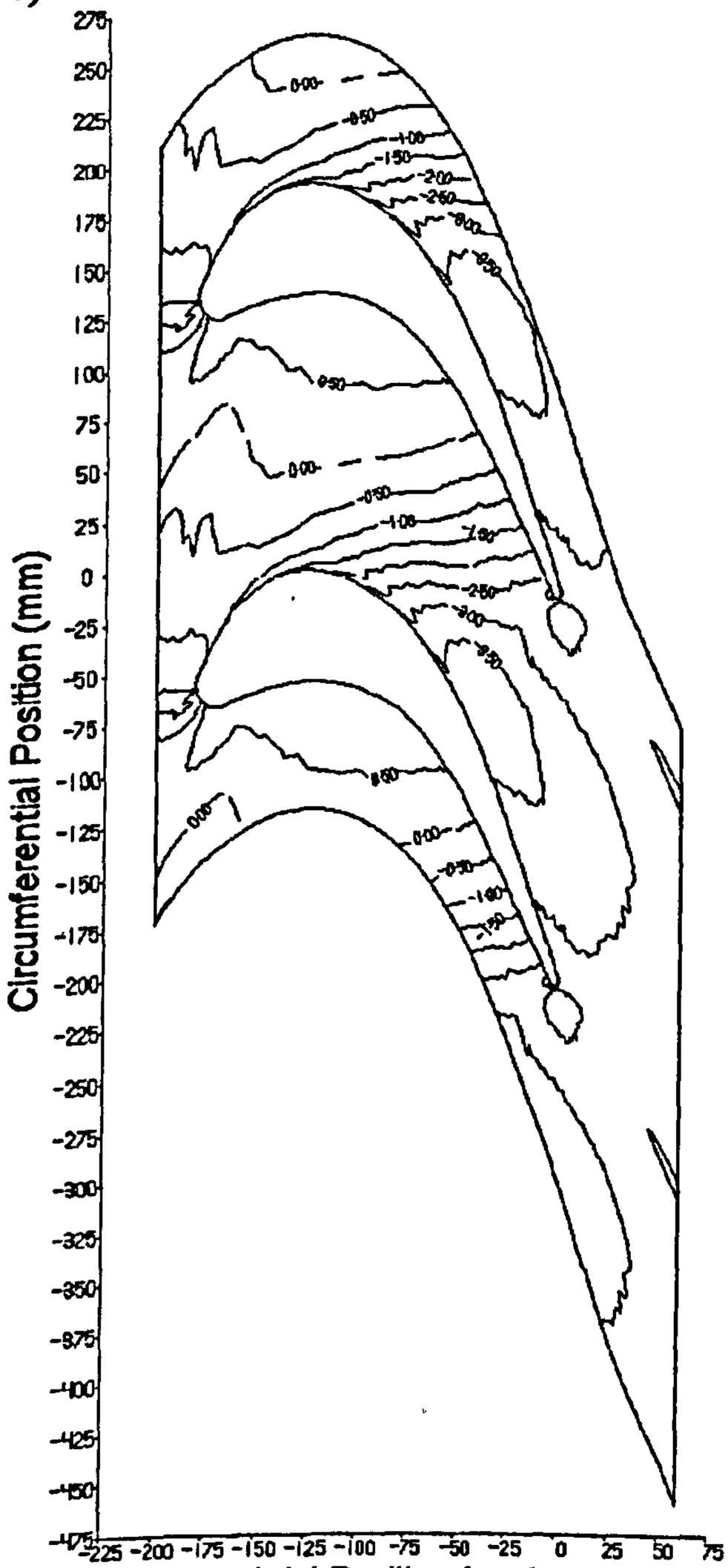

d) Planar Wall

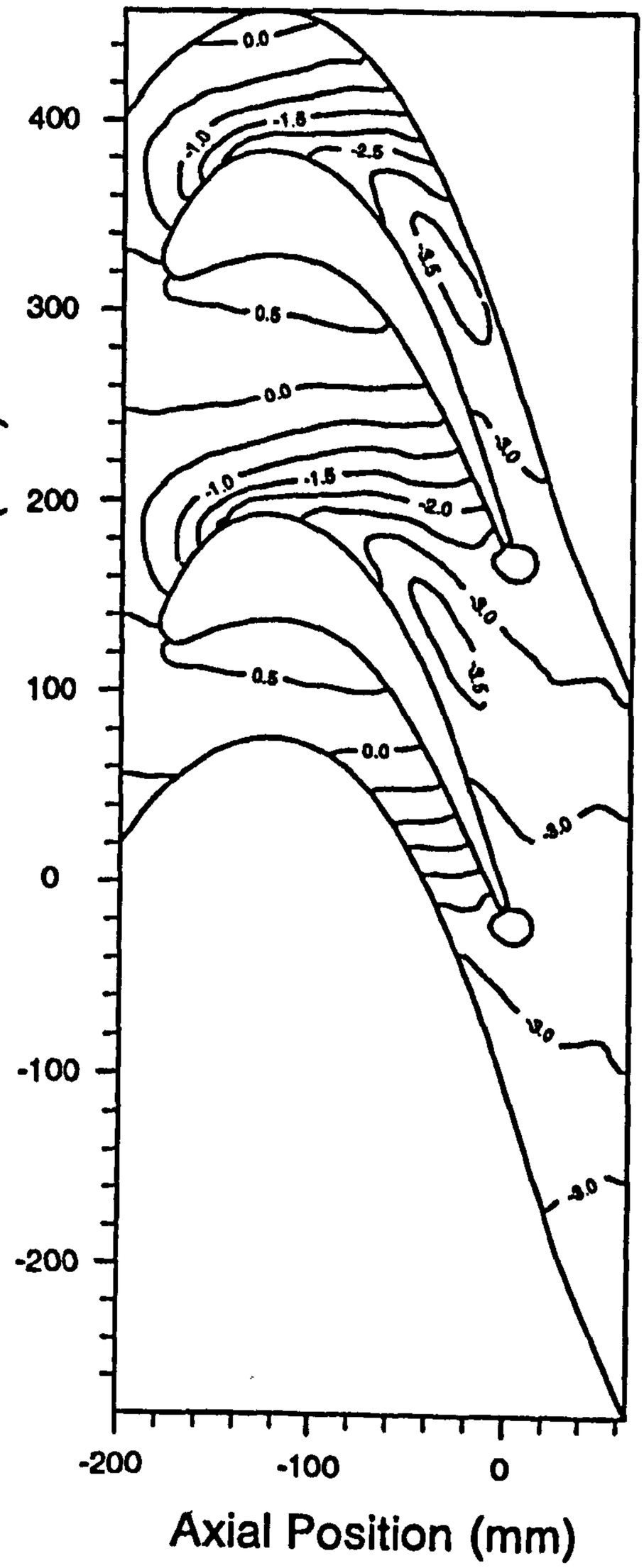

Figure 8.5 Pitch Averaged CFD Data at Slot 10 for AXM, AXM2, AXMe and Planar End-walls.

a) Total Pressure Loss Coefficient.

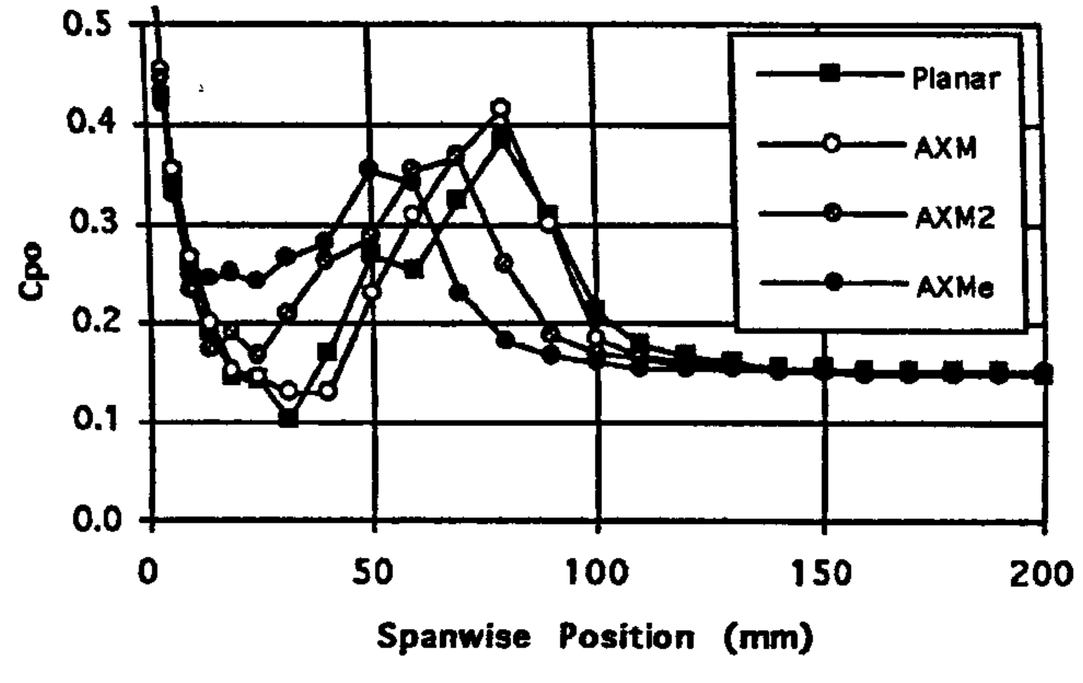

b) Yaw Angle.

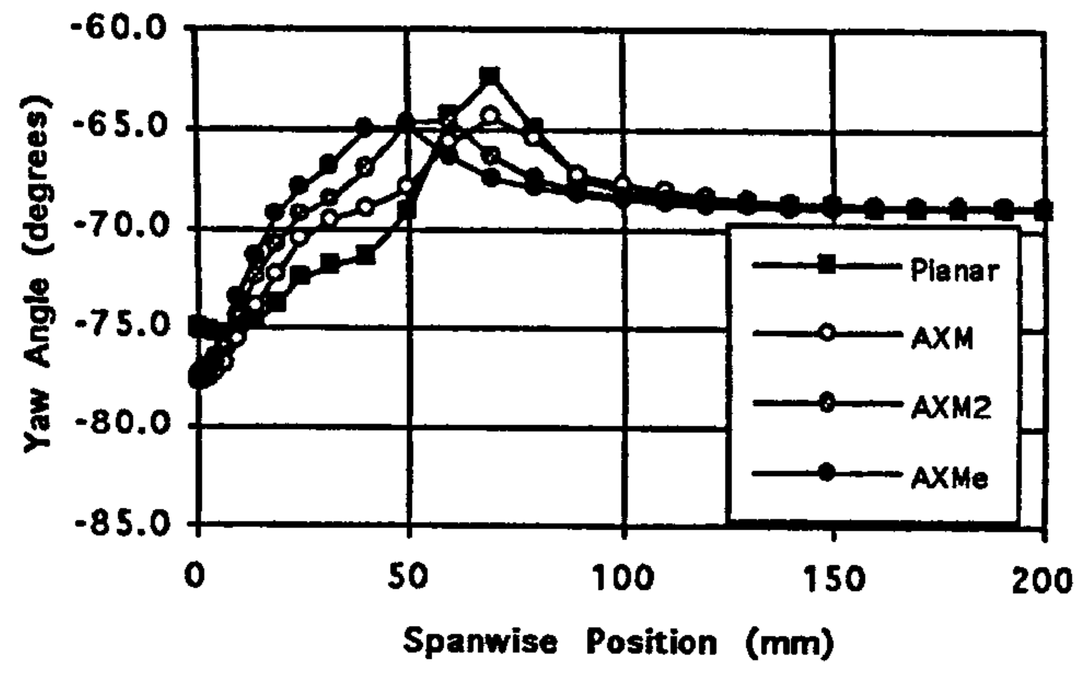

c) Pitch Angle.

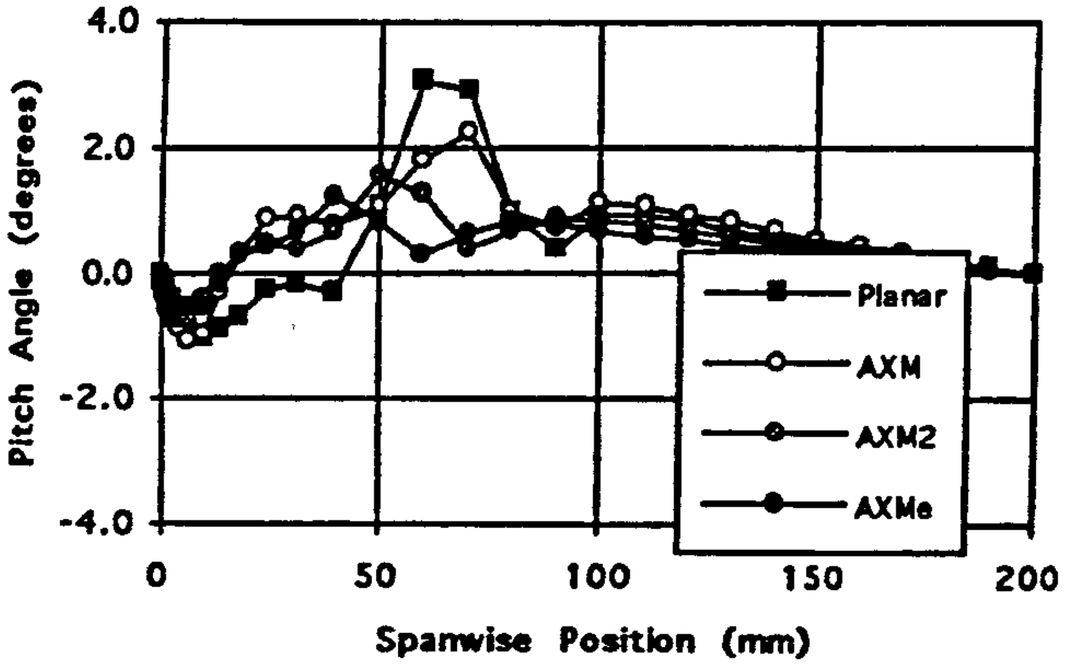

d) Secondary Kinetic Energy Coefficient.

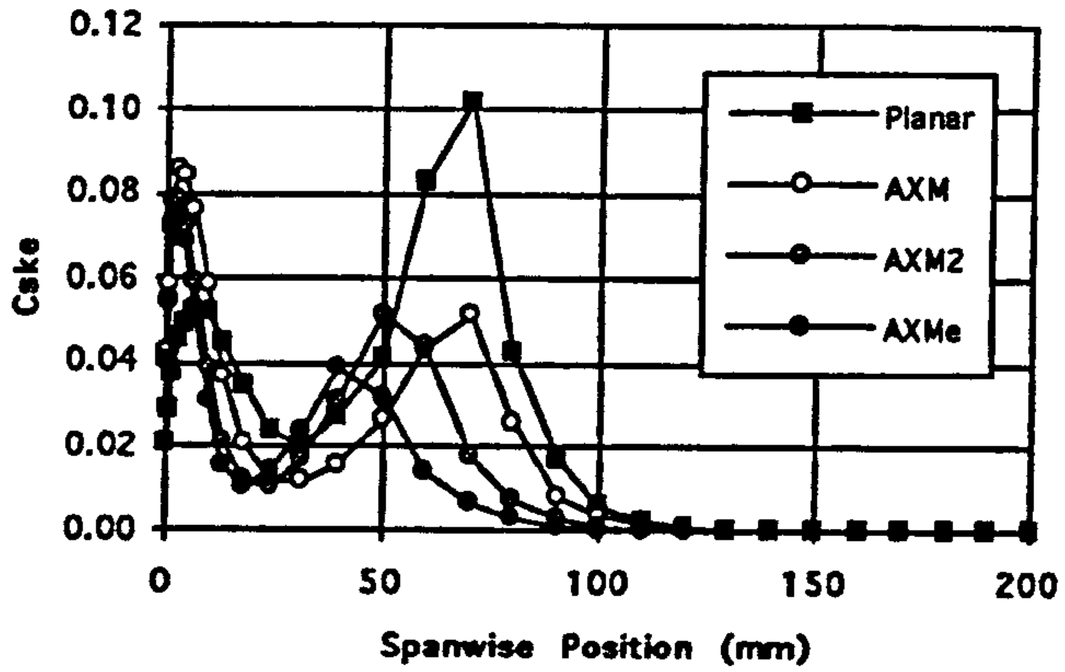

Figure 8.6 Pitch Averaged CFD Data at Slot 10 for FAITH, AXMe and Planar End-walls.

a) Total Pressure Loss Coefficient.

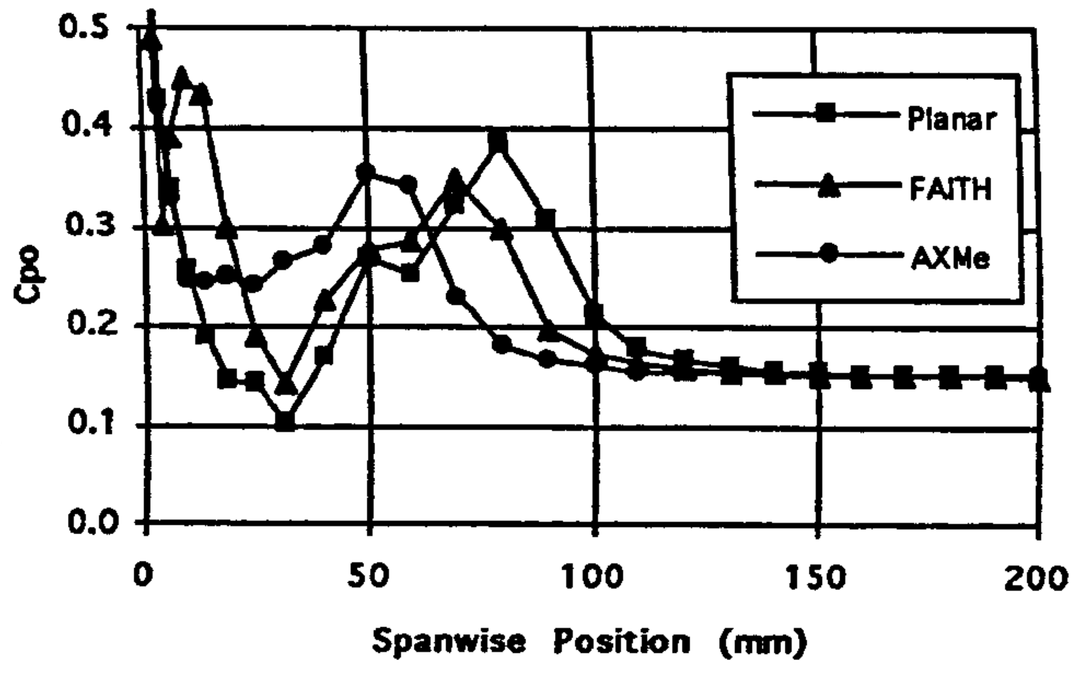

b) Yaw Angle.

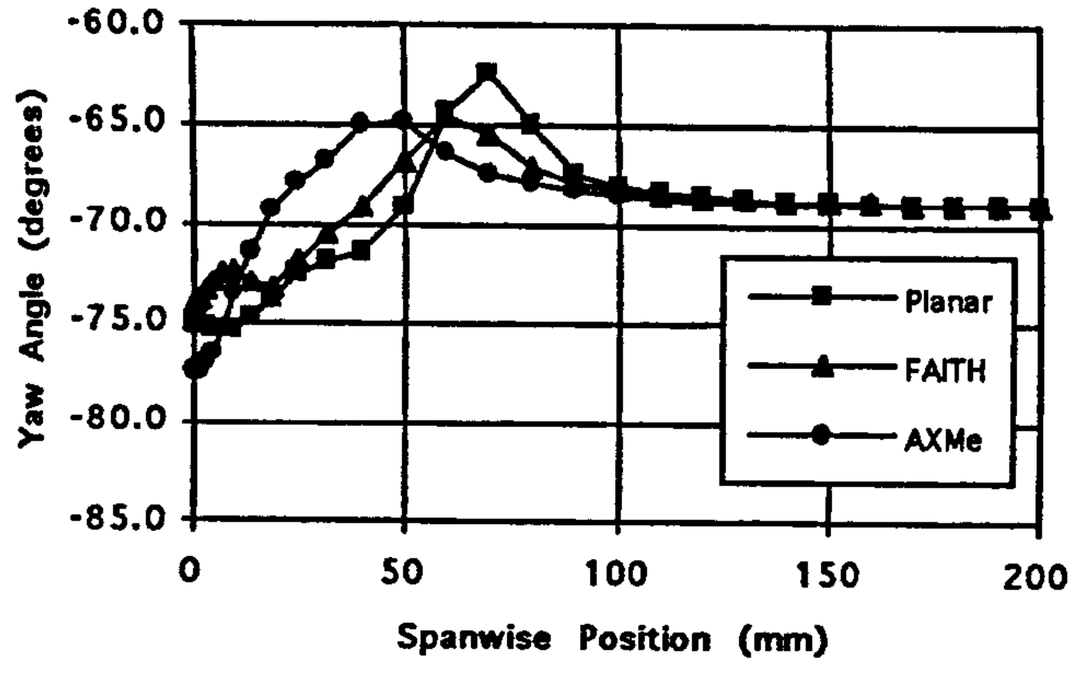

c) Pitch Angle.

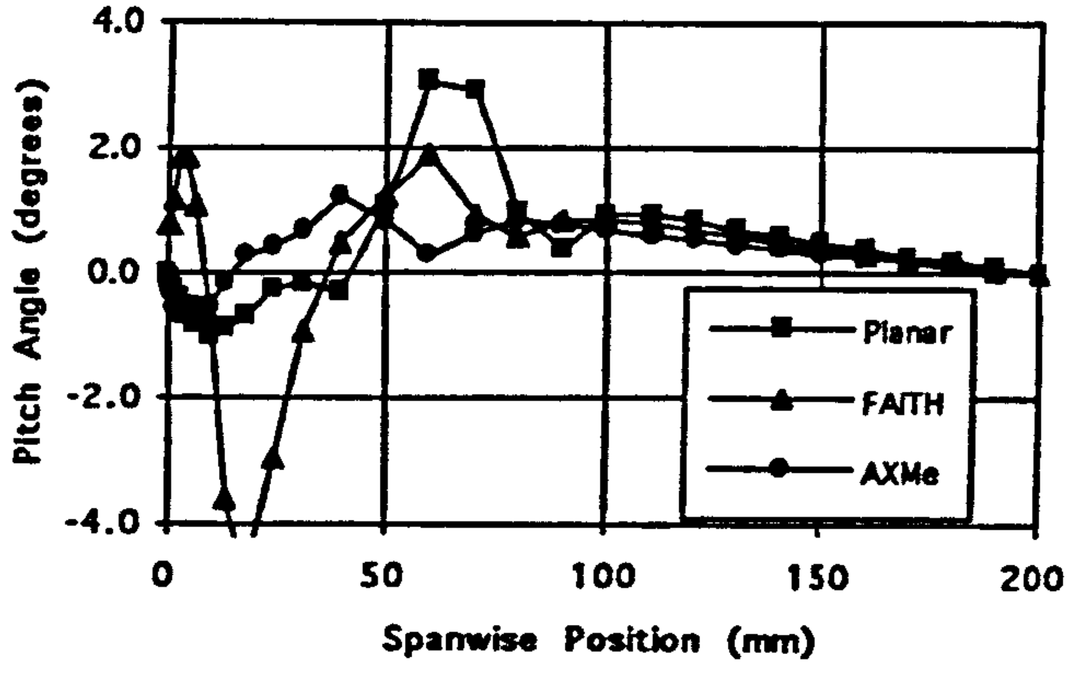

d) Secondary Kinetic Energy Coefficient.

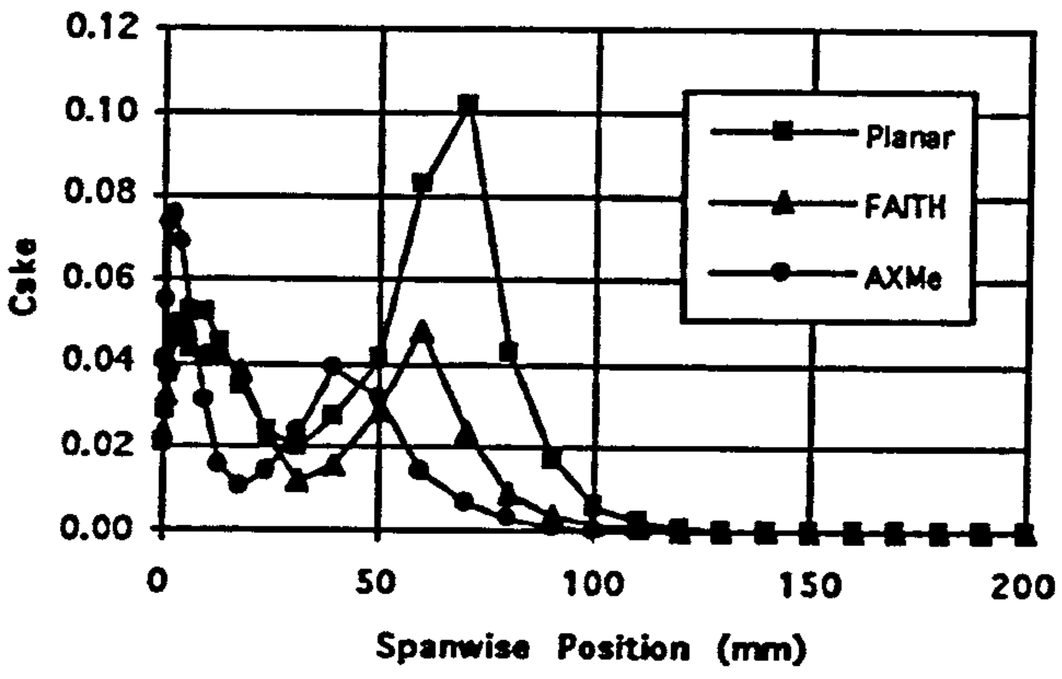

Figure 8.7 CFD Data at Slot 10

a) Secondary Velocity Vectors.

AXM Profile

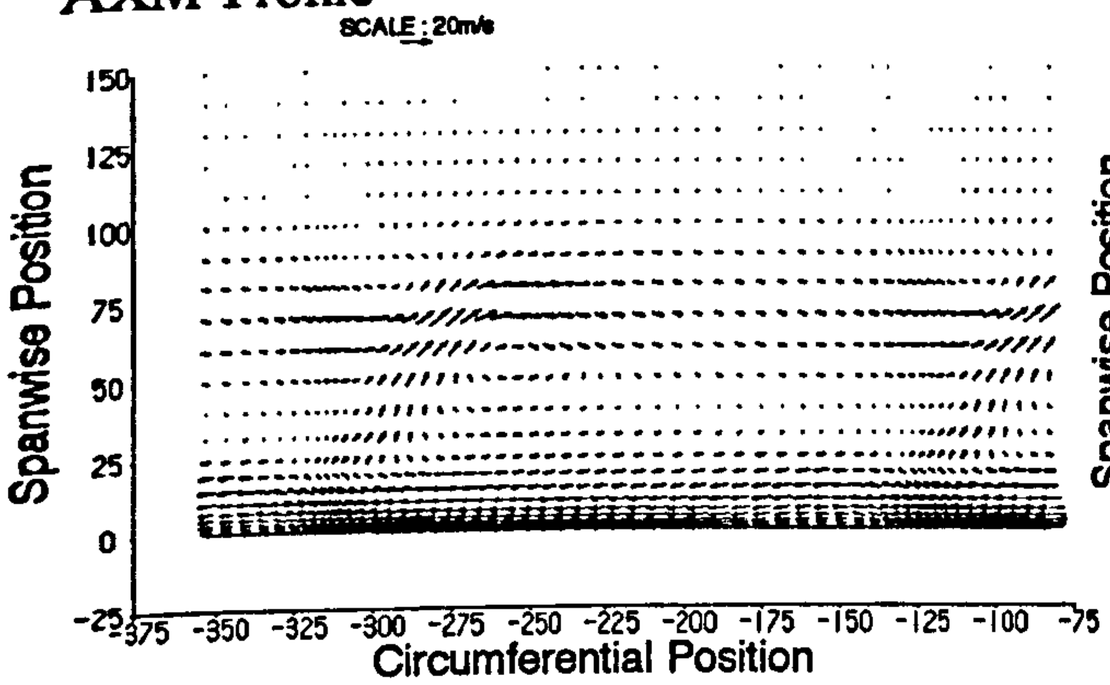

AXM2 Profile

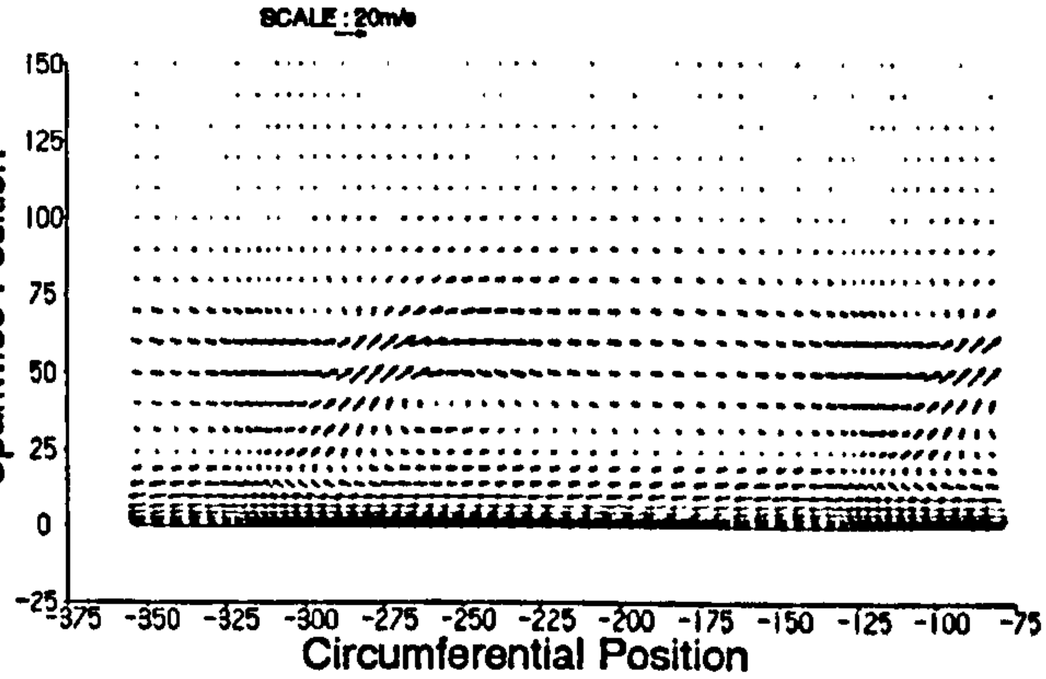

AXMe Profile

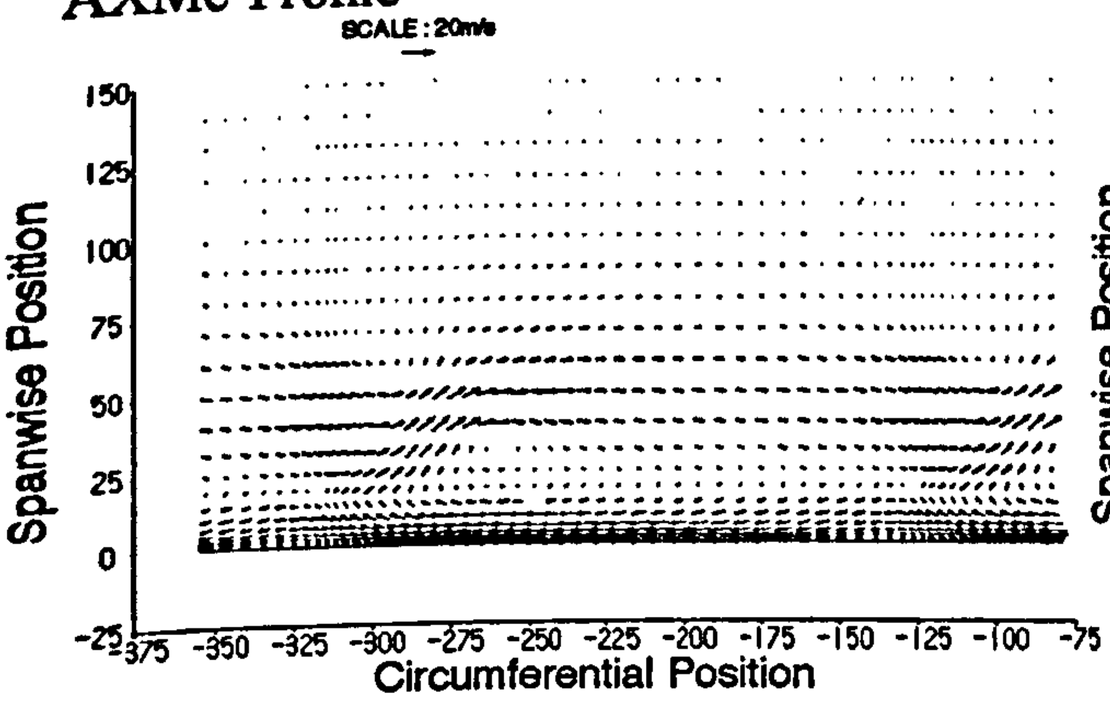

Planar Wall

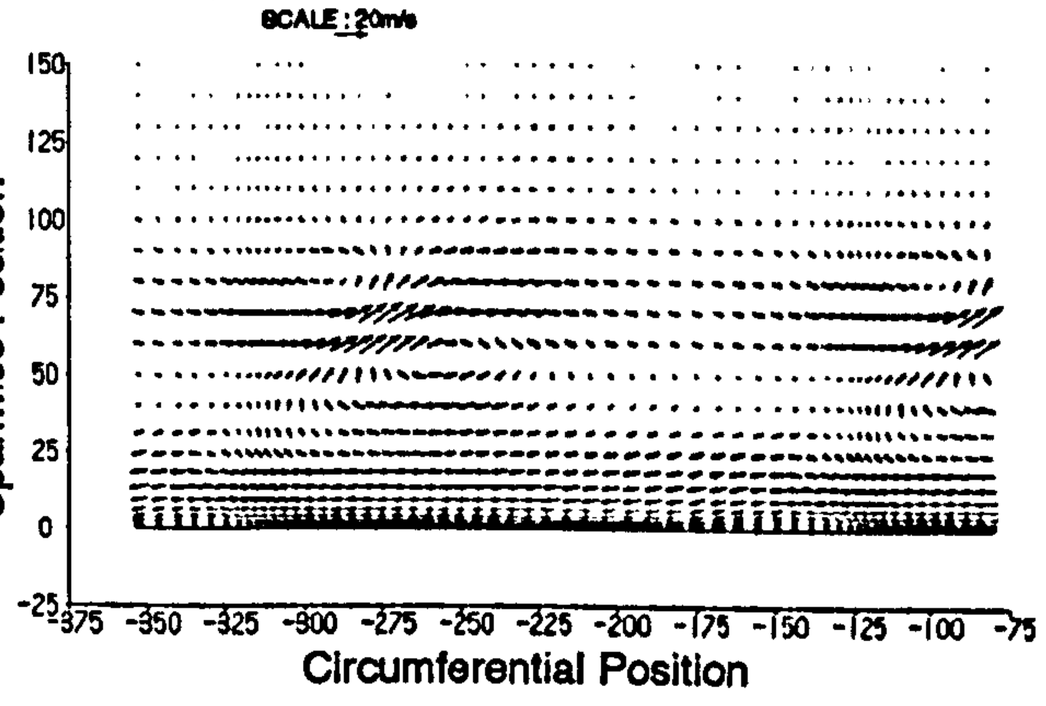

b)Total pressure Loss Coefficient.

AXM Profile

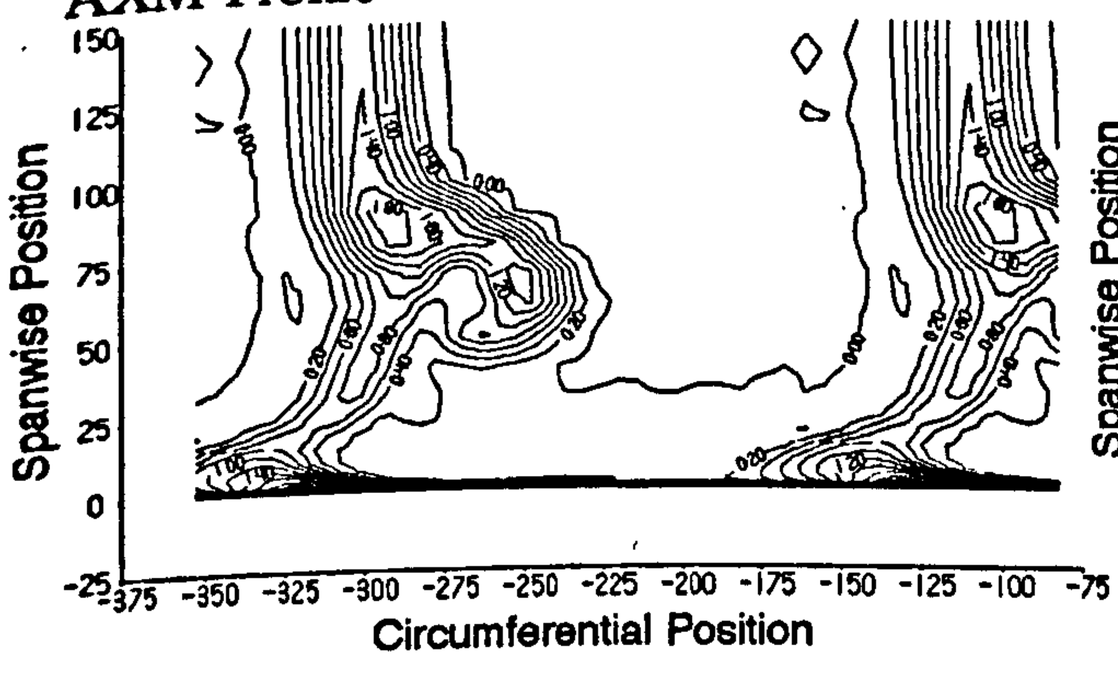

AXM2 Profile

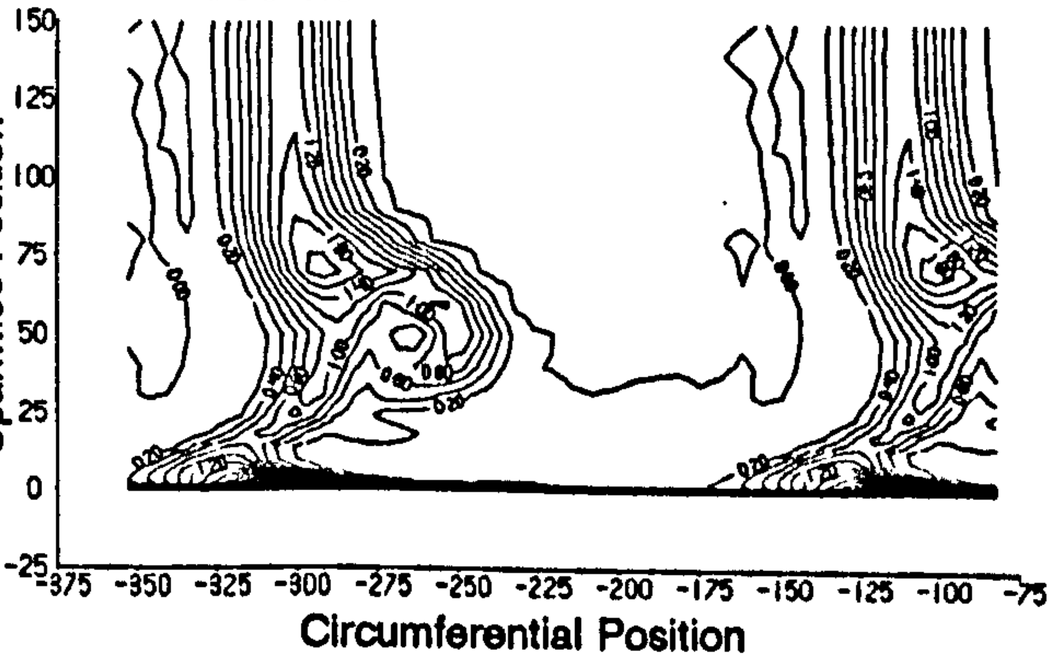

AXMe Profile

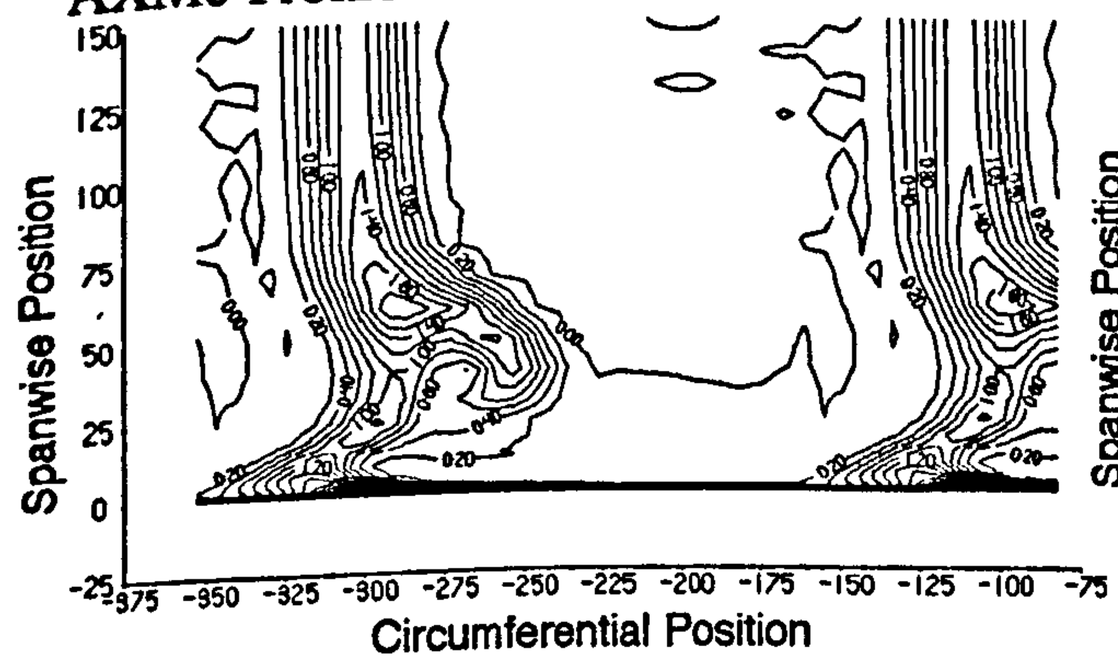

Planar Wall

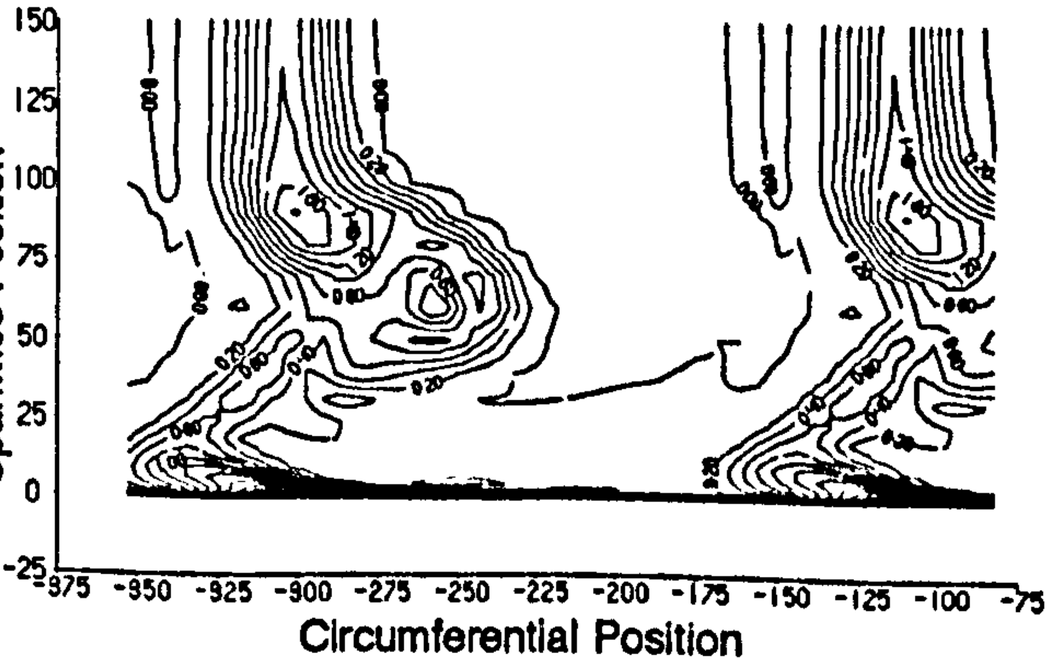

c) Yaw Angle.

AXM Profile

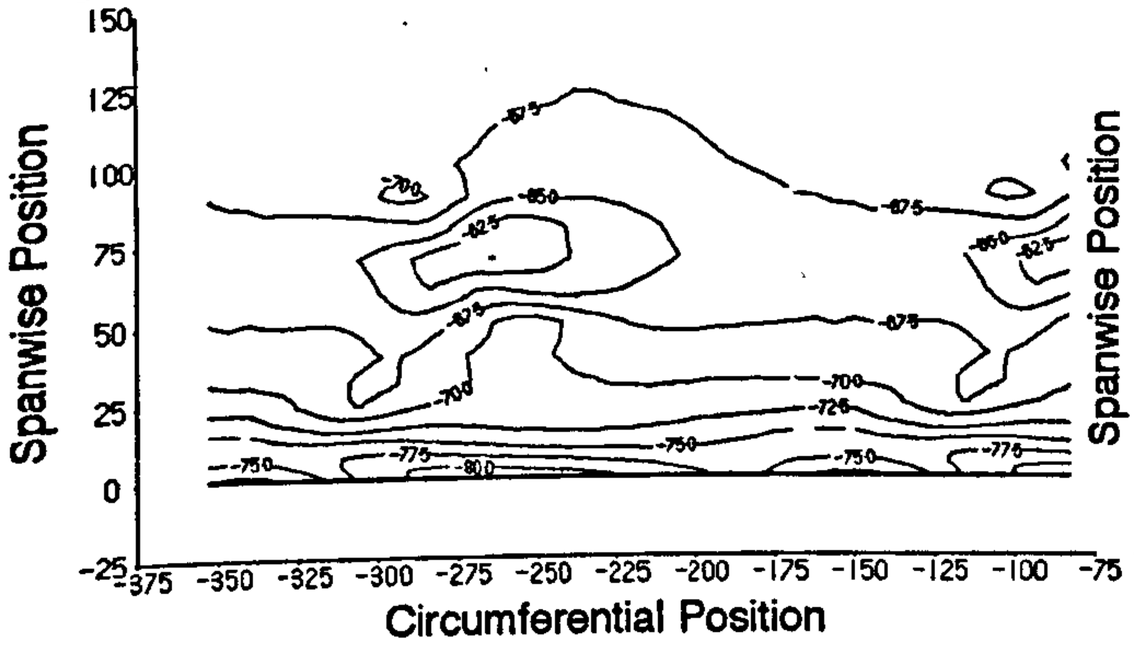

AXM2 Profile

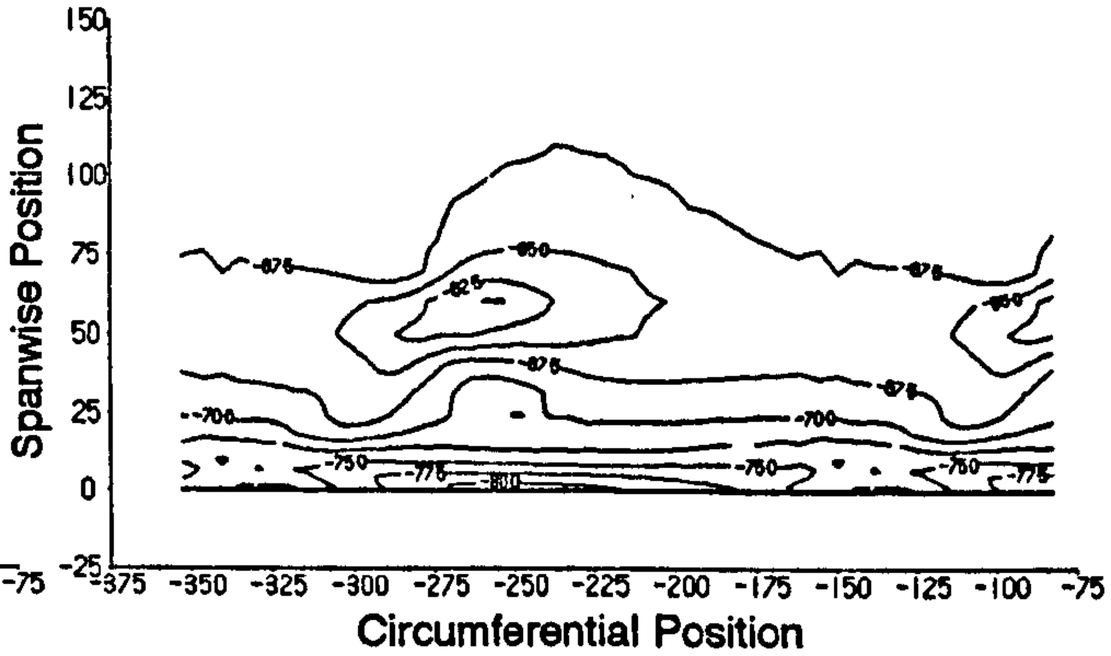

AXMe Profile

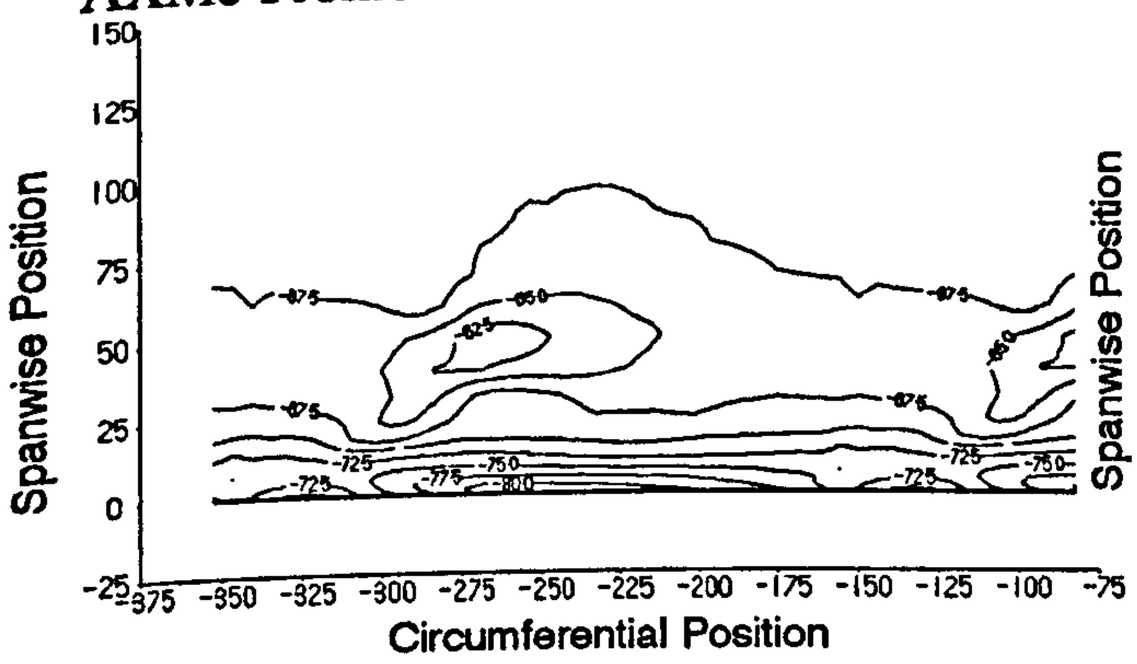

Planar Wall

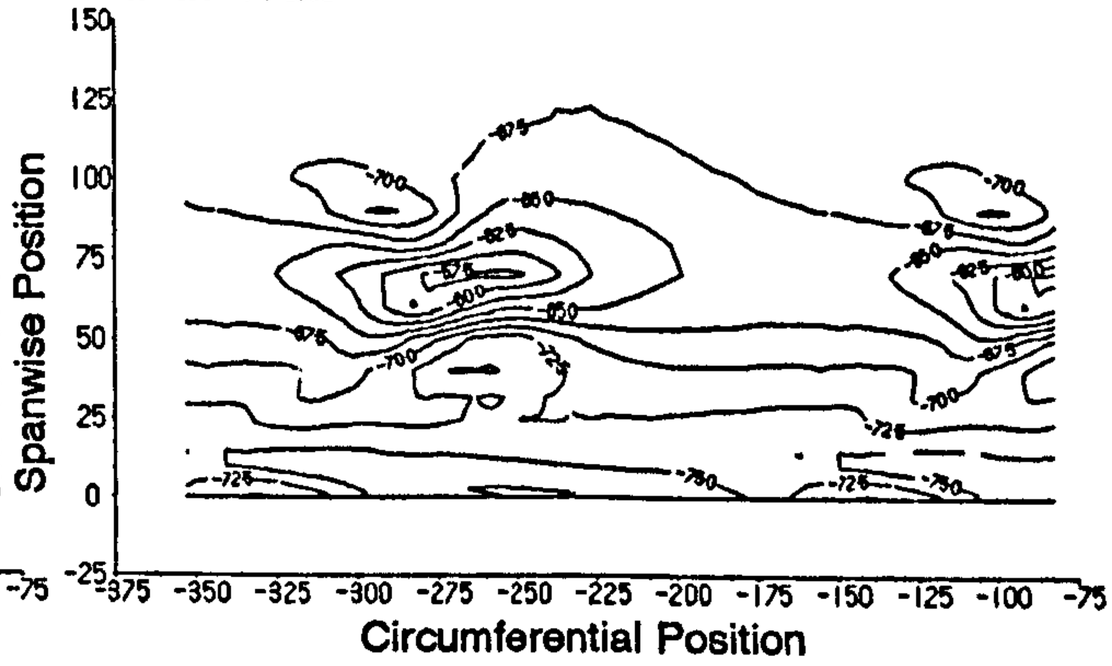

d) Secondary Kinetic Energy Coefficient.

AXM Profile

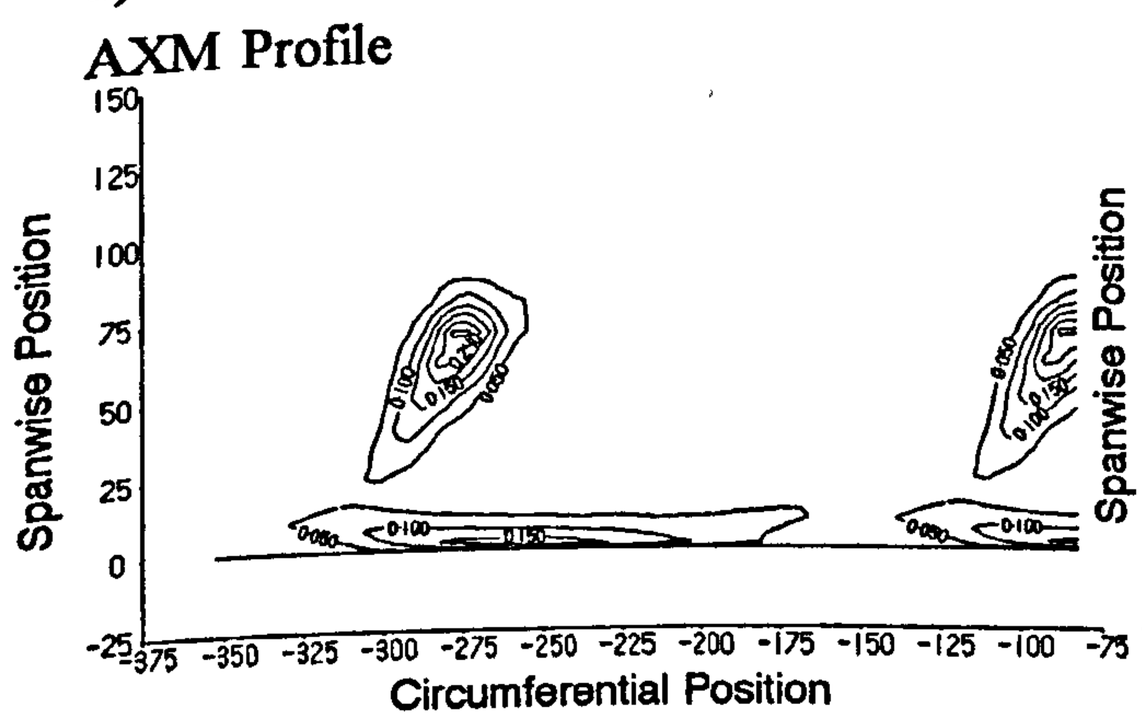

AXM2 Profile

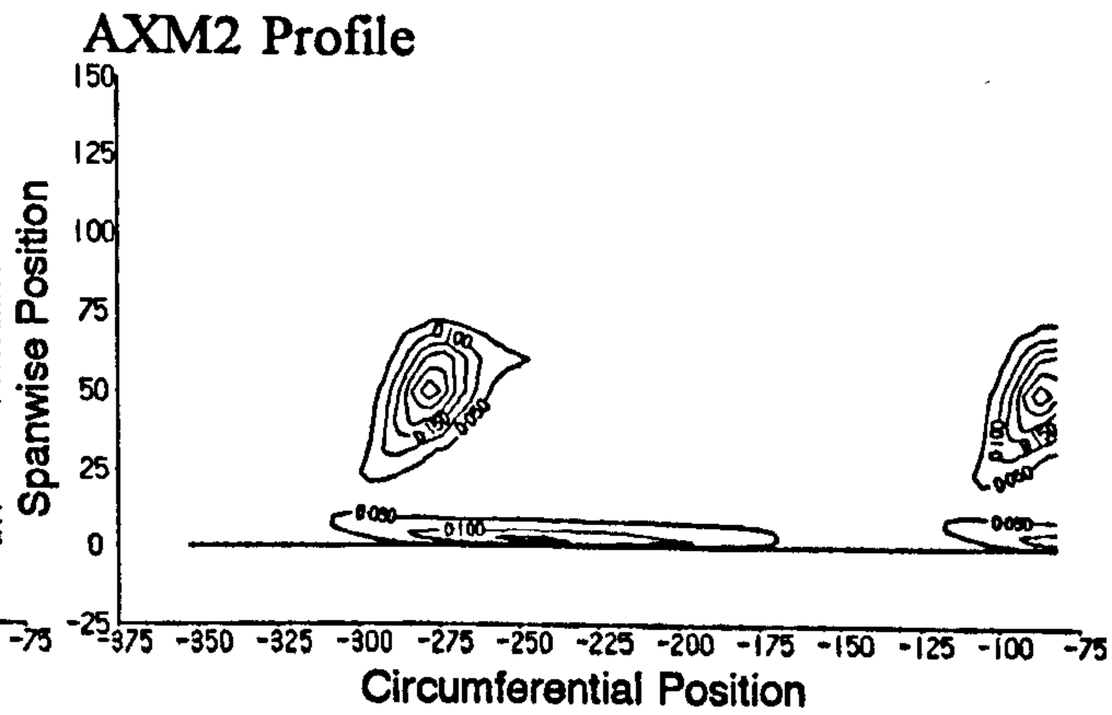

AXMe Profile

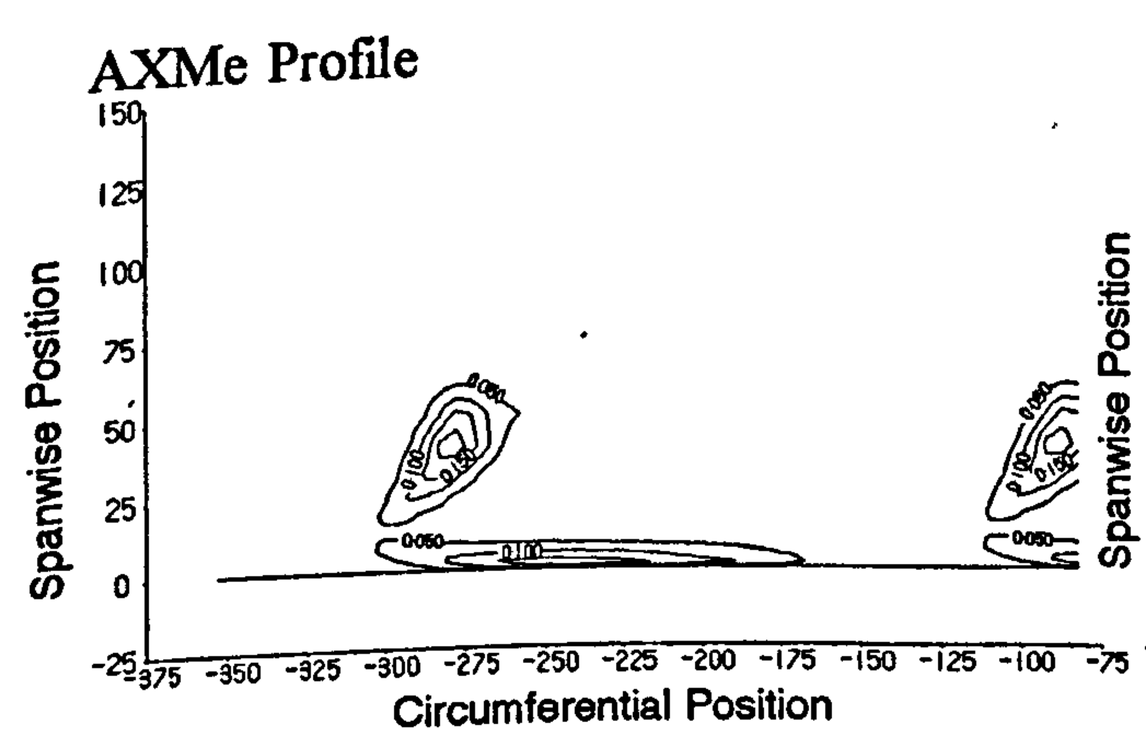

Planar Wall

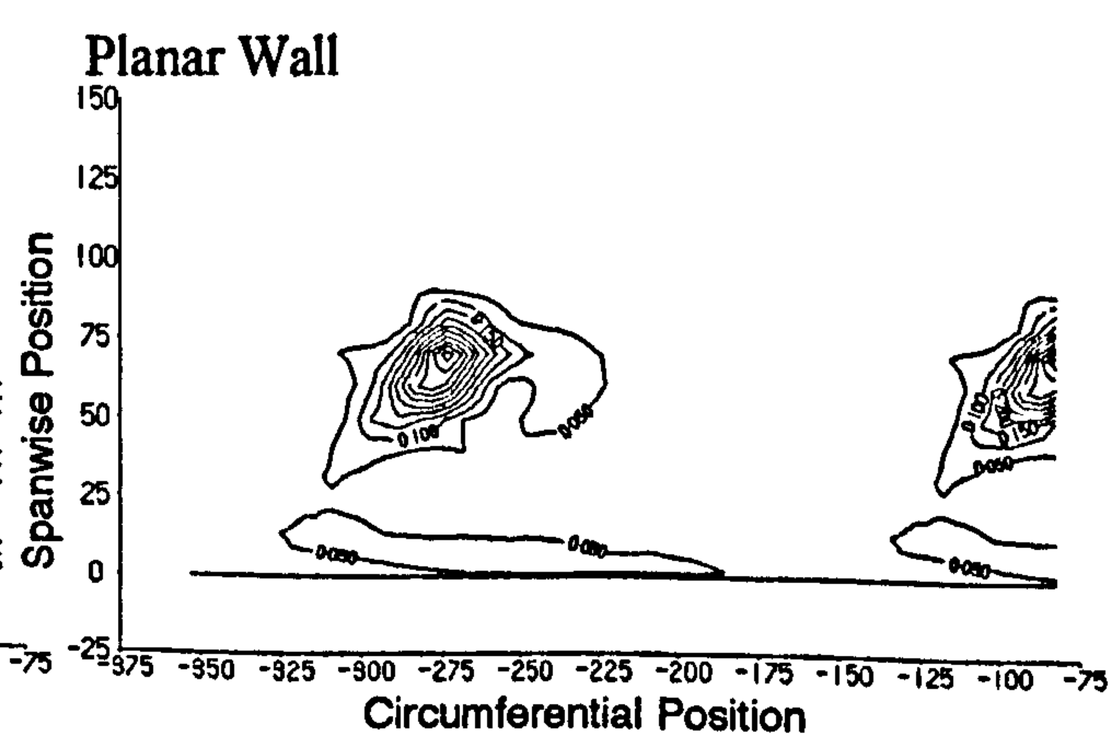

9 Overall Conclusions and Future Work.

The conclusions drawn in each chapter are summarised here, along with other general conclusions. These are followed by suggestions for further work which may be useful in understanding the effect of end-wall profiling on secondary flows, or may answer questions raised here which were not answered satisfactorily due to lack of time or resources.

9.1 Conclusions.

9.1.1 Intermittency Measurements.

A method of measuring boundary layer intermittency using surface mounted hot film gauges has been developed and tested.

The intermittency results from the hot film system over the suction surface and end-wall agree well with the findings of Moore[1995] and prove that the measurements made 1mm from the surface are accurate, similar features of the flow being identified by both detection systems. The passage vortex and its migration across the end-wall and along the blade suction surface have been captured by the hot film measurements, along with the laminar region on the end-wall and the beginnings of its transition back to a turbulent state.

The measurements over the pressure surface were not sufficiently clear to allow valid conclusions to be drawn, however if the gauges were to be more firmly affixed to the blade surface (at the risk of destroying the film on removal) then better measurements should be possible, although this region does not seem to show any features of great interest.

9.1.2 End-wall Profile Manufacture.

A method has been developed to allow arbitrary profiled end-walls to be manufactured on-site in Durham. Software written to cover the processes of extracting height data from a CFD grid, calculating a three-dimensional tool cutting path from the CFD height data and transmitting this from an IBM compatible PC to a CNC milling machine via a serial cable. The CNC machine has also been programmed to receive the data from the serial port and to carry out a number of predetermined functions defined within the CNC program in response to the received data. The cost of a set of profiles using this system (excluding time costs) is approximately £100.00, which compares favourably with an estimate obtained for rapid prototyping the profiles of £2500.00 per end-wall segment (5 segments are required in total). Considering the internal charges for technician time, it is estimated that the total cost of a set of machined profiles would be £450 which is still very competitive. A set of profiles takes approximately one week to machine, and a further week to sand and varnish. The surface finish on the profiles is very good and appears to have no effect on the flow within the cascade.

9.1.3 Repeat of Datum Case.

Whilst the change in position of the reference probe has changed the absolute values of loss when compared with previous research, the flow-field is unchanged from previously reported research in this cascade. It is therefore highly likely that the non-uniformity in inlet total pressure existed for previous data from the cascade, even though it was not referenced directly. Any effects of surface roughness caused by the end-wall manufacture method do not seem to play a significant role in the flow development within the passage in comparison to the cross passage pressure gradients near the end-wall.

The coarse grid CFD resolved the static pressures within the cascade with reasonable accuracy, as did the fine grid. However, only the fine grid was able to resolve the flow within the passage accurately.

9.1.4 Reduction of Circumferential Pressure Non-uniformities at Exit from the Cascade.

The results presented in Chapter 6 proved that it is possible to design an end-wall profile using CFD methods to directly control the end-wall static pressure distribution. The changes in end-wall pressure resulting from profiling have been shown to be directly related to the curvature of the end-wall profiling. The experimental testing of the profile confirmed the results of the CFD design used to control the pressure distribution on the end-wall. The end-wall profiling in this case does not have a significant effect on the secondary flow, although the loss is increased slightly. This is thought to be due to sharp curvature at the trailing edge, and the resulting reduction in size of the passage vortex as it fails to recover its radial location as the end-wall returns to zero height.

9.1.5 End-wall Profiling to Reduce Secondary Loss.

The profile designed using the FAITH design code has been very successful in reducing the secondary flow and secondary losses. The experimental net secondary loss through the cascade is reduced by over 21%, and the net mixed out secondary loss is reduced by almost 26% with the profile in place. Although the CFD results indicated a slight increase in loss, the trends predicted by the pitch averaged loss and loss contours are correct. The experimental secondary kinetic energy at Slot 10 is reduced by 48%, and the CFD predicted this very well, giving a 49% reduction. The velocity vectors show that the CFD predicts of flow features are accurately. From the results presented in Chapter 7, CFD design based on secondary flow rather than secondary loss would appear to be an achievable goal.

9.1.6 Alternative End-wall Design Method.

The three alternative end-wall profiles designed based on the mean line of the blades should all be effective in reducing the secondary flow within the cascade. The best profile was the AXMe profile which extended upstream and downstream of the blades to attempt to overcome the problems associated with the sharp curvature with the AXM and AXM2 profiles.

The CFD investigation predicted a 6% reduction in secondary loss and a 61% reduction in C_{SKE}. Whilst the loss predictions are not expected to be accurate, the reduction in C_{SKE} is likely to be similar to that achieved if the profile were tested experimentally, and the loss reduction should be larger than predicted.

9.2 Future Work.

A number of areas where additional work may be necessary, or desirable to further understand or extend the work carried out here have become apparent. These are briefly outlined below.

9.2.1 Intermittency Measurements.

Whilst the intermittency measurements on the blade suction surface and end-wall proved to be accurate, those on the pressure surface gave no useful information. This was ascribed to there being a gap between the gauge and blade surface caused by a combination of the concave curvature and the method used to removably attach the gauges to the surface. It would be necessary to attach the gauges firmly to the blade pressure surface to overcome this which would result in destruction of the gauge. Either further work to investigate an alternative method of gauge mounting, or a significant investment would be needed to supply sufficient gauges to account for their "one-shot" nature.

9.2.2 Reduction of Circumferential Pressure Non-uniformities at Exit from the Cascade.

The profile generated in this work only aimed to reduce the first harmonic of the platform trailing edge pressure non-uniformity, and further iterations using the same procedure could potentially eliminate the pressure non-uniformity altogether. A more advanced profile than that tested would need to be designed, manufactured and tested to prove that this is in fact the case. It would also be of interest to investigate the effect of this profile on the boundary layer within the cascade and the near wall flow. This could be carried out using the hot wire anemometry method of Moore [1995] or the hot film method describe in Chapter 3 and using firmly mounted gauges. Finally, the effects of this profiling method need verifying within a rotating blade row to investigate the upstream potential effects of the following blade row on the profile.

9.2.3 End-wall Profiling to Reduce Secondary Loss.

The results of the FAITH designed profile had a number of shortcomings which could be eliminated. The effect of the sharp re-entrant corner along the suction-surface intersection should be investigated further, as a potential cause of the large counter-vortex generated by the profile tested here. Intermittency measurements should also be taken to investigate the inability of the CFD to predict the losses within the cascade with a profiled end-wall. Further work is also needed to redesign a profile with upstream and downstream limits more within the scope of actual turbine design. Again, it is important that this profile, or a similar profile addressing the above comments, be tested within a rotating blade row to investigate the effects of upstream and downstream blades on the profiling.

9.2.4 Alternative End-wall Design Method.

The brief investigation into the three AXM profiles provided very promising results and the design philosophy is very simple. Further study into these profiles is required to find the optimum method of gaining a smooth transition from the planar end-wall upstream to the profiled wall within the passage using the minimum amount of profiling outside the axial limits of the blades. Once this has been done, the resulting profile should be tested experimentally to verify the CFD predictions.

Appendix A Data Processing.

Definitions.

A1 Total pressure coefficient

$$C_{Po} = \frac{P_{0inlet} - P_0}{\frac{1}{2}\rho U_{inlet}^2}$$

A2 Static pressure coefficient

$$C_{Ps} = \frac{P - P_{inlet}}{\frac{1}{2}\rho U_{inlet}^2}$$

A3 Yaw angle

$$\beta = \tan^{-1}\left(\frac{U_2}{U_1}\right)$$

A4 Pitch angle

$$\alpha = \tan^{-1}\left(\frac{U_3}{U_1}\right)$$

A5 Secondary kinetic energy coefficient

$$C_{SKE} = \frac{U_{ts}^2 - U_3^2}{U_{inlet}^2}$$

$$\text{Where } U_{ts} = \frac{U_1 \sin(\beta - \beta_{mid})}{\cos(\beta)}$$

A6 Inviscid compensated secondary kinetic energy coefficient

$$C_{SKE(i)} = \frac{\left(U_1 \frac{\sin(\beta - \beta_{inv})}{\cos(\beta)}\right)^2 + \left(\frac{U_1 \sin(\alpha - \alpha_{inv})}{\cos(\alpha)}\right)^2}{U_{inlet}^2}$$

Pitch and Area Mass Averages.

Pitch averages are denoted by a single bar, $\overline{\phi}$, and area averages are denoted by a double bar, $\overline{\overline{\phi}}$.

A7 Total pressure loss coefficient

$$\overline{C_{Po}} = \frac{\int_{s_0}^{s_1} C_{Po} U_1 \Delta r \, dy}{\int_{s_0}^{s_1} U_1 \Delta r \, dy} \qquad \overline{\overline{C_{Po}}} = \frac{\int_{h_0}^{h}\int_{s_0}^{s_1} C_{Po} U_1 \, dydz}{\int_{h_0}^{h}\int_{s_0}^{s_1} U_1 \, dydz}$$

Where $\Delta r = \frac{(h-z)(h_{0planar} - h_{0profiled})}{(h-h_{0planar})(h-h_{0profiled})} + 1$ is the relative height of the integration path, $z = \frac{(z_0 - h_{0planar})(h-h_{0profiled})}{(h-h_{0planar})} + h_{0profiled}$, z_0 is the equivalent planar path and $h_{0profiled}$ is the varying pitchwise end-wall height.

A8 Yaw angle

$$\overline{\beta} = \tan^{-1}\left[\frac{\left(\int_{s_0}^{s_1} U_2 U_1 \Delta r \, dy\right)\left(\int_{s_0}^{s_1} \Delta r \, dy\right)}{\left(\int_{s_0}^{s_1} U_1 \Delta r \, dy\right)^2}\right] \qquad \overline{\overline{\beta}} = \tan^{-1}\left[\frac{\left(\int_{h_0}^{h}\int_{s_0}^{s_1} U_2 U_1 \, dydz\right)\left(\int_{h_0}^{h}\int_{s_0}^{s_1} 1 \, dydz\right)}{\left(\int_{h_0}^{h}\int_{s_0}^{s_1} U_1 \, dydz\right)^2}\right]$$

A9 Secondary kinetic energy coefficient

$$\overline{C_{SKE}} = \frac{\int_{s_0}^{s_1} C_{SKE} U_1 \Delta r \, dy}{\int_{s_0}^{s_1} U_1 \Delta r \, dy} \qquad \overline{\overline{C_{SKE}}} = \frac{\int_{h_0}^{h}\int_{s_0}^{s_1} C_{SKE} U_1 \, dydz}{\int_{h_0}^{h}\int_{s_0}^{s_1} U_1 \, dydz}$$

Mixed out Loss Values.

A10 Mixed out loss (after Moore[1995])

$$C_{P\infty} = 1 + \frac{1}{U_{inlet}^2}\left[U_{1\infty}^2 - U_{2\infty}^2 + \frac{1}{\int_{h_0}^{h}\int_{s_0}^{s_1} 1\ dydz}\left(U_{inlet}^2 \int_{h_0}^{h}\int_{s_0}^{s_1} C_{Ps}\ dydz - 2\int_{h_0}^{h}\int_{s_0}^{s_1} U_1\ dydz\right)\right]$$

Where $U_{1\infty} = \dfrac{\int_{h_0}^{h}\int_{s_0}^{s_1} U_1\ dydz}{\int_{h_0}^{h}\int_{s_0}^{s_1} 1\ dydz}$ and $U_{2\infty} = \dfrac{\int_{h_0}^{h}\int_{s_0}^{s_1} U_2U_1\ dydz}{\int_{h_0}^{h}\int_{s_0}^{s_1} U_1\ dydz}$

Appendix B End-wall Manufacture Software.

Batch File For IBM PC "MACHINE.BAT".

```
MODE COM1: BAUD=9600 PARITY=O STOP=2

SEND2 %1
```

C Program "SEND2.C".

```
#include <stdio.h>

#include <conio.h>

#include <string.h>


#define MCR     0x3fe   /* Modem ctrl register          */

#define TB      0x3f8   /* Tx buffer                    */

#define LSR     0x3fd   /* Line status register         */


#define CTS     0x10    /* Clear to send                */

#define DSR     0x20    /* Data set ready               */

#define THRE    0x20    /* Tx holding register empty    */


main(int argc, char *argv[]) /* argc = Number of arguments in command line :

argv[] = Arguments */

{

char temp,*p;

FILE *fp;

char st[100];


if( argc != 2) /* If not started with "program_name datafile_name" */

      {

      printf("Command is : %s filename",argv[0]);
```

```
        exit(1);
        }

if( (fp=fopen( argv[1] , "r" ) ) == NULL ) /* Open file given in string at
*argv[1] */
        {
        printf("No such file as %s\n",argv[1]);
        exit(1);
        }

/*      read string and send to m/c tool, if not busy and cts */

while(1)
        {
        if( fscanf( fp , "%s" , st ) != 1 ) /* Read current number from file
checking for EOF */
                {
                printf("End of file\n");
                exit(1);
                }

        if(st[0] == '#') /* "#" is a comment, read until next "#" and only
print to screen */
                {
                fscanf( fp , "%s" , st );
                while(st[0] != '#')
                        {
                        printf( "%s " , st );
                        fscanf( fp , "%s" , st );
                        }
                printf( "\n");
                }
```

```
        else
                {
                printf( "%s\n" , st );
                p = st ;

                while( *p != '\0' ) /* Null character "\0" denotes end of data
held in string st */
                        {
                        while( ! ( (inp(MCR) & CTS )
                                && (inp(LSR) & THRE ) ) ) ; /* Wait for clear to
send pulse to arrive, and Tx holding register empty */
                        outp( TB , *p++ ) ; /* send string */
                        }
                while( ! ( (inp(MCR) & CTS )
                        && (inp(LSR) & THRE ) ) ) ;
                outp( TB , '\r' ) ; /* send cr to end current data set */
                }
        }
}
```

CNC Machine Program.

```
N5 G4 B102
N10 G4 (0)10 *@R* B101
N15 G4 (0)#10
N20 G4 (0)/-123001
N25 G4 M80
N30 G4 (0)/100
N35 G50 L#0
N40 G4 M71 B100
N45 G4 M3
N50 G4 (0)10 *@R* B5
N55 G4 (0)11 *@R*
N60 G4 (0)12 *@R*
N65 G4 (0)13 *@R*
N70 G50 L#10
N75 G00 X#11 Y#12 Z#13 B11
N80 G50 L5
N85 G01 X#11 Y#12 Z#13 F150 B22
N90 G50 L5
N95 G00 X#11 Y#12 Z#13 B33 M2
```

Clear Buffer (Wait for 123001).

Set metric units (mm) then

start tool.

Read control then x,y,z from RS232

read x into variable 11

read y into variable 12

read z into variable 13

Jump to relevant subroutine.

11: Rapid traverse to x,y,z then

return to B5 (N50).

22: Machine to x,y,z at of 150 mm/min then

return to B5.

33: Rapid traverse to x,y,z then stop!

Control
11 Rapid
22 Machine
33 End

Serial Cable Pin Connections.

9 Pin Female D Type	25 Pin Male D Type
2	3
3	2
5	7
8	4

Example CNC File.

```
# Draw test pattern #
# Magic number 123001 starts CNC cycle #
123001
# Rapid Traverse from centre to 45 degrees at 10mm height #
11      0.000      0.000      10.000
11      17.678     17.678     10.000
# Machine a 50 mm diameter circle, anticlockwise #
22      17.678     17.678     0.000
22      21.651     12.500     0.000
22      24.148     6.470      0.000
22      25.000     0.000      0.000
22      24.148     -6.470     0.000
22      21.651     -12.500    0.000
22      17.678     -17.678    0.000
22      12.500     -21.651    0.000
22      6.470      -24.148    0.000
22      0.000      -25.000    0.000
22      -6.470     -24.148    0.000
22      -12.500    -21.651    0.000
22      -17.678    -17.678    0.000
22      -21.651    -12.500    0.000
22      -24.148    -6.470     0.000
22      -25.000    0.000      0.000
22      -24.148    6.470      0.000
22      -21.651    12.500     0.000
22      -17.678    17.678     0.000
22      -12.500    21.651     0.000
22      -6.470     24.148     0.000
22      0.000      25.000     0.000
```

```
22      6.470     24.148    0.000

22      12.500    21.651    0.000

22      17.678    17.678    0.000

# Finished circle so lift pen. #

11      17.678    17.678    10.000

# Rapid Traverse to centre then stop CNC machine! #

33      0.000     0.000     10.000
```

References/Bibliography.

Arts T, 'Effects of Tip Endwall Contouring on the Three-Dimensional Flow-Field in an Annular Turbine Nozzle Guide Vane: Part 2 - Numerical Investigation', Journal of Engineering for Gas Turbines and Power Vol. 108, 1986, pp426-428

Atkins M J, 'Secondary Losses and Endwall Profiling in a Turbine Cascade', Proceedings of the IMechE, Paper C255/87, 1987, pp29-42

Bellhouse B J, Schultz D L, 'Determination of Mean and Dynamic Skin Friction, Separation and Transition in Low-Speed Flow with a Thin-Film Heated Element', Journal of Fluid Mechanics Vol. 24 part 2, 1966, pp379-400

Bellhouse B J, Schultz D L, 'The Measurement of Fluctuating Skin Friction in Air with Heated Thin-Film Gauges', Journal of Fluid Mechanics Vol. 32 part 5, 1968, pp 675-680

Biesinger, T e, 'Secondary Flow Reduction Techniques in Linear Turbine Cascades', PhD Thesis, University of Durham, 1993

Boletis E, 'Effects of Tip Endwall Contouring on the Three Dimensional Flow-Field in an Annular Turbine Nozzle Guide Vane: Part 1 - Experimental Investigation', Journal of Engineering for Gas Turbines and Power Vol. 107, 1985, pp983-990

Bonnett P, Jones T V, McDonnell D G, 'Shear-Stress Measurement in Aerodynamic Testing Using Cholesteric Liquid Crystals', Liquid Crystals Vol. 6 No. 3, 1989, pp271-280

Cook W J, 'Response of Hot Element Wall Shear Stress Gages in Unsteady Turbulent Flows', AIAA Journal Vol. 32, No. 7, 1994, pp1464-1471

Debruge L L, 'The Aerodynamic Significance of Fillet Geometry in Turbocompressor Blade Rows', ASME Paper 80-GT-41, 1980

Deich M E, Fillipov G A, Lazarev L Ya, 'Atlas of Axial Turbine Blade Characteristics. Part 1: Method of Profiling and the Aerodynamic Characteristics of Cascades', CEGB Info Services, CE Trans. 4563, 1965 (Original: Mashinostroenie Publishing House, Moscow 1965)

Deich M E, Zaryankin A E, Filippov G A, Zatsepin M F, 'Method of Increasing the Efficiency of Turbine Stages With Short Blades', AEI (Manchester) Ltd, Translation No 2816 (Original: Teploenergetika No2, Feb. 1960, p.18-24), 1960

Denton J D, 'Loss Mechanisms in Turbomachines', Journal of Turbomachinery Vol.115, 1993, pp621-656

Devenport W J, Agarwal N K, Dewitz M B, Simpson R L, Poddar K, 'Effects of a Fillet on the Flow Past a Wing-Body Junction', AIAA Journal Vol. 28 No. 12, 1990, pp2017-2024

Dominy R G, Hodson H P, 'An Investigation of Factors Influencing the Calibration of 5-Hole Probes for 3-D Flow Measurements', ASME, 92-GT-216, 1992

Ewen J S, Huber F W, Mitchell J P, 'Investigation of the Aerodynamic Performance of Small Axial Turbines', Journal of Engineering for Power, 1973, pp326-332

Gregory-Smith D G, 'Calculations of the Secondary Flow in a Turbine Cascade', Draft Paper

Gregory-Smith D G, 'Secondary Flows and Losses in Axial Flow Turbines', Journal of Engineering for Power Vol. 104, 1982, pp819-822

Haas J E, 'Analytical and Experimental Investigation of Stator Endwall Contouring in a Small Axial-Flow Turbine. 1: Stator Performance', NASA TP-2023, 1982

Han Wanjin, Wang Zhongqi, Tan Chunqing, Shi Hong, Zhou Mochun, 'Effects of Leaning and Curving of Blades With High Turning Angles on the Aerodynamic Characteristics of Turbine Rectangular Cascades', Journal of Turbomachinery Vol.116, 1994, pp417-424

Harrison S, 'Secondary Loss Generation in a Linear Cascade of High-Turning Turbine Blades', ASME Paper 89-GT-47, 1989

Harrison S, 'The Influence of Blade Lean on Turbine Losses', ASME Paper 90-GT-55, 1990

Hodson H P, 'Boundary-Layer Transition and Separation Near the Leading Edge of a High-Speed Turbine Blade', Journal of Engineering for Gas Turbines and Power Vol. 107, 1985, pp127-134

Hodson H P, Huntsman I, Steele A B, 'An Investigation of Boundary Layer Development in a Multi-Stage LP Turbine', Journal of Turbomachinery Vol.116, 1994, pp375-383

Horton G C, 'The Effects of Profiled Endwalls on the Secondary Flows Within a Turbine Nozzle Guide Vane Row: Part 1 - A Theoretical Investigation', Royal Aircraft Establishment Technical Memo P1027, 1984

Joslyn D, Dring R, 'Three Dimensional Flow in an Axial Turbine: Part 1 - Aerodynamic Mechanisms', Journal of Turbomachinery Vol.114, 1992, pp61-70

Joslyn D, Dring R, 'Three Dimensional Flow in an Axial Turbine: Part 1 - Profile Attenuation', Journal of Turbomachinery Vol.114, 1992, pp71-78

Klein A, 'Untersuchungen Über den Einfluss der Zuström-grenzschicht auf die Sekundärströmung in den Beschaufelungen von Axialturbinen', Forsch. Ing., Bd 32, Nr 6, 1966; (English Translation" 'Investigation of the Entry Boundary Layer on the Secondary Flows in the Blading of Axial Turbines', BHRA T 1004, 1966

Langston L S, 'Crossflows in a Turbine Cascade Passage', ASME Journal of Engineering for Power Vol.102, No. 4, Oct. 1980, pp866-874

Kopper F C, Milano R, Vanco M, 'Experimental Investigation of Endwall Profiling in a Turbine Vane Cascade', AIAA Journal Vol. 19 No. 8, 1981, pp1033-1040

Lewis R I, Hill J M, 'The Influence of Sweep and Dihedral in Turbomachinery Blade Rows', Journal of Mechanical Engineering Science Vol. 13 No. 4, 1971, pp266-285

Marchal P, Sieverding C H, 'Secondary Flows Within Turbomachinery Bladings', AGARD-CP-214 Paper No. 11, 1977

Massey B S, 'Mechanics of Fluids', 6th Edition, VanNostrand Reinhold, 1989, pp238-239

Mayle R E, 'The Role of Laminar-Turbulent Transition in Gas Turbine Engines', ASME Paper 91-GT-261, 1991

Moore H, 'Experiments in a Turbine Cascade for the Validation of Turbulence and Transition Models', PhD First Year Report, University of Durham , 1993

Moore H, 'Experiments in a Turbine Cascade for the Validation of Turbulence and Transition Models', PhD Progress Reports, University of Durham, 1993 - 1995

Moore H, 'Experiments in a Turbine Cascade for the Validation of Turbulence and Transition Models', PhD Thesis, University of Durham, 1995

Moore J, Moore JG, 'Performance Evaluation of Linear Turbine Cascades Using Three-Dimensional Viscous Flow Calculations', Journal of Engineering for Gas Turbines and Power, Vol 107, 1985, pp 969

Morris A W H, Hoare R G, 'Secondary Loss Measurements in a Cascade of Turbine Blades with Meridional Wall Profiling', 75-WA/GT-13, 1975

Moustapha S H, 'Investigation of the Effect of Two Endwall Contours on the Performance of an Annular Nozzle Cascade', AIAA Paper 85-1218, 1985

Moustapha S H, Paron G J, Wade J H T, 'Secondary Flows in Cascades of Highly Loaded Turbine Blades', Journal of Engineering for Gas Turbines and Power Vol. 107, 1985, pp1031-1038

Rose M G, 'Non Axisymmetric Endwall Profiling in the HP NGV's of an Axial Flow Gas Turbine', ASME Paper 94-GT-249, 1994

Schneider S P, 'Improved Methods for Measuring Laminar-Turbulent Intermittency in Boundary Layers', Experiments in Fluids 18, 1995, pp370-375

Sieverding C H, 'Recent Progress in the Understanding of Basic Aspects of Secondary Flows in Turbine Blade Passages', Journal of Engineering for Gas Turbines and Power Vol. 107, 1985, pp248-257

Sieverding C H, 'Reduction of Secondary Losses in Turbines', Von Karmen Institute for Fluid Dynamics Coursenote 95, 1975

Tall W A, 'Understanding Turbine Secondary Flow', AGARD-CP-214, 1977

Topunov A M, Nikolaev N I, 'Increasing the Operating Economy of HP Steam Turbine Stages', Izv Vozov Seriya Energetika, Translation 20972, 1975, pp57-62

Walker G J, Solomon W J, 'Turbulent Intermittency Measurement on an Axial Compressor Blade', 11th Australasian Fluid Mechanics Conference, University of Tasmania, Hobart, Australia, 1992, pp 1277-1281

Wright T, Simmons W E, 'Blade Sweep for Low-Speed Axial Fans', Journal of Turbomachinery Vol.112, 1990, pp151-158